The University of Nottingham

UNITED KINGDOM · CHINA · MALAYSIA

AIDING TAKE-OFF AND REDUCING CIVIL AIRCRAFT WEIGHT USING THE ELECTROMAGNETIC CATAPULT

LUCA BERTOLA, MENG.

Thesis submitted to the University of Nottingham
for the degree of Doctor of Philosophy

July 2017

Abstract

The engine size of modern aircraft is principally determined by take-off conditions, since initial acceleration requires the maximum engine power. An Electromagnetic Launch (EML) system could provide some or all of the energy required during the take-off phase of the flight so that the engine power requirement and fuel use could be significantly reduced. EML also has the potential of reducing the required runway length by increasing aircraft acceleration. Expensive airport extensions to face constant air traffic growth might then be avoided by allowing large aircraft to operate from short runways at small airports. The proposed system has positive impacts on total aircraft noise and exhaust emissions near airports and improves overall aircraft efficiency through reducing engine design constraints.

So far, EML for aircraft has been adopted only for military applications to replace steam catapults on the deck of aircraft carriers. This thesis considers the feasibility of different technologies for EML systems to assist civil aircraft take-off. The research develops, models, designs and compares three possible linear motor topologies which may be used to propel an A320-200 sized aircraft up to the take-off speed. The theories exploited to design the motors are thoroughly explained while the comparison of the performance is made on results from both analytical and finite element analysis (FEA).

The work is validated using a small experimental setup to launch a UAV weighing 4.5 kg. The electromagnetic analysis developed for civil aircraft launchers has been employed to size the scaled down motors and the methods proposed to design all the other components of the test rig are also presented.

Acknowledgements

Firstly, I would like to express my sincere gratitude to my supervisors Prof. Pat Wheeler and Dr. Tom Cox for the continuous support of my Ph.D study and related research, for their suggestions, motivations and contributions. Their guidance helped me throughout the whole research and their hard questions incented me to widen my research from various perspectives.

I would like to thank the rest of my supervisor committee: Prof. Seamus Garvey and Prof. Herve Morvan, for their insightful comments and encouragement.

My sincere thanks also goes to Dr. Fred Berg and Dr. Nicolas Fouquet, who provided me an opportunity to join Airbus Group Innovations as a research engineer, and who gave me access to laboratories and research facilities. Without they precious support it would not be easy to conduct the research about superconductors, cryogenic technology and cryocooler for aerospace applications.

This research was possible for the funding from the People Programme (Marie Curie Actions) of the European Union's Seventh Framework Programme (FP7/2007-2013) under REA grant agreement no 608322.

I am grateful to all the INNOVATE members for the stimulating discussions, for all the time we worked together before deadlines, and for all the fun we had in the last three years.

Thanks to the technicians who helped me during my experimental work and offered their time to contribute to the rig assembling.

My parents and my sisters deserve a substantial share of the credit for everything I have done. Thanks to my family for supporting me spiritually throughout my research experience and my life in general.

Last but not the least, an heartfelt thanks goes to my girlfriend for her patience, her support in difficult situations and her love.

List of Publications

Conference Papers

L. Bertola, T. Cox, P. Wheeler, S. Garvey and H. Morvan, "Civil application of electromagnetic aircraft launch system" in *LDIA*, Aachen, Germany 2015

F. Berg, J. Palmer, L. Bertola, P. Miller and G. Dodds, "Cryogenic system options for a superconducting aircraft propulsion system" in *IOP Conference Series: Materials Science and Engineering*, Vol. 101, No. 1, IOP Publishing, Tucson, USA 2015

L. Bertola, T. Cox, P. Wheeler and S. Garvey, "Superconducting and conventional electromagnetic launch system for civil aircraft assisted take-off" in *IEEE Energy Conversion Congress and Expo*, Milwaukee, USA 2016

L. Bertola, T. Cox, P. Wheeler, S. Garvey and H. Morvan, "Design study and scaled experiment of induction and synchronous motors for civil applications of electromagnetic aircraft launch system" in *18th Electromagnetic Launch Technology Symposium*, Wuhan, China, 2016

Journal Papers

L. Bertola, T. Cox, P. Wheeler, S. Garvey and H. Morvan, "Electromagnetic launch systems for civil aircraft assisted take-off", *Archives of Electrical Engineering*, Vol. 64, n. 4, pp. 543-554, 2015

L. Bertola, T. Cox, P. Wheeler, S. Garvey and H. Morvan, "Superconducting

electromagnetic launch system for civil aircraft", *IEEE Transactions on Applied Superconductivity*, Vol. 26, n. 8, pp. 1-11, 2016

L. Bertola, T. Cox, P. Wheeler, S. Garvey and H. Morvan, "Reducing weight and fuel consumption of civil aircraft by EML", *International Journal of Mechanical, Aerospace, Industrial, Mechatronic and Manufacturing Engineering*, Vol. 11, n. 2, pp. 225-229, 2017

L. Bertola, T. Cox, P. Wheeler, S. Garvey and H. Morvan, "Thermal design of linear induction and synchronous motors for electromagnetic launch of civil aircraft", *IEEE Transactions on Plasma Science*, Vol. 45, n. 6, pp. 1-8, 2017

Journal Paper under Revision

L. Bertola, T. Cox, P. Wheeler, S. Garvey and H. Morvan, "Reducing aircraft weight and take-off length using electromagnetic launch system for civil applications", submitted to *Aerospace Science and Technology*

Contents

Abstract i

Acknowledgements iii

List of Publications v

List of Tables xi

List of Figures xiii

Glossary of Symbols xxi

Acronyms xxxv

1 Introduction 1

1.1 Motivations 1

1.2 Research Outline 5

1.3 Thesis Structure 6

2 Literature Review 9

2.1 Research Background on Aircraft Launchers 10

2.1.1 Asynchronous Launcher 10

2.1.2 Synchronous Launcher 18

2.1.3 MAGLEV and Superconducting Launcher 24

2.2 Research Background on Railguns 26

2.2.1 Railgun Performance Improvement 27

2.2.2 Sliding Interface Phenomena in Railguns 32

2.3 Railgun for Civil EML Applications 34
2.4 Conclusion 39

3 Take-off Segment Analysis 41
3.1 Definition of Take-Off Speeds and Distances 42
3.2 Take-off Performance Analysis 46
3.2.1 Climb Out Gradient 46
3.2.2 Take-off Speeds and Distances 55
3.2.3 Take-off Time and Fuel Consumption 62
3.3 Take-off Analysis Outcomes 66
3.3.1 Flight Performance and Fuel Consumption Reduction . . . 66
3.3.2 Runway Length Reduction 71
3.3.3 Catapult Requirements 73
3.3.4 Noise and Exhaust Emission Reduction 76
3.3.5 Engine Size Reduction 78
3.4 Contribution to Knowledge 81

4 Linear Induction Motor 83
4.1 Introduction to LIM for EML 83
4.1.1 LIM Topology Selection 84
4.2 Circuit Theory, Field Theory and Goodness Criterion 87
4.2.1 The Goodness Factor G 90
4.2.2 Field Theory and Special LIM Phenomena 93
4.3 LIM Electromagnetic Design 115
4.3.1 Parametric Optimization Algorithm for LIM 115
4.3.2 Parametric Optimization Results 125
4.3.3 Transient Equivalent Circuit Model, FEM Analysis 133
4.4 LIM's Mover Structural Analysis 138
4.5 LIM Thermal Analysis 146
4.5.1 Thermal Analysis of the Primary Windings 147
4.5.2 Heat Transfer Problem Solution for the Moving Plate . . . 152
4.6 Contribution to Knowledge 164

5 Linear Permanent Magnet Synchronous Motor 165
5.1 Introduction to LPMSM for EML 166
5.1.1 Topology Selection for the Synchronous Motor 167
5.2 Winding Selection 171
5.2.1 Stator Winding Layout 171
5.2.2 Winding Factor 174
5.2.3 Winding Sequence 182
5.3 LPMSM Electromagnetic Design 185
5.3.1 Parametric Optimization Algorithm for LPMSM 186
5.3.2 Parametric Optimization Outcomes 197
5.4 Multi-Layer Theory 204
5.5 Transient Electromagnetic Model 216
5.6 Thermal Analysis 222
5.6.1 Thermal Analysis of the Mover's Yoke 222
5.6.2 Thermal Analysis of the Magnets 225
5.7 Contribution to Knowledge 228

6 Experimental Validation 231
6.1 Test Rig Description 232
6.2 Definition of Prototype Requirements 233
6.3 Prototype Electromagnetic Design 236
6.4 Sizing of the Magnetic Brake 240
6.4.1 Safety Springs and Maximum Mover End-Speed 240
6.4.2 Electromagnetic Analysis of the Magnetic Brake 242
6.5 Structural Design of the Stator Housing 246
6.5.1 Description of Structural Components and Loads 246
6.5.2 Results of the Structural Analysis of the Frame 250
6.5.3 Structural Analysis of the Brake Framework 252
6.6 Prototype Thermal Analysis 253
6.7 Experimental Results 256
6.7.1 Test of LIM 256
6.7.2 Test of the Concentrated Winding Stator as a LIM 260
6.8 Contribution to Knowledge 263

7 Superconducting Linear Synchronous Motor 265
7.1 Introduction to SCLSM for EML 266
7.2 Definition of SCLSM Geometry 269
7.3 Electromagnetic Design of SCLSM 284
7.4 Losses in Superconductors 294
7.4.1 Eddy Current Losses 294
7.4.2 Coupling Losses 297
7.4.3 Hysteresis Losses 304
7.5 Static-Transient Model of Thermal Insulation 309
7.5.1 Static Heat Transfer Problem 313
7.5.2 Transient Heat Transfer Problem 316
7.6 Cryocoolers for Aerospace Applications 323
7.6.1 Recuperative Cooling 325
7.6.2 Cryocooler Performance 333
7.7 SCLSM Design Results 336
7.8 Contribution to Knowledge 342

8 Conclusion 343
8.1 Launcher Topology Comparison 344
8.2 EML Systems Limitations 348
8.3 Future Research 350
8.3.1 Linear Synchronous Motor with Halbach PM Array 350
8.3.2 SCLSM Configuration with Lower Cooling Power 351
8.3.3 Definition of the Electromagnetic Catapult Subsystems . . 352
8.3.4 Energy Recovery During Landing 355

Bibliography 357

List of Tables

2.1 EML system requirements for aircraft carriers 10
3.1 Average friction coefficients for different runway pavements [78] . 58
3.2 Take-off analysis outcomes for two possible mission scenarios . . 67
3.3 A320-200 take-off history comparison between engine-boosted take-off and electromagnetic launch 68
3.4 A320-200 flight data comparison between engine-boosted take-off and electromagnetic launch 69
3.5 A320-200 fuel consumption comparison between engine-boosted take-off and electromagnetic launch 70
3.6 A320-200 take-off performance comparison between engine-boosted take-off and electromagnetic launch 72
3.7 Take-off performance comparison in ISA+20 K condition at 3000 ft 74
3.8 Requirements of the EML system for civil aircraft 76
3.9 CFM56-5A1 engine exhaust emission data 77
3.10 Take-off and flight performance with reduce engine size and thrust 79
4.1 Winding arrangement of consecutive stators to limit longitudinal end-effects 114
4.2 Parametric optimization inputs and design variables for LIM . . . 116
4.3 Design variables ranges for the parametric optimization of LIM . . 126
4.4 Optimum values of the design variables after optimization 131
4.5 Geometrical features, circuit parameters and performances of LIM for EML 132
5.1 Fundamental harmonic winding factors for different combination of number of pole pairs and number of slots for a three phase machine [107] 179

5.2 Properties of pole-slot combinations for $N_s = 36$ 180
5.3 Basic binary series for several number of slots per pole per phase . 184
5.4 Repeatable winding sequence 185
5.5 Double-layer winding sequence for a 36 slots 28 pole fractional-slot LPMSM 185
5.6 Parametric optimization inputs and design variables for LPMSM . 187
5.7 Design variable ranges for the parametric optimization of LPMSM 197
5.8 Design variables selected through parametric optimization 204
5.9 Linear permanent magnet synchronous motor data 204
6.1 Aerodynamic characteristics of the UAV and small catapult requirements 237
6.2 Geometrical features, circuit parameters and performances of the LIM prototype 238
6.3 Geometrical features, circuit parameters and performances of the LPMSM prototype 238
6.4 Spring Data 241
6.5 Comparison between FEA and experimental performance 259
7.1 Coolant properties at atmospheric pressure 268
7.2 Geometrical characteristics of SCLSM 284
7.3 Comparison between electric variables computed over 1 or 5 coils 291
7.4 Thermal properties of the materials involved in the heat transfer problem model of insulation 312
7.5 Temperature distribution on the surfaces of the insulation model . 316
7.6 Comparison between efficiencies achieved by different cryocooler configurations 336
7.7 Efficiencies of double-stage cryocooler with different coolant as heat sink 339
7.8 SCLSM performance with different airgap lengths 340
8.1 Comparison between the electromagnetic performance of LIM, LPMSM and SCLSM with and without cryocooler 345

List of Figures

1.1 Axial acceleration limits for a healthy human being 2
1.2 Schematic of an EML system for civil aircraft 4
2.1 The single-sided induction motor called Electropult 11
2.2 Schematic of a multi-section double-sided LIM with constant pole pitch 12
2.3 Double-sided tubolar LIM for EML systems 14
2.4 Double-sided linear reluctance synchronous motor for EML systems 23
2.5 Diagram of the Yamanashi MAGLEV system 25
2.6 Schematic and working principle of a railgun 27
2.7 Schematic of the monolithic C-type armature 29
2.8 Schematic of augmented railgun (A) and of the multi-turn railgun (B) 31
2.9 Time variation of current and efficiency of a conventional railgun . 38
3.1 Take-off procedure and parameters for a twin-engine civil transport aircraft 42
3.2 Low speed lift polar of an A320-200 aircraft for several flap deflections [73] 44
3.3 MTO thrust rating for several Mach number in ISA+0K conditions for the two CFM56-5-A1 engines installed on A320-200 aircraft [73] 49
3.4 Comparison between thrust profiles of CFM56-5-A1 MTO rating at ISA+0K and ISA+20K [73] 50
3.5 Low speed drag polar with landing gear retracted for an A320-200 aircraft [73] 52
3.6 Experimental data for trim drag estimation [77] 53

3.7 Low speed drag polar with landing gear extended for an A320-200 aircraft [73] . . . 56
3.8 Fuel flow across CFM56-A1 engines for several Mach and ISA conditions [73] . . . 63
3.9 High speed drag polar for an A320 aircraft flying at 950 ft [73] . . . 66
3.10 Required thrust during aircraft acceleration and respective thrust components . . . 75
4.1 Derivation of LIM from rotary counterpart . . . 85
4.2 Linear induction motor topologies . . . 86
4.3 Equivalent circuit of induction machines . . . 88
4.4 Variation of the force of induction motor with the slip frequency . . . 90
4.5 Section of a single-sided linear induction motor . . . 92
4.6 Airgap fringing in a double-sided induction motor . . . 94
4.7 Primary key dimensions of a single-sided LIM . . . 98
4.8 Current density and field distribution on a secondary plate . . . 100
4.9 Representation of the flux wave in the airgap . . . 101
4.10 Double-sided LIM cross section . . . 102
4.11 Structure of the LIM mover . . . 118
4.12 End coil schematic . . . 122
4.13 Parametric optimization results . . . 127
4.14 Peak DC Voltage at the end of the launch . . . 128
4.15 Magnetic field density in the stator teeth in the hypothesis of non-linear permeability . . . 131
4.16 Induction motor equivalent circuit for transient analysis . . . 134
4.17 Comparison between thrusts calculated by FEA, transient model and parametric analysis of LIM . . . 136
4.18 Comparison between electromagnetic performances of LIM computed by FEA, transient model and parametric analysis . . . 138
4.19 Deformation and strain field of the aluminium plate under load . . . 142
4.20 Stress distribution on the aluminium plate under rated load . . . 142
4.21 Buckling factor variation with the plate thickness . . . 143
4.22 Buckling factor variation with the LIM's pole pitch and the respective mover length and width . . . 145

4.23 Buckling factor variation with the width of the LIM's active area and the respective mover width 145
4.24 Plate deformation under the buckling load 146
4.25 Effect of current density on active and reactive power 147
4.26 Temperature rise in the stator windings after the time t_1 with several current densities 149
4.27 Temperature evolution of the first stage coils after the power supply is disconnected 151
4.28 Current density profile computed by FEA at different time step during the launch 153
4.29 Thermal equilibrium of an infinitesimal volume of aluminium . . 154
4.30 Possible node configurations on the mover boundary 157
4.31 Variation of the convective heat transfer coefficient with the mover speed until the take-off point 160
4.32 Variation of the secondary Joule losses during the launch 161
4.33 Temperature profile over the mover lateral surface at different time steps 163
5.1 Double-sided LPMSM with conventional PMs array (A), with conventional buried PMs array (B) and with Halbach array (C) . . 169
5.2 Double-sided LPMSM with slot-less armature (A), and double-sided air core LPMSM with slot-less internal armature (B) 170
5.3 MMF intensity of the first 50 harmonics for a 36 slot machine with 30 and 34 poles respectively 181
5.4 MMF intensity of the first 50 harmonics for a 36 slot machine with 28 and 32 poles respectively 182
5.5 Mover of LPMSMs for electromagnetic launch application 188
5.6 Schematic of concentrated windings end-coil 195
5.7 Percentage variation of the input power with respect to its mean value 198
5.8 Amplitude of the supplied voltage at the end of the launch 199
5.9 Variation of the magnetic field density in the stator teeth for several combinations of the design variables 200

5.10 Percentage variation of the input power as a function of the last design variables . . . 201
5.11 Variation of the magnet thickness with respect to the magnetic flux density in the airgap . . . 203
5.12 Structural simplification of the MLT applied to a double-sided LPMSM . . . 205
5.13 Multi-layered structure of a double-sided LPMSM with regions and current sheets considered by MLT . . . 207
5.14 Magnetic field over a single pole pair computed by the Multi-Layer Theory . . . 212
5.15 Sketch of the slot model and of the respective frame of reference considered by the permeance function . . . 213
5.16 Magnetic flux density along the y-axis computed by the MLT and corrected with the relative permeance function of the stator slotted structure . . . 215
5.17 Time evolution of dq voltage and first phase voltage during the launch . . . 218
5.18 Comparison between thrust profiles computed using different methods . . . 220
5.19 Comparison between efficiency profiles computed using different methods . . . 221
5.20 Comparison between power factor profiles computed using different methods . . . 221
5.21 Transient variation of the Joule losses in the mover's yoke . . . 224
5.22 Interpolation of the experimental data to estimate the ratio between 2D and 3D resistivities . . . 226
5.23 Transient variation of the Joule losses in a PM segment . . . 228
6.1 Electromagnetic launcher prototype for UAVs . . . 233
6.2 Reference aircraft for the catapult prototype . . . 234
6.3 Aerodynamic drag and lift coefficients of NACA2312 airfoil . . . 235
6.4 Pictures of LIM's and LSM's stator sides taken when they were disassembled and mounted on the frame . . . 239
6.5 Location of the safety springs after the magnetic brake housing . . . 241

6.6 Magnetic brake structure 243
6.7 Comparison between the LIM's mover deceleration computed by the analytical and FEA model 245
6.8 Technical drawing of the laminated structure of LIM's and LPMSM's stators 246
6.9 Schematic of load distribution and constraints location on the stators simplified structure 247
6.10 Variation of the normal force acting in LIM and LPMSM stators during the launch 248
6.11 Technical drawing of LIM stator connected to the frame structure . 249
6.12 Deformation of LIM's stator and C-shape connectors under the maximum load 250
6.13 Deformation of U-shape plates under the maximum load 251
6.14 Deformation of all the components of the electromagnetic brake's structure 253
6.15 Temperature distribution over the surface of the aluminium plate at the end of the launch 254
6.16 3D view of the active and passive regions of the mover of the induction motor 255
6.17 Temperature distribution on the surface of aluminium as it comes to a standstill 256
6.18 Induction motor voltage, current and frequency profiles measured by the AC drive 257
6.19 Comparison between synchronous speed, measured speed and speed computed by the FEA software 259
6.20 Motor voltage, current and frequency profiles measured by the AC drive 260
6.21 Comparison between speed and thrust achieved by LIM with concentrated and distributed windings 261
6.22 Comparison between input and output power of LIM with concentrated and distributed windings 262
6.23 Comparison between efficiency and power factor of LIM and LSM 263

7.1 Section of a double-sided SCLSM stator with a four poles mover anchored to the guidance system 267
7.2 Critical current density variation with the magnetic flux density at 20 K 270
7.3 Cross section of a MgB_2 wire implemented in the EML system . . 271
7.4 Inner structure of superconducting cables adopted for the launcher 272
7.5 Simplified structure of the 132-kA superconducting cable 273
7.6 Magnetic field density on the superconducting cable cross section generated by a current density of 1750 A/mm^2 274
7.7 Magnetic field density on the superconducting cable cross section generated by a current density of 583 A/mm^2 274
7.8 Section of a superconducting cable used to reinforce the magnetic field 276
7.9 Section of the cryostat of the SCLSM's mover 276
7.10 Magnetic flux density generated by the superconducting cables over the cryostat cross section 277
7.11 Pattern followed by the bundle of superconducting cables inside the cryostat of a 4 poles SCLSM with the respective end-coil configuration 279
7.12 Top view of the cryostat of a 4 poles SCLSM 280
7.13 Section of the cryostat in proximity to the end-coils 282
7.14 Superconducting filaments considered during the integration of the Biot-Savart law with the respective tilted frame of reference . . 285
7.15 Magnetic flux density components generated by a 3-kA wire carrying 1000 A at a distance of 5 cm 288
7.16 Comparison between excitation field and ideal sinusoidal wave with the difference between magnetic fields 289
7.17 Magnetic flux density produced by a single SC over 5 neighbour stator coils 291
7.18 Schematic of the multi-layered structure and MMF harmonics amplitude used by the MLT to reconstruct the magnetic field generated by the secondary harmonics 293

7.19 Eddy current loss in all the superconducting wires and in the aluminium vessel during aircraft acceleration 297
7.20 Geometrical features of the first helix used to compute the wire inductances 299
7.21 Variation of self and mutual inductances with the helix pitch angle 303
7.22 Coupling loss in the superconducting wires during aircraft acceleration 304
7.23 Schematics of the current density distribution over the wire cross section in case of weak penetration and full penetration 306
7.24 Time variation of the hysteresis loss during the launch 308
7.25 Superconducting coil and insulation structure of MAGLEV trains 310
7.26 Schematic of the layered structure of the thermal insulation used for the 1D heat transfer model 311
7.27 Variation of temperature and heat flow across the insulation components without internal heat generation 319
7.28 Temperature evolution of thermal insulation components and cryogenic coolant during the launch 320
7.29 Double-stage reverse-Brayton cryocooler for aerospace application 324
7.30 T-P chart for the coolant in the cryocooler second stage 325
7.31 T-P chart of the second stage compression side with intercooler . . 326
7.32 Specific input power variation with the pressure ratio between compression stages and with the intercooler temperature delta . . 328
7.33 Schematic of the double-stage RBC interface 329
7.34 T_{7a} and T_{3b} temperatures variations with the pressure ration between compression stages and with the intercooler temperature delta 330
7.35 Schematic of the double-stage RBC interface with parallel-connected heat exchangers 331
7.36 Schematic of the double-stage RBC with regenerative cooling and parallel connected heat exchangers 334
7.37 Temperature-pressure chart of the double-stage RBC with regenerative cooling and parallel connected heat exchangers 335
7.38 Comparison between SCLSM efficiency and the efficiencies of an EML system including RBC's input power 341

8.1 Schematic of the structure of LIM's, LPMSM's and SCLSM's movers 346
8.2 Variation of the normal force acting on the stator side of LIM and LPMSM during the launch 355

Glossary of Symbols

a	LIM stator half width
a_e	LIM active area half width
$\overline{a}_{mov}$	Average acceleration while the mover returns to its initial position
$\overline{a}_{stop}$	Average aircraft deceleration using brakes
a_{TO}	Rated acceleration during UAV take-off
$\overline{a}_1$	Average aircraft acceleration using engines
a_1	Instantaneous acceleration on the runway
A	Any area involved in the heat transfer across thermal insulation
AC_{loss}	Total AC losses in the superconductors
A_{cryo}	Cryostat surface
A_e	Electric circuit area
A_m	Magnetic circuit area
A_{mov}	Area of the mover
A_{PM}	Equivalent permanent magnet current sheet
AR	Aircraft wing aspect ratio
A_s	Slot area
A_{sc}	Area of the superconducting material in each wire
A_{st}	Equivalent stator current sheet
A_ν	Equivalent stator current sheet for the ν^{th} harmonic
A_w	Wire cross section area
α_{Al}	Aluminium thermal diffusivity
α_G	Angle of attack at ground level
α_{LOF}	Angle of attack at lift-off
α_m	Twisting angle of superconducting cables
α_{ph}	Angle between consecutive phasors
$\alpha_{ph\nu}$	Angle between consecutive phasors of the ν^{th} harmonic
α_s	Electrical angle between consecutive slots
α_{TO}	Angle of attack at UAV take-off
b	Half width of a superconducting coil
b_s	Slot opening and slot width
b_t	Stator tooth width
$\vec{B}$	Magnetic flux density vector
B	Magnetic flux density

B_α	Magnetic flux density in the tilted frame of reference
B_{es}	Peak-to-peak amplitude of the orthogonal magnetic flux density
B_g	Magnetic flux density in the airgap
B_{ir}	Magnetic flux density in the stator back iron
B_r	Permanent magnet remnant flux density
B_t	Magnetic flux density in the stator teeth
$B_{w\nu}$	Flux density perpendicular to wire cross section of ν^{th} harmonic
B_y	Y-component of the magnetic flux density (orthogonal to the airgap)
$B_{y_{DS}}$	Y-component of the magnetic flux density in double-sided motor
B_{yl}	Y-component of the magnetic flux density with no excitation field
$B_{y\,MLT}$	Y-component of the magnetic flux density computed by MLT
$B_{y_{SS}}$	Y-component of the magnetic flux density in single-sided motor
β_{Air}	Expansion factor of air
β_{LH_2}	Expansion factor of liquid hydrogen
$\beta(y)$	Permeance function of conformal transformation
c	Mover half width including overhangs in Chapter 4
c	Number of coils per phase in Chapter 5
c_{air}	Speed of sound of air
c_{Air}	Specific heat at constant pressure of dry air
c_{Al}	Aluminium thermal capacity
c_{Co}	Copper thermal capacity
c_{Fe}	Stainless steel thermal capacity
c_{PM}	NdFeB permanent magnets thermal capacity
c_{GH_2}	Specific heat capacity of gaseous hydrogen
c_{H_2}	Specific heat capacity of hydrogen
c_{LH_2}	Specific heat capacity of liquid hydrogen
$\cos\phi$	Power factor
$c_{p_{He}}$	Specific heat at constant pressure of helium
C_D	Drag coefficient
C_{D_C}	Drag coefficient during cruise
C_{DHS}	High speed drag coefficient
C_{Di}	Induced drag coefficient
C_{DLS}	Low speed drag coefficient
C_{DTrim}	Rudder trim drag coefficient
C_{D2}	Drag coefficient at V_2
C_L	Lift coefficient
C_{LHS}	High speed lift coefficient
C_{LLOF}	Lift coefficient at V_{LOF}
C_{LLS}	Low speed lift coefficient
C_{Lmax}	Maximum lift coefficient
C_{L2}	Lift coefficient at V_2
d	Thickness of an insulation layer
d_{Al}	Aluminium mover thickness

d_{Alf}	Thickness of the aluminium sheets
d_{Al1}	Thickness of the outer vessel
d_{Al2}	Thickness of the inner vessel
d_{eng}	Distance between the engine and the aircaft barycentre
d_{FinAC}	Distance between fin and wing aerodynamic centres
d_{H_2}	Thickness of the liquid hydrogen layer
d_{ij}	Distance between the superconducting wires i and j
d_{ins}	Thickness of the insulation layer
d_g	Grooves diameter
d_q	Denominator of slot per pole per phase
d_r	Distance between railgun rails
$\vec{ds}$	Infinitesimal displacement vector
d_{sc}	Distance between consecutive cryostat sections
dv	Infinitesimal volume of material
d_{Vac1}	Thickness of the first vacuum layer
d_{Vac2}	Thickness of the second vacuum layer
d_w	Wire diameter
D	Aerodynamic drag
D_{cc1}	Diameter of the cooling channel 1 in Fig. 7.9
D_{cc2}	Diameter of the cooling channel 2 in Fig. 7.9
D_{cc3}	Diameter of the cooling channel 3 in Fig. 7.9
D_{fil}	Diameter of a superconducting filament
D_{Trim}	Rudder trim drag
D_{WML}	Windimilling drag
D_w	Diameter of superconducting wire
$D_{0.75kA}$	Diameter of a 0.75-kA cable
D_{132kA}	Diameter of a 132-kA cable
D_2	Aerodynamic drag at V_2
D_{3kA}	Diameter of a 3-kA cable
δ	Penetration depth
δ_{Al}	Aluminium penetration depth
δ_{ph}	Number of slots between two adjacent phasors
Δp	Pressure drop across heat exchangers
Δt	Pilot reaction time
Δt	Time step
Δs	Spring displacement at full compression
ΔS_{TO}	Distance travelled during the pilot reaction time
ΔT	Temperature variation
ΔT_c	Temperature drop across the cold heat exchanger
ΔT_i	Temperature difference between intercooler inlet and outlet
ΔT_{iHx}	Temperature drop across the intermediate heat exchanger
ΔT_{iHx2}	Second outlet-inlet temperature drop in parallel heat exchangers
ΔT_{PM}	Temperature variation in permanent magnets

ΔT_{wHx}	Temperature drop across the hot heat exchanger
ΔT_{yoke}	Temperature variation in the LPMSM mover's yoke
$\Delta x, \Delta y, \Delta z$	Distances between nodes in the 3 directions of space
e	Oswald efficiency number
ε_i	Emissivity of the radiative surface i
ε_{Al}	Emissivity of aluminium
ε_{ins}	Emissivity of thermal insulator
$\overrightarrow{E}$	Electromagnetic field vector
E	Electromotive force
E_{AC}	AC losses while the mover returns to its initial position
E_{A320}	Energy transferred to the aircraft and mover during the launch
E_c	Induced voltage per turn
E_F	Energy variation due to a force
E_{H_2}	Energy absorbed by the liquid hydrogen
E_i	Energy stored in the magnetic field generated by induced currents
E_l	Induced voltage with no excitation field
E_L	Energy stored in an inductor
E_m	Sum of the magnitudes of the EMF phasors
E_{mov}	Energy required to take the mover to its initial position
E_r	Vectorial resultant of the EMF phasors
E_s	No-load voltage induced in the stator coils
E_{tot}	Maximum energy that can be absorbed by liquid hydrogen
E_v	Energy stored in the magnetic field inside a solenoid
η	Efficiency
η_c	Compressor polytropic efficiency
η_C	Carnot efficiency
η_{RBC}	Cryocooler efficiency
η_t	Turbine polytropic efficiency
f	Frequency
f_{max}	Maximum frequency
f_r	Mover frequency
f_s	Synchronous frequency
f_{stress}	Expected thrust density
f_ν	Frequency of the ν^{th} harmonic
f_1	Primary frequency
$\vec{F}$	Force vector
F	Force
F_b	Braking force
F_B	Fuel burnt
F_{buck}	Buckling load
$F_€$	Fuel cost
F_F	Fuel flow
F_{Fr}	Friction force acting on the prototype mover

$F_{i\rightarrow j}$	Form factor between radiative surfaces i and j
F_{max}	Spring force at full compression
F_{mov}	Thrust required to accelerate the mover
F_p	Prototype thrust
F_x	Catapult thrust requirement
F_{xc}	Total catapult thrust
g	Airgap length
g_e	Equivalent airgap length
g_m	Mechanical airgap length
g_{md}	Geometric mean distance
G	Gravitational acceleration
G	Goodness factor in Section 4.2.1
G_e	Equivalent goodness factor
Gr	Grashof number
γ	Climb out gradient in Chapter 3
γ	Ratio between specific heats in Chapter 7
γ_{Air}	Isentropic expansion factor of air
γ_h	Harmonic leakage factor
γ_{LOF}	Climb out gradient at V_{LOF}
$\gamma_{LOF\,Req}$	Requirement on the climb out gradient at V_{LOF}
$\gamma_{1,2}$	Roots of characteristic equations
$\gamma_{1e,2e}$	Roots of the characteristic equation in the passive zones
γ_2	Climb out gradient at V_2
γ_{2Req}	Requirement on the climb out gradient at V_2
h	Altitude or convection coefficient
h_{Air}	Convection coefficient of air
h_f	Fin height
h_F	Fuselage height
h_{LH_2}	Convection coefficient of liquid hydrogen
h_m	Magnet thickness
h_r	Height of railgun rails
h_{ratio}	Square of the ratio between fin and fuselage heights
h_s	Slot height
h_{sc}	Cryostat height
h_{ss}	Slot tip height
h_t	Height related to the layered structure shown in Fig. 5.13
h_{TO}	Altitude at which the take-off procedure terminates
h_y	Stator back iron thickness
h_{ys}	Thickness of LPMSM mover's yoke
h_2	Safety screen altitude
$\vec{H}$	Magnetic field vector
H	Magnetic field
H_{c1}	First critical magnetic field of a superconductor

H_{c2}	Second critical magnetic field of Type-II superconductors
H_p	Magnetic field with full penetration
H_ν	External magnetic field due to the ν^{th} harmonic
H_{yentry}	Y-component of the magnetic field at the entry edge
H_{yexit}	Y-component of the magnetic field at the exit edge
H_0	Initial magnetic field in the airgap
$H^n_{2\%}$	Percentage of gaseous hydrogen at the n^{th} time step
I	Current
$\overrightarrow{I}$	Current vector
I_A	Supplied current first phase
I_B	Supplied current second phase
I_c	Critical current in a superconducting wire
I_C	Supplied current third phase
I_d	Direct current
I_m	Magnetizing current
I_q	Quadrature current
I_1	Primary current
I_2	Secondary current
I_{2T}	Maximum transport current of a superconducting wire at 2T
$\Im$	As operator it indicates the imaginary part of a complex number
$\vec{J}$	Current density vector
J	Current density
J_c	Superconductor critical current density
J_m	Amplitude of primary current sheet
J_1	Primary current density
J_2	Secondary current density
k	Conductivity of a material
k_{Al}	Aluminium thermal conductivity
k_{buck}	Buckling factor
k_{buckAl}	Buckling factor of aluminium
k_{buckFe}	Buckling factor of iron
k_c	Carter coefficient
k_{cr}	Creep coefficient
k_d	Distribution factor
$k_{d\nu}$	Distribution factor for the ν^{th} harmonic
k_{el}	Spring elastic constant
k_{es}	Eddy current loss constant
k_{Fg}	Fringing factor
k_{fill}	Fill factor
k_{gmd}	Geometric mean distance constant
k_{Hxa}	Ratio between heats transferred from the first RBC stage
k_{Hxb}	Ratio between heats transferred from the second RBC stage
k_{ins}	Thermal conductivity of the electrical insulation

k_{LOF}	Lift-off constant
k_p	Pitch factor
k_{pr}	Pressure ratio factor
$k_{p\nu}$	Pitch factor for the ν^{th} harmonic
k_{par}	Number of wires connected in parallel per turn
k_ρ	2D-3D power loss ratio
k_{skin}	Skin effect coefficient
k_{ss}	Saturation coefficient
k_{tr}	Transverse edge effect coefficient
k_{Tro}	Troposphere coefficient
k_w	Winding factor
$k_{w\nu}$	Winding factor for the ν^{th} harmonic
k_{yc}	Hysteresis loss constant
K_R	Resistance correction factor
K_X	Reactance correction factor
l	Half length of a superconducting coil
l_e	Length of the electric circuit
l_{cable}	Average length of the superconducting cables
l_{end}	End coil length
l_m	Length of the magnetic circuit in Section 4.2.1
l_m	Length of the permanent magnets
l_{mag}	Length of the area with a magnetic field
l_{mov}	Mover length
l_s	Stator width
l_w	Length of a twisted wire
λ_g	Relative airgap permeance
λ_{ld}	Differential permeance
λ_{le}	End winding permeance
λ_{lh}	Permeance associated with the secondary harmonics
λ_{ls}	Slot permeance
L	Inductance
$\overrightarrow{L}$	Inductance vector
L	Lift force in Chapter 3
L'	Inductance gradient
L_c/L_{ro}	C-type armature's root ratio
L_d	Direct inductance of LSM
L_{H_2}	Hydrogen latent heat
L_i	Self-inductance of a superconducting wire
L_l	Leakage inductance
L_{ld}	Differential leakage inductance
L_{le}	End winding leakage inductance
L_{lh}	Leakage inductance associated with the secondary harmonics
L_{long}	Longitudinal inductance

L_{ls}	Slot leakage inductance
L_{ltot}	Leakage inductance considering passive zones
L_{ph}	Inductance per turn per phase in SCLSM
L_q	Quadrature inductance of LSM
L_m	Magnetization inductance
L_{md}	Direct magnetization inductance of LSM
L_{mq}	Quadrature magnetization inductance of LSM
L_r	Railgun rail self-inductance
L_s	Resultant inductance per phase of SCLSM
L_{sc}	Length of the cryostat straight part
L_t/L_{ro}	C-type armature's C-type ratio
L_0	Spring length at rest
L_1	Primary leakage inductance
L_2	Secondary leakage inductance
m	Number of phases
$\dot{m}$	Mass flow rate
$\dot{m}_a$	Mass flow rate across the RBC first stage
$\dot{m}_{a1}$	Mass flow rate across the first parallel-connected heat exchanger
$\dot{m}_{a2}$	Mass flow rate across the second parallel-connected heat exchanger
m_a	Railgun armature mass
m_{acc}	Mass of the accelerometer
m_{Al}	Aluminium mover mass
m_{A320}	Mass of the A320-200 aircraft
$\dot{m}_b$	Mass flow rate across the RBC second stage
m_{Co}	Copper mass
m_{cryo}	Mass of the cryostat
m_{Eng}	Engine mass
m_{Fuel}	Fuel mass
m_{LH_2}	Mass of liquid hydrogen
m_{MgB_2}	Mass of MgB_2
m_{matrix}	Mass of the superconducting wire's matrix
m_{mov}	Mover mass
m_p	Mass of the test rig
m_{Stru}	Aircraft structure mass
m_{th}	Stator teeth mass
m_{UAV}	Mass of the UAV
m_{vess}	Mass of the cryostat vessel
m_{yo}	Stator yoke mass
M	Mach number
M_{ij}	Mutual inductance between the wire i and j
M_{yaw}	Yaw momentum
M_2	Mach number at V_2
μ	Friction coefficient

μ_{Air}	Dynamic viscosity of air
μ_{A320}	Friction coefficient of the A320-200 aircraft
μ_e	Equivalent friction coefficient
μ_{mov}	Friction coefficient of the prototype mover
μ_p	Friction coefficient of the test rig against its support
μ_{PM}	Permanent magnet relative permeability
μ_r	Relative permeability of the iron core
μ_x	Permeability of slotted structures in x-direction
μ_y	Permeability of slotted structures in y-direction
μ_0	Permeability of the void
$n_{\%g=6}$	Percentage variation related to $g = 6$ mm
n_q	Numerator of slot per pole per phase
n_{zq}	Minimum number of 0 after each 1 in the basic binary series
$\mathbb{N}$	Set of integer numbers
N_c	Number of turns per coil
N_{engine}	Number of engines
N_r	Number of rail pairs
N_s	Number of turns per slot in Chapter 4 and 7
N_s	Number of slots in Chapter 5
N_{tot}	Total number of turns considering passive zones
Nu	Nusselt number
N_1	Stator turns per phase
N_{132kA}	Number of 132-kA cable sections in the cryostat section
N_{21kA}	Number of 21-kA cable sections in the cryostat section
ω	Rotational speed
ω_1	Primary rotational speed
ω_2	Secondary rotational speed
ω_R	Rotational speed at nose rotation
p	Number of pole pairs
p_{Air}	Air pressure
p_{tot}	Total number of poles considering passive zones
p_0	Standard atmospheric pressure at ground level
P_a	Active power
P_{a2}	Active power of LIM secondary considering end-effects
P_c	Copper losses
P_{core}	Total iron losses
$P_{coupling}$	Coupling losses in superconductors
P_{eddy}	Eddy current loss in superconductors
P_{eddy_ν}	Eddy current loss in superconductors due to ν^{th} harmonic
P_{e2D}	Loss in PMs calculated by 2D simulations
P_{e3D}	Loss in PMs calculated by 3D simulations
P_{Hys}	Hysteresis power loss in all the superconducting wires
P_{Hys_i}	Hysteresis power loss in the superconducting wire i

P_i	Input power
$\overline{P}_{ig=6}$	Average input power related to $g = 6$ mm
P_o	Output power
P_{onet}	Net output power
Pr	Prandtl number
P_r	Reactive power
P_{RBC}	Power required by the cryocooler
P_{r2}	Reactive power of LIM secondary considering end-effects
P_{sc}	Specific cryocooler input power
P_{th}	Iron losses in the stator teeth
P_{yo}	Iron losses in the stator yoke
P_{yoke}	Iron losses in the LPMSM mover's yoke
Φ	Magnetic flux
Φ_m	Magnetic flux in the airgap
Φ_s	Flux linkage between each turn and PMs
Φ_1	Magnetic flux of a single pole
Ψ	Helix pitch angle
Ψ_{PM}	Permanent magnet flux linkage
Ψ_s	Flux linkage between each phase and PMs
Ψ_1	Primary flux linkage
Ψ_2	Secondary flux linkage
q	Slot per pole per phase
q_{Air}	Dynamic air pressure
q_v	Heat generation per unit volume
$q_{x,y,z}$	Heat fluxes in the 3 directions of space
Q	Heat flow
Q_c	RBC cooling power
Q_i	Internal energy
Q_1	Heat flow across the first heat exchanger
Q_2	Heat flow across the second heat exchanger
r	Distance between two points
r_q	Zeros to redistribute in the basic binary series
r_{mp}	Ratio of magnet span to pole pitch
r_{ts}	Ratio of tooth width to slot pitch
r_w	Radius of a superconducting wire
r_1	First boundary of the weak penetration region
r_2	Second boundary of the weak penetration region
R	Resistance
Ra	Rayleigh number
R_{Co}	Copper wire resistance
R_g	Specific gas constant of dry air
R_m	Iron loss resistance
R_r	Radius of a superconducting ring

R_{tot}	Total winding resistance considering passive zones
R_0	Initial resistance
R_1	Primary resistance
R_2	Secondary resistance
R_{2e}	Equivalent secondary resistance
$\Re$	Reluctance
$\Re$	As operator it indicates the real part of a complex number
ρ	Resistivity
ρ_{Air}	Air density
ρ_{Al}	Aluminium density
ρ_c	Copper resistivity
ρ_{Co}	Copper density
ρ_{ef}	Effective resistivity of a superconducting wire section
ρ_{Fe}	Stainless steel density
ρ_{Fuel}	Fuel density
ρ_{GH_2}	Gaseous hydrogen density
ρ_{H_2}	Hydrogen density
ρ_{ir}	Laminated silicon steel density
ρ_i	Initial resistivity
ρ_{LH_2}	Liquid hydrogen density
ρ_m	Aluminium resistivity
ρ_M	Monel resistivity
ρ_{ma}	Resistivity of the superconducting wire matrix
ρ_{mag}	Permanent magnets resistivity
$\rho_{mag_{2D}}$	Equivalent 2D permanent magnets resistivity
ρ_{MgB_2}	MgB_2 density
ρ_{Mo}	Monel density
ρ_{PM}	NdFeB permanent magnet density
ρ_0	Standard air density at ground level and 20°C
s	Distance travelled by railgun's armature
s	Slip frequency in Chapter 4
s_{Air}	Aircraft airborne distance
s_{max}	Slip frequency at maximum thrust
s_{Run}	Aircraft acceleration distance
s_{stop}	Distance travelled from an engine failure to a standstill
s_x	Distance between superconducting cables in x-direction
s_y	Distance between superconducting cables in y-direction
s_1	Distance travelled before an engine failure in Chapter 3
s_1	Helical arc of the first helix in Chapter 7
s_2	Distance travelled from an engine failure to h_2 in Chapter 3
s_2	Helical arc of the second helix in Chapter 7
S_{eng}	Engine front section area
$S_{€}$	Fuel cost saving

S_w	Wing surface area
S_{wESDU}	ESDU wing surface area
S_{wire}	Wire external surface area
σ	Ratio ρ_{Air}/ρ_0 in Chapter 3
σ	Electrical conductivity
σ_{Al}	Aluminium electrical conductivity
σ_B	Boltzmann constant
σ_c	Copper electrical conductivity
σ_e	Equivalent electrical conductivity
σ_s	Carter coefficient constant
t	Time
t	Machine periodicity in Chapter 5
t_{Air}	Aircraft airborne time
t_c	Minimum time between two consecutive take-off
t_{cryo}	Thickness of the cryostat wall
t_{EF}	Time when the engine failure occurs
t_{LOF}	Take-off elapsed time at V_{LOF}
t_{Ret}	Time required to return to the initial position
t_{Run}	Aircraft acceleration time
t_{TO}	Time spent to reach h_{TO} from h_2
t_{TOF}	Time required by the catapult to accelerate the aircraft
t_{vess}	Thickness of all the aluminium sheets of the cryostat vessel
t_1	Time the current is supplied to the primary windings
t_2	Take-off elapsed time at V_2
θ_0	Angular offset between two helices
θ_1	Helical angle of the first helix
θ_2	Helical angle of the second helix
T	Temperature
T	Engine/s Thrust
T_{Air}	Air temperature
T_C	Minimum temperature in the RBC cycle
T_{cr}	Creep temperature
T_i	Initial temperature
T_H	Maximum temperature in the RBC cycle
T_{H_2}	Temperature of liquid hydrogen
T_m	Melting temperature
T_x	Coil equilibrium temperature
T_w	Wall temperature
T_0	Standard atmospheric temperature at ground level
T_∞	Temperature of a fluid far from the wall
τ	Pole pitch
τ_c	Coil pitch
τ_s	Slot pitch

τ_w	Pitch of a twisted wire
u	Permeance function parameter
U	Voltage
$\overrightarrow{U}$	Voltage vector
U_A	Supplied voltage first phase
U_B	Supplied voltage second phase
U_C	Supplied voltage third phase
U_d	Direct voltage
U_{ind}	Induced voltage
U_q	Quadrature voltage
U_1	Primary voltage
U_2	Secondary voltage
v	Volume
v_A	Volume of the cryostat part A in Fig. 7.12
v_B	Volume of the cryostat part B in Fig. 7.12
v_C	Volume of the cryostat part C in Fig. 7.12
v_{cable}	Volume of the a superconducting cables
v_{cryo}	Volume of the cryostat
v_{LH_2}	Volume of liquid hydrogen
v_{PM}	Permanent magnets volume
v_r	LIM mover speed
$\overrightarrow{v_{rel}}$	Relative speed
v_s	Synchronous speed
v_{sc}	Volume of the superconducting wires
$v_{s\nu}$	Synchronous speed of the ν^{th} harmonic
v_{TO}	Catapult end-speed
v_{wire}	Volume of each wire in the primary coils
v_{yoke}	Volume of the LPMSM mover's yoke
V	Aircraft Speed
V_{Air}	Aircraft mean airborne speed
V_{EF}	Critical engine failure speed
V_{LOF}	Lift-off speed
V_{MC}	Minimum control speed
V_R	Nose rotation speed
V_s	Stall speed
V_{sp}	Maximum mover speed at spring location
V_{TO}	Speed at h_{TO}
V_x	General take-off speed
V_1	Critical decision speed
V_2	Take-off safety speed
ν	Harmonic order
ν_{Air}	Kinematic viscosity of air
w_{mag}	Width of the area with a magnetic field

w_{mov}	Width of the mover
w_r	Width of the railgun rails
w_s	Number of turns per slot in Chapter 4
w_{sc}	Width of the cryostat cross section
W	Aircraft weight
$x_\alpha, y_\alpha, z_\alpha$	Tilted frame of reference axes
X_m	Magnetizing reactance
X_{me}	Equivalent magnetizing reactance
x_P, y_P, z_P	Coordinate of the integartion point
$X_{parameter}$	Non-dimensional parameter of momentum intensity
X_2	Secondary leakage reactance
ξ	Ratio of aluminium thickness to penetration depth
y_c	Coordinate at which the current density changes sign
y_0	Longitudinal offset between two helices
y_1	Distance along the first helix axis
y_2	Distance along the second helix axis
z_q	Difference between numerator and denominator of q
Z_s	Secondary impedance

Acronyms

AC	Alternated Current
AEO	All Engine Operative
ASTM	American Society for Testing and Materials
BFL	Balanced Field Length
CAA	Civil Aviation Authority
CERN	European Centre of Nuclear Research
DC	Direct Current
dq	Direct Quadrature
EASA	European Aviation Safety Agency
EASD	Emergency Accelerating and Stop Distance
EM	Electro-Migration
EMALS	Electromagnetic Aircraft Launch System
EMCAT	Electromagnetic Catapult
EMF	Electro-Motive Force
EML	Electromagnetic Launch
EPA	Environmental Protection Agency
ESDU	Engineering Science Data Unit
FAR	Federal Aviation Regulation
FDM	Finite Difference Method
FEA	Finite Element Analysis
FEM	Finite Element Method
FID	Flight Idle rating
GA	General Atomics
GCD	Greatest Common Divisor
HTS	High Temperature Superconductor

ICAO	International Civil Aviation Organization
IHS	Information Handling Service
ISA	International Standard Atmosphere
ISO	International Standard Organization
LCM	Least Common Multiple
LIM	Linear Induction Motor
LPMSM	Linear Permanent Magnet Synchronous Motor
LRSM	Linear Reluctance Synchronous Motor
LSM	Linear Synchronous Motor
LTS	Low Temperature Superconductor
MAGLEV	Magnetically Levitated
MCL	Maximum Climb rating
MCR	Maximum Cruise rating
MCT	Maximum Continuous Thrust rating
MLI	Multi-Layer Insulator
MLT	Multi-Layer Theory
MMF	Magneto-Motive Force
MTO	Maximum Take-Off rating
MTOW	Maximum Take-Off Weight
OEI	One Engine Inoperative
PDRR	Program Definition and Risk Reduction
PM	Permanent Magnet
RBC	Reverse Brayton Cryocooler
RMS	Root Mean Square
SCLSM	Superconducting Linear Synchronous Motor
SEP	Specific Excess Power
SMES	Superconducting Magnetic Energy Storage system
TOD	Take-Off Distance
TOFL	Take-Off Field Length
UAV	Unmanned Air Vehicle

Chapter 1

Introduction

This chapter outlines the topic of this research and describes the aims and objectives of the work. The chapter introduces the concept of the civil aircraft application of electromagnetic launch (EML) systems as well as the possible benefits and drawbacks of the exploitation of such an external energy source to aid aircraft acceleration during take-off. The chapter presents the rationale behind the selection of the reference aircraft and defines the acceleration requirement of an electromagnetic catapult in this application. The methods and the technologies that have been employed to address the design challenges of such a complex system are summarized and the thesis structure is presented.

1.1 Motivations

The power required to accelerate modern civil aircraft on the airport runway during take-off sets the engine size and thrust requirement. An EML system may significantly reduce the engine power and fuel use by providing some or all of the energy required at the launch stage.

Most of modern aircraft accelerate at 0.3 G since the engines thrust peak is about 30-35% of the maximum take-off weight. The thrust provided by the engines gradually decreases with the speed gained by the aircraft while the aerodynamic drag increases. Therefore, the acceleration profile at take-off has a negative slope. The thrust level that can be delivered by an EML system allows for accelerations

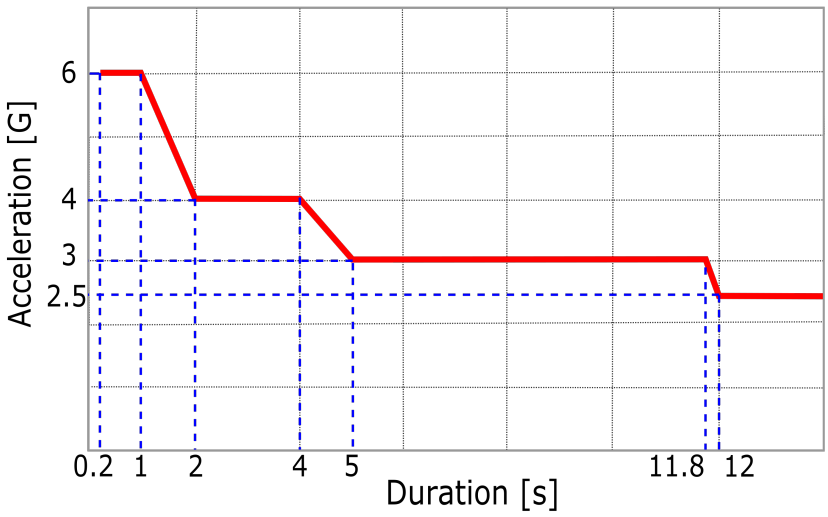

Figure 1.1: Axial acceleration limits for a healthy human being

that cannot be reached by aircraft engines alone and do not depend on aircraft speed and aerodynamic drag. The intensity of the acceleration that the electromagnetic catapult delivers for the whole duration of the take-off procedure must not jeopardize safety and comfort of the passengers of any physical condition and age.

There are no regulations in aviation which limit the maximum axial take-off acceleration for passengers, but the American Society for Testing and Materials developed standards for allowable acceleration in amusement rides [1]. This document establishes the limits of accelerations acting from different directions upon a person without any specific physical limitations. Fig. 1.1 shows the axial acceleration intensity that a healthy person can withstand for a specific time span. This chart is valid only for an axial acceleration acting perpendicularly to the chest of a passenger seated with backrest and headrest [1]. The duration of the take-off procedure is expected to exceed 12 seconds which allow a maximum axial acceleration of 2.5 G according to the curve reported in Fig. 1.1. In order to take into account all the possible health conditions of the passengers, less than the 50% of the maximum limit has been considered (< 1.25 G).

Besides passenger safety, passenger comfort plays an important role in the selection of an appropriate acceleration level. Independently from the max acceleration that can be withstood, every passenger differently perceives accelerations

according to personal and psychological factors. Since discomfort may be caused by low accelerations as well as high accelerations, the rated acceleration considered in this work is conservatively assumed to be 0.6 G. This acceleration intensity guarantees passengers safety and comfort while exceeding the usual engines acceleration peak on civil aircraft.

The increased acceleration and the consequent reduction of the runway length required at take-off is one of the major benefits of EML systems. Existing runways could respond to the air traffic growth without the need of expensive airport extension through the implementation of an electromagnetic catapult. Beside the possibility of avoiding airport extensions, an EML system may, for example, allow the use of existing runways to serve two aircraft taking off simultaneously from the center of the runway and accelerating in opposite directions, virtually doubling the airport capacity.

An EML system may be a viable alternative to airport extension in city airports like London Heathrow. For instance, the foreseen cost for the construction of a third runway in Heathrow is £17.6 billion whereas the runway extension proposals quote the total expense £14.4 billion [2]. The installation cost of an EML system for civil aircraft is difficult to predict, but it may roughly reach £700 million per launcher, considering the cost of the electrical motor, excavation work, holding structure, power supply, power electronics and work force required to build it. The cost of two launchers would approximately be one tenth of the cost reported in the official proposal for the Heathrow runway extension.

The suggested technology may not have only a significant economic impact, but it could also affect the local communities living around airport by preventing the need of mandatory home purchase, 242 for the runway extension and 783 for the third runway [2].

City airport extension also required additional incentives to take affective measures to mitigate the noise impact in the broader area. The electromagnetic catapult is an electrical motor whose noise envelope is negligible compare to the noise emitted by combustion engines. The electromagnetic catapult reduces the engine usage and fuel consumption at ground level and actively contributes to the mitigation of the airport noise emission. The benefit of fuel consumption reduction during take-off has a significant impact on pollution at ground level and might

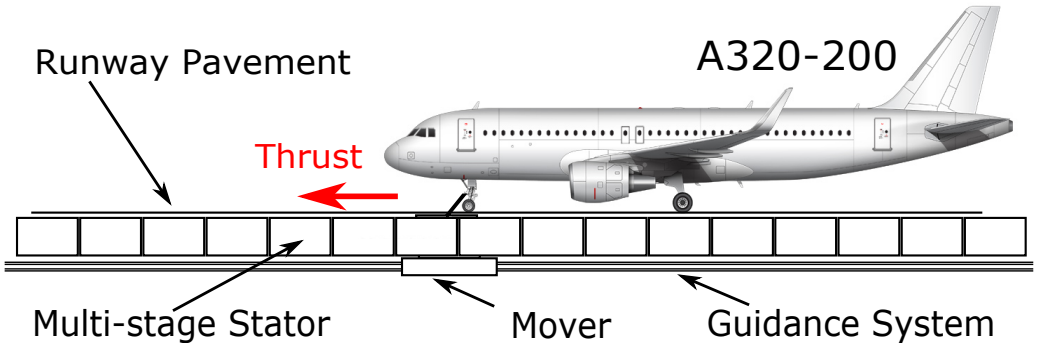

Figure 1.2: Schematic of an EML system for civil aircraft

push research toward the implementation of EML as a greener technology.

The fuel saving could be accentuated by the reduction of engine thrust requirements which may lead to the installation of smaller engines with lower weight and lower fuel consumption. The consequent cost saving for airline operator may encourage investors to cover the expenses for the catapult installation and for the reconfiguration of the undercarriage framework. However, the reduction of the engine size may be possible only on the basis of a large scale implementation of EML systems in several airports. Indeed, an aircraft with reduced engine size may only be able to fly routes between airports with an EML system.

The global expansion of the aviation market is expected to continue over the next 20 years, with single-aisle airplanes commanding the largest share of new deliveries (70%) [3]. A large number of single-aisle aircraft will be ordered to face the local air traffic growth and to replace aircraft with obsolete technologies. Innovations and technological improvements for this aircraft category might have a significant impact on the worldwide aviation economy. For this reason, the EML system proposed in this work has been designed to aid the take-off for single-aisle aircraft rather than larger airplanes. The single-aisle aircraft category is well represented by the Airbus A320 family, and in particular by the A320-200 model which has a maximum take-off weight of 73.5 tons. A schematic of the EML system that will be considered as baseline for the calculation of electromagnetic catapult thrust and speed requirements is shown in Fig. 1.2.

In conclusion, EML may allow a sensible runway length reduction by increasing the aircraft acceleration rate at take-off. This system has also the potential

of reducing the engine fuel consumption, noise emission and exhaust emission at ground level. For an aircraft flying to airports with an EML system, it could be even possible to reduce the engine thrust and size while further decreasing the total fuel consumption. Nevertheless, the installation of such a large electrical machine needs consistent investments and the interruption of some or all of the airport services. The aircraft operations at an airport with a shorter runway are dependant on the correct functioning of the EML system both at take-off and landing. Furthermore, an aircraft with reduced engine thrust can take-off only from airports where an EML system is available. The take-off procedures that guarantee passengers safety with conventional take-off should be revised to consider the EML system. Additionally, the technology readiness level may not be sufficient to engineer a system capable of launching large aircraft.

1.2 Research Outline

An EML system is a complex electric machine which can be composed of a power source, an electrical motor and power electronics for control. The power source may be either an external power station or an energy storage system on site. In the latter case the energy can be stored:

- electromagnetically using ultracapacitors or superconducting energy storage system;
- electrochemically employing batteries;
- kinetically through several flywheels.

The power electronics takes the energy from the source and supply the electrical motor with the required voltage and frequency to achieve the required thrust with the maximum efficiency. The power electronics also includes the electric components required to control the machine throughout the whole duration of the launch. The electrical motor is responsible to provide the required thrust and acceleration to the aircraft until the catapult end-speed is reached.

This thesis focuses only on the design and modelling of the electrical motor considering the state of the art power electronics limitations and the impact of the

catapult on modern aircraft take-off procedure. In this work three linear electrical motor topologies are considered:

Linear Induction Motor This motor topology produces the thrust through the interaction between the magnetic field produced by the primary coils and the current induced by the same field in a conductive plate. This solution is highly attractive for its light structure and simple control technique, but it suffers poor electromagnetic performance;

Linear Permanent Magnet Synchronous Motor In this machine the thrust is generated by the interaction of the field produced by the stator coils and the excitation field sustained by rare earth permanent magnets. This system is particularly attractive for its good electromagnetic performance, even though a close-loop control, expensive materials and high supply frequencies are needed;

Superconducting Linear Synchronous Motor This topology includes linear motors in which parts of the machine are made out of special material that cooled down below their transition temperature show superconducting properties. In this work, the superconducting part of the linear motor generates the excitation field whereas the travelling magnetic wave is produced by conventional conductors. Superconducting motors are particularly attractive for the exceptional electromagnetic performance, even though they need complex cryogenic technologies and a cooling system whit high input power demand.

The electromagnetic design and the thermal-structural characterization of the machines presented in this thesis are applied to EML system in particular, but the same techniques can be extended to any linear motor with similar configurations.

1.3 Thesis Structure

Chapter 2 explores military applications of EML, such as kinetic weapons and electromagnetic catapults for jet aircraft. The recent developments in superconducting magnetic levitated trains are also presented. The preliminary design of a simple railgun is carried out to assess the performance of this system during the aircraft launch.

Chapter 3 presents the implementation of the electromagnetic catapult in the take-off procedure of an A320-200 aircraft. The take-off analysis is carried out to estimate the impact of the catapult on all the take-off characteristics, in particular on runway length, fuel consumption and operational cost. On the basis of a thorough analysis of the engines performance, the catapult requirements are determined. This chapter also presents an investigation of the effects of engine size reduction on the take-off and in-flight performance.

The topology selection and the design of a linear induction motor for EML applications is presented in Chapter 4. The theories to model the phenomena related to the limited dimensions of the mover are explained and applied. The electromagnetic design is developed on the basis of the geometrical parameters selection through the parametric optimization analysis. The transient analytical model of the machine is validated through the comparison with the results of the finite element analysis. The buckling analysis and thermal analysis are performed to verify the structural stability and to evaluate the temperature rise in the conductive components of the machine.

Chapter 5 presents the topology selection and the electromagnetic design of a linear synchronous motor. The algorithm to determine the optimum phase sequence for a tooth-winding machine with a large number of slots is reported. The parametric optimization method is exploited to determine the geometrical parameters which minimize the input power. The multi-layer theory for the double-sided linear synchronous motor is presented, being essential part of the transient model of the machine. The thermal analysis of the permanent magnets and of the mover's yoke was carried out to reckon possible risks of demagnetization.

The design procedures of the linear induction motor presented in Chapters 4 are validated using experiment results in Chapter 6. The calculation of the requirements for the launch of an UAV with a take-off weight of 4.5 kg is presented. The sizing procedures of the asynchronous and synchronous launchers presented in the previous chapters are applied to determine the geometrical features of the small prototype. The structural design of the motor housing is presented, as the same techniques are applicable to the large scale launcher. The methods used to size the braking system and the safety measures taken to avoid any hazard are shown. The experimental results are compared with analytical and finite element

analysis outcomes.

Chapter 7 introduces the definition of the geometrical properties of a superconducting linear synchronous motor for EML application, with particular attention on the superconducting material distribution in the airgap. The magnetic flux across the machine and its harmonic content are reconstructed using the Biot-Savart law and the multi-layer theory. The secondary harmonics of the magnetic field are used to estimate the AC losses in superconductors due to wires coupling, hysteresis and eddy current. The static and transient thermal model of the insulation are presented to evaluate the cooling capability of the system to prevent quenching during the launch. The cryocooler used to remove the heat absorbed by the coolant is modelled to estimate the input power required by the cooling system. The performance of the motor is eventually estimated by considering the power requirements of the cooling system as well as the machine itself.

In Chapter 8 the machines topologies proposed in this research are compared. The points of the analyses presented in this thesis that can be further developed are discussed. Research topics that may be of interest in the future are presented.

Chapter 2

Literature Review

This chapter presents a review of relevant literature on viable technologies for electromagnetic launch (EML) applications to assist civil aircraft take-off. Although an electromagnetic launcher for civil aircraft has never been designed before, similar technologies have been considered for military planes and transportation industries.

EML systems have been investigated for military applications as aircraft launcher to replace the steam catapult on the deck of aircraft carriers [4]. In the transportation field superconducting linear electric motors with power requirements similar to military EML systems have also been used to propel and levitate trains for urban and interurban purposes [5].

Therefore this chapter considers the relevant research which has been reported on military aircraft launchers and superconducting linear motors for magnetically levitated trains. The main research achievements in these areas can then be exploited for the design of the civil aircraft launcher.

EML systems have been also studied as kinetic weapons to launch heavy projectiles [6]. Since this technology involves a railgun with output energy comparable with that of an EML system for military planes [7], a railgun could also represent a viable solution for a civil aircraft launcher. Besides the vast research undertaken on railguns, this chapter introduces an investigation on the performance of a railgun for a civil aircraft EML system.

Table 2.1: EML system requirements for aircraft carriers

Take-off speed	28 - 103 m/s
Max Aircraft Mass	25000 kg
Acceleration	2.5 - 5 G
Launch Energy	122 MJ
Runway Length	< 110 m
Cycle Time	45 s

2.1 Research Background on Aircraft Launchers

Electromagnetic launch system have been studied as an alternative technology to replace the existing steam and hydraulic catapult on the deck of aircraft carriers. The steam catapult has many years of operation, but the inexorable trend towards heavier jet aircraft results in a launch energy requirements that exceeds the catapult capability, approximately 95 MJ [8]. Moreover, the catapult operates without a feedback control, has an efficiency of only 4-6%, requires several hours of maintenance and occupies a large volume [4]. Modern ship configurations require a launch system that could overcome the limitations of steam catapults while delivering more maintainability, reliability, capability and efficiency at lower cost.

All the scientific articles published in this research area proposed either an asynchronous linear motor or a synchronous linear motor able to satisfy the requirements reported in Table 2.1.

2.1.1 Asynchronous Launcher

An electrical machine topology that can be considered for the launch of civil aircraft is the linear induction motor (LIM). This section presents only the research done on induction launchers for military and light aircraft, since a LIM for civil aircraft launch has never been studied or developed.

2.1.1.1 The Electropult

In order to address the issue of launching jet-propelled aircraft and heavy bombers from shipboard without the initial impact of steam catapult, the Westinghouse

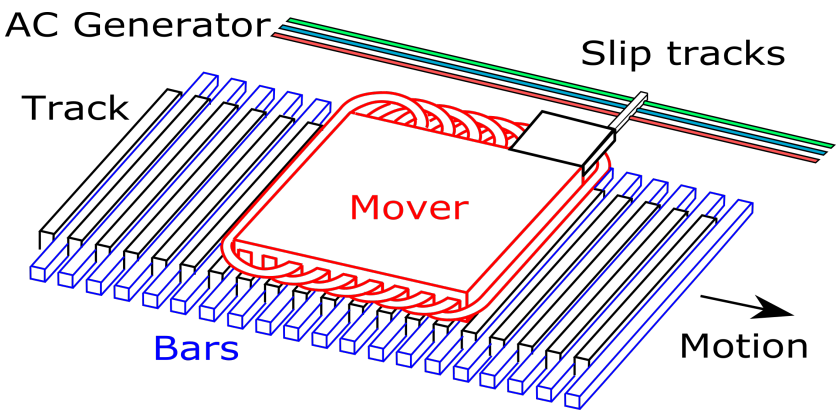

Figure 2.1: The single-sided induction motor called Electropult

Electric Corporation designed and built for the United States Navy a linear induction motor known as the "Electropult" [9] in 1946.

The power supply for the Electropult was a Pratt and Whitney 1100 horsepower aircraft engine which drove a DC generator coupled to a DC motor. The DC motor in turn drove a 24 tons flywheel which stored the amount of kinetic energy required by the launch rotating at 1300 rpm. The energy stored in the flywheel was used to drive an AC generator, which supplied 12 MW of electrical power to the Electropult.

The Electropult was a single-sided motor 420 m long whose illustration is shown in Fig. 2.1. The Electropult's moving member hosted the primary windings and three collector brushes sliding along the slip tracks were used to supply the power input to the moving carriage [10]. The use of these collectors led to considerable problems as the current per phase was approximately 7000 A. The magnetic circuit was closed by the electrical steel track with 17000 high resistance metal bars embedded in slots [9]. The last section of the runway was used in conjunction with a DC braking system that used 10000 A in order to bring the mover to rest.

The induction motor successfully accelerated a 4500 kg jet aircraft from rest to 52 m/s. A serious problem that occurred during tests was the force generated on the moving part of the machine which acted perpendicularly to the motion [10]. The downward force required to keep the mover stable effectively multiplied the weight of the aircraft by a factor of 10 reaching approximately 500 kN.

Another unattractive feature of the Electropult was the low slip frequency which

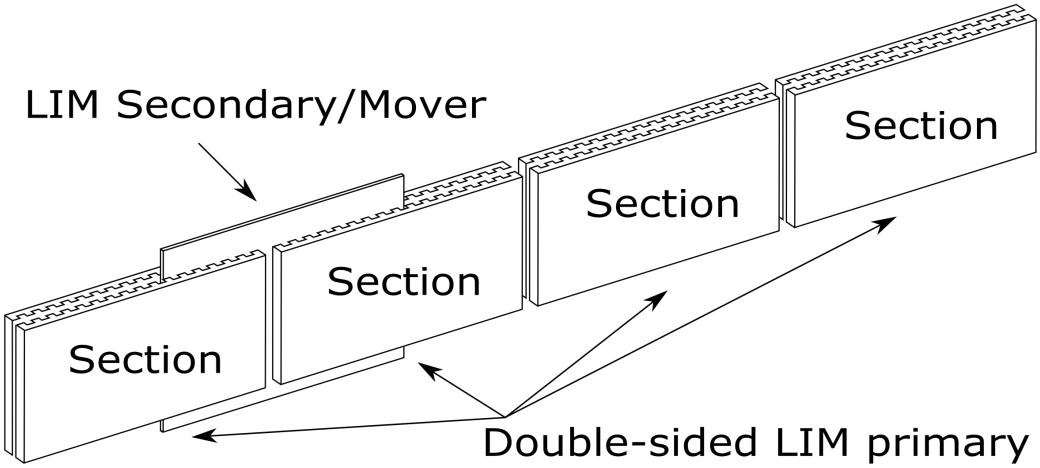

Figure 2.2: Schematic of a multi-section double-sided LIM with constant pole pitch

at take-off was only 66% of the synchronous speed [10]. Therefore, the overall energy efficiency of the Electropult was less than 50% and a considerable amount of energy was consumed in heating the runway. Eventually, the Electropult project was abandoned because of the high initial costs and the development of the steam catapult.

2.1.1.2 The EMALS program

The Electromagnetic Aircraft Launch System (EMALS) is the latest technology being inducted by the US Navy for assisted take-off systems on aircraft carriers. The system is being developed by General Atomics, for the Gerald R. Ford-class aircraft carriers which are currently being built [11].

The EMALS uses a double-sided LIM which configuration is similar to the one shown in Fig. 2.2. This system is particularly versatile being capable of launching light to heavy aircraft without any restrictions and independently from the wind conditions over the flight deck. Unlike steam catapults, which instantly release the launch energy, the linear induction motor allows for smoother acceleration while reducing stress, wear and tear on the aircraft frames.

The induction motor of EMALS is formed by 25 sections 3.65 m long which comprise a row of stator coils that pull an aluminium plate 6.7 m long [12]. To minimize losses and provide maximum available power, only the sections of the

stator that surround the vicinity of the mover are fed with current at a particular time. The coils are energized in carefully controlled succession via very-high-power SCRs (silicon-controlled rectifiers). The applied power is controlled through a closed loop so that the actual launch profile is matched to the requirements of a particular aircraft load and to overall system-performance variations.

The energy storage subsystem uses rotors of a disk alternator as a flywheel to kinetically store the energy it draws from the ship's power system [12]. Each rotor stores more than 100 MJ, spinning at more than 6000 rpm. Ford-class carriers are able to generate 13800 V of electrical power which drives the rotors to their target rotational speed. Then the power correction subsystem uses the same coils that drive the rotor to draw off their power as the rotor shifts from its motor mode to its alternator mode. The rotors operate in a vacuum chamber to eliminate air drag and increase efficiency above 90%. The power delivered from each rotor at maximum speed is approximately 80 MW and is released through a cycloconverter, which is a controllable source of rising frequency and voltage for the linear induction motor.

2.1.1.3 The EMCAT Project

ALSTOM power conversion Ltd and the British Ministry of Defence developed the Electromagnetic Catapult (EMCAT) project for light aircraft launching [13]. The double-sided LIM implemented in the EMCAT launch system delivers a thrust of 4.4 kN and is able to reach a maximum operating velocity of 80 m/s.

Since first LIMs were connected to an AC supply with constant frequency, the winding pitch gradually increased to speed up the load [14]. However, LIM's performance can be significantly increased using the same winding pitch on the whole length of the motor, while the frequency of the power supply gradually increases. This motor configuration can operate at very low slip frequencies with high speed control accuracies and open loop control. As will be further explained in Chapter 4, low slip frequencies are associated with efficient electrical machines whereas an open loop is a simple control method that requires less electronics to operate.

Therefore, a LIM with constant winding pitch was also adopted for the EMCAT

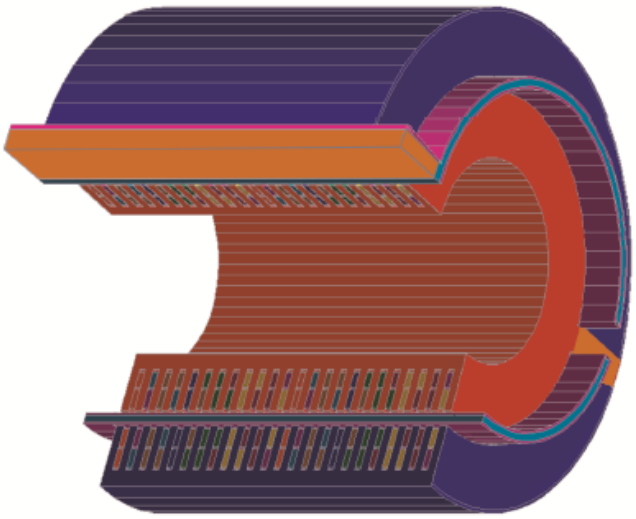

Figure 2.3: Double-sided tubolar LIM for EML systems

project and open loop control was implemented with only two critical data as inputs: speed and aircraft mass [13]. If there was to be an error on the data measurements the system automatically adjusted according to the particular thrust/frequency dependency of LIM. The reported experiments proved the feasibility and the technology readiness of linear induction motors with high power requirements for this very demanding application.

2.1.1.4 Tubular LIM

A double-sided tubular LIM similar to the one shown in Fig. 2.3 was proposed for EML system and modelled with a quasi-analytical method and numerical simulations to satisfy the requirements reported in Table 2.1 [15]. Even though the quasi-analytical results presented a good agreement with the numeric outcomes, the double-sided tubular LIM performance were not compared with those of either the single-sided counterpart or the conventional flat double-sided LIM with similar specifications. Therefore it cannot be asserted with certainty which topology performs better than the others.

For manufacturing reasons a linear tubular launcher is usually comprised of sets of separate stator units each one fed separately as the mover's motion progresses. Recent work proposed a dimensioning methodology to determine the optimum

number of LIM sections to reduce the impact of the reactive power by diminishing the leakage inductance of the inactive areas of the machine [16]. The selection of the number of sections also aimed to achieve the maximum efficiency accounting for mechanical loads, thermal stresses and voltage limits.

Besides aircraft launching applications, single-sided linear asynchronous motors with a tubular structure have also been proposed to accelerate heavy cylindrical masses such as torpedoes [17]. The high thrust density can also be exploited during breaking after the load detaches. At the same time, the kinetic energy of the mover without the load can be partially recovered: a numerical test on a single-sided tubular LIM showed that a recovery of about 46.5% is possible. However this amount of energy is negligible in practice as it represents only the 3% of the overall acceleration energy.

2.1.1.5 Modelling Methods for LIMs

The design of LIMs for EML applications must take into account the phenomena associated with the finite dimensions of the mover. The finite dimensions of the primary cause the so called end-effects that have enormous influence on the thrust and performance of the linear motor [18]. End-effects include transverse end-effect and longitudinal end-effect which are characterized by strong non-linearity and time dependency. The theory used to model linear induction machines can be still derived from the equivalent circuit often used for modelling rotary induction motor, using revised magnetizing inductance and secondary resistance to compensate for these effects [19].

Transverse end-effects cause an uneven distribution of the magnetic flux along the direction perpendicular to the motion and a thrust reduction [20]. In order to evaluate their impact on the equivalent circuit parameters a simplified bi-dimensional theory can be applied to the transversal section of a linear induction motor. The performance was shown to depend from three non-dimensional parameters, which are functions of the design data and of the slip frequency.

Longitudinal end-effects can cause a reduction of the rated thrust, efficiency and power factor especially at high speed [18]. The performance reduction due to longitudinal end-effects can be analysed assuming the existance of different

travelling magnetic flux waves, one representing the fundamental wave and the others the end-effects. The ratio between the magnetomotive force of these additional waves to the fundamental magnetomotive force return the end-effect factor which can be used to calculate the proper value of the equivalent circuit parameters. In particular, an additional impedance in parallel to the secondary resistance and magnetizing inductance should be added to the equivalent circuit to take into account longitudinal end-effect [21].

Longitudinal end-effects are particularly significant at high speed in LIMs with a moving short primary and a stationary secondary [18]. Conversely, in long-primary LIMs the secondary moves while the primary itself is stationary. In this case the correction factor for the end-effect reduces with the slip frequency and can be neglected at high speed [22].

2.1.1.6 Control Techniques for LIMs

In order to successfully construct and test a LIM for EML applications, the control system must take into account the performance reduction due to end-effects. The end-effects of LIM cause attenuation of the airgap flux that, in general, becomes more severe as the speed increases [23]. In order to reduce the impact of flux variations on LIM performance, special vector control strategies have been applied to the *dq* model of LIMs. The validity of the LIM model was checked by comparing currents from an experiment of a LIM acting upon a rotating disk. The problem of flux attenuation caused by speed increase was not observed with the proposed control scheme [23].

Similar control techniques were also implemented in a subscale integration test rig which was developed for the US Navy EMALS program [24]. This scaled LIM was 10 m long and capable of producing 8 kN of thrust operating at 100 kW. Tests were performed to compare various aspects of the system model with the hardware response before the final implementation of the launcher on board aircraft carriers. The control scheme based on the *dq* model of LIMs was successfully validated by comparing the simulation results with the test data.

Since any electromagnetic launch system requires high reliability, the mover could be driven by multiple separately excited stators [25]. Redundant stators

were considered in literature for synchronous machines, since the motor are essentially identical and uncoupled. In LIMs multiple stators acting on the same secondary are coupled by the common path of the induced current in the conductive plate. Since the motor mover is driven by multiple stators, an indirect vector control algorithm that accommodates the intense cross-coupling between stators and allows for independent control of flux in each stator and total motor force has been derived [25]. Since one of the purposes of the multiple stator geometry is fault tolerance, several methods for tolerating failed stator have been presented and tested on the EMALS PDRR (Program Defintion and Risk Reduction) built by General Atomics. This machine has the same section of the full scale launcher, but half the length.

2.1.1.7 Methods to Improve LIMs Power Factor

The main drawback of LIMs is the low power factor that they can achieve in comparison with other linear machines [18]. The low power factor increases the design difficulty, particularly the size and the mass of the power inverter. The low power factor is not only a consequence of the large airgap, but it also depends on the edge transients that occur in linear machines. In particular the rotor current tends to oppose the stator magnetomotive force at the entry edge reducing the flux density across the airgap.

A technique known as the asynchronous condenser has been used to effectively reduce the edge effects [26]. In this method the two undesirable transients at the LIM edges can be attenuated by having a space-transient magnetic wave travelling at rotor speed artificially created by two distinct windings of different pole pitch.

Another method that led to power factor improvements is based on a gradual shrinking of the pole pitch so that a primary section has a pole pitch which is $1-s$ times the pole pitch of the previous section (where s is the slip frequency) [27]. In this way the oscillating currents in the rotor would appear as continuous, but a phase step is required between the coils of different sections. From the evaluation of the experimental results it turned out that the phase steps clearly improved the power factor and allowed the demonstration motor to achieve a power factor of 80% compared to the more usual value of 30-40%.

2.1.1.8 LIMs as Kinetic Weapons

Linear induction launchers have also been proposed to accelerate light projectiles at end speeds of 150-1500 m/s [28]. The advantage of using an induction machine as railgun is that there is no wear of the projectile and no sliding contact, allowing repeated firings without maintenance of any sort. However, at such a speed the exit edge effect will cause a magnetic drag and a loss of magnetic flux that would make any solution very impracticable. In order to attenuate the end-effects the asynchronous condenser technique was used with dual pole-pitches operating at the same time. The launcher was built and tested by NASA Dryden and Embry Riddle Aeronautical University, and reached a speed of 180 m/s [28].

2.1.2 Synchronous Launcher

Synchronous motors and especially Linear Permanent Magnets Synchronous Motors (LPMSMs) have attracted the interest of many researchers for their capability of achieving high electromagnetic performance when compared with other linear motor topologies [29]. Since LPMSMs allow greater power factors than LIMs, they need an energy storage system with reduced capacity and a power conditioning system with less demanding requirements. However, LPMSMs operate at higher frequencies and their heavier movers absorb a larger amount of energy to accelerate at the same rate. Additionally, the expensive rare earth permanent magnets which are often adopted in synchronous EML system further increase the cost of the launcher.

2.1.2.1 The Kaman Launcher

Before implementing a LIM in Ford-class aircraft carriers, the U.S. Navy in partnership with Kaman Electromagnetics developed an Electromagnetic Aircraft Launch System (EMALS) to satisfy the requirements listed in Table 2.1 [8]. This EMALS consisted in a LPMSM that accelerated the aircraft while providing closed loop control. The machine layout is similar to the EMALS shown in Fig. 2.2 where the aluminium plate is replaced by an array of permanent magnets.

The launch starts when the electric power at 4160 V from the carrier (old Nimtz-

class carriers [12]) is rectified and fed to inverters. The power is then sent to the four disk alternators where it is used to spin up the rotors that kinetically store the energy required by the launcher. The disk alternators are six-phase permanent magnet machines with a dual stator and axial field [8]. Each stator has two separate windings: one for power generation and the other for motoring. Each rotor operates at a maximum rotational speed of 6400 rpm and stores a total energy of 121 MJ which gives an output power of 81.6 MW into a matched load.

The machine excitation field comes from 35 neodymium iron boron (NdFeB) permanent magnets that are housed in the rotor. These magnets create an average working air gap flux density of 0.976 T. The stator is a radially slotted laminated core with 240 slots and develops a maximum back EMF of 1122 V. The maximum output voltage is 1700 V peak while the maximum current per phase is 6400 A peak. The overall efficiency of each disk alternator is 89.3% with a total loss of 127 kW. These heat losses are transferred out of the disk alternator through a cold plate on the outside of the stators [8].

The LPMSM is energized through a cycloconverter which increases the voltage and frequency according to the speed of the aircraft. The output of a cycloconverter can vary from 0-644 Hz and from 0-1520 V. The cycloconverter must be cooled with liquid cooled plates to dissipate the 528 kW loss [8].

The LPMSM has a dual vertical stator configuration with the active area facing outwards. The stator consists of 298 segments, 149 per side which are actively cooled down to allow a cycle time of 45 seconds. Each segment is 640 mm long, 686 mm high and 76 mm wide. The segment is wound as a three-phase winding with 24 slots and 6 turns per slot resulting into 8 poles per segment and a pole pitch of 8 cm. These coils are epoxied on a slot-less stator structure which keeps the phase inductance as low as 18 μH with a phase resistance of 41 mΩ and bus resistance of 0.67 mΩ.

The mover contains 160 NdFeB magnets, is restrained in two axes by rollers and is passively cooled by air convection, since eddy currents losses cause negligible heat dissipation. These rollers help to maintain a consistent air gap of 6.35 mm with a magnetic flux density of 0.896 T.

The launcher has a projected efficiency of 70% and peak losses of 13.3 MW [8]. With this power loss intensity, active cooling is necessary. The launcher uses

an aluminium cold plate to remove the heat from the attached stator windings and back iron.

Unfortunately, the EMALS proposed by Kaman Electromagnetics has a few drawbacks [10]. One of the drawbacks is that high power electromagnetic motors create electromagnetic interference with electronic equipment. This presents a problem because the aircraft that is launched has a large amount of sensitive electronic equipment. Another drawback of this EMALS design is the disk alternators. These highspeed pieces of rotating machinery are spinning at about 6400 rpm storing a total of 484 MJ. While these disk alternators work in a laboratory setting, the jarring and motion of an aircraft carrier could cause the disk alternators to be less effective and possibly even malfunction.

2.1.2.2 Patterson Launcher Model

Later studies were carried out on the components of the EMALS proposed by Kaman Electromagnetics and US Navy, starting from the requirements reported in Table 2.1 [30]. A synchronous motor with NdFeB permanent magnets supported in a composite structure was proposed. The particularly challenging and ambitious aspects of this design are the required current intensity (18 kA), the shear stress of 220 kN/m^2 and the 60% fill factor especially considering the high applied voltage (4.8 kV).

The authors asserted that the proposed LPMSM layout could operate without a cooling system, despite the likely temperature rise that should occur in the stator coils due to 30 A/mm^2 current density and multiple launches with a cycle time of only 45 seconds. High current densities are usually applied to the primary windings to get the desired magnetic flux density in airgap. The current density increases the copper temperature and might cause serious damages to motor especially after several launches.

The thermal behaviour of a LPMSM with short primary has been analysed by solving the heat transfer problem for the stator coils [31]. The research proposed a bi-dimensional thermal model that can establish the need of particular cooling system in the most critic area. In a single launch the temperature rise does not threaten the coil insulation, but a limited number of launches is allowed without

an active cooling system that absorbs part of the heat produced during the accelerations. Similar techniques and conclusions can be extended to a section of a synchronous launcher with a long primary as well.

Some researchers attempted to improve the performance of the model presented by Patterson [30] by using different machine structures, coil arrangements and permanent magnets arrays [32]. In particular, the stators with active areas facing inward (*blade* structure) and outward (*inverted-U* structure) were compared. Three stator winding strategies were adopted: distributed windings, juxtaposed windings with a reduced step ($q = 1/2$) and juxtaposed winding with a polar step ($q = 1$). Their performances were evaluated implementing the conventional north-south magnets array and the Halbach array. The research results show that the configuration based on the Halbach array, distributed windings and blade structure achieves the highest thrust density. Nevertheless, the slot-pole combinations selected by the author of the paper for the LPMSM with concentrated windings are well known for their low performance with respect to the distributed windings configuration. The performance can be significantly improved with the optimum selection of number of slots and poles.

2.1.2.3 Modelling and Control Methods for LPMSM

As for LIMs, LPMSMs for EML applications are usually built in sections to reduce the leakage flux that would occur feeding the full track continuosly while only a part of the stator interacts with the mover. In order to model the sectioned LPMSM not only self and the mutual phase inductances of a single section should be considered, but also the mutual inductance between two phases in two different sections should be taken into account [33].

When the motor is divided into sections the problem to control the mover at the section transitions arises [34]. In order to reduce the thrust ripple and the potential damage of the launcher that may occur during transition, a fuzzy PI regulator was implemented to adjust the mover velocity and prevent magnetic flux overshoots using the measurements taken by current trackers. The current trackers were employed in the adjacent windings of two primary sections allowing the magnetic field at the transition to smoothly move forward.

2.1.2.4 Other Synchronous Motor Topologies

The traditional LPMSM has a laminated iron structure which may suffer large iron losses and low efficiency at high frequency and high speed. To solve this issue a decentralized coreless linear motor was proposed [35]. Experiment and numerical transient simulation showed that the proposed coreless machine had higher efficiency than the respective iron-core LPMSMs at very high speed whereas the iron-core machine is more efficient at lower speed. Since the iron-core LPMSM efficiency is larger than coreless machine for the speed range in which EML systems operate, the former configuration is usually adopted. However, to reduce the iron losses that may occur at high speed, the yoke thickness can be increased while diminishing the intensity of the average flux density in the laminated structure.

The synchronous machines proposed in literature usually employ expensive permanent magnets to produce the excitation field. Under the severe conditions of electromagnetic launch system the magnetic material may suffer demagnetization and decrease of the magnetic performance due to temperature variations and large adverse magnetic fields. For these reasons, some researchers proposed a linear reluctance synchronous motor (LRSM) as the one shown in Fig. 2.4 which does not have any permanent magnet on the mover, but exploits the different permeance of a ferromagnetic structure [36].

The design of the LRSM for electromagnetic launch applications was developed using the Patterson model and the requirements in Table 2.1 as reference. This system needs grain-oriented silicon steel to avoid excessive saturation losses in the ferromagnetic material of the mover. Indeed, when the crystals of the ferromagnetic material assume the direction of the magnetic flux higher magnetic flux densities are allowed before saturation. However, due to the large airgap, extremely high current densities are needed to assure the required magnetic flux density to produce the thrust.

2.1.2.5 LPMSM Disadvantages at System Level

One of the disadvantages of the conventional AC-fed long primary is that the whole launch path should be equipped with power electronics circuit. In order to reduce the power electronic costs and to increase the reliability of the system a

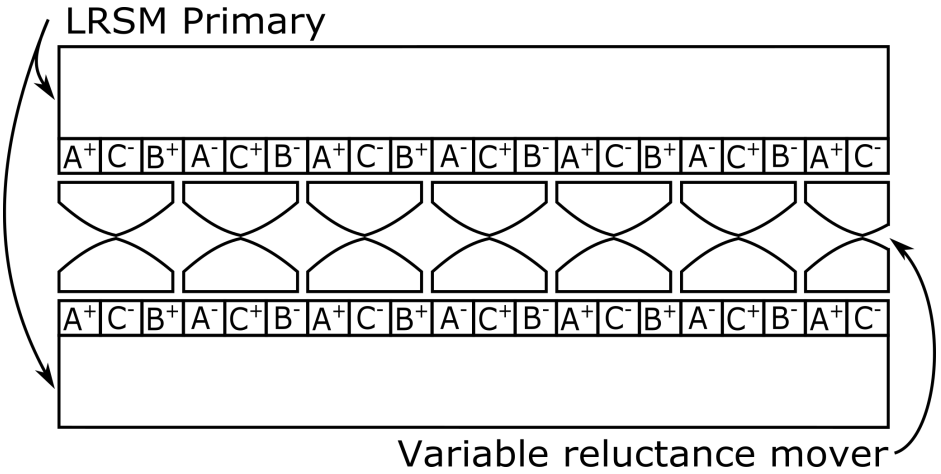

Figure 2.4: Double-sided linear reluctance synchronous motor for EML systems

linear PM DC machines was proposed [37]. However, DC machines can operate only at low voltage (<1000 V) and carbon dust is generated by the mechanical brush wear. To reduce commutation problems the voltage induced in a single coil should be shared among several commutator bar separators. This study showed that a DC machine for EML applications required higher current density and more poles than the Patterson model [30] to achieve the same thrust.

2.1.2.6 Comparison between LIM and LPMSM for EML systems

Several studies on electromagnetic launch applications compared the performance of LIMs and LPMSMs with the same geometrical features and they indicate synchrnous machines as the best motor topology for EML systems [22]. However, a good comparison cannot be made on the same stator geometry without significantly penalizing one of the topologies under investigation. For instance, the performance of LIMs tends to increase with longer pole pitches while the synchronous motor performance is improved by shorter pole pitches.

Similar studies proposed a comparison between synchronous and asynchronous motors with concentrated windings and same stator geometry [38]. In this case, LIMs are further penalized by the high harmonic content that characterizes the concentrated winding layout. Indeed strong secondary harmonics may induce intense currents in the moving conducting material which in turns may produce

significant disturbances or even arresting forces.

2.1.3 MAGLEV and Superconducting Launcher

Since the discovery of the superconductivity three main issues have prevented the widespread use of superconducting machines and technologies [39]:

- the continued developments of the technologies that use normal conductors;
- the loss of superconductivity when a superconductor is crossed by a current intensity above a specific limit;
- the very low operating temperatures at which superconductivity takes place which requires an expensive refrigeration system and an efficient insulation system.

However, the recent advances in the performance of superconducting materials and the improvements on the reliability and efficiency of refrigeration systems have led to a gradual replacement of the conventional components with their superconductive equivalent in some applications [39]. In particular, the discovery of high temperature superconductors (HTSs) that present transitional temperatures above 30 K and can operate with high magnetic fields up to 40 K allowed applications that required less energy to cool down the system [40].

2.1.3.1 The Yamanashi MAGLEV Train

To date, proposed superconducting linear motors have included both synchronous and asynchronous machines [5]. However, synchronous motors with superconducting coils (magnets) or bulk HTS materials in place of PMs have gained interest due to their high power density and good electromagnetic performance.

As an example, a superconducting synchronous motor has been adopted in trasportation industry to develop a MAGLEV train capable to reach speeds above 500 km/h [41]. The train was tested on the Yamanashi MAGLEV test line and reached the top speed of 581.7 km/h exceeding the maximum design speed. The power conversion substation of the MAGLEV system shown in Fig. 2.5 receives power from two lines at 154 kV and transforms the voltage to 66 kV [42]. A 24

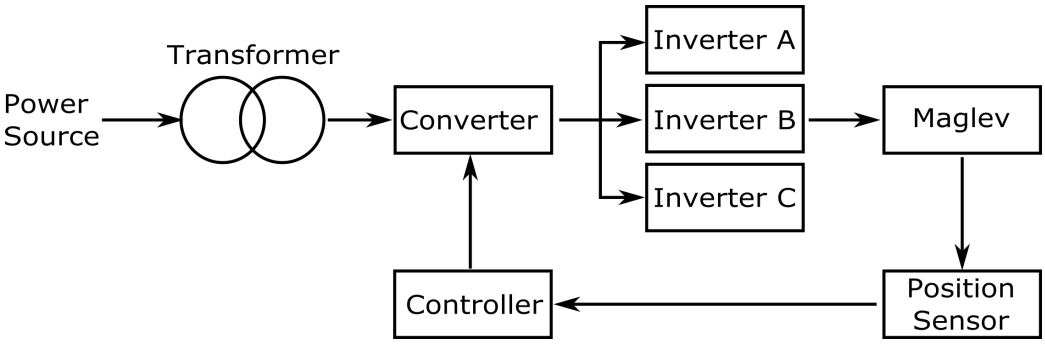

Figure 2.5: Diagram of the Yamanashi MAGLEV system

phase thyristor converter with a capcity of 69 MW changes the utility power into direct current. Three 38 MVA PWM inverter units deliver a current amplitude among 0-960 A with a max frequency of 56.6 Hz and an applied voltage between 0 and 12.7 kV according to the position and the acceleration required by the vehicle. The existing superconducting MAGLEV vehicle adopts niobium titanium (NbTi) wires cooled by liquid helium at 4 K, via pool cooling method and their radiation shield is kept at 77 K by liquid nitrogen [43]. The magnets are energized at the train depot and operate in persistent current mode.

2.1.3.2 Superconducting Motors for EML Applications

The feasibility of superconducting machines for electromagnetic launch systems has been investigated exploiting the latest HTS developments with practical magnetic fields at high current density [44]. Successful operation of HTS were verified in the temperature range from 20 K to 30 K with a liquid hydrogen environment being ideal. The research has also investigated the motor performance with liquid nitrogen as main coolant due to reduced cost of the refrigeration system. Oberly in [44] asserted that with the current performance of superconductors it would be very difficult to extend the operations of superconducting magnets to 77 K.

A superconducting linear synchronous motor (SCLSM) with bulk HTS magnets has been proposed for electromagnetic aircraft launch systems [45]. The HTS magnets were made out of Yttrium Boron Carbon Oxygen (YBCO) material that can trap a magnetic field of 3.7 T at 77 K. Since the cooled block of YBCO can produce flux densities above 2 T, an iron-core stator could not be used to

avoid saturation. The permanent magnets were embedded into the rotor frame that consisted of a non-magnetic and non-conductive material. The results presented in this research have also been compared with those of the LPMSM and LIM designed in [38] and show that the power factor of SCLSM is far superior with respect to the other topologies. However, the performance obtained at 77 K were not so attractive due to the heavy mover and to the relatively limited flux density of the magnets. Conversely, when the temperature is reduced to 40 K a much smaller mover can be used and almost unity power factor was achieved.

It is worth mentioning that the work presented in [45] does not consider the energy required to cool down the motor; this work also neglects any insulation system in the definition of the geometrical features of the motor and does not mention any additional losses due to the alternating currents induced in the superconductors especially when implementing concentrated stator windings.

Other researchers have proposed a SCLSM with bulk HTS magnets in the mover and $Bi_2Sr_2Ca_2Cu_3O_{10+x}$ HTS tapes (Bi-2223) in place of the conventional stator windings [46]. In this case all the machine is cooled down to 77 K and the stator coils are supplied with an alternating current. In this work the authors were not concerned about thermal insulation and alternating current losses in the superconducting magnets and tapes which may significantly change the geometry and the configuration of the proposed motor layout.

2.2 Research Background on Railguns

When two parallel metals (rails) connected to a power supply are short circuited by third conductor (armature) free to slide along them, an electromagnetic force acts on the armature accelerating it to the desire speed. The force is due to the electromagnetic interaction between the current that crosses the armature and the magnetic field generated by the current that flows in the rails, as shown in Fig. 2.6.

The railgun's capability to accelerate a projectile at a hypersonic velocity (>2000 m/s) has attracted the interest of US Navy and US Army to electromagnetic launch systems used as kinetic weapons with long-range, precision and high energy impact shots [47]. General Atomics successfully, developed, built and tested a 32

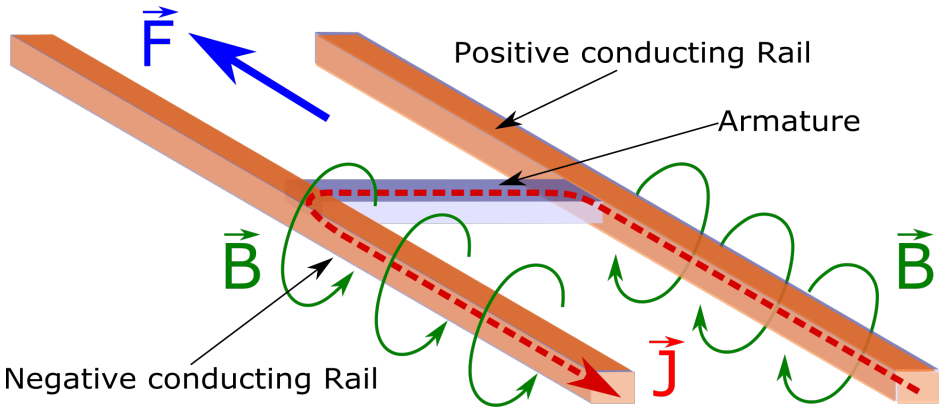

Figure 2.6: Schematic and working principle of a railgun

MJ railgun which may be used to fire a projectiles of a few kilos up to a speed of 2.5 km/s [7].

NASA has also proposed this technology as a possible solution for the next generation of space launchers. The idea is to accelerate a spacecraft horizontally on an electrified track on ground and then use wings and scramjet to reach the outer atmosphere [48].

Despite its simplicity, a railgun system requires a very high controlled current to get acceptable performance, usually from several hundreds of kA to several MA [49]. This section presents the ways many researchers have attempted to reduce the magnitude of the driving current without reducing the electromotive force generated on the armature by modifying the rail topology or the projectile shape.

This section also presents the studies on the behaviour of the material under high contact pressures and current densities to enhance the understanding of the phenomena that cause the rail wear in an EML system. Indeed, high current intensity and the harsh conditions at the rail-armature interface can also cause serious damages to the rails after just a few firings.

2.2.1 Railgun Performance Improvement

Research on electromagnetic launch systems based on the railguns principle has investigated the possible ways to improve the total thrust for a given magnitude

of current. The thrust $\vec{F}$ from a railgun is determined by the calculation of the Lorentz's force on the armature as

$$\vec{F} = \iiint_v \vec{J} \times \vec{B}\, dv = \vec{I} \times \int \vec{B}\, dl \tag{2.1}$$

where v is the volume of the armature, $\vec{J}$ is the rated current density, $\vec{I}$ is the driving current, integral of the current density over the armature cross section, and $\vec{B}$ is the magnetic flux density generated by the conductive rails as shown in Fig. 2.6.

Another expression of the railgun thrust is based on energy stored by the inductance L of the system:

$$E_L = L\frac{I^2}{2} \tag{2.2}$$

Since the interaction between the current and the magnetic field produces a force that causes a displacement of the armature, the energy variation of the system can be expressed as

$$E_F = \int \vec{F} \cdot \vec{ds} \tag{2.3}$$

Since $E_L = E_F$ based on the principle of conservation of energy, an expression of the thrust can be derived:

$$F = \frac{1}{2}L'I^2 \tag{2.4}$$

where L' is the inductance gradient. As it will be shown in this section, past researches have considered effects of armature and rail geometry on the current distribution to maximize the inductance gradient which is proportional to the thrust according to eq. 2.4.

One of the main geometrical parameters that has an impact on the value of the inductance gradient is the shape of the rail cross section [50]. Two commonly used rail cross sections have rectangular and circular shapes. The performance of the two rail cross sections were simulated by FEM assuming equal surface. Due to the different current distribution and magnetic field a circular section has a smaller inductance gradient and lower efficiency with respect to rectangular rails.

The inductance gradient is also affected by the rail aspect ratios w_r/d_r and h_r/d_r,

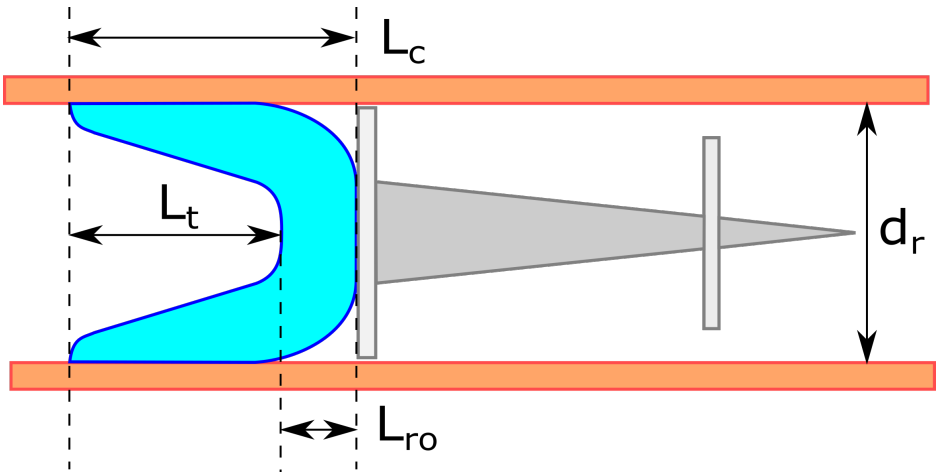

Figure 2.7: Schematic of the monolithic C-type armature

being d_r the distance between the rails and the w_r, h_r the width and the height of the rectangular cross section respectively [51]. The effect of different aspect ratios was tested on the railgun inductance gradient, magnetic field and total thrust. 2D finite element analysis of the copper rails with one MA of driving current showed that the lower is the rail aspect ratio w_r/d_r the higher are the rail performances. The analysis of the performance of the rails with different height demonstrated that and optimum condition was reached when $h_r/d_r = 0.5$.

As well as the rail geometry affecting the EML performance, the type of armature plays an important role [52]. The right type of armature is often selected to reduce the armature resistance and achieve high system efficiency. The armature layout can be either block-type armature shown in Fig. 2.6 or monolithic C-type armature shown in Fig. 2.7. The block-type armature is considered the simplest configuration while the C-type armature achieves the best performance and is retained to be more practical to maintain good sliding contact and reduce the rail wear over the acceleration.

Researchers at The University of Texas have investigated how the C-type armature geometry affects the current density distribution and the gradient inductance of the railgun system [53]. In particular the effects of the rail overhang, the root ratio (L_c/L_{ro} in Fig. 2.7) and the C-type ratio (L_t/L_{ro} in Fig. 2.7) were observed. It was found that the current density distribution over the rail/armature interface significantly changed with some of the geometrical parameters. As the overhang

ratio increased the current distribution moved to the front and the sides of the armature causing the inductance gradient L' to decrease. The inductance gradient also seemed to have no dependence on the root ratio and C-type ratio that characterized the armature shape.

The independence of the gradient inductance of the projectile geometry was analytically proven and numerically validated by the 3D finite-element analysis presented in [54].

The inductance gradient is not only affected by the geometry of the railgun, but also by the magnetic permeability and electrical conductivity of the rail material [55]. 2D FEA showed that high values of the magnetic permeability and low values of the electric conductivity cause an increment of the flux density between the rails. Consequently, to increase the gradient inductance the conductivity must be decreased while the permeability must be increased. However a material with high conductivity allows for significant ohmic loss reduction, whereas high magnetic permeabilities mean that the current flows across a narrower area resulting in increased losses.

As seen so far, L' has been increased by either adjusting the geometrical features of the railgun or adopting a rail material with the best compromise between electrical conductivity and magnetic permeability. Much more significant improvements were achieved replacing the conventional railgun configuration in Fig. 2.6 with different railgun architectures. These new railgun topologies were first introduced by McNab in [56] and are known under the names *augmented railgun* and *multi-turn railguns*, as shown in Fig. 2.8. The Institute for Advanced Technology of the University of Texas has tested these machines proving their improved performance [6].

An augmented railgun increases L' by adding one or more pairs of rails close to the main one. With the same current flowing in N_r rail pairs, the force acting on the projectile is proportional to $(2N_r - 1)I^2$ [57]. A series-connected augmented railgun has the advantage of reducing the current through the main rails and armature to achieve the same thrust, thereby reducing the wear of the rails. At the same time, an augmented railgun with $N_r = 2$ delivers three times the thrust of a conventional railgun when it is supplied with the same current. These advantages are offset by the added mechanical and electrical complexity and by the increased

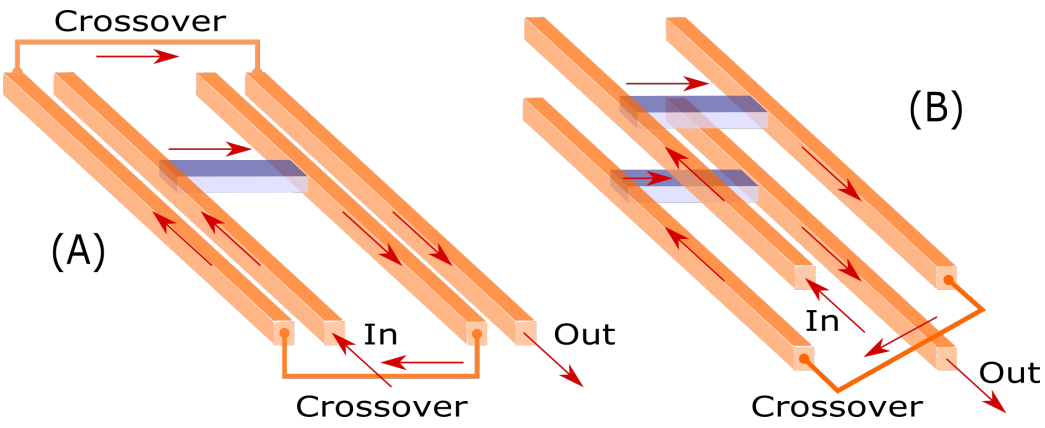

Figure 2.8: Schematic of augmented railgun (A) and of the multi-turn railgun (B)

resistive losses.

A multi-turn railgun increases the gradient inductance adding rails pairs to the system, each pair with its own armature. In this case, the propulsive force is proportional to $N_r^2 I^2$ [57]. The multi-turn railguns have the advantage to effectively reduce the current density at the interface for the same driving force. The multi-turn has also the advantage of dividing the driving force between more rails [49]. Beside the several advantages, this architecture suffers a degradation of the efficiency due to longer current paths and higher resistive losses.

Augmented and multi-turn railguns require an insulation between rails to prevent arcing due to the voltage difference between rails [6]. Since the multi-turn railgun has two armatures with different voltages, the moving conductors must be insulated from each other for the same reason. Conversely, augmented railguns use a single armature that does not need extra insulation.

The crossovers of augmented and multi-turn railguns shown in Fig. 2.8 are components which carry the driving current across two parallel rails. Since the crossovers transfer the same current of the armature, they experience a repulsive force equal to roughly the 75% of the railgun thrust [57]. The repulsive force must be handled by a containment structure which must be cable of absorbing the impulsive load. The crossovers may also represent an obstacle that makes the reload procedure more difficult.

2.2.2 Sliding Interface Phenomena in Railguns

The rail/armature interface is the place of many physical phenomena that impact the system performance and cause severe damage to the gun after few firings [47]. This section illustrates the research that has been developed to describe the underling physics and nature of the interface phenomena with the purpose of reducing the wear of the railgun during operation.

The rail and armature interaction cannot be characterized without the definition of their materials [58]. Copper is the ideal candidate as rails and armature material for its low resistivity, high melting temperature and high thermal conductivity. Nevertheless, aluminium alloys are the preferred as armature material for their low density and relatively good electrical properties. Aluminium can be also used as lubricant since at the rail/armature interface liquid metal forms as a result of frictional and Joule heating.

In order to satisfy the requirement of a good electrical couple, the behaviour of copper and aluminium was studied under high current densities and contact pressures [58]. The aim was to determine a model of the additional electric resistance across the sliding surface. The contact resistance decreases with increasing current density, but a little difference was found between two different contact pressure.

Since direct observation of the active interface is very difficult, the liquid aluminium flow from the armature has been characterized from post-launch metal deposit studies to describe the melting process, the involved chemical reactions and the heat load along the rails [59]. These analysis allowed the understanding of the rail damage mechanism which is strictly related with the metal deposit formation process. When the deposit solidifies and stays attached to the copper, the rail surface remains smooth. However, periodically the thickest parts of the metal layer detach from the copper surface, causing rail damage.

When a metallic conductor is subject to current density of approximately 10^4 A/mm^2 a significant atomic flux is set up by the electron flow and matter is transferred across the conductive region by diffusional transport [60]. This phenomenon, known as electro-migration (EM), causes the debris on the negative rail to become progressively thicker than those on the positive rail. Thus, EM en-

hances the damage of the negative rail. In order to reduce any potential adverse impact of EM during the railgun operations, it was proposed to regularly switch the polarity between consecutive shots.

The current distribution on the cross section of both rails and armature is not uniform due to the combination of skin effect and velocity skin effect [61]. Skin effect occurs in railguns used as kinetic weapons since the current is applied as an impulse that lasts for few milliseconds. Due to the high frequency of the impulse the current tends to flow on the outer surfaces of the conductors. The velocity skin effect is a type of diffusion time phenomenon that occurs when there is relative motion between two conductive materials. Because of the high velocity of the armature relative to the rails, the current tends to flow through a narrow constriction at the corner of the rail/armature interface. The current and magnetic field distribution due to velocity skin effect were modelled in steady state in [62] and in [63].

The current crowding due to skin effect and velocity skin effect is the first cause of melting the material at the contact surface [64]. The peak armature temperature is associated with the location of the peak current density according to the experimental results.

The effect of the current crowding was also investigated to determine the fundamental velocity limits based upon Joule heating for different rail/armature configurations and materials [65]. According to this model, the maximum speed of the projectile is reached when the whole rail/armature interface warms up to the melting temperature of the armature material.

The real contact between rail and armature is accomplished by microscopic asperities on the conductor surfaces [66]. The presence of current conduction through the continuous making and unmaking of contact gives rise to magnetic forces that tend to separate the armature from the rails. Metal armature contacts often transit from low voltage to a high voltage with arcing and considerable rail damage. The transition take place when the entire contact surface reaches the vaporization temperature which can be predicted using the model of the rail/armature contact presented in [66].

The heat load on the interface surface is exacerbated by the friction between armature and rails [67]. In presence of high current densities, local melting, metal

vapour and arcing the prediction of the friction coefficient can be very difficult. The coefficient of friction in the presence of high current density was measured using a modified mesoscale friction tester. When similar contact pressure are applied and current is flowing, the friction coefficient was found to be lower than the case whit no supplied current.

Materials subject to heat pulses of short duration and high intensity are exposed to large mechanical forces that can leads to plastic deformations of the material [68]. The mechanical properties measured under thermal equilibrium are likely to be very conservative in railgun applications. Experimental tests were use to characterize the mechanical response under short duration heating.

A similar investigation was carried out to quantify the effects of thermal loading on the life cycle of the cladding material on the rail surface [69].

2.3 Railgun for Civil EML Applications

This section introduces a simplified one-dimensional model of a railgun to investigate whether is possible to employ this technology to efficiently launch an heavy object like an aircraft A320-200 to a speed much lower than that reached by kinetic weapons.

The model that aims to estimate the railgun performance during the launch is based on the following assumptions:

- The simple railgun configuration in Fig. 2.6 is considered;
- The rails are made out of copper and have a rectangular section 20 cm high (h_r) and 10 cm wide (w_r);
- The armature has the same geometry of the rails, has a length d_r of 2 m and is made out of copper as well. The block-type armature is considered for simplicity;
- The current is uniformly distributed in the rails and armature cross section. Current crowding caused by skin effect and velocity skin effect is not considered;

- The rail/armature interface is characterized by an ideal electric contact with no resistance;
- The friction between armature and rails is neglected;
- The magnetic field is assumed to be perpendicular to the armature and to the current direction at any point within the volume occupied by the armature itself.

The required thrust F_x reported in Table 3.8 is considered to define the launcher thrust requirement. The thrust that the railgun has to deliver also includes the force required to accelerate the armature and the framework that connects it to the aircraft undercarriage. The total thrust can be computed as:

$$F_{xc} = F_x + 3m_a \cdot 0.6\,G \tag{2.5}$$

where the number 3 is introduced to consider the weight of the structure connecting the armature to the aircraft, $0.6\,G$ is the required acceleration and m_a is the mass of the armature that can be calculated as

$$m_a = \rho_{Co} d_r h_r w_r \tag{2.6}$$

where ρ_{Co} is the copper density.

The one-dimensional model of railgun is based on an iterative algorithm that at each time steps calculates the electromagnetic parameters and the performance of the launcher. The algorithm within each iteration proceeds as follow:

1. The mutual inductance of the rails depends on the shape of their cross section and on the distance between them. Since the sizes h_r and w_r are much smaller than the distance d_r, the formula for the mutual inductance of two parallel conductive filaments with negligible thickness [70] can be safely applied to get an acceptable approximation of the rails mutual inductance as

$$M_r = \frac{\mu_0}{2\pi}\left[s \ln\left(\frac{s+\sqrt{s^2+d_r^2}}{d_r}\right) - \sqrt{s^2+d_r^2} + d_r\right] \tag{2.7}$$

where s is the distance travelled by the armature during the motion.

2. The self inductance of a single rail L_r can be computed using eq. 2.7 by replacing the armature length d_r with the geometric mean distance of the rectangular cross section. The calculation of the geometric mean distance of a rectangle is not simple, but the exact expression is known as

$$g_{md} = k_{gmd}(h_r + w_r) \tag{2.8}$$

where the value of the constant k_{gmd} depends on the aspect ratio of the rectangle. For the aspect ratio of rail cross section under investigation the constant is $k_{gmd} = 0.2236$ [71].

3. The self inductance of the railgun can be computed from the self inductance of the single rail and the mutual inductance of the rails in eq. 2.7 as [70]

$$L = 2(L_r - M_r) \tag{2.9}$$

4. The inductance gradient can be computed from the definition of spatial derivative as

$$L' = \frac{\partial L}{\partial x} = \frac{L^n - L^{n-1}}{s^n - s^{n-1}} \tag{2.10}$$

where n represents the current time step and $n-1$ represents the previous time step.

5. The current required to produce the rated thrust can be determine from eq. 2.4 as

$$I = \sqrt{\frac{2F_{xc}}{L'}} \tag{2.11}$$

6. The average magnetic field over the armature can be computed from the expression of the Lorentz force in eq. 2.1 as

$$B = \frac{F_{xc}}{I\, d_r} \tag{2.12}$$

7. When a conductor moves in a magnetic field a voltage appears at its terminals and a current flows as to generate a magnetic field in opposite direction of the

external magnetic field. The results is a braking affect that tends to slow down the conductor. In railguns the voltage provided by the power supply has to overcome the induced voltage to prevent any breaking effect and to allow the rated current to flow for the whole duration of the launch. The induced voltage can be computed as

$$U_{ind} = V B d_r \tag{2.13}$$

where V is the speed of the armature and of the connected aircraft.

8. The electric resistance of the system changes during the acceleration for the longer path that the rated current has to travel to close the electric circuit. The value of the resistance at each time step is computed as

$$R = R_0 + \frac{1}{\sigma_c} \frac{2s + d_r}{h_r w_r} \tag{2.14}$$

where σ_c is the copper conductivity and R_0 is the resistance of the power supply terminals.

9. The voltage applied to the rails that allows the rated current I to flow is

$$U = R \cdot I + U_{ind} \tag{2.15}$$

10. The input power is $P_i = U \cdot I$

11. The output power is $P_o = F_{xc} V$

12. The efficiency of the railgun is $\eta = P_o / P_i$

This procedure is repeated iteratively until the electromagnetic launcher end-speed is reached.

The time variation of the current that flows into rails and armature is reported in Fig. 2.9a. The peak current intensity is reached at the end of the launch and correspond to a current density of about 43 A/mm^2 in the hypothesis of homogeneous current distribution over the rail cross section. Since the current is applied continuously for 15 seconds and cannot be represented by an impulse as in kinetic weapons, the skin effect should not affect the current distribution over the

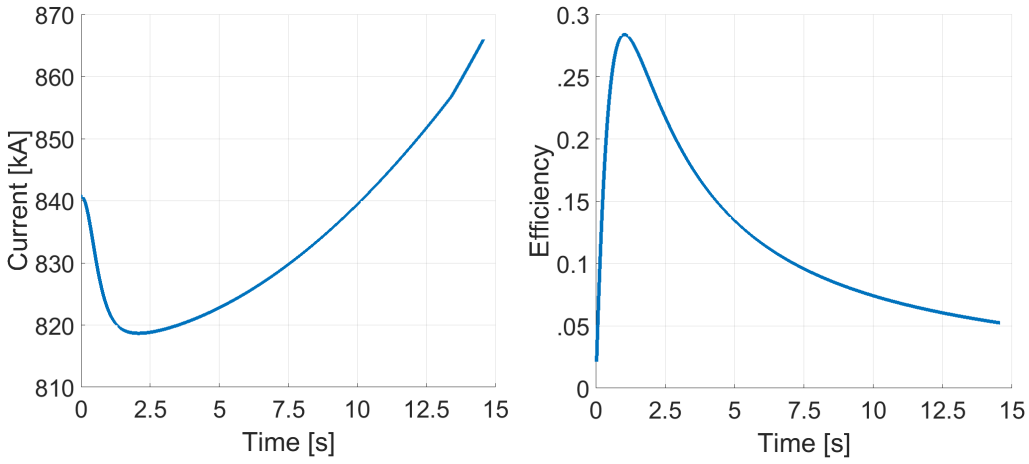

(a) Current (b) Efficiency

Figure 2.9: Time variation of current and efficiency of a conventional railgun

rail cross section. On the contrary, the velocity skin effect compels the current flow across a narrower area increasing the current density, the electric resistance and the related Joule losses especially in proximity of the armature trailing edge. However, the end-speed of the launcher is two order of magnitude slower than the projectile ejection speed of kinetic weapons, and the current crowding due to the velocity skin effect is expected to be less relevant.

The efficiency of the electromagnetic launcher is reported in Fig. 2.9b and reaches a peak of 0.284 after approximately 1.0 seconds. The decrease of the efficiency is mainly due to the increase of the resistance with the length of current path. The efficiency of the system is so low that almost 680 MW are required to the power supply at the end of the launch. Even neglecting contact resistance, friction, velocity skin effect and the degradation of the electrical properties with the Joule heating at rail/armature interface, satisfactory electric performance are not achieved.

It may be argued that the implementation of augmented or multi-turns railguns might lead to an increase of the efficiency for the reduced current required to achive the same thrust. Indeed, even considering that the resistance doubles, the augmented and multi-turns railguns can achieve an efficiency 1.5 and 2 times greater than the one shown in Fig. 2.9b respectively. However, after the initial peak, the efficiency would inexorably decrease as for the simple railgun configu-

ration. Another possible alternative to improve the performance is the *distributed energy storage arrangement* in which multiple terminals are located along the rails so that the proper current amplituted can be provided at the right time and place to maximize the efficiency [56]. This configuration might be capable of performing with a constant efficiency up to 40% for the whole duration of the launch, but the losses will always largely exceeds the output power requiring a supply with an enormous capacity.

2.4 Conclusion

The research on asynchronous and synchronous linear motors for military aircraft launch systems presented in Section 2.1 suggests that these technologies could also be viable solutions for civil aircraft launch applications. The installation of an electromagnetic catapult on board contemporary Ford-class aircraft carriers bolsters the research on linear induction and synchronous motors for a launcher with similar power requirements and for civil applications.

In a similar way the results achieved in the design, construction and tests of the Yamanashi MAGLEV train indicates another possible technology that could be adopted for a civil aircraft launcher. Additionally, the research carried out on superconducting linear motors for EML systems is rather poor, inconclusive and often limited to the evaluation of the motor electromagnetic performance. Therefore, the work presented in this thesis is particularly concerned with the thermal management of the superconducting launcher and the additional energy required by the refrigeration system.

The simplified model of a railgun for civil EML application presented in Section 2.3 proves that, despite its simplicity, this technology achieves very low efficiency and cannot be used for the launching of civil aircraft unless very large power sources are available. Since more efficient EML systems can be built, the research on railguns to assist civil aircraft take-off was not further developed.

Since the application of an EML system to civil aircraft launching is completely new, before proceeding with the design of the possible linear motor topologies, a methodology to define the catapult requirements and to quantify the possible benefits of assisted civil aircraft take-off is introduced in the next chapter.

Chapter 3

Take-off Segment Analysis

This chapter presents the take-off analysis of an Airbus A320-200 aircraft and the impact of electromagnetic catapult on the take-off performance. Initially, the definition of the take-off distances and speeds is presented together with the description of the take-off procedure. One of the main objective of this chapter is to determine the requirements of the electromagnetic catapult which will be used to size synchronous and asynchronous launchers in the next chapters.

The take-off analysis algorithm is reported in order to show the potential of reducing runaway length using the electromagnetic catapult. The take-off analysis outcomes for an A320-200 aircraft accelerating with and without the launcher assistance are also compared to determined the fuel saved during take-off and the exhaust emission reduction at ground level. In this contest, the possible annual cost saving, noise emission and pollutant emission reduction are estimated in a busy city airport like Heathrow.

Since actual engines are sized to allow the aircraft to take-off, electromagnetic launch systems allow the installation of engines with a reduced cross section and a lower rated thrust. The engine thrust reduction does not imply a sensible extension of the required runway length since the catapult is responsible to provide the aircraft with the proper speed. The consequent aircraft weight and fuel consumption reductions bring significant saving for airlines in terms of annual operational cost.

The principles of take-off field length determination reported in this chapter ap-

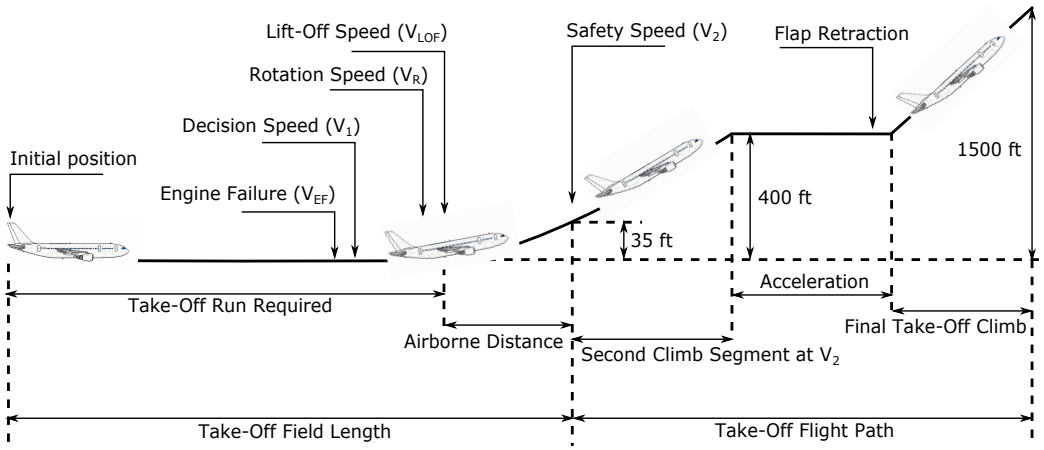

Figure 3.1: Take-off procedure and parameters for a twin-engine civil transport aircraft

ply to civil transport aircraft whose maximum take-off weight (MTOW) is bigger than 5760 kg, but the methods of analysis may well be used for other aircraft categories, e.g. light aircraft.

3.1 Definition of Take-Off Speeds and Distances

The lift-off and the initial climb are two of the most critical safety phases of a civil aircraft flight. The combined analysis of both phases can be referred to as the aircraft take-off performance analysis. This analysis allows an estimation of take-off distances and take-off speeds as defined by the Federal Aviation Regulation (FAR) [72]. The speeds and distances associated with the take-off analysis are shown in Fig. 3.1.

In order to determine the impact of the catapult on the take-off performance and on the fuel consumption it is important to define the take-off characteristics of the reference aircraft, the Airbus A320-200.

The take-off phase starts when the aircraft is in standstill position at the beginning of the runway and terminates when the aircraft reaches the altitude of 1500 ft. The Take-Off Distance (TOD) is the distance needed to accelerate the aircraft to the lift-off speed V_{LOF} with all the engines operative, plus a portion of the airborne distance until the height of 35 ft (screen altitude). V_{LOF} is the airspeed at which the aircraft first becomes airborne. TOD must not exceed the take-off

ground available.

The Take-Off Field Length (TOFL) in Fig. 3.1 is the greatest distance between the TOD and the Balanced Field Length (BFL). BFL is the Emergency Accelerate-Stop Distance (EASD) covered when the engine failure occurs at the critical engine failure speed V_{EF}. In general, the EASD is the distance covered by the aircraft until any speed $V_x \leq V_{EF}$ when an engine critical failure occurs and the pilot decides to abort the take-off, plus the distance to come to a standstill by means of braking. The speed V_{EF} is determined considering the situation where the EASD coincides with the TOD with an engine failure. EASD must not exceed the length of the take-off ground plus the clearway (if present).

The maximum speed at which the pilot can abort the take-off is usually called the decision speed V_1 [72]. This speed is determined by the aircraft manufacturer considering V_{EF} and the speed gained in One-Engine-Inoperative (OEI) condition during the time interval between the critical engine failure and the reaction of the pilot. When the aircraft speed exceeds V_1 the pilot must proceed with the lift-off phase even if one engine is inoperative.

In establishing take-off performance the operational flight speeds must have a specified safety margin relative to the stalling speed V_s. Stall is an aerodynamic phenomenon associated to downstream flow separation over the aircraft wing. Stall does not depend on the air speed, but on the angle of attack which is the angle between the chord line of the airfoil and the vector representing the relative motion between the aircraft and the air through which the airplane is moving. When the angle of attack exceeds its critical value the flow separates, the lift force decreases and the aircraft loses altitude.

In order to understand the reason why a stall speed and not a stall angle is considered, the expression of lift force L generated over the A320's wings and the dependency of the lift coefficient C_L on the angle of attack become useful. The lift force is defined as

$$L = \frac{1}{2}\rho_{Air} S_w C_L V^2 \tag{3.1}$$

where ρ_{Air} is the air density, S_w is the reference wing surface and V is the speed of the aircraft with respect the surrounding air. The dependency of the lift coefficient

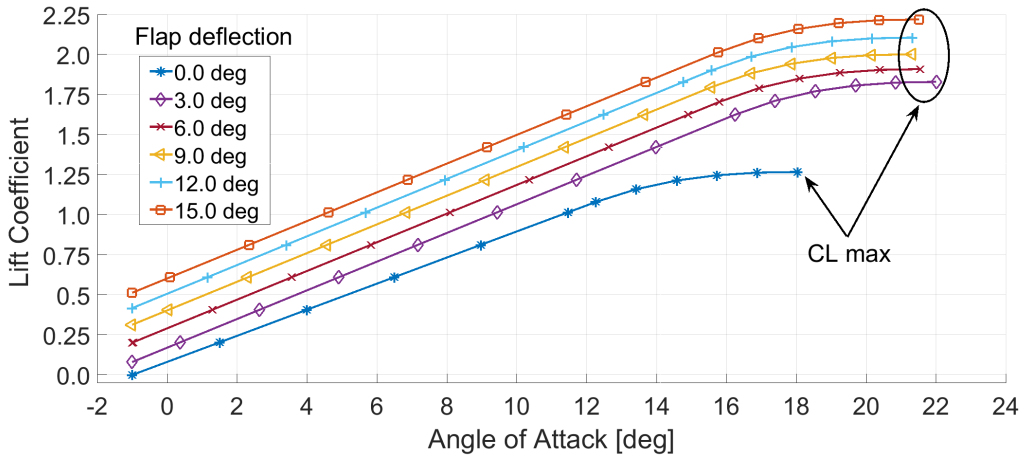

Figure 3.2: Low speed lift polar of an A320-200 aircraft for several flap deflections [73]

C_L of the A320 aircaft on the angle of attack for several flap deflections is shown in Fig. 3.2 [73]. The critical angle of attack for each flap deflection is represented by the last point of the respective curve in Fig. 3.2 where the lift coefficient reaches its maximum.

When a flying aircraft loses speed at constant altitude (constant ρ_{Air}), the same lift force can be achieved increasing the lift coefficient as it can be deduced from eq. 3.1. Fig. 3.2 shows that the lift coefficient for a given flap deflection can increase only whit higher angles of attack. When the aircraft speed decreases to the point that the angle of attack reaches its critical value, stall occurs. The speed that generates a lift force equal to the aircraft weight with the maximum lift coefficient at the critical angle of attack is called stall speed V_s.

Using eq. 3.1 and the maximum lift coefficient C_{Lmax} in Fig. 3.2, the stall speed for each flap deflection can be determined as

$$V_s = \sqrt{\frac{2L}{\rho_{Air} S_w C_{Lmax}}} \tag{3.2}$$

Other useful reference speeds that are needed to study the impact of the catapult on the take-off phase can be defined as:

- Minimum Control Speed V_{MC}: the lowest airspeed at which the aircraft manufacturer has proved it to be possible to control the aircraft with one en-

gine inoperative using the rudder control alone with the maximum available power from the remaining engines. This speed will not be considered in the evaluation of the take-off performance, but it is mentioned here because it represents a requirements for the take-off safety speed and the rotation speed;

- Take-off Safety Speed V_2: the aircraft speed over the screen height of 35 ft. V_2 must be greater than the minimum take-off safety speed V_{2min} which must not be less than

$$V_{2min} = 1.2 \cdot V_s \tag{3.3}$$

for safe operations above the stall speed V_s. This limitation provides the pilot with some measure of freedom to manoeuvre avoiding stalling due to vertical wind gusts. In order to grant enough controllability V_2 must be greater than 110% of V_{MC} [72]. Since V_{2min} is always considered in take-off performance analyses, it is commonly identified using the more generic symbol V_2.

- Rotation Speed V_R: the reference speed for the pilot to raise the nose landing gear. The nose is rotated when the pilot decides to proceed with take-off even in case of engine failure. Thus V_R must be greater than V_1 and greater than 105% V_{MC} to guarantee aircraft controllability.

The rotation speed V_R represents the end-speed requirement for the electromagnetic catapult and when it is reached the aircraft detaches to continue the take-off procedure. The mover of the launcher can be connected to the nose landing gear, as is done with steam catapults for military applications. When V_R is reached the aircraft detaches and completes the nose rotation before taking off. It may be argued that the catapult should be connected to the main landing gear to accelerate the aircraft even further, to lift-off speed V_{LOF} and gain the maximum benefit from the catapult installation. The main landing gears are connected to the central spar, which is the strongest point of the aircraft structure. If the catapult would be connected to the main landing gear the aircraft framework would not have to undergo significant modifications to sustain the additional load from the catapult.

The nose landing gear is designed to sustain only landing and push-back loads and would have to be reconfigured to withstand the catapult force. However, the main landing gears are positioned behind the aircraft's center of gravity and therefore a pulling force on this point is intrinsically unstable.

For safety reasons the catapult is assumed to be engaged with the nose landing gear until V_R is reached. It is accepted that this system will require some essential changes to the aircraft's front undercarriage framework.

3.2 Take-off Performance Analysis

3.2.1 Climb Out Gradient

To ensure a sufficient level of safety the take-off procedure is investigated considering a possible engine failure occurring at any stage. The take-off requirements with one-engine-inoperative (OEI) are so demanding, that the analysis of the aircraft performance in all-engine-operative (AEO) condition is not necessarily required.

The first step in estimating the take-off performance is to establish the climb out gradient at 35 ft γ_2 and the respective flap deflection during the initial acceleration with OEI. The minimum climb out gradient requirement considered during the take-off design procedure ensures that the aircraft crosses the 35 feet obstacle at the end of the runway with enough clearance and with a sufficient thrust excess to allow safe operation even with an engine failure. The flap deflection affects the performance of the wing and is proportional to the aerodynamic lift and drag. The rated flap deflection assures enough lift force and minimum drag to allow a safe flight even with OEI.

The minimum climb out gradient requirement γ_{2Req} at speed V_2 with retracted landing gear can be computed as [72]:

$$\gamma_{2Req} = 0.018 + 0.003 \cdot N_{engine} \tag{3.4}$$

where N_{engine} is the total number of engines. A second climb out gradient requirement is defined in eq. 3.5 for lift-off when extended landing gears cause an

additional drag force.

$$\gamma_{LOF\,Req} = 0.002 \cdot (N_{engine} - 2) + 0.001 \tag{3.5}$$

The coefficients in eqs. 3.4 and 3.5 are determined on a statistical basis by considering a deviation from the nominal flight path of 0.8%, 0.9% or 1.0% for aircraft with 2, 3 or 4 engines respectively. Normally the requirement with landing gear retracted in eq. 3.4 is considered for take-off distances and speeds estimation since it is more demanding than the climb out gradient requirement with landing gear extended in eq. 3.5. Nonetheless, the climb gradient requirement at lift-off $\gamma_{LOF\,Req}$ is later verified by take-off analysis procedure.

A useful general term for specifying the climb performance is the Specific Excess Power, SEP:

$$SEP = \frac{T-D}{W}V = \frac{V}{G}\frac{\partial V}{\partial t} + \frac{\partial h}{\partial t} \tag{3.6}$$

where T is the overall thrust, D is the aerodynamic drag, W is the aircraft weight, G is the gravitational acceleration and h is the aircraft altitude. The specific excess power represents the amount of available power per unit of weight. For horizontal flight and a load factor $n = L/W \sim 1$, the SEP is equivalent to the rate of increase of kinetic energy and is a measure of the time required to accelerate from one speed to another. In case of a specified climb rate for $n = 1$ and steady flight (no acceleration), the climb gradient is

$$\gamma = \frac{1}{V}\frac{\partial h}{\partial t} = \frac{SEP}{V} \tag{3.7}$$

Since the aircraft does not accelerate from the screen altitude to 400 ft as shown in Fig. 3.1, the derivative $\partial V/\partial t$ in eq. 3.6 is zero during this phase and the climb out gradient γ_2 can be expressed using eq. 3.7 as

$$\gamma_2 = \frac{SEP}{V} = \frac{T-D}{W} \tag{3.8}$$

Eq. 3.8 shows that to calculate the climb out gradient at screen altitude it is necessary to determine the thrust and the drag force in OEI conditions at V_2. The procedure to accurate estimate these quantities is discussed in Sections 3.2.1.1

and 3.2.1.2.

3.2.1.1 Engine Thrust

The engine thrust figures provided by engine manufacturers are usually measured in a controlled environment with a standard atmosphere and anchoring of the engine on the ground. Under these conditions the engine performance in terms of thrust are maximized. During a flight, pressure, temperature and air speed change continuously and the thrust of the engines may be sensibly reduced. This section aims to show the methodology that can be applied to get an accurate estimation of the thrust available at any flight condition.

When the aircraft speed and altitude change, the engines deliver different levels of thrust according to the rating the pilot can select for each particular flight conditions. The most important engine ratings are:

- Maximum Take-Off rating (MTO): this is the maximum thrust the engine can deliver for 5 minutes during the take-off phase. The peak thrust is achieved in static conditions at sea level and is usually reported in engine's public datasheet;

- Maximum Continuous Thrust rating (MCT): outside the take-off phase MCT defines the maximum thrust the engine can deliver continuously within specific limits in terms of engine speed and temperature;

- Maximum Climb rating (MCL): the manufacturers often recommend the use of this specific rating during the climb phase. It may be the same or very similar to the MCT;

- Maximum Cruise rating (MCR): this is the rating that should be ideally used during cruise, but a pilot actually uses the thrust required to maintain altitude and speed to meet the air traffic control requirements.

- Flight Idle rating (FID): the idle rating is the minimum thrust that can be used when the aircraft is in flight. This rating is also used to defined the fuel consumption during the airport ground movements when the engine runs

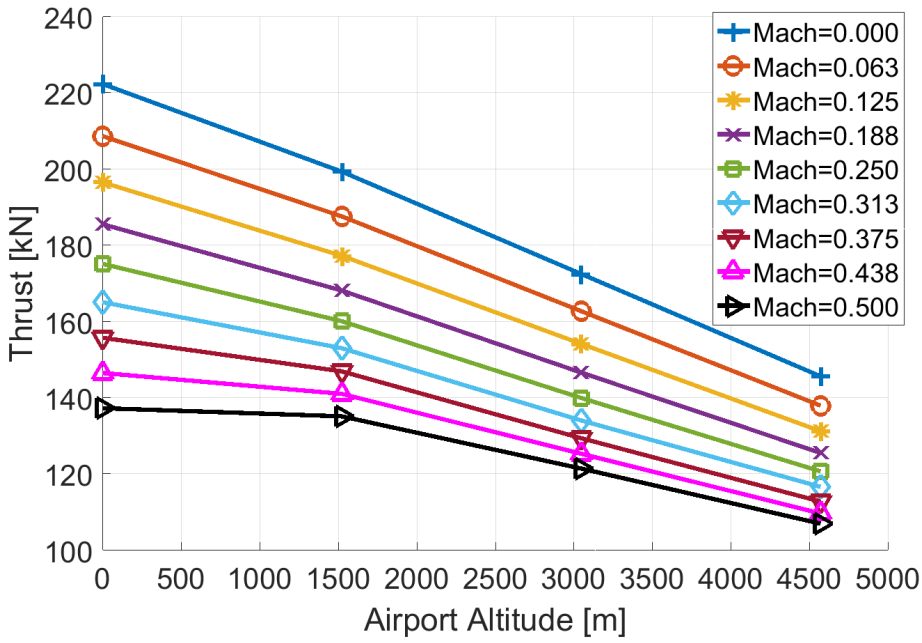

Figure 3.3: MTO thrust rating for several Mach number in ISA+0K conditions for the two CFM56-5-A1 engines installed on A320-200 aircraft [73]

to supply the secondary utilities, for example hydraulic and electric power systems.

The engine rating that is involved in take-off envolope is the MTO rating. The A320-200 aircraft has two CFM56-5-A1 turbofan engines from CFM International whose maximum certified thrust at sea level is 111.2 kN [74]. The MTO rating of the two CFM56-5-A1 engines is shown in Fig. 3.3. The curves indicate the variation of the thrust with the altitude and the Mach number M which is the ratio between the aircraft velocity and the speed of sound c_{air}.

The thrust profiles in Fig. 3.3 were evaluated from experimental tests in a International Standard Atmosphere (ISA): atmospheric pressure 101325 Pa, air density 1.225 kg/m^3 and air temperature 20 °C [75]. Though the atmospheric conditions during take-off may differ from the ISA depending on altitude and latitude of the airport and on the weather conditions. The deviation from the standard conditions is expressed as a temperature delta, either in Kelvin or in degree Celsius. Engine manufacturers usually provide several sets of curves like the one in Fig. 3.3 for each engine rating and specific atmospheric conditions. The impact of the tem-

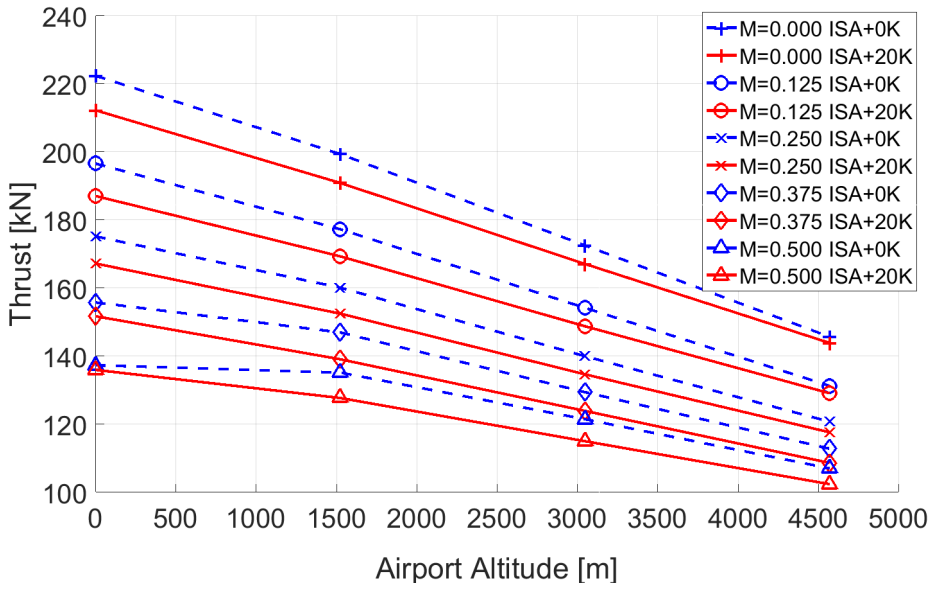

Figure 3.4: Comparison between thrust profiles of CFM56-5-A1 MTO rating at ISA+0K and ISA+20K [73]

perature on the MTO thrust performance of the CFM56-5-A1 at ISA+0K and at ISA+20K can be seen in Fig. 3.4. In particular Fig. 3.4 shows that the engines thrust does not just decrease only with the airport altitude (air density), but with the environmental temperature as well. Despite the thrust reduction under adverse environmental conditions, the take-off performance analysis is always performed considering standard atmospheric conditions (ISA+0K) whilst the effects of altitude and temperature are later evaluated.

In order to determined the engine thrust at the screen altitude from the data in Fig. 3.3 the respective Mach number has to be calculated. The Mach number at speed V_2 is by definition

$$M_2 = \frac{V_2}{c_{air}} \tag{3.9}$$

where the speed of sound can be computed treating air as an ideal gas like in the most of the applications:

$$c_{air} = \sqrt{\frac{\gamma_{Air} p_{Air}}{\rho_{Air}}} \tag{3.10}$$

where p_{Air} is the atmospheric pressure and γ_{Air} is the isentropic expansion factor, i.e. the ratio of specific heats of a gas at constant pressure and of a gas a constant volume. Even though eq. 3.9 will be used to defined the Mach number at several key points along the take-off path, at this design stage the speed V_2 is not available and the definitions of dynamic pressure q_{Air} can be used in place of eq. 3.9 to calculate the Mach number.

$$q_{Air} = \frac{\gamma_{Air}}{2} p_{Air} M^2 \qquad q_{Air} = \frac{1}{2}\rho_{Air} V^2 \tag{3.11}$$

Combining eq. 3.1 with the second expression of the dynamic pressure in eq. 3.11 and inserting the result in the first expression of the dynamic pressure in eq. 3.11 yields

$$M_2 = \frac{2L}{C_{L2} S_w \rho_{Air} \gamma_{Air} p_{Air}} \tag{3.12}$$

where C_{L2} is the lift coefficient at V_2.

The computation of the lift coefficient C_{L2} and of the respective Mach number requires the assumption of the initial value of flap deflection. The combination of the low speed drag polar curves with retracted landing gear in Fig. 3.2 and the selected flap deflection allows the calculation of the maximum lift coefficient C_{Lmax}. For the A320-200 the initial flap deflection can be assumed 15° and from Fig. 3.2 the respective C_{Lmax} is 2.22.

At this point the requirement on the speed V_2 with respect to the stall speed V_s in eq. 3.3 can be exploited to calculate the lift coefficient C_{L2}. Since the lift force must be equal to aircraft weight at V_2, combining eqs. 3.1 and 3.2 with eq. 3.3 yields

$$\begin{aligned} L &= \frac{1}{2}\rho_{Air} S_w C_{L2} V_2^2 = \frac{1}{2}\rho_{Air} S_w C_{L2} (1.2 \cdot V_s)^2 = \\ &= \frac{1}{2}\rho_{Air} S_w C_{L2} \left(1.2 \cdot \sqrt{\frac{2L}{\rho_{Air} S_w C_{Lmax}}}\right)^2 \qquad \Rightarrow \qquad C_{L2} = \frac{C_{Lmax}}{1.2^2} \end{aligned} \tag{3.13}$$

Once the Mach number M_2 is known, the interpolation of the engine MTO rating dataset in Fig. 3.3 with airport altitude and no ISA deviations allows the calculation of the engine thrust T at V_2 in OEI or AEO condition.

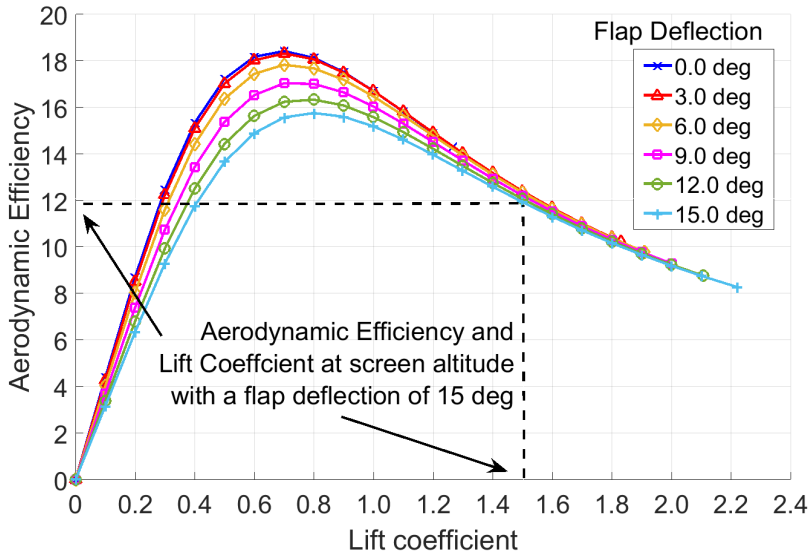

Figure 3.5: Low speed drag polar with landing gear retracted for an A320-200 aircraft [73]

3.2.1.2 Aerodynamic Drag

Once lift coefficient C_{L2} and flap deflection are known, it is possible to determine the drag coefficient using the low speed drag polars reported in Fig. 3.5 [73]. The aerodynamic efficiency E in the y-axis of Fig. 3.5 is the ratio between the aerodynamic lift and drag coefficients. Thus, the drag coefficient C_{D2} at V_2 is given by the ratio C_{L2}/E_2. As an example, Fig. 3.5 also shows the lift coefficient and the respective aerodynamic efficiency of an A320-200 flying at V_2 with a flap deflection of 15°.

The aerodynamic drag D_2 at the screen altitude can be computed as

$$D_2 = q_{Air} C_{D2} S_w \tag{3.14}$$

In a OEI condition D_2 does not represent the total drag of the aircraft and additional contributions should be considered.

When an engine fails the pressure losses in the air flow across the engine due to the movements of the fan, compressor and turbine blades are associated with a drag increment called the windmilling drag. The windimilling drag D_{WML} can be computed with an expression similar to eq. 3.14 where the drag coefficient of

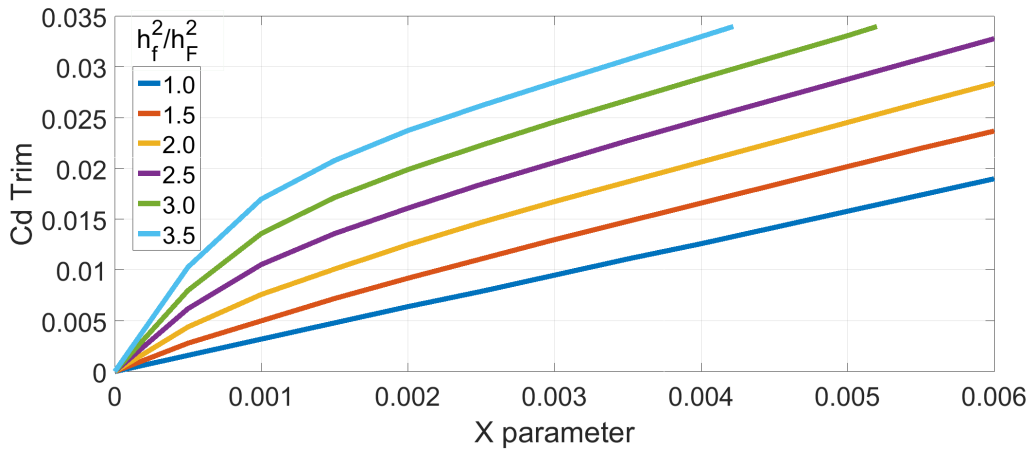

Figure 3.6: Experimental data for trim drag estimation [77]

moving blades inside subsonic turbofan engines is assumed to be about 0.3.

$$D_{WML} = 0.3 q_{Air} S_{eng} \tag{3.15}$$

where S_{eng} is the area of the engine front section, a circle with a diameter which is often assumed to be 80% of the nacelle diameter [76].

When an engine fails the asymmetric thrust generates a momentum M_{yaw} around the yaw axis of the aircraft (vertical axis) that tends to destabilize the aircraft motion.

$$M_{yaw} = d_{eng}(T + D_{WML}) \tag{3.16}$$

where d_{eng} is the distance between the engine and the aircraft's centre of gravity and T, in this case, is the total thrust in OEI condition. The A320-200 has only two engines so T in eq. 3.16 is equal to the thrust of a single engine. M_{yaw} is compensated by a rudder deflection that generates a counteracting force that allows the aircraft to continue the take-off maintaining the desired direction.

Any rudder deflection causes an additional drag force called trim drag that can be estimated using the method proposed by the Engineering Science Data Unit (ESDU) [77]. This procedure is based on the interpolation of experimental data like those shown in Fig. 3.6 to compute the drag coefficient increment C_{DTrim}. ESDU performed a series of wind tunnel tests on aircraft's tail with different ra-

tios between the fin height h_f and the fuselage height h_F applying different yaw momentum and rudder deflection. The curves in Fig. 3.6 express the C_{DTrim} as a function of a non-dimensional parameter which represents the momentum intensity and the geometrical characteristics of the aircraft:

$$X_{parameter} = \frac{\pi}{2} \frac{{M_{yaw}}^2}{{q_{Air}}^2 {d_{FinAC}}^2 {h_f}^2 S_{w_{ESDU}}} \tag{3.17}$$

where d_{FinAC} is the distance between the fin and the wing aerodynamic centres and $S_{w_{ESDU}}$ is the wing area of a fully trapezoidal wing [77]. The A320-200's $S_{w_{ESDU}}$ is not equal to the wing surface S_w, since the part of the A320's wing close to the fuselage is more rectangular than trapezoidal. The curves shown in Fig. 3.6 are plotted for several value of $X_{parameter}$ keeping constant the value of the ratio:

$$h_{ratio} = \frac{{h_f}^2}{{h_F}^2} \tag{3.18}$$

From the geometrical features of the aircraft and the momentum intensity the coefficient C_{DTrim} can be derived and the trim drag D_{Trim} can be computed as

$$D_{Trim} = q_{Air} C_{DTrim} S_{w_{ESDU}} \tag{3.19}$$

At this point all the parameters required to calculate the climb out gradient at V_2 in OEI condition are known. Substituting the thrust and all the drag contributions in eq. 3.8 yields

$$\gamma_2 = \frac{T - (D_2 + D_{WML} + D_{Trim})}{W} \tag{3.20}$$

In case that the result of eq. 3.20 is smaller than γ_{2Req} calculated using eq. 3.4, the procedure to determine thrust and drag at V_2 has to be iterated by reducing the flap deflection until the safety requirement $\gamma_2 \geq \gamma_{2Req}$ is satisfied. Indeed, a lower flap angle sensibly reduces the aerodynamic drag while the engine thrust slightly decrease for an higher Mach number at the screen altitude is required to generate the same lift force. The overall effect of the flap deflection angle reduction is an increase of climb out gradient γ_2.

3.2.2 Take-off Speeds and Distances

Once the flap deflection and climb out gradient γ_2 are known, the take-off speeds and distances can be estimated. This data can then be used to evaluate the impact of the electromagnetic catapult on the take-off phase and flight.

The stall speed V_s and the take-off safety speed V_2 are calculated using eqs. 3.2 and 3.3 respectively, using the flap deflection obtained from the iterative procedure described in Section 3.2.1. The lift-off speed V_{LOF} can be calculated as shown in eqs. 3.21 and 3.22 [76].

$$k_{LOF} = \frac{1}{2}(\frac{V_2}{V_s} + 1) \tag{3.21}$$

$$V_{LOF} = k_{LOF} V_s \tag{3.22}$$

Since at lift-off the lift force is equal to the aircraft weight, the lift coefficient $C_{L_{LOF}}$ can be computed as done for the lift coefficient at the screen altitude C_{L2} in eq. 3.13.

$$C_{L_{LOF}} = \frac{C_{Lmax}}{{k_{LOF}}^2} \tag{3.23}$$

The requirement of the climb out gradient at lift-off expressed by eq. 3.5 can be now verified. The available climb gradient at lift-off γ_{LOF} can be calculated by adopting the procedure used to determine γ_2 in Section 3.2.1 and considering the drag polar with extended landing gear shown in Fig. 3.7 [73] in place of the drag polar with retracted landing gear shown in Fig. 3.5. The drag polar with extended landing gear considers the contribution of the undercarriage to the aerodynamic drag. Since the landing gear has no impact on the generation of the lift force the aerodynamic efficiency decreases as can be seen by comparing Figs. 3.5 and 3.7. Fig. 3.7 also shows the aerodynamic efficiency that corresponds to the lift coefficient $C_{L_{LOF}}$ with a flap deflection of 15° in ISA conditions at sea level. In case the requirement in eq. 3.5 is not satisfied, the procedure in Section 3.2.1 needs to be reiterated with a reduced flap deflection.

Once the lift-off speed and the respective climb out gradient are known, it is possible to calculate the aircraft rotation speed V_R. The aircraft rotation occurs just before the aircraft reaches the lift-off speed. The rotation speed is usually

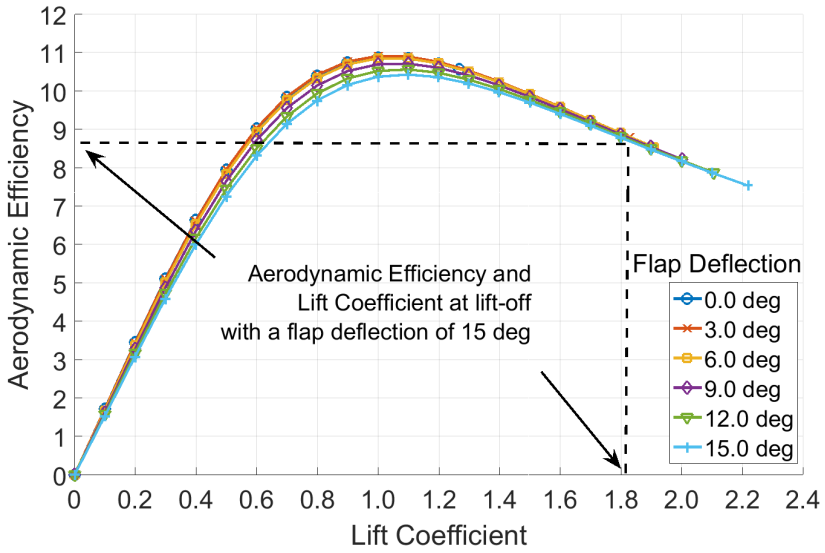

Figure 3.7: Low speed drag polar with landing gear extended for an A320-200 aircraft [73]

estimated assuming uniform acceleration between the time the rotation starts and the instant the aircraft leaves the ground. It has already been mentioned how the climb out gradient for a straight path with unity load factor can be envisioned as an non-dimensional acceleration between one speed and another. Therefore, the aircraft acceleration during the rotation can be assumed to be approximately $G \cdot \gamma_{LOF}$. Assuming the mean rate of rotation about the lateral axis equal to ω_R, the rotation speed V_R can be estimated as

$$V_R = V_{LOF} - G \cdot \gamma_{LOF} \frac{\alpha_{LOF} - \alpha_G}{\omega_R} \tag{3.24}$$

where α_G is the angle of attack at ground level and α_{LOF} is the angle of attack at lift-off. During the initial acceleration on the runway, the angle of attack coincides with the wing incidence which is 0° for the A320-200. The lift polars in Fig. 3.2 can be used to determine the angle of attack at lift-off α_{LOF} by finding the intesection between the curve for the current flap deflection and $C_{L_{LOF}}$. Typical values of the rate of rotation ω_R are: 3 to 4 degrees/s for large transport aircraft and 4 to 5 degrees/s for small transport aircraft [78].

The methodology described so far to determine the take-off characteristics is not

affected by the presence of the electromagnetic catapult. For instance, the take-off speeds depend on the safety requirement at V_2, engine performance, aerodynamic characteristics of the aircraft and environmental conditions. Since the electromagnetic catapult affects the rate the aircraft accelerates to the required speeds, an EML system has a significant impact on the take-off distances.

Therefore the take-off field length (TOFL) in Fig. 3.1, which comes from a comparison between the take-off distance (TOD) and the maximum emergency accelerate-stop distance (BFL), is expected to be reduced by the implementation of an EML system. Sections 3.2.2.1 and 3.2.2.2 explain the methodology applied to calculate TOD with all the engines operative and BFL in case of engine failure.

3.2.2.1 Take-Off Distance

Section 3.1 has introduced the take-off distance TOD as the distance covered by the aircraft in the AEO condition until the screen height of 35 ft. The TOD is the sum of the distance s_{Run} travelled by the aircraft until the lift-off point and the distance s_{Air} covered during the first airborne phase until the height of 35 ft is reached. In order to consider the errors due to the approximations and to the possible deviations of real aircraft paths from the statistical mean trajectory a common practice is to consider a safety margin of 15% [78].

$$TOD = 1.15 \cdot (s_{Run} + s_{Air}) \tag{3.25}$$

The distance initially travelled on ground by the aircraft propelled by the engines can be calculated as

$$s_{Run} = \int_0^{V_{LOF}} \frac{V}{a_1} dV = \frac{1}{2} \int_0^{V_{LOF}} \frac{dV^2}{a_1} \tag{3.26}$$

where the instantaneous value of the acceleration a_1 is

$$a_1 = \frac{T - D - \mu(W - L)}{m_{A320}} \tag{3.27}$$

where the thrust T, in this case, is the one provided by both the engines, W is the weight of the aircraft, μ is the friction coefficient, $(W - L)$ is the instantaneous value of the force perpendicular to the ground and m_{A320} is the mass of the aircraft.

Table 3.1: Average friction coefficients for different runway pavements [78]

hard runways (concrete, tarmac)	$\mu = 0.02$
hard turf or gravel	$\mu = 0.04$
short dry grass	$\mu = 0.05$
long grass	$\mu = 0.10$
soft ground	$\mu = 0.10 \rightarrow 0.30$

Substituting the acceleration expressed by eq. 3.27 and the expressions of lift and drag defined in eqs. 3.1 and 3.14 respectively into eq. 3.26 yields

$$s_{Run} = \frac{1}{2G} \int_0^{V_{LOF}} \frac{dV^2}{\frac{T}{W} - \mu - (C_D - \mu C_L)\frac{1}{2}\frac{\rho_{Air} V^2 S_w}{W}} \tag{3.28}$$

Engine thrust, drag coefficient, lift coefficient and aircraft weight are not constant during the acceleration so an approximated formula can be derived assuming the aircraft weight equal to the Maximum Take-off Weight (MTOW) as [78]

$$s_{Run} = \frac{{V_{Run}}^2}{G\left(\frac{\overline{T}}{MTOW} - \mu_e\right)} \tag{3.29}$$

where the mean thrust $\overline{T}$ is evaluated at speed $V_{Run} = V_{LOF}/\sqrt{2}$ using the engine MTO rating dataset shown in Fig. 3.4 and the equivalent friction coefficient μ_e can be calculated as [78]

$$\mu_e = \mu + 0.01 \cdot C_{Lmax} \tag{3.30}$$

Typical value of rolling friction coefficient μ are listed in Table 3.1. The time required to reach the lift-off speed can be simply approximated as

$$t_{Run} = s_{Run}/V_{Run} \tag{3.31}$$

The electromagnetic catapult has the capability to drastically reduce the take-off run, increasing the aircraft acceleration. Most of civil aircraft accelerate at 0.3 G since the maximum engines thrust is about 30-35% of the MTOW. In order to shorten the TOD, an acceleration of 0.6 G was chosen as this will ramp the velocity up at increased rate without the experience being uncomfortable to the

passengers (see Section 1.1). The controllability that can be achieved with an electromagnetic launch allows the assumption of an uniform accelerated motion until the rotation speed V_R. Therefore, the take-off run can be calculated as

$$s_{Run} = \frac{{V_R}^2}{2 \cdot 0.6G} \tag{3.32}$$

The time required by the electromagnetic catapult to reach the rotation speed can be simply calculated

$$t_{Run} = V_R/(0.6G) \tag{3.33}$$

While the catapult effects both the intensity of the acceleration on the ground and the length of take-off run s_{Run}, it has no impact on the airborne phase. The length of the airborne segment does not change with the catapult installation since the aircraft detaches at V_R, just before lifting off. In order to determine the airborne distance the duration of the airborne phase should be first estimated integrating by variable separation the definition of the Specific Excess Power in eq. 3.6 as

$$\begin{aligned} \int_{t_{LOF}}^{t_2} \frac{T-D}{W} V \, dt &= \int_{V_{LOF}}^{V_2} \frac{V}{G} dV + \int_0^{h_2} dh \Rightarrow \\ t_{Air} &= \left(\frac{{V_2}^2 - {V_{LOF}}^2}{2G} + h_2 \right) \frac{1}{\gamma_{LOF} V_{LOF}} \end{aligned} \tag{3.34}$$

where h_2 is the altitude of the safety screen. The integration of the SEP is equivalent to the application of the energy conservation principle to an accelerating body that is gaining potential energy changing altitude. The average speed V_{Air} between V_{LOF} and V_2 and the respective distance travelled during the airborne phase can be estimated as

$$V_{Air} = V_{LOF} + \frac{V_2 - V_{LOF}}{\sqrt{2}} \tag{3.35}$$

$$s_{Air} = t_{Air} V_{Air} \tag{3.36}$$

3.2.2.2 Balanced Field Length

By definition BFL is equal to the TOD in OEI condition when the engine failures occurs at V_{EF}. The subdivision of the aircraft path adopted to determine the max-

imum emergency accelerate-stop distance considers a first phase s_1 starting from standstill until the engine failure at V_{EF} and a second phase s_2 after the engine failure up to the moment of attaining the screen height at speed V_2. The distance travelled by the aircraft during the first phase is

$$s_1 = \frac{V_{EF}^2}{2\overline{a}_1} \tag{3.37}$$

where $\overline{a}_1$ is the initial acceleration with all engines operative. Eq. 3.6 can be integrated to determine the distance covered after the engine failure as

$$\int_{t_{EF}}^{t_2} \frac{T-D}{W} V\,dt = \int_{V_{EF}}^{V_2} \frac{V}{G}\,dV + \int_0^{h_2} dh \Rightarrow s_2 = \frac{1}{\overline{\gamma}}\left(\frac{V_2^2 - V_{EF}^2}{2G} + h_2\right) \tag{3.38}$$

where the mean climb gradient $\overline{\gamma}$ is defined as follow

$$\overline{\gamma} = \frac{1}{s_2}\int_{s_1}^{s_2} \frac{T-D}{W} ds \tag{3.39}$$

The distance to come to a standstill aborting take-off after engine failure can be written as

$$s_{stop} = \frac{V_{EF}^2}{2\overline{a}_{stop}} + V_{EF}\Delta t \tag{3.40}$$

where Δt is the average pilot reaction time to an engine failure and $\overline{a}_{stop}$ is the average braking deceleration. The balanced field length is determined imposing the total accelerate-stop distance s_{stop} equal to the take-off distance in one-engine-inoperative condition s_2. This condition of balancing the field length can be expressed as a ratio between the critical decision speed V_1 and the safety screen speed V_2 [78].

$$\frac{V_1}{V_2} = \sqrt{\left(1 + \frac{2Gh_2}{{V_2}^2}\right) \Big/ \left(1 + \frac{\overline{\gamma}}{\overline{a}_{stop}/G}\right)} - \frac{\overline{\gamma} G(\Delta t - 1)}{V_2} \tag{3.41}$$

The combination of eqs. 3.37 through 3.41 yields the expression

$$BFL = \frac{{V_2}^2}{2G\left(1 + \frac{\overline{\gamma}}{\overline{a}_{stop}/G}\right)}\left(\frac{1}{\overline{a}_1/G} + \frac{1}{\overline{a}_{stop}/G}\right)\left(1 + \frac{2Gh_2}{{V_2}^2}\right) + \frac{\Delta S_{TO}}{\sqrt{\sigma}} \tag{3.42}$$

where

- the mean climb gradient can be approximated as $\overline{\gamma} = 0.06 + \gamma_2 - \gamma_{2Req}$ on the basis of several assumptions regarding undercarriage drag and ground effect;

- $\overline{a}_{stop}$ is the average aircraft deceleration that can be assumed 0.37 G even though with optimum brake pressure on dry concrete 0.45 G $\rightarrow$ 0.55 G can be achieved;

- $\overline{a}_1$ is the medium acceleration until the critical decision speed V_1 which can be approximated as $\overline{T}/MTOW - \mu_e$;

- ΔS_{TO} is a distance that the aircraft travel without changing speed before the pilot react to the engine failure. The reaction time Δt and distance ΔS_{TO} may be assumed to be approximately 4.5 seconds and 200 m respectively;

- σ is the ratio between the air density ρ_{Air} and the average atmospheric density ρ_0 which is $\simeq 1$ for most of the cases.

Introducing these approximations into eq. 3.42 the BFL becomes

$$BFL = \frac{0.863}{1 + 2.3(\gamma_2 - \gamma_{2Req})} \left(\frac{MTOW}{\rho G S_w C_{L2}} h_2 \right) \left(\frac{1}{\frac{\overline{T}}{MTOW} - \mu_e} + 2.7 \right) + 200 \quad (3.43)$$

The method proposed for engine-boosted aircraft cannot be applied to calculate the BFL required by an aircraft taking off with the electromagnetic catapult. In the case of an engine failure the catapult power supply can be interrupted allowing the aircraft to slow down using its braking system. In the case where the engine failure occurs at an early stage of the launch the catapult could be even used in generation mode as a brake, partially recovering the energy transmitted during the acceleration. In order to be conservative, the BFL is calculated in the hypothesis the launcher accelerates the aircraft until V_R rather than V_1. This event may occur in the case of miss detachment and with the catapult propelling the aircraft until the speed V_R. Then an aircraft decelerating at $\overline{a}_{stop} = 0.37$ G would cover the

distance s_{stop}:

$$s_{stop} = \frac{{V_R}^2}{2\overline{a}_{stop}} + V_R \Delta t \tag{3.44}$$

The balanced field length with an electromagnetic launch system is

$$BFL = s_{stop} + s_{Run} \tag{3.45}$$

3.2.3 Take-off Time and Fuel Consumption

The fuel that is burnt during take-off changes across the several take-off phases shown in Table 3.3 according to the required thrust, aircraft speed, altitude and environmental conditions of each phase. The mass of fuel burnt F_B depends on the elapsed time of each phase and the respective fuel flow F_F that the engines require to produce the thrust. The fuel flow that is injected into the engines changes with the thrust according to the curves reported in Fig. 3.8. With the altitude, thrust and Mach number obtained from the take-off analysis presented in the previous sections, the fuel flow can be estimated interpolating the data in Fig. 3.8.

The fuel flow and the elapsed time of each take-off phase allow the calculation of the fuel burnt:

$$F_B = F_F \cdot t \tag{3.46}$$

To accurately estimate the variation of variables involved in the take-off analysis, the total mass of the plane is updated after each phase subtracting the amount of fuel burnt F_B calculated using eq. 3.46 to the initial mass of the aircraft. This is allowed by the computation of the time required to complete each take-off phase.

The time required by the engine-boosted aircraft to accelerate on the runway and to complete the airborne phase until the safety screen altitude were computed in Section 3.2.2 with eqs. 3.31, and 3.34 respectively. When the aircraft accelerates with the aid of the electromagnetic catapult the engines do not need to provide any thrust and could work under an idle condition. Since the engines usually take approximately 4 seconds to pass from the idle to the full-throttle condition, the changing of the engine rating could happen a few seconds before the lift-off.

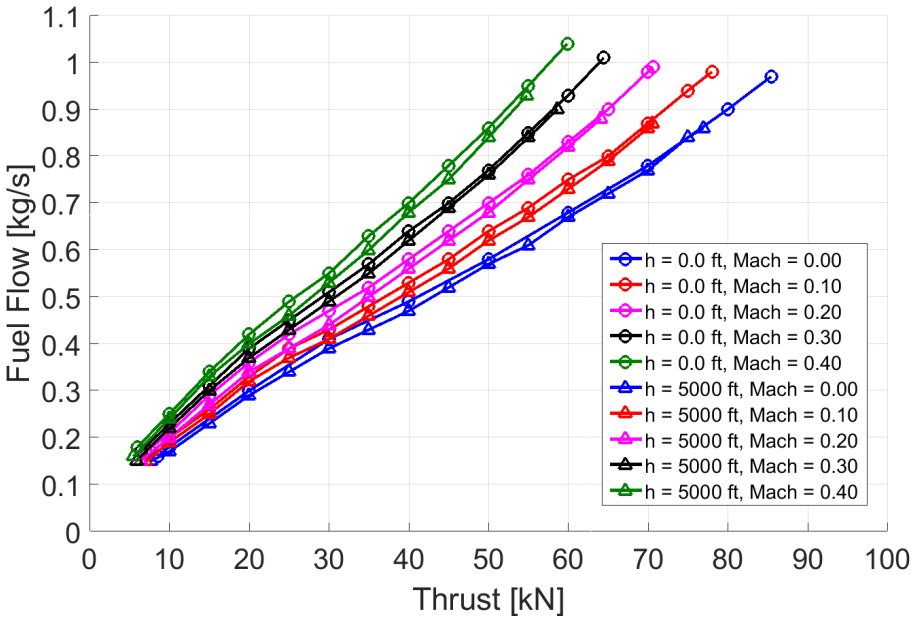

Figure 3.8: Fuel flow across CFM56-A1 engines for several Mach and ISA conditions [73]

This particular operating mode is taken into account to correctly estimate the fuel consumption during the aircraft run in the case where the electromagnetic catapult is implemented.

The take-off terminates at the height $h_{TO} = 1500$ ft where the aircraft begins to climb up to the cruise altitude. In general, the airline operators opt for a fast climb between h_2 and h_{TO} to reduce the fuel consumption as much as they can in the limits allowed by air traffic control. The time required to fly to h_{TO} from the screen altitude h_2 can be determined by integrating the partial differential equation shown in eq. 3.6 using the variables separation method.

$$\int_0^{t_{TO}} dt = \frac{\overline{W}}{\overline{T}-\overline{D}} \left(\int_{V_2}^{V_{TO}} \frac{dV}{G} + \frac{1}{\overline{V}} \int_{h_2}^{h_{TO}} dh \right) \tag{3.47}$$

where V_{TO} is the speed at h_{TO} which is assumed 250 kts (131.4 m/s) and the average speed $\overline{V}$ is calculated as $(V_{TO}+V_2)/2$. The solution of the integrals gives

$$t_{TO} = \frac{\overline{W}}{\overline{T}-\overline{D}} \left[\frac{V_{TO}-V_2}{G} + \frac{2(h_{TO}-h_2)}{V_{TO}+V_2} \right] \tag{3.48}$$

In order to solve eq. 3.48, the average weight $\overline{W}$, the average thrust $\overline{T}$ and the average aerodynamic drag $\overline{D}$ need to be estimated.

During take-off the aircraft burns an amount of fuel that is equal to approximately 0.4% of its initial weight. Thus the average weight can be assumed equal to the 99.8% of the maximum take-off weight. The average thrust $\overline{T}$ is computed from the MTO engine rating dataset in Fig. 3.4 using the average altitude $\overline{h} = (h_{TO} + h_2)/2$ and the average Mach number $\overline{M}$. $\overline{M}$ is calculated at $\overline{V}$ considering the speed of sound at altitude $\overline{h}$.

The average aerodynamic drag can be computed from the average air density $\overline{\rho}_{Air}$, the average drag coefficient $\overline{C_D}$ and the average speed $\overline{V}$ as

$$\overline{D} = \frac{1}{2}\overline{\rho}_{Air}\overline{C_D}S_w\overline{V}^2 \tag{3.49}$$

The air density changes with altitude and atmospheric conditions and the mean value between two different heights can be found using

$$\overline{\rho}_{Air} = \frac{1}{h_{TO} - h_2}\int_{h_2}^{h_{TO}} \frac{p_{Air}}{R_g T_{air}} dh \tag{3.50}$$

where $R_g = 287.05$ kJ/kg/K is the specific gas constant of dry air, p_{Air} is the air pressure and T_{air} is the air temperature. The atmospheric pressure p_{Air} in the troposphere (below 11000 ft) can be expressed as [75]

$$p_{Air} = p_0 \left(\frac{T_{air}}{T_0}\right)^{\frac{G}{R_g k_{Tro}}} \tag{3.51}$$

where the standard atmospheric pressure p_0 is 101325 Pa, the standard atmospheric temperature T_0 is 288.15 K and the troposphere coefficient k_{Tro} is 0.0065. The temperature in the troposphere varies with the altitude h according to the expression [75]

$$T_{air} = T_0 - k_{Tro}h \tag{3.52}$$

Substituting eqs. 3.52 and 3.51 into eq. 3.50 and integrating, the average value of

the air density between the screen altitude and h_{TO} becomes

$$\overline{\rho}_{Air} = \frac{p_0}{G(h_{TO}-h_2)} \left[\left(1 - \frac{k_{Tro}h_2}{T_0}\right)^{\frac{G}{\overline{R_g k_{Tro}}}} - \left(1 - \frac{k_{Tro}h_{TO}}{T_0}\right)^{\frac{G}{\overline{R_g k_{Tro}}}} \right] \quad (3.53)$$

The mean drag coefficient $\overline{C_D}$ in eq. 3.49 takes into consideration the flap retraction at 400 ft as indicated in Fig. 3.1, and that the low speed drag polar can no longer be considered at high speed above 400 ft. Indeed, the low speed drag polar lacks in accuracy near or above of Mach 0.3 due to the air compressibility effect on the aerodynamic drag. The high speed drag polar considers the air compression of the flow above the airfoil and the changing of the pressure distribution over the wings. The drag increase is particularly significant above Mach 0.7 where the acceleration of the upstream can cause shock waves [79]. The airfoil of the A320-200 is designed to operate at high Mach number ($\simeq 0.73$) and to delay the formation of shock waves. However, when an airfoil shape is optimized for cruise the low speed aerodynamic is usually described by different drag polars.

The average drag coefficient is estimated under the hypothesis that the aircraft spends the same time between 35 ft and 400 ft, at 400 ft and between 400 ft and 1500 ft. This assumption is made to simplify the calculation and causes negligible errors on the estimation of the average drag coefficient although it is not necessarily respected during real flight. Under this assumption the average drag coefficient can be calculated

$$\overline{C_D} = \frac{C_{D2} + C_{DLS} + C_{DHS}}{3} \quad (3.54)$$

Since the flap setting of the wings does not change during the climb segment between the screen height and the altitude of 400 ft, the drag coefficient remains equal to the drag coefficient C_{D2} obtained in Section 3.2.1.2. The drag coefficient at 400 ft C_{DLS} is calculated using the low speed drag polar with landing gear retracted in Fig. 3.5 with no flap deflection and considering the low-speed lift coefficient

$$C_{LLS} = \frac{2\overline{W}}{S_w \overline{\rho}_{Air} \overline{V}} \quad (3.55)$$

The drag coefficient between 400 ft and 1500 ft C_{DHS} can be determined using

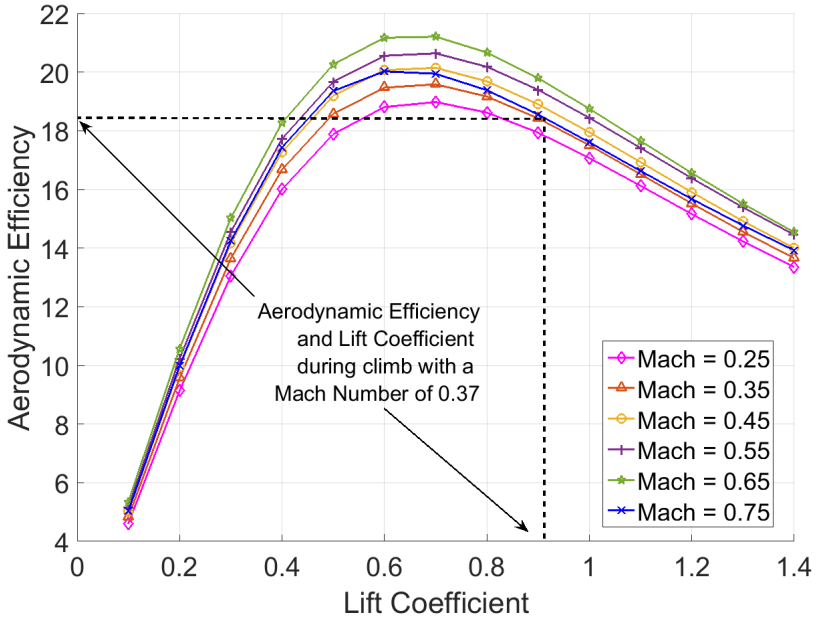

Figure 3.9: High speed drag polar for an A320 aircraft flying at 950 ft [73]

the high speed drag polar in Fig. 3.9 [73] with the Mach number $\overline{M}$ and assuming the high-speed lift coefficient $C_{LHS} = C_{LLS}$. Even though the variation of the high-speed drag and lift coefficients with the altitude is negligible within few hundreds feet, the curves in Fig. 3.9 are plotted for mean altitude between 400 ft and h_{TO} to get higher accuracy.

Once the time t_{Run}, t_{Air} and t_{TO} are known, they can be substituted in eq. 3.46 to estimate the respective amount of fuel burnt.

3.3 Take-off Analysis Outcomes

3.3.1 Flight Performance and Fuel Consumption Reduction

The take-off analysis presented above can be used to investigate the take-off performance of an A320-200 with CFM56-5-A1 engines with and without the aid of an electromagnetic catapult.

The equations described in the previous sections were implemented in a software for civil aircraft design called PACE [73]. In particular the C# scripts of

Table 3.2: Take-off analysis outcomes for two possible mission scenarios

	Aircraft mission		
Parameter	**A320 certification**	**EML constant MTOW**	**EML constant Range**
MTOW	73500 kg	73500 kg	73447 kg
Payload	14058 kg	14058 kg	14058 kg
Fuel	18273 kg	18273 kg	18221 kg
Range	2450 NM	2460 NM	2450 NM

the software main repository were edited to take into account the electromagnetic catapult impacts on the take-off phases. The data presented in this section are computed by PACE activating or deactivating the electromagnetic launch option from the modified software interface.

When the aircraft takes off with maximum weight, the fuel saved exploiting the electromagnetic catapult can be used to fly longer distances. On the other hand, the aircraft that takes off with the catapult can travel the same distance consuming less fuel and with a reduced take-off weight. Therefore, two possible mission scenarios can be envisaged:

- constant take-off weight and different mission range;
- mission with a predetermined range and a reduced take-off weight.

The range and the take-off weight calculated under these two circumstances are given in Table 3.2.

The analyses whose results are shown in Table 3.2 have been carried out for aircraft transporting the same payload. The payload mass of the A320-200 corresponds to the weight of 138 passengers travelling in economy class and 12 passengers travelling in business class. Including the luggage, the passenger average weight is 93 kg for economy class and 102 kg for the business class.

Considering the case of a flight with constant range shown in the third column of Table 3.2, the aircraft that takes off using the electromagnetic catapult accomplishes the mission consuming less fuel. In this situation the maximum take-off weight reduces and the launcher thrust required to achieve the take-off speed is less demanding. For this reason, the mission of the aircraft with an initial weight equal to the A320-200 certified MTOW has been considered to determine the

Table 3.3: A320-200 take-off history comparison between engine-boosted take-off and electromagnetic launch

Take-off history of existing A320-200				
	Start	**Full throttle**	**Safety Screen**	**Climb**
Altitude [ft]	0.0	0.0	35	1500
Time [s]	0.0	23.4	29.6	96.0
Weight [kg]	73500	73439	73422	73252
Fuel Burnt [kg]	0.0	61.4	77.72	248.37
Mach Number	0.0	0.215	0.234	0.388
Speed [m/s]	0.0	72.99	79.66	131.4
Fuel Flow [kg/s]	2.584	2.622	2.630	2.619
Thrust [kN]	222.4	181.1	177.74	163.04

Take-off history with EML					
	Start	**Idle Mode**	**Full throttle**	**Safety Screen**	**Climb**
Altitude [ft]	0.0	0.0	0.0	35	1500
Time [s]	0.0	7.6	11.6	17.8	84.0
Weight [kg]	73500	73498	73487	73471	73300
Fuel Burnt [kg]	0.0	2.14	12.63	28.95	199.8
Mach Number	0.0	0.132	0.215	0.234	0.388
Speed [m/s]	0.0	44.81	72.99	79.66	131.4
Fuel Flow [kg/s]	2.584	0.281	2.622	2.630	2.619
Thrust [kN]	222.4	0.0	181.1	177.74	163.04

catapult requirements. All the results in this section are calculated under this assumption unless otherwise specified.

Table 3.3 shows a comparison between the conventional and assisted take-off history in order to further describe the impact of the catapult across the take-off phases. When the aircraft is propelled by the electromagnetic catapult, the engines do not need to provide any thrust and they initially work in idle condition. Since the engines usually take approximately 4 seconds to pass from idle to full throttle, the fuel consumption increases only few seconds before the aircraft leaves the ground. This particular operating mode is highlighted in the second part of Table 3.3 where an extra column is used to distinguish the two engine ratings adopted during the take-off run. The engines in idle condition requires a reduced fuel flow which has a positive impact on the amount of fuel burnt during take-off.

Table 3.3 also shows the elapsed time and the cumulative amount of fuel burnt across the take-off segments. The acceleration increase due to the electromagnetic catapult allows the completion of the take-off operation in a shorter time. Addi-

Table 3.4: A320-200 flight data comparison between engine-boosted take-off and electromagnetic launch

Flight Profile with conventional take-off				
Parameter	**Fuel [kg]**	**Time [min]**	**Mass [kg]**	**Distance [NM]**
Taxi out	74.6	6.0	73575	0.0
Take-off	248.4	1.6	73500	0.0
Climb	1488.1	15.0	73252	84.9
Cruise	12521.8	319.2	71763	2233.4
Descent	265.1	20.6	59242	123.1
Landing	85.0	5.0	58977	0.0
Taxi-in	74.6	6.0	58892	0.0
Flight Profile with EML				
Parameter	**Fuel [kg]**	**Time [min]**	**Mass [kg]**	**Distance [NM]**
Taxi out	74.6	6.0	73575	0.0
Take-off	199.8	1.4	73500	0.0
Climb	1489.6	15.1	73300	95.0
Cruise	12569.0	320.3	71811	2241.2
Descent	265.1	20.6	59242	123.1
Landing	85.0	5.0	58977	0.0
Taxi-in	74.6	6.0	58892	0.0

tionally, shorter is the time spent under MTO engine rating at high fuel flows. A comparison of the total amount of fuel burnt after the take-off shows that the electromagnetic catapult allows a fuel saving of 48.5 kg.

In order to quantify the benefit of an EML system across the whole flight, the analysis of the aircraft performance was not limited only to take-off, but it was extended to the other flight phases: taxiing, climb, cruise, descent and landing. The techniques needed to estimate the quantities shown in Table 3.4 are beyond the scope of this work. A way to obtained these results may be found in several aircraft design manuals [78, 76, 79]. The analysis of the full flight is useful to estimate the effect of radical aircraft configuration changes such as the installation of new engines proposed in Section 3.3.5.

The analysis of the whole flight allows the visualization of the fuel burnt in each flight segment. For example, the flight analyses in Table 3.4 show that the A320-200 takes off and lands with the same weight and the same amount of propellant in the tanks, but different quantities of fuel are burnt across the several flight segments. The fuel saved with assisted take-off is redistributed among cruise and

Table 3.5: A320-200 fuel consumption comparison between engine-boosted take-off and electromagnetic launch

Fuel details for a 2450 NM mission		
Parameter	**Engine Take-off**	**EML take-off**
Trip	14758 kg	14708 kg
Flight	14608 kg	14559 kg
Reserves	3590 kg	3588 kg
Total	18273 kg	18221 kg

climb to enable the aircraft to travel longer distances.

The summation of the fuel consumed during the several flight segments in Table 3.4 does not correspond to the total amount of fuel in the tanks reported in Table 3.2. The extra fuel has to be carried to cope with unforeseen events such as:

- air traffic control preventing the aircraft flying at its optimum altitude. The thrust required to withstand a fiercer aerodynamic drag increases and the fuel consumption rises;
- the head wind might be stronger than forecast;
- thunderstorms might force the aircraft to depart from the planned flight path and follow longer routes to reach the final destination;
- the destination airfield may have traffic problem and the aircraft may have to fly in holding position until cleared to land;
- the flight may be diverted due to sudden closure of the destination airport for weather conditions, accidents or other operational reasons;

Table 3.5 shows the amount of fuel burnt to complete a mission of 2450 NM including the reserves and reports the fuel required to reach the destination for an aircraft starting with conventional take-off and assisted take-off. The meaning of each variable is explained as follow:

- "Trip" is the summation of the fuel consumed from the moment the aircraft exit the departure gate to the instant it reaches the destination gate. It may be calculated summing the fuel burnt during the several flight segments reported in Table 3.4;

- "Flight" represents the fuel consumed when the aircraft flies, takes off and lands. It is calculated subtracting from "Trip" the fuel consumed during taxiing operations;
- "Reserves" represents the amount of fuel that is loaded into the aircraft for safety reasons and is required to cope with the aforementioned events. The fuel reserve calculation must include [80]:
  1. the fuel required to cover 200 NM on top of the mission range in cruise condition in case of diversion to another airport;
  2. 30 min of extra landing operations at 1500 ft in case the destination runway is momentarily inaccessible;
  3. 5% of the fuel consumed during the flight ("Flight" in Table 3.5), for any other possible contingency.

  The fuel reserve generally includes the fuel required for the Taxi-Out operations;
- "Total" is the amount of fuel that is loaded into the aircraft and is computed summing to "Trip" the fuel reserves and subtracting the fuel required during Taxi-Out operations.

3.3.2 Runway Length Reduction

The comparison between the outcomes of conventional take-off analysis and assisted take-off analysis is presented in Table 3.6. The electromagnetic catapult does not affect the flap deflection required during the initial acceleration and the climb gradient γ_2 attained at screen altitude. Consequently, the characteristic speeds V_s, V_2, V_{LOF} and V_R in Table 3.6 do not change with the implementation of the launcher. The catapult increases the average acceleration during the take-off run reducing the time and the distance required to reach the rotation speed as shown in Table 3.6.

Since the aircraft detaches before the lift-off, the catapult has no effect on the time and on the distance required to complete the airborne phase. Assisted take-off allows significant Take-Off Distance and Balanced Field Length reduction with

Table 3.6: A320-200 take-off performance comparison between engine-boosted take-off and electromagnetic launch

Take-off performance		
Parameter	**Engine Take-off**	**EML take-off**
Climb gradient	2.471%	2.471%
Max lift coefficient	2.181	2.181
Aerodynamic Efficiency	11.89	11.89
Flap deflection	14°	14°
Stall Speed	66.35 m/s	66.35 m/s
Rotation speed	68.35 m/s	68.35 m/s
Lift-off speed	72.99 m/s	72.99 m/s
Screen Speed	79.62 m/s	79.62 m/s
Run time	23.41 s	11.62 s
Airborne time	6.21 s	6.21 s
Run distance	1208 m	397 m
Airborne distance	482 m	482 m
TOD	1944 m	1011 m
BFL	2256 m	1348 m
TOFL	2256 m	1348 m

respect to a conventional take-off achieving a runway length reduction (TOFL in Table 3.6) of the 40%.

EML systems have the potential of reducing runway length even further considering that the data shown in Table 3.6 for assisted take-off was computed using the same technique adopted for conventional take-off. In particular, the distance s_{stop} in eq. 3.44 depends on the deceleration due to the action of a conventional braking system whose performance depends on the pavement condition. The EML system may be used as electromagnetic brake that can decelerate the aircraft at higher rates and independently from external and environmental factors in case of engine failure. For, instance with a deceleration equal to the aircraft acceleration during assisted take-off, a runway length reduction of 51% can be estimated. Section 3.3.3 will also show in Table 3.7 that the TOFL reduction using an electromagnetic catapult in adverse environmental conditions can reach 52% of the runway length required by engine-boosted aircraft in the same atmospheric conditions.

The reduction of the runway length required at take-off is one of the major benefits of EML systems. Actual runways could respond to the air traffic growth without the need of expensive airport extension through the implementation of an electromagnetic catapult. Beside the possibility of avoiding airport extensions,

Table 3.6 shows that the EML system implementation may allow the use of actual runways to serve two aircraft taking off simultaneously from the center of the runway and accelerating in opposite directions, thereby doubling airport capacity. For this reason, EML launch systems may be a viable alternative either to Heathrow third runway or to the Heathrow runway extension proposals of £17.6 billion and £14.4 billion respectively [2].

3.3.3 Catapult Requirements

The take-off analysis outcomes in Section 3.3.1 were calculated under the hypothesis of an aircraft operating in ISA condition at sea level. However, the rotation speed V_R, which represents the end-speed requirements of the electromagnetic catapult, may sensibly vary in different environments. Since the catapult has to cope with all the weather conditions, this section aims to find the worst case combination of environmental factors that allow the right selection of the end-speed requirement to size the launcher.

What mainly affects the rotation speed is the engine thrust decrease with low air density and high environmental temperature. These conditions may be encountered at airport located above sea level and at low latitude. In order to determine the catapult end-speed requirement under adverse environemental conditions, the take-off analysis was carried out at 35 °C (ISA+20 K [79]) and at an altitude of 3000 ft (approximately 915 m). The results of the take-off analysis under these conditions are shown in Table 3.7, and conventional and assisted take-off are compared.

Table 3.7 shows a rotation speed which is 6 m/s faster than the rotation speed calculated at ISA conditions at sea level, shown in Table 3.6. As expected, the value of V_R at ISA+20K shows that the end-speed requirement of the electromagnetic catapult should consider the variation of the engine performance with environmental conditions in order to attain a speed that allows the aircraft to proceed with the climbing phase. If only the ISA+0K conditions are considered, in adverse environmental conditions engines will be used to accelerate the aircraft to V_R after the catapult detaches.

A successful design of an electrical motor imposes the selection of a safety

Table 3.7: Take-off performance comparison in ISA+20 K condition at 3000 ft

Parameter	Engine Take-off	EML take-off
Climb gradient	2.427%	2.427%
Max lift coefficient	1.881	1.881
Lift-Drag Ratio	13.92	13.92
Flap deflection	5°	5°
Stall Speed	71.44 m/s	71.44 m/s
Rotation speed	**74.32 m/s**	**74.32 m/s**
Lift-off speed	78.58 m/s	78.58 m/s
Screen Speed	**85.73 m/s**	**85.73 m/s**
Run time	33.41 s	12.63 s
Airborne time	7.52 s	7.52 s
Run distance	1857 m	469.4 m
Airborne distance	629.1 m	629.1 m
TOD	2779 m	1263 m
BFL	3208 m	1565 m
TOFL	**3208 m**	**1565 m**

margin with respect to the desired end-speed requirement. The safety screen speed V_2 is approximately 15% greater than the rotational speed V_R and this margin is considered adequate for EML design purposes. With such an achievable speed excess the EML system will be capable of coping with any take-off condition. Therefore, the sizing technique presented in Chapters 4, 5 and 7 will consider the speed V_2 shown in Table 3.7 as end-speed requirement even though the speed to attain remains V_R.

The electromagnetic catapult has to provide the same acceleration rate during the whole take-off procedure overcoming the aerodynamic drag and the friction with the runway pavement. In order to be conservative on the thrust requirement calculation, the weight of the aircraft will be considered constant over the acceleration phase and the aerodynamic drag coefficient estimated at V_2 using the air density at sea level will be applied during the whole acceleration. Therefore instantaneous required thrust can be estimated as

$$F_x = 0.6\,G\,m_{A320} + D + \mu_{A320}(m_{A320}\,G - L) \tag{3.56}$$

where μ_{A320} is the friction coefficient with the ground (0.02 for a paved runway), and D and L are the aerodynamic drag and lift that can be respectively computed

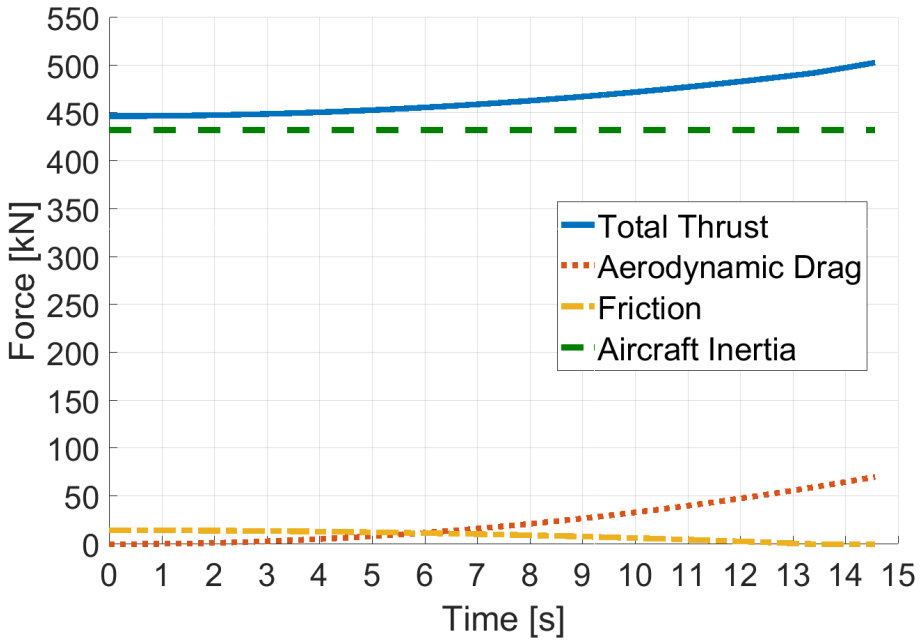

Figure 3.10: Required thrust during aircraft acceleration and respective thrust components

as

$$D = \frac{1}{2}\rho_{Air} S_w C_{D2} V^2 \tag{3.57}$$

$$L = \frac{1}{2}\rho_{Air} S_w C_{L2} V^2 \tag{3.58}$$

The thrust profile needed to accelerate a fully loaded A320-200 aircraft until the required end-speed and the respective thrust components are shown in Fig. 3.10. Since the aerodynamic drag grows with the square of the aircraft velocity, the maximum thrust is delivered when the aircraft reaches the end-speed.

The main catapult requirements are summarized in Table 3.8. The minimum time between two consecutive launches is defined as cycle time in Table 3.8. A minimum cycle time must be imposed between aircraft taking off, to ensures safety both at take-off and in-flight. Since wake vortices are left behind aircraft wings, they might affect following aircraft if they take-off too soon. The selected cycle time allows the vortices to viscously dissipate their energy and prevents any deterioration of the aerodynamic performance of next aircraft. This time separation between take-off should be at least one minute [81], but it is considered to

Table 3.8: Requirements of the EML system for civil aircraft

Catapult end-speed	85.73 m/s
Max Thrust	502.9 kN
Acceleration	0.6 G
Cycle time	90 s

be 90 seconds to enlarge the safety margin. The minimum separation between launches corresponds to the time the machine spends at rest and it is a useful data for the thermal design of the electrical catapult.

The take-off performance analysis in adverse environmental conditions presented in this section does not consider the common practice of reducing the thrust losses at high atmospheric temperatures through water-methanol injection. A mixture of water and methanol is usually sprayed into the compressor inlet or injected in the combustion chamber and, as the liquid evaporates, it cools and thickens the air and with the same air speed the mass flow through the engine increases. However, since high temperature is needed after the combustion chamber, the turbine entry temperature is restored by the combustion of methanol which normally releases more energy than the aircraft propellant. With the use of water-methanol injection the rated thrust can be maintained up to a deviation of 20 K from the standard atmosphere and if required it can be increased by about 3% to 7% in ISA conditions [78].

3.3.4 Noise and Exhaust Emission Reduction

The comparison between take-off histories and performances in Tables 3.3 and 3.6 has shown that the catapult impacts the take-off distances and times leading to lower fuel consumption. The 48.5 kg of fuel that can be saved during each A320-200 aircraft take-off can be used to extend flight distances or can be removed to fly with a lighter aircraft. Even though the propellant saved in a single flight is just a small portion of the total amount of fuel on board the aircraft at the departure, considering an airport like Heathrow with approximately 650 flights per day and assuming the same fuel saving for each take-off, about 31525 kg of fuel can be saved on a daily basis. Although there are many kinds of airplanes

Table 3.9: CFM56-5A1 engine exhaust emission data

Mode	Power Setting	Emission Indices [g/kg]		
		HC	CO	NOx
Take-off	100%	0.23	0.9	24.6
Climb out	85%	0.23	0.9	19.6
Approach	30%	0.40	2.5	8
Idle	7%	1.4	17.6	4
Emission reduction at Heathrow [g/day]		7251	28373	775515
Exhaust emission for passenger cars [g/day]		35.4	309.0	22.78
Equivalent number cars		205	92	34044

with different fuel consumptions, maximum thrusts and take-off times that depart from Heathrow every day, the A320-200's class of aircraft can be considered as an average in terms of fuel consumption. The fuel that would not be burnt in Heathrow with an EML system leads to a cost saving $S_{€}$ that can be estimated as

$$S_{€} = \frac{m_{Fuel}}{\rho_{Fuel}} F_{€} \tag{3.59}$$

where m_{Fuel} is the mass of fuel saved, ρ_{Fuel} is the fuel density (approximately 0.803 kg/l) and $F_{€}$ is the fuel price per litre (which is approximately 0.603 €/l in this study, but it may significantly change). Applying eq. 3.59 to Heathrow airport yields a daily saving of 23670 €/day and an annual saving of 8.64 M€/year in fuel investment. This fuel saving is not particularly relevant with respect to the total annual fuel investment in Heathrow (which is roughly estimated 6200 M€), but it may significantly impact pollution at ground level.

The engine emission indices per kilo of fuel burnt given in Table 3.9 [82] allow an estimation of the daily exhaust emission reduction. For every type of pollutant, the daily emission reduction at ground level is 19.6%. In order to understand the impact of EML systems the emissions of each pollutant in Table 3.9 were compared with the respective car daily emission [83]. For instance, the NOx emission reduction at the airport is equivalent to the average daily emissions of 34044 cars.

As already mentioned in this thesis, aircraft engines usually take 4 seconds to pass from idle condition to maximum power. Comparing the time that the engines spend at full power during conventional take-off and during EML take-off (29.6

and 10.2 seconds respectively from Table 3.3), approximately 66% noise emission reduction at ground level may be expected. This noise emission will occur only near the take-off point, since during most of the acceleration the engine will be kept in idle condition.

3.3.5 Engine Size Reduction

Sections 3.3.1 to 3.3.4 have shown how the electromagnetic launcher brings significant benefits to city airports in terms of take-off field length, fuel consumption, noise emission and exhaust emission reduction. However it does not seem to imply drastic cost reduction for airline operators which do not experience consistent annual saving on aircraft operational costs. Indeed, considering that a civil transport aircraft completes approximately 750 flight every year, eq. 3.59 computes an annual saving of 27315 €/year which is negligible compared to the total annual expense of 8.227 M€/year.

The take-off analysis presented in Section 3.2 can be applied to estimate whether it is possible to reduce the engine thrust when implementing an EML system and respecting the minimum climb out gradient requirement $\gamma_2 > \gamma_{2_{Req}}$. When the installed thrust reduces, size and cross section of the engines decrease proportionally. This section investigates the effect of different rated thrust on the flight performances of aircraft which have to accomplish the same mission: reach a destination 2450 NM distant carrying a payload of 14058 kg in ISA condition at sea level. In particular, this analysis aims to quantify the possible fuel and cost saving that can be achieved by the installation of smaller engines.

Table 3.10 shows the results of the investigation across a thrust range that spans from the CFM56-5-A1 rated thrust to the minimum thrust level that satisfies the requirement $\gamma_2 > \gamma_{2_{Req}}$.

Assuming constant flap deflection, the reduced engine cross section can only have a beneficial impact on the aerodynamic drag of the aircraft at take-off for the reduce nacelle cross section and wet area. The thrust reduction has also a secondary effect on the aerodynamic drag at take-off: since lighter engines are installed, the aircraft weight decreases and the lift force required to take-off diminishes along with it; lower lift means lower take-off speed and lower aerodynamic

Table 3.10: Take-off and flight performance with reduce engine size and thrust

Thrust [kN]	γ_2 **%**	**Flap [deg]**	C_{D_C}	V_2 **[m/s]**	V_R **[m/s]**	**TOFL [m]**	**MTOW [kg]**	m_{Fuel} **[kg]**	m_{Eng} **[kg]**	m_{Stru} **[kg]**
A320 engine-boosted take-off										
111.2	2.471	14	.03231	79.62	68.35	2256	73500	18273	5921	20929
A320 EML take-off										
111.2	2.471	14	.03231	79.59	68.32	1347	73447	18273	5921	20929
110.0	2.525	13	.03229	80.21	68.91	1368	73291	18159	5856	20906
107.5	2.472	12	.03224	80.74	69.51	1389	72988	18054	5719	20860
105.0	2.417	11	.03219	81.26	70.12	1411	72674	17936	5583	20814
102.5	**2.486**	**9**	**.03214**	**82.45**	**71.24**	**1451**	**72357**	**17816**	**5447**	**20767**
100.0	2.421	8	.03209	82.95	71.79	1471	72061	17715	5312	20721
97.5	2.449	6	.03204	84.08	72.84	1510	71751	17602	5176	20675
95.0	2.434	4	.03199	85.12	73.84	1547	71448	17493	5042	20629
92.5	2.415	1	.03194	86.58	75.09	1594	71157	17397	4907	20583
90.0	2.974	0	.03189	102.5	90.85	2247	70832	17267	4773	20536
87.5	2.793	0	.03184	102.3	90.78	2245	70538	17167	4639	20490
85.0	2.606	0	.03179	102.1	90.74	2243	70270	17092	4506	20445
82.5	2.418	0	.03174	101.9	90.70	2241	69997	17008	4373	20402

drag.

The decrease of the nacelle cross section and wet area causes an additional drag reduction not only during take-off, but across all the flight phases as well. For instance, Table 3.10 shows the value of the drag coefficient C_{D_C} at 35000 ft and Mach 0.75 to demonstrate the impact of the nacelle size reduction on the aerodynamic drag during cruise. The aerodynamic drag reduction across the flight phases causes a fuel consumption reduction that sensibly decreases the amount of fuel that needs to be carried on board.

The engine thrust and size reductions cause a decrease in the engine mass m_{Eng}. In turn, the reduced engine mass has a positive impact on the mass of the aircraft structure m_{Stru}, for the decrement of the mass of the nacelle and of the engine structural supports. Aerodynamic drag, engine mass and structure mass reductions significantly decrease the mass of fuel m_{Fuel} needed to reach the final destination and the maximum take-off weight MTOW as shown in Table 3.10.

Even though the engine size reduction has a such a positive impact on the overall flight performance and aircraft mass, the installed thrust cannot be indefinitely decreased. Despite the drag and weight reductions, a lower thrust has such a strong effect on the take-off characteristics in one engine inoperative condition

that the flap deflection must decrease to guarantee the passenger safety (condition represented by the requirement $\gamma_2 > \gamma_{2Req}$). Eq. 3.8 used to calculate γ_2 shows that a thrust decrease implies a climb out gradient reduction unless the aerodynamic drag diminishes as well. The aerodynamic drag reduction at take-off due to the aforementioned effects is not enough to achieve the required climb out gradient. As in normal take-off operations the aerodynamic drag must then be reduced by retracting the flaps.

The effect of the flap deflection reduction prevails on the other positive effects and the impact of the reduced nacelle cross section on the aerodynamic drag can be only seen in Table 3.10 looking at the characteristic speeds V_2 and V_R and at the TOFL when the flaps are fully retracted and when the thrust is lower than 92.5 kN. For thrusts equal or greater than 92.5 kN, the reduced flap deflection causes a increment of the speed required to generate the same lift force across the whole take-off phase. In particular, Table 3.10 shows the increment of the safety-screen speed V_2 and of the rotation speed V_R until the flaps are not deflected any more.

Since the catapult is responsible for the aircraft acceleration, the distance s_{Run} required to propel the aircraft until the catapult's end-speed is proportional to the square of V_R. When the nose rotation speed rises for the lower flap deflection required at take-off, the acceleration distance exponentially increases. The airborne distance s_{Air} increases as well for the lower thrust available between the lift-off point and the screen altitude. These effects cause a gradual increase of the TOFL until the thrust reaches 92.5 kN and the flaps have a minimum deflection. When the flaps are fully retracted, the TOFL reported in Table 3.10 sharply increases and becomes comparable with the distance required by conventional A320-200 take-off. With such a low installed thrust the advantage of reducing the runway length through the EML system implementation is lost. For this reason, it is not practical to reduce the installed thrust below 92.5 kN. Nevertheless, even this value of the installed thrust cannot be selected as other important factors need to be taken into account.

Indeed, the data shown in Table 3.10 was obtained from analyses performed in standard atmospheric condition at sea level, but the aircraft also needs to operate in several weather conditions. The engine performance decrease with the altitude and the environmental temperature imposes a limit on the thrust reduction

and on the respective minimum value of flap deflection at take-off. A maximum flap deflection reduction of 5° with respect to the rated value can be considered acceptable in ISA conditions to guarantee successful aircraft operations also in adverse environments. For this reason, the minimum acceptable installed thrust highlighted in Table 3.10 is not 92.5 kN, but 102.5 kN which corresponds to 9° flap deflection. Water-methanol injection can be always used to increase the take-off thrust if needed.

Therefore, accounting for all the benefits and drawbacks that the engine size reduction brings, the installation of an EML launch system may allow future A320-200 aircraft with an installed thrust of about 102.5 kN to operate. With this total thrust the aircraft would save 457 kg of fuel each flight if travelling a distance of 2450 NM.

Eq. 3.59 can be applied to estimate the annual cost saving of airline operators that will own the A320-200 with reduced installed thrust. Considering 750 flights per year, 257380 €/year can be saved, approximately 3.10% of the total amount that the airline operator spends to fuel existing aircraft. This cost saving extended to the full fleet might push airline operators to invest in the installation of multiple EML systems at several airports.

3.4 Contribution to Knowledge

For the very first time the take-off performance analysis of aircraft including the effects of an electromagnetic catapult has been carried out in compliance with the requirements established by Federal Aviation Regulation (FAR). Indeed, the researchers who have investigated EML systems for military applications have been more concern with the launcher design than with the study of the take-off performance of aircraft. In this work, the safety requirements in the case of an engine failure have received particular attention while research on military technology is not usually limited by strict safety regulations.

The key findings presented for the first time in this chapter (runway length, fuel consumption, noise emission and exhaust emission reductions) are an important added value that may push future research on EML systems for civil applications. For a very first time a method that can significantly reduce the installed thrust on

board aircraft without compromising passenger safety and aircraft performance in case of engine failure was proposed. To achieve these results a software for civil aircraft design has been edited and improved to simulate the electromagnetic catapult at take-off.

Chapter 4

Linear Induction Motor

This chapter deals with the design of a Linear Induction Motor (LIM) accounting for special phenomena like transverse and longitudinal edge effects, which do not occur or have a negligible impact on rotary machines. An accurate description of the electromagnetic design procedure of a LIM for a civil aircraft Electromagnetic Launch (EML) system is proposed, together with an explanation of the methods that were used to structurally and thermally characterize the moving plate. The analytical theories are compared with Finite Element Analysis (FEA) results to validate the adopted design procedures.

4.1 Introduction to LIM for EML

Linear induction machines are particularly attractive for EML application since they have a cheaper and simpler mover structure than other launcher topologies which either involve expensive materials like rare earth permanent magnets and superconducting ceramics or require very precise closed loop position feedback. Induced current is generated into the LIM's armature which can be a simple aluminium or copper plate. With a low mass mover, LIMs can achieve the maximum kinetic energy transfer to the aircraft with respect to other motor topologies that employ heavy materials on the moving part of the machine.

Nevertheless LIMs are characterized by low electromagnetic performances when compared with other linear electrical machines and the cost increase due to the

power conditioning requirements might sensibly affect the decision on the most suitable technology for EML applications. The large mechanical airgaps commonly required in practical EML systems are augmented by the thickness of the armature causing significant flux fringing and requiring large magnetising currents, which in turn increase drive output rating and reduce system power factor. The limited length of the machine both in parallel and perpendicular direction to the motion causes phenomena that tend to further reduce the machine power factor increasing the size, mass and design difficulty of the power inverter.

Despite the expected low electromagnetic performance, the simplicity of the machine and the possibility of open loop operation make LIM a valid candidate to investigate for electromagnetic launch applications.

4.1.1 LIM Topology Selection

A linear induction motor can be described as a conventional rotary machine which has been cut along an axial plane and unrolled to form a flat structure as shown in Fig. 4.1. This 'unrolling' routine to generate the single-sided linear machine from the rotary counterpart can be applied to the primary winding arrangement as well.

Distributed windings are associated with a low harmonic content and are usually preferred to concentrated windings for the primary of induction machines. In order to improve the thrust generation capability of the electromagnetic launcher, the slots of LIM will host distributed winding disposed in a double-layer configuration. Nevertheless, double-layer distributed windings demand additional installation costs when compare with the simpler tooth winding configuration that can be implemented in synchronous machines.

In linear motors a normal force acts between rotor and stator, while in rotary induction machines the normal force cancels due to its symmetrical distribution. The single-sided configuration can be exploited for active magnetic suspension taking advantage of the normal force. In single-sided stator configuration the tooth-slot structure of the flat cage secondary can also be replaced by a conductive sheet with a ferromagnetic backing plate. The slotted cage secondary allows for a lower magnetic airgap than the conductive sheet on iron secondary and produces higher normal forces which can be an advantage when suspension is required [18].

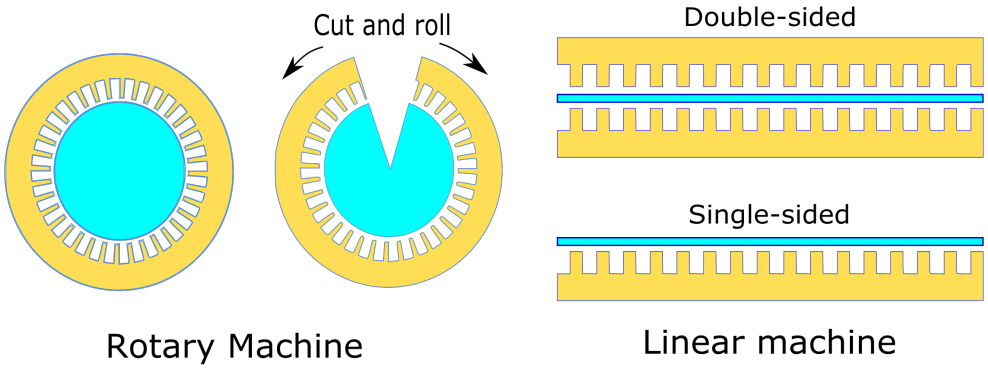

Figure 4.1: Derivation of LIM from rotary counterpart

To get a net zero normal force a second stator may be added on the other side of a mover consisting only of a conductive sheet without the ferromagnetic backing plate, leading to a double-sided LIM configuration as shown in Fig. 4.1. In double-sided LIMs the ferromagnetic backing plate is not required since the complete flux path passes through both stators and across both airgaps, with symmetry along the center line of the secondary. Thus, the conductive sheet can be used alone leading to a particularly light and simple mover structure.

The double-sided motor does not produce normal force when the mover is symmetrically placed between the stators. In this case the slotted secondary topology could still be used to reduce the magnetic airgap, but the normal force would no longer be stable. Since electromagnetic launch systems do not require magnetic suspension and they benefit from having light and simple movers in equilibrium within the airgap, the double-sided topology has been considered as the most suitable for LIM launchers.

LIMs can be classified as passive guideway LIMs or active guideway LIMs as shown in Fig. 4.2. Two single-sided motors are shown in place of the respective double-sided version for clarity. In the former case, the conductive plate is stationary and the full power is either transferred to or generated on the mover. This topology has been commonly adopted in transportation for MAGLEV trains, where the cost of an active guideway can be considerable. The on board generation of tens of MW required by the electromagnetic launch would drastically increase the weight of the mover and a considerable portion of the input energy

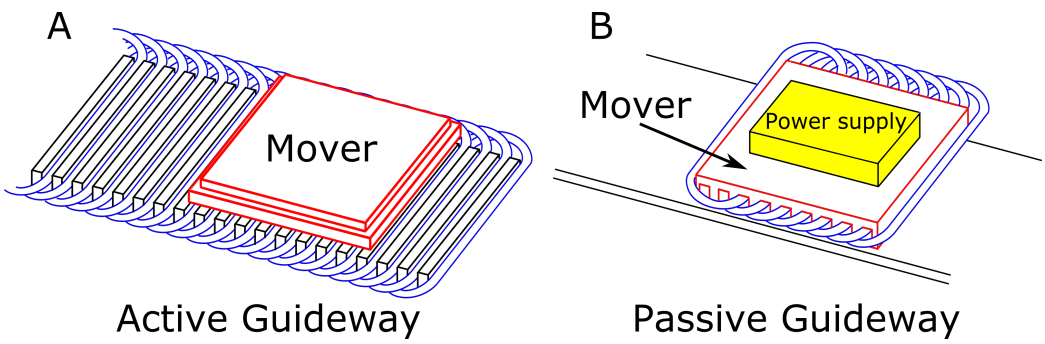

Figure 4.2: Linear induction motor topologies

would be wasted to accelerate the heavy power supply. In LIMs with passive guideways power can be also transferred on board through moving electric contact. The transfer of the full power on the mover would require an on board power conversion system with consequent additional weight, energy waste, and non negligible engineering challenges. Alternatively, a LIM with an active guideway has a moving conductive plate and stationary stators fed by external power systems and no power supply or power conditioning systems are required on board the vehicle.

The conductive sheet is often made out of aluminium for its low density, high electrical conductivity and good structural properties while copper may be selected to take advantage of its higher electrical conductivity and melting point. Aluminium is preferred for EML applications to reduce the active power needed from the catapult and transfer the most of the kinetic energy to the aircraft. Nevertheless, an accurate estimation of the temperature increase on the conductive plate is required to prevent structural failures or melting. Therefore a double-sided LIM with an active guideway and an aluminium secondary has been selected for EML to improve the energy transfer to the aircraft while reducing the weight and complexity of the mover.

It is worth mentioning another possible classification of LIMs: long primary LIM (with short secondary) and long secondary LIM (with short primary). The former option coincides with the active guideway LIM in Fig. 4.2A. The latter topologies is similar to the motor B in Fig. 4.2 where the conductive sheet becomes the moving part and the short mover becomes stationary. This option is not suitable for EML since it would entail a moving plate with the runway length.

4.2 Circuit Theory, Field Theory and Goodness Criterion

A simple model of electromagnetic forces produced between conductors carrying currents is necessary if any progress is to be made in designing linear induction motor. In rotating machine studies the *equivalent circuit model* is extensively used for it enables the designer to consider the machine as a network of resistors and inductors, temporally forgetting that he is dealing with moving objects.

Every electrical machine may be considered as an electric circuit and a magnetic circuit which interact together to convert electrical power into mechanical power or vice versa. Any other form of energy conversion can be considered as losses in the machine. For instance, the heat dissipated in conductors while current is flowing is modelled as a resistance in series with an otherwise perfect electric circuit. The heat losses in the primary electric circuit are modelled as a resistance R_1, while the rotor losses are represented by the resistance R_2 as shown in Fig. 4.3. Part of the energy of the magnetic circuit is used to link the primary and secondary and this effect is modelled through an inductance L_m in parallel with the rotor resistance R_2. Unlike the electric losses, the magnetic energy in the inductances is not dissipated under the form of heat, but it is stored in the magnetic field without contributing to the generation of mechanical power. The electric circuit losses are connected in series while magnetic circuit inductances are connected in parallel. This means the more efficient the electric circuit the lower R_1 and R_2, whereas the more efficient the magnetic circuit the larger L_m. Since not all the magnetic flux is routed exactly across the airgap, the portion that does not link both primary and secondary circuits can be regarded as a series leakage inductances L_1 and L_2 respectively.

The magnetic circuit has a second kind of loss due to eddy currents and hysteresis loop of ferromagnetic materials. Eddy currents can be treated as a third electric circuit with an electromotive force induced by the same flux and therefore to be regarded as an impedance in parallel with the magnetizing reactance $X_m = \omega L_m$. The eddy currents effect is proportional to the magnetic flux Φ_m^2 and can be represented as a fictitious resistance connected across a voltage proportional to Φ_m, i.e. in parallel with X_m. The same parallel-connected resistor is used to repre-

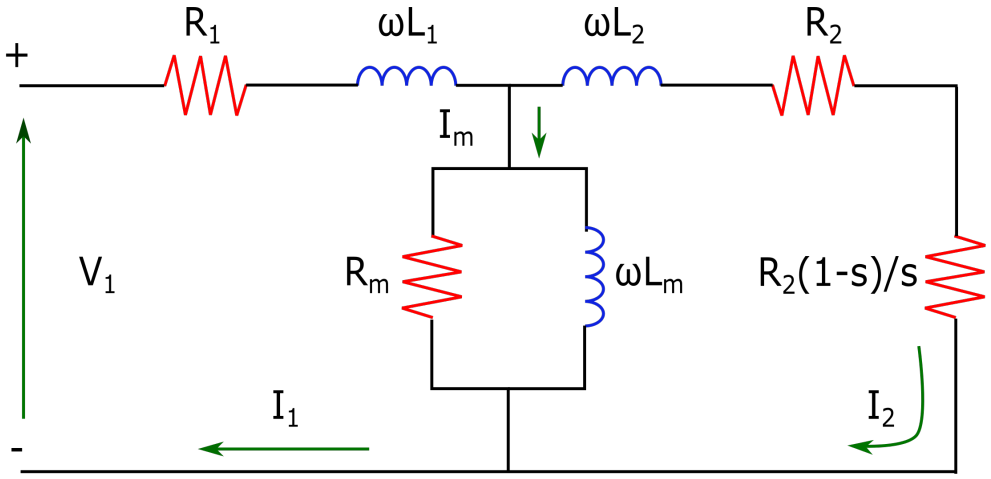

Figure 4.3: Equivalent circuit of induction machines

sent hysteresis losses, even though they do not behave as eddy currents. As first approximation hysteresis losses are considered proportional to B^2.

Linear and rotary induction machines can be sized by the mean of the steady state equivalent circuit shown in Fig. 4.3. Since the force F produced on the mover by the magnetic field wave which travels at synchronous speed v_s is equal to the force produced by the mover on the load at speed v_r, the mover power equation may be written as

$$Fv_s - Fv_r = P_2 \tag{4.1}$$

where P_2 is the power lost in the secondary. Each side of eq. 4.1 for the linear case can be divided by Fv_s leading to eq. 4.2.

$$\frac{v_s - v_r}{v_s} = \frac{P_2}{Fv_s} = \frac{P_2}{P_i} = s \tag{4.2}$$

where s is also called slip frequency. Since all the mover losses can be attributed to an equivalent resistance R_2 and having defined the mover efficiency as

$$\frac{P_i - P_2}{P_i} = 1 - \frac{P_2}{P_i} = 1 - s \tag{4.3}$$

the mover power input may be represented as a fictitious resistance R_2/s. The resistance R_2/s is often subdivided into R_2 to represent the mover losses $R_2 I_2^2$ and

the reminder $R_2(1-s)/s$ for the mover power output as shown in Fig. 4.3.

Any required information on induction machines can be extracted from the equivalent circuit, but the complexity of the computation to determine the motor performance may need some approximations. The most common assumption is that the iron loss resistance R_m is much larger than any other components. This assumption introduces larger and larger errors as the mover speed approaches to synchronism, but if the full-load force occurs at sufficient large slip the approximate equivalent circuit will give results of the required accuracy for most of the values of slip frequency. It is a common practice to reconsider the iron loss on the computation of the total active power and efficiency.

Based on the electromagnetic power definition, the force generated along the direction of the motion by three phase secondary current may be computed as

$$F = 3\frac{R_2}{s}\frac{I_2^2}{v_s} \tag{4.4}$$

The Kirchoff laws applied to the equivalent circuit in Fig. 4.3 allow to express the secondary current as a function of the primary current.

$$I_2^2 = \frac{X_m^2}{(R_2/s)^2 + (X_2 + X_m)^2} I_1^2 \tag{4.5}$$

where $X_2 = \omega L_2$ is the secondary leakage reactance. Substituting the secondary current (eq. 4.5) in eq. 4.4 the synchronous thrust may be expressed as a function of the primary current as

$$F = \frac{3(R_2/s)X_m^2}{v_s\left[(R_2/s)^2 + (X_2 + X_m)^2\right]} I_1^2 \tag{4.6}$$

having a maximum where

$$s_{max} = \frac{R_2}{X_2 + X_m} \tag{4.7}$$

The general relation between thrust and slip frequency of an induction motor is shown in Fig. 4.4.

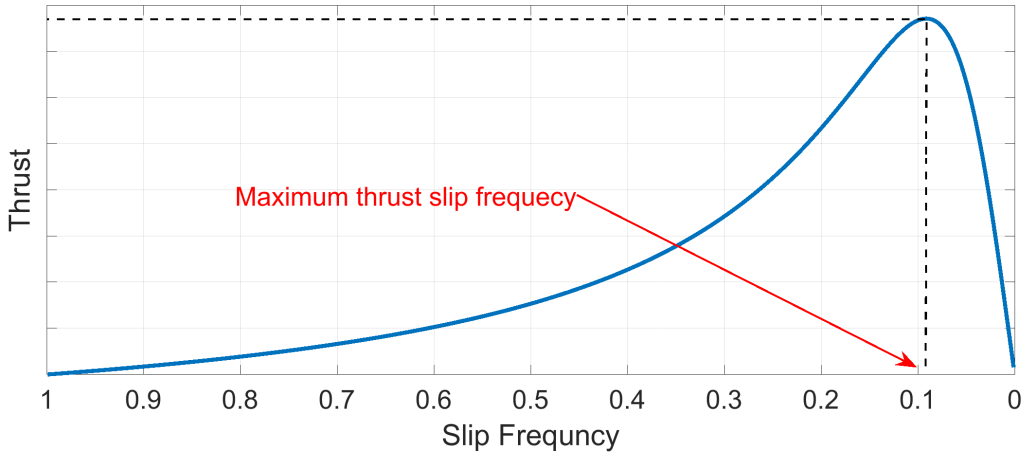

Figure 4.4: Variation of the force of induction motor with the slip frequency

4.2.1 The Goodness Factor G

The circuit model can be easily used to compute fundamental machine properties like efficiency with reasonable accuracy. The value of efficiency of an induction machine indicates the portion of real power that is converted to useful mechanical power and is not dissipated under the form of heat. However, the quality of a machine cannot be only determined by the calculation of its efficiency, because other factors such as power factor, power density, etc also have a significant effect on the overall system. The quality of an induction machine has to be evaluated on the basis of its capability to convert the input power into the desired form of power.

The *goodness factor* of an induction machine has been introduced to express the ability to convert power from one form to another as mentioned in [84] page 23. The mechanical power is the product of force and speed while the force in an electrical machine is proportional to the product of current and flux. The goodness factor is therefore concerned with the ability of the electric circuit to produce a current I from a given electromotive force E and the ability of the magnetic circuit to produce a flux Φ from a given current. Consequently,

$$G \propto \frac{I}{E} \cdot \frac{\Phi}{I'} \tag{4.8}$$

The ratio I/E in eq. 4.8 is equal to the reciprocal of the resistance R from the

Ohm's law while Φ/I' is proportional to the inductance L. Eq. 4.8 can be rewritten as

$$G \propto \frac{L}{R} \tag{4.9}$$

The goodness factor in eq. 4.8 has the dimension of time, but it should be dimensionless. Since the product $\Phi \cdot I$ is the work done by the force, while the goodness factor is more concerned about machine power conversion, the final expression of G should contain the angular frequency ω which dimension is the reciprocal of time.

$$G = \frac{\omega L}{R} \tag{4.10}$$

To understand which is the correct value of L and R to considered in eq. 4.10, it is important to note that the series of impedance of the primary circuit (R_1 and ωL_1 in Fig. 4.3) is independent of the electromagnetic action. The circuit which really matters for power conversion purposes is the rotor one, whence in absence of secondary leakage reactance the value of G is simply given by

$$G = \frac{\omega L_m}{R_2} = \frac{X_m}{R_2} \tag{4.11}$$

It is now important to correlate the expression of G with the physical dimensions of the induction machine. Equations 4.8 and 4.10 have shown how the goodness factor is proportional to the product of the following quantities

$$G \propto \frac{1}{R} \cdot \frac{1}{\mathfrak{R}} \cdot f \tag{4.12}$$

where $\mathfrak{R}$ is the reluctance of the machine and the reciprocal of the inductance L. Calling A_e and l_e the area and the length of the electric circuit and A_m and l_m the area and the length of the magnetic circuit eq. 4.12 can be rewritten as

$$G \propto \frac{A_e}{\rho l_e} \cdot \frac{\mu_0 A_m}{l_m} \cdot f \tag{4.13}$$

where ρ is the resistivity of the material and μ_0 the permeability of the void. Considering the dimensions illustrated in Fig. 4.5 the length of the magnetic circuit

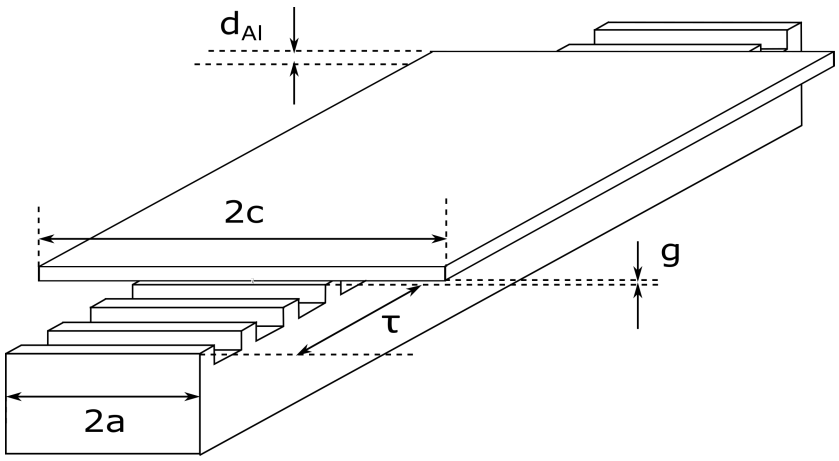

Figure 4.5: Section of a single-sided linear induction motor

may be taken, in the first instance, to be the length of the airgap, while the length of the electric circuit is the stator width $2a$. The area of the electric circuit is given by the product between the pole pitch τ and the mover thickness d_{Al}, while that of the magnetic circuit is the product between the pole pitch and the stack width. Eq. 4.13 can be rewritten as

$$G \propto \frac{\tau d_{Al}}{\rho 2a} \cdot \frac{\mu_0 \tau 2a}{g} \cdot f \propto \frac{\mu_0 \tau^2 f d_{Al}}{\rho g} \tag{4.14}$$

The constant of proportionality needed to write eq. 4.14 as an equality is $2/\pi$ [84]. This constant takes into account the sinusoidal distribution of flux and current and relates the inductance to the inverse of reluctance on any given system of units. The goodness factor becomes

$$G = \frac{\mu_0 \tau^2 \omega \sigma d_{Al}}{\pi^2 g} \tag{4.15}$$

where $\omega = 2\pi f$ and $\sigma = 1/\rho$.

In application like electromagnetic launch system the value of G is necessary to evaluate the performance of the machine. Thermal and structural requirements of EML systems fix the aluminium plate thickness and the airgap length so that the goodness factor is proportional to $\tau^2\omega$. The launch end-speed $v_{TO} = \tau\omega/\pi$ depends on the aircraft take-off performances and the product $\omega\tau$ is given. The

goodness factor of LIM for EML application is therefore proportional to the pole pitch τ. To increase the power output for a given stator loss, large pole pitch and low frequency are needed to get high goodness factors.

4.2.2 Field Theory and Special LIM Phenomena

Both linear and rotary induction machines can be modelled through the equivalent circuit in Fig. 4.3. However, linear machines present some specific phenomena that either do not exist, do not have the same extent or are negligible in the rotary case. Linear induction machines suffer larger airgap fringing and skin effect than their rotary counterparts, while the finite length and width of the mover cause so called end-effect and edge-effect respectively. An accurate model of LIMs needs to consider these phenomena to correctly estimate the machine performance.

The impact of airgap fringing, skin effect, edge-effect and end-effect on the performance can be modelled by the mean of factors which multiply either the airgap length g or the rotor electric conductivity σ. In turns, both electric conductivity and airgap length are parameters involved in the calculation of the machine goodness factor as shown in eq. 4.15. Therefore, the sizing techniques for rotary induction machines can be employed in the linear case once the factors related to special LIM phenomena are estimated.

4.2.2.1 Airgap Fringing

When the magnetic airgap becomes rather large a portion of primary flux does not cross the airgap following a straight path, but it tends to bulge following a longer path as shown in Fig. 4.6. This phenomenon causes an increase of the affective area of the airgap and a decrease of the magnetic field density within it. This effect is often indicated as airgap fringing and this section introduces the field theory to model it.

The total magnetic airgap of a double-sided LIM g_m is larger than the mechanical airgap g and depends on the reaction plate thickness as shown in eq. 4.16.

$$g_m = K \times g + d_{Al} \tag{4.16}$$

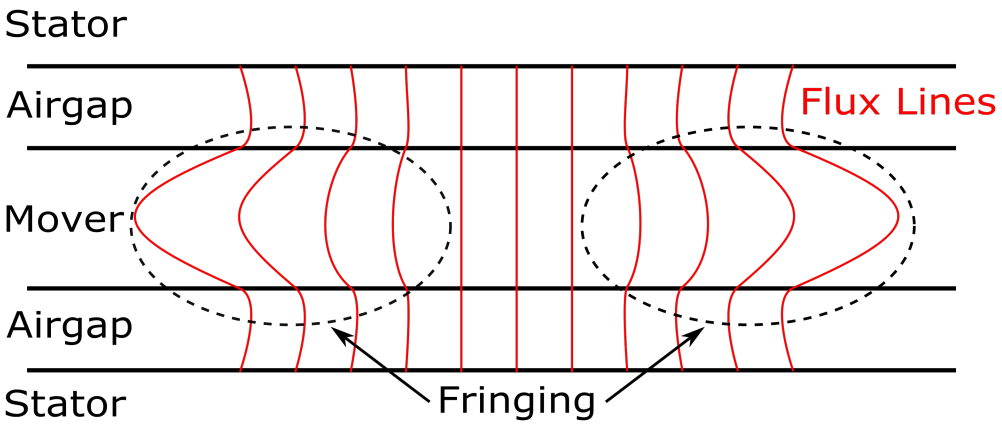

Figure 4.6: Airgap fringing in a double-sided induction motor

where $K = 1$ for single-sided LIM while $K = 2$ for double-sided LIM. The reaction plate is likely to be thick to withstand the mechanical and thermal stresses, especially for applications like EML systems where high traction forces and high current densities are involved.

The fringing effect due to the mechanical airgap g_m can be described by considering a fictitious machine with a larger airgap where the flux is assumed to cross normally at all points. A fringing factor k_{Fg} is introduced to represent the ratio between the mechanical airgap of the fictitious motor and the mechanical airgap of real induction machine. The equivalent circuit can be applied to the machine with larger airgap where no fringing is imposed considering an airgap length equal to $k_{Fg} \cdot g_m$.

The fringing factor depends on the flux distribution between stators which can be determined assuming that [85]:

- the excitation field is supposed to exit on an infinitely thin sheet of a perfectly conducting material according to the law $\vec{J}_2 = J_2 \sin(\pi x/\tau)$ where x is the direction of the motion;
- the stator is considered to be one meter wide, but part of an infinitely large system to neglect edge effect;
- the stator is also considered to be infinitely long to ignore end effects.

Under these assumptions, the vector potential A due to a filament of current positioned between the stators can be computed using the method of images derived by Moullin [86]. When the current filament $\vec{J}_2 dl$ is located on one boundary surface of the mover the vector potential becomes

$$A = \frac{\vec{J}_2 dl}{2\pi} \log \left[\cosh\left(\frac{\pi x}{g_m}\right) - \cos\left(\frac{\pi y}{g_m}\right) \right] \tag{4.17}$$

The magnetic field along x direction due to the current filament is given by

$$H_x = \frac{\partial A}{\partial y} = \frac{\vec{J}_2 dl}{2g_m} \frac{\sin\left(\frac{\pi y}{g_m}\right)}{\cosh\left(\frac{\pi x}{g_m}\right) - \cos\left(\frac{\pi y}{g_m}\right)} \tag{4.18}$$

Integrating eq. 4.18 with respect to dl from $-\infty$ to ∞ on one side of the gap yields

$$H_x = J_2 \sin\left(\frac{\pi x}{\tau}\right) \frac{\sinh\left(\frac{\pi(g_m - y)}{\tau}\right)}{\sinh\left(\frac{\pi g_m}{\tau}\right)} \tag{4.19}$$

Since $\nabla \times H = 0$ then $\partial H_x/\partial y = \partial H_y/\partial x$ and the magnetic field along y axis can be expressed as

$$H_y = J_2 \cos\left(\frac{\pi x}{\tau}\right) \frac{\cosh\left(\frac{\pi(g_m - y)}{\tau}\right)}{\sinh\left(\frac{\pi g_m}{\tau}\right)} \tag{4.20}$$

When a double-sided stator is considered the excitation filaments $\vec{J}_2 dl$ are located on both the boundary surfaces of the mover. By superposition of the effects of the current filaments eqs. 4.19 and 4.20 for the double-excited system become

$$H_x = J_2 \sin\left(\frac{\pi x}{\tau}\right) \frac{\sinh\left(\frac{\pi(g_m - y)}{\tau}\right) - \sinh\left(\frac{\pi y}{\tau}\right)}{\sinh\left(\frac{\pi g_m}{\tau}\right)} \tag{4.21}$$

$$H_y = J_2 \cos\left(\frac{\pi x}{\tau}\right) \frac{\cosh\left(\frac{\pi(g_m - y)}{\tau}\right) - \cosh\left(\frac{\pi y}{\tau}\right)}{\sinh\left(\frac{\pi g_m}{\tau}\right)} \tag{4.22}$$

When the flux is assumed to cross the airgap normally at all points, the magnetic

flux density can be calculated as

$$B_g = \frac{\mu_0 \tau J_2}{\pi g_m} \cos\left(\frac{\pi x}{\tau}\right) \tag{4.23}$$

For the single-sided case, the magnetic flux density $B_{y_{SS}} = \mu_0 H_y$ along the excitation plane ($y = 0$) can be derived from eq. 4.18 as

$$(B_{y_{SS}})_{y=0} = \mu_0 J_2 \cos\left(\frac{\pi x}{\tau}\right) \coth\left(\frac{\pi g_m}{\tau}\right) \tag{4.24}$$

The ratio of the magnetic field densities in eqs. 4.23 and 4.24 yields an expression of the fringing factor for a single-sided LIM.

$$k_{Fg} = \frac{(B_{y_{SS}})_{y=0}}{B_g} = \frac{\pi g_m}{\tau} \coth\left(\frac{\pi g_m}{\tau}\right) \tag{4.25}$$

In a similar way the the magnetic field density $B_{y_{DS}}$ of a double-sided LIM can be computed from eq. 4.22 as

$$(B_{y_{DS}})_{y=0} = \mu_0 J_2 \cos\left(\frac{\pi x}{\tau}\right) \tanh\left(\frac{\pi g_m}{2\tau}\right) \tag{4.26}$$

and the fringing factor becomes

$$k_{Fg} = \frac{(B_{y_{DS}})_{y=0}}{2B_g} = \frac{\pi g_m}{2\tau} \tanh\left(\frac{\pi g_m}{2\tau}\right) \tag{4.27}$$

4.2.2.2 Slot Opening Effect

The ideal magnetic flux density distribution in the airgap is represented by a sinusoidal wave. The slot openings modulate this shape reducing the performance of the machine. These disturbances can be represented by a larger mechanical airgap g_{me} where the magnetic flux density is supposed to vary sinusoidally. The ratio g_{me}/g_m is also called Carter coefficient k_c and it is also used for rotary induction machines design. Carter introduced this coefficient proposing eqs. 4.28 and 4.29 to compute it [87].

$$k_c = \frac{\tau_s}{\tau_s - \sigma_s b_s} \tag{4.28}$$

$$\sigma_s = \frac{2}{\pi}\arctan\left(\frac{b_s}{2g_m}\right) - \frac{2g_m}{\pi b_s}\log\left(1+\frac{b_s^2}{2g_m}\right) \tag{4.29}$$

where b_s and τ_s are slot width and slot pitch respectively as shown in Fig. 4.7.

Many other formulas have been proposed to calculate either the Carter coefficient k_c or the tooth width reduction factor σ_s. For instance, when the airgap length is rather large the Carter coefficient can be estimated as

$$k_c = 1 + \frac{\tau_s}{2\pi g_m}\left[\left(1+\frac{b_s}{\tau_s}\right)\log\left(1+\frac{b_s}{\tau_s}\right) + \left(1-\frac{b_s}{\tau_s}\right)\log\left(1-\frac{b_s}{\tau_s}\right)\right] \tag{4.30}$$

Matagne [88] established regions where eqs. 4.28 and 4.30 should be used alternatively to get higher precision. In combination with the Carter coefficient in eq. 4.28 he proposed the tooth width reduction factor

$$\sigma_s = \frac{2}{\pi}\left[\arctan\left(\frac{b_s}{2g_m}\right) - \frac{2g_m}{b_s}\log\sqrt{1+\left(\frac{b_s}{2g_m}\right)^2}\right] \tag{4.31}$$

In particular, to correctly calculate the Carter coefficient of LIM for EML application eq. 4.30 should be used.

Lower Carter coefficient can be obtained reducing the slot opening implementing semi-closed slots with wider tooth tips. Since the tooth tip reactance is lower than the one of the airgap, magnetic flux tends to concentrate inside the ferromagnetic material. This phenomenon may cause saturation, especially in those application where the magnetic flux density in the airgap is rather large. Linear induction machines for electromagnetic launch systems require strong magnetomotive forces to produce the required thrust and the rated magnetic flux density in the stator is close to the saturation point of the material. For this reason teeth with the shape shown in Fig. 4.7 were adopted for the induction launcher despite the increase of the Carter coefficient.

Carter coefficient and the fringing factor k_{Fg} can be combined together to express the equivalent airgap g_e as

$$g_e = g_m \cdot k_{Fg} \cdot k_c \tag{4.32}$$

The equivalent airgap is used in place of the real airgap to estimate the perfor-

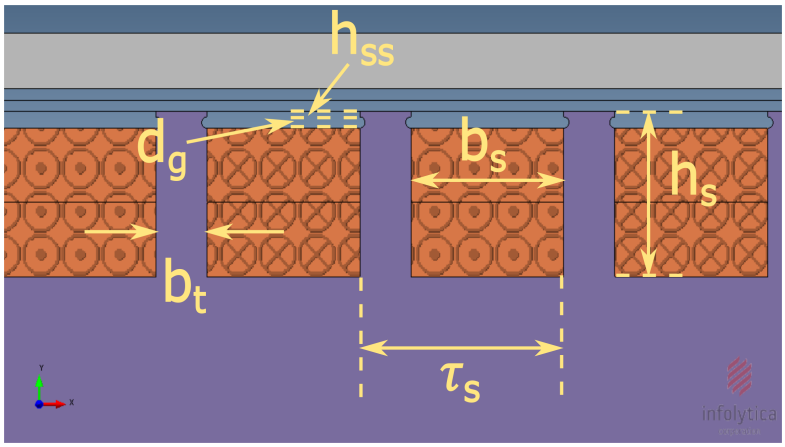

Figure 4.7: Primary key dimensions of a single-sided LIM

mance of the machine, and in particular it replaces g in the calculation of the goodness factor using eq. 4.15.

4.2.2.3 Skin Effect

The synchronous speed v_s of an induction machine is the speed of the travelling magnetic wave in the airgap. The induced currents in the conducting plate generate a magnetic field which interacts with the existing synchronous field producing a force. This force tends to align the two fields till an ideal synchronism is reached. In reality the secondary wave never reaches synchronization with the primary field, but travels at a lower speed that is calculated as

$$v_r = (1 - s) \cdot v_s \tag{4.33}$$

where v_r is also the mover speed. The difference in speed between the travelling magnetic wave and the mover induces a current with a frequency

$$f_r = s \cdot f_s \tag{4.34}$$

where the primary frequency f_s is related to the synchronous speed by the formula $v_s = 2\tau f_s$.

In general the rated slip frequency s of LIMs is rather large with respect to rotary IMs and, according to eq. 4.34, the secondary frequency sf_s is large as well.

Alternating current has the tendency to flow close to the surface of a conductor within a layer of material whose thickness is inversely proportional to the current frequency. This phenomenon is called *skin effect* and the penetration depth of the alternating current δ in the material of conductivity σ_{Al} is

$$\delta = \sqrt{\frac{2}{2\pi s f_s \mu_0 \sigma_{Al}}} \tag{4.35}$$

The penetration depth represents the distance form the surface where the current density reaches 63% of its rated value. For higher precisions, the penetration depth may be corrected by considering the travelling field variation along the motion direction in a simplified bidimensional airgap field model, rather than using the AC characteristic of rotary IMs, leading to eq. 4.36 [18].

$$\delta = \Re\left(\sqrt{\frac{1}{(\tau/\pi)^2 + j s f_s 2\pi \mu_0 \sigma_c}}\right) \tag{4.36}$$

The thickness of the conductive plate of the launcher is constrained by structural and thermal requirements and can be longer than the penetration depth of the induced currents. Therefore, skin effect causes the effective resistance of the aluminium plate to increase for the reduced effective cross section of the conductor.

Skin effect may be modelled by reducing the conductivity of a factor k_{skin}. Having defined $\xi = d_{Al}/\delta_{Al}$, the skin effect coefficient k_{skin} can be computed as [18]

$$k_{skin} = \xi \frac{\sinh(2\xi) + \sin(2\xi)}{\cosh(2\xi) - \cos(2\xi)} \tag{4.37}$$

In the case of double-sided LIM, d_{Al} has to be replaced by $d_{Al}/2$ in the calculation of ξ because the field penetrates from both the sides of the conducting plate. The skin effect coefficient is always grater than one, but if the penetration depth is larger than the plate thickness its impact can be neglected.

4.2.2.4 Transverse Edge Effect

The conductive plate which has been employed for LIM launchers presents electrical isotropy to the induce electromotive force in all the directions. To portray

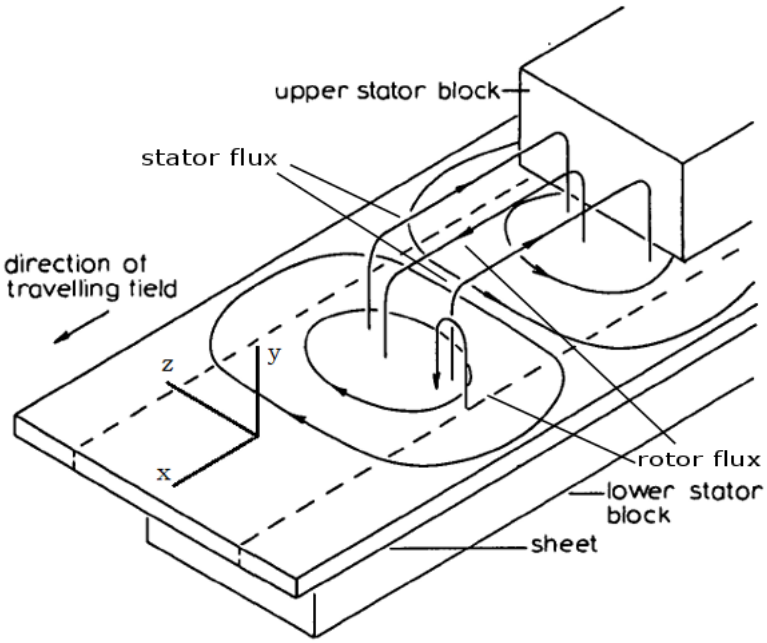

Figure 4.8: Current density and field distribution on a secondary plate

the distribution of the induced current density through the thickness and along the mover length, a three-dimensional analysis should be carried out. In this section, the transverse edge effect will be modelled by a simplified bi-dimensional theory [20]. This field theory will be applied to a double-sided linear induction motor as the electromagnetic catapult, but it can be generalized for single-sided configuration as well.

The machine secondary can be subdivided in an active zone between the stators and a passive zone which corresponds to the lateral regions overhanging the primary. These regions are illustrated in Fig. 4.8 where part of the top stator has been removed to show the instantaneous flux distribution and current loops in the secondary. In a cage rotor the high resistivity of the bars confined the current paths, but in a sheet rotor the plate overhangs and the presence of the stator restrict the current to follow patterns like those in Fig. 4.8. The transverse component J_{2z} of the secondary current density J_2 produces the thrust in the active region. The presence of the longitudinal component J_{2x} represents an additional loss both in active and passive zones.

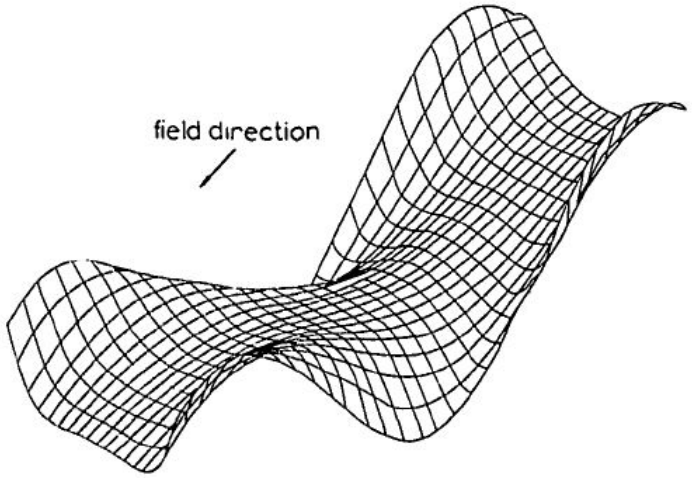

Figure 4.9: Representation of the flux wave in the airgap

When the airgap is small J_{2x} in the active region is minimized by the large impeding flux which is set up by any current in x-direction in the passive region. The resultant currents in the active region flow mainly in transverse direction. With a large airgap more longitudinal current can flow in proximity or inside the active region. In this case the flux lines generated by J_{2x} close inside the active zone and modify the flux density distribution. An example of the resultant flux travelling wave formed by the summation of the effect of J_{2z} and J_{2x} for large airgaps is shown in Fig. 4.9 [20]. The net flux alternatively decreases and increases in density and advances in phase from the middle to the sides of the plate. The overall effect is a decrease in sheet equivalent electrical conductivity and an increment of the secondary rotor resistance represented by the coefficient k_{tr}.

The inhomogeneous distribution of magnetic flux density also affects the magnetization reactance, but the decrement may be neglected in most practical cases. Therefore, the variation of the magnetization reactance due to edge effect will be only shown in this section for completeness of the analysis, but it will not be reconsidered in the launcher model.

In order to determine the field equations to describe the edge effect and define an analytical expression of the coefficient k_{tr} some assumptions have to be made.

- The equivalent magnetic airgap g_e in eq. 4.32, will be considered in place of the mechanical airgap g_m to account for slotting effect and airgap fringing;

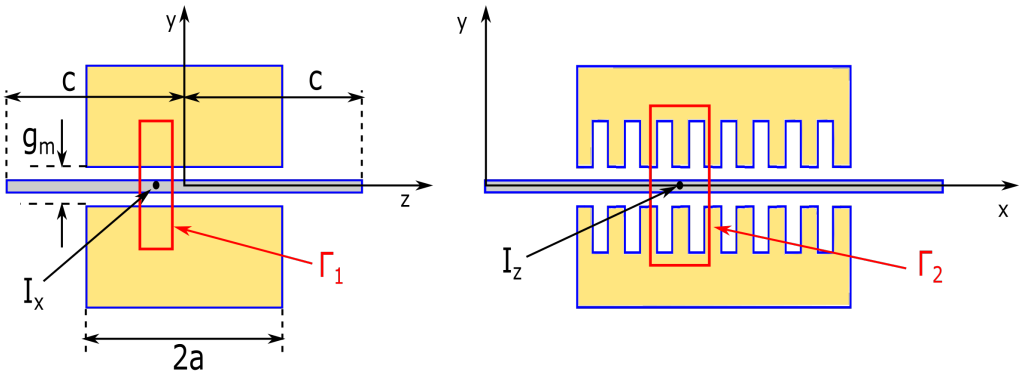

Figure 4.10: Double-sided LIM cross section

- All the electromagnetic quantities vary sinusoidally in the airgap. In particular the magnetomotive force (MMF) is represented by its fundamental travelling wave in secondary coordinates

$$MMF(x,t) = \frac{3\sqrt{2}N_1 I_1 k_w}{\pi p} e^{-j\left(s\omega_1 t - \frac{\pi}{\tau}x\right)} \tag{4.38}$$

  where N_1, I_1, k_w, p and $s\omega_1$ are turns per phase in series, primary current, winding factor, number of pole pairs and secondary frequency of induced currents respectively. This assumption allows the removal of time dependency, hence the theory is applied only to the wave magnitude;

- Outside the boundaries of the active region the field is assumed to be zero, so that the Laplace's equation holds for either component of the current density;

$$\frac{\partial^2 J_{2z}}{\partial z^2} + \frac{\partial^2 J_{2z}}{\partial x^2} = 0 \qquad \frac{\partial^2 J_{2x}}{\partial z^2} + \frac{\partial^2 J_{2x}}{\partial x^2} = 0 \tag{4.39}$$

- The motor length is so large along the motion direction that longitudinal end effect can be neglected.

The active zone of the double-sided LIM in Fig. 4.10 is the area having z-coordinate respecting the inequality $|z| \leq a_e$. The coordinate of the margins of active zone a_e

can be computed as

$$a_e \approx a + g \tag{4.40}$$

where a is half of the stack width. Outside the active zone $\nabla \cdot J_2 = 0$ which means

$$\frac{\partial J_{2x}}{\partial x} + \frac{\partial J_{2z}}{\partial z} = 0 \tag{4.41}$$

The general form of Ampere's law is given by eqs. 4.42 and 4.43 in implicit and explicit form respectively.

$$\nabla \times \vec{H} = \vec{J} \tag{4.42}$$

$$\left(\frac{\partial H_z}{\partial y} - \frac{\partial H_y}{\partial z}\right)\vec{i} + \left(\frac{\partial H_x}{\partial z} - \frac{\partial H_z}{\partial x}\right)\vec{j} + \left(\frac{\partial H_y}{\partial x} - \frac{\partial H_x}{\partial y}\right)\vec{k} = \vec{J} \tag{4.43}$$

The transverse edge effect is due to a non-uniform distribution of y-component of the magnetic field H_y in the airgap while H_x and H_z are normally negligible in the active region. Therefore, the curl product reduces to

$$\nabla \times \vec{H} = -\frac{\partial H_y}{\partial z}\vec{i} + \frac{\partial H_y}{\partial x}\vec{k} \tag{4.44}$$

The Ampere's law is applied to the contour Γ_1 and Γ_2 shown in Fig. 4.10.

$$-g_e \frac{\partial H_y}{\partial z} = J_{2x} d_{Al} \tag{4.45}$$

$$g_e \frac{\partial (H_y + H_0)}{\partial x} = J_m + J_{2z} d_{Al} \tag{4.46}$$

where the H_0 is the initial field in the airgap in the absence of secondary currents and J_m expressed in A/m is the primary current sheet

$$J_m = \frac{\partial [MMF(x,t)]}{\partial x} = j\frac{3\sqrt{2} N_1 I_1 k_w}{\tau p} \tag{4.47}$$

where the time dependency of the magnetomotive force has not been considered. H_0 can be obtained from eq. 4.46 imposing $J_{2z} = 0$ and $H_y = 0$.

$$H_0 = -j\frac{J_m \tau}{\pi g_e} \tag{4.48}$$

A further equation can be derived applying the Faraday's law shown in eq. 4.49 to the active zone yielding eq. 4.50.

$$\nabla \times \vec{E} = \frac{\partial \vec{B}}{\partial t} \Rightarrow \nabla \times \frac{\vec{J}}{\sigma} = \mu_0 \frac{\partial \vec{H}}{\partial t} \tag{4.49}$$

$$\frac{\partial J_{2x}}{\partial z} - \frac{\partial J_{2z}}{\partial x} = -js\omega_1 \mu_0 \sigma_e (H_y + H_0) \tag{4.50}$$

Eq. 4.50 considers only the component of the curl product along y-direction. The equivalent conductivity in eq. 4.50 accounts for skin effect and is calculated as $\sigma_e = \sigma_{Al}/k_{skin}$. Substituting eqs. 4.45, 4.46 and 4.48 into eq. 4.50 yields

$$\frac{\partial^2 H_y}{\partial z^2} + \frac{\partial^2 H_y}{\partial x^2} - js\omega_1 \mu_0 \sigma_e \frac{d_{Al}}{g_e} H_y = js\omega_1 \mu_0 \sigma_e \frac{d_{Al}}{g_e} H_0 \tag{4.51}$$

The solution of eq. 4.51 is

$$H_y = H_0 \frac{js\omega_1 \mu_0 \sigma_e \frac{d_{Al}}{g_e}}{\left(\frac{\pi}{\tau}\right)^2 + js\omega_1 \mu_0 \sigma_e \frac{d_{Al}}{g_e}} \left[A \cosh(\alpha z) + B \sinh(\alpha z)\right] \tag{4.52}$$

$$\text{with} \qquad \alpha^2 = \left(\frac{\pi}{\tau}\right)^2 + js\omega_1 \mu_0 \sigma_e \frac{d_{Al}}{g_e}$$

where A and B are integration constants. The magnetic field H_y in eq. 4.52 can be expressed as a function of the equivalent goodness factor G_e as

$$H_y = H_0 \frac{jsG_e}{1 + jsG_e} \left[A \cosh(\alpha z) + B \sinh(\alpha z)\right] \tag{4.53}$$

$$\text{with} \qquad \alpha^2 = \left(\frac{\pi}{\tau}\right)^2 (1 + jsG_e)$$

Eq. 4.53 can be inserted into eqs. 4.45 and 4.46 to obtain an expression for the current densities J_{2x} and J_{2z} as

$$J_{2x} = \frac{J_m}{d_{Al}} \frac{jsG_e}{1 + jsG_e} \frac{\pi}{\tau} \alpha \left[A \sinh(\alpha z) + B \cosh(\alpha z)\right] \tag{4.54}$$

$$J_{2z} = -\frac{J_m}{d_{Al}} \frac{jsG_e}{1 + jsG_e} \left(\frac{\pi}{\tau} \alpha\right)^2 \left[A \cosh(\alpha z) + B \sinh(\alpha z)\right] \tag{4.55}$$

In order to determine the final expression of magnetic field and secondary current density some extra equation are needed to compute the integration constants

in eqs. 4.53, 4.54 and 4.55. On the conductive sheet overhangs the Laplace's law expressed by eq. 4.39 can be solved for one current density components whereas the condition $\nabla \cdot J_2 = 0$ can be applied to the other one leading to

$$\begin{aligned} J_{2z} &= -C \sinh\left[\frac{\pi}{\tau}(c-z)\right], \\ J_{2x} &= jC \cosh\left[\frac{\pi}{\tau}(c-z)\right], \\ J_{2z} &= -D \sinh\left[\frac{\pi}{\tau}(c+z)\right], \\ J_{2x} &= jD \cosh\left[\frac{\pi}{\tau}(c+z)\right]. \end{aligned} \qquad \begin{aligned} &\text{for} \quad a_e < z \leq c \\ &\\ &\\ &\text{for} \quad -c \leq z < -a_e \end{aligned} \tag{4.56}$$

where C and D are integrations constants. For the current density continuity the integration constants can be calculated equating eqs. 4.54, 4.55 and 4.56 in $z = \pm a_e$.

Once constants A and B are computed they can be replaced in eq. 4.53 and using the relation $B_y = \mu_0 H_y$ the expression of the magnetic field density across the airgap can be derived as

$$B_y = -j\frac{\mu_0 J_m \tau}{g_e \pi (1 + jsG_e)}\left[1 - \frac{jsG_e}{1 + jsG_e}\lambda \frac{\cosh(\alpha z)}{\cosh(\alpha a_e)}\right], \tag{4.57}$$

$$\text{where} \quad \lambda = \frac{1}{1 + \sqrt{1 + jsG_e}\tanh(\alpha a_e)\tanh[\frac{\pi}{\tau}(c - a_e)]}$$

The impact of the edge-effect on the value of R_2 and X_m of the induction motor equivalent circuit can be found by calculating the net voltage induced by the flux wave in one phase of an ideal stator winding having sinusoidal distribution of the coil turns. The induced voltage in any turn E_c can be computed integrating the product between wave velocity and magnetic field density along the z-coordinate.

$$\begin{aligned} E_c =& \frac{\tau}{\pi}\frac{\omega}{\sqrt{2}}\int_{-a_e}^{a_e} B_y dy = \\ =& -j\frac{\sqrt{2} a_e \mu_0 \omega \tau^2 J_m}{g_e \pi^2 (1 + jsG_e)}\left[1 - \frac{jsG_e}{1 + jsG_e}\frac{\lambda}{\alpha a_e}\tanh(\alpha a_e)\right] \end{aligned} \tag{4.58}$$

The phase winding induced voltage under a single pole can be computed integrating the product between the induced voltage in a single conductor and the ideal full pitched coil distribution which varies sinusoidally along x. To get the entire

induce voltage E it is necessary to consider all the $2p$ poles of the machine.

$$\begin{aligned} E &= 2p\int_0^{\tau} E_c \frac{N_1}{2p} k_w \Re\left(e^{-j\frac{\pi}{\tau}x}\right) dx \\ &= -j\frac{2\sqrt{2}\pi a_e J_m N_1 k_w G_e}{\sigma_e d_{Al}(1+jsG_e)}\left[1+j\frac{sG_e\lambda}{\alpha a_e}\tanh(\alpha a_e)\right] \end{aligned} \tag{4.59}$$

Eq. 4.47 can be inserted in eq. 4.59 to compute the secondary impedance $Z_s = -E/I$

$$Z_s = \frac{12a_e(N_1k_w)^2}{\sigma_e d_{Al}\tau p}\frac{s+j/G_e}{s^2+1/G_e^2}\left[1+j\frac{sG_e\lambda}{\alpha a_e}\tanh(\alpha a_e)\right] \tag{4.60}$$

Considering that the secondary resistance can be expressed as

$$R_2 = \frac{12a_e(N_1k_w)^2}{\sigma_e d_{Al}\tau p} \tag{4.61}$$

the secondary impedance can be rewritten as

$$Z_s = R_2\frac{1}{s^2+1/G_e^2}\left(sK_R + j\frac{1}{G_e}K_X)\right) \tag{4.62}$$

where the correction factors K_R and K_X are given by

$$K_R = 1-\Re\left[(1-jsG_e)\frac{\lambda}{\alpha a_e}\tanh(\alpha a_e)\right] \tag{4.63}$$

$$K_X = 1+\Re\left[(sG_e+j)sG_e\frac{\lambda}{\alpha a_e}\tanh(\alpha a_e)\right] \tag{4.64}$$

By equating real and imaginary parts, the equivalent parallel connected resistance and reactance are found to be

$$\frac{R_{2e}}{s} = \frac{R_2}{s}\frac{K_X^2}{K_R}\frac{1+(sG_eK_R/K_X)^2}{1+(sG_e)^2} \tag{4.65}$$

$$X_{me} = X_m K_X \frac{1+(sG_eK_R/K_X)^2}{1+(sG_e)^2} \tag{4.66}$$

The ratio between the equivalent secondary resistance R_{2e}/s in eq. 4.65 and the

real secondary resistance R_2/s is

$$k_{tr} = \frac{K_X^2}{K_R} \frac{1 + (sG_e K_R/K_X)^2}{1 + (sG_e)^2} \tag{4.67}$$

which can be used to express the impact of the edge-effect on the machine performance.

The equivalent conductivity σ_e considers both skin effect and transversal edge effect and can be calculated as

$$\sigma_e = \frac{\sigma_{Al}}{k_{skin} k_{tr}} \tag{4.68}$$

The equivalent conductivity σ_e replaces the real aluminium conductivity σ in the expression of the goodness factor in eq. 4.15.

4.2.2.5 Longitudinal End Effect

When the conductive plate of an induction machine moves along the primary, it experiences flux transients at its entry and exit edge. The reaction of the mover is to generate an induced current in such a direction as to oppose the change of flux. This additional current affects the flux distribution along the airgap so that non-uniform propulsive forces and normal forces are generated. The end-effect force at the rated slip frequency that acts along the direction of the motion may be propulsive or braking, whereas the net normal force might not be zero. Furthermore, higher current density in the conductive plate increases Joule losses and absorbed reactive power, reducing the motor efficiency and power factor respectively. This phenomenon particularly compromises the performance of induction motors travelling at such a speed that the distance covered by induced current before it decays is comparable or grater than the mover length. Indeed, longitudinal end-effect mainly affects LIMs with short primary and long secondary, but it can also involve LIMs with long primary and short secondary.

As for the edge-effect in Section 4.2.2.4, longitudinal end-effect may be analysed with a simplified two-dimensional theory assuming that

- the permeability of the core is infinite, so the reluctance of the stator core can be neglected;

- the current flows only along z direction in the active region;
- only the effect of the fundamental harmonic is considered while the secondary harmonics are neglected;
- there is no magnetic field outside the stator.

The active region under investigation is the area of the mover whose x-coordinate satisfies the inequality $0 < x < 2p\tau$. The Ampere's law in eq. 4.42 can be applied along the contour Γ_2 in Fig. 4.10 as done during the edge-effect analysis yielding a similar equation.

$$g_e \frac{\partial H_y}{\partial x} = J_1 + J_2 d_{Al} \tag{4.69}$$

where the sinusoidal space and time variation of the primary current sheet J_1 can be expressed as

$$J_1 = J_m e^{j(\omega_1 t - \frac{\pi}{\tau} x)} \tag{4.70}$$

and the magnetizing current sheet J_m can be expressed as

$$J_m = \frac{3\sqrt{2} N_1 I_1 k_w}{\tau p} \tag{4.71}$$

Faraday's law applied to a body moving in a magnetic field is

$$\nabla \times \overrightarrow{E} = -\frac{\partial \overrightarrow{B}}{\partial t} + \nabla \times (\overrightarrow{v_{rel}} \times \overrightarrow{B}) \tag{4.72}$$

where the relative speed v_{rel} is given by the difference between the synchronous speed v_s and the mover speed v_r. The theory proposed to investigate longitudinal end-effect considers the magnetic field component H_y across the airgap. The other components H_x and H_z are negligible in the active zone. Under these assumptions the vectors in the in eq. 4.72 assume the form

$$\overrightarrow{E} = \{0, 0, J_2/\sigma_e\} \qquad \overrightarrow{B} = \mu_0 \{0, H_y, 0\} \qquad \overrightarrow{v_{rel}} = \{v_{rel}, 0, 0\} \tag{4.73}$$

Assuming that the field H_y varies sinusoidally in time eq. 4.72 may be rewritten

as

$$\frac{\partial J_2}{\partial x} = j\mu_0\sigma_e\omega_1|H_y|e^{j\omega_1 t} + \mu_0\sigma_e v_{rel}\frac{\partial|H_y|}{\partial x}e^{j\omega_1 t} \tag{4.74}$$

Substituting eq. 4.74 in eq. 4.69 and simplifying the time dependency yields

$$\frac{\partial^2 H_y}{\partial x^2} - \mu_0\sigma_e v_{rel}\frac{d_{Al}}{g_e}\frac{\partial H_y}{\partial x} - j\mu_0\sigma_e\omega_1\frac{d_{Al}}{g_e}H_y = -j\frac{\pi}{\tau}\frac{J_m}{g_e}e^{-j\frac{\pi}{\tau}x} \tag{4.75}$$

The characteristic equation of the differential equation in eq. 4.75 is

$$\gamma^2 - \mu_0\sigma_e v_{rel}\frac{d_{Al}}{g_e}\gamma - \mu_0\sigma_e\omega_1\frac{d_{Al}}{g_e} = 0 \tag{4.76}$$

whose roots are

$$\gamma_{1,2} = \frac{\mu_0\sigma_e v_{rel}d_{Al}}{2g_e}\left(1 \pm \sqrt{1 + j\frac{4\omega_1}{\mu_0\sigma_e v_{rel}^2 d_{Al}/g_e}}\right) \tag{4.77}$$

that written in the complex form $\gamma = \gamma_\Re + j\gamma_\Im$ become

$$\gamma_{1,2} = \frac{\mu_0\sigma_e v_{rel}d_{Al}}{2g_e}\left[1 \pm \left(\sqrt{\frac{\sqrt{1+\frac{16\omega_1^2}{\mu_0^2\sigma_e^2 v_{rel}^4 d_{Al}^2}}+1}{2}} + j\sqrt{\frac{\sqrt{1+\frac{16\omega_1^2}{\mu_0^2\sigma_e^2 v_{rel}^4 d_{Al}^2}}-1}{2}}\right)\right] \tag{4.78}$$

Substituting the expression of the equivalent goodness factor G_e (which is eq. 4.15 with equivalent conductivity σ_e defined by eq. 4.68 and equivalent airgap length g_e defined by eq. 4.32), in eq. 4.78 yields

$$\gamma_{1,2} = \frac{G_e}{2}\frac{\pi}{\tau}(1-s)\left[1 \pm \left(\sqrt{\frac{\sqrt{1+\frac{16}{G_e^2(1-s)^4}}+1}{2}} + j\sqrt{\frac{\sqrt{1+\frac{16}{G_e^2(1-s)^4}}-1}{2}}\right)\right] \tag{4.79}$$

The final solution of the differential equation in eq. 4.75 is a function of the roots of the characteristic equation plus a particular root as shown in eq. 4.80.

$$H_y = C_1 e^{\gamma_1 x} + C_2 e^{\gamma_2 x} + j\frac{\tau J_m}{\pi g_e(1+jsG_e)}e^{-j\frac{\pi}{\tau}x} \tag{4.80}$$

Inserting eq. 4.80 in the Ampere's law shown in eq. 4.69, an expression of the

secondary current may be derived as

$$J_2 = C_1 \frac{\gamma_1 g_e}{d_{Al}} e^{\gamma_1 x} + C_2 \frac{\gamma_2 g_e}{d_{Al}} e^{\gamma_2 x} - j \frac{s G_e J_m}{d_{Al}(1 + j s G_e)} e^{-j\frac{\pi}{\tau}x} \tag{4.81}$$

The magnetic field in the passive zones where $x < 0$ and $x > 2p\tau$ is not the same for LIMs with short primary and long secondary and LIMs with long primary and short secondary. Both these topologies need to be investigated because, as far as end-effects are concerned, the electromagnetic catapult represents an intermediate case.

The runway length for an aircraft gaining speed at the rated acceleration exceeds several hundreds of meters, consequently the launcher's stator cannot be built as a single, but it is composed by a large number of stages each one with a length that can be easily manufactured. Depending on stator and system design, the sections may be grouped together forming a continuous magnetic path or may have significant gaps among them. Half filled end slots of double-layer distributed windings also produce discontinuities between consecutive stator segments. The length of the mover may go beyond the length of a single section depending on the thrust requirement to launch aircraft of different size and the number of active poles required to produce the propulsive force.

In the case the length of the mover exceeds the length of the active section considering the discontinuites, the longitudinal end-effect would be better represented by the case of LIMs with short primary a long secondary. The longitudinal end-effect of LIMs with short primary and long secondary has been proved to increase with the frequency and mainly affect the perfromance at high speed [21]. When the length of the active area is comparable with the length of the mover, the end-effect of LIMs with long primary and short secondary should be considered. Junyong in [89] proved that the influence of this longitudinal end-effect reduces with increasing frequency and can be neglected at high speed.

In LIMs with a short primary and long secondary, there is no primary current in the passive zones and the equivalent airgap g_e may be approximated as τ/π which corresponds to an average flux line in air with a periodicity of τ [90]. The magnetic field generated by the secondary currents outside the primary can be

expressed as

$$\begin{aligned} H_{y\,exit} &= C_3 e^{\gamma_{1e} x} && \text{for } x \le 0, \\ H_{y\,entry} &= C_4 e^{\gamma_{2e}(x-2p\tau)} && \text{for } x \ge 2p\tau, \\ \gamma_{1e} &= (\gamma_1)_{g_e=\tau/\pi} && \gamma_{2e} = (\gamma_2)_{g_e=\tau/\pi} \end{aligned} \tag{4.82}$$

The integration constants can be found imposing the continuity of the field and secondary current at the mover boundaries.

$$\begin{aligned} (H_{y\,exit})_{x=0} &= (H_y)_{x=0} & (H_y)_{x=2p\tau} &= (H_{y\,entry})_{x=2p\tau} \\ \left(\frac{\partial H_{y\,exit}}{\partial x}\right)_{x=0} &= (J_2)_{x=0} & \left(\frac{\partial H_{y\,exit}}{\partial x}\right)_{x=2p\tau} &= (J_2)_{x=2p\tau} \end{aligned} \tag{4.83}$$

In order to get more realistic results the fourth boundary condition in eq. 4.83 may be replaced by

$$\int_{-\infty}^{\infty} H_y dx = 0 \tag{4.84}$$

Imposing these boundary conditions the integration constants become

$$\begin{aligned} C_1 &= \frac{C_2\left(\frac{1}{\gamma_2} - \frac{1}{\gamma_{1e}} - \frac{e^{2p\tau\gamma_2}}{\gamma_2} + \frac{e^{2p\tau\gamma_2}}{\gamma_{2e}}\right) - j\frac{\tau J_m}{\pi g_e(1+jsG_e)}\left(\frac{1}{\gamma_{1e}} - \frac{1}{\gamma_{2e}}\right)}{\frac{1}{\gamma_{1e}} + \frac{e^{2p\tau\gamma_1}}{\gamma_1} - \frac{1}{\gamma_1} - \frac{e^{2p\tau\gamma_1}}{\gamma_{2e}}} \\ C_2 &= \frac{j\frac{\tau J_m}{\pi g_e(1+jsG_e)}\left[\frac{\frac{1}{\gamma_{1e}} - \frac{1}{\gamma_{2e}}}{\frac{1}{\gamma_{1e}} + \frac{e^{2p\tau\gamma_1}}{\gamma_1} - \frac{1}{\gamma_1} - \frac{e^{2p\tau\gamma_1}}{\gamma_{2e}}}\left(\gamma_{1e} - \gamma_1\frac{g_e}{d_{Al}}\right) - \gamma_{1e}\right] - j\frac{sG_eJ_m}{\pi d_{Al}(1+jsG_e)}}{\frac{\frac{1}{\gamma_2} - \frac{1}{\gamma_{1e}} - \frac{e^{2p\tau\gamma_2}}{\gamma_2} + \frac{e^{2p\tau\gamma_2}}{\gamma_{2e}}}{\frac{1}{\gamma_{1e}} + \frac{e^{2p\tau\gamma_1}}{\gamma_1} - \frac{1}{\gamma_1} - \frac{e^{2p\tau\gamma_1}}{\gamma_{2e}}}\left(\gamma_{1e} - \gamma_1\frac{g_e}{d_{Al}}\right) + \gamma_{1e} - \gamma_2\frac{g_e}{d_{Al}}} \\ C_3 &= C_1 + C_2 + j\frac{\tau J_m}{\pi g_e(1+jsG_e)} \\ C_4 &= C_1 e^{2p\tau\gamma_1} + C_2 e^{2p\tau\gamma_2} + j\frac{\tau J_m}{\pi g_e(1+jsG_e)} \end{aligned} \tag{4.85}$$

As done in most of literature [18], eq. 4.86 can be simplified using γ_1 instead of γ_{1e} in the exit zone and γ_2 instead of γ_{2e} in the entry zone introducing small errors

in the system. Under this assumption the integration constants become

$$\begin{aligned} C_1 &= j\frac{J_m}{1+jsG_e}\frac{\left(sG_e+\frac{\tau}{\pi}\gamma_2\right)e^{-2p\tau\gamma_1}}{\gamma_1 d_{Al}-\gamma_1 d_{Al}e^{-2p\tau\gamma_1}+\gamma_1 g_e e^{-2p\tau\gamma_1}-\gamma_2 g_e} \\ C_2 &= -j\frac{J_m}{1+jsG_e}\frac{sG_e+\frac{\tau}{\pi}\gamma_1}{\gamma_1 d_{Al}-\gamma_1 d_{Al}e^{-2p\tau\gamma_1}+\gamma_1 g_e e^{-2p\tau\gamma_1}-\gamma_2 g_e} \\ C_3 &= C_1\left(1-e^{2p\tau\gamma_1}\right) \\ C_4 &= C_2\left(e^{2p\tau\gamma_2}-1\right) \end{aligned} \tag{4.86}$$

In case of LIMs with long primary and short secondary, the equations to express the field in the passive zones has to consider the presence of primary current. In this case the airgap of the passive zones is the same of the one considered for the active area.

$$H_{y\,exit} = j\frac{\tau J_m}{\pi g_e}e^{-j\frac{\pi}{\tau}x} \qquad \text{for } x \le 0 \tag{4.87}$$

$$H_{y\,entry} = j\frac{\tau J_m}{\pi g_e}e^{-j\frac{\pi}{\tau}(x-2p\tau)} \qquad \text{for } x \ge 2p\tau \tag{4.88}$$

Since only two integration constants have to be determined the continuity can be imposed using only the first two boundary conditions in eq. 4.83 obtaining

$$C_1 = -\frac{\tau J_m}{\pi g_e}\frac{sG_e}{1+jsG_e}\frac{e^{2p\tau\gamma_2}-1}{e^{2p\tau\gamma_2}-e^{2p\tau\gamma_1}} \tag{4.89}$$

$$C_2 = -\frac{\tau J_m}{\pi g_e}\frac{sG_e}{1+jsG_e}\frac{1-e^{2p\tau\gamma_1}}{e^{2p\tau\gamma_2}-e^{2p\tau\gamma_1}} \tag{4.90}$$

The magnetic field density in the airgap $B_y = \mu_0 H_y$ can be written for both the LIM topologies as

$$B_y = \mu_0 C_1 e^{\gamma_1 x} + \mu_0 C_2 e^{\gamma_2 x} + j\frac{\mu_0 \tau J_m}{\pi g_e(1+jsG_e)}e^{-j\frac{\pi}{\tau}x} \tag{4.91}$$

The third term of eq. 4.91 represents the conventional magnetic field density distribution that is generated by the primary current in the active zone. The other two terms represent two end-effect magnetic waves which travel in different directions according to the sign of $\gamma_{1\Re}$ and $\gamma_{2\Re}$. Since $\mid \gamma_{1\Re} \mid \neq \mid \gamma_{2\Re} \mid$, the magnetic waves decay differently along the direction of the motion for different decay times $\tau/\gamma_{1\Re}$

and $\tau/\gamma_{2\Re}$. Since $\gamma_{1\Im} = \gamma_{2\Im} = \gamma_{\Im}$, both waves are characterized by the same pitch $\tau_e = 1/\gamma_{\Im}$.

The main consequences of the end-effect are

- Thrust reduction;
- Secondary Joule losses increase and efficiency reduction due to higher secondary current density;
- Reactive power increase and power factor reduction;
- Non-uniform magnetic flux and normal force distribution which becomes particularly important for double-sided LIMs where the nominal normal force is zero

For a practical investigation of the end-effect impact on thrust, active power and reactive power the current density and the magnetic field density may be assumed constant along the mover thickness and along the stack width. This assumption is consistent with the present two-dimensional analysis on the longitudinal end-effect, since the lateral edge effects have been considered separately.

The propulsive force is produced by the interaction of the currents induced into the mover and the magnetic field in the airgap. By definition, the thrust can be calculated integrating the product between magnetic field density and current density over the mover's volume according to eq. 4.92.

$$F = \Re\left(\iiint_v \overline{J_1}\cdot\overline{B}^* \, dx\,dy\,dz\right) \tag{4.92}$$

where the symbol $\overline{B}^*$ indicates the complex conjugate of $\overline{B}$. The conventional thrust without longitudinal end-effects can be computed as

$$F_x = 2a_e\mu_0\Re\left(\int_0^{2p\tau} J_m e^{-j\frac{\pi}{\tau}x}\cdot\left(j\frac{\tau J_m}{\pi g_e(1+jsG_e)}e^{-j\frac{\pi}{\tau}x}\right)^* dx\right) \tag{4.93}$$

Combining eqs. 4.91 and 4.70 in eq. 4.92 leads to the expression of the total propulsive force that takes into account the disturbances due to end-effects.

$$F_{xe} = 2a_e d_{Al}\Re\left(\int_0^{2p\tau} \overline{J_1}\cdot\overline{B_y}^* \, dx\right) \tag{4.94}$$

Table 4.1: Winding arrangement of consecutive stators to limit longitudinal end-effects

Arrangement of the primary windings		Distance between stators
First stator	Second stator	
... a, -c, b	c, -b, a, ...	$1/3\tau$
... a, -c, b	-b, a, -c, ...	$2/3\tau$
... a, -c, b	a, -c, b, ...	τ
... a, -c, b	-c, b, -a, ...	$4/3\tau$
... a, -c, b	b, -a, c, ...	$5/3\tau$
... a, -c, b	-a, c, -b, ...	2τ

The secondary active power loss can be calculated from the general expression of the Joule Losses as

$$\begin{aligned} P_{a2} =& RI_2^2 = \rho_{Al}\frac{2a_e}{l\,d_{Al}}(l\,d_{Al})^2\frac{1}{l}\int_0^l J_2^2\,dx \Rightarrow \\ \Rightarrow P_{a2} =& \frac{2a_e d_{Al}}{\sigma_e}\Re\left(\int_0^{2p\tau}\overline{J_2}\cdot\overline{J_2}^*\,dx\right) \end{aligned} \tag{4.95}$$

where the length l is the equal to the mover length $2p\tau$. The secondary reactive power losses can be calculated by integration of the specific energy density in the airgap multiplied by the primary frequency as

$$\begin{aligned} P_{r2} =& \frac{\omega_1}{2\mu_0}\iiint_V \overline{B}\cdot\overline{B}^*\,dV \Rightarrow \\ \Rightarrow P_{r2} =& \frac{\omega_1 a_e g_e}{2\mu_0}\Re\left(\int_0^{2p\tau}\overline{B_y}\cdot\overline{B_y}^*\,dx\right) \end{aligned} \tag{4.96}$$

Eqs. 4.93 to 4.96 are valid for both LIMs whit long primary and short secondary and LIMs with short primary and long secondary.

The end-effect impact on the performance may be drastically reduced by an accurate positioning of the stages, so that at the rated speed the exit magnetic field wave reaches the next stator in phase with the fundamental magnetic wave [91]. In order to align the end-effect wave and the fundamental wave the stages should be placed according to Table 4.1. The distance between consecutive stator sections depends on the winding sequence at their edges. In order to reduce the length of the magnetic path discontinuities, the shortest distance allowed by the implemented winding configuration should be selected.

4.3 LIM Electromagnetic Design

The electromagnetic design methodology for the induction launcher aims to determine the geometrical features, the current rating and voltage rating to achieve the desired thrust with the minimum input power. The input power P_i is defined as the vectorial summation of active power P_a and reactive power P_r and is modulus can be computed as

$$P_i = \sqrt{P_a^2 + P_r^2} \tag{4.97}$$

The input power can also be expressed as a function of the output power P_o as indicated by eq. 4.98.

$$P_i = \frac{P_o}{\eta \cos\phi} \tag{4.98}$$

where η and $\cos\phi$ are the motor efficiency and power factor respectively. For a given output power $P_o = F_{xc}\, v_{TO}$, the minimization of the input power coincides with the maximization of the product $\eta \cos\phi$.

4.3.1 Parametric Optimization Algorithm for LIM

The complexity of the induction machine requires a numerical algorithm which can estimate the efficiency and power factor considering requirements, constraints and special LIM phenomena as described in Section 4.2. The numerical approach that was adopted is based on the *parametric optimization* of the system which determines the impact of the design variables on the model outcomes. The parametric analysis allows for a deeper understanding of the relationships between inputs and outputs finding regions in the space of the design variables where the design objectives meet an optimum criterion (including maximization and minimization problems). Parametric optimization algorithm is particularly suitable to identify the way a model with a large number of parameters "senses" the variations of some design inputs.

This numerical method is performed by running a mathematical model a large number of times for each combination of the design variables. The number of

Table 4.2: Parametric optimization inputs and design variables for LIM

Design variables		
Description	**Sym**	**Value**
Aluminium plate thickness	d_{Al}	?
Pole pitch	τ	?
Rated slip frequency	s	?
Half stator width	a	?
Expected thrust density	f_{stress}	?
Turns per slot per phase	N_s	?
Airgap length	g	?
Primary current density	J_1	?
Slot opening on slot pitch ratio	b_s/τ_s	?
Input variables		
End-speed requirement	v_{TO}	85.73 m/s
Aluminium conductivity	σ_{Al}	$3.5 \cdot 10^{-7}\,\Omega^{-1}m^{-1}$
Vacuum permeability	μ_0	$4\pi \cdot 10^{-7}$ H/m
Copper conductivity	σ_c	$5.8 \cdot 10^{-7}\,\Omega^{-1}m^{-1}$
Number of phases	m	3
Slot per pole per phase	q	4
Required peak thrust	F_x	502.9 kN
Coil to pole pitch ratio	τ_c/τ	9/12
Stator maximum B	B_{ir}	1.7 T
Saturation coefficient	k_{ss}	0.21
Fill factor	k_{fill}	0.45
Aluminium density	ρ_{Al}	2700 kg/m^3
Silicon steel density	ρ_{ir}	7750 kg/m^3
Tooth tip height	h_{ss}	1.0 mm
Grooves Diameter	d_g	2.0 mm

iterations grows exponentially when the effect of many variables is explored. In particular, the algorithm can take a significant amount of time if a single iteration is rather complex and requires considerable computational efforts. Although the number of variables for the induction motor design is rather large, the time needed to complete a single iteration is short and tens of thousand of steps require a few seconds to be executed. In fact, the mathematical model for LIM design is a sequence of analytical equations that were obtained from simplified field theories as those described in Section 4.2.

Parametric optimization was employed to size the induction launcher selecting the optimum combination of design variables to implement in finite element and

transient analysis of LIM. The design variables of the parametric optimization algorithm for LIM are shown in Table 4.2. Before running the algorithm their value is still unknown. A combination of the design variables is not the only input of the parametric optimization algorithm: properties of the materials, catapult requirements and the other input variables shown in Table 4.2 are known as well. These inputs are assumed constant and do not vary across all iterations of the parametric optimization algorithm.

The selection process starts from the design variables that have structural and thermal constraints and proceeds with the choice of all other parameters in order to minimize the input power. Once the desired value of a design variable is selected, the parametric optimization algorithm has to be run again to verify the impact of the other variables on the system. The steps that allow the algorithm to compute the input power and the electromagnetic performance of the system are now explained.

The algorithm first calculates synchronous speed v_s, frequency f_1 and angular frequency ω_1 from the catapult end-speed requirement v_{TO}.

$$v_s = \frac{v_{TO}}{1-s} \qquad f_1 = \frac{v_s}{2\tau} \qquad \omega_1 = 2\pi f_1 \tag{4.99}$$

Substituting the equivalent conductivity σ_e (see eq. 4.68) and the equivalent airgap length g_e (see eq. 4.32) in eq. 4.15 it is possible to determine the expression of the equivalent goodness factor G_e as

$$G_e = \frac{\mu_0 \tau^2 \omega_1 \sigma_e d_{Al}}{\pi^2 g_e (1+k_{ss})} \tag{4.100}$$

The stator magnetic saturation coefficient k_{ss} accounts for the primary teeth and back iron contribution to the magnetization current and it is usually assumed between 0.2 - 0.6 [18].

The number of pole pairs is calculated rounding up to the nearest integer the ratio between the required thrust F_x and the thrust expected from a single pole pair as

$$p = \left\lceil 0.5 \frac{F_x}{2a\tau f_{stress}} \right\rceil \tag{4.101}$$

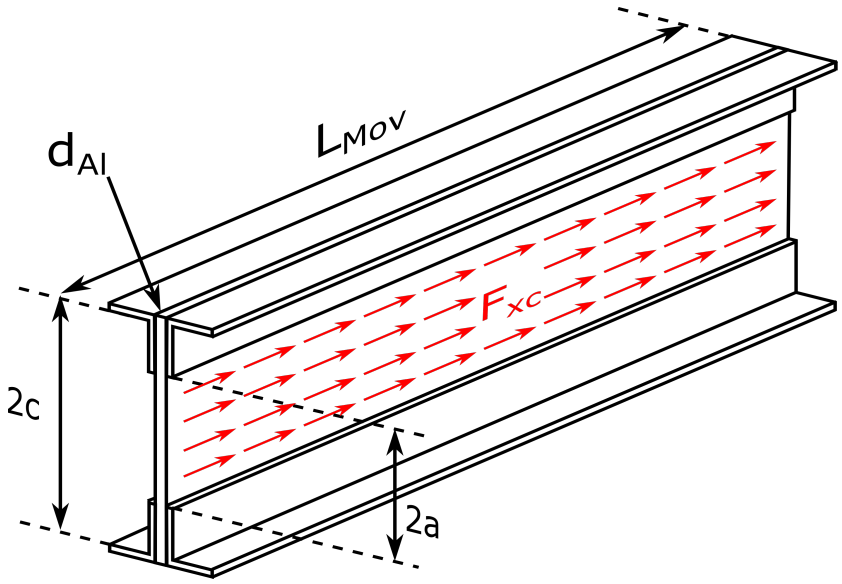

Figure 4.11: Structure of the LIM mover

The mass of the mover is given by the sum of the mass of the aluminium plate and the mass of all the other components that are used to connect the plate to the aircraft or are part of the guidance system. The mass of the structure connected to the aircraft undercarriage and the mass of the carriages that slide over the rails underneath the mover (see Fig. 1.2) are difficult to estimate. None of the design procedures for the electrical machines presented in this thesis consider the mass of the connection to the landing gear since it cannot be easily estimated and is not expected to significantly change the machine performance. Instead, the preliminary sizing of LIM takes into account the weight of the carriages adding an extra 10% to the mass of the system shown in Fig. 4.11.

$$m_{Al} = \rho_{Al}(2p+1+\frac{\tau_c}{\tau})\tau\,[2c\cdot d_{Al}+4(c-a)d_{Al}]\cdot 1.1 \tag{4.102}$$

where ρ_{Al} is the aluminium density and $c = a+\tau/\pi$ is the plate half width including overhangs.

The thrust required to propel the A320-200 aircraft has to be corrected to take into account the additional mass of the mover m_{Al}.

$$F_{xc} = F_x + 0.6G\cdot m_{Al} \tag{4.103}$$

where F_x and $0.6G$ are the required thrust and acceleration shown in Section 3.3.3.

The number of series-connected turns per phase N_1 can be computed considering the number of turns per slot per phase N_s, the number of active poles in case of double-layer distributed windings and the number of slots per pole per phase q as

$$N_1 = 2N_s(2p+1)q \tag{4.104}$$

where 2 is added for the double-sided stator configuration. The number of turns per slot N_s is selected to stay within a preset voltage limit. The number of slots per pole per phase q and coil pitch τ_c are selected in order to have a magnetic wave shape in the airgap as close as possible to a sinusoidal shape and are given in Table 4.2.

In order to investigate the induction motor using the equivalent electric circuit shown in Fig. 4.3, it is necessary to determine its components. The equivalent circuit of double-sided LIM may undergo further simplifications. The secondary leakage inductance L_2 is generally due to the flux generated by the secondary current that does not cross the airgap and returns to the mover without producing any thrust. The secondary leakage inductance may become rather large with strong variation of the current density along the mover thickness. L_2 can become significant in single-sided LIMs with a poor penetration depth in the secondary back iron. In double-sided machines the primary field is on both sides of the aluminium plate and it guarantees an uniform current density distribution across the conductor unless the machine rated frequency widely exceeds the point where the penetration depth equals half of the mover thickness. High performance double-sided LIMs tend to have long pole pitches, low frequencies and high penetration depths. Furthermore, in EML systems the input frequency ramps up so that its maximum value appears only for a short time at the end of the launch. The contribution of current density variations to the secondary leakage inductance in double-sided LIMs is expected to be very small. Eddy current induced in the conductive sheet by the secondary harmonics contributes to the leakage inductances as well. However, the winding sequence has been selected to have a low harmonic content in order to maintain eddy current intensity at such a low level that L_2 has not a great

impact even at high speed. Therefore, in double-sided LIMs for EML application the secondary leakage inductance can be neglected without introducing significant errors.

The amplitude of the magnetic flux density in the airgap may be written as a function of the amplitude of the travelling magnetomotive force in eq. 4.38 as

$$B_g = \frac{\mu_0 \mid MMF(x,t) \mid}{g_e(1+k_{ss})} = \frac{3\sqrt{2}\mu_0 N_1 k_w I_1}{\pi g_e(1+k_{ss})p} \tag{4.105}$$

The primary flux linkage Ψ_1 can be computed from the flux of a single pole Φ_1 that in turns is a function of the magnetic flux density B_g as

$$\Psi_1 = \Phi_1 N_1 k_w = \frac{2}{\pi} B_g 2a_e \tau \cdot N_1 k_w \tag{4.106}$$

where a_e is half the width of the active zone and is calculated using eq. 4.40. Combining eqs. 4.105 and 4.106 the magnetizing inductance L_m for a three phase distributed windings can be calculated as

$$L_m = \frac{\Psi_1}{\sqrt{2}I_1} = \frac{6\mu_0 (N_1 k_w)^2 2a_e \tau}{\pi^2 p g_e(1+k_{ss})} \tag{4.107}$$

The winding factor of the fundamental magnetic wave k_w is the product of the respective pitch factor k_p and distribution factor k_d. Pitch factor $k_{p\nu}$, distribution factor $k_{d\nu}$ and winding factor $k_{w\nu}$ of distributed windings for the ν^{th} harmonic can be computed as

$$k_{p\nu} = \sin\left(\nu \frac{\pi}{2} \frac{\tau_c}{\tau}\right) \qquad \nu = 6k \pm 1 \qquad \text{with} \qquad k = 1,2,3,... \tag{4.108}$$

$$k_{d\nu} = \frac{\sin\left(\frac{\nu\pi}{2m}\right)}{q \sin\left(\frac{\nu\pi}{2qm}\right)} \qquad \nu = 6k \pm 1 \qquad \text{with} \qquad k = 1,2,3,... \tag{4.109}$$

$$k_{w\nu} = k_{p\nu} k_{d\nu} \qquad \nu = 6k \pm 1 \qquad \text{with} \qquad k = 1,2,3,... \tag{4.110}$$

The expression of the motor thrust as a function of the electric circuit parameters in eq. 4.6 can be rewritten as a function of the goodness factor as

$$F_{xc} = \frac{3(R_2/s)X_m^2}{v_s\left[(R_2/s)^2 + X_m^2\right]} I_1^2 \Rightarrow F_{xc} = \frac{3\pi s G_e L_m}{\tau(1+s^2 G_e^2)} I_1^2 \tag{4.111}$$

Eq. 4.111 can be rearranged to compute the primary current required to produce the thrust to propel the aircraft as

$$I_1 = \sqrt{\frac{\tau(1+s^2G_e^2)}{3\pi s G_e L_m} F_{xc}} \tag{4.112}$$

The primary current allows for the calculation of the slot area A_s, slot height h_s and wire diameter d_w as

$$A_s = \frac{N_s I_1}{J_1 k_{fill}} \tag{4.113}$$

$$h_s = A_s / b_s \tag{4.114}$$

$$d_w = \sqrt{\frac{I_1}{J_1}\frac{4}{\pi}} \tag{4.115}$$

where k_{fill} is the filling factor and b_s is the slot width.

The filling factor of high packed coils may be up to 55% of the slot area or more, depending on construction technique, applied voltage and insulation material properties. To be conservative, the launcher preliminary design considers a filling factor k_{fill} of 45%. In order to fit the conductors in a slot layer parallel connections of multiple wires can be considered in place of a single series-connected wire. Selecting the number of parallel connections k_{par}, the copper wire diameter can be calculated as $d_w/\sqrt{k_{par}}$. This relation assures that the bundle of parallel-connected wires has same electric resistance of the single series-connected conductor of diameter d_w.

The primary leakage inductance L_1 is the sum of slot leakage inductance L_{ls}, end winding leakage inductance L_{le}, differential leakage inductance L_{ld} and leakage inductance due to high order harmonics L_{lh}. Each inductance can be expressed as a function of the respective specific permeance λ as

$$L_1 = L_{ls} + L_{le} + L_{ld} + L_{lh} = 2\mu_0 \frac{2a_e N_1^2}{pq}(\lambda_s + \lambda_e + \lambda_d + \lambda_h) \tag{4.116}$$

The slot leakage permeance λ_s for double layer windings is

$$\lambda_s = \left(\frac{h_s}{3b_s} + \frac{h_{ss}+d_g}{b_s}\right)\frac{3\tau_c/\tau + 1}{4} \tag{4.117}$$

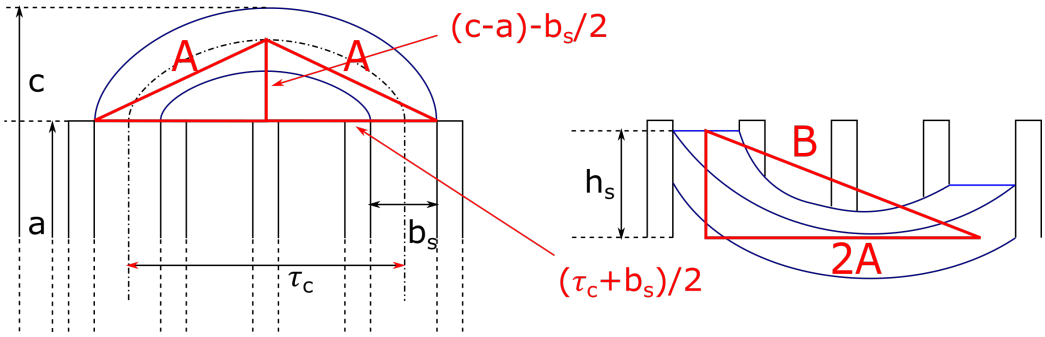

Figure 4.12: End coil schematic

where h_{ss} is the height of the tooth tip and d_g is the grooves diameter as shown in Fig. 4.7. The grooves are used during the manufacturing process to block the coils inside the slots with a solid insulting material. The specific end-turn permeance λ_e is estimated on the basis of experiments and for double layer high voltage windings it can be expressed as [29]

$$\lambda_e = 0.42 \frac{q l_{end}}{2 a_e} \left(1 - \frac{2}{\pi} \frac{\tau_c}{l_{eend}}\right) k_w^2 \tag{4.118}$$

where the length l_{end} of a generic end-coil can be approximately calculated as the 105% of the length of hypotenuse B of triangle in Fig. 4.12 which sides are the slot height h_s and the sum of the hypotenuses A. The expressions to calculate the length of the sides of the triangles A are reported in Fig. 4.12 whereas the end-coil length can be calculated as

$$l_{end} = 1.05 \sqrt{2 \left(\sqrt{\left(c - a - \frac{b_s}{2}\right)^2 + \left(\frac{\tau_c + b_s}{2}\right)^2} \right)^2 + h_s^2} \tag{4.119}$$

The differential specific permeance λ_d is [18]

$$\lambda_d = \frac{5 k_c g / b_s}{5 + 4 k_c g / b_s} \tag{4.120}$$

The specific leakage permeance λ_h due to high order harmonics for three phase

windings can be computed as [29]

$$\lambda_h = 3\frac{q\tau k_w^2}{\pi^2 g_e(1+k_{ss})}\gamma_h \tag{4.121}$$

where the harmonics leakage factor γ_h is

$$\gamma_h = \frac{1}{k_w^2}\sum_{\nu>1}\left(\frac{k_{w\nu}}{\nu}\right)^2 \tag{4.122}$$

The last elements of the induction motor equivalent circuit that the parametric optimization algorithm calculates are the primary resistance R_1 and the secondary resistance R_2. The primary resistance can be directly calculated from the resistance definition as

$$R_1 = \rho_c\frac{l}{A} = \frac{1}{\sigma_c}\frac{N_1(2a+l_e)}{I_1/J_1} \tag{4.123}$$

where ρ_c is the resistivity of copper, σ_c is the conductivity of copper, $N_1(2a+l_e)$ is the length of all the conductors connected in series for each phase considering both the stator sides, and $A = I_1/J_1$ is the area of a single conductor. The secondary resistance can be determined by the definition of goodness factor in eq. 4.11.

$$R_2 = \frac{\omega L_m}{G_e} = \frac{12a_e k_w^2 N_1^2}{p\tau\sigma_e d_{Al}} \tag{4.124}$$

The secondary current that flows across the secondary resistance can be computed applying the Kirchoff law to the induction motor equivalent circuit yielding

$$I_2 = I_1\frac{sG_e}{\sqrt{1+s^2G_e^2}} \tag{4.125}$$

In a similar way the magnetization current I_m can be computed as

$$I_m = I_1\frac{1}{\sqrt{1+s^2G_e^2}} \tag{4.126}$$

Once all the equivalent circuit parameters have been defined, it is possible to proceed with the calculation of the last features of LIM. The magnetic flux density in the stator teeth B_t can be obtained from the magnetic flux density in the airgap

B_g calculated using eq. 4.105, assuming that the most of the magnetic flux does not cross the slots, but it is channelled through the stator teeth themselves. Equating the magnetic flux across the airgap and the teeth, the magnetic flux density B_t can be computed as

$$\frac{2}{\pi}B_g\tau_s 2a = B_t(\tau_s - b_s)2a \quad \Rightarrow \quad B_t = \frac{2}{\pi}B_g\frac{\tau_s}{\tau_s - b_s} \tag{4.127}$$

In a similar way, equating the flux across the slots over a single pole and the flux across the stator yoke, it is possible to determine the yoke thickness h_y that maintains the flux density in the iron below the max threshold B_{ir}. The maximum admissible magnetic flux density in the stator depends on the properties of the ferromagnetic material. The material that has been selected for the launcher stator is a non-oriented electrical silicon steel grade M-47, with 0.47 mm lamination thickness. To be conservative the peak magnetic field density B_{ir} is 1.7 T even though some stator materials allow magnetic field densities up to 2.2 T. The flux across a single pole is shared between two neighbour poles so that h_y can be computed as

$$q\,m\,B_t(\tau_s - b_s)2a = 2B_{ir}h_y 2a \quad \Rightarrow \quad h_y = \frac{1}{2}q\,m\frac{B_t}{B_{ir}}(\tau_s - b_s) \tag{4.128}$$

where m is the number of phases.

The Steinmetz's equation for the M-47 steel can be applied to calculate the iron loss per mass unit in the teeth and in the stator core [92]. The total iron losses in the stator teeth P_{th} and in the stator yoke P_{yo} can be obtained multiplying the Steinmetz equation by the respective mass as shown in eqs. 4.129 and 4.130.

$$P_{th} = \left(5.61999\cdot 10^{-3} f_1^{1.33629} B_t^{1.91523} + 7.62268\cdot 10^{-5} f_1^2 B_t^2\right) m_{th} \tag{4.129}$$

$$\text{where} \qquad m_{th} = 2ah_s(\tau_s - b_s)\left[m\left(2p + 1 + \frac{\tau_c}{\tau}\right)q + 1\right]\rho_{ir}$$

$$P_{yo} = \left(5.61999\cdot 10^{-3} f_1^{1.33629} B_{ir}^{1.91523} + 7.62268\cdot 10^{-5} f_1^2 B_{ir}^2\right) m_{yo} \tag{4.130}$$

$$\text{where} \qquad m_{yo} = 2a\left[\left(2p + 1 + \frac{\tau_c}{\tau}\right)\tau + \tau_s - b_s\right]h_y\rho_{ir}$$

where m_{th} is the mass of the teeth, m_{yo} is the mass of the stator yoke and $\rho_{ir} = 7750$ kg/m^3 is the density of the stator material. The overall iron loss in the stator of the

double-sided LIM is calculated as

$$P_{core} = 2(P_{yo} + P_{th}) \tag{4.131}$$

Once all the geometrical and electromagnetic features of the launcher are determined, the parametric optimization algorithm calculates the performance of the catapult:

Net Output Power:	$P_{o\,net} = F_x v_{to}$	(4.132)
Output Power:	$P_o = F_{xc} v_{to}$	(4.133)
Active Power:	$P_a = P_o + P_{core} + 3R_1 I_1^2 + 3R_2 I_2^2$	(4.134)
Reactive Power:	$P_r = 3\omega_1 \left[L_1 I_1^2 + L_m (I_1^2 - I_2^2) \right]$	(4.135)
Input Power:	$P_i = \sqrt{P_a^2 + P_r^2}$	(4.136)
Efficiency:	$\eta = P_o / P_a$	(4.137)
Power Factor:	$\cos\phi = P_a / P_i$	(4.138)

The input voltage of the primary windings can be computed from the machine performance as

$$U_1 = \frac{P_a}{3 I_1 \cos\phi} \tag{4.139}$$

4.3.2 Parametric Optimization Results

The parametric optimization algorithm explained in Section 4.3.1 is iterated for each combination of the design variables listed in Table 4.3. The design variables are assumed to vary across the respective range in Table 4.3 where the optimal combination which minimizes the input power and satisfies thermal and structural constraints should be found.

The main outcome of the parametric analysis are charts like those shown in Fig. 4.13 which present in the y-axis the percent variation of an output with respect to its mean value. The x-axis presents the percent variation of each design variable with respect to the mean value of the respective range in Table 4.3. Each marked points in Figs. 4.13a, 4.13b and 4.13c correspond to the medium effect of

Table 4.3: Design variables ranges for the parametric optimization of LIM

Variable description	**Sym**	**Range**	**Iterations**
Rated slip frequency at v_{TO}	s	$[0.01 \Rightarrow 0.05]$	9
Aluminium mover thickness	d_{Al}	$[0.015 \Rightarrow 0.030]$ m	4
Airgap length	g	$[0.006 \Rightarrow 0.010]$ m	5
Pole pitch	τ	$[0.51 \Rightarrow 0.69]$ m	7
Stator half width	a	$[0.6 \Rightarrow 1.2]$ m	4
Slot width and slot pitch ratio	b_s/τ_s	$[0.4 \Rightarrow 0.8]$	5
Primary slot current density	J_1	$[30 \Rightarrow 90]$ MA/m^2	4
Axial stress on the mover	f_{stress}	$[80 \Rightarrow 120]$ kN/m^2	3
Number of turns per slot	N_s	$[4 \Rightarrow 8]$	3
Total Iterations			**907200**

a specific value of a design parameter on the output variable under examination. Hence, each point is calculated averaging all the combinations where an input has the same value. The slope of the curves represents the sensitivity of the system to the respective design parameter variation.

The rationale behind the selection of each parameter is presented listing the variable in the order they were chosen:

1. The thickness of the aluminium plate d_{Al} is the result of a multi-physics optimization that takes into account structural and thermal limitations. The aluminium thickness is a key parameter to determine the structural resilience and the thermal capacity of the mover. These aspects will be addressed in Sections 4.4 and 4.5 in more details, but in general the thicker is the plate the better are its structural and thermal properties, but the worse are its electromagnetic properties as shown in Figs. 4.13b and 4.13c. From the electromagnetic point of view, large d_{Al} and large equivalent airgap g_e cause a rapid decrease of all the equivalent circuit parameters. Despite the inductances and resistances reduction, the active and reactive power rapidly increase due to the primary and secondary current increments needed to produce the required thrust. Consequently the input power sharply increase with d_{Al} as shown in Fig. 4.13a.

2. The number of turns per slot N_s does not affect the total input power, but it impacts the voltage and current ratings of the machine: the higher the number

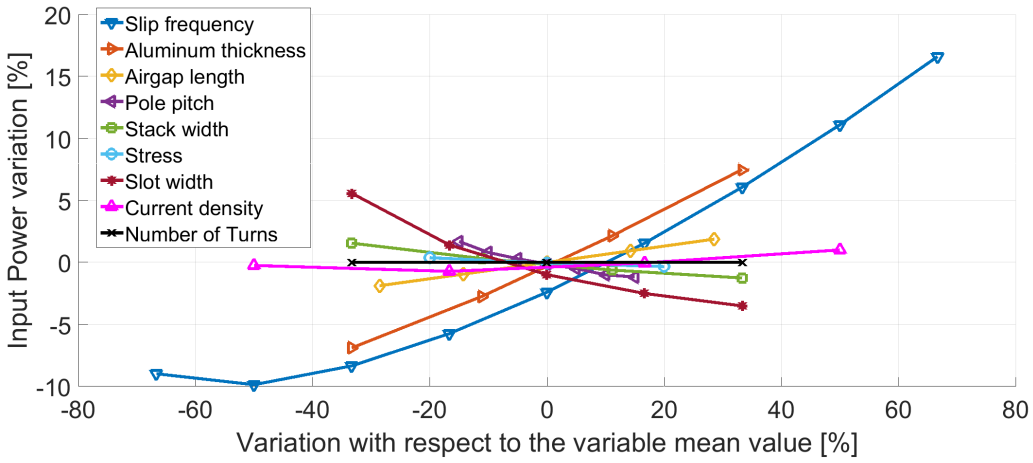

(a) Input Power

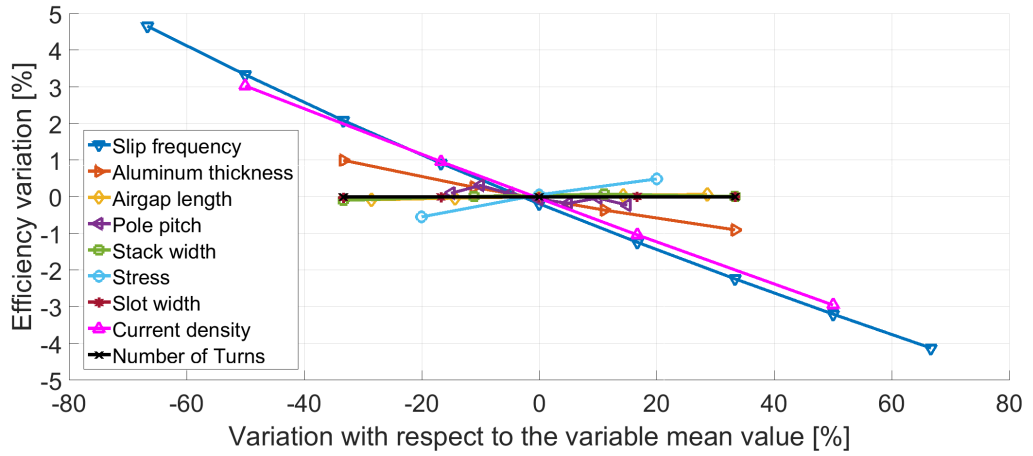

(b) Efficiency

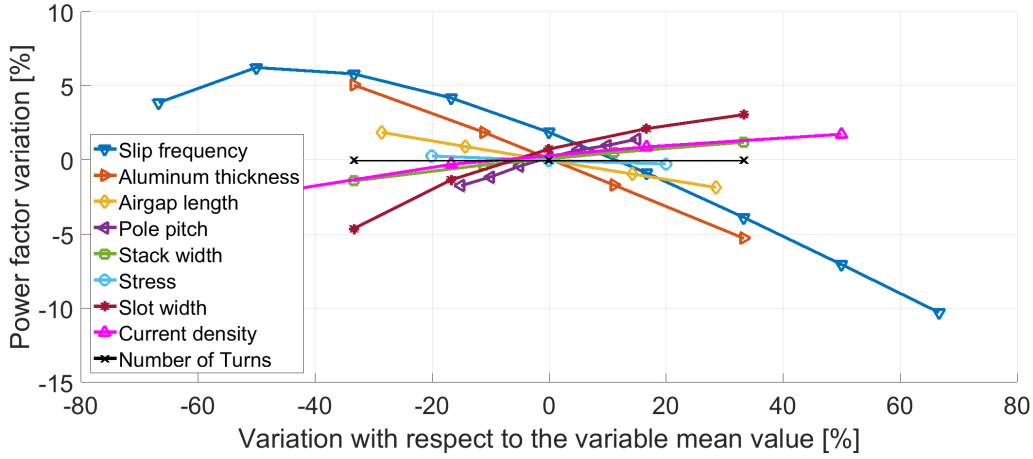

(c) Power Factor

Figure 4.13: Parametric optimization results

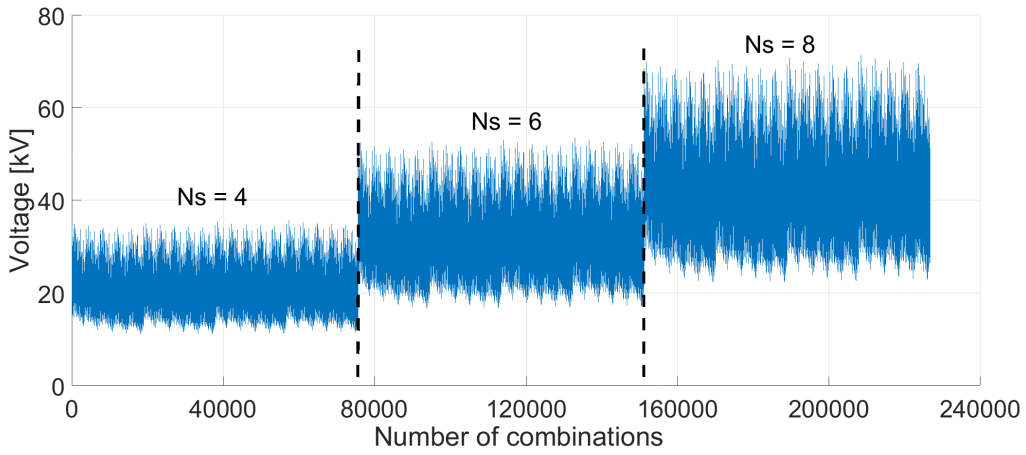

Figure 4.14: Peak DC Voltage at the end of the launch

of turns, the lower the current rating and the higher the voltage rating. Since double-layer windings are considered the number of turns per slot must be an even integer number. Since one major limitation of EML systems is the voltage required at the end of the launch, the number of turns in series needs to be appropriately selected to minimize it. The way the peak voltage varies with N_s is shown in Fig. 4.14.

3. The thrust density f_{stress} is proportional to the number of active poles and to the length of the mover as shown in eqs. 4.101. The impact of the thrust density on the electromagnetic performance is not significant with respect to other input parameters, but high values of f_{stress} are preferable since small and light movers can be implemented. Since load distribution and plate dimensions depend on thrust density, the value of f_{stress} is linked to the structural characteristics of the plate as will be shown in Section 4.4.

4. High values of current densities J_1 can be exploited since the primary windings are fed for a very short time. The current density is limited by the properties of the electrical insulation. The temperature increase of copper wires subject to intense current density will be further investigated in Section 4.5. From the electromagnetic point of view, an intense current density affects the slot geometry reducing the slot height h_s and the slot permeance λ_s. The consequent decrease of the primary leakage inductance L_1 reduces the reactive power needed

by the machine. Nevertheless, high current densities increase the Joule losses in the primary circuit for the reduction of the wire cross section leading to a lower motor efficiency. These counteracting effects cause an input power minimum as can be seen in Fig. 4.13a.

5. The airgap length g represents the distance between the coil surface and the aluminium plate. The length of g includes the tooth tip height h_{ss} and the grooves diameter d_g. From the electromagnetic point of view, the airgap length g affects the length of the equivalent airgap g_e. With short airgap, the power factor increases as shown in Fig. 4.13c for the reduction of inductances L_m and L_1 while the primary current I_1 remains approximately the same. Since active power and efficiency are not affected by g, the input power decreases with short airgap. However, the airgap length needs to be large enough to prevent any contact between aluminium plate and the stators during operations. Possible lateral displacements are due to vibrations and structural deformations.

6. The variable with a greater impact on the input power P_i is the rated slip frequency s as shown in Fig. 4.13a. Reactances and reactive power are mainly affected by s and they tend to increase as the rated slip frequency grows. The inductances do not depend directly on s, but they are affected by the variation of the slot geometry with the primary current. At the same time, Joule losses in the mover and active power increase with the slip frequency causing a decrement of the motor efficiency. The slip frequency curve in Fig. 4.13a presents a minimum at 0.015, but such a low value cannot be selected for FEA simulation which are run at constant current. Indeed, the rated current for the slip frequency is optimized to produce the required thrust only during the last part of the launch. High goodness factors are expected at the end of the runway since the supplied frequency and the magnetizing reactance X_m along with it, linearly increase during the launch. The curve in Fig. 4.4 at the end of the acceleration will be very steep for $s < s_{max}$, being the peak thrust slip frequency s_{max} which satisfy the relation $s_{max} G_e = 1$, very close to zero. At low speed, low frequency and low goodness factor the peak of the thrust-speed curve in Fig. 4.4 moves backward so that high slip frequencies intersect the thrust curve at points where the propulsive force is not sufficient to accelerate

the aircraft leading to de-synchronization. In real EML application, the control system would try to keep the slip frequency constant slightly changing current amplitude to deliver the rated thrust with the minimum loss according to the instantaneous value of the system parameters. The FEA of LIM does not consider any control system and the current amplitude is set constant while the frequency given in input varies continuously during the launch starting from zero to reach the rated value at the end of the acceleration. To simplify the analysis high values of the slip frequency were selected to increase the rated primary current and grant sufficient thrust for the whole duration of the launch. According to these considerations, the final slip frequency computed by FEA is expected to be lower that the value selected by the parametric optimization.

7. The b_s/τ_s ratio is related with the slot width b_s. When the slot width is large, the Carter coefficient k_c increases while the magnetization inductance L_m decreases as can be seen in eqs. 4.30 and 4.107 respectively. Large slot widths have a significant impact on the slot specific permeance λ_s calculated using eq. 4.117 and on the differential specific permeance λ_d calculated using eq. 4.120 causing a sensible decrement of the primary leakage inductance L_1. The reduction of all the inductances causes a significant decrement of the reactive power which in turns gives an input power reduction. Despite the reactive power reduction, the b_s/τ_s ratio augments the magnetic field density in the stator teeth causing saturation. Considering the non-linearity of the magnetic permeability, the magnetic field density in the stator teeth varies as shown in Fig. 4.15. The stator teeth are expected to be saturated, but their mass in eq. 4.129 is so small compare to the rest of the stator that the hysteresis losses remains negligible even with high b_s/τ_s ratios.

8. Since the stator length is fixed by the speed and acceleration requirements, the bulk of the stator entirely depends on its width $2a$. The installation and material costs depend on the stator dimensions, but from the electromagnetic point view the stack width is not subject to any particular limitations. The stack width, and consequently the mover width, affects the structural response of the aluminium plate to the electromagnetic force density which will be investigated in Section 4.4. Since the thrust density f_{stress} was previously selected, when

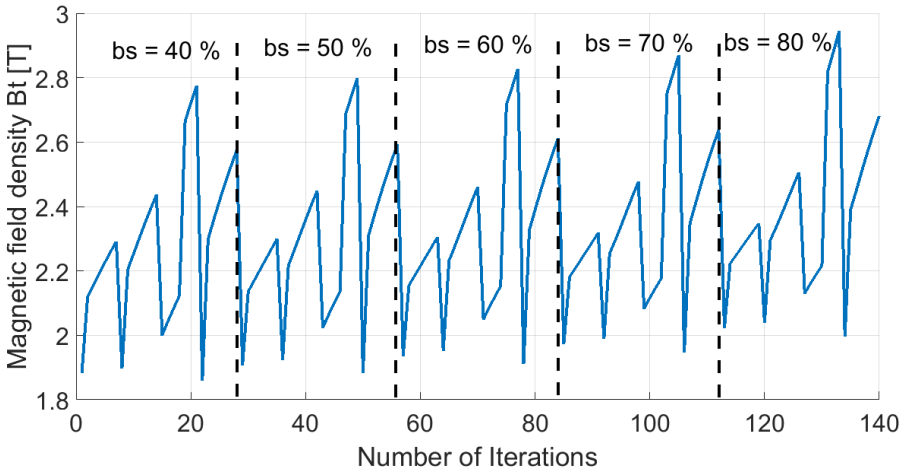

Figure 4.15: Magnetic field density in the stator teeth in the hypothesis of non-linear permeability

Table 4.4: Optimum values of the design variables after optimization

d_{Al}	20 mm
w_s	4
f_{stress}	100 kN/m^2
J	50 A/mm^2
g	7.0 mm
s	0.035
b_s/τ_s	0.75
a	1000 mm
τ	600 mm

wide machines are considered the number of poles required to produce the rated thrust reduces. Even though the length of a single coil $2a + l_{end}$ varies with the stack width, the number of turns N_1 decrease with the number of poles and the length of the wires in series of a single phase does not change. Thus, the primary resistance and the efficiency of the motor do not vary with the stack width. The magnetization inductance L_m in eq. 4.107 is proportional to the stack width so that the primary current I_1 decreases according to 4.112. The sum of the inductances does not substantially change, thus the reactive power follows the tendency of the primary current. The overall effect is a power factor increase and an input power reduction with large stack widths.

Table 4.5: Geometrical features, circuit parameters and performances of LIM for EML

Geometrical features		**Circuit Parameter**		**LIM Performance**	
Slot width	37.5 mm	Peak frequency	74.0 Hz	Field B_g	1.383 T
Slot height	5.1 mm	Sync. speed	88.84 m/s	Field B_t	3.522 T
Wire diameter	1.3 mm	End speed	85.73 m/s	Mover thrust	5115 N
Wires in parallel	16	I_1 (RMS)	1086.0 A	Total thrust	508010 N
Airgap g_m	34.0 mm	I_2 (RMS)	1080.6 A	Thrust density	70.56 kN/m^2
Airgap g_e	36.4 mm	I_m (RMS)	107.8 A	Carter coeff.	1.0643
Plate width	2382 mm	Voltage U_1	16635 V	Fringing factor	1.0005
Yoke height	311 mm	Winding factor	0.8848	Skin-effect fac.	1.0017
Mover length	4650 mm	Poles	6	Edge-effect fac.	1.1818
Mover mass	868.9 kg	Number of turns	224	Iron loss	0.366 MW
Teeth mass	93.8 kg	Resistance R_1	0.4631 Ω	Active Power	49.716 MW
Yoke mass	17353 kg	Resistance R_2	0.4506 Ω	Reactive Power	23.751 MW
Coil pitch	450 mm	Inductance L_1	11.7 mH	Input Power	54.197 MW
End coil length	626.8 mm	Inductance L_m	277.6 mH	Peak Efficiency	0.894
Mover width	2382 mm	Goodness factor	286.4	Power factor	0.899

9. The pole pitch τ is a key design parameter and its minimum length is limited by the maximum frequency that semiconductor switching devices can safely handle. Nevertheless the goodness factor G and therefore the capability of the machine to convert electrical power in mechanical power, is proportional to the pole pitch τ as discussed in Section 4.2.1. Therefore the optimum pole pitch is usually longer that the limit imposed by the switching technology. Also the current I_1 calculated using eq. 4.112 increases with τ to deliver the same thrust. Since the current density is given, an current increase enlarges the conductor cross section reducing the primary resistance. A longer pole pitch also entails a heavier mover and a greater output power. Therefore the Joule losses increase while the efficiency slightly reduces as shown in Fig. 4.13b. Since magnetization and leakage inductances decrease, the power factor increment results sharper than the efficiency decrement causing an overall reduction of the input power.

Table 4.4 lists the values of the design variables that were selected and used in FEA simulation and transient LIM analysis whose results will be compared in Section 4.3.3. The machine geometrical features and performances that were calculated through the parametric analysis with the optimal combination of design variables are reported in Table 4.5.

4.3.3 Transient Equivalent Circuit Model, FEM Analysis

When transients of motor speed are accounted for, differential equations are introduced to characterize the response of the machine and the analytical method proposed in Section 4.3.1 to size the electromagnetic launcher becomes inaccurate. The equivalent circuit model for transient problems needs to take into account the changes of the primary and secondary flux linkage over time as indicated in Fig. 4.16.

The direct-quadrature (d-q) equivalent circuit model of the motor provides a convenient way of modelling the machine and it is most suitable for induction machine transient analysis. This method describes the motor parameters in terms of complex variables with respect to a frame of reference which may be stationary or in motion. According to the linear induction motor model in Fig. 4.16 the voltage equations expressed with respect to a frame of reference moving at synchronous speed are

$$\overline{U_1} = R_1\overline{I_1} + \frac{\partial\overline{\Psi_1}}{\partial t} + j\omega_1\overline{\Psi_1} \tag{4.140}$$

$$\overline{U_2} = 0 = R_2\overline{I_2} + \frac{\partial\overline{\Psi_2}}{\partial t} + j(\omega_1 - \omega_2)\overline{\Psi_2} \tag{4.141}$$

$$\overline{I_m} = \overline{I_1} + \overline{I_2} \tag{4.142}$$

where the primary flux linkage $\overline{\Psi_1}$ and secondary flux linkage $\overline{\Psi_2}$ are defined as

$$\overline{\Psi_1} = L_m\overline{I_m} + L_{1l}\overline{I_1} \tag{4.143}$$

$$\overline{\Psi_2} = L_m\overline{I_m} \tag{4.144}$$

The complex currents and voltage used by eqs. 4.140 to 4.144 can be expressed as function of their d-q axis components as

$$\overline{I_1} = I_{1d} + jI_{1q} \tag{4.145}$$

$$\overline{I_2} = I_{2d} + jI_{2q} \tag{4.146}$$

$$\overline{I_m} = I_{md} + jI_{mq} \tag{4.147}$$

$$\overline{U_1} = U_{1d} + jU_{1q} \tag{4.148}$$

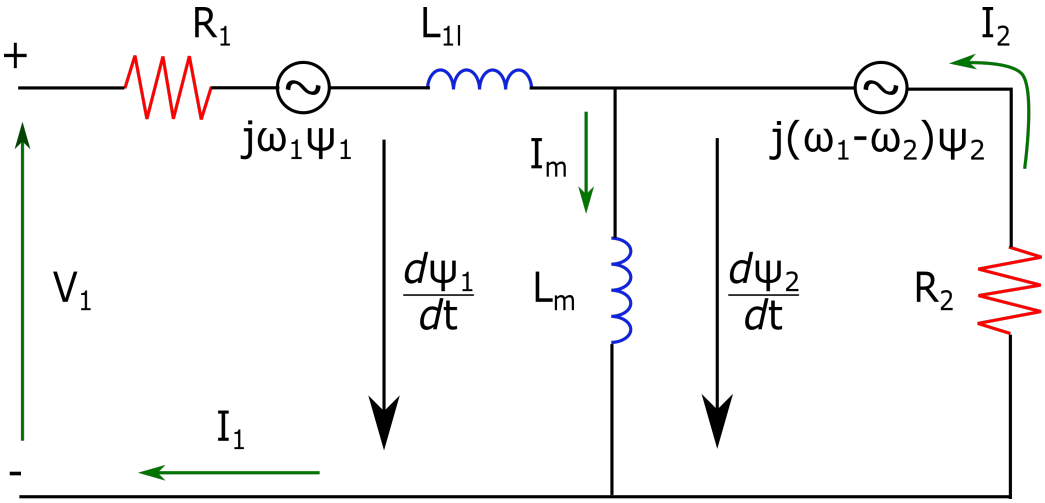

Figure 4.16: Induction motor equivalent circuit for transient analysis

In order to solve the system of differential equations that includes eqs. 4.140 to 4.142, the Root Mean Square (RMS) value of primary current I_1 reported in Table 4.5 was considered. This current represents the known variable in input for both finite element analysis and transient LIM model. Indeed, the three phase current supplied to the system has an amplitude $\sqrt{2}I_1$ which remains constant during the whole launch. In electromagnetic launch systems the frequency linearly increases over time and the instantaneous frequency can be expressed as

$$f(t) = kt = \frac{0.6G}{2\tau}t = \frac{v_s}{2\tau} \tag{4.149}$$

The angular velocity of any oscillating signal is 2π times the integral of the frequency over time. For the frequency shown in eq. 4.149 the angular velocity becomes

$$\omega = \frac{2\pi}{t}\frac{k}{2}t^2 = 2\pi\frac{0.6G}{4\tau}t = \frac{\pi}{\tau}\frac{v_s}{2} \tag{4.150}$$

The quantity $\pi v_s/(2\tau)$ is called chirp frequency where a chirp is a signal in which the frequency varies with time. Thus, each current phase supplied to the stator coils at increasing frequency varies in time according to the relations

$$I_A = \sqrt{2}I_1 \cos\left(\frac{\pi}{\tau}\frac{v_s}{2}t\right)$$

$$I_B = \sqrt{2} I_1 \cos\left(\frac{\pi}{\tau}\frac{v_s}{2}t - \frac{2}{3}\pi\right) \tag{4.151}$$
$$I_C = \sqrt{2} I_1 \cos\left(\frac{\pi}{\tau}\frac{v_s}{2}t + \frac{2}{3}\pi\right)$$

The three phases I_A, I_B and I_C can be expressed with respect to the direct-quadrature frame of reference using Park's mathematical transformation [93].

$$\begin{bmatrix} I_{1d} \\ I_{1q} \\ I_0 \end{bmatrix} = \frac{2}{3} \begin{bmatrix} \sin\left(\frac{\pi}{\tau}\frac{v_s}{2}t\right) & \sin\left(\frac{\pi}{\tau}\frac{v_s}{2}t - \frac{2}{3}\pi\right) & \sin\left(\frac{\pi}{\tau}\frac{v_s}{2}t + \frac{2}{3}\pi\right) \\ \cos\left(\frac{\pi}{\tau}\frac{v_s}{2}t\right) & \cos\left(\frac{\pi}{\tau}\frac{v_s}{2}t - \frac{2}{3}\pi\right) & \cos\left(\frac{\pi}{\tau}\frac{v_s}{2}t + \frac{2}{3}\pi\right) \\ \frac{1}{2} & \frac{1}{2} & \frac{1}{2} \end{bmatrix} \begin{bmatrix} I_A \\ I_B \\ I_C \end{bmatrix} \tag{4.152}$$

Since the primary current oscillates at synchronous frequency, eq. 4.152 yields $I_{1d} = 0$ and $I_{1q} = \sqrt{2} I_1$.

The magnetization current can be defined as $\overline{I_m} = \overline{\Psi_2}/L_m$ according to eq. 4.144. Inserting eqs. 4.144 and 4.142 to replace the secondary current $\overline{I_2}$ in eq. 4.141 yields

$$\frac{\partial \overline{\Psi_2}}{\partial t} + \left[\frac{R_2}{L_m} + j(\omega_1 - \omega_2)\right] \overline{\Psi_2} = R_2 \overline{I_1} \tag{4.153}$$

Eq. 4.153 can be integrated to calculate the variation of the secondary flux linkage $\overline{\Psi_2}$ over time. Once the secondary flux is known, the currents in the circuit ($\overline{I_1}$, $\overline{I_2}$ and $\overline{I_m}$), the primary voltage $\overline{U_1}$ and the primary flux linkage $\overline{\Psi_1}$ can be determined. The thrust that the machine delivers during its transient can be obtained from

$$F_x = -\frac{3}{2}\frac{\pi}{\tau}\Im(\overline{\Psi_1} \cdot \overline{I_1}^*) \tag{4.154}$$

where $\overline{I_1}^*$ is the complex conjugate of $\overline{I_1}$. Solving the imaginary part of the product in eq. 4.154 and considering that $I_{1d} = 0$ and $I_{md} = I_{2d}$ yields

$$F_x = \frac{3}{2}\frac{\pi}{\tau} L_m I_{2d} I_{1q} \tag{4.155}$$

The thrust calculated by d-q equivalent circuit model using eq. 4.154 is compared with thrust computed by finite element and parametric analysis in Fig. 4.17.

The software that performs electromagnetic finite element simulations uses the

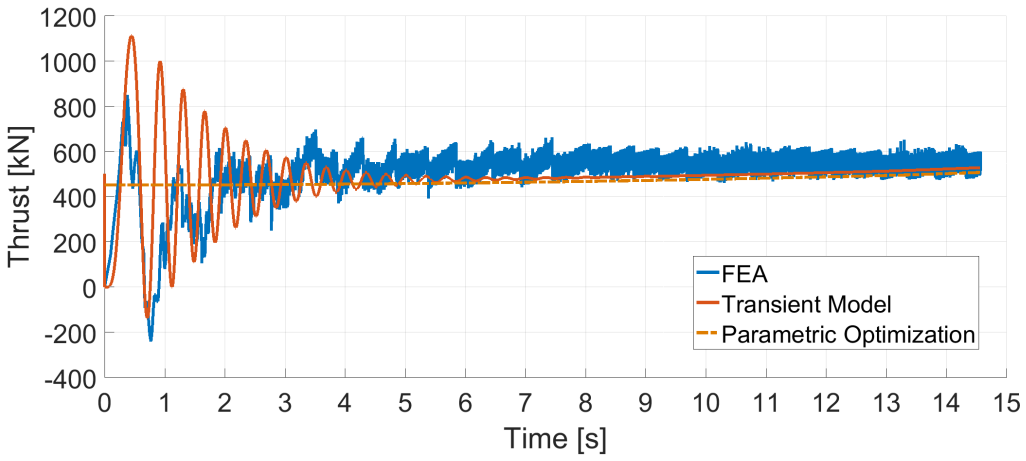

Figure 4.17: Comparison between thrusts calculated by FEA, transient model and parametric analysis of LIM

geometry of LIM determined through parametric optimization. Therefore the geometrical parameters of the induction motor shown in Tables 4.4 and 4.5 are loaded into the software to draw the machine. The finite element simulations are performed on a 2D section of the machine while transverse edge effect is simulated modifying the aluminium conductivity with the factor k_{tr}. In order to reduce the computational time, FEA is executed on half the stator geometry taking advantage of the longitudinal symmetry. Since the flux is assumed to cross the symmetry plane perpendicularly, orthogonal boundary conditions are imposed along the symmetry line. Additionally, electromagnetic simulations are carried out only on a single stage which has $2p$ active poles (see Table 4.5). The full length of the launcher is simulated imposing even periodic boundary conditions on planes beside the stator which are located to reproduce the exact distance between stages. The machine is wound following the distributed winding method for double-layer configurations and considering the coil pitch and the slot per pole per phase shown in Table 4.2. The magnitude of the primary current supplied to the stator windings remains constant for the whole duration of the launch. On the contrary, the frequency linearly change according to eq. 4.151.

The thrust computed by FEA shown in Fig. 4.17 becomes negative at the beginning of the launch when the mover exceeds the synchronous speed for a short time. The oscillations of the FEA thrust profile are due to the transition effect

between one stage and the next one. The transient analytical model of LIM does not consider transition effects between consecutive stator sections and the wide oscillations that can be observed when the mover starts to accelerate are due to numerical instabilities during the integration of the differential equations. However, the amplitude of the oscillations gradually damps until the system delivers exactly the required thrust which is represented by the curve computed using the parametric optimization method and shown in Fig. 4.17.

The thrust profiles calculated by the FEA software is generally greater that the thrust computed with the analytical model because the 2D simulation does not account for Joule losses and leakage inductance associated with the end windings which on the contrary were considered by d-q model and parametric optimization algorithm.

The effect of resistance and leakage inductance due to the end windings were later considered in the calculation of efficiency and power factor after the data extraction from the finite element software. With this method the efficiency and power factor profiles computed using the FEA data are very similar to those calculated by the d-q equivalent circuit model of LIM as shown in Figs. 4.18a and 4.18b.

The oscillations of efficiency and power factor profiles computed by the transient model are not only due to the numerical integration instabilities, but fluctuations are exacerbated by the difficulty of extracting the data from alternating currents and voltages with variable frequency and magnitude. However, both FEA and transient model compute efficiency and power factor profiles that at the end of the launch tend towards the respective value calculated by the parametric optimization algorithm (see Table 4.5).

The d-q equivalent circuit model was proved to provide machine performances which are comparable with FEA and parametric optimization results. This tool can be used to predict the transient behaviour of LIM in place of time expensive FEA during the preliminary design phase of electromagnetic launch system even though some inaccuracies appear at the beginning of the launch. Indeed, the solution of the differential equations requires 27 seconds whereas the full launch FEA simulation lasts approximately 72 hours.

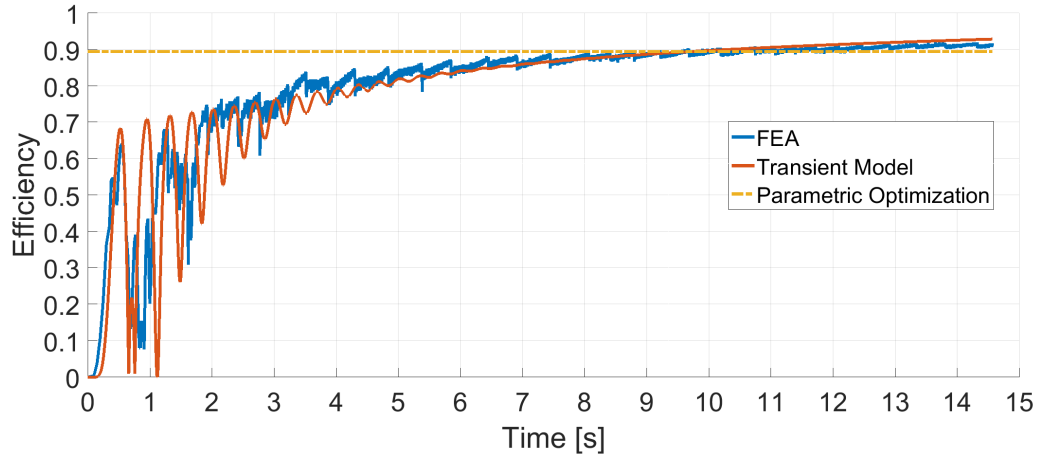

(a) Efficiency

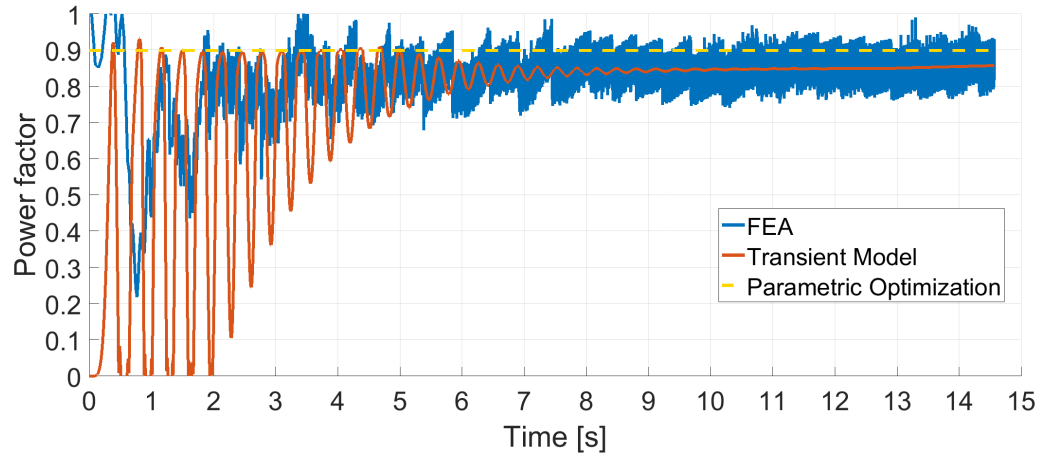

(b) Power factor

Figure 4.18: Comparison between electromagnetic performances of LIM computed by FEA, transient model and parametric analysis

4.4 LIM's Mover Structural Analysis

Slender objects like the aluminium plate of the induction launcher may undergo a structural instability phenomenon called buckling. Buckling is characterized by sudden failure of a structure subject to a compressive stress that occurs at a load lower than the ultimate compressive load of the material. The LIM mover is subject to a distributed load acting in the direction of the motion that with the reaction force due to the aircraft inertia and aerodynamic drag generates compressive

stresses that could cause undesirable buckling deformations.

The propulsive force stretches the plate along the direction of the motion, but the displacement does not affect the electromagnetic performance of the machine. On the contrary, buckling typically provokes ripples on the material surface with strong deviation from the original shape of the loaded object. From the structural point of view, the buckled plate can continue to carry the propulsive load without braking if the deformation is not catastrophic. However any transverse deformation due to the buckling of the plate is associated with an uneven airgap distribution and a generation of a normal force F_n proportional to the plate displacement. Normal forces exerted by two opposite stators would counteract the plate deformation, trying to re-establish the equilibrium condition $F_n = 0$. Despite the balancing action of the double-sided motor, the buckling condition should never be reached to avoid unpredictable reactions of the machine.

The structural and buckling analyses have been carried out to define range of values that the geometrical design parameters can assume granting the structural integrity of the plate. The structural analysis defines the maximum displacement and the stress distribution while the buckling analysis allows the calculation of the buckling factor k_{buck} under the operative load. The buckling factor may be interpreted as the distance between operative condition and instability and it is computed as

$$k_{buck} = \frac{F_{buck}}{F_{xc}} \tag{4.156}$$

where F_{buck} is the buckling load and F_{xc} is the corrected thrust calculated using eq. 4.103.

In the aerospace field the load factor for high stressed structural components is set up to 3.8 by the international Federal Aviation Regulation [94]. This means that the aircraft structure is capable of withstanding 3.8 times the maximum nominal load for safety reason. Due to the uncertainty of the final structural layout, this study considers acceptable a structure that has a buckling factor greater than 10.

The structural and buckling analyses have been carried out considering a fixed constraint on the top edge of the plate where the aircraft is connected and a guide

on the bottom edge that impedes transversal displacements. The load is applied as a distributed force in x-direction to all the nodes of the active area of the plate as shown in Fig. 4.11. The same load is considered throughout all the structural investigations and its value is reported in Table 4.5. Since the applied load is constant the buckling factor in eq. 4.156 proportionally varies with the buckling load.

The plate's material considered in the structural and buckling analyses is isotropic aluminium with invariant physical properties all over the volume. In order to fully characterize the structural response of an isotropic material two mechanical properties must be employed. The mechanical property that is equal to the ratio between stress (force per unit area) and strain in a material is called Young's modulus. The Young's modulus is a measure of the stiffness of a material and is proportional to the force needed to stretch or compress a material sample. The Young's modulus remains constant until the load reaches the yield point of the material when it loses its elastic behaviour, i.e. the capability of returning to the initial shape after the load is removed, and undergoes permanent plastic deformation. The second parameter used to describe the structural behaviour of the plate is the Poisson's ratio which is the quotient between axial extension and transverse contraction when the material is stretched in one direction. The 1050A H14 aluminium alloy considered for the LIM's mover for its high electrical conductivity has a Young's modulus of 71 GPa, a yield strength of 105-145 MPa and a Possion's ratio of 0.334.

The structural analysis has to be solved before the buckling analysis to find the strain and stress distribution over the plate. Even for simple geometries the buckling analysis of structures reaches such a level of complexity that the aid of specialized FEA software is required. Implementing the material properties and the constraint conditions previously described in the FEA software, the structural analysis determines the strain and the stress fields reported in Figs. 4.19 and 4.20 respectively. The mover's thickness, width and length considered during the analyses are those reported in Table 4.5. Both the figures show an exaggerated plate deformation to visualize the stretching of the material under the applied load. Fig. 4.19 shows that the maximum displacement is only about 0.4 mm and is expected on the corners opposite to the connection with the aircraft and in proximity of

the guidance system. The deformation of the plate under load should be taken into account in the design of the supporting structure, but it does not affect the electromagnetic performance of the motor. In particular, the displacement along z-direction affects the total load used to size the linear bearings of the guidance system.

Considering the yield strength of aluminium 1050 (105-145 MPa), the stress distribution shown in Fig. 4.20 proves that the material elastically deforms under load without incurring in any permanent deformation. The plate undergoes the greater stress in proximity of the aircraft connection while the tension gradually decreases toward the guidance system. The maximum stress reaches 34.5 MPa and is located in small areas on the top corners of the plate in Fig. 4.20, but it rapidly dwindles in the surrounding area. The average stress in proximity of the aircraft connection may be assumed approximately 15 MPa which is sensibly smaller than the yield strength of the material.

Once the structural analysis is completed the FEA software can use the solutions to perform the buckling analysis of the plate. The geometrical parameter which has the strongest effect on the instability load is the thickness of the plate. In order to study the impact of this geometrical feature on the buckling factor the analysis was carried out varying the plate thickness while all the other geometrical parameters were kept constant. The variation of the buckling factor with respect to the aluminium thickness is shown in Fig. 4.21 where the plate thickness presented by the parametric optimization in Section 4.3.2 and the relative buckling factor are highlighted.

Fig. 4.21 shows that an high thickness not only increments the load-carrying capability of the plate, but also delays the occurrence of the instability phenomenon. Indeed, the buckling load is proportional to the second moment of inertia of the rectangular cross section of sides d_{Al} and $2c$ in Fig. 4.11 which in turns varies with the cube of the thickness. However, a thick plate has a greater mass and it negatively affects the electromagnetic performance of the induction machine as shown in Fig. 4.13. Therefore, the plate thickness was selected in order to minimize the deterioration of the electromagnetic performance and to satisfy the structural requirement $k_{buck} > 10$. The combination of electromagnetic, structural and buckling analyses allow the implementation of a plate 20 mm thick with a buckling

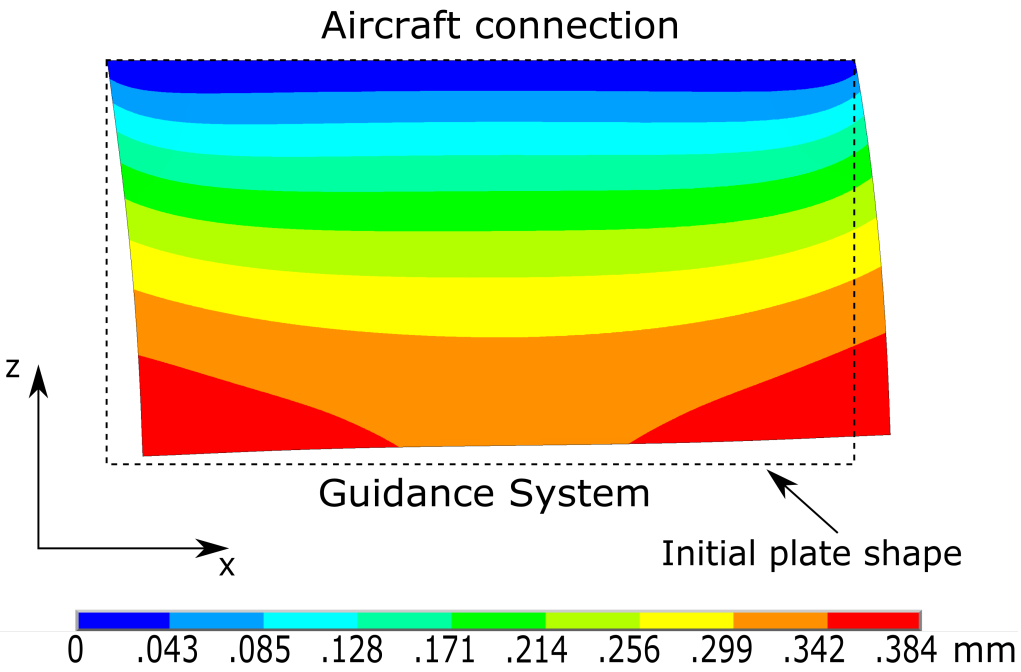

Figure 4.19: Deformation and strain field of the aluminium plate under load

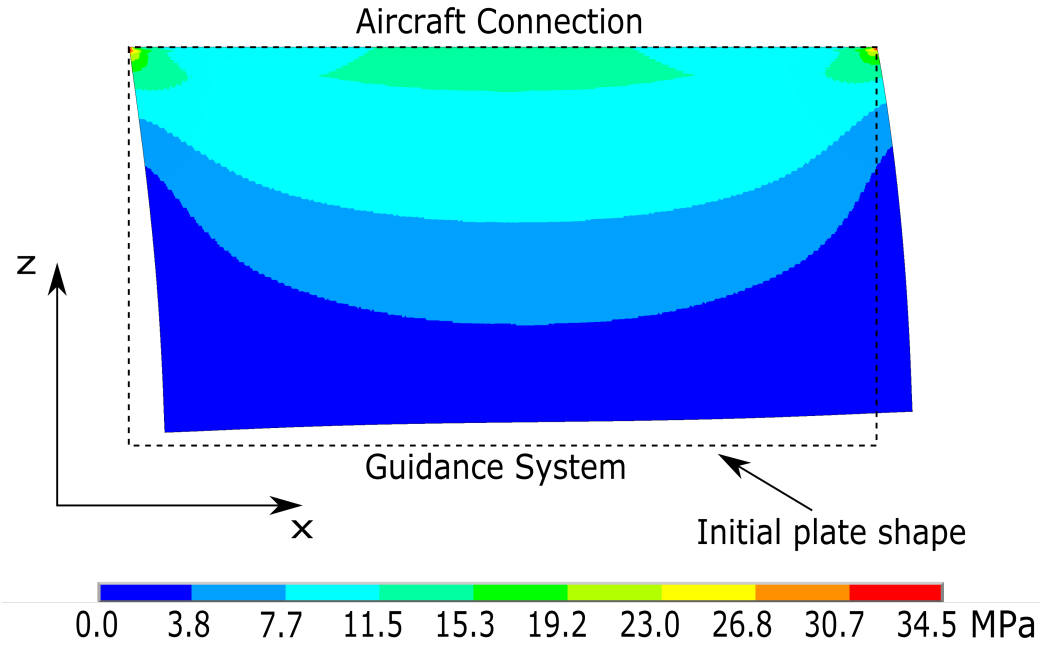

Figure 4.20: Stress distribution on the aluminium plate under rated load

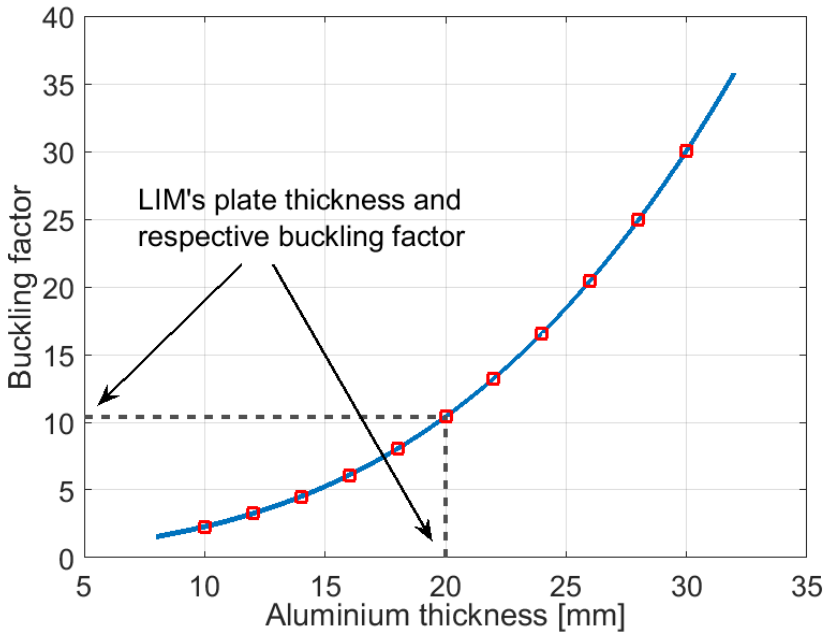

Figure 4.21: Buckling factor variation with the plate thickness

factor of 10.4. The value of the plate thickness will be further validated by the thermal analysis presented in Section 4.5.

The aluminium thickness is not the only LIM's design variable that affects the structural performance of the aluminium plate. Indeed, the pole pitch of the motor τ and the width of the active area $2a$ influence the other two dimensions of the plate. The pole pitch is directly proportional to the length of the mover l_{mov} as shown in eq. 4.157. The pole pitch also affects the mover width $2c$ since it is involved in the calculation of the plate overhangs length as shown in eq. 4.158.

$$l_{mov} = \left(2p + 1 + \frac{\tau_c}{\tau}\right)\tau \tag{4.157}$$

$$2c = 2\left(a + \frac{\tau}{\pi}\right) \tag{4.158}$$

Eq. 4.158 shows that the mover width is also affected by the width of the active area $2a$. The dependencies of the buckling factor on the pole pitch and on the width of the active area are reported in Figs. 4.22 and 4.23 respectively. The buckling analysis outcomes reported in Figs. 4.22 and 4.23 were achieved varying the respective variable while maintaining constant the other design parameters

which affect the plate dimensions.

In order to understand the behaviour of the buckling factor with respect to the variation of the mover's length and width, it should be mentioned that the more a structure is constrained the greater the instability load becomes. When the mover length extends, the percentage of the plate perimeter under constraints increases as well as the buckling load. This effect can be observed on the tendency of the buckling factor in Fig. 4.22 which varies proportionally to the pole pitch and to the length of the mover. Furthermore, a longer pole pitch broadens the active surface of the plate and since the applied load remains the same, the thrust density becomes weaker. The decrease of the thrust density intensifies the load required to buckle the aluminium plate even considering the impact of the pole pitch on the width of the plate overhangs. Fig. 4.22 allows to compare the value of the buckling factor with both the mover width and the mover length and it highlights the selected value of the plate dimensions as shown in Section 4.3.2.

The mover width does not have any impact on the length of the constrained part of the perimeter and the instability appears at lower loads. As the width increases the buckling factor reduces as shown in Fig. 4.23. As the plate thickness, the plate width is a dimension perpendicular to the direction of the load and it is directly affected by the instability phenomenon. For this reason, the the buckling factor dependency on the mover width is cubic rather than linear.

The buckling analysis allows the calculation of the deformation under the buckling load as shown in Fig. 4.24. The ripples of the material are located on the far edge of the plate with respect to the direction of the motion and of the applied force. In this area the compressive stress reaches its maximum intensity and here is where the material first becomes unstable. According to the minimum requirement for the buckling factor this deformation appears with a load 10 times greater than the rated one. Considering the stress distribution in Fig. 4.20, the buckling load would generate an average stress of 150 MPa and would reach 345 MPa in small areas near the aircraft connection. In this case, the stress would exceed the yield strength of the material causing a plastic deformation. Above the yield point the buckling analysis loses linearity and the method applied in this section can no longer be used to describe structural instability. Therefore, the buckling deformation shown in Fig. 4.24 might not happen at the same load predicted by the linear

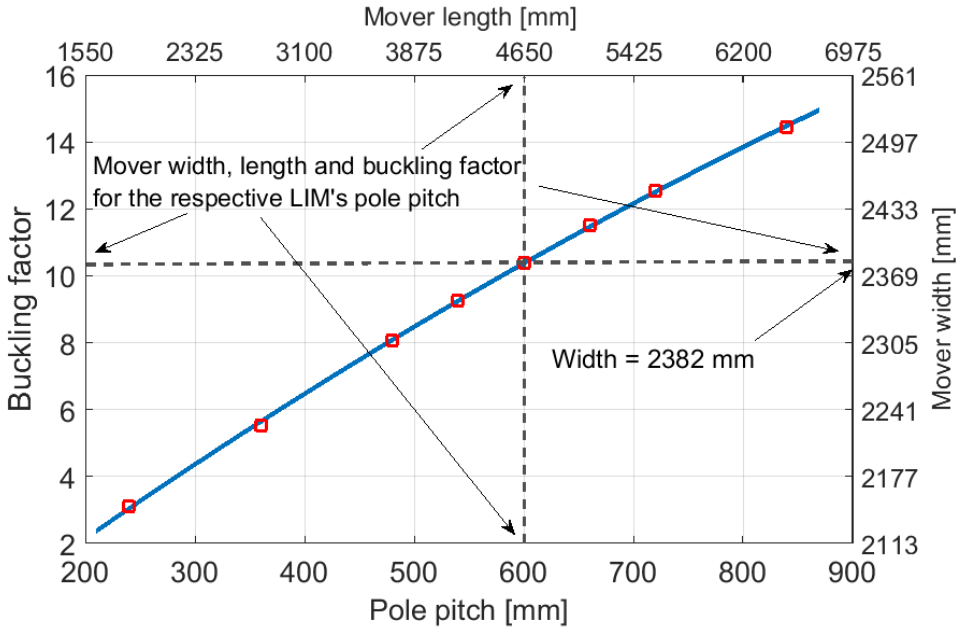

Figure 4.22: Buckling factor variation with the LIM's pole pitch and the respective mover length and width

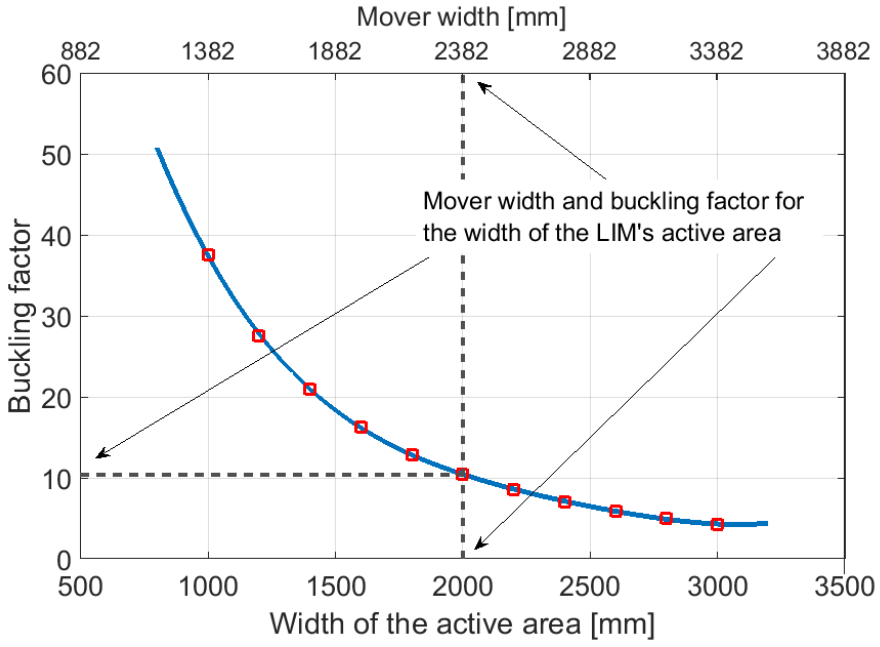

Figure 4.23: Buckling factor variation with the width of the LIM's active area and the respective mover width

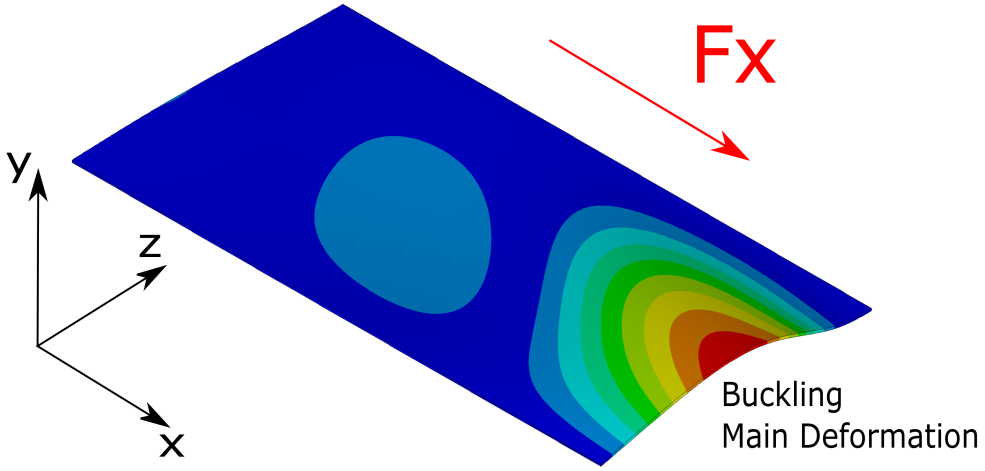

Figure 4.24: Plate deformation under the buckling load

analysis. However, the selected geometry safely copes with the operative load and the structure would rather yield than buckle as the load increases.

4.5 LIM Thermal Analysis

The thermal management of electrical machinery is an issue that has to be carefully addressed, especially in high performance applications where high forces and power densities are needed. Since the electromagnetic induction launcher is formed by a high number of stages fed for a very short time, the machine can exploit higher current densities than any motor designed for continuous operations. The thermal analysis is concerned with LIM's components where intense current flows: the stator windings and the conductive plate.

In general high current densities in the stator windings are desired since primary leakage inductance and reactive power exponentially decrease for the reduction of the slot depth. Since the area of the conductors crossed by the rated current shrinks when the current densities augments, the primary resistance and the active power linearly grow as shown in Fig. 4.25. Since high current densities cause an

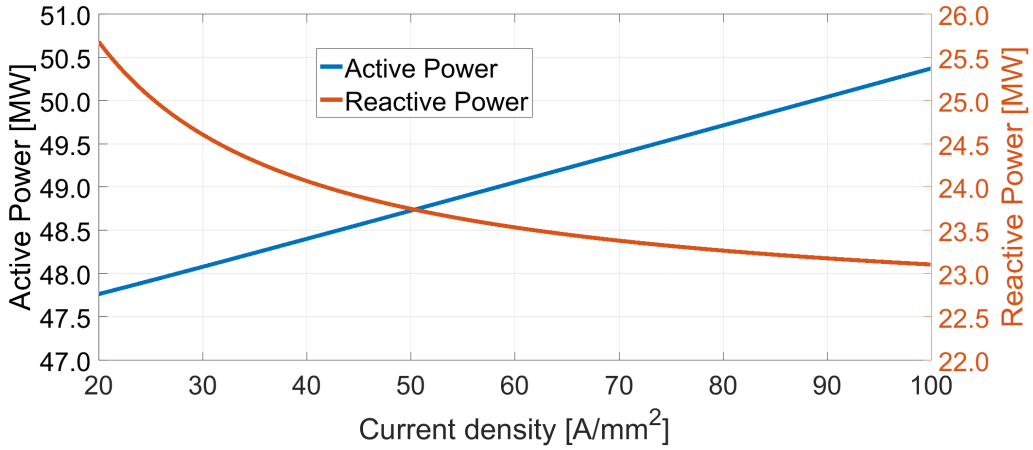

Figure 4.25: Effect of current density on active and reactive power

increase of the Joule losses into the conductive components of the machine, the thermal analysis aims to verify whether the machine is able to passively extract the excess heat without the aid of an active cooling system.

Two different approaches were used to solve the heat transfer problem for stator windings and moving plate. In both the cases the heat transfer problem cannot be solved looking at the static thermal equilibrium, but the transient evolution of temperature has to be considered.

4.5.1 Thermal Analysis of the Primary Windings

This section aims to determine the maximum current density J_1 that can flow through the primary coils without thermally damaging the insulation. The class of insulating material that is considered in this section can operate under the maximum temperature of 180 °C. Other classes of insulating material can resist to temperature above 220 °C, but at this design stage it is preferred to adopt conservative insulation properties.

Since the electrical insulation has a low thermal conductivity all the wires inside the slots can be considered thermally isolated from one another and the thermal analysis of the stator windings may be reduced to the study of the short-time current carrying capacity of a single copper conductor. Since the temperature drops in the insulation matrix between wires, the insulation cannot be damaged if

the temperature rise in each single wire remains within the limits.

The Onderdonk's law was first introduce to study the short-term current required to bring the temperature of copper conductors to the melting point [95]. The Onderdonk's law can be also applied in its more general form to determine the temperature increase ΔT in a single wire [96].

$$33.5\left(\frac{I_1}{A_w}\right)^2 t_1 = \log\left(\frac{\Delta T}{234+T_i}+1\right) \tag{4.159}$$

where I_1 is the rated primary current, A_w is the wire area in circular mils (1 circular mils = $5.067 \cdot 10^{-10}$ m^2), t_1 is the time in seconds and T_i is the initial temperature in °C. Eq. 4.159 represents the balance over time between the heating due to the electrical energy and the thermal energy gained by the wire material. It can be calculate by integrating the energy balance equation:

$$c_{Co} m_{Co} \partial T = R_{Co} I_1^2 \partial t \tag{4.160}$$

where c_{Co}, m_{Co} and R_{Co} are the thermal capacity, the mass and the resistance of the copper wire respectively.

The Onderdonk's law can be rewritten to express the temperature increment as a function of current and time as

$$\Delta T = (234+T_i)\left[10^{33.5(I_1/A_w)^2 t_1} - 1\right] \tag{4.161}$$

Since the wire section, the primary current and the initial temperature are known, eq. 4.161 can be used to determine the temperature increase of the a copper wire once the time t_1 is calculated.

Each stage of the induction launcher is connected to the power source for the time required by the mover to cross the stage itself. Since the mover accelerates the time needed to pass each stage is gradually shorter as the motion progresses. Therefore, the primary windings of the first stage will be connected to the power supply for the longest period and will experience the strongest temperature rise.

The time spent to build up the magnetic flux in each stage of the machine must also be considered to estimate the total time the power source needs to be connected. Current and magnetic flux reach their rated value after a time that cor-

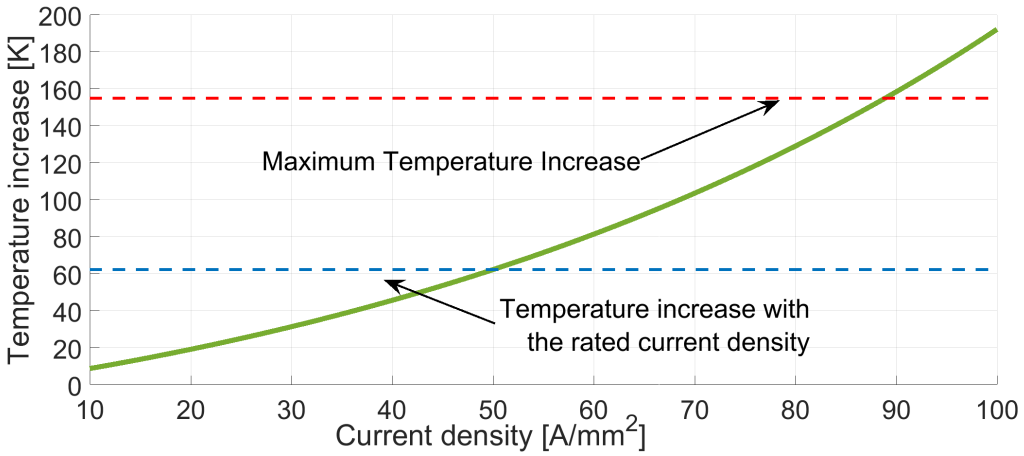

Figure 4.26: Temperature rise in the stator windings after the time t_1 with several current densities

responds to five times the time constants of the machine. In a similar way the current takes other five time constants to return to zero once the power source is disconnected. Since the current profiles during charging and discharging are complementary, the thermal analysis considers the rated primary current flowing for only 5 time constants. For an inductive/resistive electric circuit like the equivalent circuit of the induction motor the time constant is given by the ratio between the primary inductance and the primary resistance.

The sum of time spent to charge and discharge the motor and the time to cross the first stage can be calculated as

$$t_1 = \sqrt{\frac{2(2p+1+\tau_c/\tau)\tau}{0.6G}} + 5\frac{L_m + L_1}{R_1} \tag{4.162}$$

where $(2p+1+\tau_c/\tau)\tau$ is the length of the stages. Eq. 4.162 can be used together with eq. 4.161 to calculate the temperature variation of the copper wires.

Fig. 4.26 shows the variation of the temperature increase ΔT with the current density. The ΔT profile was calculated using eq. 4.161 considering the initial temperature of the copper wire $T_i = 25$ °C. The parametric optimization in Section 4.3.1 proposes a rated current density $J_1 = 50$ A/mm^2 considering all the design constraints. The current density J_1 causes the copper wire to increase their temperature of only 62.3 K after a time t_1 of 4.35 seconds as shown in Fig. 4.26.

The current density required to take the wire to the maximum temperature allowed by the insulation in a time t_1 is 86 A/mm^2. The maximum temperature increase shown in Fig. 4.26 is calculated $\Delta T_{max} = 180 - T_i$.

Even though the rated current density of the induction launcher is greater than the current densities of induction machines for continuous operations, the thermal analysis has shown that the temperature increase of the copper wire is below the insulation limits. The launcher can operate without any active cooling of the stator windings. Special precaution must be taken when a stator stage is fed for more than 9.5 s which is the time required to reach the insulation temperature limit with the rated current density J_1, although this should not occur during normal operations.

Even though the temperature rise during a single launch can be handled by the thermal insulation, the launcher has to performed multiple launches to cope with the air traffic of an airport. Busy airports like Heathrow reach an average number of movements (take-off and landing) of about 1300 flights per day [97], so that the time between two consecutive launches may reduce to as little as 90 seconds during peak times. Within this time the initial coil temperature of 25 °C should be passively or actively re-established.

In order to model the temperature profile of a coil of the first stage after the current ceases to flow a simple mono-dimensional thermal model is introduced:

$$\frac{\partial T}{\partial t} = \frac{k_{ins} S_{wire}}{b_s/2 \cdot \rho_{Co} c_{Co} v_{wire}} (T - T_i) \tag{4.163}$$

where k_{ins} is the thermal conductivity of the insulation (Mica 0.528 W/m/K), S_{wire} is the external surface of the wire, ρ_{Co} is the copper density, c_{Co} is the copper heat capacity and v_{wire} is the volume of the wire. The analysis is restricted to a single wire since all the turns of a coil behave in a similar fashion. Moreover, the heat transfer model studies the temperature evolution of the part of the wire inside a single slot, since the heat flow along the wire length is neglected. The slowest passive cooling occurs when the wire is located in the middle of the slot with an insulation thickness equal to $b_s/2$ as shown in eq. 4.163. The integration of eq. 4.163 for a time span of ten minutes yields the result reported in Fig. 4.27.

The temperature profile in Fig. 4.27 shows that after 90 seconds the temperature

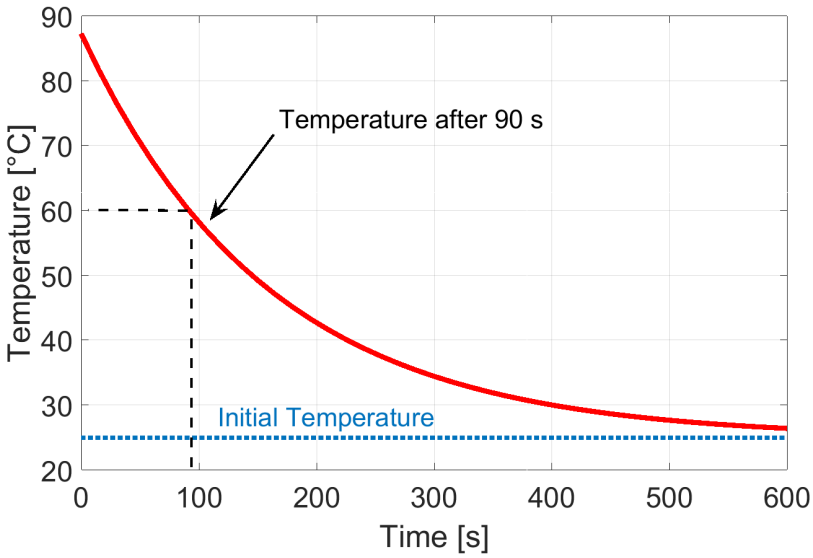

Figure 4.27: Temperature evolution of the first stage coils after the power supply is disconnected

of the coil reaches 60.5 °C and that a time longer than 10 minutes is required to return to the initial temperature T_i. After 90 s another launch would heat the stator windings up to a temperature of approximately 123 °C. However, the hotter is the motor with respect to its environment the faster it exchanges heat with the surrounding. The temperature of the coil T_x at which the heat absorbed during the launch is equal to the heat dissipated through the insulation in 90 seconds can be computed as

$$T_x = \frac{\Delta T + T_i e^{90 \cdot A}}{1 - e^{90 \cdot A}} \qquad \text{where} \qquad A = \frac{k_{ins} S_{wire}}{b_s/2 \cdot \rho_{Co} c_{Co} v_{wire}} \tag{4.164}$$

Solving eq. 4.164 with the geometrical data of the linear induction motor yields an equilibrium temperature of 169.6 °C. Even though the temperature T_x can be handled by high class insulations, the presence of hot spot due to material defects might locally compromise the electrical insulation. Furthermore the presented method assumes that each launch causes the same ΔT. The variation of the coil resistivity can easily increase the equilibrium temperature computed by eq. 4.164

above the insulation limit leading to the need of an active cooling system. The extra heat could be removed with the aid of fans located along the track or using a cold plate behind the stators. Since the stator sections at the end of the track are fed for a time shorter than t_1, an active cooling system will be probably required only in the first part of the launch track.

4.5.2 Heat Transfer Problem Solution for the Moving Plate

This section illustrates the thermal model employed to analyse the heat transfer across the aluminium plate. The thermal heat transfer problem is solved to estimate the temperature evolution of the mover to prevent the *creep* of the aluminium plate. Creep is the tendency of a material to deform permanently under high mechanical stresses and heat loads especially when they are applied for a long time. The rate of deformation depends on the temperature, applied structural load and exposure time. Creep is observed in all metals, provided that the operating temperature exceeds $k_{cr} \cdot T_m$, where T_m is the absolute melting temperature and k_{cr} is a coefficient that depends on the material. The melting temperature of aluminium is 933.3 K and the creep coefficient is 0.54 [98]. Under the temperature T_{cr} of 504 K (231 °C) creep can be neglected.

The temperature of the solid aluminium changes during the launch because of the heat generation due to the induced current. The current density J_2 induced in the secondary was extracted from the two-dimensional FEA software and implemented in the three-dimensional thermal model. The current density distribution computed by FEA is defined along the thickness and the length of the aluminium plate. The current density distribution along the third dimension is assumed to be constant in the active area of the mover and edge-effects are neglected.

The current density profiles over the aluminium plate section after 1.0 second and after 14.0 seconds are shown in Figs. 4.28a and 4.28b respectively. As can be seen in Fig. 4.28, the skin effect cause the current density to gather close to the aluminium boundary as the frequency increases during the launch. Therefore, the external layer of the aluminium plate is subject to the most severe thermal conditions.

The thermal heat transfer problem is solved using the Finite Difference Method

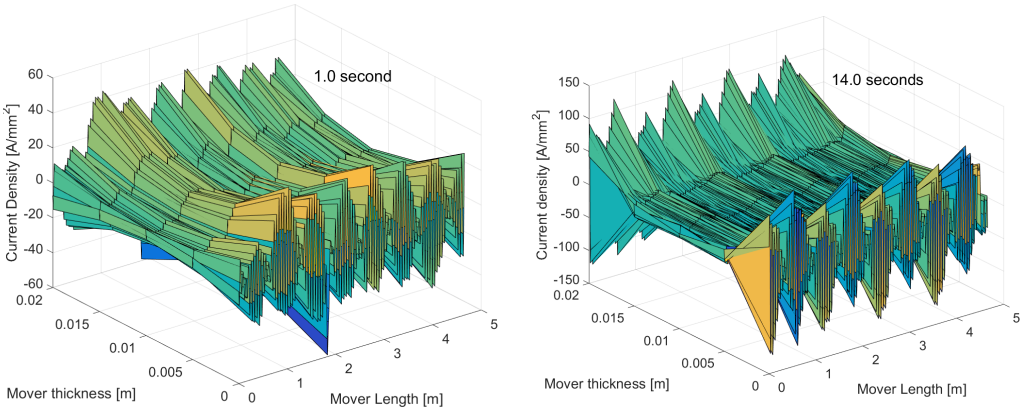

(a) 1.0 second

(b) 14.0 seconds

Figure 4.28: Current density profile computed by FEA at different time step during the launch

(FDM) which approximates the derivatives of a solving equation with finite differences. The algorithm produces a set of discrete numerical equations after dividing the domain into a uniform orthogonal grid. FDM is mainly applied to simple geometries like the aluminium plate when the grid is not distorted by any irregularities. Like all the numerical methods, FDM produces a discretization error which can be limited by the correct selection of the step size.

When the solving equation involves time derivatives it can be discretized adopting either an explicit or an implicit technique. The explicit method finds the state of the system at each node of the grid at the time step $n+1$ from the state of the system at the time step n. The results is a series of algebraic equations that can be solved in sequence and that converges to the solution only when the time and space stepping respects certain criteria. The implicit method solves the system of equations at the time step $n+1$ considering the state of the system in all the nodes of the grid at the time step $n+1$. The implicit method does not have strict convergence criteria, but it requires more computational efforts since it solves a system of algebraic equations with one equation for every node of the grid. The implicit method was selected to solve the heat transfer problem of the moving plate since it always converges and is more stable than the explicit method.

The transient heat transfer model of the aluminium plate is based on the solution

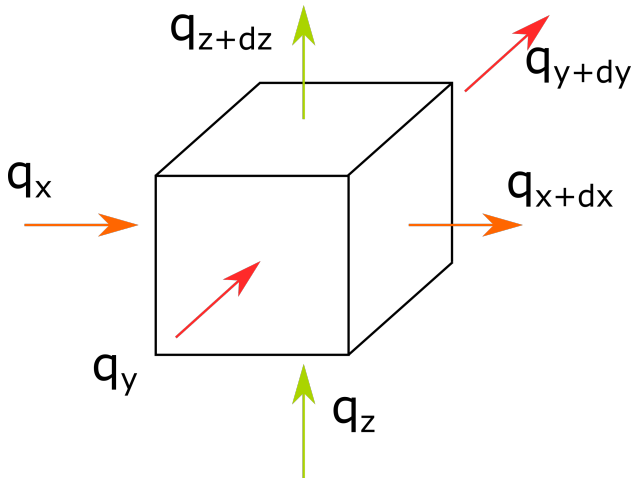

Figure 4.29: Thermal equilibrium of an infinitesimal volume of aluminium

of the first law of thermodynamics with no heat radiation. The change of the internal energy Q_i of the infinitesimal volume of material dv in Fig. 4.29 can be expressed as

$$\begin{aligned} Q_i &= \left(\frac{q_{x+dx} - q_x}{dx} + \frac{q_{y+dy} - q_y}{dy} + \frac{q_{z+dz} - q_z}{dz} \right) dv \\ &\Rightarrow \left(\frac{\partial q_x}{\partial x} + \frac{\partial q_y}{\partial y} + \frac{\partial q_z}{\partial z} \right) dv \end{aligned} \tag{4.165}$$

where the heat fluxes q_x, q_y and q_z are reported in Fig. 4.29. Substituting the Fourier's law of thermal conduction $\vec{q} = k_{Al} \nabla T$ in eq. 4.165 yields

$$Q_i = \left[\frac{\partial}{\partial x} \left(k_{Al} \frac{\partial T}{\partial x} \right) + \frac{\partial}{\partial y} \left(k_{Al} \frac{\partial T}{\partial y} \right) + \frac{\partial}{\partial z} \left(k_{Al} \frac{\partial T}{\partial z} \right) \right] dv \tag{4.166}$$

where k_{Al} is the aluminium conductivity. The change of the internal energy can be also expressed in terms of the temperature variation of a mass of volume dV over time as

$$Q_i = \rho_{Al} c_{Al} \frac{\partial T}{\partial t} dv - q_v dv \tag{4.167}$$

where ρ_{Al} is the aluminium density, c_{Al} is the aluminium thermal capacity and q_v is the heat generation per unit volume. The general form of the heat transfer equation with heat generation can be derived by comparing eqs. 4.166 and 4.167

as

$$\rho_{Al} c_{Al} \frac{\partial T}{\partial t} - q_v = \nabla \cdot (k_{Al} \nabla T) \tag{4.168}$$

Since the plate is made out of an isotropic material the thermal conductivity is constant in space and it can be moved outside the scalar product of eq. 4.168.

When a current flows inside a conductive material it generates a volumetric heat flux $q_v = J_2^2/\sigma$ where σ is the electrical conductivity of the material. After few algebraic operations eq. 4.168 may be rewritten as

$$\frac{1}{\alpha_{Al}} \frac{\partial T}{\partial t} = \frac{\partial^2 T}{\partial x^2} + \frac{\partial^2 T}{\partial y^2} + \frac{\partial^2 T}{\partial z^2} + \frac{J_2^2}{\sigma_{Al} k_{Al}} \tag{4.169}$$

where $\alpha_{Al} = k_{Al}/(\rho_{Al} c_{Al})$ is the thermal diffusivity of the material. Eq. 4.169 was solved using FDM imposing convective boundary conditions upon all the plate surfaces. The discretized implicit form of eq. 4.169 is

$$\begin{aligned} \frac{1}{\alpha} \frac{T_{i,j,k}^{n+1} - T_{i,j,k}^{n}}{t^{n+1} - t^{n}} = \frac{T_{i+1,j,k}^{n+1} - 2T_{i,j,k}^{n+1} + T_{i-1,j,k}^{n+1}}{\Delta x^2} + \\ \frac{T_{i,j+1,k}^{n+1} - 2T_{i,j,k}^{n+1} + T_{i,j-1,k}^{n+1}}{\Delta y^2} + \frac{T_{i,j,k+1}^{n+1} - 2T_{i,j,k}^{n+1} + T_{i,j,k-1}^{n+1}}{\Delta z^2} + \frac{{J_2}_{i,j,k}^{n}{}^2}{\sigma_{Al}^{n} k_c} \end{aligned} \tag{4.170}$$

where i, j, k are the indexes of the node along x, y, z directions respectively, Δx, Δy, Δz are the distances between nodes along x, y, z directions respectively and n is the time step index. The distances between nodes are considered constant along the grids, but the same equation can still be used with inhomogeneous node distribution replacing Δx^2 with $\Delta x_{i+1} \Delta x_{i-1}$, Δy^2 with $\Delta y_{j+1} \Delta y_{j-1}$ and Δz^2 with $\Delta z_{k+1} \Delta z_{k-1}$. Eq. 4.170 can be rearranged separating the unknown from the known terms yielding

$$\begin{aligned} \left(\frac{1}{\alpha_{Al} \Delta t^n} + \frac{2}{\Delta x^2} + \frac{2}{\Delta y^2} + \frac{2}{\Delta k^2} \right) T_{i,j,k}^{n+1} - \frac{T_{i+1,j,k}^{n+1}}{\Delta x^2} - \frac{T_{i-1,j,k}^{n+1}}{\Delta x^2} - \frac{T_{i,j+1,k}^{n+1}}{\Delta y^2} \\ - \frac{T_{i,j-1,k}^{n+1}}{\Delta y^2} - \frac{T_{i,j,k+1}^{n+1}}{\Delta z^2} - \frac{T_{i,j,k-1}^{n+1}}{\Delta z^2} = \frac{1}{\alpha_{Al} \Delta t^n} T_{i,j,k}^{n} + \frac{{J_2}_{i,j,k}^{n}{}^2}{\sigma_{Al}^{n} k_c} \end{aligned} \tag{4.171}$$

where the time step is $\Delta t^n = t^{n+1} - t^n$.

Eq. 4.171 was implemented to calculate the temperature evolution on the in-

ternal nodes of the grid. However, this equation cannot be used to calculate the temperature evolution on the boundary nodes. The plate external boundary exchanges heat with the surrounding air through convection and different equations have to be implemented. When the volume of material in Fig. 4.29 is located on the boundary the variation of the internal energy along the direction where convection occurs can be expressed as

$$Q_i = \frac{k_{Al}}{\Delta x}\frac{\partial T}{\partial x}dv + h\frac{\partial T}{\partial x}dv \tag{4.172}$$

where h is the convective heat transfer coefficient. The heat transfer equation for the boundary nodes can be derived equating eqs. 4.172 and 4.167 yielding

$$\rho_{Al}c_{Al}\frac{\partial T}{\partial t}dv - q_v dv = (k_{Al}\cdot dA + h_{Air}\cdot dV)\nabla T \tag{4.173}$$

where dA is the area of the surfaces of volume dv where the convective heat transfer occurs.

The discretized form of eq. 4.173 changes depending on the location of the nodes. As can be seen in Fig. 4.30, three cases can be identified: A) surface node, B) edge node and C) corner node. The discretized form of eq. 4.173 for a node located on the surface which is represented by the case A in Fig. 4.30 becomes:

$$\begin{aligned}
&\rho_{Al}c_{Al}\frac{T^{n+1}_{i,j,k} - T^{n}_{i,j,k}}{t^{n+1}-t^{n}}\frac{dxdydz}{2} - \frac{{J2^{n}_{i,j,k}}^2}{\sigma^{n}_{Al}}\frac{dxdydz}{2} = \\
&h^{n}_{Air}dxdy\left(T_{Air} - T^{n+1}_{i,j,k}\right) + \frac{k_{Al}}{dx}dydz\left(T^{n+1}_{i+1,j,k} - T^{n+1}_{i,j,k}\right) + \\
&\frac{k_{Al}}{dx}dydz\left(T^{n+1}_{i-1,j,k} - T^{n+1}_{i,j,k}\right) + \frac{k_{Al}}{dy}dxdz\left(T^{n+1}_{i,j+1,k} - T^{n+1}_{i,j,k}\right) + \\
&\frac{k_{Al}}{dy}dxdz\left(T^{n+1}_{i,j-1,k} - T^{n+1}_{i,j,k}\right) + \frac{k_{Al}}{dz}dxdy\left(T^{n+1}_{i,j,k+1} - T^{n+1}_{i,j,k}\right)
\end{aligned} \tag{4.174}$$

The terms of eq. 4.174 can be rearranged to separate the unknowns from the known terms as

$$\begin{aligned}
&\left(h^{n}_{Air}dxdy + 2\frac{k_{Al}}{dx}dydz + 2\frac{k_{Al}}{dy}dxdz + \frac{k_{Al}}{dz}dxdy + \frac{\rho_{Al}c_{Al}dxdydz}{2\Delta t^{n}}\right)T^{n+1}_{i,j,k} - \\
&\frac{k_{Al}}{dx}dydzT^{n+1}_{i+1,j,k} - \frac{k_{Al}}{dx}dydzT^{n+1}_{i-1,j,k} - \frac{k_{Al}}{dy}dxdzT^{n+1}_{i,j+1,k} - \frac{k_{Al}}{dy}dxdzT^{n+1}_{i,j-1,k}
\end{aligned} \tag{4.175}$$

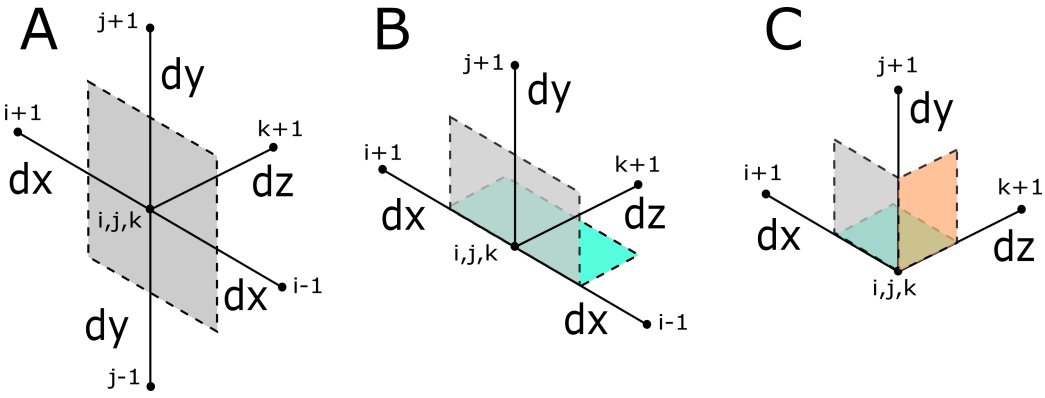

Figure 4.30: Possible node configurations on the mover boundary

$$-\frac{k_{Al}}{dz}dxdyT^{n+1}_{i,j,k+1} = h^n_{Air}dxdyT_{Air} + \frac{{J2^n_{i,j,k}}^2}{\sigma^n_{Al}}\frac{dxdydz}{2} + \frac{\rho_{Al}c_{Al}dxdydz}{2\Delta t^n}T^n_{i,j,k}$$

When a node is located on the plate edge B in Fig. 4.30 the discretized form of eq. 4.173 becomes

$$\begin{aligned}
&\rho_{Al}c_{Al}\frac{T^{n+1}_{i,j,k}-T^n_{i,j,k}}{t^{n+1}-t^n}\frac{dxdydz}{4} - \frac{{J2^n_{i,j,k}}^2}{\sigma^n_{Al}}\frac{dxdydz}{4} = h^n_{Air}\frac{dxdy}{2}\left(T_{Air}-T^{n+1}_{i,j,k}\right)+\\
&h^n_{Air}\frac{dxdz}{2}\left(T_{Air}-T^{n+1}_{i,j,k}\right)+\frac{k_{Al}}{dx}dydz\left(T^{n+1}_{i+1,j,k}-T^{n+1}_{i,j,k}\right)+\\
&\frac{k_{Al}}{dx}dydz\left(T^{n+1}_{i-1,j,k}-T^{n+1}_{i,j,k}\right)+\frac{k_{Al}}{dy}dxdz\left(T^{n+1}_{i,j+1,k}-T^{n+1}_{i,j,k}\right)+\frac{k_{Al}}{dz}dxdy\left(T^{n+1}_{i,j,k+1}-T^{n+1}_{i,j,k}\right)
\end{aligned} \tag{4.176}$$

and rearranging the terms

$$\begin{aligned}
&\left(h^n_{Air}\frac{dxdy}{2}+h^n_{Air}\frac{dxdz}{2}+2\frac{k_{Al}}{dx}dydz+\frac{k_{Al}}{dy}dxdz+\frac{k_{Al}}{dz}dxdy+\frac{\rho_{Al}c_{Al}dxdydz}{4\Delta t^n}\right)\cdot\\
&T^{n+1}_{i,j,k}-\frac{k_{Al}}{dx}dydzT^{n+1}_{i+1,j,k}-\frac{k_{Al}}{dx}dydzT^{n+1}_{i-1,j,k}-\frac{k_{Al}}{dy}dxdzT^{n+1}_{i,j+1,k}-\frac{k_{Al}}{dz}dxdyT^{n+1}_{i,j,k+1}\\
&=\left(h^n_{Air}\frac{dxdy}{2}+h^n_{Air}\frac{dxdz}{2}\right)T_{Air}+\frac{{J2^n_{i,j,k}}^2}{\sigma^n_{Al}}\frac{dxdydz}{4}+\frac{\rho_{Al}c_{Al}dxdydz}{4\Delta t^n}T^n_{i,j,k}
\end{aligned} \tag{4.177}$$

The discretized form of the heat transfer equation for the node on the corner C in Fig. 4.30 may be written as

$$\rho_{Al}c_{Al}\frac{T^{n+1}_{i,j,k}-T^n_{i,j,k}}{t^{n+1}-t^n}\frac{dxdydz}{8} - \frac{{J2^n_{i,j,k}}^2}{\sigma^n_{Al}}\frac{dxdydz}{8} = h^n_{Air}\frac{dxdy}{4}\left(T_{Air}-T^{n+1}_{i,j,k}\right)+$$

$$h_{Air}^{n}\frac{dxdz}{4}\left(T_{Air}-T_{i,j,k}^{n+1}\right)+h_{Air}^{n}\frac{dydz}{4}\left(T_{Air}-T_{i,j,k}^{n+1}\right)+ \tag{4.178}$$
$$k_{Al}\left[\frac{dydz}{dx}\left(T_{i+1,j,k}^{n+1}-T_{i,j,k}^{n+1}\right)+\frac{dxdz}{dy}\left(T_{i,j+1,k}^{n+1}-T_{i,j,k}^{n+1}\right)+\frac{dxdy}{dz}\left(T_{i,j,k+1}^{n+1}-T_{i,j,k}^{n+1}\right)\right]$$

and rearranging the terms

$$\begin{aligned}&\left(h_{Air}^{n}\frac{dxdy}{4}+h_{Air}^{n}\frac{dxdz}{4}+h_{Air}^{n}\frac{dydz}{4}+\frac{k_{Al}}{dx}dydz+\frac{k_{Al}}{dy}dxdz+\frac{k_{Al}}{dz}dxdy\right)T_{i,j,k}^{n+1}+\\&\frac{\rho_{Al}c_{Al}dxdydz}{8\Delta t^{n}}T_{i,j,k}^{n+1}-\frac{k_{Al}}{dx}dydzT_{i+1,j,k}^{n+1}-\frac{k_{Al}}{dy}dxdzT_{i,j+1,k}^{n+1}-\frac{k_{Al}}{dz}dxdyT_{i,j,k+1}^{n+1}=\\&\left(h_{Air}^{n}\frac{dxdy}{4}+h_{Air}^{n}\frac{dxdz}{4}+h_{Air}^{n}\frac{dydz}{4}\right)T_{Air}+\frac{{J2}_{i,j,k}^{n}{}^{2}}{\sigma_{Al}^{n}}\frac{dxdydz}{8}+\frac{\rho_{Al}c_{Al}dxdydz}{8\Delta t^{n}}T_{i,j,k}^{n}\end{aligned} \tag{4.179}$$

The boundary conditions expressed in eqs. 4.175, 4.177 and 4.179 were written for surface, edge and corner with the geometrical features shown in Fig. 4.30, but the same procedure can be applied to determine the descretized form of the heat transfer equation for all the other boundary nodes. The boundary conditions shown in eqs. 4.175, 4.177 and 4.179 and the discrete equation for the internal nodes expressed by eq. 4.171 complete the system of the equations that computes the transient evolution of the temperature in the aluminium plate.

The convective coefficient expresses the heat transfer between a solid surface and a fluid. The amount of heat that crosses the boundary depends on the relative speed between the solid surface and the surrounding fluid. The temperature of the solid material and the fluid physical properties affect the convective heat transfer as well. In an electromagnetic launch system the mover changes speed and its temperature varies because of the Joule losses in the system. In order to correctly describe the instantaneous state of the moving plate the value of the convective coefficient has to be updated according to the changing of the system parameters.

The convective heat transfer coefficient is often computed by means of non-dimensional numbers as

$$h_{Air}=\frac{k_{Al}}{L}Nu \tag{4.180}$$

where Nu is the Nusselt number and L represents the ratio between the volume of fluid and the surface area where the convection occurs. For the induction motor, L is the length of the mover l_{mov}. The Nusselt number is a non-dimensional quantity

that expresses the ratio between the convective and conductive heat transfer that occurs in the mean flow. When the mover is at rest before the launch the relative speed with respect to the surrounding air is zero and natural convection occurs. The Nusselt number for natural convection is a function of the Prandtl number Pr in eq. 4.181 and of the Rayleigh number Ra in eq. 4.183 which in turn is a function of the Grashof number Gr in eq. 4.182.

$$Pr = \frac{c_{Air}\mu_{Air}}{k_{Al}} \tag{4.181}$$

$$Gr = \frac{G\beta_{Air}|T_w - T_{Air}|l_{mov}^3}{\nu_{Air}^2} \tag{4.182}$$

$$Ra = Gr \cdot Pr \tag{4.183}$$

where c_{Air} is the specific heat at constant pressure of air, μ_{Air} is its dynamic viscosity, G is the gravitational acceleration, β_{Air} is the expansion factor of air, T_w is the wall temperature, T_{Air} is the air temperature and ν_{Air} is its kinematic viscosity. The Prandtl number is a non-dimensional number that represents the ratio of the momentum diffusivity in the fluid to thermal diffusivity in the solid material. The Grashof number is an non-dimensional number that represents the ratio of the upward force exerted by the fluid on a submerged solid object against its weight to the viscous force acting on the fluid.

The relations used to express the Nusselt number as a function of the Rayleigh number are empirical formulas that depend on both the type of fluid and the value of Rayleigh number itself. The Nusselt number for gaseous air is calculated using eq. 4.184 [99].

$$\begin{cases} Nu = 0.68 + \dfrac{0.67Ra^{0.25}}{\left[1 + \left(\dfrac{0.492}{Pr}\right)^{\frac{9}{16}}\right]^{\frac{4}{9}}} & 0.1 < Ra < 10^9 \\ Nu = \left\{ 0.825 + \dfrac{0.387Ra^{\frac{1}{6}}}{\left[1 + \left(\dfrac{0.492}{Pr}\right)^{\frac{9}{16}}\right]^{\frac{8}{27}}} \right\}^2 & 10^9 < Ra < 10^{12} \end{cases} \tag{4.184}$$

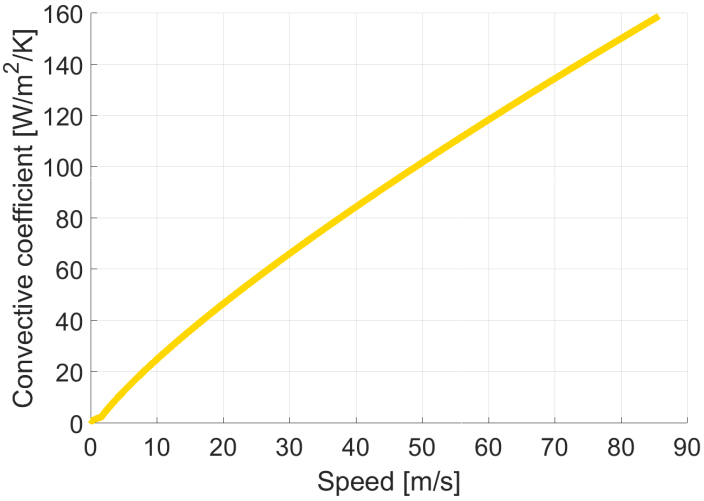

Figure 4.31: Variation of the convective heat transfer coefficient with the mover speed until the take-off point

When the mover starts to accelerate the convective coefficient h_{Air} changes with the speed. The convective coefficient can be still computed using eq. 4.180, but the formulas for force convection should be used in place of those for natural convection to compute Nu. The Nusselt number of force convection is a function of the Prandtl number and of the Reynolds number $Re = \rho_{Air} V l_{mov} / \mu_{Air}$. The Reynolds number represents the ratio between the momentum forces and the viscous forces inside a fluid in motion and it is used to characterize flow regime.

$$\begin{cases} Nu = 0.664 \cdot Re^{\frac{1}{2}} Pr^{\frac{1}{3}} & Re < 5 \cdot 10^5 \\ Nu = 0.664 \left(5 \cdot 10^5\right)^{\frac{1}{2}} Pr^{\frac{1}{3}} + 0.037 \left[Re^{\frac{4}{5}} - \left(5 \cdot 10^5\right)^{\frac{4}{5}} \right] Pr^{\frac{1}{3}} & Re > 5 \cdot 10^5 \end{cases} \tag{4.185}$$

The variation of the convective coefficient h_{Air} expressed by eq. 4.180 with Nusselt number Nu expressed by eqs. 4.184 and 4.185 is shown in Fig. 4.31. The correct value of the convective coefficient is selected during the solution of the heat transfer problem of the aluminium plate by interpolation of the data in Fig. 4.31 as the speed increases.

The resistance of a conductor to a current flow is the result of the collision between the current electrons and crystallographic structure of the conductor. The temperature of a solid material represents the amplitude of the oscillation of the atoms around their average position in the inner structure. When the oscillations

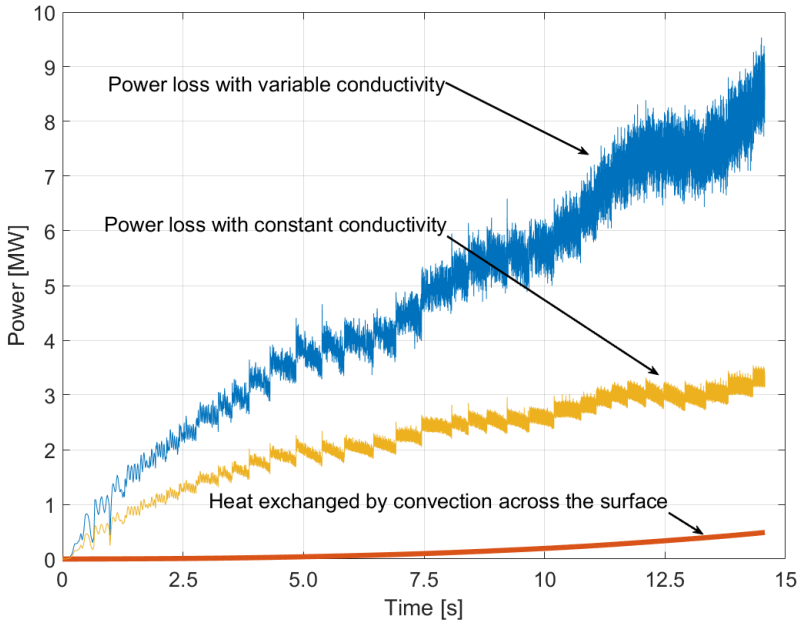

Figure 4.32: Variation of the secondary Joule losses during the launch

amplitude augments the chances of collision with the electrons of a current flow increases. The results is a increment of the conductor resistivity ρ_m as

$$\rho_m = \rho_i [1 + \alpha_c (T - T_i)] \tag{4.186}$$

where α_c is the temperature coefficient of resistance and ρ_i is the resistivity at the temperature T_i. Therefore, the conductivity of the aluminium plate σ_{Al} of the induction motor changes during the launch due to temperature variation as

$$\sigma_{Al} = \frac{1}{\rho_i [1 + \alpha_c (T - T_i)]} \tag{4.187}$$

The reduction of the conductivity and the respective Joule losses increase is taken into account during the solution of the heat transfer problem. Fig. 4.32 compares the Joule losses computed by the thermal analysis software with variable conductivity with those computed by the FEA software with constant conductivity. Fig. 4.32 reports the total heat exchanged at the boundary through convection as well.

The decrement of the aluminium conductivity with temperature was not con-

sidered during the electromagnetic design in Section 4.3.1 even though the conductivity at the end of the launch is 56% of the initial σ_{Al}. A reduced aluminium conductivity increases the heat generation when the same current flows in the conductor. However, a decrease of the aluminium conductivity entails a reduction of the induced current intensity which in turns implies less heat generation. The analysis of the electromagnetic performance variation with temperature would required a combined thermal and electromagnetic finite element analysis which is beyond traditional computational resources. Indeed no advantage can be taken from parallel calculation of multi-processor computer being the electromagnetic time iterations performed in series. For preliminary catapult sizing, it is accepted to undertake the electromagnetic and thermal analysis separately.

It may be argued that the additional heat losses might be removed by an active cooling system during the acceleration to keep constant the value of the conductivity. However, a cooling system that acts on the mover along the track is impractical and difficult to implement. In case an active cooling system would be required, a pre-cooled plate at liquid nitrogen temperature may represent a viable and cheap solution to maintain the conductivity around the desired value.

The solution of the heat transfer problem yields the time evolution of the temperature over the aluminium plate volume. The most severe temperature increase occurs over the lateral surface of the moving plate which is subject to skin effect. Fig. 4.33 shows the temperature profile on the nodes located on the lateral surface at several time steps. In particular Fig. 4.33d shows the temperature profile at the end of the launch. It can be seen that the creep temperature of 504 K is never reached as 499.7 K is the maximum temperature of plate. Even though the maximum temperature is close to the creep point, the average temperature of the lateral surface at the end of the launch is 447.4 K while the average temperature of the whole plate is 442.9 K.

These results demonstrate that the thermal requirement for the aluminium plate is satisfied and that the launcher can operate safely without deforming the mover permanently under the combination of thermal and structural load. The aluminium thickness d_{Al} that was selected during LIM electromagnetic design is large enough to guarantee the necessary thermal capacity to avoid large temperature rise. Shorter d_{Al} would increase the electromagnetic performances, but would

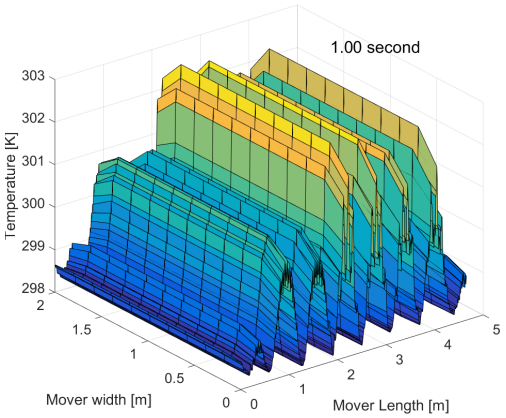

(a) Temperature profile after 1.00 second

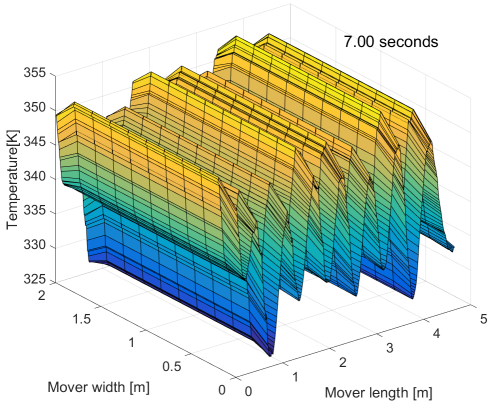

(b) Temperature profile after 7.00 seconds

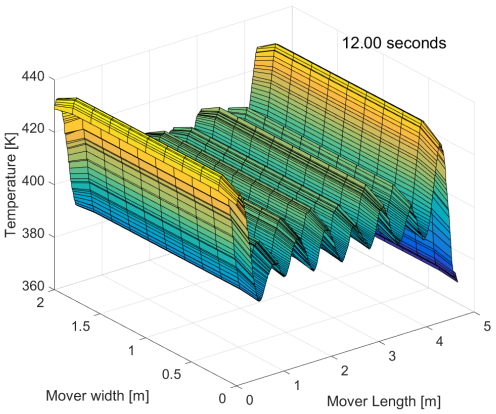

(c) Temperature profile after 12.00 seconds

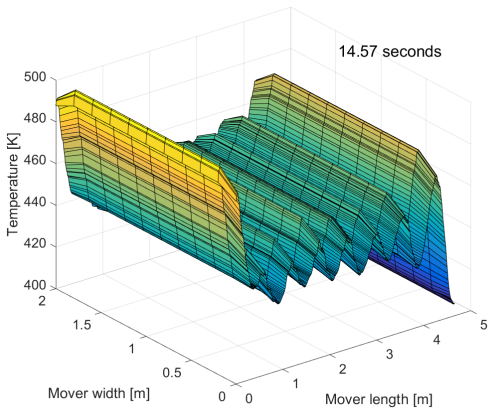

(d) Temperature profile after 14.57 seconds

Figure 4.33: Temperature profile over the mover lateral surface at different time steps

rise the temperature above the creep limit.

When the effect of multiple launches is considered, the temperature on the mover would gradually build up unless the aluminium plate has enough time to passively cool down to the initial temperature or unless it reaches the equilibrium between the heat absorbed during the launch and the heat dissipated through convection. Since the peak temperature computed by the 3D thermal analysis is very close to the creep point (504 K), any additional launch would cause creep to occur before reaching any heat equilibrium. An active cooling system might be required

to bring the plate to its initial temperature before the next launch. Unlike the primary coils, the aluminium plate can be replaced by other movers for the next launches until the temperature is passively restored.

4.6 Contribution to Knowledge

This chapter proposed a sizing methodology for LIM which unifies field theories developed by several researchers in literature. The partial differential equations that are usually solved to characterize the behaviour of LIMs including edge-effects were replaced by coefficients calculated using algebraic equations. For the first time these theories were applied to size a LIM for civil aircraft launch applications. Due to the high forces and current densities involved in an EML system of such a size, the structural and thermal analysis of the launcher were carried out. Very little work has been published on thermal and structural analyses of the aluminium plate especially when the temperature behaviour is investigated to prevent creep of the conductive material and when the structural response to the load is studied to avoid buckling.

Chapter 5

Linear Permanent Magnet Synchronous Motor

This chapter presents the sizing procedure of a Linear Permanent Magnet Synchronous Motor (LPMSM) for an electromagnetic launch (EML) system to assist civil aircraft take-off. The rationale behind the choice of the motor topology is introduced together with the algorithm to select the winding sequence that generates a travelling magnetic field wave shape as close as possible to a sinusoidal shape. The parametric optimization introduced in Chapter 4 has been employed to size the synchronous machine as well. An analytical algorithm that is solved iteratively to find the combination of the design parameters that minimizes the required input power is presented. The selected geometrical and electric features were implemented in both Finite Element Analysis (FEA) and a transient model of the machine. The field theory used to reconstruct the magnetic flux in the synchronous motor and to determine the forces involved in the motion is accurately described and the results are verified using FEA. Heat generation due to eddy current losses is analysed to determine the transient temperature of the mover's components and prevent any risk of demagnetization.

5.1 Introduction to LPMSM for EML

A linear synchronous motor (LSM) is an electrical machine where the mechanical motion is synchronized with a travelling magnetic field wave. This means that the motor's moving part and the magnetic field in the airgap travel at same speed. The thrust is produced by the interaction of the multi-phase field produced by the alternating current in the motor's winding and either a variable reluctance ferromagnetic structure, a magnetic field produced by dc electromagnets or a magnetic field generated by an array of magnets. The part producing the travelling magnetic field is called *armature* while the part that provides the continuous flux is called *excitation system*. The terms *primary* and *secondary* used in Chapter 4 for LIM are usually abandoned, as they are justified for linear induction motors and transformers where the secondary field exists only in relation with the primary field [29].

Linear synchronous machines generally operate with heavy and complex movers, independently from the moving part of the machine being used to either host the armature winding, provide the variable ferromagnetic reluctance or produce field excitation through dc or permanent magnets. Indeed, most mover components are made out of high density ferromagnetic materials which increase the total mass that has to be accelerated. This implies that a significant part of the energy produced by the launcher is converted into the kinetic energy of the mover and is not transferred to the aircraft. Synchronous machines also need to operate with a closed loop control to provide position/speed feedback and so supply the correct voltage, frequency and load angle to produce the required thrust.

An additional drawback of synchronous machines with permanent magnets is the possible deterioration of the performance due to demagnetization. In electromagnetic launch applications, the main factors that may cause magnets to lose their strength are: magnet temperature rise (potentially over multiple launches) and adverse field produced by the stator's current carrying conductors. Temperature will cause irreversible loss of magnetization if the magnet is driven past the knee point of the material demagnetization curve. Considering the same demagnetization curve, it is also possible to understand whether the stator field is strong enough to cause demagnetization in conjunction with temperature loss.

Despite these disadvantages, LSMs are particularly attractive in many applications for their high efficiency, high power factor and so reduced cost of the power conditioning system with respect to LIMs. Moreover, the possibility to use the concentrated winding layout almost eliminates the transition effect between consecutive stator sections and further reduces the cost of the machine. Unlike the induction motor, synchronous motors suffer negligible performance reduction due to the limited length and width of the machine. Indeed, the excitation field generation and distribution are almost independent from these geometrical features. These characteristics make LSMs a viable solution for EML applications.

5.1.1 Topology Selection for the Synchronous Motor

As for LIMs, linear synchronous machines can be classified as double-sided or single-sided electrical motors. The force perpendicular to the motion which is normally generated by single-sided machine is not required by EML systems. A double-sided linear synchronous motor generates a zero nominal force on the mover and is adopted for EML applications where only the propulsive force is required. A short mover - long stator configuration is more suitable for EML systems than the respective long mover - short stator layout, since in the latter case the moving part of the machine would have the same length of the runway.

Moving electrical connections to transfer several MWs of power between the supply and the mover represent a significant engineering challenge. Therefore, in the case of moving armature, the power conditioning system should be installed on board the mover. The mass of the additional components would add such a significant amount of weight that a large amount of energy produced by the motor would be used to accelerate the mover rather than the aircraft. Therefore, a double-sided synchronous motor with a short mover that generates the excitation field and with a long static armature is the machine topology that is selected for the synchronous launcher.

The choice of the mover and track topologies themselves requires an investigation of the possible benefits and drawbacks of the several solutions that can be adopted for EML systems.

5.1.1.1 Mover Topology

The LSM's mover topology depends on the way the excitation field is generated. The excitation field of synchronous motors can be produced by dc current flowing in coils wrapped around iron cores which compel the magnetic flux in a direction perpendicular to the airgap. In a mover with no sliding electrical connection, the direct current should be generated on board by an exciter. Especially in applications like EML systems where there is no need to control the excitation field intensity and where on board storage and generation systems would add undesired extra weight to the mover, the excitation field is developed by permanent magnets (PMs). Linear synchronous motor whose excitation field is produced by PMs are called Linear Permanent Magnet Synchronous Motors (LPMSMs).

Synchronous thrust can be also generated by exploiting the variable reluctance of special ferromagnetic features of the mover. In particular, Linear Reluctance Synchronous Motors (LRSMs) generate a thrust proportional to the difference between the reluctances in the d-axis and q-axis of the machine. When fed with comparable current intensity the electromagnetic performance of a LRSM is usually low due to the low ratio between the d-axis and the q-axis reluctances [29]. Better performance can be obtained when using special steel lamination in the reaction plate or flux barriers made out of any non-ferromagnetic material. However, LRSMs would deliver the thrust required by EML with such a high current density [36] that the stator coils would need an active cooling system to maintain the temperature within the range allowed by the insulation. Additionally, LRSM's movers are quite thick to prevent saturation of the laminated ferromagnetic material. The additional thickness increases the mechanical airgap and the mover's weight further reducing the machine's performance and increasing losses.

After these considerations, LRSMs were discarded in favour of LPMSMs that are considered the most suitable synchronous motor topology for the civil aircraft launcher.

LPMSMs can be further classified according to the magnets arrangement on the moving plate. Fig. 5.1A shows a double-sided surface-mounted LPMSM whereas Fig. 5.1B shows a double-sided interior magnet LPMSM. Interior magnets are normally magnetized in the direction of the motion and the yoke should be non-

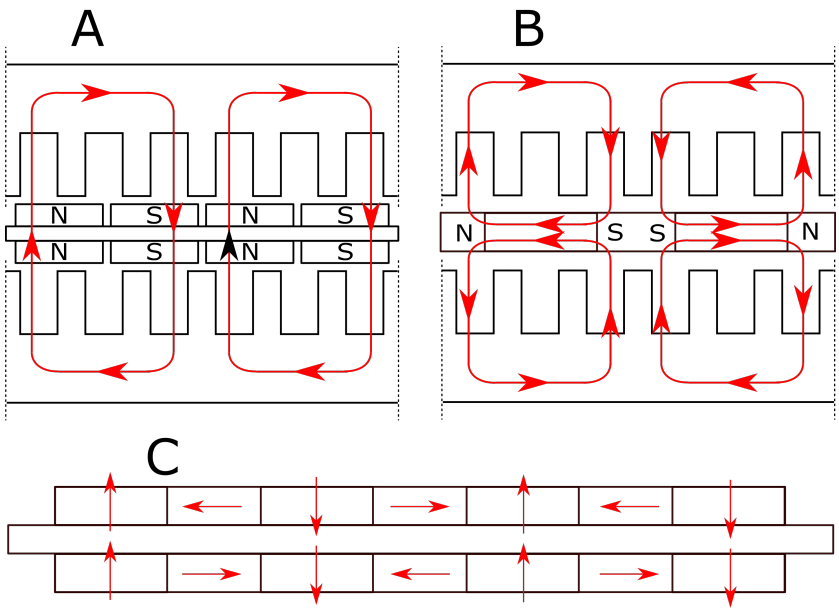

Figure 5.1: Double-sided LPMSM with conventional PMs array (A), with conventional buried PMs array (B) and with Halbach array (C)

ferromagnetic otherwise the majority of the flux would tend to stay in the mover and return to the magnet without crossing the airgap. Interior permanents magnets are difficult to cool down while heat can be removed more easily through convection from surface-mounted PMs. Moreover, the surface-mounted structure gives the highest force density when compared with the equivalent interior PM congurations [100].

On the other hand, a machine with interior PMs experiences less force ripple with respect to a machine with surface-mounted PMs. Force ripple in machines with surface-mounted PMs can be reduced by the selection of proper winding arrangement and slot/pole combinations. Moreover, force ripples below a certain amplitude do not represent an issue for EML systems since special dampers in the structure of the mover-aircraft connection can stop the propagation of the vibrations to the aircraft. Therefore, surface-mounted PMs are preferred to buried PMs for EML systems.

Surfaced-mounted PMs may be arranged to form an Halbach array as shown in Fig. 5.1C in order to produce a stronger magnetic field density and thrust while

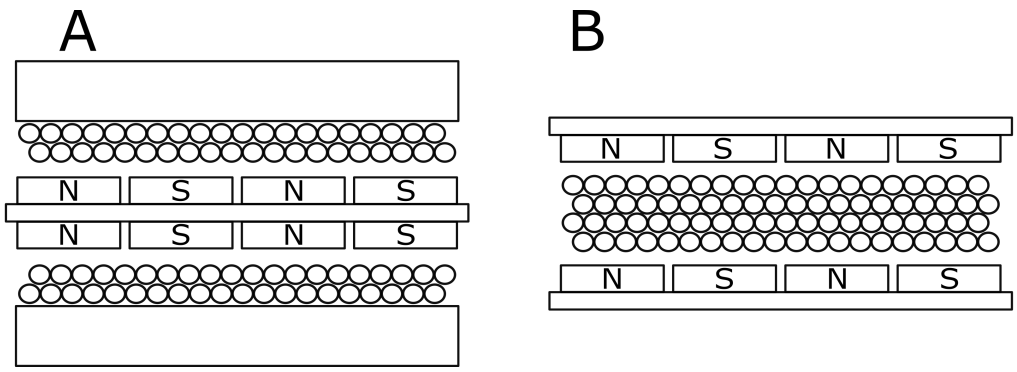

Figure 5.2: Double-sided LPMSM with slot-less armature (A), and double-sided air core LPMSM with slot-less internal armature (B)

reducing the mover weight and size. An Halbach array generates a magnetic flux wave shape closer to a sinusoid than a conventional south-north PMs arrangement [101]. Halbach arrays can improve the performance of LPMSMs, but in this work a conventional array of surface mounted PMs was implemented leaving space for future research to investigate possible improvements.

5.1.1.2 Armature Topology

Synchronous machines can also be classified depending on the armature topologies and in particular slotted and slot-less structures can be distinguished. In the slot-less motors in Fig. 5.2 the primary windings are uniformly distributed on a flat armature core and the motor provides propulsive forces with low force ripple. On the other hand, the large airgap of a slot-less armature requires thick PMs to produce an acceptable value of magnetic flux and high current densities are needed to produce the required thrust. Due to the increased volume of the active region, the thrust density is lower than that of slotted motors.

Armatures can be also classified according to the type of core, in particular iron core and air core can be implemented. Air core machines like the one in Fig. 5.2 B are particularly useful to reduce the iron losses that would occur at high speeds, frequencies and magnetic field densities. Air core linear machines are often used in automation because they minimize the cogging force [18].

Since EML systems require high thrust densities the slotted configuration is preferred and cogging force will be reduced by an adequate winding arrangement

and an accurate selection of the geometrical features. The field density in the EML system is high, but does not generate significant enough eddy current and hysteresis losses (W/m^3) to require an air cored machine. Indeed, saturation is expected only on the stator teeth which have a low volume compare to the full stator.

5.2 Winding Selection

The operating principle of the electrical machine is based on the interaction between the magnetic fields and the current flowing in the windings of the machine. The windings construction and connections together with the currents and voltages fed into the windings determine the operating mode of the machine. The armature windings are copper conductors with rectangular or circular cross section that can be arranged in different ways to improve the electromagnetic performance of synchronous machines. Indeed, the shape of the travelling magnetic wave and the thrust profile strongly depend on the current-carrying conductor distribution inside the machine. This section reports the rationale behind the choice of the final winding layout and presents a detailed description of the distribution algorithm for an optimized winding sequence that achieves low cogging force and an almost sinusoidal magnetic wave shape.

5.2.1 Stator Winding Layout

In general, electrical machines have at least three common winding constructions:

1. single-layer winding;
2. double-layer winding with coils horizontally separated inside the slot;
3. double-layer winding with coils vertically separated inside the slot.

The two parts of a slot of double-layer winding may belong to different phases, so that the windings can be distributed along the direction of the motion to reproduce a magnetic wave shape as close as possible to the sinusoidal shape. Double-layer vertically separated windings minimize the end coil length since they are

positioned closer to each other with respect other winding constructions [100]. This solution better satisfies the EML requirements than single-layer winding and double-layer winding with horizontally separated slot, since it produces less Joule losses.

Electrical machines can be wound adopting two main different techniques which are often identified with the name *distributed windings* and *concentrated windings* (also called *tooth windings*). The former method consists in distributing homogeneously the conductors along the direction of the travelling magnetic wave so that each phase is hosted in an integer number of slots below each pole. The distance between slots that host conductors carrying the same phase is constant along the whole length of the machine. On the contrary, concentrated windings are wound around a single tooth and the distance between slots with the same phase might not be constant. With this winding configuration, the number of slots with coils carrying the same phase under a single pole is not an integer number. For this reason, motors with tooth windings are also called *fractional-slot* winding motors [102]. Both winding configurations present advantages and drawbacks.

One of the main advantages of distributed windings is their ability to produce a magnetic wave with lower harmonic contents with respect to the concentrated distribution. Indeed, the travelling wave shape of distributed windings is closer to the sinusoidal shape than the magnetic wave of tooth winding machines. Since secondary harmonics travel at different speeds with respect to the mover, they induce current in the moving conductors of the shuttle causing additional losses. The induced current associated with secondary harmonics of a concentrated winding may be reduced by employing materials with low conductivity. For this reason, concentrated windings are not usually adopted for induction motors with high conductivity material in the secondary. On the contrary, the mover of a PM synchronous machine is usually made out of low conductivity stainless steel while Neodymium Iron Boron (NdFeB) PMs are relatively poor conductors.

The minimization of the end-winding length is one the objective of an electrical motor design that aims to achieve a high performance machine. Indeed, the part of the coil outside the active region of the machine does not contribute to the thrust production and generates additional Joule losses and leakage flux. Since concentrated windings do not overlap, they can be wound without crossovers reducing

end-winding length.

Synchronous motors are affected by force oscillations which may represent an excessive structural stress or may transfer unwanted vibrations to the load. The force oscillations are commonly distinguished as cogging forces and force ripple. Cogging forces are caused by the tendency of the mover to line up with the stator where the permeance of the magnetic circuit is maximized. This happens in correspondence to the stator teeth even when no current is flowing in the armature. When the motor is running, there are some additional oscillatory force components resulting from the interaction between the magnets and the space harmonics in the airgap. These alternating forces are generally referred to as force ripple.

Cogging force amplitude is often reduced by increasing the cogging force frequency. Since the number of cogging force oscillations is proportional to the least common multiple (LCM) between number of slots and number of poles [103], fractional-slot machines can achieve a higher LCM than synchronous motors with distributed windings. Force ripple depends on many geometrical parameters and is usually lower for machines with minimum slot openings, skewed permanent magnets, chamfered magnets, chamfered stator teeth, concentrated windings with high number of slots per pole per phase and fractional-slot machines. [100].

Fractional-slot synchronous machines are characterized by lower cogging force and are particularly attractive for EML application for their short end-windings and low Joule losses. Concentrated windings are also cheaper to manufacture and can be easily installed with respect to distributed windings. Additionally, concentrated winding configuration are more efficient for a segmented stator since the stages can be positioned next to each other so that transition effects between segments can be neglected. For these significant advantages concentrated windings were selected for the synchronous electromagnetic launcher for civil aircraft assisted take-off.

Nevertheless, as a consequence of the presence of secondary harmonics, a correct choice of the number of slots and poles together with the winding arrangement is imperative. The choice of the number of slots and poles is also important to determine the winding factor and the harmonic content of the machine.

5.2.2 Winding Factor

The winding factor k_w for a specific winding distribution expresses the ratio of the flux linked by that winding and the total flux that would be linked by a full-pitch distributed winding. The flux linked by the winding depends on the distribution of the coils in the slots and on coil pitch, so that the winding factor of the ν^{th} harmonic is

$$k_{w\nu} = k_{d\nu} \cdot k_{p\nu} \tag{5.1}$$

where $k_{d\nu}$ and $k_{p\nu}$ are the distribution factor and the pitch factor of the ν^{th} harmonic respectively. Since the linked flux is proportional to the thrust delivered by the motor, the winding factor should be maximized during the preliminary design selecting the appropriate number of slots and poles. In the following sections the method to calculate distribution and pitch factor for fundamental and secondary harmonics is shown.

5.2.2.1 Distribution Factor

When the mover is synchronized with the magnetic field speed, the magnetic flux Φ induces in the w_s turns in each slot a voltage called electromotive force (EMF). Since the flux is sinusoidally distributed, the electromotive force is sinusoidal and its peak value E is

$$E = 2\pi f w_s \Phi \tag{5.2}$$

where f is the frequency of the supplied voltage. The w_s conductors inside a slot lie close to each other and they are linked by the same flux at any instant of time. Conversely, the EMF induced in individual coils of a phase group of concentrated windings machine is out of phase. The EMF of each coil can be represented by phasors which are tilted with respect to one another by the electrical angle

$$\alpha_{ph} = \frac{2\pi t}{N_s} \tag{5.3}$$

where N_s is the number of slots and t is the periodicity of the machine. The angle between two phasors coincides with the electrical angle between two slots

$\alpha_s = 2\pi p/N_s$ only when the number of slots per pole per phase is an integer number, that is with distributed windings. For fractional-slot windings the ratio between the two angles is

$$d_q = \frac{\alpha_s}{\alpha_{ph}} = \frac{p}{t} \tag{5.4}$$

where d_q is also the denominator of the number of slots per pole per phase ($q = n_q/d_q$).

The machine periodicity t represents the number of identical parts in which the machine can be split and corresponds to the maximum number of parallel circuits allowable by a specific combination of slots and poles. The machine periodicity can be computed as the greatest common divisor (GCD) between slots and pole pairs p, that is

$$t = GCD(N_s, p) \tag{5.5}$$

Considering a machine with m phases the number of slots that belongs to the same phase is N_s/m and the same amount of phasors should be considered to evaluate the total EMF. The vectorial resultant E_r of these phasors represents the total EMF induced in a coil group. Since all the phasors are shifted with respect to one another of an angle α_{ph}, the magnitude of the resultant EMF E_r is smaller than the sum of the magnitudes of the phasors E_m. The distribution factor expresses the reduction of the resultant EMF of a coil distribution with respect to the sum of the EMFs induced in the machine coils and it is computed as

$$k_d = \frac{E_r}{E_m} \tag{5.6}$$

In order for the winding to be feasible, the number of coil per phase must be an integer number and each phase must have the same amount of slots. These conditions are satisfied when

$$\frac{N_s}{m \cdot t} \in \mathbb{N} \tag{5.7}$$

where $\mathbb{N}$ is the set of integer number. First grade windings are identified by even number of the ratio N_s/mt and both single-layer and double-layer windings are

possible. Odd value of the ratio N_s/mt are associated with second grade windings that allow the existence of the double-layer configuration only [104]. The distribution factor of the fundamental harmonic of first grade double-layer windings can be computed as [102]

$$k_d = \frac{\sin\left(\frac{\pi}{2m}\right)}{\frac{N_s}{2mt}\sin\left(\frac{\alpha_{ph}}{2}\right)} \tag{5.8}$$

In a similar way the distribution factor of the fundamental harmonic of second grade windings can be computed as

$$k_d = \frac{\sin\left(\frac{\pi}{2m}\right)}{\frac{N_s}{mt}\sin\left(\frac{\alpha_{ph}}{4}\right)} \tag{5.9}$$

Equations 5.8 and 5.9 for the fundamental harmonic can be still used to calculate the distribution factor for the ν^{th} harmonic using an appropriate value of the electrical angle between two consecutive phasors. The angle between two adjacent phasors for the ν^{th} harmonic can be expressed as [102]

$$\alpha_{ph\nu} = \alpha_{ph}\left(1 + \delta_{ph}\frac{\nu - p}{t}\right) \tag{5.10}$$

$\alpha_{ph\nu} = \alpha_{ph}$ only when $\nu = p$ which is the condition that corresponds to the fundamental harmonic. δ_{ph} is an integer number that is equal to the number of slots between two adjacent phasors. Since the $(i+1)^{th}$ phasor is obtained from the i^{th} phasor by a rotation of an angle $\alpha_{ph} + 2k\pi$ with $k \in \mathbb{N}$, in fractional-slot machines the slot angle α_s is related to the phasor angle α_{ph} by the expression

$$\delta_{ph}\alpha_s = \alpha_{ph} + 2k\pi \tag{5.11}$$

Substituting the eq. 5.3 and the expression $\alpha_s = 2\pi p/N_s$ in eq. 5.11 yields

$$\delta_{ph} = \frac{kN_s/t + 1}{p/t} \tag{5.12}$$

where k is the minimum integer number that makes δ_{ph} an integer number.

Not all the harmonic orders ν are produced by the winding sequence imple-

mented in the fractional-slot machine. For instance, the harmonic contents of the winding distribution when N_s/t is even includes only harmonics of odd order multiplied by the periodicity t. There are no harmonics of even order because the effects of two opposite coils always cancel out. Thus, when N_s/t is even the harmonic order can be calculated as

$$\nu = k_\nu \cdot t \qquad \text{where} \qquad k_\nu = 1, 3, 5, 7, 9, 11 \ldots \tag{5.13}$$

For the synchronous harmonic $\nu = p$ and therefore $k_\nu = d_q$ according to eq. 5.4. The number of subharmonics is $(d_q - 1)/2$ [105].

Conversely, when N_s/t is odd the winding distribution includes harmonics of both even and odd order multiplied by the periodicity t, since no opposite phasors reciprocally null their effects. The harmonic orders to consider when N_s/t is odd become

$$\nu = k_\nu \cdot t \qquad \text{where} \qquad k_\nu = 1, 2, 3, 4, 5, 6 \ldots \tag{5.14}$$

In this case the synchronous harmonic corresponds to $k_\nu = d_q/2$ whereas the number of subharmonics is $(d_q - 2)/2$. For both even and odd value of the ratio N_s/t the harmonics which are multiple of the number of phases do not exist.

5.2.2.2 Pitch Factor

In order to reduce the turn length and the harmonic contents, the coil pitch τ_c can be smaller than the pole pitch τ of the machine. In short pitched coil, the phase angle between the EMFs induced in two opposite coil sides is less than π (electrical angle), whereas in full pitched coil the phase angle between the EMFs induced in two coil sides is exactly π. Hence, the pitch factor is the measure of resultant EMF of short pitched coil in comparison with resultant EMF of full pitched coil. The magnitude of the pitch factor k_p depends upon the ratio of coil pitch τ_c and pole pitch. The pitch factor of the fundamental harmonic can be written as

$$k_p = \sin\left(\frac{\pi}{2}\frac{\tau_c}{\tau}\right) = \sin\left(\pi\frac{p}{N_s}\right) \tag{5.15}$$

since the coil pitch is equal to the slot pitch τ_s and the slot pitch can be expressed as $\tau_s = 2p/N_s$. The pitch factor for the ν^{th} can be computed using

$$k_{p\nu} = \sin\left(\pi \frac{\nu}{N_s}\right) \tag{5.16}$$

where the number of pole pairs p was substituted with the harmonic order. Eq. 5.16 can be still used for the fundamental harmonic since in this case $\nu = p$.

5.2.2.3 Selection of Number of Slots and Poles

The selection of the number of poles $2p$ and number of slots N_s is correlated with the thrust density (shear stress) of the machine and the dimensions of the active area of the mover. In particular the number of poles can be expressed as a function of the mover length l_{mov} as

$$2p = \frac{l_{mov}}{\tau} \tag{5.17}$$

In general, synchronous motor with short pole pitches have increased electromagnetic performance. However, the minimum length of the pole pitch for high voltage application is limited by the maximum frequency allowed by state of the art silicon carbide switches (a few kHz with a maximum admissible output frequency of approximately 300 Hz). With a required end-speed of approximately 85.7 m/s (as shown in Section 3.3.3), the minimum pole pitch is about 15 cm. According to eq. 5.17, the number of poles is proportional to the length of the mover when the pole pitch τ is given. Hence, it is sufficient to define a range of values for the mover length to know the number of poles that LPMSM may implement.

The mover length can be determined form the other dimension of the mover's active area and from the rated thrust density of the electrical motor. The shear stress on the moving plate of synchronous machines designed for continuous operations for aerospace applications ranges between 45-75 kN/m^2 [106]. The thrust density can reach higher values, but complex cooling systems are often required. Since the peak thrust needed to launch an A320-200 is approximately 500 kN, the area of the mover is expected to vary between 7-11 m^2.

The width of the LPMSM's mover can be determined from structural consid-

Table 5.1: Fundamental harmonic winding factors for different combination of number of pole pairs and number of slots for a three phase machine [107]

$N_s \backslash p$	2	3	4	5	6	7	8	9	10	11	12	13	14	15	16	17	18	19	20
6	.866	X	.866		X		.866	X	.866		X		.866	X	.866		X		.866
9		.866	.945	.945	.866			X			.866	.945	.945	.866			X		
12	1	X	.866	.933	X	.933	.866	X			X			X	.866	.933	X	.933	.866
15		X		.866	X	.951	.951	X	.866		X			X			X		.866
18		1			.866	.902	.945	X	.945	.902	.866						X		
21					X	.866	.890	X	.953	.953	X	.890	.866	X			X		
24			1		X		.866	X	.933	.950	X	.950	.933	X	.866		X		
27								.866	.877	.915	.945	.954	.954	.945	.915	.877	.866		
30				1	X			X	.866	.874	X	.936	.951	X	.951	.936	X	.874	.866
$N_s \backslash p$	11	12	13	14	15	16	17	18	19	20	21	22	23	24	25	26	27	28	29
33	.866	X	.903	.928	X	.954	.954	X	.928	.903	X	.866		X			X		
36		.866	.867	.902	.933	.945	.953	X	.953	.945	.933	.902	.867	.866			X		
39		X	.866		X	.918	.936	X	.954	.954	X	.936	.918	X		.866	X		
42		X		.866	X	.890	.913	X	.945	.953	X	.953	.945	X	.913	.890	X	.866	
45					.866		.866	X	.927	.945	.951	.955	.955	.951	.945	.927	X	.866	
48		X			X	.866		X	.905	.933	X	.950	.954	X	.954	.950	X	.933	.905
51		X			X		.866	X	.880	.901	X	.933	.944	X	.955	.955	X	.944	.933
54								.866		.877	.902	.915	.930	.945	.949	.954	X	.954	.949
57		X			X			X	.866		X	.932	.912	X	.937	.946	X	.955	.955

erations on the plate thickness and material. Since the shuttle is made out high density stainless steel, in order to reduce the weight of the LPMSM's mover the yoke thickness should be reduced as much as possible. As can be seen in Fig. 4.21 a thickness reduction must be compensated either by the enhanced structural characteristics of the yoke material or by a decrease of the mover width (Fig. 4.23) to guarantee a buckling factor greater than 10. As it will be later shown in Section 5.3.1, the thickness is reduced to get a mover width comparable with that of the LIM's aluminium plate found in Section 4.4 accounting for the structural properties of steel. Therefore the mover width of the LPMSM is expected to vary between 1.5-3.0 m.

From the values that have just been established for the active area and the mover's width, the mover length ranges between 2.3-7.3 m. Inserting the values of mover length in eq. 5.17 together with the minimum pole pitch length, the number of poles of the synchronous launcher varies between 16 and 48 (8 to 24 pole pairs).

Within the 8-24 pole pairs range, a large number of slot-pole combinations with

Table 5.2: Properties of pole-slot combinations for $N_s = 36$

p	12	13	14	15	16	17	19	20	21	22	23	24
k_w	.866	.867	.902	.933	.945	.953	.953	.945	.933	.902	.867	.866
LCM	72	468	252	180	288	612	684	360	252	396	828	144
t	12	1	2	3	4	1	1	4	3	2	1	12
N_s/t	3	36	18	12	9	36	36	9	12	18	36	3
	X	X	√	X	√	X	X	X	X	X	X	X

different winding factors can be found. Table 5.1 reports the winding factors of the fundamental harmonic of several combinations of slots and pole pairs [107]. Only winding factors greater than 0.866 are reported as they are more interesting from the design point of view. Cells with winding factor lower than 0.866 are left blank. The combinations of slots and pole pairs marked with a red cross in Table 5.1 are not allowed.

Table 5.1 shows that dozens of combinations are possible within the the 8-24 pole pairs range. The technique proposed to select the pole-slot combination for the LPMSM does not follow any optimization criteria, but it is based on considerations that lead to satisfactory results. Indeed, in case an optimal solution exists, it would require the comparison of the electromagnetic performance of all the possible pole-slot combinations. It is accepted to consider a pole-slot combination with winding factor greater than 0.9, low force ripple and low content of magnetic material.

The number of slots that presents the largest number of combinations with a winding factor greater than 0.9 in the 8-24 pole pairs range is 36. The properties of all the possible pole-slot combinations with $N_s = 36$ are reported in Table 5.2. The cells of Table 5.2 are coloured either in green or red depending on whether the value of the respective parameters is satisfactory or not according to the selection criteria.

In order to limit the cost and the length of the active area, solutions with maximum 34 poles (17 pole pairs) were considered in Table 5.2. Indeed, high number of poles are associated with long movers with large quantities of magnetic material. Least Common Multiple (LCM in Table 5.2) greater than 200 are demanded to reduce the cogging force due to the interaction between magnets and stator

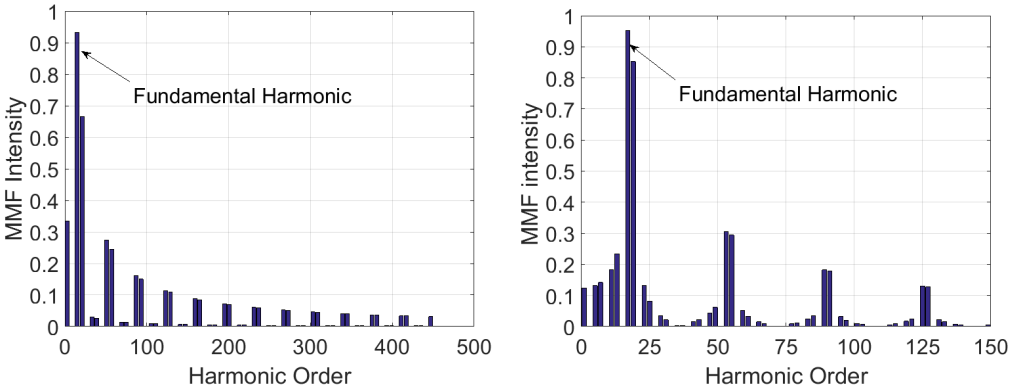

(a) 30 poles, q =2/5 (b) 34 poles, q =6/17

Figure 5.3: MMF intensity of the first 50 harmonics for a 36 slot machine with 30 and 34 poles respectively

teeth. Low values of the periodicity t were neglected since they are often associated with high harmonic content. This can be verified comparing the MMF intensity of the harmonics of different pole combinations. The normalized MMF intensity is computed as

$$MMF_\nu = \frac{kw_\nu}{\nu} p \tag{5.18}$$

The harmonic content of the 30-poles and 34-poles machine in Table 5.2 are compared in Fig. 5.3. In particular, Fig. 5.3b shows that the first 50 harmonics of the 34-poles have lower orders than those of the 30-poles machine. At the same time, the 34-pole solution presents an high intensity secondary harmonic very close to the fundamental which may cause significant force ripple during operation.

Another reason why the solutions in Table 5.2 with unitary periodicity were discarded is that t corresponds to the number of parallel circuit that can be implemented in a single stage of the synchronous motor. In high voltage application, high periodicities provide a way of reducing the applied voltage by increasing the number of parallel circuits despite increasing both the current and the complexity of the machine winding.

Even though the harmonics order is mainly related with the value of the periodicity t also the ratio N_s/t affects the harmonic distribution as explained in Section 5.2.2.1. In particular, odd values of N_s/t are associated with a higher harmonic

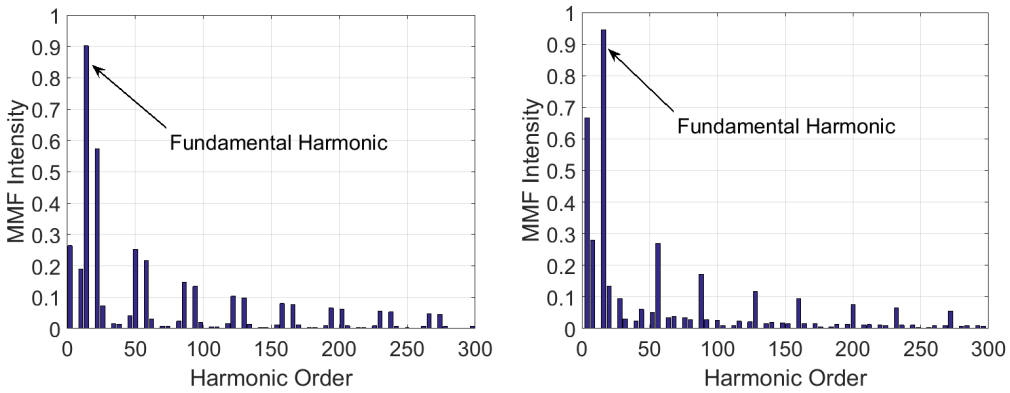

(a) 28 poles, q =3/7 (b) 32 poles, q =3/8

Figure 5.4: MMF intensity of the first 50 harmonics for a 36 slot machine with 28 and 32 poles respectively

content than pole-slot combinations with even N_s/t and same periodicity. Odd values of N_s/t are still acceptable, but they are indicated in yellow in Table 5.2.

After these considerations, only two combinations remain in Table 5.2 to be selected. The MMFs of the 28-poles and of the 32-poles machines are compared in Fig. 5.4. The 32-poles solution presents winding factor and LCM slightly larger than the 28-poles solution, but the mover hosts four more poles and is expected to be at least 60 cm longer. In this work higher importance was given to the minimization of the magnetic material on board the mover rather than to other parameters. Additionally, the sub-harmonics of the 32-poles are more intense than the 28 poles solution and they are expected to absorb more flux during operations. The sub-harmonic flux may cause saturation of the magnetic circuit leading to severe drop of the fundamental thrust and consequently the motor speed. Therefore, the LPMSM considered for EML application mounts 28 poles on both the sides of the mover while the travelling magnetic field is produced by the current flowing in 36 slots. Hence, each stage of the LPMSM is formed by two opposite stators each one with 36 slots.

5.2.3 Winding Sequence

A major difficulty in the design of concentrated winding machines lies in the determination of the distribution of the phases under each pole in order to achieve high

electromagnetic performance. This section proposes a systematic method that can be used to position the phase windings in the slots not only for the number of slots and poles selected in Section 5.2.2.3, but for all the possible combinations. The method applied to locate the conductors of each phase in the slots is similar to the one proposed for large rotary synchronous generators [108]. This method that was accurately described in [107] is adapted to the linear motion and it is modified to allow for software implementation.

The method is based on the decomposition of the number of slots per pole per phase q which is defined as

$$q = \frac{N_s}{2p \cdot m} = \frac{n_q}{d_q} \tag{5.19}$$

where n_q, d_q are integer number. The denominator d_q represents the number of poles of the basic unit of the fractional-slot winding sequence, whereas the nominator n_q represents the number of slots per phase within d_q poles. Therefore, the total number of slots within d_q poles is $m \cdot n_q$. The difference between the denominator and the numerator of q is

$$z_q = d_q - n_q \tag{5.20}$$

The winding layout of fractional-slot machines is determined through the comparison between the distributed winding sequence A-C'-B-A'-C-B' and a sequence of 1 and 0 which is determined from q. The conductors of the distributed winding sequence having the same position of the ones in the binary series are kept to form the optimum winding sequence of the fractional-slot machine. It can be deduced that the optimum binary sequence contains N_s/t ones and that the associated winding layout is repeated t times to fill all the slots.

The basic binary series instead contains d_q digits and is formed by n_q ones and z_q zeros. In order to find the optimum distribution of 1 and 0 in the basic binary series some additional variable must be defined. The minimum number of zeros after each 1 in the basic binary series is defined as

$$n_{zq} = \left\lfloor \frac{z_q}{n_q} \right\rfloor \qquad \text{where} \qquad n_{zq} \in \mathbb{N} \tag{5.21}$$

Table 5.3: Basic binary series for several number of slots per pole per phase

q	Binary Series
1/2	1 0
3/8	1 0 0 1 0 0 1 0
3/10	1 0 0 1 0 0 1 0 0 0
2/5	1 0 0 1 0
2/7	1 0 0 1 0 0 0
3/7	1 0 1 0 1 0 0
3/11	1 0 0 0 1 0 0 0 1 0 0
7/22	1 0 0 1 0 0 1 0 0 1 0 0 1 0 0 1 0 0 1 0 0 0
9/26	1 0 0 1 0 0 1 0 0 1 0 0 1 0 0 1 0 0 1 0 0 1 0 0 1 0

The remainder of the ratio z_q/n_q corresponds to the number of zeros r_q to redistribute in the basic binary series.

In order to facilitate the software implementation the basic binary sequence is initialized as a vector of d_q zeros while the position indexes i of the "1" are computed according to

$$\begin{aligned} &i+(n_{zq}+1)\cdot(i-1) && \text{for } i=1,\ 2,\ ...r_q \\ &i+n_{zq}\cdot(i-1)+r_q && \text{for } i=r_q+1,\ r_q+2,\ ...n_q \\ &i+n_{zq}\cdot(i-1) && \text{only if } r_q=1 \text{ and } d_q\neq 5 \end{aligned} \tag{5.22}$$

The indexes distributions law in eq. 5.22 were determined in order to have the first phase A at the beginning of the winding sequence. This has to be done for linear machines whereas in rotary machines it is not necessary. Indeed, no matter the phase the sequence starts, the slots of rotary machines are filled correctly since the edges of the sequence coincide. The basic binary series for several numbers of slots per pole per phase are shown in Table 5.3. In particular, the binary sequence for the slot-pole combinations selected in Section 5.2.2.3 is highlighted.

The obtained sequence is subsequently repeated a number of times equal to the number of phases in order to represent the total number of slots $n_q \cdot m$ within d_q poles. This binary sequence is than compared with the sequence of distributed windings as shown in Table 5.4 for the selected slot-pole combination with $q = 3/7$.

In case d_q is odd the repeatable winding sequence is antiperiodic and the trans-

Table 5.4: Repeatable winding sequence

1	0	1	0	1	0	0	1	0	1	0	1	0	0	1	0	1	0	1	0	0
A	C'	B	A'	C	B'	A	C'	B	A'	C	B'	A	C'	B	A'	C	B'	A	C'	B
Repeatable winding sequence for $q = 3/7$														A B C C' A' B' B C A						

Table 5.5: Double-layer winding sequence for a 36 slots 28 pole fractional-slot LPMSM

| | | | | | | | | | | | | | | | | | | |

variables, a simple analytical algorithm has to be introduced. The simplicity of the algorithm allows the calculation of the desired data in a short time, but the accuracy of the sizing procedure must not be compromised. The following section introduces the sizing algorithm that the parametric optimization iterates a large number of times for all the combinations of the design parameters. The outcome of the parametric optimization will be used to define the geometrical features of the machine that will be implemented in FEA software and in the analytical transient model based on the multi-layer theory.

5.3.1 Parametric Optimization Algorithm for LPMSM

The parametric optimization algorithm for LPMSM considers the design variables shown in Table 5.6. Before running the algorithm the value of the design variables is still unknown, but they are assumed to vary within specific ranges as will be later shown in Table 5.7. A combination of these parameters and the list of input variables shown in Table 5.6 are all the parametric optimization algorithm inputs. The input variables are assumed before running the algorithm and do not vary across all iterations. As can be seen in Table 5.6 the slot-pole combination selected in Section 5.2 is an input of the LPMSM sizing procedure.

The thickness of the mover's yoke h_{ys} in Table 5.6 is determined before running the parametric optimization algorithm from structural considerations. To prevent structural instability during operations, the buckling factor $k_{buck\,Fe}$ of the stainless steel plate must be greater than 10. The dependency of the buckling factor of the stainless steel yoke on the plate thickness is similar to that of the aluminium plate of LIM shown in Fig. 4.21 in Section 4.4. Thus the buckling factor is expected to vary with the cube of the yoke thickness. Since stainless steel has a Young's modulus of 210 GPa, whereas aluminium has a Young's modulus of 70 GPa, the buckling factor of a plate made out of steel is expected to be approximately three times greater than that of an aluminium plate with the same dimensions. Assuming that the steel plate has the same width and length of the aluminium plate and that it withstands the same load (hypotheses that are approximately true), an initial

Table 5.6: Parametric optimization inputs and design variables for LPMSM

Design variables		
Description	**Sym**	**Value**
Airgap length	g	?
Slot pitch	τ_s	?
Peak magnetic field density in the airgap	B_g	?
Number of turns per coil	N_c	?
Stator width	l_s	?
Ratio of the tooth width to the slot pitch	r_{ts}	?
Ratio of the magnet span to the pole pitch	r_{mp}	?
Input variables		
End-speed requirement	v_{TO}	85.73 m/s
Vacuum permeability	μ_0	$4\pi \cdot 10^{-7}$ H/m
Magnets relative permeability	μ_{PM}	1.033
Copper conductivity	σ_c	$5.8 \cdot 10^{-7}\,\Omega^{-1}m^{-1}$
Number of phases	m	3
Number of pole pairs	p	14
Number of slots	N_s	36
Required peak thrust	F_x	502.9 kN
Stator maximum flux density	B_{ir}	1.7 T
Magnets remnant flux density	B_r	1.39 T
Fill factor	k_{fill}	0.45
NdFeB magnets density	ρ_{PM}	7400 kg/m^3
Silicon steel density	ρ_{ir}	7750 kg/m^3
Stator windings current density	J	50 A/m^2
Tooth tip height	h_{ss}	1.0 mm
Grooves Diameter	d_g	2.0 mm

value of the yoke thickness can be estimated as

$$k_{buckFe} = k_{buckAl} \Rightarrow \begin{cases} k_{buckAl} = a \cdot d_{Al}^3 \\ k_{buckFe} = 3a \cdot h_{ys}^3 \end{cases} \Rightarrow h_{ys} = \frac{d_{Al}}{\sqrt[3]{3}} \tag{5.24}$$

where a is a generic constant. The buckling factors were imposed equal in eq. 5.24 since they have to satisfy the same requirement and the k_{buckAl} is already greater than 10. Inserting the thickness of the aluminium plate in eq. 5.24 ($d_{Al} = 20$ mm) yields a yoke thickness of approximately 14 mm. This length is initially considered although a lower thickness could be selected for the different structural features of the LPMSM's mover with respect to the LIM's. Indeed, the LPMSM's

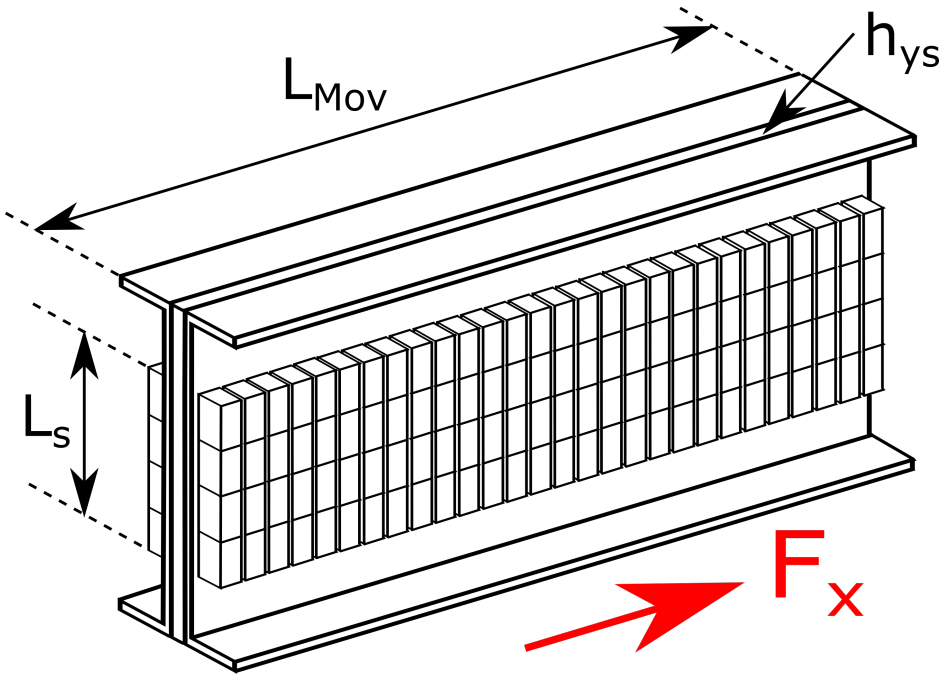

Figure 5.5: Mover of LPMSMs for electromagnetic launch application

yoke is not an isolated plate but its structural properties are enforced by the presence of extra stainless steel sheets which are used to keep the magnets in place. These plates are glued on both the sides of the yoke as shown in Fig. 5.5. The magnets themselves may offer an increased structural resilience.

A complete structural analysis of the mover in Fig. 5.5 would be required to fully characterize the response to the load and the minimum value of h_{ys} to avoid instability. The structural response should be validated with a model that includes yoke, magnets and lateral plates as shown in Fig. 5.5. This analysis would also allow the calculation of the stress tensor over the volume of the magnets and would verify whether the intensity of the load will crack the brittle magnetic material or not. However, the difficulty of simulating the action of the glue between the interfaces and the complexity of the structure limit the selection of the yoke thickness to the aforementioned considerations on the buckling factor.

The parametric optimization algorithm starts with the definition of the mover geometrical features. The slot pitch length of concentrated windings machines for a given combination of number of slots and poles is related to the pole pitch length

by the equation

$$\tau = \frac{N_s}{2p}\tau_s \tag{5.25}$$

The span of the permanent magnet is simply given by the product

$$l_m = r_{mp} \cdot \tau \tag{5.26}$$

The airgap magnetic field density B_g given in input is analytically related with the thickness of the PMs h_m through the balance of the magnetic voltage drops in the magnetic circuit [29]:

$$\frac{B_r}{\mu_{PM}\mu_0}h_m = \frac{B_g k_{Fg}}{\mu_{PM}\mu_0}h_m + \frac{B_g k_{Fg}}{\mu_0}g \tag{5.27}$$

where B_r is the PMs remnant flux density, μ_{PM} is the relative magnetic permeability of the magnet's material and k_{Fg} is the fringing factor. The fringing factor measures the increase of the effective airgap length due to tendency of the magnetic flux to cross the airgap following a curved pattern. This effect is stronger for machines with large airgaps. The fringing factor is a coefficient always greater than one that can be computed as

$$k_{Fg} = \frac{\sinh\left(\frac{\pi}{\tau}g\right)}{\frac{\pi}{\tau}g} \tag{5.28}$$

After few algebraic operations, eq. 5.27 can be used to express the thickness of the magnets as a function of known terms as

$$h_m = \frac{\mu_{PM}}{\frac{Br}{B_g k_{Fg}} - 1}g \tag{5.29}$$

The length of the mover l_{mov} in Fig. 5.5 can be calculated as

$$l_{mov} = (2p-1)\tau + l_m + 2h_{ys} \tag{5.30}$$

Considering that the lateral plates are assumed to have a thickness equal to $h_{ys}/2$ and that the length of the flanges plus that of the plate overhangs is considered to be the 40% of the width of the active area l_s, the mass of the mover can be

calculated as

$$m_{mov} = 1.1 \cdot [2\rho_{PM} l_m l_s h_m 2p + \rho_{Fe}(1.4 \cdot l_s l_{mov} 2h_{ys} - 2p l_s l_m h_{ys})] \tag{5.31}$$

where ρ_{PM} is the NdFeB PMs density, ρ_{Fe} is the stainless steel yoke density and the coefficient 1.1 is added to consider the weight of the guidance system. In order to accelerate the mover at the required rate, the motor has to deliver an additional force of

$$F_{mov} = m_{mov} \cdot 0.6G \tag{5.32}$$

The thrust needed to propel the aircraft and the mover at constant acceleration is

$$F_{xc} = F_x + F_{mov} \tag{5.33}$$

The respective thrust density which expresses the shear stress in the airgap is

$$f_x = \frac{F_{xc}}{2p\tau l_s} \tag{5.34}$$

Once the dimensions of the mover are established and the corrected thrust F_{xc} is determined, the algorithm proceeds with the calculation of the rated stator current and the armature geometrical features. A parameter that can be simply determined from the data given in input is the tooth width

$$b_t = r_{ts} \cdot \tau_s \tag{5.35}$$

whereas the slot width b_s is given by

$$b_s = \tau_s - b_t \tag{5.36}$$

Since the slots are rectangular, the slot opening coincides with the slot width. As in the LIM, the teeth of the synchronous motor present grooves of height d_g to hold the coils in place during the manufacturing process and tips of height h_{ss}. The magnetic flux density B_t in the stator teeth can be calculated assuming that the flux that crosses a slot pitch is redirected through the respective tooth to follow

the pattern with lower reluctance. It can be approximated as

$$B_t = \frac{2}{\pi} B_g \frac{\tau_s}{b_t} \tag{5.37}$$

Equating the flux across the slot teeth and the stator back iron, the back iron thickness can be computed assuming a maximum flux density $B_{ir} = 1.7$ T as

$$h_y = 2\frac{B_t b_t}{B_{ir}} \tag{5.38}$$

where the number 2 is inserted to consider the contribution of two adjacent slots. The slot height h_s can be determined from the slot area A_s as

$$h_s = \frac{A_s}{b_s} \tag{5.39}$$

The slot area must be enough wide to host the conductors and the insulating material among them. It is computed as

$$A_s = 2\frac{N_c I}{J \cdot k_{fill}} \tag{5.40}$$

where the fill factor k_{fill} is assumed to be 45% of the total slot area whereas the current density J has the same value of the rated current density of the induction launcher, since the respective temperature rise in the stator coils has been proven within the insulation limit in Section 4.5. Since the machine is a double-layer concentrated windings LPMSM, the number 2 in eq. 5.40 takes into account that every slot hosts two coils, one for each layer. The variable I in eq. 5.40 represents the current per turn that is required to produce the synchronous thrust.

At every instant of time the mechanical output power P_o must be equal to the product between the thrust and the synchronous speed v_s which in turn is

$$F_{xc} \cdot v_s = m \cdot E_s I \tag{5.41}$$

where m is the number of phases and E_s is the no-load voltage induced in the stator coils by the excitation field of the PMs. The no-load induced voltage is also called back electromotive force and it may be explained as the voltage needed from the power supply to allow the rated current I to flow and interact with the

excitation field to produce the required thrust. However, the total voltage that the power supply provides is greater than E_s since the losses of the machine have to be considered as well.

An expression of the current per turn can be derived from eq. 5.41 for a three phase machine as

$$I = \frac{\tau}{\pi}\omega\frac{F_{xc}}{3E_s} \tag{5.42}$$

where the synchronous speed was substituted with the expression

$$v_s = \frac{\tau}{\pi}\omega \tag{5.43}$$

The angular velocity ω is related with the instantaneous frequency f as

$$\omega = 2\pi f \tag{5.44}$$

The maximum frequency is provided at the end of the launch when the synchronous speed reaches the end-speed v_{TO} required at take-off.

$$f_{max} = \frac{v_{TO}}{2\tau} \tag{5.45}$$

The back electromotive force in eq. 5.41 is related to the flux linkage Φ_s between the permanent magnets and the stator windings as

$$E_s = \omega N_c c\, k_w \Phi_s \tag{5.46}$$

where c is the number of coil per phase which is

$$c = 2\frac{N_s}{m} \tag{5.47}$$

where the number 2 is used to consider both the sides of the stator. The magnetic flux Φ_s is defined as the integral over the slot surface of the magnetic flux density in the airgap $B(x)$. It is computed as

$$\Phi_s = l_s \int_0^{\tau} B(x)\, dx = \frac{2}{\pi} B_g \tau l_s \tag{5.48}$$

where the second equality comes from the integration of the sinusoidal function

$B(x)$ that represents the magnetic flux density in the airgap. Substituting eqs. 5.46 and 5.48 in eq. 5.42 yields

$$I = \frac{\tau}{\pi} \frac{F_{xc}}{3\frac{2}{\pi} B_g \tau l_s N_c c k_w} \tag{5.49}$$

Once the algorithm determines all the geometrical features of the LPMSM and the current required to produce the thrust, the parametric optimization proceeds with the calculation of the electromagnetic properties of the synchronous motor. The resistance of the current carrying conductors in the stator can be simply computed from the definition as

$$R = \rho_c \frac{l_c}{A_c} = \frac{l_s + l_{end}}{\sigma_c} \frac{J}{I} N_1 \tag{5.50}$$

where $N_1 = N_c \cdot c$ is the number of turns per phase, ρ_c is the resistivity of the conductive material and the reciprocal of the conductivity σ_c, $l_c = l_s + l_{end}$ is the length of the conductors, l_{end} is the end-coil length and $A_c = I/J$ the area of the conductive region in the slot.

The magnetization inductance can be determined from the total flux across the machine as

$$L_m = \frac{\psi_s}{\sqrt{2}I} = \frac{N_1 k_w \Phi_s}{\sqrt{2}I} \tag{5.51}$$

The expression of the magnetization inductance can be rewritten considering that the magnetic flux density in the airgap can be expresses as

$$B_g = \frac{\mu_0 \mid MMF \mid}{g_e} = \frac{3\sqrt{2}\mu_0 N_1 k_w I}{\pi g_e p} \tag{5.52}$$

where equivalent airgap g_e can be computed as

$$g_e = g k_c + h_m \tag{5.53}$$

The factor k_c is the Carter coefficient that represents the increase in effective magnetic path length due to slotting. The stator slotted structure deviates the magnetic wave shape from the ideal sinusoidal shape reducing the machine performance. This effect is quantified by the Carter's coefficient which can be computed using

the formula [87]

$$k_c = \frac{\tau_s}{\tau_s - \sigma_s b_s} \tag{5.54}$$

In literature there are many possible modifications of the Carter factor σ_s and often the calculation is done using the finite element method to improve the accuracy. The expression of the Carter factor that minimizes the discrepancies between the FEA and the analytical formulas for a surface-mounted PM synchronous motor with concentrated windings is [109]

$$\sigma_s = \frac{\tau_s}{g}\left[\frac{b_s}{\tau_s} - \frac{4g}{\pi\tau_s}\ln\left(1+\frac{\pi b_s}{4g}\right)\right] \tag{5.55}$$

The final expression of the magnetization inductance can be obtained by substituting eqs. 5.48 and 5.52 in eq. 5.51 which yields

$$L_m = \frac{6\mu_0(N_1 k_w)^2 \tau l_s}{\pi^2 g_e p} \tag{5.56}$$

The armature leakage inductance L_l represents the magnetic flux that does not link the armature and the mover, but returns to the stator without crossing the airgap and producing the thrust. In a PM machine there are several sources of flux leakage: the slot geometry, the end windings and the secondary harmonics. Every contribution to the total leakage inductance can be expressed as a function of the respective permeance as

$$L_{lx} = 2\mu_0 \frac{l_s N_1^2}{pq}\lambda_x \tag{5.57}$$

The magnetic flux that circles around the coils and crosses the slot without reaching the tooth tips and the airgap is represented by the slot leakage inductance L_{ls}. The respective permeance of double-layer windings is a function of the dimensions of the slots that can be written as

$$\lambda_s = \left(\frac{h_s}{3b_s} + \frac{h_{ss}+d_g}{b_s}\right)\frac{3\tau_c/\tau+1}{4} \tag{5.58}$$

Another part of the magnetic flux that does not contribute to the thrust generation is the flux associated with the end windings. The end winding leakage inductance

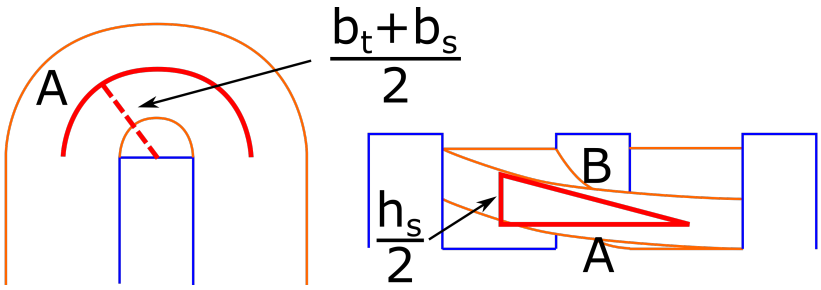

Figure 5.6: Schematic of concentrated windings end-coil

L_{le} is generated by all the conductors outside the active area of the machine. The end winding permeance for high voltage double layer windings is

$$\lambda_e = 0.42 \frac{q l_{end}}{2a} \left(1 - \frac{2}{\pi} \frac{\tau_c}{l_{end}}\right) k_w^2 \tag{5.59}$$

where the length l_{end} of a generic end-coil can be approximately computed as the 105% of the length of hypotenuse B of triangle in Fig. 5.6 which sides are half of the slot height $h_s/2$ and the semicircumference A in Fig. 5.6. Thus, the expressions to calculate the end-coil length is

$$l_{end} = 1.05 \sqrt{\frac{\pi^2}{4}(b_s + b_t)^2 + \frac{h_s^2}{4}} \tag{5.60}$$

Especially with large airgaps and narrow slot openings, part of the magnetic flux that reaches the tooth tip follows low reluctance patterns to the neighbour tooth tips rather than crossing the airgap. The associated flux leakage is represented by the differential leakage inductance L_{ld} whose permeance can be computed as

$$\lambda_d = \frac{5 k_c g / b_s}{5 + 4 k_c g / b_s} \tag{5.61}$$

The leakage inductance L_{lh} associated with the secondary harmonics is the sum of their magnetization inductances. Since the amplitude of the magnetomotive force of each harmonic is related with the fundamental MMF by the eq. 5.18, the magnetization inductance of any secondary harmonic can be calculated as

$$L_{m\nu} = \frac{L_m}{k_w^2} \left(\frac{k_{w\nu}}{\nu} p\right)^2 \tag{5.62}$$

Combining eqs. 5.57, 5.51 and 5.62, an expression for the specific leakage permeance λ_h due to high order harmonics can be derived as

$$\lambda_h = 3\frac{q\tau k_w^2}{\pi^2 g_e}\gamma_h \tag{5.63}$$

where the harmonics leakage factor γ_h is the sum of all the ratios of the magnetization inductances of high order harmonics to the fundamental MMF. The harmonic leakage factor is computed as

$$\gamma_h = \frac{1}{k_w^2}\sum_{\nu>1}\left(\frac{k_{w\nu}}{\nu}\right)^2 \tag{5.64}$$

In conclusion, the total leakage inductance gathers all the possible leakage flux contributions and it is computed as

$$L_l = L_{ls} + L_{le} + L_{ld} + L_{lh} = 2\mu_0\frac{l_s N_1^2}{pq}(\lambda_s + \frac{l_{end}}{l_s}\lambda_e + \lambda_d + \lambda_h) \tag{5.65}$$

Eventually, the parametric analysis estimates the electromagnetic performance of the synchronous motor and the input power required by the machine. The power that is dissipated as heat in the stator coils can be computed as

$$P_c = 3RI^2 \tag{5.66}$$

where the number 3 corresponds to the number of phases. The active power P_a of the machine is the sum of the mechanical power and the heat losses:

$$P_a = F_{xc}v_s + P_c \tag{5.67}$$

The hysteresis losses and the eddy current losses are not considered during parametric optimization because they are negligible compare to the Joule losses P_c assuming proper lamination and high quality magnetic material. The machine efficiency expresses the amount of active power that is converted into mechanical power:

$$\eta = \frac{P_o}{P_a} = \frac{F_{xc}v_s}{F_{xc}v_s + P_c} \tag{5.68}$$

Table 5.7: Design variable ranges for the parametric optimization of LPMSM

Variable description	**Sym**	**Range**	**Iterations**
Airgap length [mm]	g	$[4 \rightarrow 11]$	8
Slot pitch [mm]	τ_s	$[100 \rightarrow 220]$	7
Airgap flux density [T]	B_g	$[1.12 \rightarrow 1.27]$	6
Mover width [m]	l_s	$[1.5 \rightarrow 3.5]$	5
Magnet span ratio	l_m/τ	$[0.65 \rightarrow 0.95]$	7
Tooth width ratio	b_t/τ_s	$[0.3 \rightarrow 0.8]$	6
Turns per coil	N_c	$[2 \rightarrow 6]$	3
Total iterations			**211680**

The reactive power P_r of the LPMSM is a measure of the energy stored in the magnetic field which is not used to produce the thrust.

$$P_r = 3\omega(L_m + L_l)I^2 \tag{5.69}$$

Since the reactive power is in quadrature with respect to the active power the total input power can be computed as the modulus of their vectorial sum as

$$P_i = \sqrt{P_a^2 + P_r^2} \tag{5.70}$$

The power factor defines the percentage of the input power which is converted in active power and it is computed as

$$\cos\phi = \frac{P_a}{P_i} = \frac{P_a}{\sqrt{P_a^2 + P_r^2}} \tag{5.71}$$

The phase voltage applied to the motor terminals is

$$U = \frac{P_i}{3I} \tag{5.72}$$

5.3.2 Parametric Optimization Outcomes

The parametric optimization iterates the sizing algorithm for LPMSM presented in Section 5.3.1 for every possible combination of the design variables reported in Table 5.7. Table 5.7 also reports the range where the design variables vary and the number of discretizations within each range. The total number of iterations

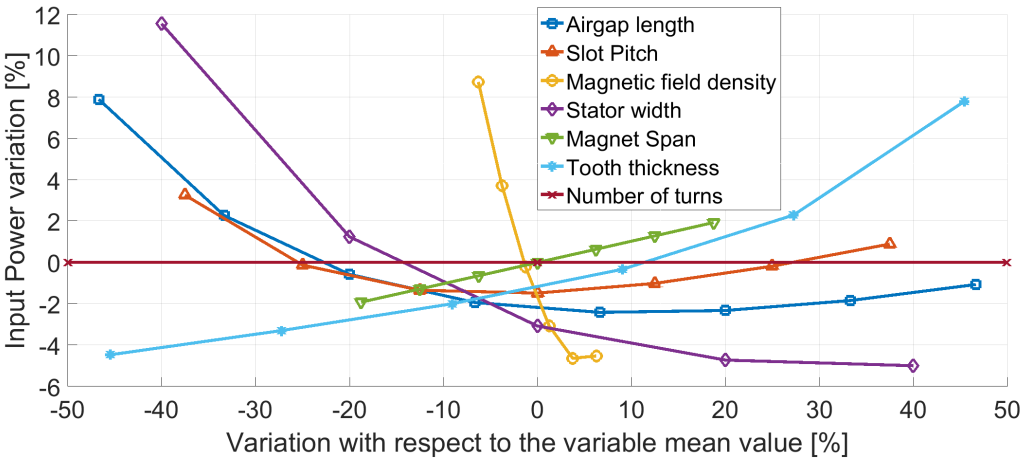

Figure 5.7: Percentage variation of the input power with respect to its mean value

of the parametric optimization algorithm corresponds to the product between the discretizations of all the variables.

The main objective of the parametric analysis is to determine the impact of the design variables on the input power. In order to determine the effect of every single value of the design variables on the power required, the power P_i computed by the algorithm in Section 5.3.1 is averaged for all the possible combinations where that value is constant. The average input power for every value of the variables is than compared with the average input power of all the possible combinations to determine the percentage variation with respect to the P_i mean value. For instance, considering the the airgap length $g = 6$ mm, the percentage variation $n_{\%g=6}$ for this variable is

$$n_{\%g=6} = \frac{\overline{P_i}_{g=6}}{\overline{P_i}} \tag{5.73}$$

where $\overline{P_i}_{g=6}$ is composed by 26460 while $\overline{P_i}$ considers all the 211680 combinations. Repeating the averaging procedure for every variable and plotting the results lead to the chart in Fig. 5.7.

In order to obtain the minimum input power with a set of variable that satisfies the design constraints, the parametric optimization algorithm has to be run every time a parameter is chosen. The parameters selection order might affect the final outcome and it is suggested to proceed either from the variable with the lowest

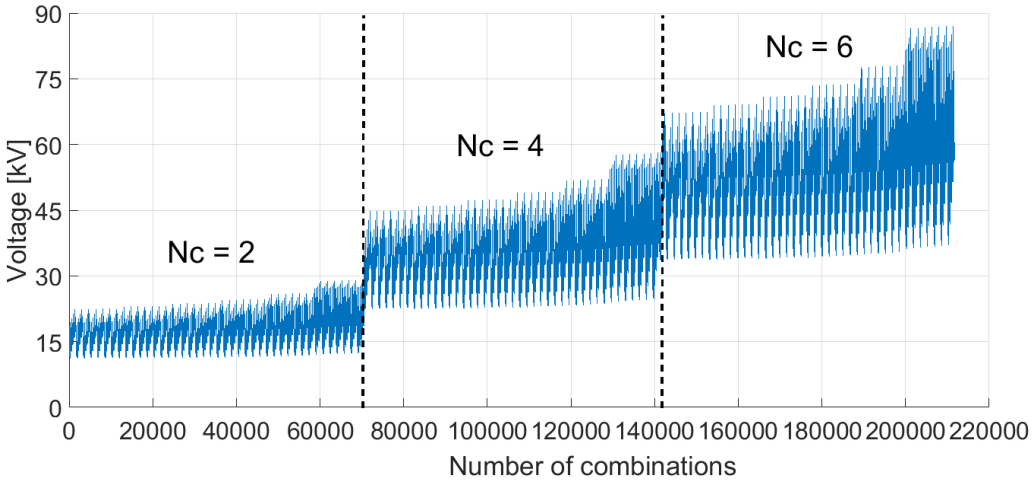

Figure 5.8: Amplitude of the supplied voltage at the end of the launch

impact on the input power or from the variable which value is constrained by other factors. Indeed, in the case a variable is constrained by any design requirement, its value is selected before the other parameters. The impact of each variable on the system is measured by the slope of the curves in Fig. 5.7. The rationale behind the choice of the parameters is presented enumerating the variables in the order they were selected.

1. The number of turns per coil N_c corresponds to the number of conductive wire connected in series in each coil. Even though the input power is not affected by number of turns per coil as shown in Fig. 5.7, the input voltage is proportional to the number of turns per phase N_1 which in turns proportionally grows with N_c. High voltage levels are difficult to handle by the power management system that supplies and controls the electromagnetic launcher. Even with the state of the art technology available today the maximum voltage should be reduced as much as possible. During the launch the voltage increases until the aircraft detaches. The peak voltage at the end of the launch for every design variable combinations is shown in Fig. 5.8. The parametric optimization shows that only low number of turns per coil are admissible. The voltage was computed considering the two sides of the stator connected in series. The applied voltage can be further reduced by considering the periodicity of concentrated windings machines and connecting all the equal parts of the motor in parallel.

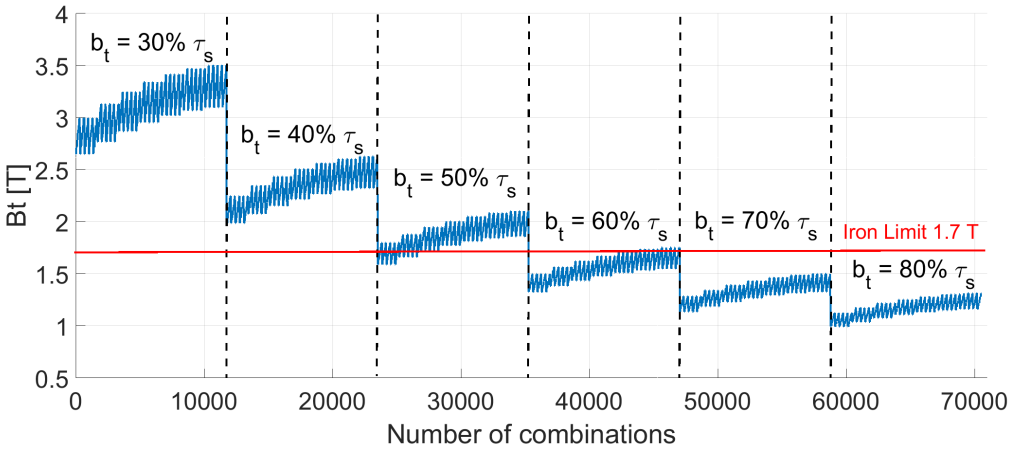

Figure 5.9: Variation of the magnetic field density in the stator teeth for several combinations of the design variables

2. The ratio b_t/τ_s is a parameter that describes the proportion between the tooth width and the slot opening. When the tooth is thin, the slot opening tends to be large and the slot tends to be short. Therefore, according to eq. 5.58 narrow teeth positively affect the slot permeance reducing the slot leakage flux. Indeed, when b_s becomes rather large the magnetic reluctance of the pattern across the slot increases and the magnetic flux tends to remain in the ferromagnetic material. At the same time, low values of the ratio b_t/τ_s increase the magnetic flux density in the stator teeth as can be seen in Fig. 5.9 where the permeability of the ferromagnetic material is supposed to have a linear behaviour. The maximum magnetic flux density in stator steel before saturation of the ferromagnetic material is assumed to be 1.7 T. Below this limit the minimum value of the ratio b_t/τ_s should be selected. However the mass of the stator teeth is so small compare to the iron yoke that a limited saturation level is acceptable.

3. The input power presents a minimum for intermediate value of the airgap length g since active and reactive powers differently behave with its variations. When g increases, the same magnetic field density in the airgap can be achieved only by thicker magnets as shown in eq. 5.29. The effective airgap length g_e sensibly increases causing a reduction of the magnetization and leakage inductances and a consequent decrease of the reactive power. Conversely,

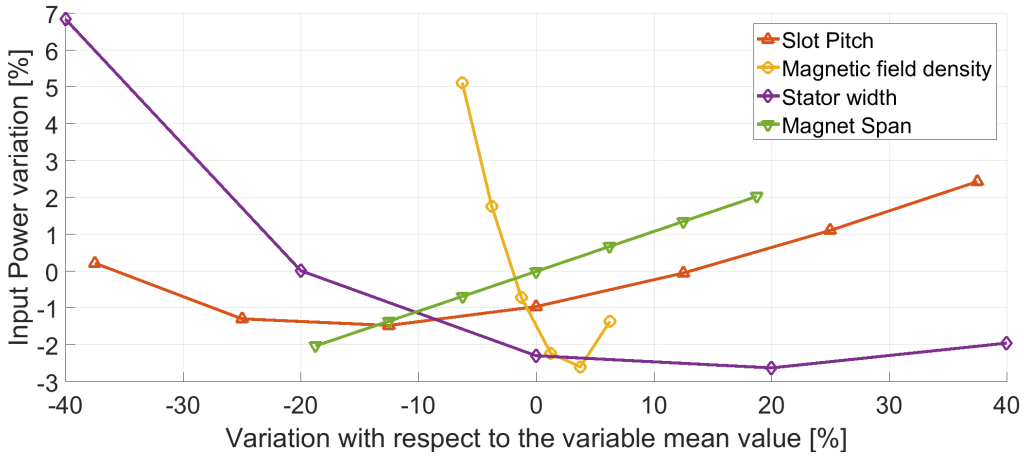

Figure 5.10: Percentage variation of the input power as a function of the last design variables

the active power increases for the higher thrust required to propel a heavier mover with larger magnets and a greater current intensity is needed to generate the thrust. In general one of these effects prevails, but in the point where they counterbalance the input power presents a minimum. The minimum of P_i appears for an airgap length of 7 mm which respects the mechanical constraints of the mover and prevents possible impacts due to vibrations. After the selection of the previous parameters the parametric optimization curves slightly change their appearance as shown in Fig. 5.10. In order to correctly select the value of the next variables these updated curves should be considered.

4. The slot pitch curve shown in Fig. 5.10 is related to the variation of the pole pitch according to eq. 5.25. The pole pitch length is limited by the max frequency that can be achieved by the state of the art switching technology commercially available today. Research is moving towards the design and testing of high voltage semiconductor switches that connected in series may be capable of handling up to 10-20 kV at 300 Hz [110]. Series connected SiC p-IGBTs with 12kV stopping voltage presented in [111] may be suitable for EML applications. Considering 300 Hz as peak frequency and an end-speed of 85.73 m/s, the minimum pole pitch is approximately 150 mm. The respective slot pitch can be computed from eq. 5.25 and is approximately 117 mm. The input power curve associated with the slot pitch in Fig. 5.10 presents a minimum because

active and reactive power differently behave with the variation of the pole pitch. When the pole pitch increases, the length and the mass of the mover grow and a thrust progressively more intense is needed. The armature current increases as well intensifying the Joule losses in stator winding causing a decrease of the efficiency. Even though the magnetizing inductance and the leakage inductance of the stator harmonics increase with the pole pitch as shown in eqs. 5.56 and 5.62 respectively, the power factor increases for the sharp decrement of the supplied frequency. In general one of these effects prevails, but when they counterbalance the input power presents a minimum. It is recommended to select of value of the slot pitch close to the minimum input power.

5. In order to correctly explain the rationale behind the selection of the stator width, the chart with updated parametric optimization curves shown in Fig. 5.10 is considered. The input power presents a minimum in correspondence to a stator width of approximately 3 m. With a larger stator the active surface of the machine increases and the current required to produce the thrust reduces. Both efficiency and power factor benefit from having a synchronous machine with a larger l_s and a lower rated current. However this effect is counteracted by an always increasing mover weight that requires more active power to accelerate it at the same rate and by the increase of the motor inductances which are proportional to l_s. In general one of the two tendencies prevails on the other, but in the point where they counterbalance the input power presents a minimum. The selection of the value of the stator width requires further structural considerations similar to those made for the linear induction motor in Section 4.4. When the yoke thickness is selected on the basis of the stainless steel structural properties as shown in eq. 5.24 and comparing the width that achieves the minimum output power and the length of the active area of the LPMSM's mover (approximately 3.0 m and 4.3 m respectively) with the curves shown in Figs. 4.23 and 4.22 a buckling factor of 4 is expected. Although the structural reinforcement provided by lateral plates and magnets should attain a buckling factor larger than 4, at this design stage is preferable to reach higher buckling factor with narrower movers. A narrow mover also entails less magnetic material and a reduction of weight and costs.

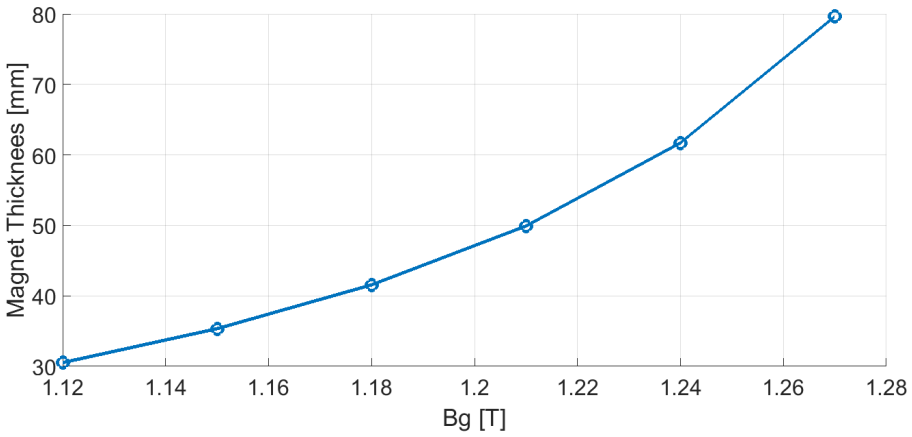

Figure 5.11: Variation of the magnet thickness with respect to the magnetic flux density in the airgap

6. According to the parametric analysis results the best performance is achieved when the ratio $l_m/\tau = 1$ as shown in Fig. 5.10. However, the algorithm does not consider the leakage that is associated with the magnetic flux that is compelled to travel to the neighbouring poles when the distance between magnets is shorter than the airgap. In order to take into account this effect the selected value of l_m/τ is such that $\tau - l_m$ is greater than g.

7. High magnetic field densities in the airgap allow the generation of the required thrust with a reduced stator current. Therefore the motors that achieves high B_g usually have higher efficiencies and power factors. However, according to eq. 5.29 the closer the required magnetic field density in the airgap is to the remnant field density of the magnets, the thicker the magnets have to be. The variation of the magnet thickness with respect to the magnetic flux density in the airgap is shown in Fig. 5.11 considering a remnant flux of 1.39 T of NdFeB magnets of grade N48 Chinese standard. The augmented magnet thickness causes an increase of the mover mass and of the thrust required to propel it. As for the previous variables the effects counterbalanced a present a minimum that also corresponds to acceptable value of h_m.

The design variables that satisfy the design constraints and achieve the minimum input power are reported in Table 5.8. The motor geometrical characteristics, the electric parameters and the electromagnetic performance that were calculated by

Table 5.8: Design variables selected through parametric optimization

g	7.0 mm
τ_s	120 mm
B_g	1.21 T
l_s	2000 mm
l_m/τ	0.90
b_{t/τ_s}	0.4
N_c	2

Table 5.9: Linear permanent magnet synchronous motor data

Geometrical Features		**Electric Parameters**		**Performance**	
Tooth width	48 mm	Frequency	277.8 Hz	Mover mass	8286 kg
Slot Opening	72 mm	Number of coils	48	Mover thrust	48.77 kN
Slot height	2.8 mm	Carter coefficient	1.774	Required thrust	551.67 kN
Back Iron	106 mm	Turns per phase	96	Thrust density	63.85 kN/m^2
Yoke thickness	14 mm	Voltage Peak	17.09 kV	Joule losses	559.2 kW
Pole pitch	154.3 mm	Current (RMS)	1128 A	Active power	47.89 MW
End-coil length	198 mm	Tooth field	2.42 T	Reactive power	32.47 MW
Magnet span	139 mm	L_l	2.8 mH	Input Power	57.86 MW
Magnet thick.	49.9 mm	L_m	2.0 mH	Efficiency	0.988
Mover length	4333 mm	Resistance	0.157 Ω	Power Factor	0.828

the parametric optimization algorithm with the input variables in Table 5.8 are listed in Table 5.9. This data will be implemented in the FEA software and in transient model based on the multi-layer theory.

5.4 Multi-Layer Theory

The evaluation of the magnetic field distribution across linear synchronous machines is fundamental to determine the forces acting upon the mover. The method that is proposed to model the magnetic field in the double-sided LPMSM was only used to represent the field distribution in single-sided linear machines [112]. This method is based on the solution of the Maxwell equations on a continuous structure organized in layers of material with different electromagnetic properties. The action of the stator currents and of the permanent magnets is simulated by current sheets opportunely located inside the machine. Due to the stratified nature of the

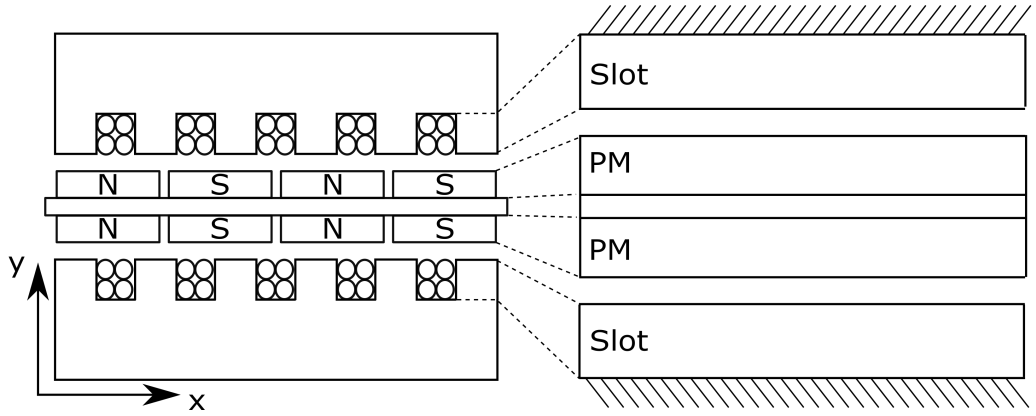

Figure 5.12: Structural simplification of the MLT applied to a double-sided LPMSM

model, the method is named Multi-Layer Theory (MLT).

The MLT is a linear 2D model that replaces the slotted structure of the stator and the permanent magnets with a continuous medium. A schematic of the layered structure that is implemented in MLT is shown in Fig. 5.12. The continuous region that replaces the stator slots is characterized by different permeabilities along the x-axis and the y-axis which are respectively

$$\mu_x = \frac{\mu_0 \mu_r}{1 + \frac{b_s}{\tau_s}(\mu_r - 1)} \tag{5.74}$$

$$\mu_y = \mu_0 \left[\frac{b_s}{\tau_s} + \mu_r \left(1 - \frac{b_s}{\tau_s} \right) \right] \tag{5.75}$$

where μ_r is the recoil permeability of the iron core. The magnet's recoil permeability μ_{PM} corresponds to the slope of the recoil line in the material hysteresis loop also called demagnetization curve. The value of the recoil permeability of NeFeB permanent magnets is very close to μ_0 ($\mu_{PM} = 1.03\mu_0$), so that the permeability of the void can be considered in its place without introducing any significant errors. Since the permeability of the air in the gaps between magnets is μ_0 as well, the layer that replaces the PMs can be considered as made out of an isotropic material with constant permeability. The permeability of the stator yoke is considered to be infinite whereas the permeability of the mover yoke is considered to be equal to μ_0. Indeed, the mover's yoke is made out of stainless steel whose magnetic permeability ranges between $1.003\mu_0 - 7\mu_0$ and no significant

errors are introduced considering μ_0 for simplicity.

MLT is based on the assumption of linear behaviour of the teeth material with given magnetic permeability which remains constant independently from the value of the magnetic field. This hypothesis limits the accuracy of the model especially at high magnetic field densities, but it is commonly accepted to neglect the non-linearity of the ferromagnetic hysteresis loop adding eventual hysteresis losses later on in the design. Even the PM material is supposed to behave linearly which holds true for the majority of the application where the stator field is not strong enough to demagnetize the magnets.

In this work only the effect of the fundamental magnetic wave is investigated, since the main purpose of the MLT is to determine the synchronous thrust. However, the effects of the secondary harmonics can be implemented adopting the superposition principle and computation techniques similar to those described for the fundamental wave. The permanent magnet and the stator magnetomotive force fundamental can be expressed respectively as

$$MMF_{PM} = \frac{4}{\pi} \sin\left(\frac{\pi}{2}\frac{l_m}{\tau}\right) \frac{B_r h_m}{\mu_{PM}} \cos\left(\frac{\pi}{\tau}x\right) \tag{5.76}$$

$$MMF_{st} = \frac{m\sqrt{2}N_1 I k_w}{\pi p} \sin\left(\frac{\pi}{\tau}x\right) \tag{5.77}$$

where l_m is the magnet span, B_r is the PM's remnant magnetic field density, h_m is the magnet thickness, N_1 is the number of turns per phase and I is the stator current. The equivalent current sheet of any magnetomotive force is given by the derivative $A = \partial MMF/\partial x$. It follows that the PM and stator equivalent current sheets are respectively

$$A_{PM} = -\frac{4}{\tau} \sin\left(\frac{\pi}{2}\frac{l_m}{\tau}\right) \frac{B_r h_m}{\mu_{PM}} \sin\left(\frac{\pi}{\tau}x\right) \tag{5.78}$$

$$A_{st} = \frac{m\sqrt{2}N_1 I k_w}{\tau p} \cos\left(\frac{\pi}{\tau}x\right) \tag{5.79}$$

The equivalent currents sheet are implemented in the layered structured as infinitely thin current filaments as shown in Fig. 5.13.

The governing equations which are used to determine the field in the various layers shown in Fig. 5.13 are two of Maxwell equations which are also called

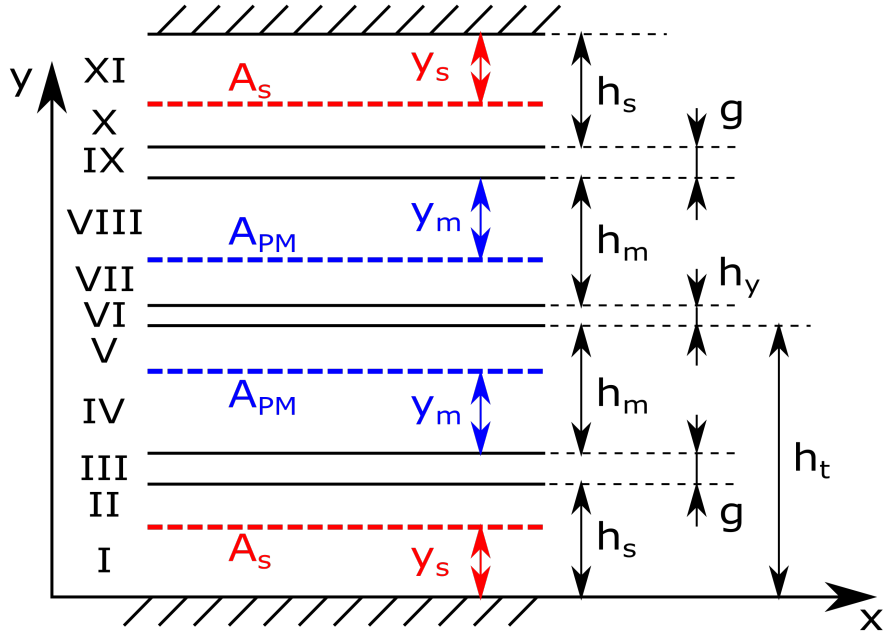

Figure 5.13: Multi-layered structure of a double-sided LPMSM with regions and current sheets considered by MLT

Faraday's law and Ampere's law:

$$\nabla \times \vec{E} = -\frac{\partial \vec{B}}{\partial t} \tag{5.80}$$

$$\nabla \times \vec{B} = \mu_0 \left(\vec{J} + \varepsilon_0 \frac{\partial \vec{E}}{\partial t} \right) \tag{5.81}$$

Both the magnetic flux density $\vec{B} = \mu \vec{H}$ and the electrostatic field $\vec{E}$ vary sinusoidally as the armature current sheet A_s and the excitation current sheet A_{PM}. In general, a sinusoidal wave both in time and space can be expressed in complex notation as

$$\vec{A} = A e^{j\left(\omega t - \frac{\pi}{\tau} x\right)} \tag{5.82}$$

The electric field in the layers of Fig. 5.13 exists only along z direction, so that the curl product in eq. 5.80 has only two components along x and y axes. Moreover, the derivative on the right hand side of the Faraday law in eq. 5.80 can be calculated considering the sinusoidal variation in eq. 5.82. Restricting the

analysis to the amplitude of the field wave yields

$$\frac{\partial E_z}{\partial y} = -j\omega\mu_x H_x \tag{5.83}$$

$$\frac{\partial E_z}{\partial x} = j\omega\mu_y H_y \tag{5.84}$$

The complex notation in eq. 5.82 allows the expression of the derivatives

$$\frac{\partial H_y}{\partial x} = -j\frac{\pi}{\tau}H_y \tag{5.85}$$

$$\frac{\partial E_z}{\partial x} = -j\frac{\pi}{\tau}E_z \tag{5.86}$$

Combining eqs. 5.84 and 5.86 yields

$$H_y = -\frac{\pi}{\tau}\frac{E_z}{\omega\mu_y} \tag{5.87}$$

Then, eq. 5.87 can be inserted in eq. 5.85 obtaining

$$\frac{\partial H_y}{\partial x} = j\frac{\pi^2}{\tau^2}\frac{E_z}{\omega\mu_y} \tag{5.88}$$

The MLT stratified structure is done in such a way that in the inner area of each layer there is no current flowing in z direction ($\vec{J} = 0$), since the current sheets are located just outside the boundaries. Considering that the second term on the right hand side of eq. 5.81 is negligible, Ampere's law can be rewritten as $\nabla \times \vec{H} = 0$. In particular, the third components of the curl product of $\vec{H}$ is

$$\frac{\partial H_y}{\partial x} - \frac{\partial H_x}{\partial y} = 0 \tag{5.89}$$

Substituting eq. 5.89 in eq. 5.88 and deriving with respect to y yields

$$\frac{\partial^2 H_x}{\partial y^2} = j\frac{\pi^2}{\tau^2\omega\mu_y}\frac{\partial E_z}{\partial y} \tag{5.90}$$

From eqs. 5.90 and 5.83 the partial differential equation for H_x becomes

$$\frac{\partial^2 H_x}{\partial y^2} - \frac{\pi^2}{\tau^2}\frac{\mu_x}{\mu_y}H_x = 0 \tag{5.91}$$

An equation for H_y can be determined from eqs. 5.85 and 5.89 as

$$H_y = j\frac{\tau}{\pi}\frac{\partial H_x}{\partial y} \tag{5.92}$$

The partial different equation 5.91 must be solved for all the layers of the structure in Fig. 5.13 to compute the field H_x, whereas the field H_y can be calculated using eq. 5.92. Using Fig. 5.13 as reference to identify the regions where Maxwell equations are solved, the solutions for all the layers are listed as follows.

Region I $(0 \leq y \leq y_s)$

$$\begin{aligned} H_{x\,I} &= H_1\left[\sinh\left(\frac{\pi}{\tau}\sqrt{\frac{\mu_x}{\mu_y}}y\right) + C_1\cosh\left(\frac{\pi}{\tau}\sqrt{\frac{\mu_x}{\mu_y}}y\right)\right] \\ H_{y\,I} &= jH_1\sqrt{\frac{\mu_x}{\mu_y}}\left[\cosh\left(\frac{\pi}{\tau}\sqrt{\frac{\mu_x}{\mu_y}}y\right) + C_1\sinh\left(\frac{\pi}{\tau}\sqrt{\frac{\mu_x}{\mu_y}}y\right)\right] \end{aligned} \tag{5.93}$$

Region II $(y_s \leq y \leq h_s)$

$$\begin{aligned} H_{x\,II} &= H_2\left[\sinh\left(\frac{\pi}{\tau}\sqrt{\frac{\mu_x}{\mu_y}}(y-y_s)\right) + C_2\cosh\left(\frac{\pi}{\tau}\sqrt{\frac{\mu_x}{\mu_y}}(y-y_s)\right)\right] \\ H_{y\,II} &= jH_2\sqrt{\frac{\mu_x}{\mu_y}}\left[\cosh\left(\frac{\pi}{\tau}\sqrt{\frac{\mu_x}{\mu_y}}(y-y_s)\right) + C_2\sinh\left(\frac{\pi}{\tau}\sqrt{\frac{\mu_x}{\mu_y}}(y-y_s)\right)\right] \end{aligned} \tag{5.94}$$

Region III $(h_s \leq y \leq h_s + g)$

$$\begin{aligned} H_{x\,III} &= H_3\left[\sinh\left(\frac{\pi}{\tau}(y-h_s)\right) + C_3\cosh\left(\frac{\pi}{\tau}(y-h_s)\right)\right] \\ H_{y\,III} &= jH_3\left[\cosh\left(\frac{\pi}{\tau}(y-h_s)\right) + C_3\sinh\left(\frac{\pi}{\tau}(y-h_s)\right)\right] \end{aligned} \tag{5.95}$$

Region IV $(h_s + g \leq y \leq h_s + g + y_m)$

$$\begin{aligned} H_{x\,IV} &= H_4\left[\sinh\left(\frac{\pi}{\tau}(y-h_s-g)\right) + C_4\cosh\left(\frac{\pi}{\tau}(y-h_s-g)\right)\right] \\ H_{y\,IV} &= jH_4\left[\cosh\left(\frac{\pi}{\tau}(y-h_s-g)\right) + C_4\sinh\left(\frac{\pi}{\tau}(y-h_s-g)\right)\right] \end{aligned} \tag{5.96}$$

Region V $(h_s + g + y_m \leq h_t)$

$$\begin{aligned} H_{xV} &= H_5 \left[\sinh\left(\frac{\pi}{\tau}(y - h_s - g - y_m)\right) + C_5 \cosh\left(\frac{\pi}{\tau}(y - h_s - g - y_m)\right)\right] \\ H_{yV} &= jH_5 \left[\cosh\left(\frac{\pi}{\tau}(y - h_s - g - y_m)\right) + C_5 \sinh\left(\frac{\pi}{\tau}(y - h_s - g - y_m)\right)\right] \end{aligned} \tag{5.97}$$

Region VI $(h_t \leq y \leq h_t + h_y)$

$$\begin{aligned} H_{xVI} &= H_6 \left[\sinh\left(\frac{\pi}{\tau}(y - h_t)\right) + C_6 \cosh\left(\frac{\pi}{\tau}(y - h_t)\right)\right] \\ H_{yVI} &= jH_6 \left[\cosh\left(\frac{\pi}{\tau}(y - h_t)\right) + C_6 \sinh\left(\frac{\pi}{\tau}(y - h_t)\right)\right] \end{aligned} \tag{5.98}$$

Region VII $(h_t + h_y \leq y \leq h_t + h_y + h_m - y_m)$

$$\begin{aligned} H_{xVII} &= H_7 \left[\sinh\left(\frac{\pi}{\tau}(y - h_t - h_y)\right) + C_7 \cosh\left(\frac{\pi}{\tau}(y - h_t - h_y)\right)\right] \\ H_{yVII} &= jH_7 \left[\cosh\left(\frac{\pi}{\tau}(y - h_t - h_y)\right) + C_7 \sinh\left(\frac{\pi}{\tau}(y - h_t - h_y)\right)\right] \end{aligned} \tag{5.99}$$

Region VIII $(h_t + h_y + h_m - y_m \leq y \leq h_t + h_y + h_m)$

$$\begin{aligned} H_{xVIII} &= H_8 \left[\sinh\left(\frac{\pi}{\tau}(y - h_t - h_y - h_m + y_m)\right) + C_8 \cosh\left(\frac{\pi}{\tau}(y - h_t - h_y - h_m + y_m)\right)\right] \\ H_{yVIII} &= jH_8 \left[\cosh\left(\frac{\pi}{\tau}(y - h_t - h_y - h_m + y_m)\right) + C_8 \sinh\left(\frac{\pi}{\tau}(y - h_t - h_y - h_m + y_m)\right)\right] \end{aligned} \tag{5.100}$$

Region IX $(h_t + h_y + h_m \leq y \leq h_t + h_y + h_m + g)$

$$\begin{aligned} H_{xIX} &= H_9 \left[\sinh\left(\frac{\pi}{\tau}(y - h_t - h_y - h_m)\right) + C_9 \cosh\left(\frac{\pi}{\tau}(y - h_t - h_y - h_m)\right)\right] \\ H_{yIX} &= jH_9 \left[\cosh\left(\frac{\pi}{\tau}(y - h_t - h_y - h_m)\right) + C_9 \sinh\left(\frac{\pi}{\tau}(y - h_t - h_y - h_m)\right)\right] \end{aligned} \tag{5.101}$$

Region X $(h_t + h_y + h_m + g \leq y \leq 2h_t + h_y - y_s)$

$$\begin{aligned} H_{xX} &= H_{10} \left[\sinh\left(\frac{\pi}{\tau}\sqrt{\frac{\mu_x}{\mu_y}}(y - 2h_t - h_y - y_s)\right) + C_{10} \cosh\left(\frac{\pi}{\tau}\sqrt{\frac{\mu_x}{\mu_y}}(y - 2h_t - h_y - y_s)\right)\right] \\ H_{yX} &= jH_{10} \left[\cosh\left(\frac{\pi}{\tau}\sqrt{\frac{\mu_x}{\mu_y}}(y - 2h_t - h_y - y_s)\right) + C_{10} \sinh\left(\frac{\pi}{\tau}\sqrt{\frac{\mu_x}{\mu_y}}(y - 2h_t - h_y - y_s)\right)\right] \end{aligned} \tag{5.102}$$

Region XI $(2h_t + h_y - y_s \leq y \leq 2h_t + h_y)$

$$\begin{aligned} H_{x\,XI} &= H_{11}\left[\sinh\left(\frac{\pi}{\tau}\sqrt{\frac{\mu_x}{\mu_y}}(y-2h_t-h_y)\right) + C_{11}\cosh\left(\frac{\pi}{\tau}\sqrt{\frac{\mu_x}{\mu_y}}(y-2h_t-h_y)\right)\right] \\ H_{y\,XI} &= jH_{11}\left[\cosh\left(\frac{\pi}{\tau}\sqrt{\frac{\mu_x}{\mu_y}}(y-2h_t-h_y)\right) + C_{11}\sinh\left(\frac{\pi}{\tau}\sqrt{\frac{\mu_x}{\mu_y}}(y-2h_t-h_y)\right)\right] \end{aligned} \tag{5.103}$$

The distribution of the magnetic field $\vec{H}$ and of the magnetic flux density $\vec{B}$ on the machine cross section can be calculated solving the equations for all the regions of the structure in Fig. 5.13. The equations contain 22 unknown constants which can be determined imposing the following boundary conditions at the respective coordinates.

$y = 0$	$H_{x\,I} = 0$	
$y = y_s$	$H_{x\,I} - H_{x\,II} = A_{st}$	$B_{y\,I} = B_{y\,II}$
$y = h_s$	$H_{x\,II} = H_{x\,III}$	$B_{y\,II} = B_{y\,III}$
$y = h_s + g$	$H_{x\,III} = H_{x\,IV}$	$B_{y\,III} = B_{y\,IV}$
$y = h_s + g + y_m$	$H_{x\,IV} - H_{x\,V} = A_{PM}$	$B_{y\,IV} = B_{y\,V}$
$y = h_t$	$H_{x\,V} = H_{x\,VI}$	$B_{y\,V} = B_{y\,VI}$
$y = h_t + h_y$	$H_{x\,VI} = H_{x\,VII}$	$B_{y\,VI} = B_{y\,VII}$
$y = h_t + h_y + h_m - y_m$	$H_{x\,VII} - H_{x\,VIII} = A_{PM}$	$B_{y\,VII} = B_{y\,VIII}$
$y = h_t + h_y + h_m$	$H_{x\,VIII} = H_{x\,IX}$	$B_{y\,VIII} = B_{y\,IX}$
$y = h_t + h_y + h_m + g$	$H_{x\,IX} = H_{x\,X}$	$B_{y\,IX} = B_{y\,X}$
$y = 2h_t + h_y - y_s$	$H_{x\,XI} - H_{x\,X} = A_{st}$	$B_{y\,X} = B_{y\,XI}$
$y = 2h_t + h_y$	$H_{x\,XI} = 0$	

The substitution of the boundary conditions leads to a non-linear system of equations because of the presence of unknowns multiplied between each other. The linearity can be recovered by replacing these products with some additional auxiliary variables. The solution of the system of the equations determines the value of the integration constants and allows to calculate the value of the magnetic field in any point of the machine cross section.

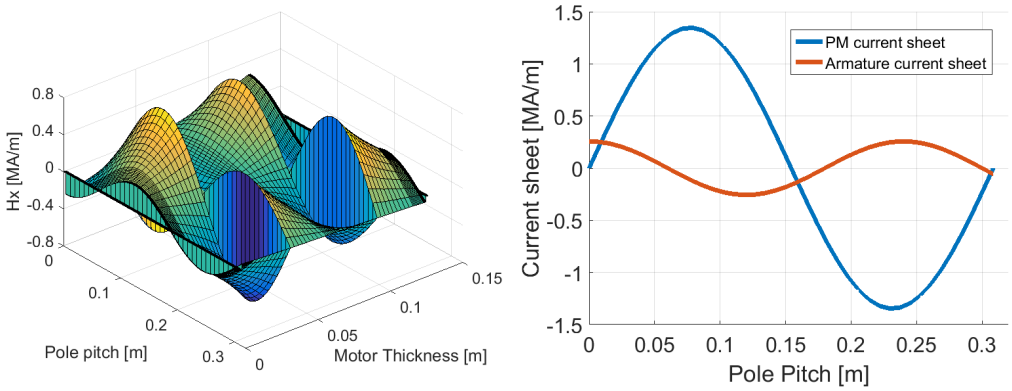

(a) Magnetic field (b) Current sheet

Figure 5.14: Magnetic field over a single pole pair computed by the Multi-Layer Theory

Since in the real machine the armature and excitation fields are not produced by infinitely thin current sheets, the location of the current filaments is varied along the slot height and along the mover height. The average of the results returns a more accurate estimation of the magnetic field across the motor which is computed as

$$H_x = \frac{1}{h_m h_s} \int_0^{h_m} \int_0^{h_s} H_x(y_m, y_s)\, dy_m\, dy_s \tag{5.104}$$

The calculation of the magnetic field is done over a grid of points that discretizes all the regions in Fig. 5.13. The discretization is limited to a single pole pair since the same wave profile periodically repeats over the other poles. The magnetic field H_x calculated by the MLT is shown in Fig. 5.14a. The discontinuities of the field in correspondence of the average location of the current sheets can be observed as well. The intensity of the armature and PM current sheets used by MLT for the synchronous launcher are reported in Fig. 5.14b.

MLT has determined the magnetic field considering a continuous anisotropic structure in correspondence of the stator slots. In order to evaluate the effects of the stator slots on the magnetic flux density distribution a correction function should be introduced. This function represents the relative permeance variation across 2D model of the synchronous motor. Accounting for slot and slot opening

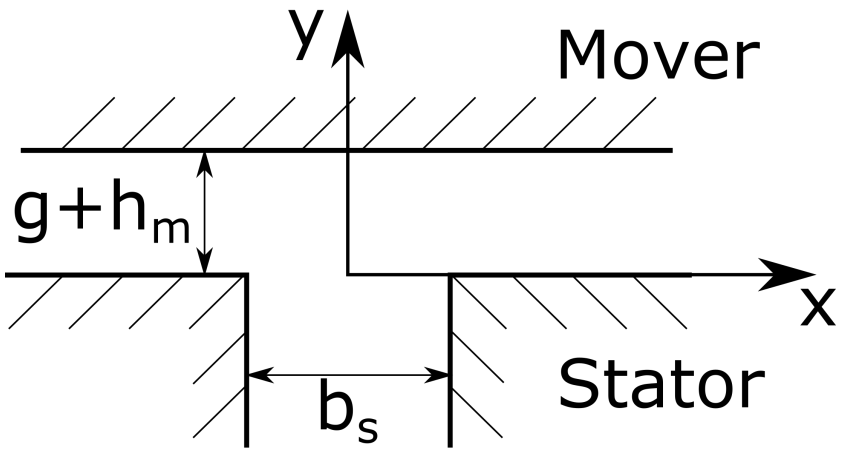

Figure 5.15: Sketch of the slot model and of the respective frame of reference considered by the permeance function

distribution the magnetic flux density becomes

$$B_y = B_{y\,MLT} \cdot \lambda_g(x,y) \tag{5.105}$$

where λ_g is the relative permeance which is a function of the Cartesian coordinate x and y and $B_{y\,MLT}$ is the magnetic flux density distribution computed by MLT.

This method can be especially applied to machine with rectilinear slots and long effective airgap $g_m = g + h_m$ like the synchronous electromagnetic launcher. In particular, the technique is applied on a single slot with a frame of reference located as it is shown in Fig. 5.15. Later the relative permeance function is extended to include all the other slots under a single pole pair. The relative permeance of the slotted region can be calculated by conformal transformation mapping applied between the mover and stator surface as [113]

$$\lambda_g(x,y) = \begin{cases} 1-\beta(y)\left[1-\cos\left(\frac{2\pi}{0.8}\frac{x}{b_s}\right)\right] & \text{for } 0 \leq \mid x \mid \leq 0.4b_s \\ 1 & \text{for } 0.4b_s \leq \mid x \mid \leq b_s/2 \end{cases} \tag{5.106}$$

where the function $\beta(y)$ depends on the transversal position and is determined by

conformal transformation as [113]

$$\beta(y) = \frac{1}{2}\left[1 - \frac{1}{\sqrt{1+\left(\frac{b_s}{2g_m}\right)^2(1+u^2)}}\right] \tag{5.107}$$

where u satisfies the equality

$$y\frac{\pi}{b_s} = \frac{1}{2}\ln\left[\frac{\sqrt{1+\left(\frac{b_s}{2g_m}\right)^2+u^2}+u}{\sqrt{1+\left(\frac{b_s}{2g_m}\right)^2+u^2}-u}\right] + \frac{2g_m}{b_s}\arctan\left(\frac{2g_m}{b_s}\frac{u}{\sqrt{1+\left(\frac{b_s}{2g_m}\right)^2+u^2}}\right) \tag{5.108}$$

The permeance function for a single slot is shown in Fig. 5.16a, whereas the permeance function for the slots under a single pole pair is shown in Fig. 5.16b. Figs. 5.16c and 5.16d compare the magnetic flux density estimated by the MLT and the flux density corrected with relative permeance.

The analytical method presented so far is useful to determine the magnetic field and the flux density distribution inside a synchronous motor. MLT can be also used to determine the no-load induced voltage E_s and the longitudinal inductance L_{long} of the machine. These parameters are very important from the design point of view, since they are related to the machine thrust F_x and to the magnetizing inductance L_m according to the laws

$$F_x = \frac{3}{2}\frac{\pi}{\tau}\frac{E_s}{\omega}I \tag{5.109}$$

$$L_m = L_{long} - L_{ls} \tag{5.110}$$

where ω is the angular velocity of the supplied voltage and L_{ls} is the slot leakage inductance that is computed as

$$L_{ls} = \frac{\mu_0 l_s}{2pq}\left(\frac{h_s}{3b_s}+\frac{h_{ss}}{b_s}\right)\left(3\frac{\tau_c}{\tau}+1\right)N_1^2 \tag{5.111}$$

The no-load induced voltage can be determined solving the MLT with $A_{st} = 0$. In this situation no power is supplied to the armature and only the action of the PMs is included. The RMS value of the voltage induced in a single phase of the

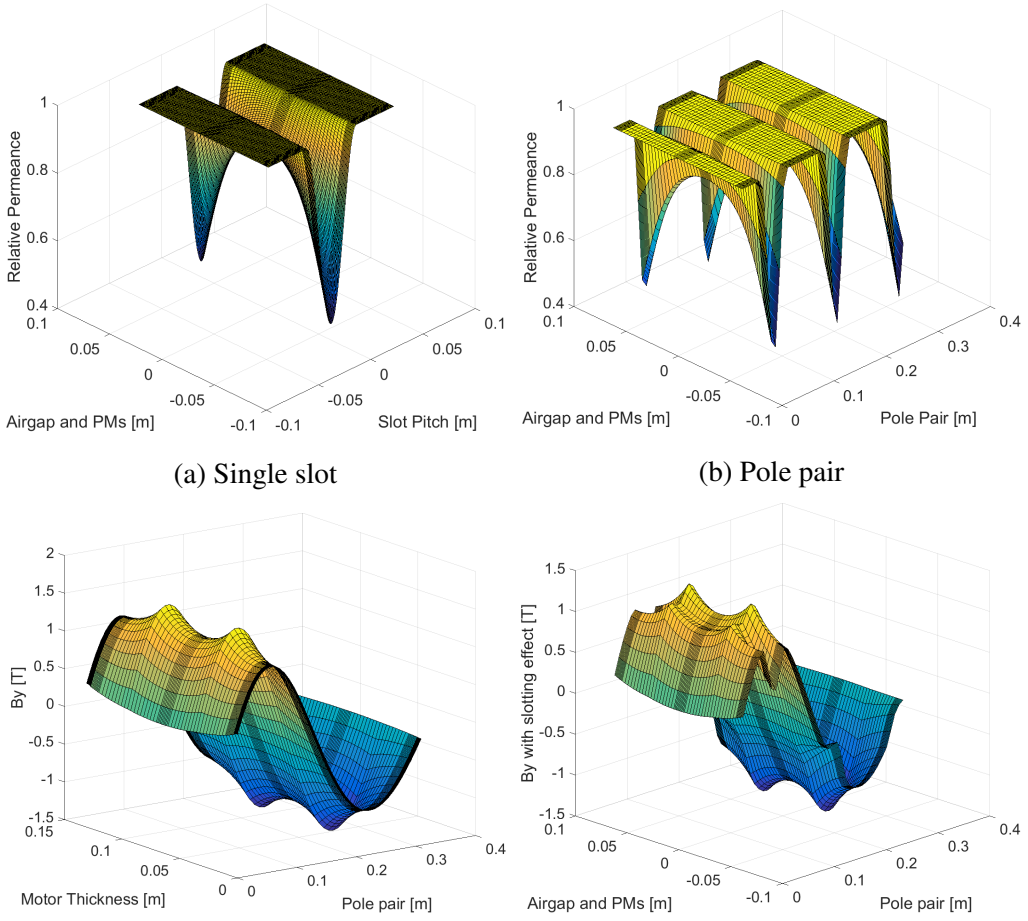

(a) Single slot

(b) Pole pair

(c) MLT flux density

(d) Corrected flux density

Figure 5.16: Magnetic flux density along the y-axis computed by the MLT and corrected with the relative permeance function of the stator slotted structure

machine is proportional to the flux linkage produced by the permanent magnets as

$$E_s = \omega \frac{\Psi_{PM}}{\sqrt{2}} \tag{5.112}$$

where the flux linkage for a single phase is

$$\Psi_{PM} = N_1 k_w \tau l_s \frac{2}{\pi} B_{ys} \tag{5.113}$$

where B_{ys} is the average of the magnetic flux density computed by the MLT over

the stator slots and is computed as

$$B_{ys} = \frac{1}{h_s}\int_0^{h_s}\frac{1}{h_m}\int_0^{h_m} B_y(y_m)dy_m dy \tag{5.114}$$

The inner integral in eq. 5.114 represents the average of the magnetic flux density produced by current sheets on different locations along the magnet thickness.

Having determined the no-load induced voltage it is possible to proceed with calculation of the longitudinal inductance. The MLT allows the calculation of the magnetic flux density distribution with no excitation field setting the current sheet $A_{PM} = 0$. The longitudinal inductance is obtained from the induced voltage E_l on the stator coils when there is no excitation field and the stator current intensity is equal to 1 A as

$$L_{long} = \frac{E_l}{\omega I} \tag{5.115}$$

The voltage induced in the stator coil by only the action of the stator current sheet A_{st} is

$$E_l = \frac{\omega}{\sqrt{2}} N_1 k_w \tau l_s \frac{2}{\pi} B_{yl} \tag{5.116}$$

where the magnetic field B_{yl} is

$$B_{yl} = \frac{1}{h_s^2}\int_0^{h_s}\int_0^{h_s} B_y(y, y_s)dy_s dy \tag{5.117}$$

where the inner integral represents the average of the effects produced by the current sheet A_{st} on different location along the stator slot. These parameters and the other machine features determined in Section 5.3 are implemented in the transient analytical model whose results will be compared with the finite element analysis outcomes.

5.5 Transient Electromagnetic Model

The transient of electrical machines is described by the mean of differential equations that characterize the response of the motor to the applied voltage or current.

A method that is widely use to represent the transient behaviour of synchronous machines is based on the *direct-quadrature axes model* also called *dq model*. The theory proposes to resolve the electromagnetic equations into two mutually perpendicular components along the direct-quadrature (dq) frame of reference. In synchronous machines the dq frame travels at the same speed of the magnetic field wave in the airgap and therefore it is synchronized with the moving part of the motor. In this frame of reference the partial differential equations that represent the transient evolution of the machine are

$$U_d = RI_d + L_d \frac{\partial I_d}{\partial t} - \omega L_d I_q \tag{5.118}$$

$$U_q = RI_q + L_q \frac{\partial I_q}{\partial t} + \omega (L_q I_d + \Psi_{PM}) \tag{5.119}$$

where the subscripts d and q indicate the axis where the respective voltage, current or inductance is evaluated, ω represents the instantaneous angular velocity and Ψ_{PM} is the the magnetic flux computed by the MLT as shown in eq. 5.113. The angular velocity of an alternating current supplied at increasing frequency can be computed as

$$\omega = \frac{\pi}{\tau} \frac{v_s}{2} \tag{5.120}$$

where 2 at the denominator is added considering the linear variation of the frequency over time (see eq. 4.149).

The model expressed by eqs. 5.118 and 5.119 is valid when the MMF and EMF waves are sinusoidal. The standard dq model of electrical machinery can not be applied to achieve high fidelity results when large secondary harmonics are present. The thrust pulsations due to the magnets-teeth interaction and to the space harmonics are not considered by the standard dq model as well. Despite these approximations, eqs. 5.118 and 5.119 are widely used to assess the basic dynamic performance of the synchronous motor.

The inductances of the dq model in eqs. 5.118 and 5.119 can be expressed as

$$L_d = L_{md} + L_l \qquad L_q = L_{mq} + L_l \tag{5.121}$$

where L_{md} and L_{mq} are the direct and quadrature magnetization inductances re-

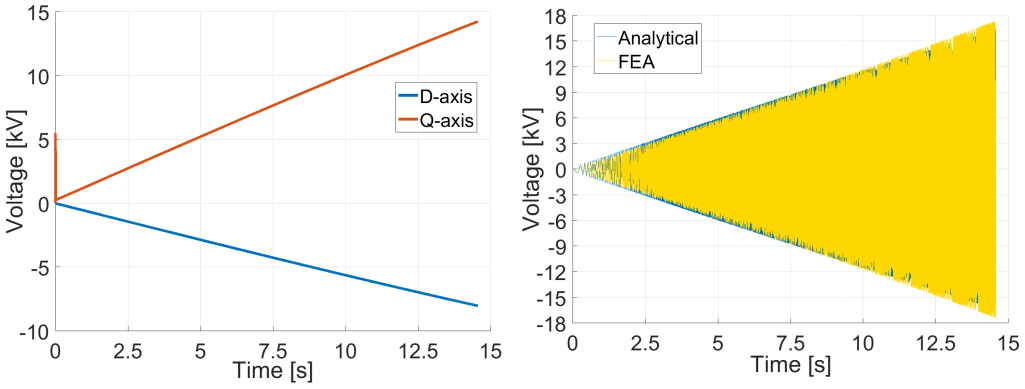

(a) dq components (b) First phase

Figure 5.17: Time evolution of dq voltage and first phase voltage during the launch

spectively. The dq model can be applied to any synchronous motor, but for surfaced-mounted PM machines it can be further simplified. Indeed, in this case L_{md} and L_{mq} are equal to the magnetization inductance L_m computed by the MLT using eq. 5.110 [18]. This means that direct and quadrature inductances L_d and L_q of surface-mounted PM motors have exactly the same value.

A three phase alternating current is supplied to the system where each phase varies in time according to

$$I_A = \sqrt{2} I \cos\left(\frac{\pi}{\tau}\frac{v_s}{2}t\right) \tag{5.122}$$

$$I_B = \sqrt{2} I \cos\left(\frac{\pi}{\tau}\frac{v_s}{2}t - \frac{2}{3}\pi\right) \tag{5.123}$$

$$I_C = \sqrt{2} I \cos\left(\frac{\pi}{\tau}\frac{v_s}{2}t + \frac{2}{3}\pi\right) \tag{5.124}$$

In order to solve the differential equation of the dq model the three phases have to be expressed with respect to the direct-quadrature frame of reference using Park's mathematical transformation [93] which is

$$\begin{bmatrix} I_d \\ I_q \\ I_0 \end{bmatrix} = \frac{2}{3} \begin{bmatrix} \sin\left(\frac{\pi}{\tau}\frac{v_s}{2}t\right) & \sin\left(\frac{\pi}{\tau}\frac{v_s}{2}t - \frac{2}{3}\pi\right) & \sin\left(\frac{\pi}{\tau}\frac{v_s}{2}t + \frac{2}{3}\pi\right) \\ \cos\left(\frac{\pi}{\tau}\frac{v_s}{2}t\right) & \cos\left(\frac{\pi}{\tau}\frac{v_s}{2}t - \frac{2}{3}\pi\right) & \cos\left(\frac{\pi}{\tau}\frac{v_s}{2}t + \frac{2}{3}\pi\right) \\ \frac{1}{2} & \frac{1}{2} & \frac{1}{2} \end{bmatrix} \begin{bmatrix} I_A \\ I_B \\ I_C \end{bmatrix} \tag{5.125}$$

The dq axis components of the current can be inserted in eqs. 5.118 and 5.119 to

find the dq axis components of the voltage which are shown in Fig. 5.17a. Using the inverse Park transformation the amplitude of the phase voltage becomes

$$\begin{bmatrix} U_A \\ U_B \\ U_C \end{bmatrix} = \begin{bmatrix} \cos\left(\frac{\pi}{\tau}\frac{v_s}{2}t\right) & -\sin\left(\frac{\pi}{\tau}\frac{v_s}{2}t\right) \\ \cos\left(\frac{\pi}{\tau}\frac{v_s}{2}t - \frac{2}{3}\pi\right) & -\sin\left(\frac{\pi}{\tau}\frac{v_s}{2}t - \frac{2}{3}\pi\right) \\ \cos\left(\frac{\pi}{\tau}\frac{v_s}{2}t + \frac{2}{3}\pi\right) & -\sin\left(\frac{\pi}{\tau}\frac{v_s}{2}t + \frac{2}{3}\pi\right) \end{bmatrix} \begin{bmatrix} U_d \\ U_q \end{bmatrix} \tag{5.126}$$

The first phase voltage U_A computed using the dq model and the MLT is compared with FEA results in Fig. 5.17b. The voltage computed with the analytical method considers the losses associated with the end windings and predicts a voltage amplitude which is slightly greater than the one computed by the finite element method.

The thrust of a synchronous machine can be computed from the electrical features of the motor as

$$F_x = \frac{3}{2}\frac{\pi}{\tau}\left[\Psi_{PM} + (L_d - L_q)I_d\right] I_q \tag{5.127}$$

For a surface-mounted PM machine the second term of eq. 5.127 disappears since $L_d = L_q$.

The transient analysis of the LPMSM is also performed through a finite element software for electromagnetic simulations. As for LIMs, the finite element software for LPMSM draws the machine using the geometrical data determined by parametric optimization. For a shorter computational time, FEA is carried out only on half machine taking advantage of the longitudinal symmetry. The analysis is performed on a single stage while the whole length of the machine is simulated by even periodic boundary conditions opportunely located to reproduce the distance between stages. The machine is wound using the coils sequence shown in Section 5.2 which are connected to a current source with variable frequency. Since the simulation is run without a control system, a linearly increasing speed is imposed to the mover.

The thrust profiles computed using MLT and FEA are compared in Fig. 5.18. The value computed by the parametric optimization procedure and the required thrust to accelerate an A320-200 aircraft are shown as well. MLT and the dq model estimates a slightly stronger magnetic interaction and a higher thrust than the parametric optimization algorithm. However, the MLT thrust profiles exactly

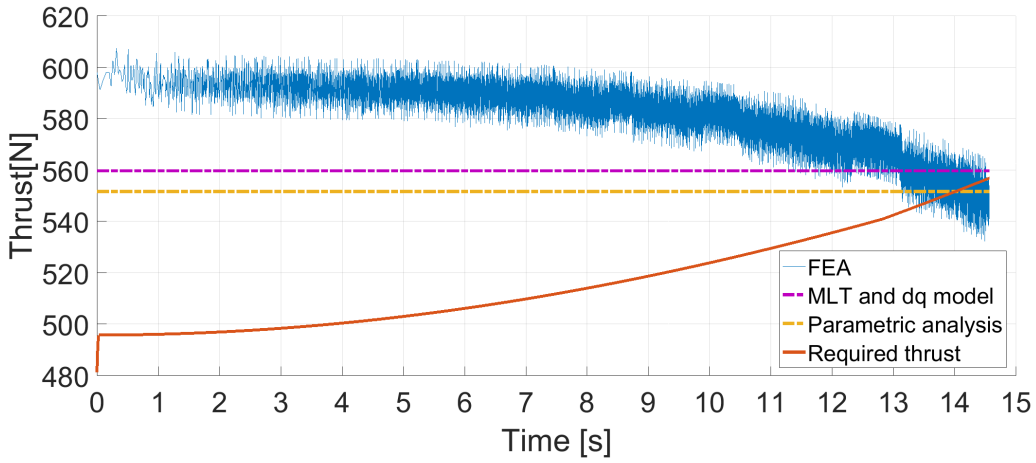

Figure 5.18: Comparison between thrust profiles computed using different methods

matches the required thrust by the A320-200 aircraft at the end of the acceleration. The thrust predicted by MLT is constant because it assumes linear behaviour of the stator material and it does not consider the effects of secondary harmonics. MLT does not consider the disturbances caused by the motion along the stator slotted structure and the respective thrust in Fig. 5.18 profile present no oscillations. On the contrary, FEA thrust profile presents several oscillations that are mainly due to the slot openings. The output thrust determined with FEA gradually decreases due to the effects of non-linear iron and of the eddy current losses in the magnets and in the mover yoke caused by secondary harmonics. Since there is no control on the power source of the machine simulated by FEA, the current intensity supplied at the begging of the launch produces a much stronger thrust that gradually matches those predicted by the other methods as the mover gains speed.

The efficiency of the PM synchronous machine can be computed as

$$\eta = \frac{F_x v_s}{F_x v_s + 3RI^2} \tag{5.128}$$

where the iron losses were not considered since they are negligible with respect to the Joule losses in the stator windings. The power factor of the LPMSM can be computed from the dq components of the voltage as

$$\cos\phi = \frac{U_q}{\sqrt{U_q^2 + U_d^2}} \tag{5.129}$$

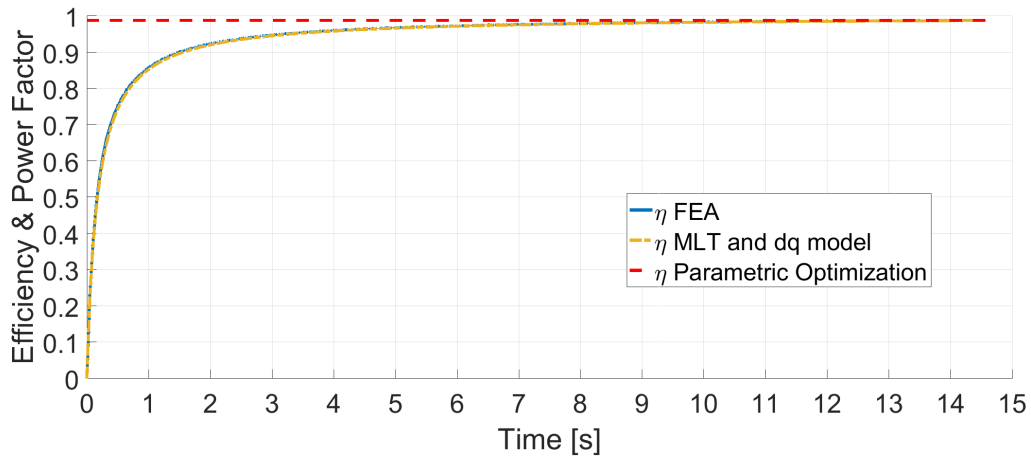

Figure 5.19: Comparison between efficiency profiles computed using different methods

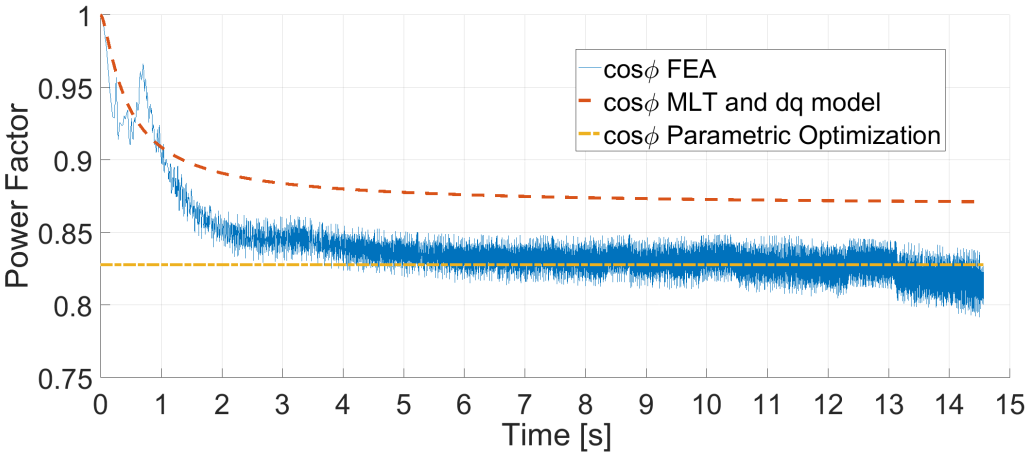

Figure 5.20: Comparison between power factor profiles computed using different methods

Efficiency and power factor computed by dq model and FEA are compared in Figs. 5.19 and 5.20 respectively. The same figures show the value of efficiency and power factor computed by parametric optimization at the end of the launch. The efficiency profiles computed using the different methods presented in this chapter present a very good agreement across the whole acceleration.

The different methods used to calculate the power factor show different tendencies in Fig. 5.20. Since the value of the power factor is proportional to the active power and to the thrust of the machine, the behaviour of the power factor computed by FEA approximately reflects the thrust profiles in Fig. 5.18. Starting from one, FEA thrust gradually decreases to match the power factor estimated by the

parametric optimization algorithm. MLT predicts the greatest power factor since the method slightly underestimates the leakage inductance.

5.6 Thermal Analysis

The thermal heat transfer model is applied to LPMSM to determine the temperature change of the surface-mounted magnets and of the yoke during the launch. It is important to estimate the temperature rise of the magnetic material to prevent demagnetization. Temperature increases in magnets are due to the Joule losses caused by eddy currents induced by the secondary harmonics of the magnetic wave in the magnetic material. The intensity of secondary harmonics is particularly significant in fractional-slot motors like the synchronous launcher under investigation.

When a strong magnetic field is established in opposition with the magnet magnetization, it will cause demagnetization if it is sufficiently intense. However, NdFeB magnets can withstand strong external demagnetizing fields due to their high intrinsic coercive force. In electromagnetic launch systems the field generated by the stator coils should not be strong enough to threaten demagnetization. However, NdFeB's demagnetization curve and coercive force are strongly temperature dependent and sharply decrease when the magnet operates at high temperatures.

The mathematical model used to estimate the temperature evolution in the mover assumes that no heat is transferred between the yoke and the magnets. The assumptions of perfect thermal insulation is supported by the low conductivity of the glue that is used to stick the magnets on the yoke surface. However, the temperature delta between magnets and yoke may generate a heat flow that in this analysis is neglected for simplicity. Under this assumption the heat transfer problem for the yoke and the magnets can be solved separately.

5.6.1 Thermal Analysis of the Mover's Yoke

The transient heat transfer problem for the LPMSM mover's yoke may be solved by adopting the same techniques exploited to determine the temperature transient of the LIM's secondary. However, in this case a detailed transient thermal analysis

is not required for the following reasons:

- Since the mover is synchronized with the magnetic wave, the eddy currents are induced only by the secondary harmonics. In LIM the currents induced in the aluminium plate are mainly due to the fundamental wave and the current density reaches higher intensities;

- The eddy current intensity is further reduced by the low conductivity of stainless steel;

- The LIM aluminium plate is located in proximity of the primary windings where the magnetic flux oscillations are more intense. The stainless steel yoke is located behind the magnets at a larger distance from the stator coils;

- Creep becomes a dominant effect when the temperature of stainless steel exceeds the limit $T_{cr} = 0.49 \cdot T_m$ where the melting temperature T_m of the material is 1723 K (1450 °C). Therefore the creep temperature limit of stainless steel is about 844 K (571 °C) which is much higher than temperature limit of aluminium (504 K or 231 °C);

- In the hypothesis of perfect thermal insulation between the magnets and the yoke, conduction occurs only between the active area and the passive area of the mover. To further simplify the problem, the analysis is restricted only to the active area where the eddy currents are generated. At the fictitious boundary surfaces between the active and passive area perfect thermal insulation is imposed. Since the passive area is always colder than the active area, with this assumption the heat that flows across the boundary between the active and passive area is neglected and the calculated temperature in the active region will be higher than in real applications;

- The convective heat flows only through the leading and trailing edge surfaces of the active area, since the lateral surfaces are covered by the PMs. Since the heat removed through convection along these surfaces is not significant, convection can be neglected. Perfect thermal insulation is also imposed along the mover leading and trailing surface.

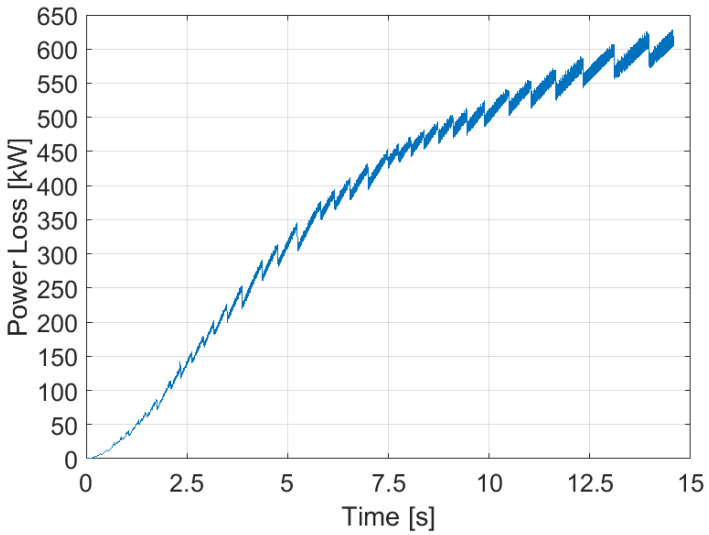

Figure 5.21: Transient variation of the Joule losses in the mover's yoke

The transient heat transfer equation for the yoke under these assumption reduces to

$$\rho_{Fe} c_{Fe} \frac{\partial T}{\partial t} = \frac{P_{yoke}(t)}{v_{yoke}} \tag{5.130}$$

where ρ_{Fe} is material density, c_{Fe} is the material specific heat capacity, v_{yoke} is the volume of the mover's yoke and $P_{yoke}(t)$ is the power which is dissipated as heat into the yoke. The time variation of the Joule losses in the stainless steel yoke during the launch was computed through FEA and it is shown in Fig. 5.21.

The integration of both sides of eq. 5.130 over the take-off time t_{TO} yields

$$\Delta T_{yoke} = \frac{1}{\rho_{Fe} c_{Fe} v_{yoke}} \int_0^{t_{TO}} P_{yoke}(t)\, dt \tag{5.131}$$

where ΔT_{yoke} is the average temperature increment. Integrating the power loss in Fig. 5.21 yields a temperature difference of approximately 20.8 K.

The analysis performed in Section 4.5 for LIMs showed that the temperature is not uniform over the plate surface and that it varied reaching values 15% greater than the average temperature. This temperature peaks that may appear on the LPMSM's yoke as well do not represent an issue during a single launch, but a cooling system might be required for multiple launches. However, the passive

cooling provided by conduction across the passive areas and by convection during the launch and the time between launches will allow several consecutive take-off without the need for an active cooling system.

5.6.2 Thermal Analysis of the Magnets

The thermal demagnetization of the magnets by the eddy current loss due to intense secondary harmonics in fractional-slot machines is one of the major problems to deal with during the machine design. A technique that is widely used to reduce the loss in the magnets consists in shortening the eddy current path by the mean of segmentation. Each magnet can be segmented both in axial and longitudinal direction. The loss reduction due to segmentation can be investigated by 3D FEA and this shows that surface-mounted PMs have more benefits from axial segmentation than from the segmentation in the direction of motion [114].

In order to correctly predict the performance of the machine and the power loss in the magnets a 3D simulation of a full launch is required. The computational resources required to complete this goal are far beyond the usual capability of research institutions and a valid alternative has to be found. The proposed methodology aims to simulate the 3D distribution of the eddy current through an equivalent 2D representation of the same problem. The alternative technique consists in adjusting the value of the PM resistivity to emulate the 3D loss in the array of segmented magnets. The resistivity correction factor k_ρ is equal to the ratio between the loss calculated by the 2D simulation $P_{e\,2D}$ and the correct 3D solution $P_{e\,3D}$ [115].

$$k_\rho = \frac{P_{e\,2D}}{P_{e\,3D}} \qquad \Rightarrow \qquad \rho_{mag\,2D} = k_q \rho_{mag} \tag{5.132}$$

From the interpolation of experimental data for a large number of segmentations it is possible to determine the curve in Fig. 5.22 [115]. The number of segments selected for the LPMSM along the axial direction is 50. The respective value of k_ρ is highlighted in Fig. 5.22. Considering that the NdFeB magnets have a resistivity of $\rho_{mag} = 1.5 \cdot 10^{-6}$ Ωm the equivalent 2D resistivity implemented in FEA is $\rho_{mag\,2D} = 2.61 \cdot 10^{-4}$ Ωm.

Since the eddy current losses in each pole of the magnet array are almost equal,

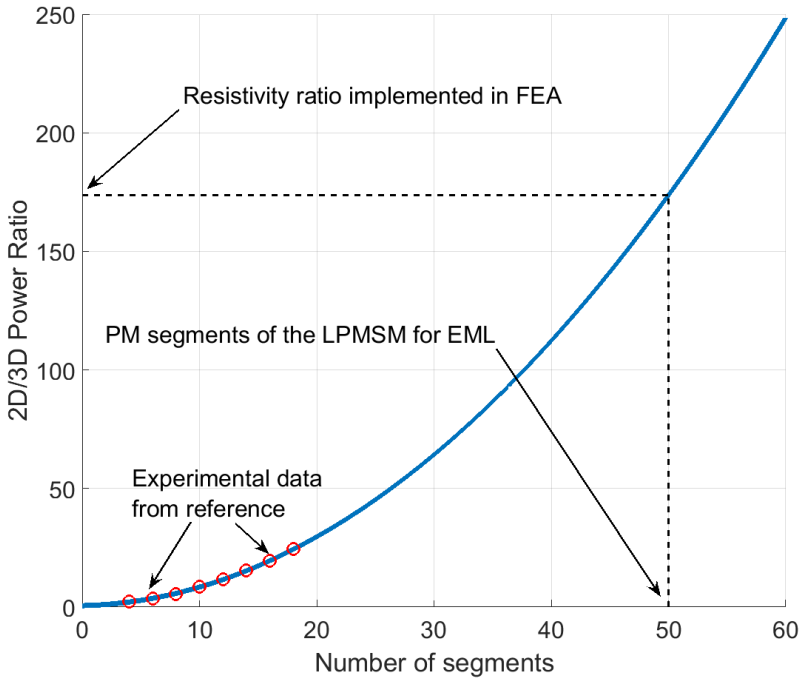

Figure 5.22: Interpolation of the experimental data to estimate the ratio between 2D and 3D resistivities

the thermal analysis of the magnets can be restricted to a single pole. Moreover axial segmentation allows the investigation of the temperature transient of a single internal segment. Considering that neighbouring magnet segments undergo approximately the same temperature rise and that the interstices between magnets are filled with a low thermal conductivity glue, the sides of each magnet segment can be considered perfectly thermally insulated. Neglecting the heat exchanged through convection on the sides exposed to air, the heat transfer problem can be solved as for the mover's yoke using equation:

$$\rho_{PM} c_{PM} \frac{\partial T}{\partial t} = \frac{P_{e2D}(t)}{v_{PM}} \tag{5.133}$$

where ρ_{PM} is the magnets density c_{PM} is the specific heat capacity of NdFeB and v_{PM} is the volume of the PM's segment. The volume of the magnet segment under investigation is

$$v_{PM} = l_m \frac{l_s}{50} h_m \tag{5.134}$$

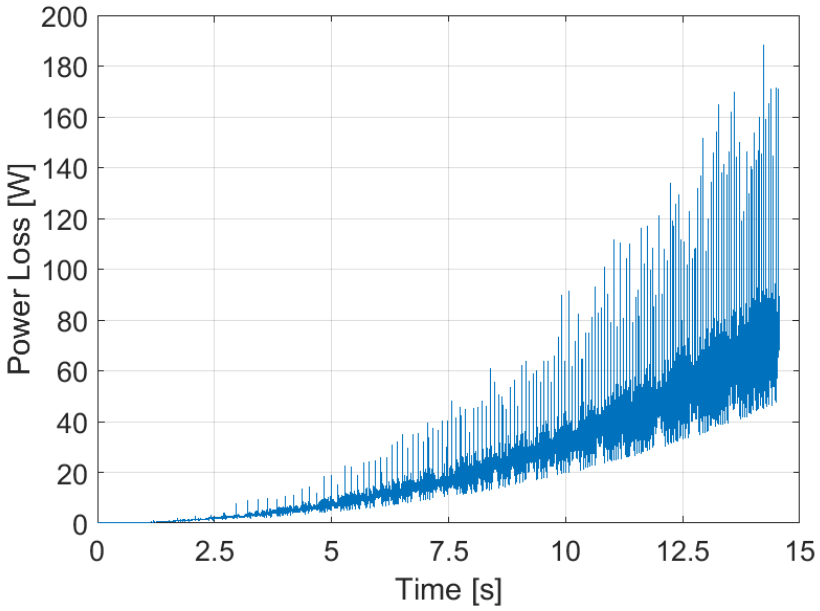

Figure 5.23: Transient variation of the Joule losses in a PM segment

The time variation of the eddy current power loss during the launch is shown in Fig. 5.23. The average temperature variation that is expected at the end of the launch can be calculated as

$$\Delta T_{PM} = \frac{1}{\rho_{PM} c_{PM} v_{PM}} \int_0^{t_{TO}} P_{e2D}(t)\, dt \tag{5.135}$$

The integration of eq. 5.135 yields a temperature rise of 0.47 K which is manageable by passive cooling even in the hypothesis of multiple launches. The temperature difference between yoke and magnets generates a heat flow that tends to cool down the yoke and heat up the magnets. However, the low conductivity of the glue between them and the short duration of the launch impede the attainment of thermal equilibrium and the temperatures of the mover's components are not expected to vary much from the values found in the present analysis.

The risk of thermal demagnetization of LPMSM with segmented PMs has been proven to be very low for the very little temperature increase ΔT_{PM} experienced during the launch. The mover component that experiences the greatest temperature rise is the stainless steel yoke. The implementation of a yoke with limited axial segmentation might further reduce the eddy current loss in the material and

completely remove the need of active cooling system for the mover even with multiple launches.

5.7 Contribution to Knowledge

The selection procedure of number of slots and poles described in this chapter was firstly introduced for large rotary PMs synchronous motor. For the first time this method has been applied to linear motors and adapted to allow software implementation. In this chapter the selection of number of slots and poles did not have the only purpose of achieving high winding factor, but it was also based on the minimization of the magnetic material on board the mover and on the reduction of the harmonic content of the respective MMF. The modelling methods which included parametric optimization, MLT, dq model and FEA were applied to size a LPMSM for civil aircraft launch applications for the very first time. These studies were combined with the thermal analysis of mover's yoke and permanent magnets. The thermal analysis was not only carried out to verify the need of an active cooling system to cope with the heating across multiple launches, but it has also assessed the absence of PMs demagnetization due to possible sharp temperature increments during operations.

Chapter 6

Experimental Validation

This chapter presents project methodology, design, construction details and test results of a reduced scale physical demonstrator concerned with the electromagnetic catapult topology presented in Chapter 4. The main aim of the prototype is to provide experimental data to compare with the results of the numerical and analytical design procedures of linear induction motors (LIMs), in order to establish a motor topology of potential use in a full scale civil aircraft launcher.

Often in literature, the performance of LIMs is compared with that of linear synchronous motors (LSMs) considering the same stator geometry [38]. Most of the times, the geometrical features of the stator are optimized to satisfy the requirement for LSM, and then the synchronous motor performance is compared with that of a LIM with the same stator. Since the two electrical machine topologies work on different principles, it is not possible to achieve the same motor performance using the same stator geometry. The experimental work presented in this chapter will prove that linear induction and synchronous machines should be sized following dedicated design procedures as done in this thesis.

Therefore, following the procedure described in Chapter 5, a linear permanent magnets synchronous motor (LPMSM) was developed and constructed to compare the two machine types and as a basis for future LSM testing. The stator of the linear synchronous motor (LSM) is tested as an induction motor to show that it cannot achieve the performance of a LIM optimally designed to meet the same requirements. In order to test the motors on the same rig and to follow the

constraints commonly applied to commercial systems, both LIM and LSM are developed to fit a common space constraint.

This chapter describes linear electrical motors that are designed to launch a small Unmanned Air Vehicle (UAV) with a maximum take-off weight of 4.5 kg. The launcher provides the energy required to accelerate the aircraft mass without the aid of the UAV's engines. When the engines are in operation, the launch capability of the prototype can be extended up to a take-off weight of 7 kg. This upper weight limit was chosen as aircraft heavier than 7 kg are of less interest, since they are not allowed to fly without special permission as stated by the British national regulatory institution, the Civil Aviation Authority (CAA) [116].

The procedures adopted to realise the small-scale prototype are described in the following sections.

6.1 Test Rig Description

The test rig components are held in place by a central beam made out of steel and shown in Fig. 6.1. The central beam is bolted to two steel frameworks: the largest is the linear motor housing whereas the other one is the magnetic brake structure. The test rig was mounted on the lab tables shown in Fig. 6.1 in order to ease assembling operations and to facilitate repositioning of the mover at the beginning of the launch track after each acceleration.

The function of the metallic components of motor and brake structures and the methods used to size them will be further described in Section 6.5. The central beam is also connected to rails along which four pairs of carriages can freely slide. The carriages are not visible in Fig. 6.1 since they are hidden by the mover structure which is at rest between the stator and brake housing.

The mover is also attached to a timing belt that conveys the motion to the position sensor. The timing belt is the white band shown in Fig. 6.1 that runs all around the central beam and is driven by pulleys. The timing belt tensioning system, which is used to move the pulley backward until the belt is straight, is positioned at the central beam edge after the brake.

The mover is connected to the aircraft undercarriage that travels on a transparent platform which is supported by the stator and brake housing. The connection

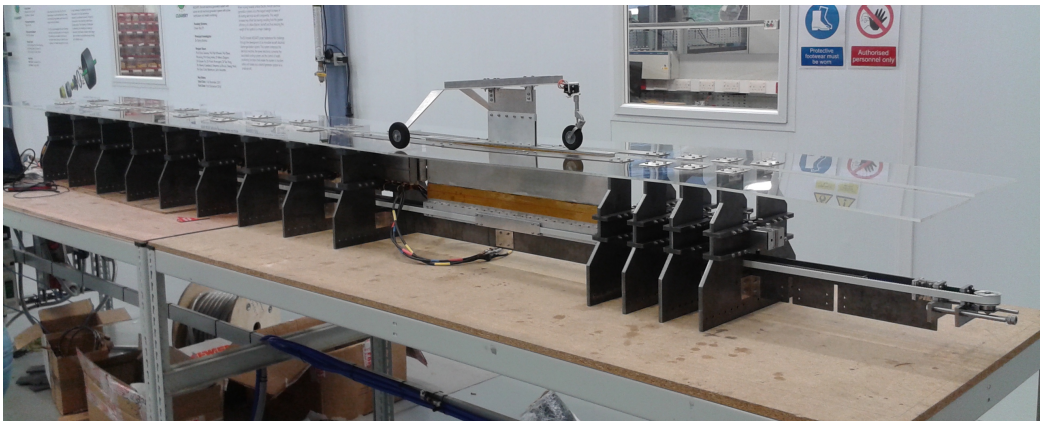

Figure 6.1: Electromagnetic launcher prototype for UAVs

between the mover and the aircraft undercarriage shown in Fig. 6.1 is fixed and impedes the aircraft detachment during indoor tests. A detachable system composed by a ring and a hook was also designed and manufactured, but it can be installed only for outdoor tests. The UAV is simulated by an iron plate which is bolted on top of the landing gear and weighs 4.5 kg.

The cables that departs from the motor in Fig. 6.1 form a star connection before joining the AC drive. The AC drive is mounted on table legs and feeds the motor with the voltage and frequency required by the operator. The parameters of the AC drive can be adjusted by the operator using a dedicated software.

6.2 Definition of Prototype Requirements

The requirements of the induction and synchronous motor were determined considering the physical properties and aerodynamic characteristics of the UAV shown in Fig. 6.2 which is manufactured by the German company Bormatec [117]. The electromagnetic catapult end-speed, peak thrust and rated acceleration depend on the aerodynamic features of the airplane at take-off. A simple method to estimate the aerodynamic characteristics of the aircraft is presented in this section.

By a comparison of the wing cross section with an online database of standard wing shapes, the airfoil that best resembles the section of the UAV's wing is the NACA2312. The aerodynamic lift and drag coefficients of the NACA2312 airfoil

Figure 6.2: Reference aircraft for the catapult prototype

vary with the angle of attack according to the curves shown in Fig. 6.3 [118]. The variation of the total aerodynamic drag coefficient of the UAV with the angle of attack also shown in Fig. 6.3 takes into account of several contributions:

- the drag coefficient of the fuselage which also considers the friction between the air flow and the aircraft. The aerodynamic drag of the fuselage does not depend on the angle of attack and it is calculated using a 3D fluid dynamics simulation software;
- the drag coefficient of the NACA2312 airfoil shown in Fig. 6.3 [118] which represents the aerodynamic resistance of an ideal wing with infinite length;
- the induced drag coefficient which is the additional aerodynamic resistance due to the finite length of the wing.

The induced drag appears every time there is a pressure difference between the top and the bottom of a wing. This pressure difference is always required to have a lift force opposite to the aircraft weight. In correspondence of the wing tips, the fast upstream low pressure air flow mingles with the slow downstream high pressure air flow causing vortices. The size of the tip whirls is proportional to the square of the aircraft speed and is associated with the induced drag. The drag coefficient

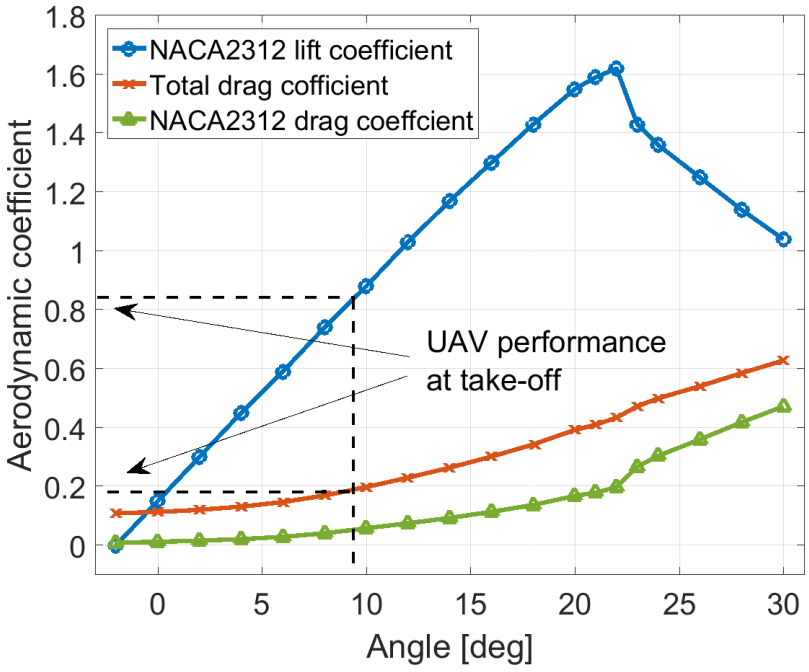

Figure 6.3: Aerodynamic drag and lift coefficients of NACA2312 airfoil

of this additional drag components can be computed as

$$C_{Di} = \frac{C_L^2}{AR\,e\,\pi} \tag{6.1}$$

where C_L is the lift coefficient, AR is the wing aspect ratio and e is the Oswald efficiency number. The Oswald efficiency represents the discrepancy between the lift distribution over the real wing and the ideal elliptical wing (with $e = 1$).

The take-off condition is reached when the lift force acting on the wing is equal to the aircraft weight ($m_{UAV} = 4.5$ kg). The speed at which take-off occurs can be computed from the lift force formula (see eq. 3.1) as

$$v_{TO} = \sqrt{\frac{2 \cdot m_{UAV} G}{\rho_{Air} S_w C_L}} \tag{6.2}$$

where S_w is the wing surface and ρ_{Air} is the air density. Knowing the take-off speed, the aerodynamic drag at take-off can be computed as

$$D = \frac{1}{2}\rho_{Air} S_w C_D v_{TO}^2 \tag{6.3}$$

The rated acceleration of the UAV launcher depends on the maximum distance that the aircraft is allowed to travel before reaching the take-off speed. The length of the motor that would be required to reach the take-off speed with the rated acceleration of the civil aircraft launcher (0.6 G) would exceed 14 m. Considering the manufacturing limitations on the length of a single stack of laminated material (approximately 2.0-2.5 m), the electrical machine would then need to be formed by at least 6-7 sections. The control difficulties, switching between stages and the cost of an apparatus of such complexity would exceed the aims and objectives of the test rig. In order to achieve the experimental goals with a simpler system and within the allocated budget, it is acceptable to reduce the system complexity and size, by implementing a single stage motor which accelerates the load at higher rate. In order to allow the aircraft to reach the take-off speed within approximately two meters, the rated acceleration must be 5 G, which is acceptable for unmanned vehicles assuming the mechanical structure is able to withstand it.

The thrust of the electromagnetic catapult must overcome the aerodynamic drag and the aircraft inertia at rated acceleration. Thus, the instantaneous required thrust can be computed as

$$F = 5\,G \cdot m_{UAV} + D \tag{6.4}$$

Since the aircraft accelerates at constant rate and since the aerodynamic drag varies with the square of the speed, the peak required thrust is delivered at the end of the launch. The aerodynamic features, the thrust and the other prototype requirements are summarized in Table 6.1.

6.3 Prototype Electromagnetic Design

The electromagnetic design of synchronous and asynchronous launchers for UAVs exploits the same theories and follows the same procedures illustrated in Chapters 4 and 5. Both the motors are sized in order to minimize the input power needed by the system through the use of the parametric optimization.

The asynchronous and synchronous motors used to accelerate the aircraft A320-200 would be formed by several stages which are progressively connected to the

Table 6.1: Aerodynamic characteristics of the UAV and small catapult requirements

Angle of attack	α_{TO}	9°
Drag coefficient	C_D	0.186
Lift coefficient	C_L	0.83
Wing aspect ratio	AR	8.8
Oswald efficiency	e	0.7
UAV mass	m_{UAV}	4.5 kg
Air density	ρ_{Air}	1.225 kg/m^3
Wing surface	S_w	0.528 m^2
Aerodynamic drag	D	9.9 N
Take-off speed	v_{TO}	12.82 m/s
Rated acceleration	a_{TO}	5G (49 m/s^2)
Thrust	F	230.6 N

power supply as the motion of the aircraft progresses. The length of the mover is supposed to cover the active coils for the whole duration of the launch. Conversely, the mover of the UAV launcher is significantly shorter than the single-stage stator. When currents flows in the stator windings, only a small part of the coils interacts with the aluminium plate of the induction motor. The energy stored in the magnetic field of the passive areas is not employed to produce the thrust and is not transformed in mechanical energy.

The parameters of the equivalent circuit of linear induction motors and the electrical features of the linear synchronous motor must take into account the passive areas of the machines. The total resistance, leakage inductance and the additional magnetization inductance related to the fundamental magnetic field wave in the passive areas are computed for both the machines as

$$R_{tot} = \frac{R}{N_1} N_{tot} \tag{6.5}$$

$$L_{l\,tot} = \frac{p \cdot L_l}{N_1^2} \frac{N_{tot}^2}{p_{tot}} \tag{6.6}$$

$$L_{ml} = L_m \frac{p_{tot} - p}{p} \tag{6.7}$$

where N_1 is the number of active turns, N_{tot} is the total number of turns, p is the number of active pole pairs, p_{tot} is the total number of pole pairs and R, L_l, L_m are the resistance, leakage inductance and magnetization inductance calculated as

Table 6.2: Geometrical features, circuit parameters and performances of the LIM prototype

Geometrical features		**Circuit Parameter**		**LIM Performance**	
Pole pitch	180 mm	Current density	14.61 A/mm^2	Field B_t	0.556 T
Thickness d_{Al}	3.0 mm	Peak frequency	40.01 Hz	Field B_g	0.437 T
Slot pitch	30 mm	Slip frequency	0.11	Mover mass	3.77 kg
Slot width	15 mm	Sync. speed	14.40 m/s	Mover thrust	175.8 N
Slot height	6.5 mm	End speed	12.82 m/s	Total thrust	449.9 N
Tooth tip height	0.5 mm	I_1 (RMS)	94.94 A	Thrust density	7.81 kN/m^2
Grooves d_g	1.0 mm	I_2 (RMS)	30.59 A	Carter coeff.	1.0417
Airgap g	5.0 mm	I_m (RMS)	89.88 A	Fringing factor	1.0086
Airgap g_m	13.0 mm	Voltage V_1	270.5 V	Skin-effect fac.	1.0000
Airgap g_e	13.7 mm	Winding factor	0.933	Edge-effect fac.	2.1298
Stator width	80 mm	Phases	3	Goodness factor	3.094
Plate width	195.6 mm	Turns per slot	6	Iron loss	0.037 kW
Yoke height	20.0 mm	Turns per phase	336	Copper loss	2.804 kW
Mover length	720 mm	Inductance L_{1l}	0.23 mH	Output Power	6.481 kW
Wire diameter	3.1 mm	Inductance $L_{1l\,tot}$	2.8 mH	Active Power	10.007 kW
Teeth mass	2.21 kg	Inductance L_m	3.1 mH	Reactive Power	76.395 kW
Yoke mass	13.41 kg	Inductance L_{ml}	6.3 mH	Input Power	77.056 kW
Coil pitch	150 mm	Inductance $L_m + L_{ml}$	9.4 mH	Peak Efficiency	0.573
End coil length	202.5 mm	Resistance R_1	0.0296 Ω	Power factor	0.131
Active poles	4	Resistance R_{tot}	0.1037 Ω	Active area η	0.715
Slot/pole/phase	2	Resistance R_2	0.2540 Ω	Active area $\cos\phi$	0.365

Table 6.3: Geometrical features, circuit parameters and performances of the LPMSM prototype

Geometrical Features		**Electric Parameters**		**Performance**	
Airgap	4.0 mm	Phases	3	Current density	13.38 A/mm^2
Slot pitch	20 mm	End speed	12.82 m/s	Iron density	8190 kg/m^3
Tooth width	9.0 mm	Frequency	249.3 Hz	PM density	7500 kg/m^3
Slot opening	11 mm	Slot/pole/phase	3/7	Mover mass	7.11 kg
Slot height	6.5 mm	Turns per coil	6	Mover thrust	348.6 N
Slot tip	0.5 mm	Turns per phase	484	Total thrust	668.6 N
Grooves diam.	1.0 mm	Remnant field	1.26 T	Thrust density	11.62 kN/m^2
Pole pitch	25.7 mm	Tooth field	0.571 T	Copper loss	3.895 kW
End-coil length	34 mm	Airgap field	0.509 T	Output power	8.572 kW
Magnet span	23.1 mm	Inductance L_l	0.57 mH	Active power	12.467 kW
Magnet thick.	2.0 mm	Inductance $L_{l\,tot}$	1.9 mH	Reactive power	17.029 kW
Mover length	722 mm	Inductance L_m	0.27 mH	Input Power	21.105 kW
Yoke thickness	1.5 mm	Inductance $L_m + L_{ml}$	0.91 mH	Efficiency	0.688
Back Iron	20.0 mm	Resistance	1.01 Ω	Power Factor	0.591
Stator width	80 mm	Voltage Peak	196.2 V	Active area η	0.915
Wire diameter	1.8 mm	Current (RMS)	35.9 A	Active area $\cos\phi$	0.880

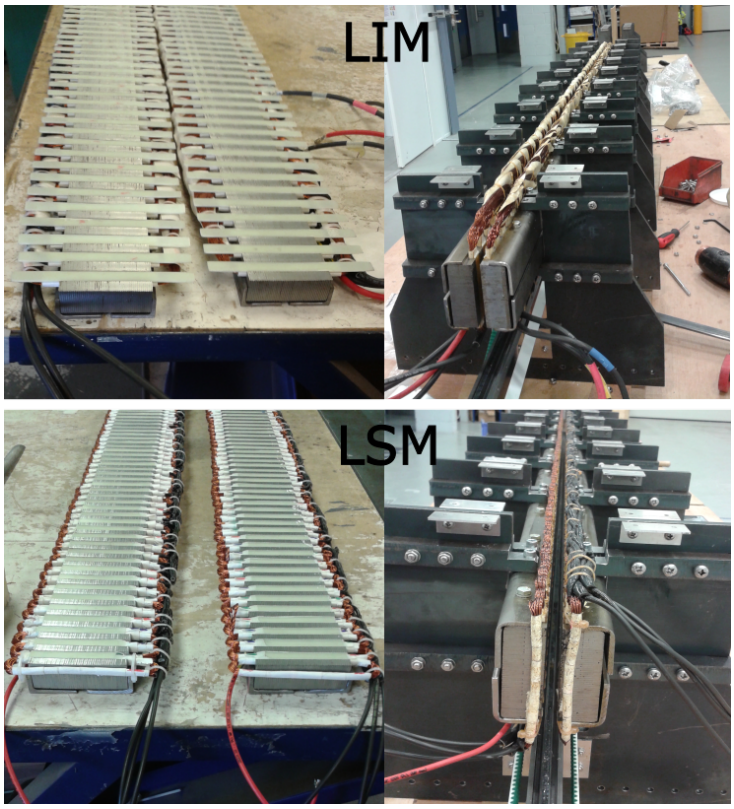

Figure 6.4: Pictures of LIM's and LSM's stator sides taken when they were disassembled and mounted on the frame

shown in Chapters 4 and 5.

The results of the parametric optimization algorithm for induction and synchronous UAV launchers are reported in Tables 6.2 and 6.3 respectively. This data was used to manufacture the stators shown in Fig. 6.4. In particular LSM's stator can be distinguished from LIM's for the shorter slot pitch and for the reduced space occupied by the end-coils of concentrated windings.

Some of the dimensions reported in Tables 6.2 and 6.3 do not come from the input power minimization algorithm of the parametric analysis, but were adjusted considering the measurements made on the launchers after they have been assembled. Additionally, the masses of the LIM's and LPMSM's movers are not computed using the same approximated methods used in Chapters 4 and 5, but they were directly weighed.

In order to compare the effects of the passive coils on the motor performance,

Tables 6.2 and 6.3 also include efficiency and power factor of the active area. As expected, a mover shorter than the stator causes a reduction of efficiency due to the Joule losses associated with the increased copper wire length required to cover the passive areas. The power factor diminishes as well due to energy stored in the magnetic field of the passive zones which is not used to produce the thrust.

6.4 Sizing of the Magnetic Brake

The system requires an end-track braking system, suitable to stop both the mover and the aircraft in the event of an unsuccessful detachment. Being able to brake the aircraft mass also considerably simplifies testing by not having to physically launch the aircraft each test. With a captive aircraft load that can be braked, the demonstrator can be shown off anywhere, indoors or outdoors. While the end stage braking could use a simple and cheap mechanical brake, this would have lifetime wear issues and reset delays in testing and demonstration. Moreover a mechanical brake has more potential for human error as this will need to be released and reset each test. Conversely, magnetic brakes with permanent magnets are absolutely fail-safe, passive and will always function.

6.4.1 Safety Springs and Maximum Mover End-Speed

As an additional precaution two springs are mounted behind the brake as shown in Fig. 6.5. The springs push the mover back into the brake, in case a single braking action is not enough to stop it. The timing belt that is employed to convey the motion to the position sensor limits the spring external diameter to 18 mm. The features of the springs available in the market that respect this dimension constraint are reported in Table 6.4, where L_0 is the spring length, k_{el} is the elastic constant of the spring, F_{max} the force that the spring exerts at full compression and Δs is the displacement at full compression.

If the mover reaches the springs location, its kinetic energy is transformed into elastic energy until the max displacement Δs is reached. If the kinetic energy is too high the mover will impact the holding structure causing serious damage to the whole test rig. The energy conservation principle allows the calculation of the

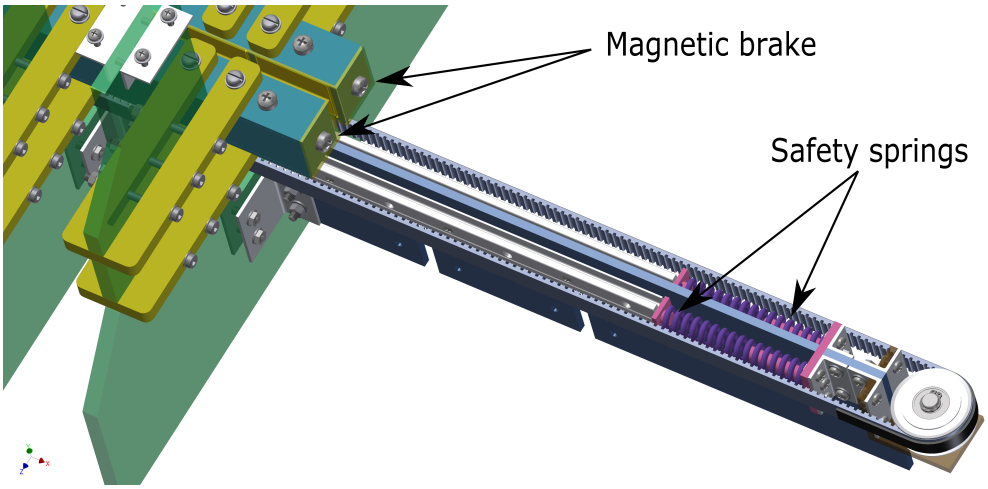

Figure 6.5: Location of the safety springs after the magnetic brake housing

Table 6.4: Spring Data

L_0 [mm]	k_{el} [N/mm]	F_{max} [N]	Δs [mm]	V_{sp} LIM [m/s]	V_{sp} LPMSM [m/s]
89	15.0	535	35.6	2.091	1.810
102	13.3	542	40.8	2.314	1.953
89	34.2	762	22.3	2.028	1.712
102	29.5	751	25.5	2.154	1.818
89	21.8	582	26.7	1.939	1.636
102	18.9	579	30.6	2.069	1.746

maximum mover speed as

$$V_{sp} = \Delta s \sqrt{\frac{2 \cdot k_{el}}{m_{UAV} + m_{mov}}} \tag{6.8}$$

where m_{mov} is the mass of the mover and the number 2 is inserted to consider the action of both the springs in Fig. 6.5.

The maximum kinetic energy that the springs are able to turn in elastic energy corresponds to the speeds listed in Table 6.4. Since the kinetic energy is proportional to the square of the mover velocity, the spring capability of safely pushing the mover back increases with the speed V_{sp}. The spring that allows the mover to travel the fastest is highlighted in green. This spring was purchased and implemented in the rig and its geometrical features are those represented in Fig. 6.5.

The speed associated with the selected spring represents the maximum mover's

velocity after the braking action. Since both the motors will be tested with the aluminium plate, only the maximum speed associated with the mass of the LIM's mover is considered. Therefore, the magnetic brake has been sized to slow down the mover to a speed lower than 2.31 m/s at the spring location.

6.4.2 Electromagnetic Analysis of the Magnetic Brake

The analytical model and the finite element simulations of the magnetic brake aim to ensure that the LIM's mover travelling at the aircraft take-off speed (approximately 12.8 m/s), reaches the springs at a velocity lower than the one highlighted in Table 6.4. The likelihood of a mover reaching a velocity higher than the take-off speed is remote, although an excess of speed and kinetic energy should be considered as a safety measure.

Since the longer the distance the aluminium plate travels across the brake the stronger the arresting action on the moving conductor, the magnetic brake analysis allows to set the minimum distance between the springs and the magnetic brake that allows the mover to come to a standstill. In order to reduce the bulk of the test rig the minimum distance is used to size the machine structural components. If the brake performs well enough to arrest the mover before it crosses the active area completely, the springs will be place at a distance shorter than the mover length.

The actual test rig hosts the magnetic brake which is shown in Fig. 6.6. The analysis presented in this section is used to evaluate the arresting capability of the installed magnetic brake and to estimate the maximum permissible mover speed which should be greater than the take-off speed.

6.4.2.1 Analytical Model of the Magnetic Brake

The braking force acting on a conductive material passing through a persistent magnetic field is caused by the interaction between the induced eddy currents and the magnetic field itself. The intensity of the eddy current and of respective braking force is proportional to speed and conductivity of the material. The total braking force can be estimated as [119]

$$F_b = \sigma_{Al} d_{Al} B_g^2 l_{mag} w_{mag} V \tag{6.9}$$

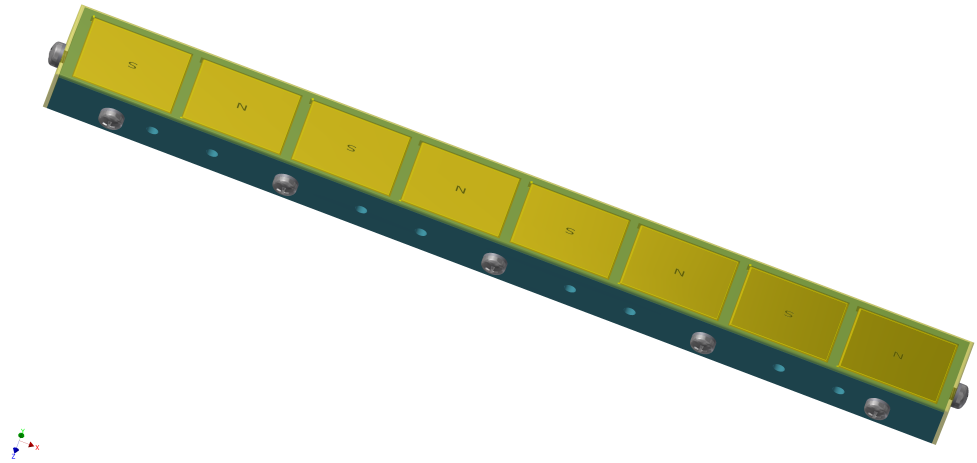

Figure 6.6: Magnetic brake structure

where σ_{Al}, d_{Al} and V are conductivity, diameter and speed of the conductor respectively, l_{mag} and w_{mag} are the length and the width of the area where the magnetic field acts and B_g is the magnetic flux density in the airgap. The length of the active area l_{mag} in eq. 6.9 depends on the motion of the plate with respect to the brake and changes with time. Since the force is proportional to the conductivity of the materials, the lower the resistivity of the aluminium alloy the better will be the braking performance.

In order to correctly model the magnetic brake using eq. 6.9, geometry and materials of the movers must be taken into account. The LIM's mover is formed by two thin aluminium sheets glued to a central aluminium plate. In order to reflect the action of different layers of material, the product between conductivity and plate thickness in eq. 6.9 is replaced by an auxiliary variable which is

$$\sigma_e = \sigma_{Al} \frac{d_{Al} \cdot d_{Al\,f}}{d_{Al} + 2d_{Al\,f}} \tag{6.10}$$

where d_{Al} and $d_{Al\,f}$ are the thickness of the central aluminium plate and aluminium sheets respectively.

The magnetic field density in the airgap in eq. 6.9 can be determined from the

remnant flux B_r of the permanent magnets as

$$B_g = \frac{h_m B_r}{k_{Fg}(h_m + \mu_{PM} g)} \tag{6.11}$$

where h_m is magnet thickness, k_{Fg} is the fringing factor (see Chapter 5), μ_{PM} is the relative magnetic permeability of the permanent magnets and g is the airgap length. Once the braking force acting on the mover is known, the speed profile is reconstructed integrating the instantaneous deceleration $F_b/(m_{UAV} + m_{mov})$.

6.4.2.2 Electromagnetic Analysis Results

The model of the magnetic brake presented in the previous section was iterated many times to find the maximum initial speed of the mover that can be slowed down to a speed lower than the maximum velocity allowed by the safety springs and highlighted in Table 6.4. The speed calculated using the analytical method is validated through comparison with the velocity computed by the FEA model of the magnetic brake.

For instance, Fig. 6.7 shows the speed profiles computed by the analytical and numerical methods with an initial mover speed of 13.7 m/s. The chart shows that at high speed, the analytical model overestimates the braking action and predicts a speed slightly lower than the one computed by the FEA software. On the contrary, at low speed, the finite element method estimates stronger magnetic forces so that the mover can slow down until it stops.

The analytical and numerical method predict the speeds at the spring location shown in Fig. 6.7. In both the cases, the speed of the mover at the safety springs is lower than the maximum allowed. The speed profile determined by analytical method is not as accurate, probably due to the fact that the simple eq. 6.9 does not consider the magnetic field generated by the induced eddy currents. For high material conductivity at high speed the eddy currents are particularly intense and they counteract the action of the magnetic field in the active area producing lower forces. On the contrary at low speed the induced current have a stronger interaction with the stationary magnetic flux. Despite the limited accuracy, the analytical model predicts a speed at the spring location very close to that computed numerically. Therefore, this simple model of the magnetic brake is good enough to

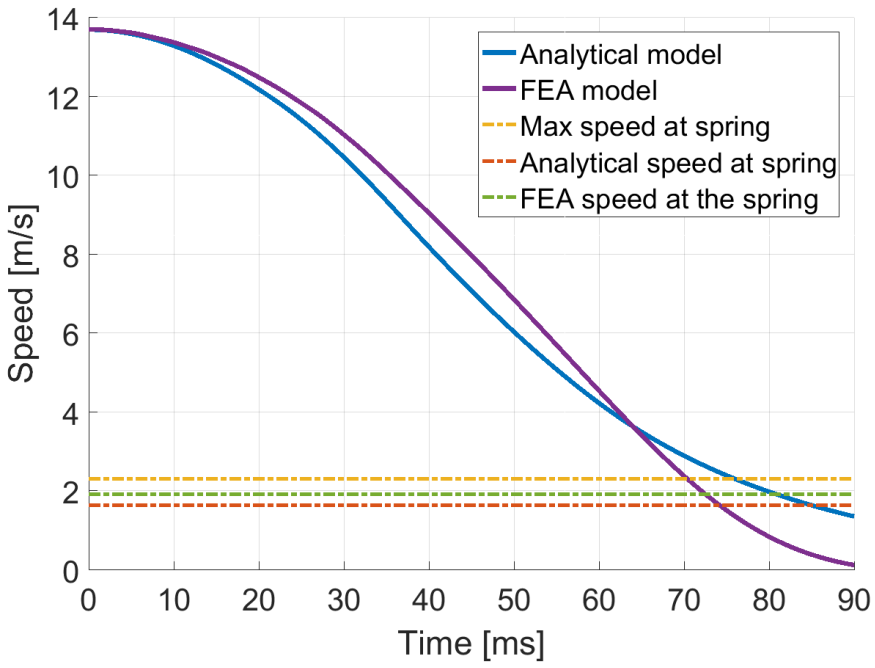

Figure 6.7: Comparison between the LIM's mover deceleration computed by the analytical and FEA model

estimate the speed without running extensive FEA simulations.

As can be seen from the results shown in Fig. 6.7, the breaking force that acts upon the aluminium sheets is strong enough to slow down a mover travelling at 13.7 m/s. This speed approximately corresponds to the maximum velocity that the mover connected to the aircraft can reach without exceeding the maximum speed allowed at the safety springs. A mover travelling at 13.7 m/s has a kinetic energy 15% larger than the kinetic energy of the mover at take-off speed.

This analysis has proved that the braking force is strong enough to decelerate the mass of mover and aircraft connected together travelling at a velocity larger than the take-off speed (12.82 m/s). The installed brake allows a 7% speed excess which guarantees safe operation. Additionally, in real launch the aircraft detaches and the brake is used to decelerate only the mass of the mover. If required, during future outdoor tests the LIM might be used to accelerate an UAV even at higher speeds.

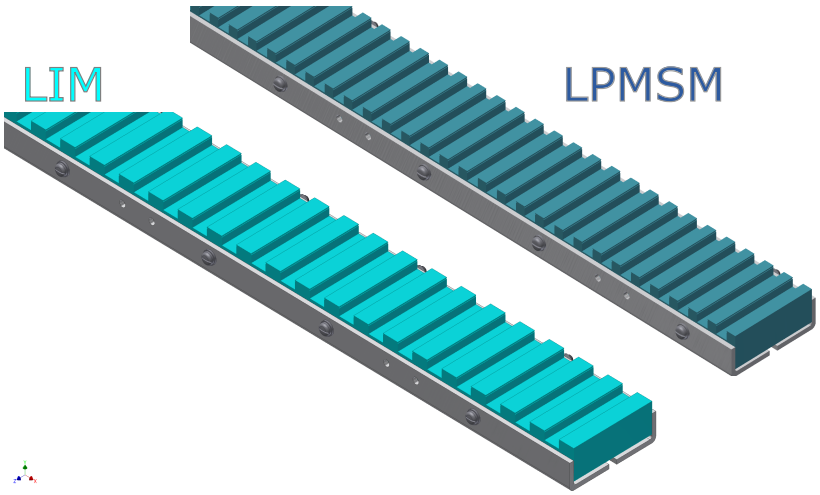

Figure 6.8: Technical drawing of the laminated structure of LIM's and LPMSM's stators

6.5 Structural Design of the Stator Housing

6.5.1 Description of Structural Components and Loads

When the current flows inside a double-sided linear motor the normal force acting on the mover is nominally zero while the stators to each side of the airgap are subject to distributed attractive forces known as normal force that tends to close the airgap. As the normal force can be 10 times greater than the propulsive thrust, the stator is commonly hold in place by a bulky and heavy structure which impedes any displacement.

The electromagnetic catapult structure has been designed to be easy to assemble and suitable for transportation. In order to accomplish this specific requirement, the launcher framework is built of components which, if not properly designed, may undergo significant deformation under operation. Intense displacements must be avoided, as they may narrow the airgap to the point of collision between the mover and the stator during operation at speed. Even though a moderate reduction of the airgap length increases the propulsive force, vibrations and small misalignments may cause impacts even with low deformations. In this work the stator housing is designed to allow a maximum displacement of 5% of the airgap length in the whole airgap region ($< 250\ \mu$m).

The structural analysis is carried out separately on all the framework compo-

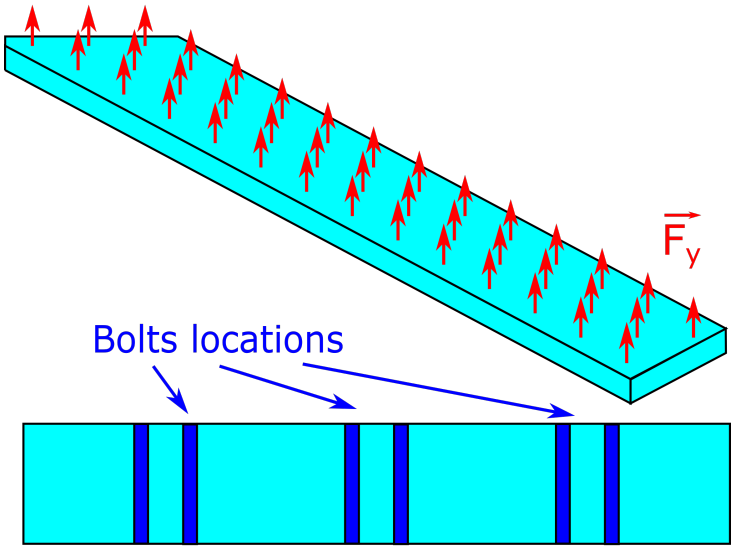

Figure 6.9: Schematic of load distribution and constraints location on the stators simplified structure

nents which are subject to the operative load. The total displacement in the airgap region is obtained summing up the contributions of all the loaded components. The structural analysis can be performed on one half of the system, taking advantage of the machine symmetry.

The motor component which is directly subject to the electromagnetic attractive load is the machine stator. The tooth-slot structure of the stators of induction and synchronous motors are shown in Fig. 6.8. They are both formed by a laminated structure of ferromagnetic material. The stainless steel angles bolted beside the stators provide further rigidity to prevent bending under flexural loads. The stainless steel angles and the laminated structure are connected to the stator housing by bolts that pass through the empty holes on the sides of the stators in Fig. 6.8.

In the hypothesis that the teeth rigidly transmit the load to the stator back iron, the structure can be represented by considering an isotropic material with the shape of a parallelepiped as shown in Fig. 6.9. The attractive load acts on one side of the stator, while the other side of the silicon steel bar is constrained by bolted connections. The blue areas highlighted in Fig. 6.9 represent the surfaces where the fix constraints are located.

The finite element electromagnetic analysis of the induction and synchronous

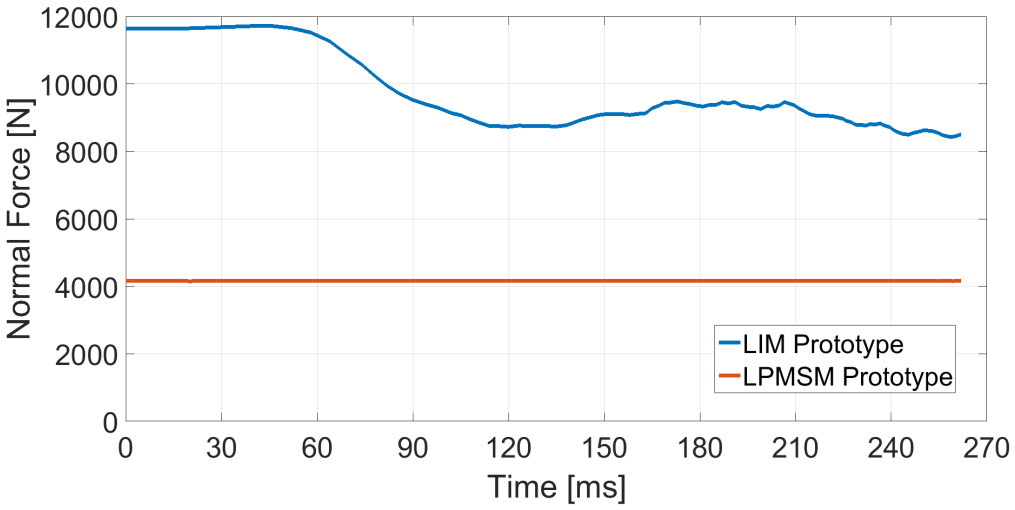

Figure 6.10: Variation of the normal force acting in LIM and LPMSM stators during the launch

motors determines the instantaneous normal forces reported in Fig. 6.10. The force acting on the induction motor is greater than the normal force of the synchronous motor due to the higher rated current and related electromagnetic interaction. Since the stator of the synchronous motor will be only used to accelerate the aluminium plate of the LIM's mover and will not be tested with the magnet array, a normal force different from the one shown in Fig. 6.10 might be produced. Even though the LSM's stator accelerating the LIM's mover was not simulated by FEA, the propulsive and normal forces are expected to be lower than those of the induction motor shown in Fig. 6.10 due to the lower rated current. Therefore the structure of the test rig will be subject to the most demanding operative load when the LIM is installed.

Since the stators of the induction and synchronous motor will be alternatively mounted on the same frame, there is no need to perform the structural analysis for each motor load and only the greatest normal force is considered to size the framework components.

The attractive load is supposed to be uniformly distributed on one side of the silicon steel plate shown in Fig. 6.9. It should be noted that, the attraction between stators is more intense in the passive areas of the machine since the induced currents in the mover generates a repulsive force at their passage. Therefore, the

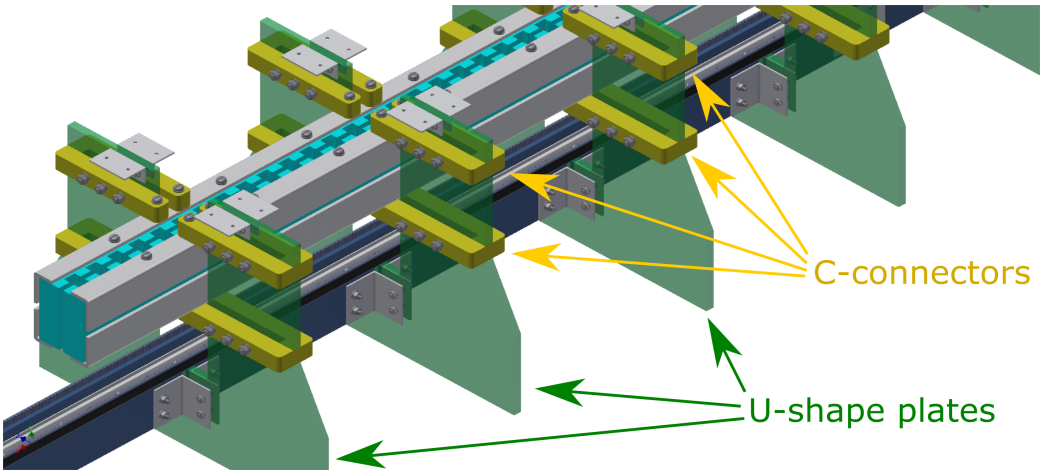

Figure 6.11: Technical drawing of LIM stator connected to the frame structure

instantaneous force resultants reported in Fig. 6.10 are not uniformly distributed along the stator lengths.

In order to simplify the structural analysis, the applied load is still considered uniformly distributed, but a safety factor of 1.5 is considered. This factor takes into account of the structural model approximations and attains sufficient operational leeway from the rated load. Considering the peak normal force in Fig. 6.10 and a safety factor of 1.5, the structure under investigation must be capable of withstanding a load of 17400 N applied on both sides of the frame with a total displacement lower than 250 μm on each side.

The motor is anchored to the frame by metallic connectors positioned below and above the stators and coloured in yellow in Fig. 6.11. The C-shape connectors transmit the load to the main structure of the frame which is formed by 9 U-shape plates linked by a central beam and coloured in green in Fig. 6.11. The attractive force acting on the stators tends to stretch the legs of C-shape connectors toward the airgap.

At the same time the load is transmitted to the lateral surface of the U-shape plate causing flexure towards the airgap. The thickness of the U-shape plates along the direction of the load is rather large to provide the structure with high bending resistance.

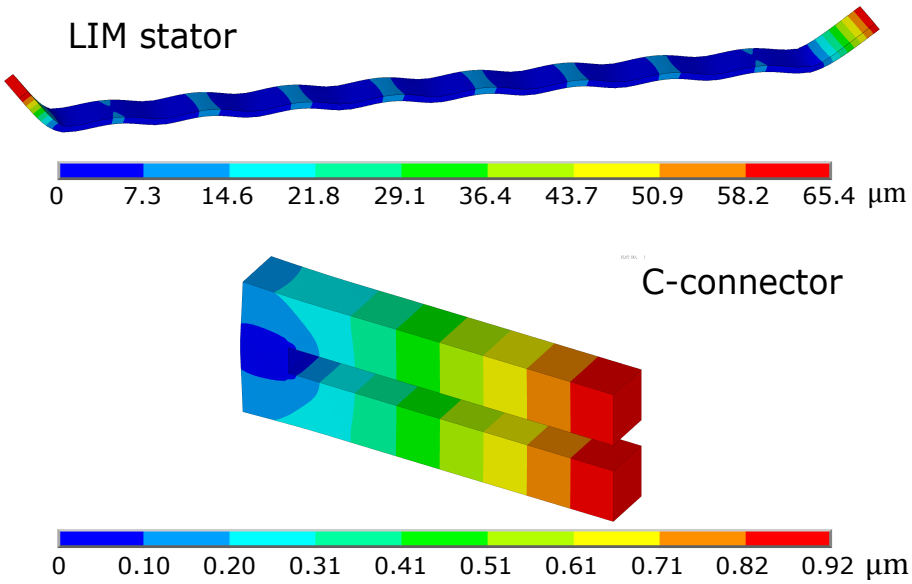

Figure 6.12: Deformation of LIM's stator and C-shape connectors under the maximum load

6.5.2 Results of the Structural Analysis of the Frame

The structural analysis performed on the simplified structure of the stator back iron with the structural constraints positioned on the bolts location shown in Fig. 6.9 and with a uniformly distributed load of 17400 N yields the deformation shown in Fig. 6.12. The displacement in the constrained area of the machine does not exceed 10 μm. The max displacement occurs where the structure is less constrained in proximity of the tip of each stator side and is about 65 μm.

Since two C-shape connectors are mounted on each side of every U-shape plate, the load which each connector withstands is $1/18^{th}$ of the distributed load (approximately 967 N). The traction load causes the deformation distribution shown in Fig. 6.12. The displacement at the connector basis is almost negligible, but it gradually increases along the connector legs. The maximum displacements occurs in correspondence of the connector tips and it is approximately 1 μm.

In turns, each U-shape plate is subject to 967 N applied in correspondence of the locations of the two C-shape connectors as shown in Fig. 6.13. The figure shows only half of the U-shape plate, since the structural analysis was solved taking

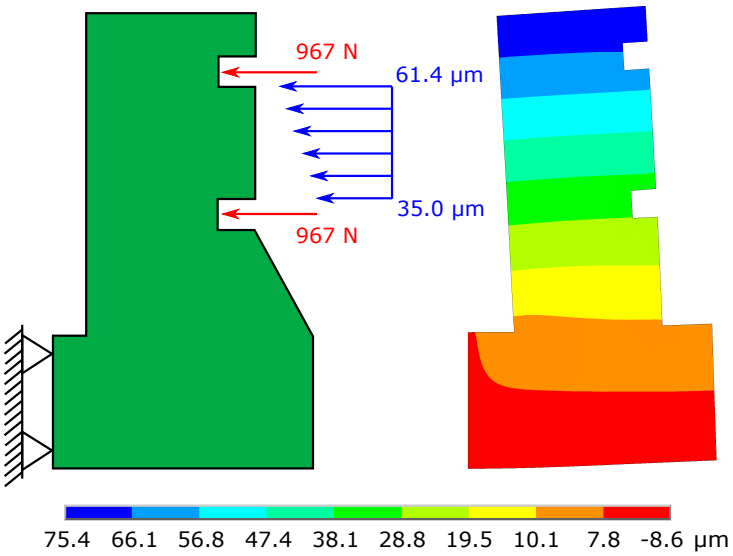

Figure 6.13: Deformation of U-shape plates under the maximum load

advantage of the frame symmetry. In order to simulate a symmetric structure a fixed constraint must be imposed on the surface located along the symmetry axis as shown in Fig. 6.13. The loads cause a deflection of the plate that gradually increases toward the top of the plate. The displacement is not uniform in the airgap region (between the two slots in Fig. 6.13 where the forces are applied) and the maximum is approximately 61 μm.

The summation of the displacements of stator housing components that are subject to the attractive force is 127 μm which is lower than the required 250 μm. The structural analysis performed on the components demonstrated that the design structure is capable of withstanding the load without excessive deformations.

Even though the normal force represents the most important requirement to size the prototype framework, the stator housing has to withstand a recoil force which acts in opposite direction to thrust. Since this force tends to accelerate the stators in the direction opposite to the motion, linear electrical machines are usually restrained to impede any movements. The catapult is designed to be easily transported and it is not anchored to any additional support. Therefore, it is important to make sure that the thrust produced by the motor does not cause any stator movements. The machine does not move under load only when the following condition

is satisfied:

$$F_p - \mu_p m_p G < 0 \tag{6.12}$$

where F_p is the prototype thrust, m_p the mass of the test rig and μ_p is the friction coefficient. Since the mass of the whole rig is 298 kg and the static friction coefficient between steel and wood is approximately 0.5, the force needed to move the rig must be larger than 1462 N. Since a propulsive force of such an intensity is never reached, the inequality in eq. 6.12 is satisfied and the stator frame does not move during operations.

6.5.3 Structural Analysis of the Brake Framework

A similar analysis can be performed on the structure that sustains the magnetic brake. Since the nominal airgap of the magnetic brake is only 1 mm, the max deformation allowed is approximately 50 μm. The maximum attractive load is experienced at high mover speeds and is approximately 2650 N per stator side which becomes about 4000 N considering a safety factor of 1.5. When this load is uniformly distributed upon the surface of the brake's stator, it causes the deformation field shown in Fig. 6.14. The max displacement is reached at the stator edges and is about 1.4 μm.

The brake's stator sides are joined to four U-shape plates by C-shape connectors similar to those used to sustain the stators of the induction motor. Each C-shape connector carries a tension load of 500 N which in turn is applied to the U-shape plate. The maximum displacement at the C-shape connector tip is about 1.0 μm whereas the U-shape plate moves at most 12.4 μm between the two slots where the load is applied.

The maximum displacement that is expected in the brake's airgap region is therefore 14.8 μm which is less than 5% of the airgap length. In conclusion, also the structure of the magnetic brake is capable of withstanding the forces that are generated by the attractive force between magnets.

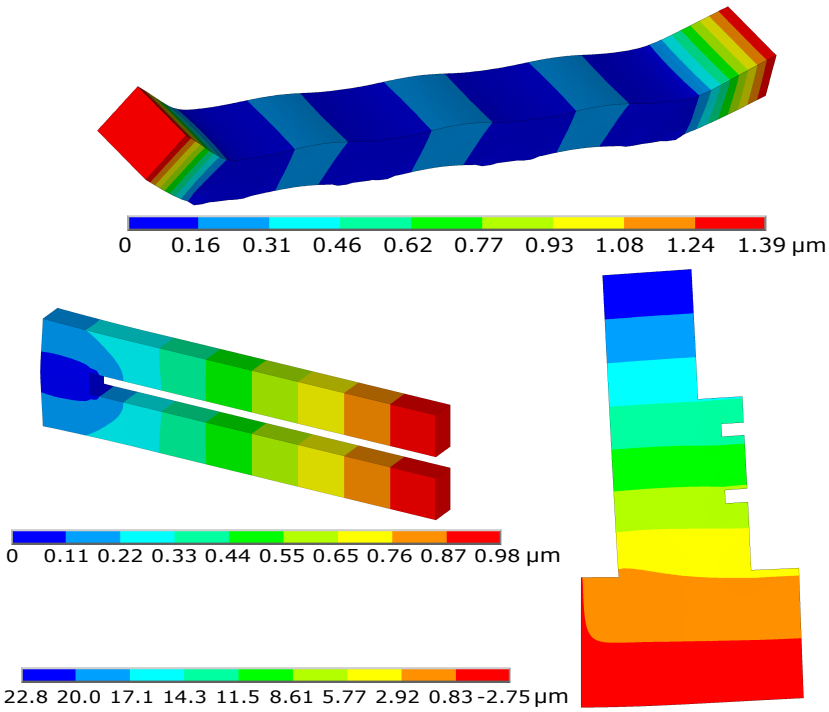

Figure 6.14: Deformation of all the components of the electromagnetic brake's structure

6.6 Prototype Thermal Analysis

The thermal analysis of the conductive components of the asynchronous motor during the launch is performed using the method developed and used for the civil aircraft launcher in Chapters 4.

Since the rated acceleration is rather intense, the mover takes only 318 ms to leave the stator completely. Adding the time required to build up the magnetic flux inside the machine, which is approximately five times the time constant of the motor (585 ms), the current is normally supplied for only 903 ms. The temperature variation of the stator winding under the rated current density can be estimated using the Onderdonk's law (eq. 4.159). Even though the current density in the motors is more intense than the current density of an electrical machine for continuous operation without active cooling, the power supply is connected for such a short time that the temperature variation of the stator windings remains within 1 K after a single launch. According to this result, the temperature rise

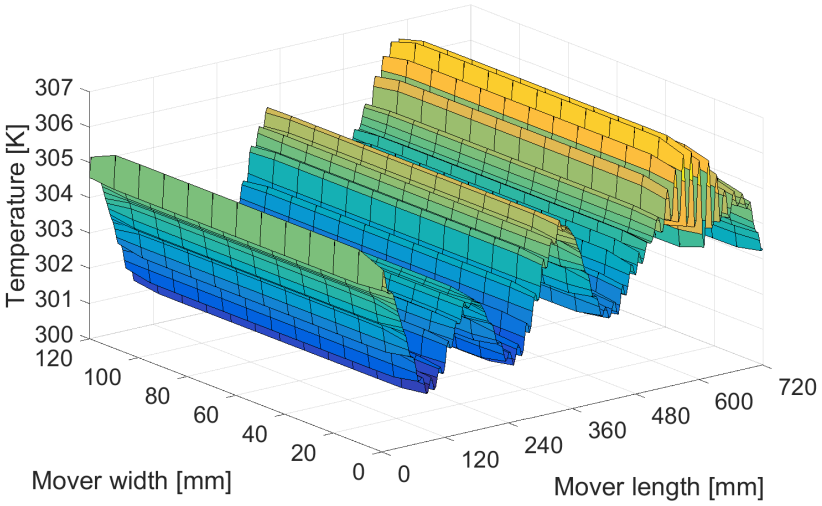

Figure 6.15: Temperature distribution over the surface of the aluminium plate at the end of the launch

in the stator windings does not represent a particular restriction on the number of launches that can be performed consecutively.

Thermal analysis is also carried out on the aluminium plate of the induction motor considering an initial room temperature of 298 K (25 °C). Since the supply frequency is rather small, the induced current distribution across the aluminium thickness is not affected by the skin effect. Consequently, the current density and the temperature distribution along the aluminium thickness is quite homogeneous. The temperature distribution at the end of the launch over the external surface of the aluminium plate is shown in Fig. 6.15. The induced current causes a temperature rise of only 9.5 K which allows limited consecutive tests before the machine cools down.

Thermal analysis has been also performed on the conductive components subject to currents induced by the magnetic brake. The strong forces that abruptly slow down the mover are caused by eddy currents with densities up to 227 A/mm^2. Thermal analysis can be used to investigate if the high density braking eddy current will cause significant enough temperature increase to compromise the structural properties of the material.

Since strong applied arresting forces may exert significant momentum on the mover carriages, the magnetic brake acts on the plate overhang located in proxim-

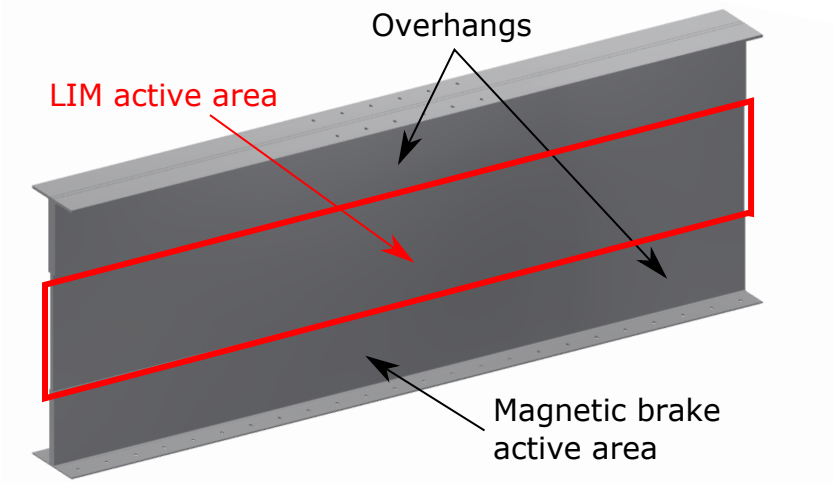

Figure 6.16: 3D view of the active and passive regions of the mover of the induction motor

ity of the guidance system as shown in Fig. 6.16. In this region, the central plate of the induction motor is glued to two aluminium angle brackets which are used to connect the main body of the mover to the carriages.

Since the angle brackets and the central plate of the induction motor are made out of the same material, the current density is homogeneously distributed across the mover thickness. Thermal analysis can be performed as if the plate is formed from a continuous material, even though the low conductivity glue between the brackets and the central plate is a thermal insulator. The layer of epoxy resin is so thin that its contribution can be neglected without leading to significant errors. The thermal models used for the mover central plate can be extended to the brake active area leading to the results in Fig. 6.17.

The maximum temperature increase occurs in proximity to the leading edge of the mover, since the magnetic field acts for a longer time in this area. Despite the high current density induced by the magnetic brake, the mover comes to a standstill in such a short time (90 ms) that the aluminium reaches only 302 K starting from an initial temperature of 298 K. It may be argued that the motor exit temperature should be used in place of the environmental temperature as initial condition, but the temperature delta will always remain 4 K. Since trailing edge of the mover does not enter the brake, the temperature of the aluminium does not change in this area.

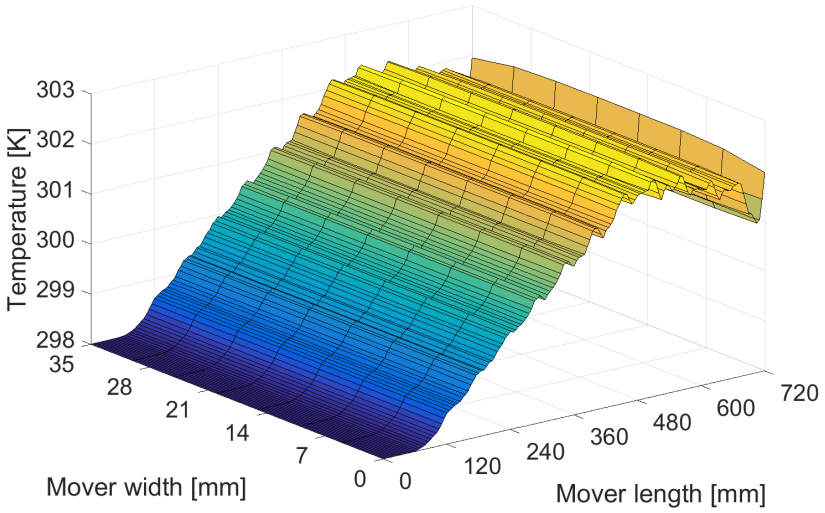

Figure 6.17: Temperature distribution on the surface of aluminium as it comes to a standstill

The thermal analysis of the conductive components of the test rig has shown that the temperature increase does not threaten the electrical insulation of the stator windings and the structural properties of the aluminium plate at any phase of the launch. Moreover, since the temperature delta after a single launch is limited to a few degrees Celsius, tests can be repeated consecutively without any particular precaution.

6.7 Experimental Results

6.7.1 Test of LIM

The LIM prototype was tested without any position feedback in open-loop mode applying the voltage-frequency profile shown in Fig. 6.18. The curves are plotted using the data measured by the AC drive during the acceleration. The applied frequency and voltage initially ramp up with an acceleration rate of approximately 125 Hz/s and 750 V/s to 21.5 Hz and 129 V respectively. After 171.5 ms the slope of the applied frequency and voltage profiles reduces to approximately 55 Hz/s and 290 V/s respectively. The launch terminates after 483 ms when the mover has travelled a distance of 2.57 m and exits the stator completely. At this point the

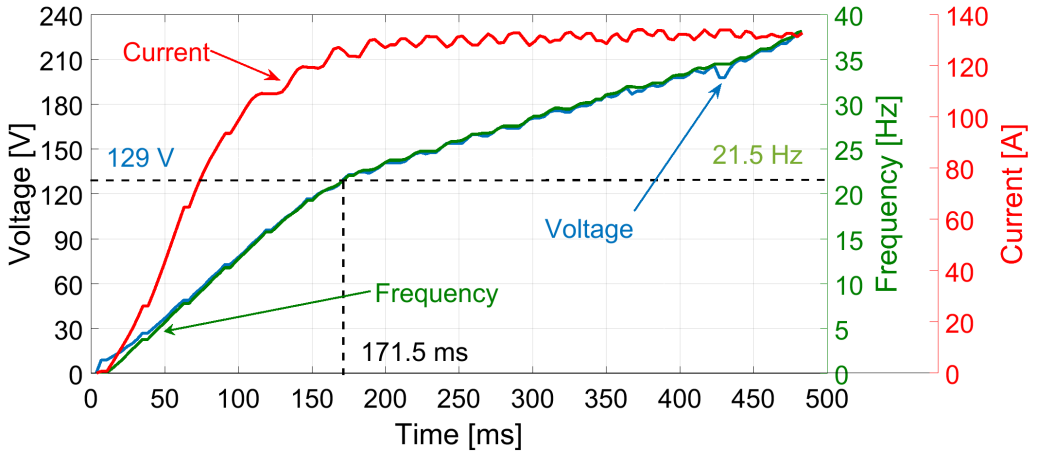

Figure 6.18: Induction motor voltage, current and frequency profiles measured by the AC drive

voltage and the frequency reach 227 V and 38.2 Hz respectively. This voltage and frequency profiles were chosen to give low slip and achieve high mover end-speed.

The frequency profile shown in Fig. 6.18 was also inserted in a finite element simulation of the LIM prototype, implementing a current wave shape varying according to the law

$$\begin{cases} I(t) = \sqrt{2} I_1 \cdot \cos\left(125\pi t^2\right) & \text{for t} < 171.5 \text{ ms} \\ I(t) = \sqrt{2} I_1 \cdot \cos\left(12\pi t + 55\pi t^2\right) & \text{for } 171.5 < \text{t} < 483 \text{ ms} \end{cases} \tag{6.13}$$

where I_1 is the root mean square of the current reported in Table 6.2.

In order to accurately model the motor with the finite element software, the moving part of LIM was loaded with the dynamic friction measured during the tests. Since the machine operates without position feedback, all the data was collected using an accelerometer mounted on the aircraft. In particular, the dynamic friction force can be calculated from the deceleration measured when no other force is acting on the mover. In the area between the stator and the magnetic brake there is not any electromagnetic force, so that the deceleration measured by the accelerometer can be only caused by the dynamic friction F_{Fr}. The force acting on the mover in this area was found to be approximately 43.5 N. Since the dynamic friction does not depend on the speed, but only on the characteristic of

the surfaces in contact, the friction force can be assumed constant along the launch track. The respective friction coefficient μ_{mov} can be calculated as

$$\mu_{mov} = \frac{F_{Fr}}{G \cdot (m_{mov} + m_{UAV} + m_{acc})} \tag{6.14}$$

where m_{acc} is the mass of the accelerometer (approximately 190 g). The friction coefficient measured during the tests is about 0.61 and includes the sliding friction between carriages and rails, the contact friction between timing belt and pulleys and the rotating friction between pulleys and their shafts.

The friction force was not only implemented in the FEA of LIM, but was also used to determine the total thrust generated by the motor during the tests. Indeed, summing the friction force to the product between the acceleration measured along the direction of the motion and the mass of the system (mover, UAV and accelerometer), it is possible to determine the instantaneous magnetic thrust that the linear induction motor delivers during the launch.

The integration of the data measured by the accelerometer allows the calculation of speed and position of the mover. The speed computed by the experimental data and the speed determined by the FEA software are compared in Fig. 6.19. FEA and experimental results show a good agreement on the speed profile except at the end of the launch when the mover exits the stator.

Fig. 6.19 also shows the synchronous speed of the travelling magnetic wave which corresponds to the frequency supplied by the AC drive to motor during the tests and implemented into the FEA software. The synchronous speed and the real speed of the mover can be used to determine the slip frequency of the induction motor using eq. 4.2. As can be seen in Fig. 6.19, the minimum slip frequency of the induction motor during the experiments is about 0.18 whereas the slip frequency reported in Table 6.2 (0.11) is never reached. The reason why the mover does not accelerate any closer to the synchronous speed could be connected to the low slope of the speed curves shown in Fig. 6.19 in the first 50 ms of the launch. The low acceleration level experienced by the mover in the initial part of the launch might be due to two main factors:

1. The launcher behaves as an inductor that needs a charging time of at least five time constants to build up the flux to the rated value. Since the time con-

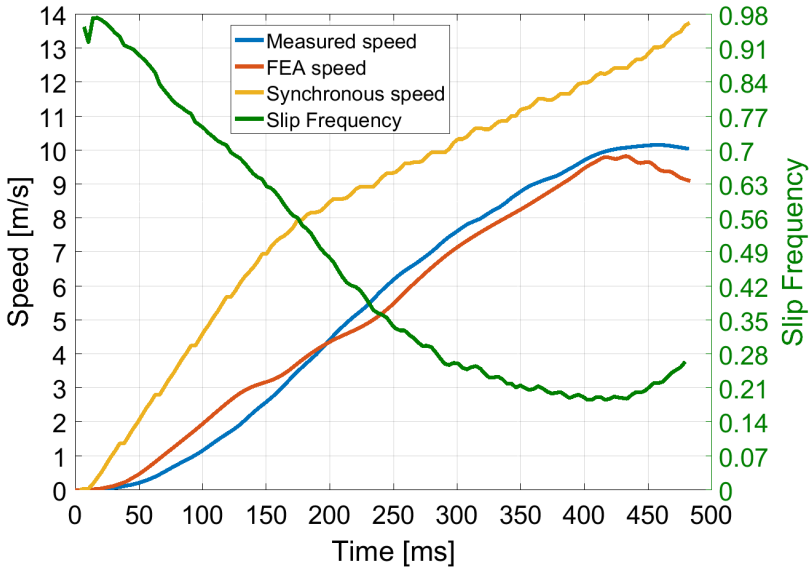

Figure 6.19: Comparison between synchronous speed, measured speed and speed computed by the FEA software

Table 6.5: Comparison between FEA and experimental performance

	Peak Efficiency	Power Factor
Finite Element Analysis	0.4327	0.1004
Experimental Data	0.4437	0.1406

stant of the motor is approximately 117 ms according to the data reported in Table 6.2 (L/R), the motor builds up the magnetic flux in about 585 ms which is a time longer than the time required to execute the launch. This is in line with the current profile measured by the AC drive during the tests.

2. The static friction when the mover is at rest is usually higher than the dynamic friction experienced along the launch track.

Since at the beginning of the launch the magnetic flux is weak, the aircraft does not move for at least 20 ms until the thrust overcomes the static friction. As soon as the aircraft moves, the total thrust that the motor can deliver is not enough to accelerate the mover at 5 G. The peak acceleration reached during the launch (approximately 4.3 G), is not enough to push the mover closer to the synchronous wave. An optimization of the launch performance could take advantage of the

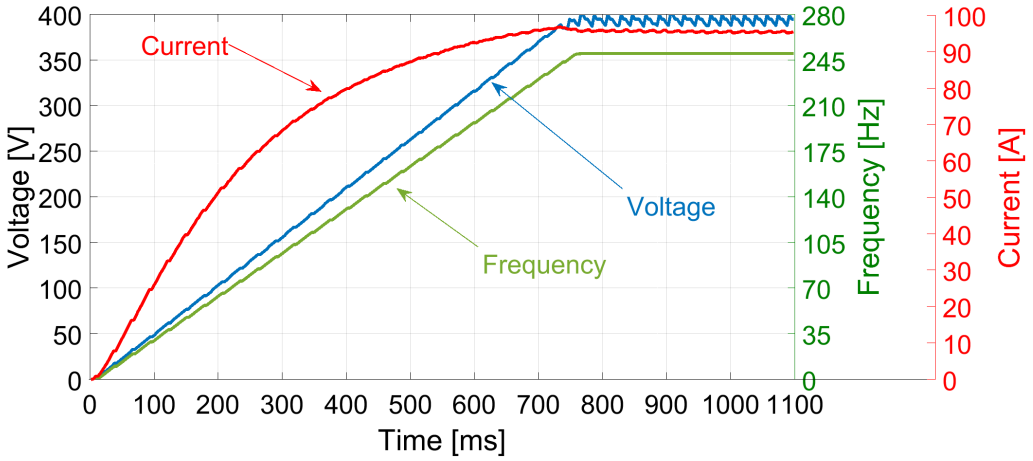

Figure 6.20: Motor voltage, current and frequency profiles measured by the AC drive

capability of the AC drive to delay the frequency ramp applying a constant low frequency voltage that does not produce any motion for an initial time span of at least 5 time constants. This procedure would allow the current to approximately reach its rated value before proceeding with the real launch.

The performance computed by FEA are compared with those calculated from the data measured during the launch in Table 6.5. The peak efficiencies are very similar whereas the power factors at take-off speed slightly differ. FEA computes a lower power factor since it slightly overestimates magnetizing and leakage inductance.

6.7.2 Test of the Concentrated Winding Stator as a LIM

The test of the LSM's stator as an induction motor was performed with the voltage and frequency profile shown in Fig. 6.20. In this case the frequency and voltage ramp up at constant rate of 327 Hz/s and 515 V/s respectively without changing slope. In this motor topology the frequency of the machine is much larger than the LIM previously tested, for the much shorter pole pitch.

The voltage required to generate a high frequency magnetic wave in the airgap is greater than the voltage applied to the previous motor and it reaches the maximum output voltage allowed by the AC drive (400 V). Even when the maximum voltage is applied the current that flows in the system does not equal the current that was

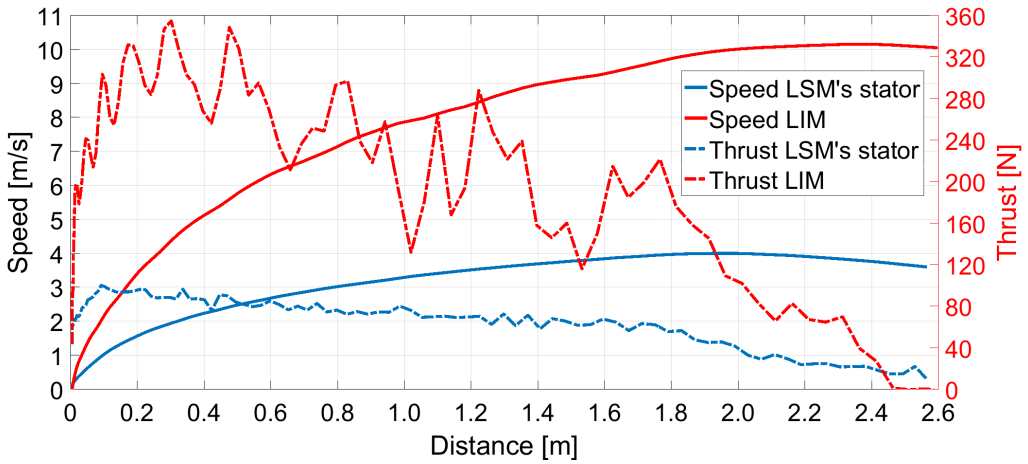

Figure 6.21: Comparison between speed and thrust achieved by LIM with concentrated and distributed windings

achieved in the LIM stators. The tendency of the current supplied by the AC drive and injected into the concentrated windings is shown in Fig. 6.20. The rated current of LIM would be reached with an applied voltage that would largely exceed the AC drive ratings.

The interaction between the magnetic flux generated by the applied voltage and the current induced in the aluminium sheet produces the magnetic force shown in Fig. 6.21. The chart also compares the thrust achieved by the LSM's stator with the thrust of the linear induction motor. The curves are plotted against the travelled distance rather than the launch time to be easily compared. Indeed the thrust delivered by the two motor topologies largely differs, so that they cover the launch track in a completely different time. Conversely, in both the experiments the acceleration of the mover is recorded across the same distance and it is easier to compare the variation of the variables with respect a constant parameter range.

Since the mass of mover used in both the tests is the same, the thrust delivered by the LSM's stator achieves lower acceleration and speed. The speed profiles of LIM and LSM's stator are compared in Fig. 6.21.

Speed and thrust profiles cannot be used as the only mean of comparison for the given motor topologies. Indeed, speed and thrust are only related to the output power of the machine whereas they do not provide any information about the input power. To fully characterize the motor performance, the AC drive used to control

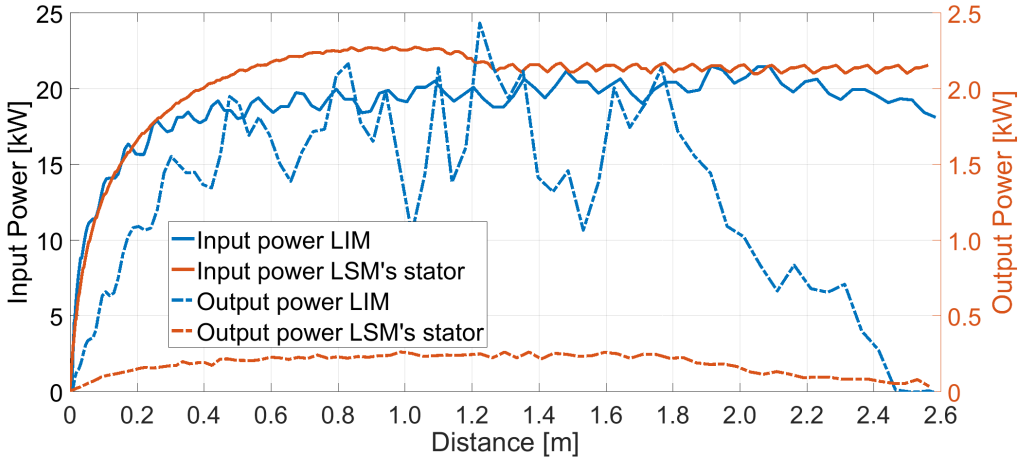

Figure 6.22: Comparison between input and output power of LIM with concentrated and distributed windings

the motor measures the power consumed by the system independently from the angle between voltage and current. The data collected from the AC drive during both the tests are plotted in Fig. 6.22. The input power profiles of LIM and LSM's stator are comparable whereas the output power tendencies largely differ.

Although Fig. 6.22 already suggests the motor with the best performance, the data available can be used to determine the machine efficiency and power factor. The output power profile P_o and the input power profile P_i in Fig. 6.22 together with the stator resistances R measured by the AC drive and listed in Tables 6.2 and 6.3 allowed the following calculations:

$$\eta = \frac{P_o}{P_o + 3RI^2} \tag{6.15}$$

$$\cos\phi = \frac{P_o}{\eta \cdot P_i} \tag{6.16}$$

where I is the stator current shown in Figs. 6.18 and 6.20. Equations 6.15 and 6.16 neglect the hysteresis losses in the stator core which especially affect the LSM's stator when it operates at high frequency. The Joule losses in the aluminium plate are also not taken into account in eqs. 6.15 and 6.16 although they affect the performance of LIM for the high value of the magnetizing inductance. Nevertheless, since hysteresis and secondary Joule losses are minor effects, eqs. 6.15 and 6.16 can be still considered a good estimation of the real power factor and efficiency.

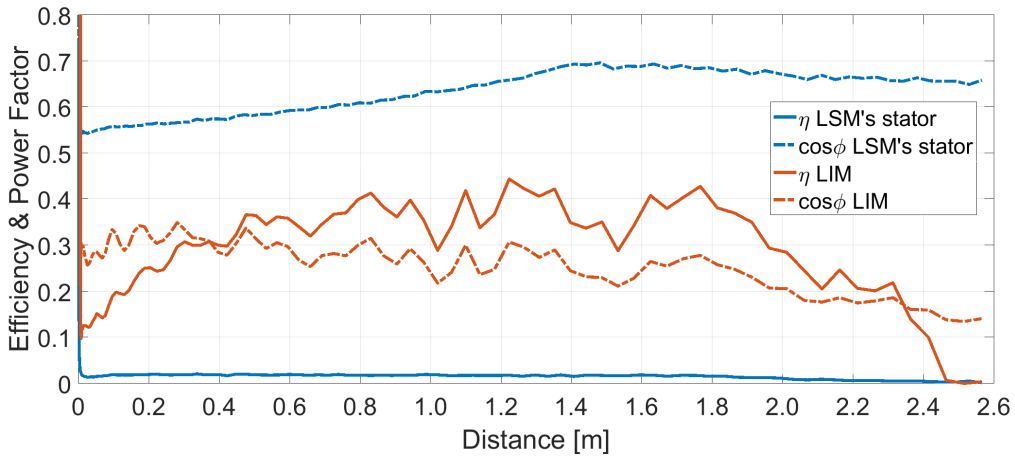

Figure 6.23: Comparison between efficiency and power factor of LIM and LSM

The variation of efficiency and power factor of LIM and LSM's stator during the launch are compared in Fig. 6.23. Since the rated current flowing the in LSM's stator (see Fig. 6.20) is rather large with respect to the design current listed in Table 6.3, the copper losses in stator windings sensibly reduce the value of the efficiency. As a consequence of the large Joule losses and active power, the power factor of the LSM's stator is rather large with respect to the power factor of LIM. On the contrary, the efficiency of LIM largely exceeds the efficiency of the LSM's stator and yields a comparable input power although the greater output power (see Fig. 6.22).

6.8 Contribution to Knowledge

The prototype represents an important added value in terms of PhD studies, especially as there has been relatively little experimental work published in this area. The expected academic outcomes from this rig will be significant. The comparison between optimised LSM and LIM systems would be of great academic and industrial interest, and would be suitable for top level journal submission. It is also of note that the "working prototype" will be a fully functioning small launcher that will serve as an excellent demonstrator during outreach events, while video of the real launch can be shown to showcase the experimental activities. Furthermore, the objective is to have a completed system that can reproduce the real catapult

system and can be used for the purposes of the Institute for Aerospace Technology and future research work.

The experimental results reported in this chapter have shown a good agreement with the numerical procedures used to model the induction motor. The theory developed to size a large scale launcher was experimentally validated and can be applied to design LIMs with different power requirements. The author is confident in extending this conclusion to the design method showed in Chapter 5 to size the LPMSM.

Additionally, this chapter experimentally proved that the LSM's stator used as an induction motor performs worse than a LIM optimized to achieve the same requirements. Therefore the procedure used to design a synchronous launcher cannot be used to size an asynchronous launcher and vice versa. The comparison of the performance of LIMs and LPMSMs with the same stator geometry often proposed in literature was proved to be inaccurate to determine the best motor topology.

This chapter has also introduced a method to design a passive, fail-safe breaking system which can be easily extended to a larger launcher. For the first time the framework of a linear motor was accurately described and designed to be as light as possible. The structural analysis of the framework components has been carried out considering the normal attractive load between stators computed by FEA. This chapter showed a structural design procedure that can be extended to the electromagnetic catapult for civil aircraft launch applications.

Chapter 7

Superconducting Linear Synchronous Motor

Chapters 4 and 5 have already shown how conventional synchronous and asynchronous machines can be used to accelerate an Airbus A320-200 to the required take-off speed. This chapter deals with the design of a superconducting linear synchronous motor (SCLSM) for electromagnetic launch applications. The chapter introduction describes the machine layout and the main operative principles suitable for the civil aircraft launcher. Next the distribution of the superconducting material inside the cryostat and the geometrical features of the machine are defined. The geometry of the superconductors will be used to determine the magnetic field distribution across the machine and the electromagnetic performance of the synchronous motor.

The electromagnetic design of a machine that operates at cryogenic temperature cannot be independent from the thermal analysis of its components. In particular the temperature evolution of the cryostat and the design of an effective thermal insulation will be shown. The oscillatory nature of the magnetic field in the airgap generates heat losses that must be removed to prevent quenching of the superconducting material. This internal heat dissipation represents the main requirement to size the refrigeration system whose static model will be introduced.

Eventually, the design results will be reported considering the impact of the cryocooler power requirements on the overall performance of the motor. The

procedure to design the non-conventional launcher is meant to be general, to be extended to any other superconducting synchronous motor.

7.1 Introduction to SCLSM for EML

Superconducting synchronous machines are recognized to offer some advantageous features like high power factor and efficiency even accounting for the input power required by the cryogenic system [46]. Existing SCLSMs with power requirements similar to those for civil EML systems employ superconducting coils to produce the excitation field in the airgap [43]. In a similar way the electromagnetic launcher proposed in this chapter generates the magnetic field to produce the required propulsive force using superconducting coils (SCs) embedded inside an evacuated mover.

The double-sided configuration of the machine's stator has been selected to avoid the generation of normal forces. Indeed, a suspension force is not needed and only the propulsive force is generated. The track is placed vertically under the runway and is subdivided in sections which are progressively connected to the power supply. The stator windings are fed at increasing frequency while the aircraft is moving. The stator operates at environmental temperature since the windings are made of conventional conducting material. Therefore, no additional stator cooling is required since the current density in the stator coil is set to a value that does not threaten the performance of the electrical insulation during the short operating time. Distributed double-layer windings were selected for the stator coils, despite the potential benefits that a synchronous machine with concentrated windings may have, as discussed in Chapter 5. Indeed, one of the main objectives of the SCLSM design is to reduce the harmonic content of the magnetomotive force in order to diminish the alternating current losses in the superconductors.

The SCLSM's cryostat is mounted on carriages that slide on rails located below the stator which are responsible for keeping the mover in straight direction during acceleration. Fig. 7.1 shows a cross section of the double-sided stator topology and a schematic of the guidance system connected to a four poles mover. The machine in Fig. 7.1 is similar to the real launcher, but the final layout might have a larger number of poles. The connections to the aircraft and the runway pavement

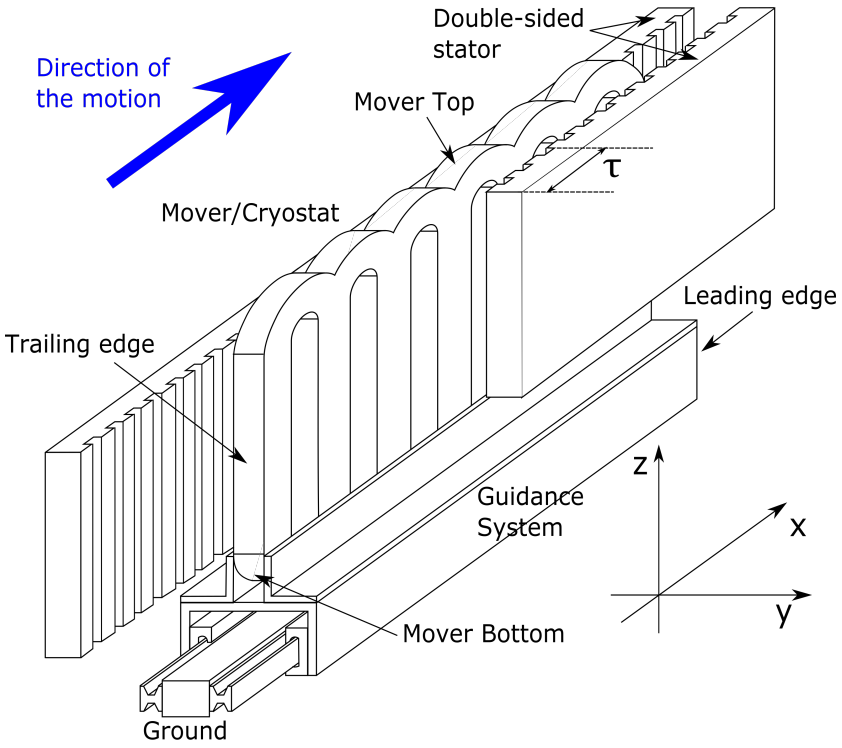

Figure 7.1: Section of a double-sided SCLSM stator with a four poles mover anchored to the guidance system

were omitted for clarity, but they are positioned above the stator.

The SCs are made out of magnesium diboride (MgB_2) which is the high temperature superconductor (HTS) with the most suitable manufacturing technology readiness level for EML application. In particular the good mechanical properties, low bending radius, round cable availability and no need for texturing are advantages that can be exploited in superconducting launchers. With the continuous developments in MgB_2 doping processes, current density improvements under high external magnetic field can be envisaged [120]. MgB_2 has a relatively low transition temperature ($T_c = 39$ K) compared to other HTSs (YBCO 92 K, BSCCO-2223 108 K), but the selected operating temperature of the mover is very close to the temperature that should be used with YBCO or BSCCO-2223 tapes. Additionally, MgB_2 wires are the most cost-effective solution being approximately 20 times less expensive than YBCO tapes [121]. So far, MgB_2 HTS has been employed to design high-power rotary synchronous generators for wind

Table 7.1: Coolant properties at atmospheric pressure

Coolant	**Melting Temperature**	**Boiling Temperature**	**Specific Heat [J/kg/K]**	**Latent Heat [kJ/kg]**
Liquid Neon (LNe)	24.6 K	27.1 K	1860 (27 K)	85.8
Liquid Hydrogen (LH_2)	14.0 K	20.3 K	9565 (20 K)	461.0
Liquid Helium (LHe)	1.0 K	4.2 K	5243 (4.2 K)	20.75

turbine applications ([122], [121]), while in this work it is proposed for the first time for EML systems.

MgB_2 presents superconducting properties at temperatures below 39 K, but its electromagnetic characteristics become interesting at operative temperatures below 25 K. At such a temperature only the three liquid coolants listed in Table 7.1 can be used. In particular it is desired to operate close to the boiling point of the coolant to take advantage of the latent heat exchanged during the phase transformation. Neon is liquid over a very narrow temperature gap and it may experience rapid phase changes under small temperature variations. Liquid Helium is the coolant that has been largely used to cool down Low Temperature Superconductors (LTSs) below their critical temperature, but its capability to remove heat is limited by its specific heat and latent heat as can be seen in Table 7.1. Moreover, helium liquefaction requires a lot of energy since the boiling temperature is close to absolute zero. Liquid hydrogen is an excellent coolant able to remove large quantities of heat before full vaporization and it is liquid in a temperature range which is ideal to enhance the MgB_2 electromagnetic properties. For this reasons, the operating temperature of the superconductors in the EML launcher is 20 K and liquid hydrogen is used to keep this temperature constant.

MgB_2 superconductors are arranged to form coils that are hosted inside the cryostat which is connected to the aircraft undercarriage. The coils are tensioned and held in place by structural supports which have the role to withstand the load during launch operations. Before each launch the cryostat is refilled with liquid hydrogen to keep the MgB_2 superconductors at the design temperature and sealed to avoid any hydrogen leakage. This cooling method has been selected to avoid any movable connection with the external refrigeration system and to reduce the number of machine components at cryogenic temperature. After the take-off

speed is reached, the aircraft detaches and the mover is decelerated by a braking system. To prevent any additional thermal load, the mover slows down without any electromagnetic interaction with the superconducting coils using a mechanical brake, an external electromagnetic brake or a combination of both. The mover can be returned to the start position using the SCLSM while producing very little additional heating loss compared to the losses generated during launch.

The mover structure is made out of aluminium for its structural and thermal properties. In particular, the low density and the high specific resilience make this material suitable to sustain the propulsive force with a light structure. Moreover, aluminium alloys represent a class of structural metals for subzero-temperature applications and they are employed for structure that operates at temperatures as low as -270 °C (3 K) [123]. Aluminium alloys also present low emissivity at cryogenic temperature which make these materials good insulators against heat transmitted through radiation. The mover is iron-less to reduce the weight and to avoid saturation of the ferromagnetic material due to the high magnetic field density.

7.2 Definition of SCLSM Geometry

The SCLSM design begins with the definition of the geometrical features of the superconducting cables that carry the DC transport current needed to produce the required magnetic field. The distribution of the superconducting material inside the cryostat is determined in order to achieve high magnetomotive forces and to prevent the quenching of the superconductors due to exceeding magnetic flux densities. Therefore, the selection of the geometrical characteristics proceeds with the estimation of the current carrying capability of the superconductors and with the calculation of the magnetic field density at their cross section.

The average magnetic flux density that is expected in the middle of the mover during the launch is approximately 2 T. Considering the MgB_2 critical current density variation with the magnetic field measured by CERN [124], the superconductor should be able to carry a transport current of 1750 A/mm^2 density with external magnetic field densities of 2 T. The dependency of the critical current density J_c on the external magnetic flux density at a temperature of 20 K is shown

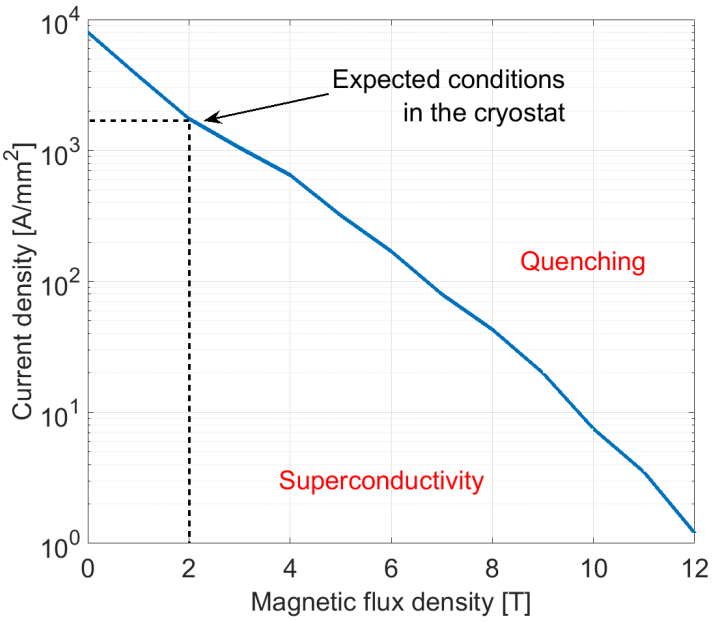

Figure 7.2: Critical current density variation with the magnetic flux density at 20 K

in Fig. 7.2. If the superconductor undergoes a combination of current density and magnetic field which defines a point above the line in Fig. 7.2, it will quench becoming a normal conductor. When quenching occurs the rapid increase of resistivity and the high current density would generate a tremendous amount of heat that would burn the entire coil. Taking into account that hot spots may appear for material defects and rapid transients, the rated current density will be set with a significant safety margin with respect to the critical value J_c.

Several wires with different section shapes and inner arrangements of the superconducting material are available on the market. The wire that is proposed for the superconducting launcher has a round shape to ensure good performance in both DC and AC environments with external magnetic fields crossing the wire section from any possible direction. This is a significant advantage with respect to other HTSs that can be manufactured only as tapes and can be subjected to fluctuating fields only in a specific direction. The MgB_2 round wire has a diameter D_w of 1.0 mm and its section includes 19 superconducting filaments as shown in Fig. 7.3. The outer sheath can be made out of nickel, monel or other alloys (both magnetic and non-magnetic) that increase the mechanical strength. The inner matrix

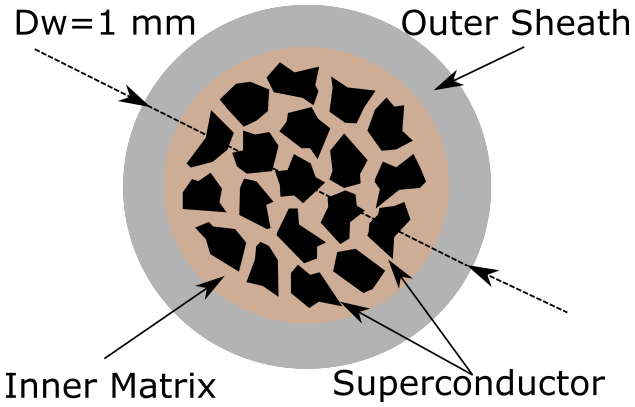

Figure 7.3: Cross section of a MgB_2 wire implemented in the EML system

is usually made out of a copper-iron alloy, but the conductive material is never in direct contact with the superconducting filaments. Copper is requested to provide electrical and thermal protection in the unlikely event of a sudden loss of superconductivity due to exogenous factors.

Considering that the 19 superconducting filaments in Fig. 7.3 can be approximated as circles with a diameter of about 10% of D_w, the area of the superconducting material in each wire is

$$A_{sc} = 19\frac{\pi}{4}D_{fil}^2 = \frac{\pi}{4}(0.1 \cdot D_w)^2 = 0.1492 \text{ mm}^2 \tag{7.1}$$

Considering the experimental data measured by CERN [124] and reported in Fig. 7.2, with an external field of 2 T the MgB_2 wire in Fig. 7.3 can carry approximately

$$I_{2T} = A_{sc} \cdot J_c \simeq 250 \text{ A} \tag{7.2}$$

An excitation field strong enough to produce the required thrust can be achieved by several superconducting wires wrapped together to form cable with a more complex structure. The structure of the cable proposed for EML systems is similar to the one adopted by CERN in 2014 to achieve the world record in transport current for a single cable [124]. This cable is in turns an assembly of smaller cables whose structure is shown in Fig. 7.4.

Twelve of the wires in Fig. 7.3 can be wrapped around a copper core to form

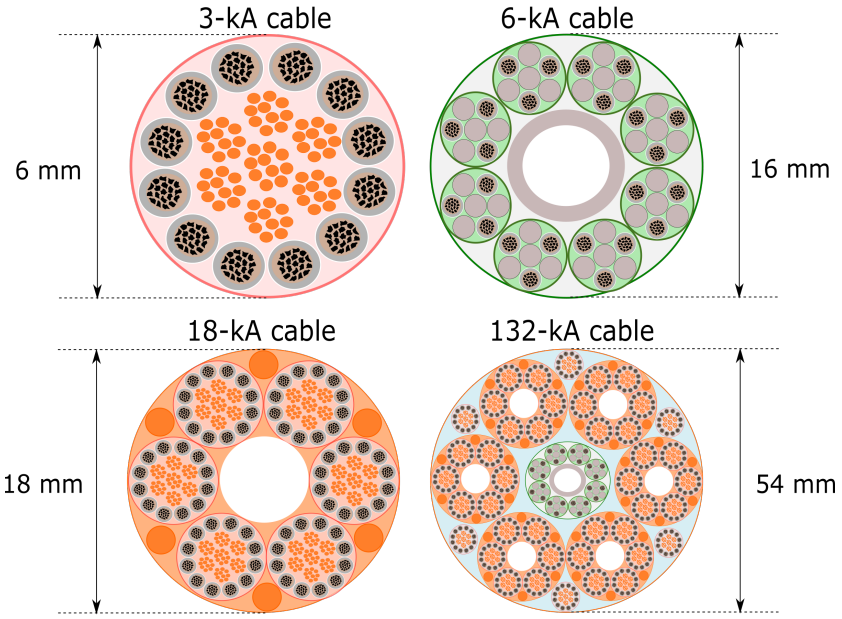

Figure 7.4: Inner structure of superconducting cables adopted for the launcher

a cable that is capable of transferring 3 kA under 2 T as shown in Fig. 7.4. Six 3-kA cables are in turn wrapped around a cooling channel of 6 mm diameter and embedded in a copper matrix to form an 18-kA cable as shown in Fig. 7.4. The cable on the top-right corner of the same figure is formed by 8 smaller cables that are twisted around a cooling channel of 8 mm diameter and are able to carry 0.75 kA apiece. An epoxy membrane surrounds the 6-kA cable and each of the 0.75-kA cables that compose it. The internal structure of the final superconducting cable is an assembly of all the previous cables which should be able to transfer 132 kA at 2 T when it is submerged in liquid hydrogen at 20 K.

In order to verify whether the selected current density really generates a magnetic field that does not exceed the critical density of 2 T, the Biot-Savart law is applied to the section of the 132-kA cable in Fig. 7.4. The structure of the 132-kA cable need some simplification before performing the calculation. Indeed, the Biot-Savart law should be applied to each of the 19 superconducting filaments within the wire in Fig. 7.3 and repeated for all the wires arranged inside the 132-kA cable. Such a level of complexity at this design stage can be avoid using the simplified structure shown in Fig. 7.5 without losing accuracy.

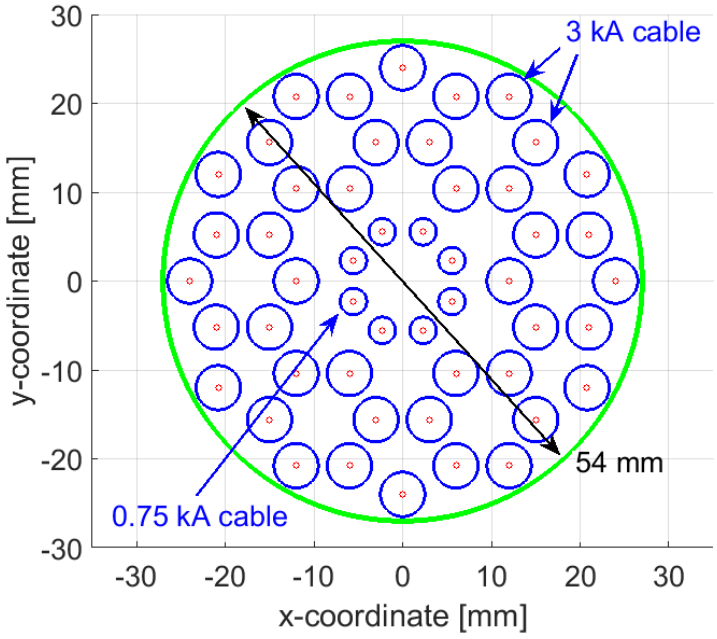

Figure 7.5: Simplified structure of the 132-kA superconducting cable

In the simplified structure in Fig. 7.5 the 3-kA cables and the 0.75-kA cables were replaced by superconducting rings of negligible thickness. The Biot-Savart law can be applied on this simplified section of the superconducting cable to compute the magnetic field density distribution. The magnetic flux density B_i generated by the i^{th} ring can be computed using eq. 7.3 for the area outside the ring and eq. 7.4 for that inside.

$$B_i = \frac{\mu_0 I_i}{2\pi r} \tag{7.3}$$

$$B_i = \frac{\mu_0 I_i}{2\pi R_{ri}} \tan \alpha_m \tag{7.4}$$

where I_i is the rated current of the conductive ring (0.75 kA or 3 kA depending on the ring under considerations); r is the distance between a generic point on the cable cross-section and the centre of the ring; R_{ri} is the radius of the ring under consideration; α_m is the twisting angle of the superconducting cable. The twisting angle used in the Biot-Savart law is the results of the minimization procedure of the cable self and mutual inductances that will be explained in Section 7.4. The field over a point of the cable cross sections with coordinate (x,y) is the sum of all

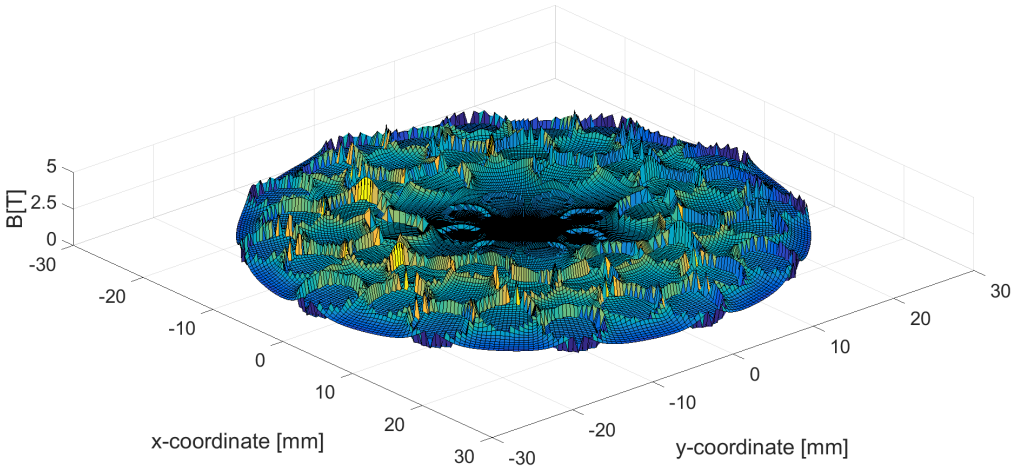

Figure 7.6: Magnetic field density on the superconducting cable cross section generated by a current density of 1750 A/mm^2

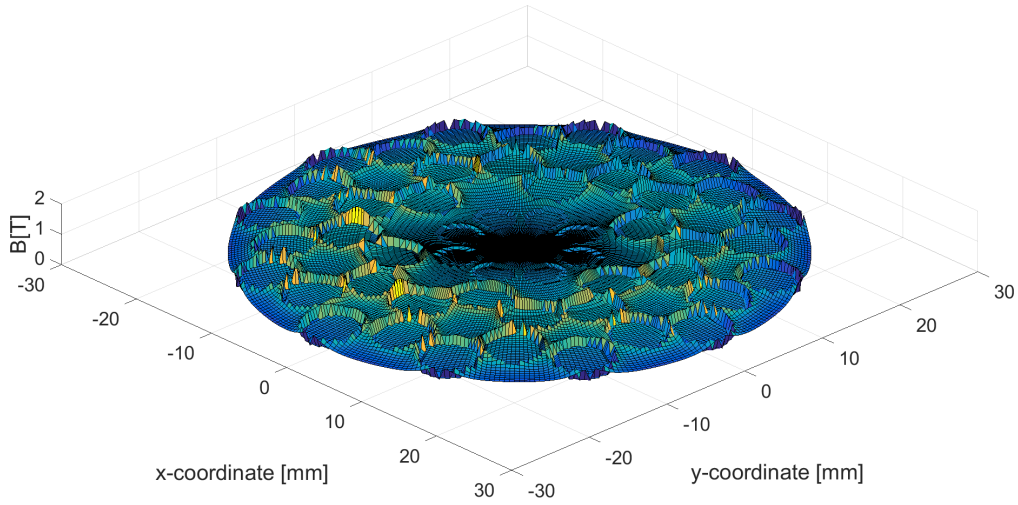

Figure 7.7: Magnetic field density on the superconducting cable cross section generated by a current density of 583 A/mm^2

the ring contributions and it is computed

$$B(x,y) = \sum_i B_i(x,y) \tag{7.5}$$

Eq. 7.5 is solved on a grid of points upon the cable cross section and the results are shown in Fig. 7.6. The peak of the magnetic field density is reached in proximity of the superconducting rings where it hits approximately 4.1 T. With such

a magnetic field density and a current density of 1750 A/mm^2, MgB_2 would lose superconductivity as shown in Fig. 7.2.

In order to restore the superconducting properties the current density was reduced to one third of the initial value. As can be seen in Fig. 7.7 the magnetic flux density reduces proportionally leading to a peak of 1.35 T. A current density of 583 A/mm^2 allows magnetic flux densities up to 4.2 T whereas a flux density of 1.35 T corresponds to a critical current density of 3020 A/mm^2 as can be seen in Fig. 7.2. The large margins between rated and the critical conditions guarantee safe operations preventing quenching due to hot spots. Moreover the superconducting cable needs to withstand the additional magnetic flux coming from the neighbouring 132-kA cables and that produced by the stator winding harmonics. Additionally, the alternating flux associated with the secondary harmonics induces currents in the superconducting filaments leading them closer to the critical conditions.

Under a current density of 583 A/mm^2, a single superconducting cable carries 44 kA. To achieve the magnetomotive force (MMF) intensity to produce the required thrust, 10 cables ($N_{132\,kA}$) were implemented in a single cryostat section. MMF of such intensity has been shown to be practically achievable in commercial magnetically levitated (MAGLEV) systems [43]. To reinforce the field strength some smaller cables, were inserted in the spaces available between the main ones. These cables are formed by seven 3-kA cables wrapped around a cooling channel with 8 mm diameter as shown in Fig. 7.8. The superconducting cables are arranged in two layers as shown in the cryostat section in Fig. 7.9.

In order to verify whether the 132-kA cable distribution inside the cryostat generates magnetic field densities above the critical value with a current density of 583 A/mm^2, the Biot-Savart law has to be applied again to all the superconducting wires shown in Fig. 7.9. To reduce the calculation complexity, the method that led to the simplified structure in Fig. 7.5 is also used in this case. Approximating both the 3-kA and 0.75-kA cables as superconducting rings and solving the Biot-Savart law over a grid that covers also the liquid hydrogen ducts yield the magnetic flux density distribution in Fig. 7.10. The 3D view of the magnetic flux density shows that the peak flux density is 2.63 T, safely below the maximum limit of the MgB_2 at 583 A/mm^2. This preliminary calculation proves that the superconduc-

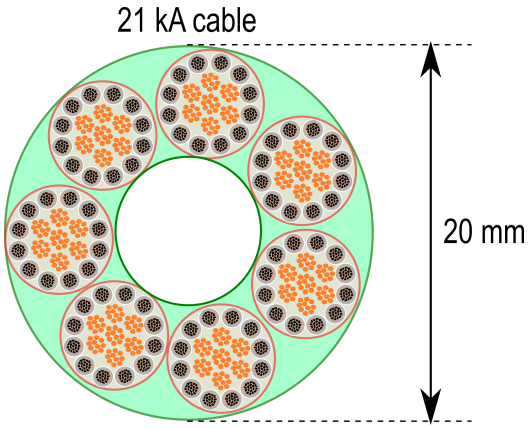

Figure 7.8: Section of a superconducting cable used to reinforce the magnetic field

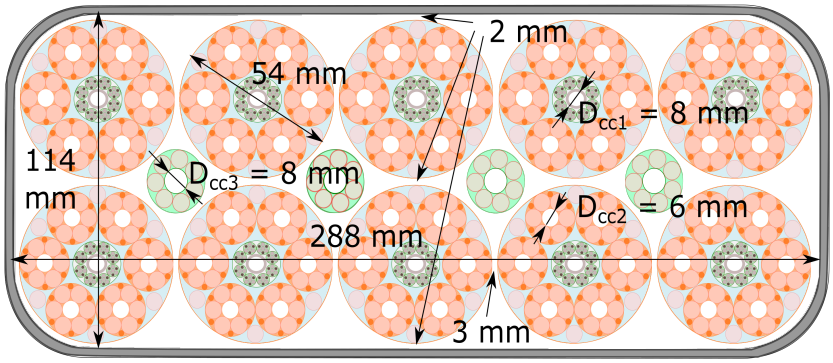

Figure 7.9: Section of the cryostat of the SCLSM's mover

tors do not quench under the combination of the rated current and magnetic field. Thus, this geometrical distribution of the superconducting material in the cryostat is adopted for the EML system.

At this point the key geometrical properties of the synchronous motor that have not been defined are the pole pitch τ, stack width l_s and the airgap length g. In the SCLSMs, the airgap length represents the distance between the symmetry plane which is located between the two layers formed by the superconducting cables and the inner surface of the stator coils. Thus, the distance between the two stator sides is $2 \cdot g$. The airgap length is related with both electromagnetic and thermal characteristics of the launcher. The value of the airgap length is initially assumed, but its final value can be determined only by an iterative procedure as will be shown in Section 7.7.

As already mentioned in Chapter 5 the minimum pole pitch that can be imple-

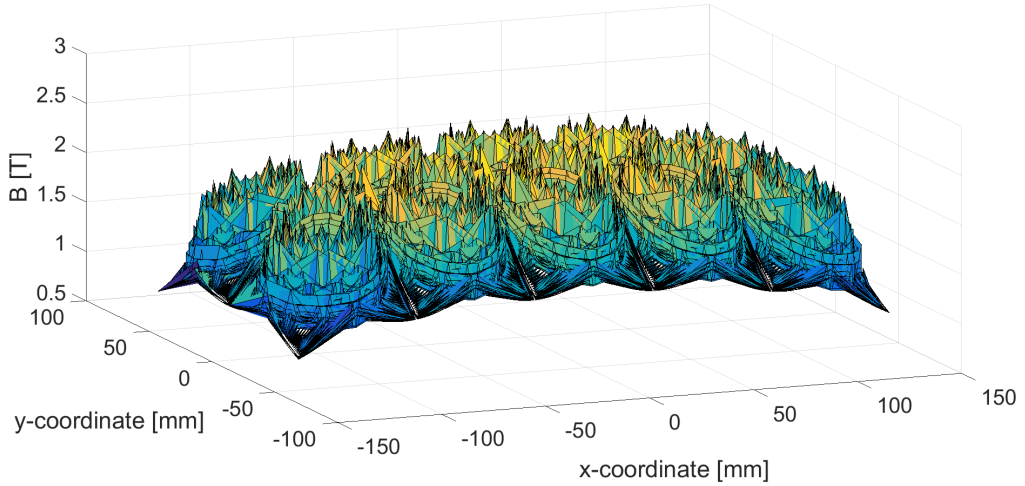

Figure 7.10: Magnetic flux density generated by the superconducting cables over the cryostat cross section

mented in synchronous machines is about 150 mm considering the maximum operating frequency that commercial medium voltage power electronics can provide (300Hz) and considering the catapult end-speed requirement (85.7 m/s). However, in SCLSMs the pole pitch length is also determined by cryostat dimensions and bending radius of the superconducting cables. The width of the cryostat cross section w_{sc} can be determined from the geometrical features of cables.

$$w_{sc} = \frac{N_{132\,kA}}{2} D_{132\,kA} + s_x \left(\frac{N_{132\,kA}}{2} + 1 \right) \tag{7.6}$$

where $D_{132\,kA}$ is the diameter of the 132-kA cable in Fig. 7.4 and s_x is the distance between cables and between the cable and the cryostat wall along x-direction. The minimum bending radius of a thin film of MgB_2 can reach value as low as 8 mm [125], but cables with complex structure cannot be usually bent with such a narrow angle. The pole pitch of the SCLSM under investigation is assumed to have a SCs bending radius at least 10 cm long. Once the pole pitch length is established, the slot pitch for the three phases distributed winding machine is $\tau/3$ since the number of slots per pole per phase is $q = 1$. Machines with a higher q may experience a significant performance improvement due to lower harmonic intensity and for the reduced slot leakage inductance. In this work a machine with a large slot pitch is first investigated while SCLSMs with larger q are proposed for

future studies. Nevertheless, the methodology proposed in this thesis to design the SCLSM, quantify the AC losses, estimate the insulation properties and calculate cryocooler performance can be still employed.

The stack width and the other geometrical features of the stator are determined from the comparison with the launchers designed in Chapters 4 and 5. In particular the ratio between the slot width and the slot pitch b_s/τ_s of LPMSM is used while the stack width l_s is assumed to be the same of both the motors. The slot height is selected to reach high current densities in the stator slot ($J > 30$ A/mm^2).

The number of poles required to produce the thrust to accelerate an aircraft A320-200 at 0.6 G depends on the maximum shear stress f_x that the cryostat structure can withstand. Considering that the structural properties of aluminium alloys for cryogenic application do not wither with the temperature and that several reinforcements hold the SCs in place and join the several layers of the insulation, the rated thrust density can be assumed within 45-75 kN/m^2 as done for the synchronous launcher in Chapter 5. Therefore, the number of poles can be computed as

$$p = \left\lceil \frac{1.1F_x}{2f_x l_s \tau} \right\rceil \tag{7.7}$$

where F_x is the peak thrust requirement and the factor 1.1 is added to consider the mass of the moving part of the machine, initially approximated as 10% of the mass of the aircraft and later calculated in details.

Once the structure of the superconducting cable and all geometrical features of the cryostat cross section are set, the technique used to wind the cables across several poles of the machine has to be defined. As shown in Fig. 7.9, the $N_{132\,kA}$ turns are arranged in two layers inside the cryostat section. The path of a superconducting cable of a four pole machine is shown in upper part of Fig. 7.11. Four poles were selected only to ease the representation of the cable's pattern, but the final machine may have more poles. The bottom part of Fig. 7.11 magnifies the end-coils that enclose two poles showing, not only a single cable, but the layout of all the 10 cables. Each end-turn of the top layer continues to the respective position of the bottom layer of the next cryostat section and vice versa for all the consecutive poles to form the pattern on the top part of same figure.

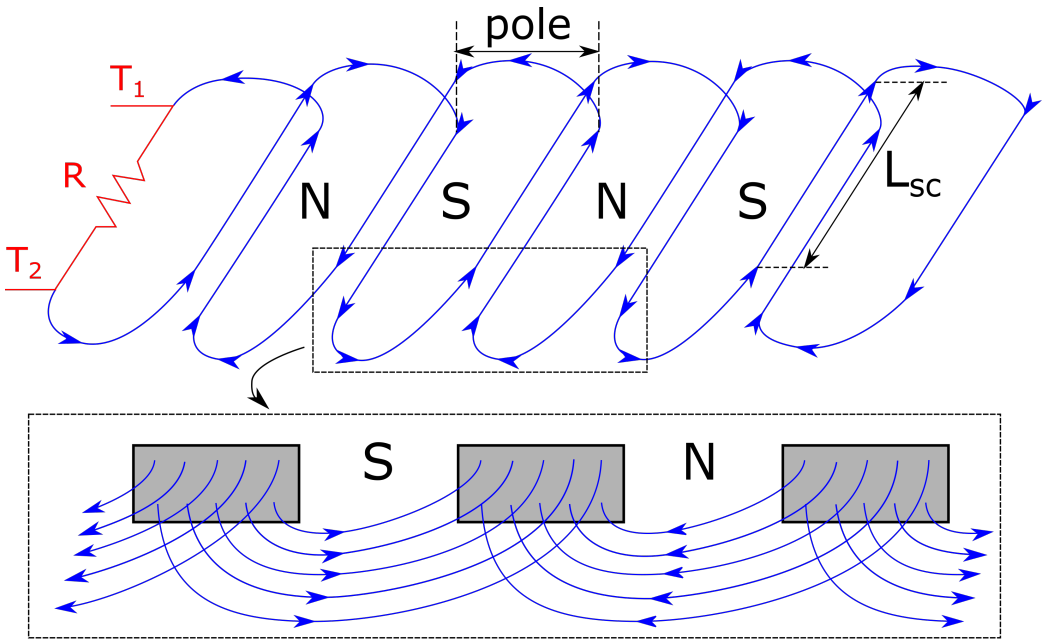

Figure 7.11: Pattern followed by the bundle of superconducting cables inside the cryostat of a 4 poles SCLSM with the respective end-coil configuration

The main 132-kA cables and the smaller 21-kA cables enter the cryostat at one end turn and are routed back and forth in parallel through the cryostat as shown in Fig. 7.11. After rounding the far end turn the cables double back through the cryostat so that each pole is surrounded by 10 cables as shown in Fig. 7.9. Eventually the cables exit from the first end turn near their starting point. Consequently, the cryostat has five closed superconducting loops, each one charged independently through a persistent-current switch whose resistor R and terminals T1 and T2 are reported in Fig. 7.11. The resistor presents no resistance at 20 K, while it is heated above the transition temperature during the SC ramping process.

The superconducting cables are wound without crossovers and they proceed in parallel configuration across the cryostat sections. Therefore the cryostat thickness does not change and remains constant even over the end turns. In general the cables on the outer side of the cryostat form loops that are longer than those on the inner side, although the mean length of the cables is considered for simplicity. It is computed as

$$l_{cable} = 2 \cdot (L_{sc} + l_{end})(2p+2) \tag{7.8}$$

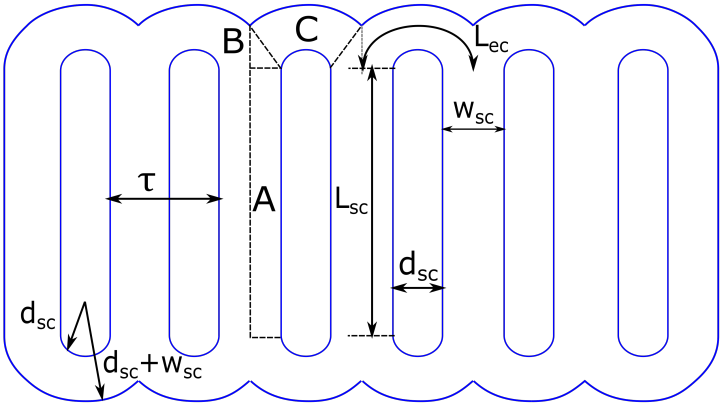

Figure 7.12: Top view of the cryostat of a 4 poles SCLSM

where L_{sc} is the length of the straight part of the SCs , l_{end} is the end-coil length and p is the number of pole pairs.

The mean end-coil length l_{end} is computed considering the cable in the middle and the average inclination of the superconducting wires.

$$l_{end} = \frac{w_{sc} + \frac{\pi}{3}\frac{d_{sc}+w_{sc}}{2}}{\cos\left[\arctan\left(\frac{D_{132\,kA}}{2}\right)\right]} \tag{7.9}$$

The total volume of the liquid hydrogen stored inside the cryostat is an important features of the SCLSM that determines the thermal capacity of the cooling system. Due to the complex shape of the hydrogen ducts, the hydrogen volume cannot be easily computed, but it can be derived from the volumes of the other components. To aid the computation, a top view of the cryostat of a four pole machine is shown in Fig. 7.12. The cryostat surface can be subdivided into simpler shapes (A, B and C in Fig. 7.12), that can be summed to calculate the total area. Considering that the cryostat thickness h_{sc} is constant everywhere the total volume can be computed as

$$v_{cryo} = (2p+2)(2v_A + 4v_B + 2v_C) + 2v_A + 4v_B \tag{7.10}$$

where the volume of the shapes in Fig. 7.12 can be computed as

$$v_A = h_{sc}\frac{w_{sc}}{2}L_{sc} \tag{7.11}$$

$$v_B = \frac{3}{8} h_{sc} w_{sc}^2 \tag{7.12}$$

$$v_C = \frac{\pi}{6} (w_{sc}^2 + 2 d_{sc} w_{sc}) h_{sc} \tag{7.13}$$

The thickness of the cryostat can be computed as

$$h_{sc} = 2 D_{132\,kA} + 3 s_y \tag{7.14}$$

where 2 represent the number of layers and s_y is the distance between cables and between the cable and the cryostat wall along y-direction. The total volume occupied by the superconducting cables is

$$v_{cable} = \frac{\pi}{4} (D_{132\,kA}^2 - D_{cc1}^2 - 6 D_{cc2}^2) l_{cable} \frac{N_{132\,kA}}{2} + \frac{\pi}{4} (D_{21\,kA}^2 - D_{cc3}^2) l_{cable} \frac{N_{21\,kA}}{2} \tag{7.15}$$

where D_{cc1}, D_{cc2} and D_{cc3} are the diameters of the cooling channels highlighted in Fig. 7.9, $D_{132\,kA}$ is the radius of the 132-kA cables, $D_{21\,kA}$ is the radius of the 21-kA cables and $N_{21\,kA}$ is the number of 21-kA cables in the cryostat section. The first term of eq. 7.15 represents the volume of the main cables, while the second term that of the smaller cables. The numbers of cable sections $N_{132\,kA}$ and $N_{21\,kA}$ shown in Fig. 7.9 are halved in eq. 7.15, since every cable doubles back on itself to cover two layers inside the cryostat section. The volume of the liquid hydrogen that the cryostat can contain is given by

$$v_{LH_2} = v_{cryo} - v_{cable} \tag{7.16}$$

The mass of the complex SCLSM's shuttle framework can be estimated through the evaluation of the masses of all its components. The mover presents the particular structure shown in Fig. 7.13 which will be used as reference to understand the following calculations. The reason why the mover framework presents the features shown in Fig. 7.13 will be further described in Section 7.5 considering the thermal insulation of the SCs.

The part of the mover outside the cryostat is a vessel which is formed by two parallel aluminium sheets whose surface is

$$A_{mov} = w_{mov} \cdot l_{mov} \tag{7.17}$$

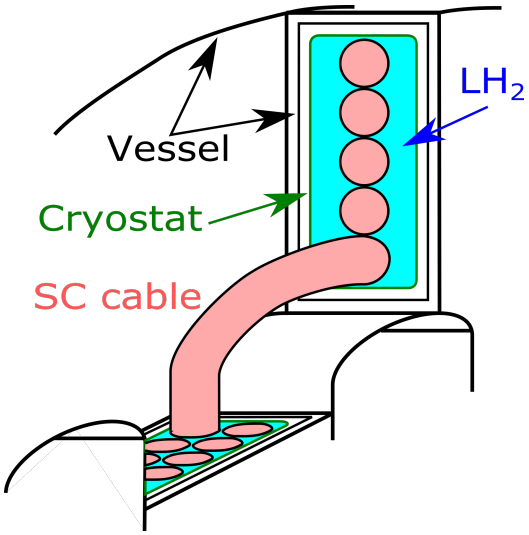

Figure 7.13: Section of the cryostat in proximity to the end-coils

where $w_{mov} = L_{sc} + d_{sc} + 2w_{sc}$ is the width of the mover and $l_{mov} = (2p+2)\tau$ is the length of the mover (see Fig. 7.12). The bending diameter can be calculated from Fig. 7.12 as $d_{sc} = \tau - w_{sc} - t_{cryo}$.

Even though the vessel forms the oval hollow shapes in Fig. 7.12, it is considered rectangular for simplicity. The mass of the vessel is approximately

$$m_{vess} = \rho_{Al} t_{vess} \left[2A_{mov} + 2g(w_{mov} + l_{mov})\right] \cdot 1.5 \tag{7.18}$$

where ρ_{Al} is the aluminium density, t_{vess} is the sum of the thickness of all aluminium sheets and g is the total airgap length which is considered in place of the vessel thickness since it is just a little longer. The factor 1.5 in eq. 7.18 is considered to take into account the mass of the structural reinforcements, of the guidance system and of the hydrogen tank.

The wall of the cryostat is an aluminium sheet with thickness t_{cryo} and surface $A_{cryo} = v_{cryo}/h_{sc}$. The mass of the cryostat can be estimated using

$$m_{cryo} = \rho_{Al} t_{cryo} \left[2A_{cryo} + 2h_{sc}(w_{mov} + l_{mov})\right] \tag{7.19}$$

The cryostat hosts the superconducting cables and a volume v_{LH_2} of liquid hydrogen as shown in Fig. 7.13. During operation only 20% of the total hydrogen can evaporate. In the very possible case that all the hydrogen in the ducts is needed to

absorb the heat dissipation in the superconductors, a coolant reservoir with four times the volume v_{LH_2} is needed. Thus, the total mass of the hydrogen corresponds to the volume of the coolant in the cryostat ducts and in the tank. It is computed as

$$m_{LH_2} = \frac{v_{LH_2}}{0.2}\rho_{LH_2} \tag{7.20}$$

The mass of the cables is estimated considering the mass of the superconducting material, the mass of the matrix of the superconducting wires in Fig. 7.3 and the mass of the copper around which the wires are wrapped. The mass of the superconducting material is

$$m_{MgB_2} = A_{sc} l_{cable} \left(528\frac{N_{132\,kA}}{2} + 84\frac{N_{21\,kA}}{2} \right) \rho_{MgB_2} \tag{7.21}$$

where ρ_{MgB_2} is the superconducting material density and 528 and 84 are the numbers of superconducting wires in the 132-kA and in the 21-kA cables respectively.

The wire matrix is made out of 70% monel and 30% copper. The percentages of the materials in the matrix are indicative and they might slightly differ in the real wire. The mass of the cable matrix is then computed as

$$m_{matrix} = \left(\tfrac{\pi}{4}D_w^2 - A_{sc}\right) l_{cable} \left(528\tfrac{N_{132\,kA}}{2} + 84\tfrac{N_{21\,kA}}{2} \right) (0.3\rho_{Co} + 0.7\rho_{Mo}) \tag{7.22}$$

where ρ_{Co} is the copper density and ρ_{Mo} is the monel density. The mass of the copper around which the 3-kA cables are wrapped can be computed as

$$m_{Co} = 6\frac{\pi}{4}\left[(D_{3kA} - D_w)^2 + (2D_w)^2\right] \cdot 6 l_{cable} \frac{N_{132\,kA}}{2}\rho_{Co} \tag{7.23}$$

where D_{3kA} is the diameter of the 3-kA cables, 6 are the 3-kA cables in the 18-kA cables and 6 are the 18-kA cables in the 132-kA cable.

In conclusion the total mass of the mover is

$$m_{mov} = m_{vess} + m_{LH_2} + m_{cryo} + m_{Co} + m_{matrix} + m_{MgB_2} \tag{7.24}$$

The geometrical properties of the cryostat and of the SCLSM's stator described in this section are listed in Table 7.2.

Table 7.2: Geometrical characteristics of SCLSM

132 kA cable diameter	54 mm	Straight cryostat length	2.50 m
18 kA cable diameter	18 mm	Cryostat height	114 mm
21 kA cable diameter	20 mm	Cryostat thickness	3.0 mm
3 kA cable diameter	6.0 mm	Cryostat surface	10.82 m^2
0.75 kA cable diameter	4.0 mm	Cryostat volume	1.234 m^3
Wire diameter	1.0 mm	Cryostat width	288 mm
Area of MgB_2 inside wire	0.1492 mm^2	Mover surface	15.66 m^2
Filament diameter	0.1 mm	Mover width	3.131 m
Cooling channel diameter 1	8 mm	Mover length	5.0 m
Cooling channel diameter 2	6 mm	End coil length	550 mm
Cooling channel diameter 3	8 mm	Length of the cables	61.0 m
N. of 132 kA cable sections	10	Volume of the cables	0.664 m^3
N. of 21 kA cable sections	4	Liquid hydrogen volume	0.570 m^3
Twisting angle	$\pi/6$	Vessel total thickness	30 mm
Dist. between cables along x	3.0 mm	Copper density	8940 kg/m^3
Dist. between cables along y	2.0 mm	Monel density	8800 kg/m^3
Pole pitch	500 mm	MgB_2 density	2570 kg/m^3
SCs bending diameter	206 mm	Liquid hydrogen density	70 kg/m^3
Slot pitch	166.7 mm	Aluminium density	2700 kg/m^3
Slot width	83.4 mm	Hydrogen mass	200 kg
Tooth width	83.4 mm	Cryostat mass	190 kg
Stator width	2.0 m	Copper mass	2236 kg
Slot height	10 mm	Matrix mass	963 kg
Airgap	150 mm	MgB_2 mass	66 kg
Number of poles	8	Vessel mass	4101 kg
Stator width	2000 mm	Mover mass	7755 kg

7.3 Electromagnetic Design of SCLSM

Once all the geometrical properties of the cryostat and of the superconducting cables are defined, it is possible to reconstruct the magnetic field in the space around the superconducting coils. In particular, the magnetic field density in correspondence of the stator slots surface allows the calculation of the magnetic flux that crosses the stator windings, the induced electromotive force and the current needed to produce the required thrust.

The extended form of the Biot-Savart's law is applied a third time to determine the magnetic flux density in the 3D space around the superconducting coils.

$$\vec{B} = \frac{\mu_0 I}{4\pi} \int \frac{\vec{dl} \times \vec{r}}{\| \vec{r} \|^3} \tag{7.25}$$

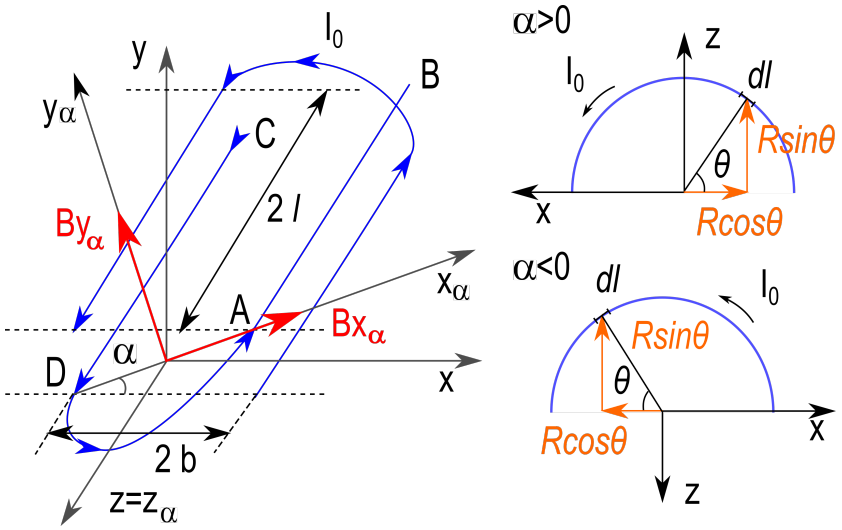

Figure 7.14: Superconducting filaments considered during the integration of the Biot-Savart law with the respective tilted frame of reference

where $\vec{dl}$ is the infinitesimal length of a conductor carrying the current I and $\vec{r}$ is the vector distance between $\vec{dl}$ and the point where $\vec{B}$ is computed. Since the Biot-Savart law in eq. 7.25 can be solved for current-carrying conductors with negligible thickness, it should be applied to the 19 MgB_2 filaments of every wire inside the cryostat. In order to simplify the calculation without introducing significant errors, the 3-kA and 0.75-kA cables are approximated as current carrying filaments located in the respective centres. The analysis is then restricted to the portion of the filaments that enclosed a single pole to take advantage of the machine periodicity.

Considering the pattern followed by the wire shown in Fig. 7.11, the integration of eq. 7.25 to calculate the field $\vec{B}$ generated by a single pole is based on the evaluation of the contribution of U-loops similar to those in Fig. 7.14. The U-loops in Fig. 7.14 represent a pair of generic 3-kA or 0.75-kA cables that travel from the top layer of a cryostat section to the respective position in the bottom layer of the next cryostat section and vice versa. Since the cryostat is aligned with the machine frame of reference x, y, z shown in Fig. 7.14, the wire around a single pole must tilt with respect to the cryostat of an angle $\pm\alpha$ around the z-axis. The tilt angle α reported in Fig. 7.14 changes for each U-loop according to the location of the cables in the cryostat section. Therefore the set of angles α counts a number

of element equal to the amount of 3-kA and 0.75-kA cables in the cryostat section.

Since each U-loop lies on a plane, the integration of the Biot-Savart law can be more easily performed in the tilted frame of reference of axes $x_\alpha, y_\alpha, z_\alpha$ in Fig. 7.14 to compute the magnetic flux density $\vec{B_\alpha}$. Considering the filament CDAB in Fig. 7.14, the integration is done separately for the straight parts and on the curved parts of the winding. The magnetic flux density components generated by the filaments AB in a generic point of coordinate x_P, y_P, z_P can be computed as

$$\vec{dl}_{AB} = \begin{bmatrix} 0 & 0 & -dz_\alpha \end{bmatrix} \qquad \vec{r}_{AB} = \begin{bmatrix} x_P - b & y_P & z_P - z_\alpha \end{bmatrix}$$

$$\vec{dl}_{AB} \times \vec{r}_{AB} = y_P dz_\alpha \vec{i} - (x_P - b) dz_\alpha \vec{j} \Rightarrow$$

$$\vec{B}_{\alpha AB} = \begin{bmatrix} B_{\alpha x AB} & B_{\alpha y_{AB}} & 0 \end{bmatrix} = \frac{\mu_0 I}{4\pi} \int_{-l}^{l} \frac{y_P \vec{i} - (x_P - b)\vec{j}}{[(x_P - b)^2 + y_P^2 + (z_P - z_\alpha)^2]^{\frac{3}{2}}} dz_\alpha$$

$$B_{\alpha x AB} = \frac{\mu_0 I}{4\pi} \frac{y_P}{(x_P - b)^2 + y_P^2} \left[\frac{l - z_P}{\sqrt{(x_P - b)^2 + y_P^2 + (z_P - l)^2}} + \frac{l + z_P}{\sqrt{(x_P - b)^2 + y_P^2 + (z_P + l)^2}} \right] \tag{7.26}$$

$$B_{\alpha y_{AB}} = \frac{\mu_0 I}{4\pi} \frac{x_P - b}{(x_P - b)^2 + y_P^2} \left[\frac{z_P - l}{\sqrt{(x_P - b)^2 + y_P^2 + (z_P - l)^2}} - \frac{l + z_P}{\sqrt{(x_P - b)^2 + y_P^2 + (z_P + l)^2}} \right] \tag{7.27}$$

where b and l are half width and half length of the coil respectively and $\vec{i}$ and $\vec{j}$ are the unit vectors of the x-axis and the y-axis respectively. The magnetic flux density components generated by the filaments CD can be computed in a similar way as

$$B_{\alpha x CD} = \frac{\mu_0 I}{4\pi} \frac{y_P}{(x_P + b)^2 + y_P^2} \left[\frac{z_P - l}{\sqrt{(x_P + b)^2 + y_P^2 + (z_P - l)^2}} - \frac{l + z_P}{\sqrt{(x_P + b)^2 + y_P^2 + (z_P + l)^2}} \right] \tag{7.28}$$

$$B_{\alpha y_{CD}} = \frac{\mu_0 I}{4\pi} \frac{x_P + b}{(x_P + b)^2 + y_P^2} \left[\frac{l - z_P}{\sqrt{(x_P + b)^2 + y_P^2 + (z_P - l)^2}} + \frac{l + z_P}{\sqrt{(x_P + b)^2 + y_P^2 + (z_P + l)^2}} \right] \tag{7.29}$$

While the integrals on the straight parts do not depend on the tilt angle of the integration plane, the curved part switches orientation and current direction. Fig. 7.14 shows the two different geometries to consider when $\alpha > 0$ or $\alpha < 0$. When $\alpha > 0$ the current in the filament proceeds from the bottom layer to the top layer

and the expression of the magnetic flux density becomes

$$\vec{dl}_{DA} = \begin{bmatrix} Rd\theta\sin\theta & 0 & Rd\theta\cos\theta \end{bmatrix}$$

$$\vec{r}_{DA} = \begin{bmatrix} x_P + R\cos\theta & y_P & z_P - l - R\sin\theta \end{bmatrix}$$

$$\begin{aligned}\vec{dl}_{DA} \times \vec{r}_{DA} =& -y_P Rd\theta\cos\theta\vec{i} + [Rd\theta\cos\theta(x_P + R\cos\theta) \\ & - Rd\theta\sin\theta(z_P - l - R\sin\theta)]\vec{j} + y_P Rd\theta\sin\theta\vec{k}\end{aligned}$$

$$B_{\alpha xDA} = \frac{\mu_0 I}{4\pi}\int_0^{\pi} \frac{-y_P R\cos\theta}{[(x_P + R\cos\theta)^2 + y_P^2 + (z_P - l - R\sin\theta)^2]^{\frac{3}{2}}} d\theta \tag{7.30}$$

$$B_{\alpha yDA} = \frac{\mu_0 I}{4\pi}\int_0^{\pi} \frac{R\cos\theta(x_P + R\cos\theta) - R\sin\theta(z_P - l - R\sin\theta)}{[(x_P + R\cos\theta)^2 + y_P^2 + (z_P - l - R\sin\theta)^2]^{\frac{3}{2}}} d\theta \tag{7.31}$$

$$B_{\alpha zDA} = \frac{\mu_0 I}{4\pi}\int_0^{\pi} \frac{y_P R\sin\theta}{[(x_P + R\cos\theta)^2 + y_P^2 + (z_P - l - R\sin\theta)^2]^{\frac{3}{2}}} d\theta \tag{7.32}$$

When $\alpha < 0$ the current in the filament in Fig. 7.14 proceeds from the top layer to the bottom layer and the components of the magnetic flux density are

$$\vec{dl}_{BC} = \begin{bmatrix} -Rd\theta\sin\theta & 0 & Rd\theta\cos\theta \end{bmatrix}$$

$$\vec{r}_{BC} = \begin{bmatrix} x_P + R\cos\theta & y_P & z_P + l + R\sin\theta \end{bmatrix}$$

$$\begin{aligned}\vec{dl}_{BC} \times \vec{r}_{BC} =& -y_P Rd\theta\cos\theta\vec{i} + [Rd\theta\cos\theta(x_P + R\cos\theta) \\ & + Rd\theta\sin\theta(z_P + l + R\sin\theta)]\vec{j} - y_P Rd\theta\sin\theta\vec{k}\end{aligned}$$

$$B_{\alpha xBC} = \frac{\mu_0 I}{4\pi}\int_0^{\pi} \frac{-y_P R\cos\theta}{[(x_P + R\cos\theta)^2 + y_P^2 + (z_P + l + R\sin\theta)^2]^{\frac{3}{2}}} d\theta \tag{7.33}$$

$$B_{\alpha yBC} = \frac{\mu_0 I}{4\pi}\int_0^{\pi} \frac{R\cos\theta(x_P + R\cos\theta) + R\sin\theta(z_P + l + R\sin\theta)}{[(x_P + R\cos\theta)^2 + y_P^2 + (z_P + l + R\sin\theta)^2]^{\frac{3}{2}}} d\theta \tag{7.34}$$

$$B_{\alpha zBC} = \frac{\mu_0 I}{4\pi}\int_0^{\pi} \frac{-y_P R\sin\theta}{[(x_P + R\cos\theta)^2 + y_P^2 + (z_P + l + R\sin\theta)^2]^{\frac{3}{2}}} d\theta \tag{7.35}$$

The integrals to compute the flux density components generated by the curved part of the filaments were solved numerically because they cannot be written in a close form like for the straight parts.

The contributions of the straight and the curved parts are then summed up to evaluate the field generated by the superconducting wire. The magnetic flux density components over a plane parallel to the wire's plane and 5 cm distant in y-

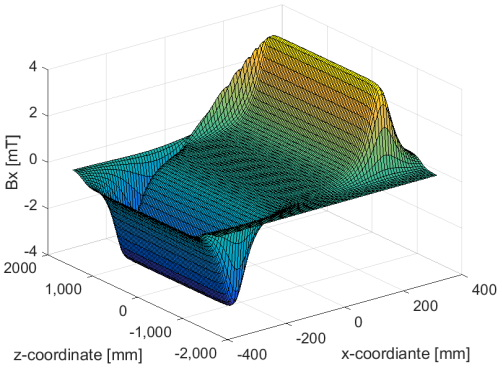

(a) $B_{\alpha x}$

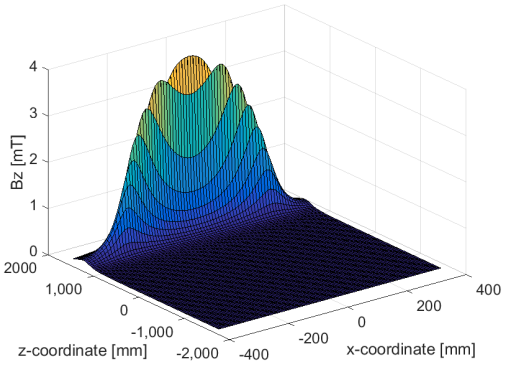

(b) $B_{\alpha z}$

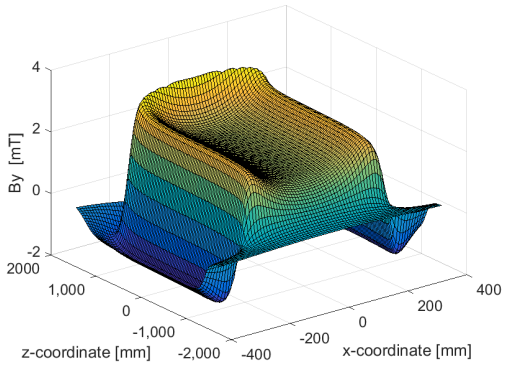

(c) $B_{\alpha y}$

Figure 7.15: Magnetic flux density components generated by a 3-kA wire carrying 1000 A at a distance of 5 cm

direction, produced by a 3-kA cable tilted of an angle $\alpha > 0$ and carrying the rated current density are reported in Figs. 7.15a, 7.15c and 7.15b.

Since the magnetic flux density $\vec{B}_\alpha$ resulting from the integration is expressed in the tilted frame of reference, a coordinate transformation is required to find the magnetic flux density $\vec{B}$ in the machine frame of reference.

$$\vec{B} = \begin{bmatrix} B_x \\ B_y \\ B_z \end{bmatrix} = \begin{bmatrix} \cos\alpha & -\sin\alpha & 0 \\ \sin\alpha & \cos\alpha & 0 \\ 0 & 0 & 1 \end{bmatrix} \begin{bmatrix} B_{\alpha x} \\ B_{\alpha y} \\ B_{\alpha z} \end{bmatrix} \tag{7.36}$$

The total magnetic flux density in the point of coordinate x_P, y_P, z_P expressed with respect to the machine frame of reference is computed summing the contributions $\vec{B}$ of all the superconducting cable within the cryostat.

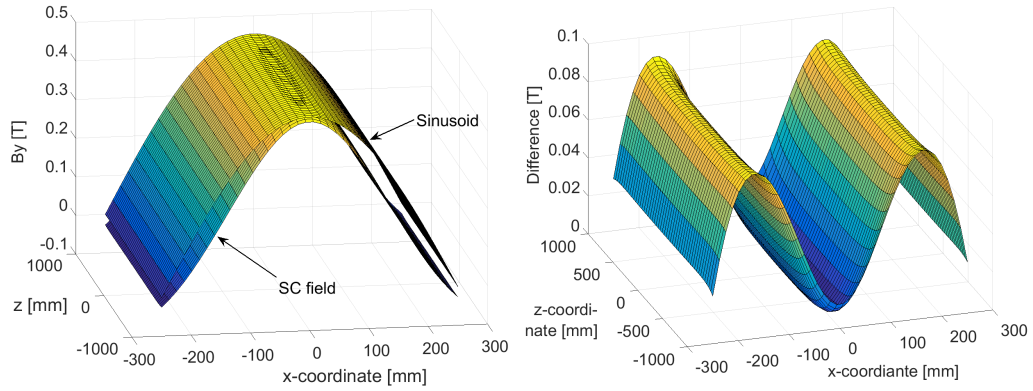

(a) Comparison (b) Difference

Figure 7.16: Comparison between excitation field and ideal sinusoidal wave with the difference between magnetic fields

The magnetic field generated by the superconducting coils in the airgap has a shape that depends on the dimensions of the SCs themselves. The aim of the designer is to select the coil aspect ratios b/τ and L_{sc}/l_s to achieve an excitation field shape as close as possible to a sinusoidal shape. For the particular winding layout selected for the SCLSM the ratio b/τ is bound to be 1/2. Indeed, any different value would entail a stator pole pitch and a mover pole pitch with different length. On the contrary, the length of the straight part of the superconducting cable L_{sc} can be varied to achieve a sinusoidal magnetic wave shape in the airgap.

It was found that the longer the SCs are, the more sinusoidal is the shape of the magnetic wave in the active area of the machine which is located at the coil centre. However, L_{sc} cannot be indefinitely increased since the weight and the cost of the mover would sharply rise as well. The best compromise was found in selecting $L_{sc}/l_s = 1.25$. The magnetic field generated on the slot surface by the coil with this aspect ratio is compared with the sinusoidal shape in Fig. 7.16a. The magnetic flux density component that is reported in Fig. 7.16a is the one that interacts with the stator current to produce the thrust and crosses the airgap perpendicularly along y-direction. The difference between the sinusoidal and the SC's magnetic flux densities is shown in 7.16b.

Since in the MLT approximation the slotted structure of the stator is replaced by an uniform layer, it is possible to compute the average magnetic flux density in

the layer of material as

$$B_{y_{avg}}(x,z) = \frac{1}{h_s}\int_0^{h_s} B_y(x,y,z)\,dy \tag{7.37}$$

By definition the magnetic flux across a surface is the integral of the magnetic flux density upon the same surface. In the hypothesis that the stator current is uniformly distributes inside the slot, the interaction with the magnetic flux is well represented by its mean value. Since the magnetic flux density is almost constant along z-direction the magnetic flux over a single pole becomes

$$\Phi = \int_0^{l_s}\int_0^{\tau} B_{y_{avg}}(x,z)\,dx\,dz = l_s\int_0^{\tau} B_{y_{avg}}(x)\,dx \tag{7.38}$$

The no-load induced voltage on the stator coil can be computed using the relation

$$E_s(x) = v_s\frac{\partial\Phi(x)}{\partial x} \tag{7.39}$$

where v_s is the synchronous speed and the derivative of the flux is computed from eq. 7.38 as

$$\frac{\partial\Phi(x)}{\partial x} = l_s\cdot B_{y_{avg}}(x) \tag{7.40}$$

The total thrust can be defined as

$$F_x + F_{mov} = \frac{3}{2}\frac{\pi}{\tau}2\Phi N_1 k_w I_s \tag{7.41}$$

where $F_{mov} = 0.6G\cdot m_{mov}$ is the thrust to accelerate the mover, k_w is winding factor, the number 2 that multiplies the flux Φ is inserted to consider both the stator sides and N_1 is the number of turns per phase on a single stator side. The stator current I can be computed from the thrust expression as

$$I = \frac{\tau}{\pi}\frac{F_x + F_{mov}}{3\Phi N_1 k_w} \tag{7.42}$$

Eq. 7.38 is used to determined the magnetic flux that crosses the track coil positioned exactly below one SC. However the magnetic field generated by a superconducting coil is strong enough to interact with the neighbour stator coils as well. The effect of a single SC was evaluated over five neighbour stator coils lo-

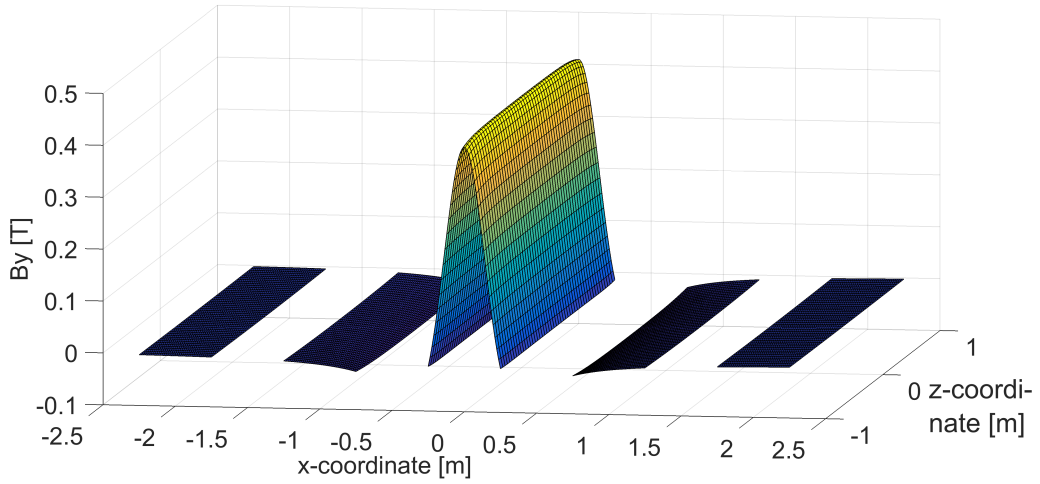

Figure 7.17: Magnetic flux density produced by a single SC over 5 neighbour stator coils

Table 7.3: Comparison between electric variables computed over 1 or 5 coils

	1 coil	**5 coils**
No-load voltage per phase	122.6 V/turn	97.9 V/turn
Stator current peak	1178 A	1475 A

cated below SCs with the same polarity. The magnetic flux density over the slot surface of the five stator coils is shown in Fig. 7.17. The stator coils beside the central one are crossed by a magnetic flux with opposite direction which produces a braking effect that must be taken into account. Indeed, the no-load induced voltage is reduced and the stator current required to produce the same thrust is higher. Neglecting this effect would lead to an erroneous estimation of the no-load voltage and the rated current as shown in Table 7.3.

The current I circulating in the stator coils generates a magnetic field whose fundamental harmonic is synchronized to the mover speed by the control system. The stator windings also generate a series of secondary harmonics with different intensities, synchronous speeds and frequencies. The superconducting coils "see" the secondary harmonics moving at a speed equal to difference between their synchronous velocities and the fundamental one. These moving magnetic waves induce alternating currents in the superconductors which cause the losses that will be estimated using techniques explained in Section 7.4. In this section

the methodology used to calculate the secondary harmonics magnetomotive force and the associated magnetic flux density in the airgap is illustrated.

The full spectrum of the magnetomotive force for a three phase machine with distributed windings can be expressed as [29]

$$\begin{aligned} MMF(x,t) = \frac{N_1 I}{\pi p}\Bigg[& \sin(\omega t)\sum_{\nu=1}^{\infty}\frac{1}{\nu}k_{w\nu}\cos\left(\nu\frac{\pi}{\tau}x\right) + \\ & + \sin\left(\omega t - \frac{2}{3}\pi\right)\sum_{\nu=1}^{\infty}\frac{1}{\nu}k_{w\nu}\cos\nu\left(\frac{\pi}{\tau}x - \frac{2}{3}\pi\right) + \\ & + \sin\left(\omega t - \frac{4}{3}\pi\right)\sum_{\nu=1}^{\infty}\frac{1}{\nu}k_{w\nu}\cos\nu\left(\frac{\pi}{\tau}x - \frac{4}{3}\pi\right)\Bigg] \end{aligned} \tag{7.43}$$

The time-space distribution of the magnetomotive force in eq. 7.43 includes harmonics that travel in the same direction of the fundamental wave and the harmonics that move in opposite direction. The forward harmonics have order

$$\nu = 2mk + 1 \qquad \text{for k = 0, 1, 2, 3, 4, 5, ...} \tag{7.44}$$

whereas the backward harmonics have order

$$\nu = 2mk - 1 \qquad \text{for k = 1, 2, 3, 4, 5, ...} \tag{7.45}$$

where m is the number of phases. The winding factor of distributed windings for the ν^{th} harmonic can be computed as

$$k_{w\nu} = k_{d\nu} \cdot k_{p\nu} \tag{7.46}$$

where the distribution factor for the ν^{th} harmonic is

$$k_{d\nu} = \frac{\sin\left(\frac{\nu\pi}{2m}\right)}{q\sin\left(\frac{\nu\pi}{2mq}\right)} \tag{7.47}$$

and the pitch factor for the ν^{th} harmonic is

$$k_{p\nu} = \sin\left(\nu\frac{\pi}{2}\frac{\tau_c}{\tau}\right) \tag{7.48}$$

where τ_c is the coil pitch. Imposing the equality $\omega t = \pm\nu\pi x/\tau$ the synchronous

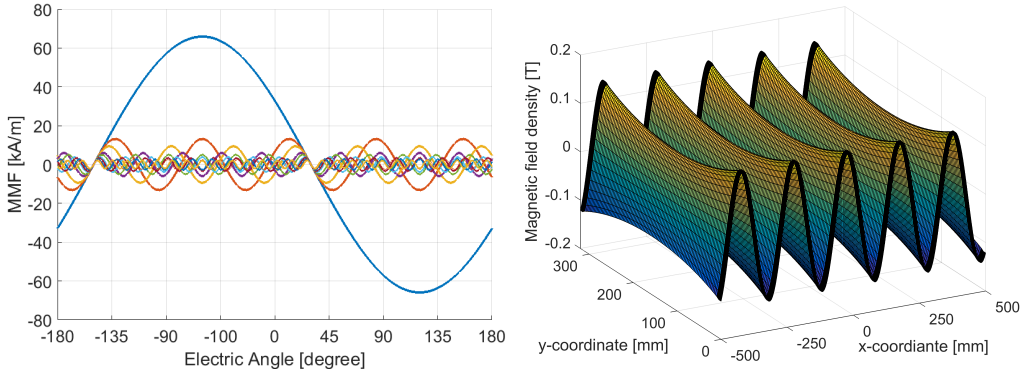

(a) Intensity of the first 10 MMF harmonics (b) Magnetic field of 2^{nd} harmonic

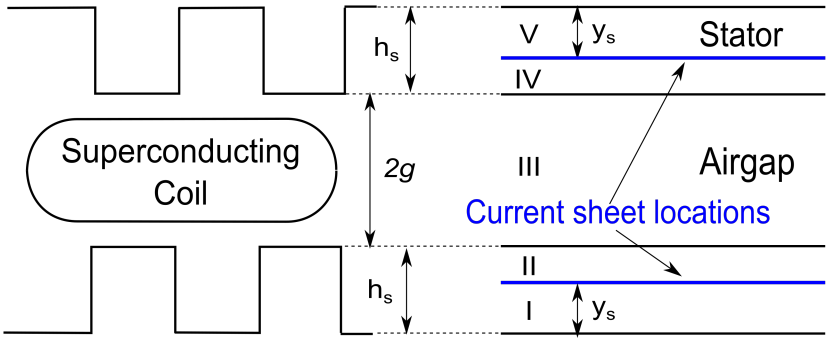

(c) Schematic of the layered structure of MLT applied to SCLSM

Figure 7.18: Schematic of the multi-layered structure and MMF harmonics amplitude used by the MLT to reconstruct the magnetic field generated by the secondary harmonics

speed of the ν^{th} harmonic wave is

$$v_{s\nu} = \pm \frac{2f\tau}{\nu} \tag{7.49}$$

The first 10 harmonics, whose magnetomotive force intensity is reported in Fig. 7.18a, were considered during the electromagnetic design. The Multi-Layer Theory (MLT) presented in Chapter 5 is applied to reconstruct the harmonic content of the field generated by the stator windings. MLT replaces superconducting coils and the airgap with a single layer having the permeability of air, while the slotted structure of stator is replaced by an anisotropic region where the permeabilities along x and y directions change. In order to determine all the secondary magnetic field waves, each harmonic is represented by a current sheet located in

correspondence of the stator slots whose intensity is

$$A_\nu = \frac{3N_1 k_{w\nu} I}{\nu \tau p} \tag{7.50}$$

The MLT is based on the solution of the Maxwell equation for every layer in the simplified machine structure in Fig. 7.18c. The procedures employed to determine the governing equations and the boundary conditions for each layer are very similar to those explained in Chapter 5 and are not reported here to avoid repetitions. As an example, the magnetic field waveform determined by the MLT for the third order harmonic is shown in Fig. 7.18b.

Once the electromagnetic properties of the machine are defined and the magnetic field generated by the secondary harmonics in the airgap is reconstructed, the AC losses in the superconductors can be calculated with the procedure illustrated in the next section.

7.4 Losses in Superconductors

During the aircraft acceleration, the mover is synchronized with the fundamental electromagnetic wave in the airgap. Since the speeds of the secondary harmonics are different from the fundamental, they are unsynchronized with the motion. The alternating field of the secondary harmonics causes losses that can be classified as coupling losses, eddy current losses and hysteresis losses.

It is worth mentioning that the high conductivity of the aluminium structure will certainly provide a protection from the alternating magnetic field harmonic produced by the stator current. Thus, the total AC losses of the SCLSM for EML might be lower that those calculated in this work. The shielding effect of the aluminium structure is not considered here in order to investigate the worst case that the cooling system has to cope with.

7.4.1 Eddy Current Losses

The travelling harmonic magnetic fields induce eddy currents which mainly flow in radial direction in the superconducting wire's matrix. Eddy currents are also

induced in the hydrogen vessel and in the aluminium structure of the cryostat. As it has been proved in [126], the losses on the aluminium vessel are negligible (below 1.0 W per pole), but they were added to the final eddy current loss for analysis completeness.

An analytical formula to describe the eddy current losses in a helical wire subject to an external alternating magnetic field has been proposed in [127].

$$P_{eddy} = \frac{B_{es}^2}{2\mu_0 \frac{\pi\omega k_{es}}{\omega^2 k_{es}^2 + 1}} A_w \qquad \text{with} \qquad k_{es} = \frac{\mu_0}{2\rho_{ef}} \left(\frac{\tau_w}{2\pi}\right)^2 \tag{7.51}$$

where B_{es} is the peak-to-peak amplitude of the magnetic flux density perpendicular to the wire axis, A_w is the cross section area of the wire, ρ_{ef} is the effective resistivity of the wire section and τ_w is the pitch of the twisted wire. Eq. 7.51 cannot be directly used to estimate the total eddy current loss P_{eddy} in the SCLSM and some considerations and minor amendments have to be done.

The cryostat of superconducting synchronous launcher hosts several wires like the one in Fig. 7.3 that are subject to different instantaneous values of the magnetic field density. Taking advantage of the machine periodicity, the analysis can be restricted to a single cryostat section and later extended to the whole machine. The magnetic flux density generated by ν^{th} harmonic which is perpendicular to any wire of the cryostat section can be computed as

$$B_{w\nu}(x,y,z) = \sqrt{B_{wx\nu}^2(x,y,z) + B_{wy\nu}^2(x,y,z)} \tag{7.52}$$

where $B_{wx\nu}$ and $B_{wy\nu}$ are the magnetic field components that result from the interpolation between the flux densities $B_{x\nu}$ and $B_{y\nu}$ computed by the MLT and the wire locations of coordinates (x,y,z). The position of a wire inside the cryostat does not change along third axis and is given by the coordinate (x,y). Conversely, the magnetic flux density varies along the z axis as it shown by the concave shape of the second harmonic field in Fig. 7.18b. The best accuracy would be achieved by removing the dependency on the coordinate z of variables in eq. 7.52 through the calculation of the average $B_{x\nu}$ and $B_{y\nu}$ along the wire length. To reduce the

computation time, it is accepted to use as mean value the magnetic field components calculated by the MLT in the middle of the gap between the two stators (at distance g by the stator coils). Being the perpendicular magnetic field in eq. 7.51 the peak-to-peak amplitude, two times the field $B_{w\nu}$ in eq. 7.52 must be considered.

The effective resistivity ρ_{ef} in eq. 7.51 takes into account the field penetration depth and the coupling between the internal MgB_2 filaments. Even though resistivity is a key parameter for eddy current losses calculation, P_{eddy} is so small compared to the other sources of loss that the effort to accurately compute ρ_{ef} is not strictly required. The effective resistivity is often approximated as the resistivity of the metal matrix ρ_{ma} [127]. The superconducting wire are embedded in an alloy of 70% monel and 30% copper whose electrical resistivity can be approximated as

$$\rho_{ma} = \frac{30\rho_c + 70\rho_M}{100} \tag{7.53}$$

where ρ_c and ρ_M are the copper and monel resistivity respectively. The twist pitch of an helix can be computed using the geometrical relation with the twist angle α_m which will be later selected to minimize self and mutual inductances.

$$\tau_w = \pi D_w \tan\alpha_m \tag{7.54}$$

The energy loss P_{eddy} in eq. 7.51 represents the amount of heat dissipated into a meter of wire during a single period of the alternating magnetic field. However, the power losses are usually expressed as energy dissipated in the unit time. In order to consider the full length of the machine and all the magnetic field periods within a second, the energy loss P_{eddy} must be multiplied by the relative frequency of the magnetic wave and the length of the cable. Therefore, the eddy current loss in the i^{th} wire due to the ν^{th} harmonic becomes

$$P_{eddy_{\nu i}} = 2B_{w\nu i}\frac{(f-f_\nu)^2 4\rho_{ma}D_w^2\tan^2\alpha_m}{(f-f_\nu)^2\mu_0^2 D_w^4\tan^4\alpha_m + 16\rho_{ma}^2} \tag{7.55}$$

where the angular velocity ω in eq. 7.51 was replaced by the expression $2\pi(f - f_\nu)$ and where $f - f_\nu$ represents the relative frequency. The total eddy current loss

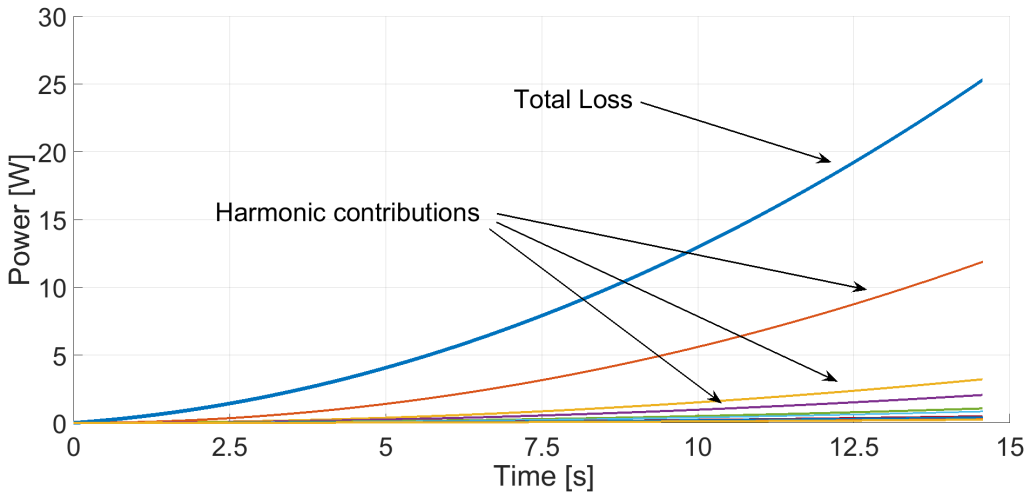

Figure 7.19: Eddy current loss in all the superconducting wires and in the aluminium vessel during aircraft acceleration

is obtained summing the contributions of the N_w wires in the cryostat for all the N_ν harmonics.

$$P_{eddy} = \sum_{\nu=2}^{N_\nu} \sum_{i=1}^{N_w} P_{eddy\,\nu\,i} \tag{7.56}$$

Since the first term at the denominator in eq. 7.55 is negligible with respect to ρ_{ma}^2, P_{eddy} can be considered inversely proportional to the matrix resistivity. For the same reason, the eddy current loss is proportional to $(f - f_\nu)^2$ in the range of frequency under consideration. The variation of the total eddy current loss during the launch is therefore quadratic as shown in Fig. 7.19.

7.4.2 Coupling Losses

When a conducting wire is subject to an oscillating field a current I is induced and a voltage U appears at the wire terminals. In general, the voltage and the induced current are linked by the law

$$U = L\frac{\partial I}{\partial t} + RI \tag{7.57}$$

where L is the inductance of the wire and R its resistance. Since superconductors present no or negligible resistance, the voltage equation for the set of superconducting wires inside the cryostat subject to a sinusoidal alternating field becomes

$$\begin{bmatrix} U_1 \\ U_2 \\ \vdots \\ U_{N_w} \end{bmatrix} = j2\pi(f - f_{\nu}) \begin{bmatrix} L_1 & M_{12} & \cdots & M_{1N_w} \\ M_{21} & L_2 & \cdots & M_{2N_w} \\ \vdots & \vdots & \ddots & \vdots \\ M_{N_w1} & M_{N_w2} & \cdots & L_{N_w} \end{bmatrix} \begin{bmatrix} I_1 \\ I_2 \\ \vdots \\ I_{N_w} \end{bmatrix} \tag{7.58}$$

where M_{ij} are the mutual inductances between cables with indexes i and j. The total power loss due to the coupling of the superconducting wires is

$$P_{Coupling} = \vec{U} \cdot \vec{I} \tag{7.59}$$

where the vectors $\vec{U}$ and $\vec{I}$ contain the voltage and the induced current of all the N_w wires respectively. In order to solve eq. 7.59 the inductances and induced currents of each wire must be found.

The vector of the induced currents $\vec{I}$ can be determined using the energy conservation principle. The total energy stored in the magnetic field generated by the induced currents into all the superconducting wires is

$$E_i = \frac{1}{2}\vec{L} \cdot \vec{I}^2 \tag{7.60}$$

The MgB_2 filaments inside each wire are wrapped together to form a solenoid. The energy that is stored in the magnetic field inside the solenoid where the induced current flows is

$$E_{\nu} = \frac{1}{2} \sum_{\nu=2}^{N_{\nu}} \frac{\vec{B}_{w\nu}}{\mu_0} v_{sc} \tag{7.61}$$

where v_{sc} is the volume of the superconducting wires. Since the energy stored in the inductor E_i must be equal to the energy stored in the solenoid E_{ν}, an expression of the induced currents can be derived as

$$\vec{I} = \sum_{\nu=2}^{N_{\nu}} \left[\frac{\vec{B}_{wx\nu}}{|\vec{B}_{wx\nu}|} \sqrt{\frac{\vec{B}_{wx\nu}^{\,2}}{\mu_0} \frac{v_{sc}}{\vec{L}}} + \frac{\vec{B}_{wy\nu}}{|\vec{B}_{wy\nu}|} \sqrt{\frac{\vec{B}_{wy\nu}^{\,2}}{\mu_0} \frac{v_{sc}}{\vec{L}}} \right] \tag{7.62}$$

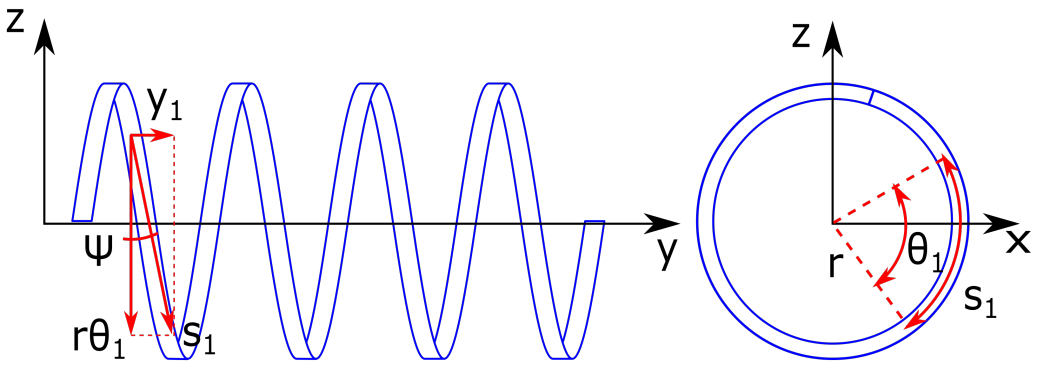

Figure 7.20: Geometrical features of the first helix used to compute the wire inductances

The components of the magnetic field harmonics $\vec{B_{wx}}$ and $\vec{B_{wy}}$ were considered separately in eq. 7.62 to take into account the direction of the respective induced currents. Indeed, the induced currents can flow in opposite directions along the wire according to the sign of the magnetic field components. Currents flowing in opposite direction cancel out, so that the vector $\vec{I}$ contains the set of the net induced currents. In order to solve eqs. 7.59 and 7.62 mutual and self inductances of the superconducting wires must be determined.

The calculation of the self and mutual inductances must take into account that some wires are wrapped together to form the 3-kA and the 0.75-kA cables. The pattern of a single superconducting wire inside the cable forms an helix similar to the one shown in Fig. 7.20. The value of the self and mutual inductances are effected by the helicity of the wires and depends on the pitch angle of the helix itself.

Fig. 7.20 shows only a single helix for simplicity, but the calculation of the mutual inductance considers a second helical wire with the same geometry of the first one and a non-zero angular offset. The helical arc s_1 shown in Fig. 7.20 represents the true length of the first helix and it can be computed as

$$s_1 = \sqrt{(r\theta_1)^2 + y_1^2} \tag{7.63}$$

where the radius r can be either $D_{3kA}/2$ or $D_{0.75kA}/2$ according to the cable under investigation, θ_1 is the helical angle and y_1 is the distance along the helix axis. In

a similar way the helical arc of a second helix s_2 can be defines as

$$s_2 = \sqrt{r^2(\theta_2 + \theta_0)^2 + y_2^2} \tag{7.64}$$

where θ_0 is the angular offset of the second helix. The helical angles θ_1 and θ_2 are related with the pitch angle ψ showed in Fig. 7.20 as

$$\begin{aligned} \theta_1 &= s_1 \frac{\cos\Psi}{r} \\ \theta_2 &= s_2 \frac{\cos\Psi}{r} + \theta_0 \end{aligned} \tag{7.65}$$

In cartesian coordinate the first helix is defined by three parametric equations that can be written as

$$\begin{aligned} x_1 &= r\cos(k_\psi s_1) \\ y_1 &= s_1 \sin\psi \\ z_1 &= -r\sin(k_\psi s_1) \end{aligned} \tag{7.66}$$

where $k_\psi = (\cos\psi)/r$. The second helix can be expressed with similar parametric equations which has to include the longitudinal offset y_0 and the angular offset θ_0.

$$\begin{aligned} x_2 &= r\cos(k_\psi s_1 + \theta_0) \\ y_2 &= s_1 \sin\psi + y_0 \\ z_2 &= -r\sin(k_\psi s_1 + \theta_0) \end{aligned} \tag{7.67}$$

The longitudinal offset y_0 of the wires within the same superconducting cable is always zero since they are supposed to depart from the same point. The angular offset is $\pi/6$ for the 3-kA cables and $2\pi/3$ for the 0.75-kA cables.

The mutual inductance between the helical filaments 1 and 2 can be calculated solving the Neumann integral [128]

$$M_{12} = \frac{\mu_0}{4\pi} \oint \oint \frac{\vec{ds}_1 \cdot \vec{ds}_2}{R} \tag{7.68}$$

where R is the Euclidean distance between the infinitesimal helical arcs $\vec{ds}_1$ and

$\vec{ds}_2$ and can be expressed as

$$R^2 = (x_1 - x_2)^2 + (y_1 - y_2)^2 + (z_1 - z_2)^2 \tag{7.69}$$

The vectorial product between the unit vector $\vec{ds}_1$ and $\vec{ds}_2$ in the numerator of eq. 7.68 is equal to the vectorial product between the direction cosines and can be expressed as

$$\begin{gathered} \vec{ds}_1 \cdot \vec{ds}_2 = \frac{\partial x_1}{\partial s_1}\frac{\partial x_2}{\partial s_2} + \frac{\partial y_1}{\partial s_1}\frac{\partial y_2}{\partial s_2} + \frac{\partial z_1}{\partial s_1}\frac{\partial z_2}{\partial s_2} \\ \text{where} \qquad \vec{ds}_1 = \begin{bmatrix} \frac{\partial x_1}{\partial s_1} & \frac{\partial y_1}{\partial s_1} & \frac{\partial z_1}{\partial s_1} \end{bmatrix} \qquad \vec{ds}_2 = \begin{bmatrix} \frac{\partial x_2}{\partial s_2} & \frac{\partial y_2}{\partial s_2} & \frac{\partial z_2}{\partial s_2} \end{bmatrix} \end{gathered} \tag{7.70}$$

Substituting the parametric equations 7.66 and 7.67 in eqs. 7.69 and 7.70, the mutual inductance in eq. 7.68 becomes

$$M_{12} = \frac{\mu_0}{4\pi} \int_0^{l_w} ds_2 \int_0^{l_w} \frac{\cos^2\psi \cos[k_\psi(s_1 - s_2) - \theta_0] + \sin^2\psi}{\sqrt{2r^2 - 2r^2\cos[k_\psi(s_1 - s_2) - \theta_0] + [(s_1 - s_2)\sin\psi - y_0]^2}} ds_1 \tag{7.71}$$

Following the method proposed in [128], in order to further simplify eq. 7.71 a new variable $\phi = s_1 - s_2$ is introduced. Substituting the variable ϕ in eq. 7.71, considering that $d\phi = ds_1$ and breaking the integral over two different regions yields

$$\begin{gathered} M_{12} = \frac{\mu_0}{4\pi}\left[\int_{-l_w}^{0} (l_w + \phi) f(\phi)\, d\phi + \int_0^{l_w} (l_w - \phi) f(\phi)\, d\phi\right] \\ \text{where} \qquad f(\phi) = \frac{\cos^2\psi \cos[k_\psi\phi - \theta_0] + \sin^2\psi}{\sqrt{2r^2 - 2r^2\cos[k_\psi\phi - \theta_0] + [\phi\sin\psi - y_0]^2}} \end{gathered} \tag{7.72}$$

and l_w is the twisted wire length. The integrals in eq. 7.72 cannot be further simplified and they are solved numerically to calculate the mutual inductances of all the superconducting wires in the cryostat.

When a formula for the mutual inductance between two identical parallel filaments exists, it can be used to calculate the self inductance of a conductor with the same geometry as well. The calculation of the self inductance can be performed considering a second filament located at a distance equal to the geometric mean distance g_{md} of the conductor's cross section [129]. The geometric mean distance

of the round wire shown in Fig. 7.3 is given by

$$g_{md} = \frac{D_w}{2} e^{-\frac{1}{4}} \tag{7.73}$$

In order to determined the value of the self inductance integrating eq. 7.72, the proper values of the longitudinal and angular offsets associated with the geometric mean distance must be found.

Being g_{md} the distance separating the two filaments, it can be expressed using the general definition of distance in eq. 7.69. The parametric equations 7.66 and 7.67 can be substituted in 7.69 considering that in this case $x_1 = D_w/2$, $y_0 = y_1 - y_2$ and $z_1 = 0$. After a few algebraic operations, an expression of the geometric mean distance as a function of the angular offset is found as

$$g_{md}^2 - \frac{D_w^2}{2}(1 - \cos\theta_0) - \frac{D_w^2}{4}\theta_0^2 \tan^2\psi_0 = 0 \tag{7.74}$$

where the pitch angle ψ_0 is $\pi/2 - \psi$. The angular offset can be found solving eq. 7.74 numerically whereas the longitudinal offset can be calculated from θ_0 and g_{md} as

$$y_0 = \sqrt{g_{md}^2 - \frac{D_w^2}{2}(1 - \cos\theta_0)} \tag{7.75}$$

The variations of the self and mutual inductances of the superconducting wires with the pitch angle are reported in Figs. 7.21a and 7.21b respectively. They are compared with the self and mutual inductance of the straight wires that have length

$$l_w = \frac{l_{cable}}{\tan\psi}\sqrt{\tan^2\psi + 1} \tag{7.76}$$

The mutual inductances of the wires inside a 0.75-kA cable are all equal, since the three wires are uniformly distributed along a circumference and have the same angular offset among themselves. Conversely, the angular offset of the six wires inside a 3-kA cables are all different as well as the respective mutual inductances as shown in Fig. 7.21b. The pitch angle above which the self and mutual inductance can be considered almost constant is approximately $\pi/6$. This value of the pitch angle is selected for the previously introduced variable α_m since it is a good

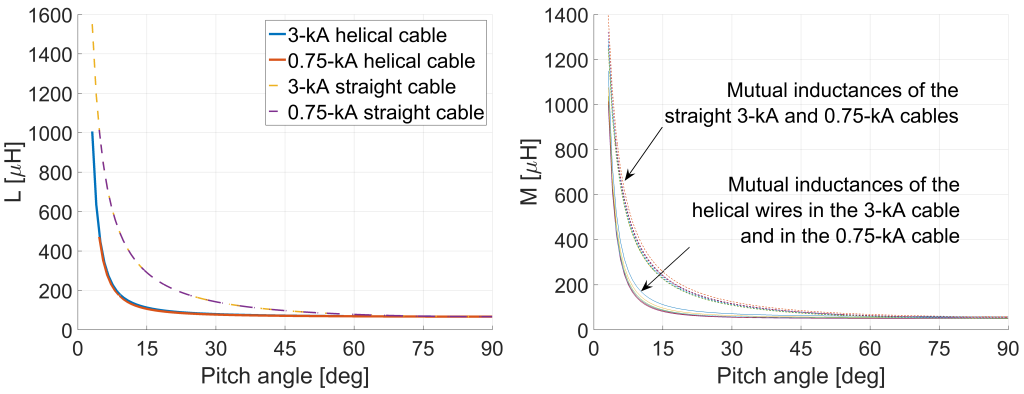

(a) Self Inductance (b) Mutual Inductance

Figure 7.21: Variation of self and mutual inductances with the helix pitch angle

compromise between inductances minimization and cable integrity. Indeed, the cable under load might fray with high pitch angles.

Eq. 7.72 was used to calculate the mutual inductances between wires wrapped around the core of the same cable, whereas a different technique was employed to estimate the mutual inductances between wires of different cables. The highest accuracy would be achieved by the integration of the Neumann formula in eq. 7.68 applied to non-coaxial helices, but the complexity of integrals discouraged such approach. Therefore, the pairs of superconducting wires of different cables were treated as straight parallel wires. In this case the integral of eq. 7.68 can be solved in a closed form as [70]

$$M_{ij} = 0.2 \left[\frac{l_{cable}}{2} \ln \left(\frac{\frac{l_{cable}}{2} + \sqrt{\frac{l_{cable}^2}{4} + d_{ij}^2}}{d_{ij}} \right) - \sqrt{\frac{l_{cable}^2}{4} + d_{ij}^2} + d_{ij} \right] \tag{7.77}$$

where M_{ij} is expressed in μH and d_{ij} is the distance between the wires i and j .

Once all the mutual and self inductances are known, the induced voltage at the wire terminals and the total coupling loss can be computed using eqs. 7.58 and 7.59 respectively. Eq. 7.58 shows that the coupling losses are proportional to the relative frequency of the secondary harmonics. Since speed and frequency increase at constant rate during the launch, the power loss linearly grows while the aircraft accelerates as shown in Fig. 7.22.

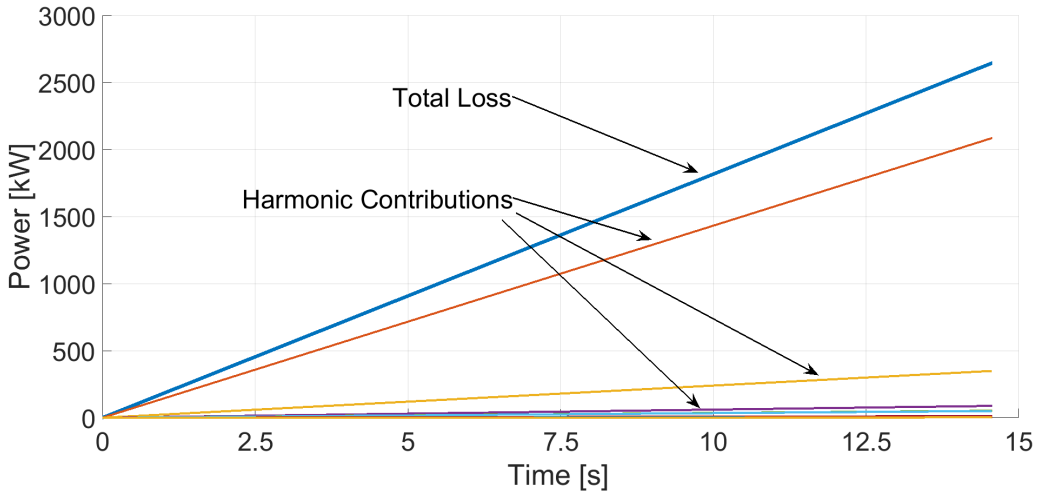

Figure 7.22: Coupling loss in the superconducting wires during aircraft acceleration

7.4.3 Hysteresis Losses

A superconductor is a material that at low temperature is capable of carrying current without electric resistance. When exposed to a magnetic field the superconductor expels the magnetic flux outside the material's boundaries. This effect is called Meissner effect and represents a characteristic feature of all the superconductors at low temperatures. When the superconductor is exposed to a magnetic field above its critical field H_{c1}, the magnetic flux penetrates the material and superconductivity is lost.

Some superconducting materials do not immediately lose their superconducting properties above H_{c1}, but they operate in a condition called mixed state where the magnetic field partially penetrates inside the superconductor. The superconducting material has then microscopic domains of normal conductive state, through which a magnetic flux passes forming a pinned structure that remains even if external forces like magnetic field or transport current are removed. These materials are called Type-II superconductors and present a second critical magnetic field H_{c2} above which superconductivity is lost.

MgB_2 is a Type-II superconductor which can operate above the first critical magnetic field H_{c1}. When an alternating magnetic field penetrates the superconductor, the movement of the magnetic flux lines of the pinned structure causes hysteresis losses and heat dissipation. The same phenomenon happens when an

alternating current flows in superconductors subject to a constant external magnetic field above H_{c1}. However, the superconductors of SCLSMs carry a dc transport current under the alternating magnetic field associated with the secondary harmonics, so the former case is investigated.

The hysteresis phenomenon can be described by the Maxwell equations in the Bean's critical state model approximation which are [130]:

$$\nabla \times \vec{E} = -\mu_0 \frac{\partial \vec{H}}{\partial t} \tag{7.78}$$

$$\nabla \times \vec{H} = \vec{J} \tag{7.79}$$

$$\nabla \cdot \vec{E} = 0 \tag{7.80}$$

$$\nabla \cdot \vec{H} = 0 \tag{7.81}$$

For a wire in z-direction the derivative with respect to the z-coordinate vanishes and $\vec{E} = E_z$, $\vec{J} = J_z$ and $H_z = 0$. Under this condition Maxwell equations in cylindrical coordinates (r, θ, z) reduce to

$$\frac{1}{r}\frac{\partial E_z}{\partial \theta} = -\mu_0 \frac{\partial H_r}{\partial t} \tag{7.82}$$

$$\frac{\partial E_z}{\partial r} = \mu_0 \frac{\partial H_\theta}{\partial t} \tag{7.83}$$

$$\frac{1}{r}\frac{\partial r H_\theta}{\partial r} - \frac{1}{r}\frac{\partial H_t}{\partial \theta} = J_z \tag{7.84}$$

$$\frac{1}{r}\frac{\partial r H_r}{\partial r} + \frac{1}{r}\frac{\partial H_\theta}{\partial \theta} = 0 \tag{7.85}$$

The solution of the Maxwell equations aims to compute the electric field E_z since the instantaneous power loss per unit volume for the i^{th} circular superconducting wire inside the cryostat is computed as

$$\begin{aligned} \frac{P_{Hys_i}}{v_{sc}} &= \frac{1}{\pi r_w^2} \int_0^{2\pi} d\theta \int_0^{r_w} \vec{E} \cdot \vec{J} r dr \\ &= \frac{J_c}{\pi r_w^2} \int_0^{2\pi} d\theta \int_0^{r_w} E_z r dr \end{aligned} \tag{7.86}$$

where $r_w = D_w/2$ is the radius of the superconducting wire and J_c is the critical current density.

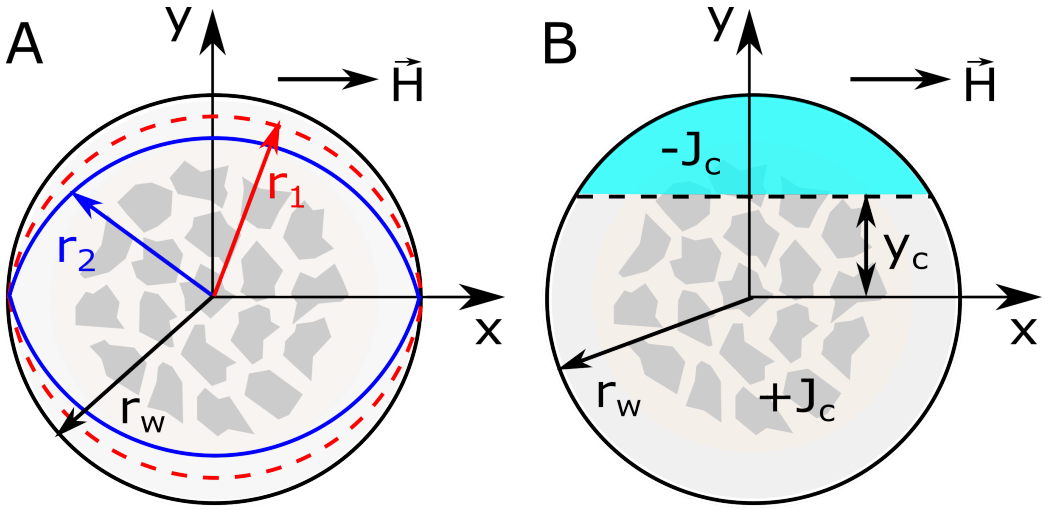

Figure 7.23: Schematics of the current density distribution over the wire cross section in case of weak penetration and full penetration

In the limit cases of magnetic field full penetration and weak penetration the Maxwell equations can be solved directly [130]. Intermediate conditions are treated by approximation. The Maxwell equations in the Bean's critical model approximation do not consider the flux shielding due to the initial Meissner effect and for field in proximity of H_{c1} or less, the hysteresis loss is overestimated.

In case of magnetic field weak penetration a narrow region of the wire cross section is crossed by a the critical current density J_c. The boundary of this region of radius r_1, alternatively oscillates between the radius r_2 and r_w as shown in Fig. 7.23A. Solving the Maxwell equations for the current distribution in the wire cross section in Fig. 7.23A and substituting E_z in eq. 7.86 yields

$$\frac{P_{Hys_i}}{v_{sc}} = (f - f_\nu)\frac{128}{9\pi}\mu_0\frac{H_\nu^3}{r_w J_c} \tag{7.87}$$

where the field $H_\nu = B_{w\nu}/\mu_0$ is the external magnetic field due to the ν^{th} harmonic.

When a wire is carrying a fixed dc current with an external alternating transverse field that leads to full penetration, the whole cross section is crossed by the critical current density J_c. The location of the boundary at which the current density changes sign, has coordinate y_c and depends on the value of the dc transport

current according to the expression

$$\frac{I}{I_c} = \frac{2}{\pi}\left[\frac{y_c}{r_w}\sqrt{1-\frac{y_c^2}{r_w^2}} + \arcsin\left(\frac{y_c}{r_w}\right)\right] \tag{7.88}$$

where I is the total induced current calculated by eq. 7.62. Since eq. 7.88 is a transcendental function of y_c, the unknown coordinate y_c can be obtained only numerically.

Since the electric field must vanish when the current density changes sign, E_z in case of full penetration can be expressed as

$$E_z = \mu_0 \frac{\partial H_v}{\partial t}(y_c - y) \tag{7.89}$$

Substituting this expression of the electric field in eq. 7.86 yields

$$\frac{P_{Hys_i}}{v_{sc}} = \mu_0 \frac{J_c}{\pi r_w^2}\left|\frac{\partial H_v}{\partial t}\right| \iint |\, y_c - y \,| \, dxdy \tag{7.90}$$

In the hypothesis of sinusoidal behaviour of the external field, the magnitude of the field derivative may be rewritten as $2\pi(f - f_v)H_v$. The evaluation of the integral to estimate the power loss in the i^{th} superconducting wire in case of full penetration leads to

$$\begin{aligned} \frac{P_{Hys_i}}{v_{sc}} =& \frac{8}{3}\mu_0 J_c r_w (f - f_v) H_v k_{yc} \\ \text{where} \qquad k_{yc} =& \left(1 - \frac{y_c^2}{r_w^2}\right)^{\frac{3}{2}} + \frac{3\pi}{4}\frac{|\, y_c I \,|}{r_w I_c} \end{aligned} \tag{7.91}$$

The magnetic field inside the cryostat of the SCLSM has an intermediate intensity with respect to the magnetic field in the case of superconductor weak and full penetration. Therefore, the SCLSM's hysteresis loss is represented by none of the described equations, although they can still be used to describe an intermediate case. Indeed, an analytical formula based on the interpolation of eqs. 7.87 and 7.91 is proposed to estimate the hysteresis losses generated by intermediate magnetic fields. Writing the loss in eqs. 7.87 and 7.91 as $C_1(H_v/H_p)^3$ and $C_2(H_v/H_p)$ respectively, the expression of the hysteresis loss with intermediate

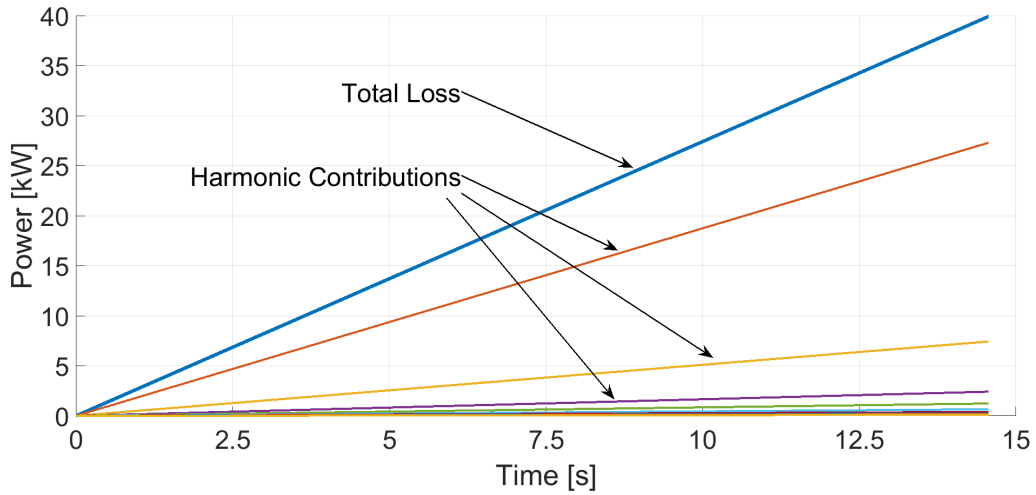

Figure 7.24: Time variation of the hysteresis loss during the launch

magnetic fields becomes [130]

$$\frac{P_{Hys_i}}{v_{sc}} = \frac{C_1\left(\frac{H_v}{H_p}\right)^3 \cdot C_2\frac{H_v}{H_p}}{C_1\left(\frac{H_v}{H_p}\right)^3 + C_2\frac{H_v}{H_p}} = \frac{C_2\left(\frac{H_v}{H_p}\right)^3}{\frac{C_1}{C_2} + \left(\frac{H_v}{H_p}\right)^2} \tag{7.92}$$

where $H_p = 2r_w J_c/\pi$. The hysteresis loss per unit volume caused by the v^{th} harmonic into the i^{th} wire is calculated from eq. 7.92 substituting the value of C_1 and C_2 as

$$\frac{P_{Hys_i}}{v_{sc}} = (f - f_v)\frac{\frac{4\pi}{3}\mu_0 H_p^2 k_{yc}\left(\frac{H_v}{H_p}\right)^3}{\frac{3\pi^3}{64}k_{yc} + \left(\frac{H_v}{H_p}\right)^2} \tag{7.93}$$

The total hysteresis loss considers the contribution of all the wires and of all the harmonics and can be computed as

$$P_{Hys} = \frac{l_{cable}}{2}\pi r_w^2 \sum_{v=2}^{N_v}\sum_{i=1}^{N_w}(f - f_v)\frac{\frac{4\pi}{3}\mu_0 H_p^2 k_{yc}\left(\frac{H_v}{H_p}\right)^3}{\frac{3\pi^3}{64}k_{yc} + \left(\frac{H_v}{H_p}\right)^2} \tag{7.94}$$

It must be underlined that the variables H_p and k_{yc} in eq. 7.94 change from wire to wire and depend on the harmonic order as well. Indeed, not only the induced current I and the field H_ν of the ν^{th} harmonic vary over the cryostat cross section, but also the critical current density J_c of each wire changes with applied magnetic field density according to the data in Fig. 7.2.

The total loss calculated using eq. 7.94 is shown in Fig. 7.24 together with the contributions of each magnetic field secondary harmonic. Since the hysteresis loss in eq. 7.94 is proportional to the harmonic frequency, the curves in Fig. 7.24 linearly increase during the aircraft acceleration.

7.5 Static-Transient Model of Thermal Insulation

In order to prevent quenching of the superconducting material, the operative temperature inside the cryostat must be kept constant by a thermal insulation system. The thermal insulation reduces the heat that flows from the hot external environment to the cold superconductors. The AC losses determined in Section 7.4 dissipate a large quantity of heat in the superconducting material that has to be absorbed by the liquid coolant. The SCLSM topology presented so far is feasible only if the thermal management system is capable of withstanding the thermal load due to the AC losses to keep the superconductors at 20 K during the whole launch. In order to verify the feasibility of the superconducting launcher, the solution of the heat transfer problem of the thermal insulation is presented in this section.

The thermal insulation system that is proposed for SCLSM is similar to the one adopted for magnetically levitatated (MAGLEV) trains [29]. The superconducting coils are hosted inside an insulated inner vessel separated by a radiation shield from the outer vessel as shown in Fig. 7.25. The space between the outer and inner vessels is evacuated to allow only radiation heat to be exchanged. Conduction occurs only through the sustaining structure, but it can be limited with thermal insulator opportunely located across the cryostat framework.

In MAGLEV systems the superconductors are made out of niobium-tin (Nb_3Sn) which requires liquid helium to cool down the material at the operating temperature (4.2 K). Additionally, liquid nitrogen is used to cool down the radiation

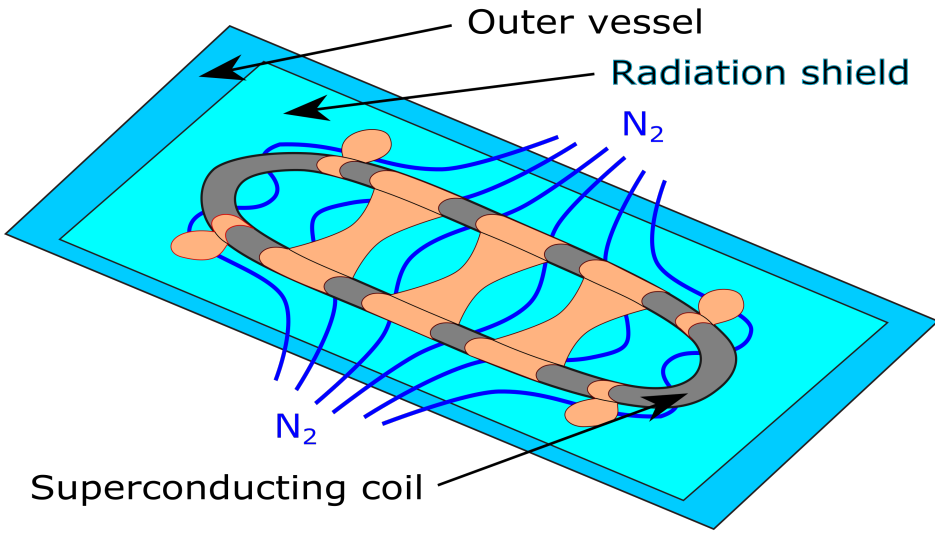

Figure 7.25: Superconducting coil and insulation structure of MAGLEV trains

shield to further reduce the heat flow across the insulation. Since MgB_2 replaces the Nb_3Sn superconductors in EML applications, the operative temperature rises from 4.2 K to 20 K, and there is no need to cool the radiation shield. Additionally, liquid hydrogen replaces liquid helium as the main coolant to exploit its excellent thermal properties at 20 K.

The thermal insulation model first solves the static heat transfer problem to obtain the temperature distribution along the mover thickness which is later used as the initial condition for the transient heat transfer problem. This method represents what happens in the real application: between two launches the mover is connected to the cryocooler and the system is cooled down to the desired temperatures (calculated by the static model); immediately afterwards, the launch procedure begins and the temperature evolves as predicted by the transient model.

The heat transfer model represents the mover structure as a series of layers of different materials as shown in Fig. 7.26. The model allows the heat to flow in a single direction. This one-dimensional model neglects the conduction heat that flows through the support structure and the heat that is transferred across the mover leading edge, trailing edge, bottom surface and top surface (see Fig. 7.1). These contributions are marginal with respect to the total heat that flows across the lateral surfaces and the heat that is generated internally. Therefore, the one-

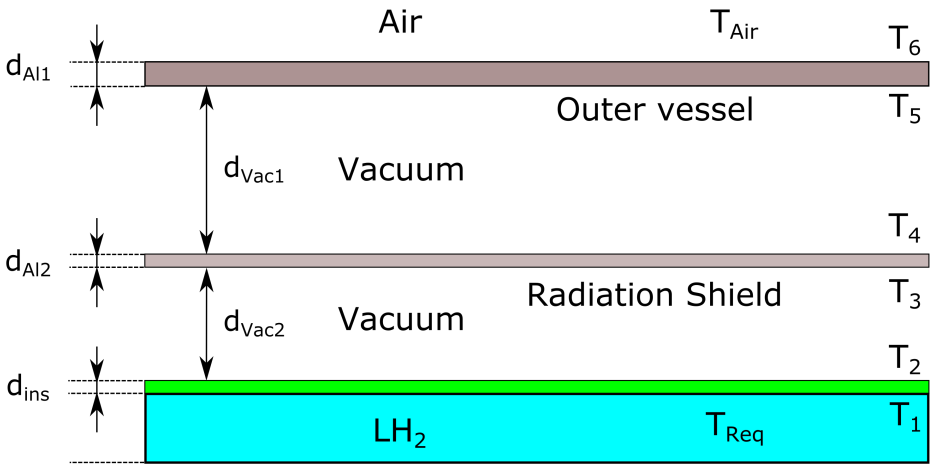

Figure 7.26: Schematic of the layered structure of the thermal insulation used for the 1D heat transfer model

dimensional approximation does not lead to significant errors and can be safely applied.

The total thickness of the structure under study is equal to the airgap length that has been considered for the electromagnetic design. The airgap length corresponds to the distance between the stator and the symmetry plane of the machine. While most of the mover dimensions, surfaces and volumes were determined in Section 7.2, the thicknesses of the various layers of the thermal insulation have to be defined.

Chapter 4 has proved that an aluminium slab with 20 mm of thickness is able to withstand the max propulsion force without reaching the buckling instability condition. Therefore, it is reasonable to assume that the sum of the thicknesses of the aluminium layers has to be equal or greater than this value. One might object that splitting the total thickness of the LIM's aluminium plate in more layers should make the structure intrinsically more unstable under the same axial load. However, in SCLSM the aluminium layers are connected by several supports which constrain the layers displacement and help to prevent buckling instability.

To be conservative, the total thickness of all the aluminium layers of the cryostat is assumed to be 30 mm, so that the insulation thermal model considers an overall thickness of 15 mm due to the machine's symmetry. The outer vessel is supposed to withstand the greatest part of the load and its thickness $d_{Al\,1}$ is assumed to be

Table 7.4: Thermal properties of the materials involved in the heat transfer problem model of insulation

	Air	**Aluminium**	**Aerogel**	**Liquid Hydrogen**
Density [kg/m^3]	1.25	2700	3-350	71.28
Dynamic viscosity [kg/m/s]	$1.82 \cdot 10^{-5}$	-	-	$2.26 \cdot 10^{-5}$
Specific Heat [J/kg/K]	1005	900	840	9565
Conductivity [W/m/K]	$2.58 \cdot 10^{-2}$	237	0.008	0.084
Emissivity	-	0.02	0.9	-

three times the thickness of the inner vessel $d_{Al\,2}$ as shown in Fig. 7.26.

The air thickness outside the cryostat is supposed to be 7 mm, exactly equal to the airgap length adopted for the conventional synchronous launcher designed in Chapter 5. Since the heat flow is almost independent from the distances between the aluminium layers, the vacuum thicknesses $d_{Vac\,1}$ and $d_{Vac\,2}$ are assumed to be equal. The cryostat wall is considered 3 mm thick whereas the thickness of the insulating material is 5 mm. With this data, the geometrical features of the layered structure of the thermal insulation are fully characterized.

The layer of insulating material outside the cryostat is used to prevent rapid fluctuations of the internal temperature. The most efficient insulators for cryogenic applications are aerogel and Multi-Layer Insulators (MLIs). MLIs are insulators formed by several layers of different materials separated by vacuum which are ideal for deep space applications and for evacuated environments. Aerogel identifies a group of foamy materials with nanometric pores and very low thermal conductivity. Aerogels present different insulation properties according to the type of foam, but in general a MLI can achieve better performance. However, MLIs are fragile and difficult to handle whereas aerogel has good structural property and is preferred for EML applications.

The thermal properties of the materials of the cryostat structure that will be used in the static and transient heat transfer problem of thermal insulation are reported in Table 7.4.

7.5.1 Static Heat Transfer Problem

The equation that has been used in the static model to express the conductive heat transfer across the solid layers of the structure in Fig. 7.26 is

$$Q = \frac{kA}{d}\Delta T \tag{7.95}$$

where Q is the heat that crosses the layers, k is the conductivity of the material, A is the area of the vessels or the cryostat computed in Section 7.2 and d is the layer thickness. The convective heat transfer across the boundary in proximity to a fluid is

$$Q = hA\Delta T \tag{7.96}$$

where h is the convective heat transfer coefficient that can be computed as

$$h = \frac{k}{l_{mov}}Nu \tag{7.97}$$

where l_{mov} is the length of the mover computed in Section 7.2 and Nu is the Nusselt number. The Nusselt number of gaseous air can be computed using the relations introduced in Chapter 4 Section 4.5, whereas the Nusselt number of liquid hydrogen is [131]

$$\begin{cases} Nu = 0.308 \cdot Ra^{0.2184} & Ra < 10^9 \\ Nu = 0.504 \cdot Ra^{0.2126} & 10^9 < Ra < 10^{11} \\ Nu = 0.801 \cdot Ra^{0.1931} & Ra > 10^{11} \end{cases} \tag{7.98}$$

The Grashof number and the Rayleigh number are computed as shown in Chapter 4 Section 4.5 using the expansion factor of liquid hydrogen $\beta_{LH_2} = 0.019$ K $^{-1}$ [132].

The general equation for the heat radiation between body 1 and body 2 is

$$Q = \frac{\sigma_B(T_1^4 - T_2^4)}{\frac{1-\varepsilon_1}{A_1\varepsilon_1} + \frac{1}{A_1F_{1\to2}} + \frac{1-\varepsilon_2}{A_2\varepsilon_2}} \tag{7.99}$$

where σ_B is the Boltzmann constant, $F_{1\to2}$ is the form factor between two ra-

diative surfaces and T_1, T_2, ε_1, ε_2, A_1 and A_2 are temperatures, emissivities and areas of the first and second body respectively. The form factor of two radiative bodies expresses the fraction of radiation emitted by one surface that reaches the other surface. The form factor only depends on the geometrical properties of the radiative surfaces and on their respective position.

When complex radiative shapes are involved in the solution of an heat transfer problem numeric integrations are often required. Since the outer vessel completely encloses the ineer vessel, the form factor can be approximated to represent the heat that would be exchanged between two rectangular surfaces with the same area of the vessels and positioned at the same reciprocal distance. The form factor between two rectangular surfaces of sizes x and y and placed at distance l between each other can be computed as [133]

$$F_{1\to 2} = \frac{2}{\pi\bar{x}\bar{y}}\left[\ln\left(\sqrt{\frac{(1+\bar{x}^2)(1+\bar{y}^2)}{1+\bar{x}^2+\bar{y}^2}}\right)+\bar{x}\sqrt{1+\bar{y}^2}\arctan\left(\frac{\bar{x}}{1+\bar{y}^2}\right)\right. \\ \left.+\bar{y}\sqrt{1+\bar{x}^2}\arctan\left(\frac{\bar{y}}{1+\bar{x}^2}\right)-\bar{x}\arctan(\bar{x})-\bar{y}\arctan(\bar{x})\right] \tag{7.100}$$

where $\bar{x} = x/l$ and $\bar{y} = y/l$. Eq. 7.100 can be used to calculate the form factor between the internal surface of the outer vessel and the external surface of the radiation shield.

Unfortunately a formula for the form factor between surfaces with the complex shape of the cryostat shown in Fig. 7.12 cannot be easily found. For an accurate calculation of the radiative heat exchanged between the inner surface of the radiation shield and the outer surface of the cryostat a numeric integration would be required. In order to avoid computationally expensive integrals the problem can be simplified without introducing significant errors. Indeed, exploiting the identity $F_{1\to 2}\cdot A_1 = F_{2\to 1}\cdot A_2$ and assuming that 95% of the radiation emitted by the cryostat hits the radiation shield ($F_{2\to 1} = 0.95$), the form factor $F_{1\to 2}$ between the internal surface of the radiation shield and the cryostat can be easily computed as

$$F_{1\to 2} = 0.95\frac{A_1}{A_2} \tag{7.101}$$

The percentage of radiative heat that is not transferred to the radiation shield

hits the structural supports of the cryostat structure.

The system of equations that has to be solved to calculate the temperature distribution across the insulation contains the heat transfer equations for all the layers:

$$\begin{cases} Q_{Air\to 6} = h_{Air} A_{mov} (T_{Air} - T_6) \\ Q_{6\to 5} = \dfrac{k_{Al} A_{mov}}{d_{Al\,1}} (T_6 - T_5) \\ Q_{5\to 4} = \dfrac{\sigma_B \varepsilon_{Al} (T_5^4 - T_4^4) A_{mov}}{2 + \varepsilon_{Al} \left(\frac{1}{F_{5\to 4}} - 2 \right)} \\ Q_{4\to 3} = \dfrac{k_{Al} A_{mov}}{d_{Al\,2}} (T_4 - T_3) \\ Q_{3\to 2} = \dfrac{\sigma_B (T_3^4 - T_2^4)}{\dfrac{1-\varepsilon_{Al}}{A_{mov}\varepsilon_{Al}} + \dfrac{1}{A_{mov} F_{3\to 2}} + \dfrac{1-\varepsilon_{ins}}{A_{cryo}\varepsilon_{ins}}} \\ Q_{2\to 1} = \dfrac{k_{ins} A_{cryo}}{d_{ins}} (T_2 - T_1) \\ Q_{1\to LH_2} = h_{LH_2} A_{cryo} (T_1 - T_{H_2}) \\ Q_{Air\to 6} = Q_{6\to 5} = Q_{5\to 4} = Q_{4\to 3} = Q_{3\to 2} = Q_{2\to 1} = Q_{1\to LH_2} \end{cases} \tag{7.102}$$

where the temperature T_{Air} and T_{H_2} are 298 K and 16 K respectively. The temperature of the liquid hydrogen is lower than the operative temperature of the superconductors because the cryocooler cools the liquid hydrogen below its boiling temperature to take advantage of the extra heat that can be absorbed before reaching the boiling point. The temperature subscripts refer to the layer surfaces as shown in Fig. 7.26.

The system of equations 7.102 cannot be directly solved since the Grashof numbers of air and hydrogen are both function of the respective wall temperatures which are part of the system unknowns. If the convective coefficients h_{LH_2} and h_{Air} would be considered as unknowns and two equations would be added to the system 7.102, the non-linear relation between the Nusselt number and the Grashof number would prevent the possibility to express the temperatures in a closed form. Therefore, the solution is found iteratively assuming an initial value for both the wall temperatures and updating them at each step until the stopping criteria are satisfied.

Even with such simplifications the system remains non-linear because of the

Table 7.5: Temperature distribution on the surfaces of the insulation model

T_{H_2} [K]	T_1 [K]	T_2 [K]	T_3 [K]	T_4 [K]	T_5 [K]	T_6 [K]	T_{Air} [K]	Q [W]
16	16.58	18.75	225.0	225.0	295.3	295.3	298	75.07

dependency of the radiation heat on the fourth power of the temperature. The roots of the transcendental equations in the system 7.102 are then found numerically before calculating all the other temperatures. The solution of the system of equations 7.102 is reported in Table 7.5.

The temperatures across the aluminium layers look constant in Table 7.5 since they vary of only 1 mK because of the high conductivity of the metal. The heat reported in Table 7.5 is two times the heat computed by solving the system of equations 7.102 to consider both sides of the cryostat.

7.5.2 Transient Heat Transfer Problem

The transient heat transfer model of the thermal insulation simulates the variation of the temperature distribution during the launch and after the aircraft detaches. The transient heat transfer model uses the data reported in Table 7.5 as initial condition. The Fourier's law for one-dimensional heat transfer problems is applied to describe the variation of the temperature on layer surfaces shown in Fig. 7.26.

$$\frac{\partial T}{\partial t} = \alpha \frac{\partial^2 T}{\partial x^2} \tag{7.103}$$

where $\alpha = k/(\rho c_p)$ is the thermal diffusivity. The finite difference method is used to transform the partial differential equation into discrete equations whose solution can be easily computed numerically. The Fourier's law is then solved over a grid of points which discretises the domain only along the insulation thickness.

The discrete form of the heat transfer equation for the i^{th} node located inside an insulation layer is

$$\frac{1}{\alpha}\frac{T_i^{n+1} - T_i^n}{\Delta t} = \frac{T_{i+1}^{n+1} - 2T_i^{n+1} + T_{i-1}^{n+1}}{\Delta x^2} \tag{7.104}$$

where the index n refers to the current time step. The second derivative on the right hand side of eq. 7.104 is evaluated at the time step $n+1$ because an implicit

method is applied. When the node is located on a boundary where convection occurs, the condition that expresses the heat transfer across the surface is

$$k\frac{T_{i+1}^{n+1}-T_i^{n+1}}{\Delta x}=h(T_i^{n+1}-T_\infty) \tag{7.105}$$

where T_∞ can be either the hydrogen or the air temperature depending on the boundary where eq. 7.105 is solved. The convective heat coefficient of air varies with the speed according to the graph shown in Fig. 4.31 in Section 4.5. The convective coefficient of liquid hydrogen can be still computed using eq. 7.98 considering the variation of the physical properties with the temperature. Since part of the hydrogen evaporates during take-off, the expression of the Nusselt number for liquid hydrogen cannot be used to describe the convective heat exchanged in the vapour. The convective coefficient of the hydrogen gaseous phase can be computed using the following expression of Nusselt number [134].

$$Nu=0.104\cdot Ra^{0.352} \tag{7.106}$$

On the boundaries where radiation takes place the heat equation is solved as

$$k\frac{T_{i+1}^{n+1}-T_i^{n+1}}{\Delta x}=\frac{\sigma_B(T_i^{n4}-T_{i-1}^{n\ 4})}{\frac{1-\varepsilon_i}{\varepsilon_i}+\frac{1}{F_{i\to i-1}}+\frac{A_i}{A_{i-1}}\frac{1-\varepsilon_{i-1}}{\varepsilon_{i-1}}} \tag{7.107}$$

where the node i is located on the radiative surface, the node $i+1$ is inside the layer and exchange heat with the node i through conduction and the node $i-1$ lays on the other radiating boundary. The areas and emissivities in eq. 7.107 refer to the boundary where the node with the same index is located. The temperatures at power four in eq. 7.107 are considered at the n^{th} time step and are not treated as unknowns (evaluated at $n+1$ as the implicit method would require). This introduces negligible errors in the numerical solution, but removes the strong non-linearity introduced by the Boltzmann equation. When the heat exchanged through the radiation is expressed using eq. 7.107, the radiative surfaces are considered as boundaries and the vacuum layers do not need to be discretised.

As it was observed after the solution of the stationary model, the temperatures shown in Table 7.5 across the aluminium layers do not significantly change due to

the high conductivity of the material. A similar results is expected after the solution of the transient heat transfer problem. Therefore, it is not necessary to use a large number of nodes to describe the temperature variation inside the aluminium layers. Five nodes per layer were considered enough for this purpose leading to a system of 15 equations to solve at each time step.

During every time iteration, the system of equations that computes the temperature distribution on the insulation layers is solved keeping the hydrogen temperature T_{H_2} constant. The temperature of the liquid hydrogen is then updated after each iteration using

$$T_{H_2}^{n+1} = \frac{Q^n + AC_{loss}^n}{\rho_{H_2}^n c_{H_2}^n d_{H_2} A_{Cryo}} \Delta t + T_{H_2}^n \tag{7.108}$$

where d_{H_2} is the thickness of the liquid hydrogen layer, Q^n is the heat flow across the insulation at the instant n and AC_{loss}^n is the sum of the eddy current loss, hysteresis loss and the coupling loss computed in Section 7.4. The hydrogen density $\rho_{H_2}^n$ and the specific heat capacity $c_{H_2}^n$ change with time and with the hydrogen phase state as shown in eq. 7.112.

The cryostat is initially filled with liquid hydrogen at 16 K that starts to heat up under the action of Q and AC_{loss} as soon as the launch begins. The liquid hydrogen temperature rise can be estimated using eq. 7.108 using the physical property of the liquid phase at temperature $T_{H_2}^n$ until the boiling point at 20.324 K is reached. At this temperature the coolant starts to evaporate and exchange latent heat with the superconductors and the cryostat walls. When the hydrogen evaporation occurs, the temperature remains constant and the coolant absorbs the energy

$$E_{H_2}^n = (Q^n + AC_{loss}^n)\Delta t \tag{7.109}$$

The energy required to evaporate the full amount of hydrogen stored inside the cryostat is

$$E_{tot} = L_{H_2} \cdot m_{LH_2} \tag{7.110}$$

where L_{H_2} is the hydrogen latent heat of evaporation shown in Table 7.1 and m_{LH_2}

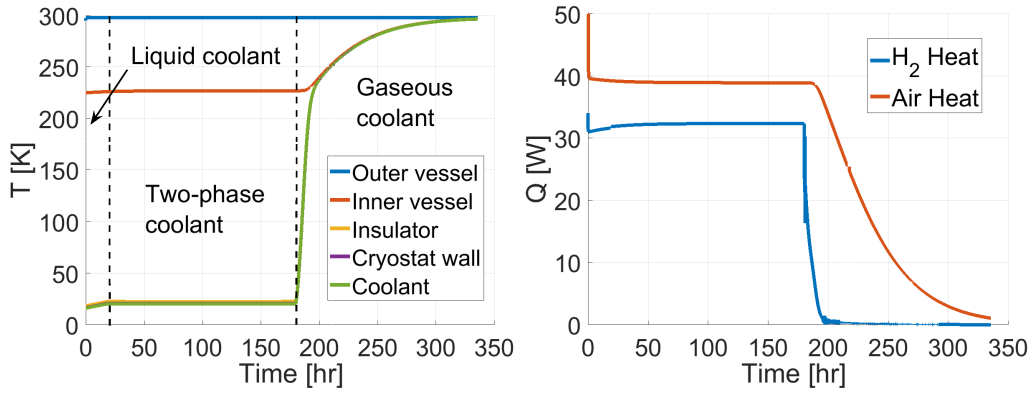

(a) Temperature (b) Heat Flow

Figure 7.27: Variation of temperature and heat flow across the insulation components without internal heat generation

is the mass of the liquid hydrogen in the cryostat which is 20% of the one shown in Table 7.2. The percentage of hydrogen in gaseous form at the n^{th} time step can be computed as

$$H^n_{2\%} = \frac{1}{E_{tot}} \sum_{i=1}^{n} E^i_{H_2} \tag{7.111}$$

The value of the physical properties of the two-phase hydrogen used in eq. 7.108 at the n^{th} time step can be estimated as

$$\begin{aligned} \rho^n_{H_2} &= (1 - H^n_{2\%})\rho_{LH_2} + H^n_{2\%}\rho_{GH_2} \\ c^n_{H_2} &= (1 - H^n_{2\%})c_{LH_2} + H^n_{2\%}c_{GH_2} \end{aligned} \tag{7.112}$$

where ρ_{LH_2}, ρ_{GH_2}, c_{LH_2} and c_{GH_2} are the density and the specific heat capacity of the liquid phase and of the gaseous phase at 20.324 K respectively. During boiling, the two phase hydrogen's Nusselt number and the physical properties required to compute it are estimated with the same technique proposed in eq. 7.112. When hydrogen fully evaporates, the temperature rise can be still estimated using eq. 7.108 with the physical property of the hydrogen vapour at temperature $T^n_{H_2}$.

The quality of the thermal insulation can be verified evaluating the time required to reach full evaporation solving the transient heat transfer problem without considering the internal heat generation due to the AC losses. In this case the con-

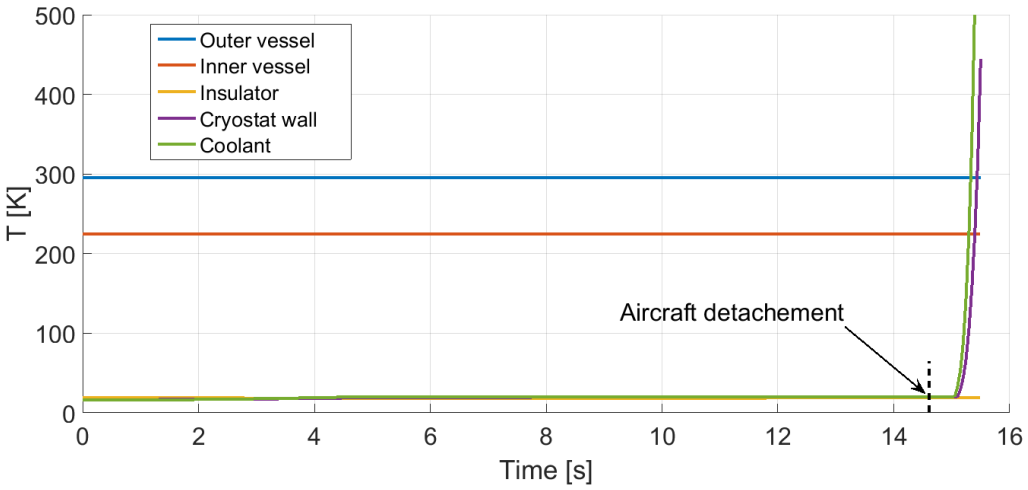

Figure 7.28: Temperature evolution of thermal insulation components and cryogenic coolant during the launch

vective coefficient of air is assumed to be the value that is reached at launcher end-speed (85.73 m/s).

Fig. 7.27a shows the temperature variation of the insulation components with time. It can be clearly seen that when hydrogen is boiling, the temperature distribution of the system does not change until full evaporation. This happens after 180 hours (about 7 days), because the amount of hydrogen stored inside the mover is able to absorb 18.73 MJ before changing phase completely, and the heat that flows across the insulation is very low as shown in Fig. 7.27b. The difference between the heat extracted from air and the heat absorbed by the hydrogen in Fig. 7.27b corresponds to the energy required to heat up the vessels and the insulator. After the hydrogen evaporation the system tends to the temperature of air which is reached after 335 hours.

When the AC losses are included, the liquid hydrogen heats up at much higher rate, but it does not reach the vaporization before the end of the launch as shown in Fig. 7.28. If the AC losses continue to dissipated heat into the coolant at their maximum rate even after the aircraft detachment, the hydrogen would fully evaporate after 15.1 s as shown in Fig. 7.28. However, the heat generation ceases after 14.57 s and only the heat flow across the insulation continues to warm the liquid hydrogen. This heat would cause the evaporation of the remnant liquid hydrogen

after approximately 11 hours and 10 minutes.

Nevertheless, the mover needs to return to its initial position and must be capable of absorbing the additional AC losses produced in the process. Assuming that the mover returns in 30 seconds (t_{Ret}) with an uniformly accelerated motion, the energy required to take the mover to its initial position is

$$E_{mov} = \int F(s)ds = \overline{F} \cdot s_{Run} = m_{mov}\overline{a}_{mov}s_{Run} = 2m_{mov}\left(\frac{s_{Run}}{t_{Ret}}\right)^2 \tag{7.113}$$

where $\overline{F}$ is the average thrust, $\overline{a}_{mov}$ is the average acceleration, m_{mov} is the mass of the mover reported in Table 7.2 and s_{Run} is the distance travelled by the aircraft during the acceleration (about 625 m). The mover needs 6.732 MJ to return to its initial position in 30 seconds.

Assuming that the SCLSM efficiency during the return operations is the same of the launch, the additional AC losses can be approximated as

$$E_{AC} = AC_{loss}\frac{E_{mov}}{E_{A320}} \tag{7.114}$$

where AC_{loss} is the energy absorbed by the liquid hydrogen during the launch (total AC losses) and E_{A320} is the total energy transferred to the aircraft and the mover during the launch which is computed as

$$E_{A320} = 2(m_{A320} + m_{mov})\left(\frac{s_{Run}}{t_{TOF}}\right)^2 \tag{7.115}$$

where t_{TOF} is the take-off time (14.57 s). Considering the additional heating $E_{AC} = 0.44$ MJ computed by eq. 7.114, the time window for post-launch operations before full hydrogen evaporation is approximately 7 hours and 10 minutes.

The thermal model presented in this chapter assumes forced convection on the air side and natural convection on the liquid hydrogen side. The amount of heat removed by the SCs can be increased by a hydrogen flow inside the narrow ducts of the cryostat forced by a pump located in the hydrogen tank. The pump would grant a homogeneous temperature distribution and would prevent the superconductors quenching during operations. In this case, the heat transfer equation for forced convection must replace the one for natural convection presented in this

model.

Additionally, the model considers only the mass of the liquid hydrogen stored in the cryostat ducts to estimate the total energy that the coolant is able to absorb. Conversely, the SCLSM's mover hosts an extra volume of liquid hydrogen in the reservoir that largely extends the post launch operation time. In this way the results presented in this chapter prove that the cooling system is able to cope with the internal heat generation maintaining 20 K during the whole duration of the launch even when only the coolant inside the cryostat is considered.

The model of the thermal insulation presented in this section does not considered the pressure variation inside the cryostat during the hydrogen vaporization. This aspect is very important for both structural and thermal design of the SCLSM's mover. Indeed, the structure of the cryostat must be capable of withstanding the internal pressure increase without cracking. The extra volume provided by the hydrogen tank may alleviate the load on the cryostat structure, but a safety valve should be implement to prevent the pressure exceeding the safety limits. Since the impact of the pressure variation on the cryostat structure requires a definition of all the geometrical characteristics to a level of detail which is beyond the purpose of this work, the structural analysis of the system is left for future research.

In a similar way, the exact solution of the thermal problem requires the calculation of the physical properties of the coolant subject to a pressure variation through the interpolation of complex data tables. Again, the knowledge of the exact value of the pressure would require an accurate definition of the geometrical properties of the cryostat. This topic is not addressed in this work because the thermal model that does not consider the pressure variation estimates an exacerbated vaporization with respect to what happens in the real cryostat. Indeed, the changing of pressure improves the thermal properties of the coolant and more heat is absorbed by the hydrogen liquid phase before reaching the boiling point. Therefore from the thermal point of view, the simplified model in this section presents some safety margins with respect to the real application.

7.6 Cryocoolers for Aerospace Applications

The functioning of a superconducting machine cannot be described independently from its cooling system which is composed of an insulation system, coolant and a refrigerator. The cryostat insulation with liquid hydrogen as coolant has been studied for EML application in Section 7.5. The chosen configuration was proven suitable to maintain the SCs at the operating temperature despite the intense internal losses. At the beginning of every launch the coolant needs to be liquid at 16 K and the heat absorbed during the previous launch has to be removed by an external refrigeration system. The coolers used to achieve cryogenic temperatures are inefficient and their input power considerably penalizes the performance of the launcher.

This section proposes a method to estimate the input power required by a cryocooler to remove the heat produced during the launch. The method describes the static performance of a cryoocoler for aerospace applications that was developed by the author to improve the performance of an existing model [135]. Palmer in [135] identifies the Reverse-Brayton cryocoolers (RBCs) as the most suitable refrigeration system for aerospace applications because of high reliability, efficient heat exchange due to the working fluid high speed, high power density and continuous displacement compression. With helium as working fluid, RBC can achieve the desired cold temperature with high flow rates and heat exchange effectiveness. The RBC configuration that better satisfies the requirements is a double-stage cryocooler as shown in Fig. 7.29.

Palmer's model is solved on the basis of assumptions made according to the current best practice for similar aerospace grade Reverse-Brayton cryocoolers.

- The system is closed and there are not helium leakages;
- No transport losses across the ducts connecting the refrigeration cycle components;
- Constant specific heat capacity even at low temperature;
- Within the heat sink heat exchanger the latent heat capacity is shared in a 50% split with the specific heat capacity of the coolant;

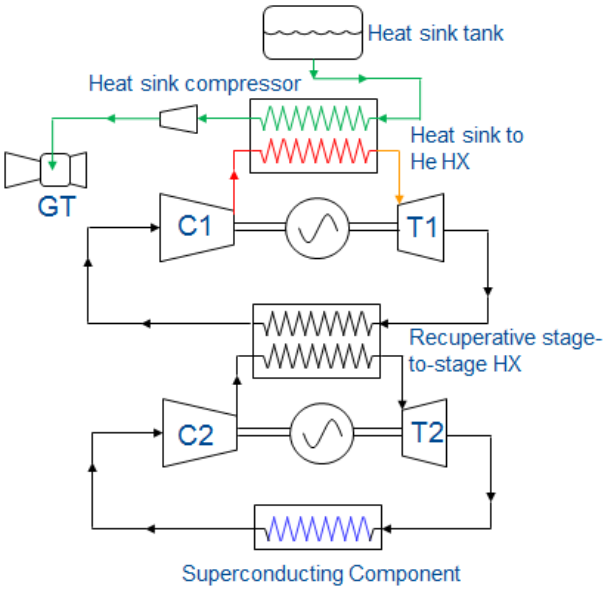

Figure 7.29: Double-stage reverse-Brayton cryocooler for aerospace application

- The motors used to move compressors and turbines are superconducting and achieve efficiencies above 99%;
- The minimum pressure in each stage is 2 bar whereas the pressure drops across heat exchangers is $\Delta p = 5\%$.
- The cold heat exchanger temperature drop is $\Delta T_c = 10$ K, the hot heat exchanger helium output temperature is $\Delta T_{wHx} = 10$ K more than the heat sink coolant on both sides and the temperature difference between input and output flow of the intermediate heat exchanger is $\Delta T_{iHx} = 10$ K on both sides;
- The temperature ratio is equally shared between both stages;
- The compressor polytropic efficiency is $\eta_c = 92\%$, whereas the turbine polytropic efficiency is $\eta_t = \eta_c + 3\%$.

The model of the cryocooler proposed in this chapter for SCLSM application is based on the same assumptions and attempt to improve the cryocooler efficiency of the Palmer's model using recuperative cooling.

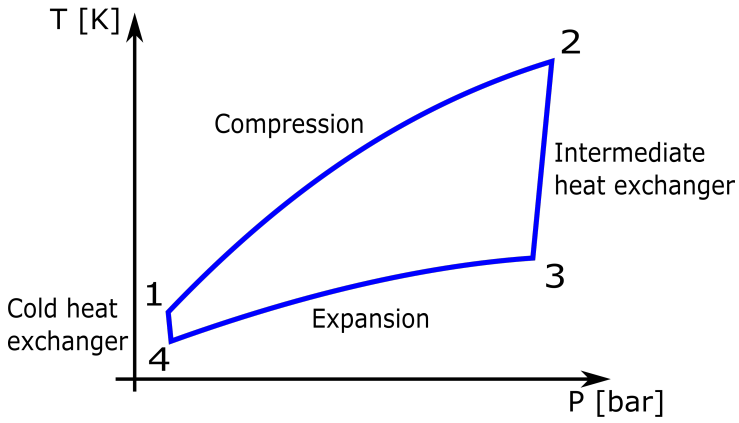

Figure 7.30: T-P chart for the coolant in the cryocooler second stage

7.6.1 Recuperative Cooling

Recuperative cooling is a common way to improve the efficiency of a thermal cycle exchanging heat between cold and hot coolant. Recuperation aims to optimize the working temperature of compressors and turbines to reduce the input power required from the external source. This section presents the implementation of recuperative cooling on the double-stage RBC showed in Fig. 7.29 and estimates the input power reduction.

Since the two stages of the cryocooler operate in the same manner, the research of a possible way to improve the performance can be restricted to a single stage and later extended to the second one. The temperature-pressure transformation that the coolant undergoes in the second stage of the cryocooler is shown in Fig. 7.30.

According to the cryocooler requirements and assumptions, temperatures T_1, T_4, T_3 and the pressures p_1 and p_4 in Fig. 7.30 are known and cannot be modified. In fact, T_1 is the cold temperature required by the superconductors; T_4 is a function of T_1 and of the cold heat exchanger performance (temperature delta ΔT_c given in input); T_3 is fixed by the assumption of equal temperature drop across stages; p_1 is known as minimum pressure and p_4 is a function of p_1 and of the cold heat exchanger performance (pressure drop Δp given in input).

The objective of the analysis is the minimization of the input power of the cycle

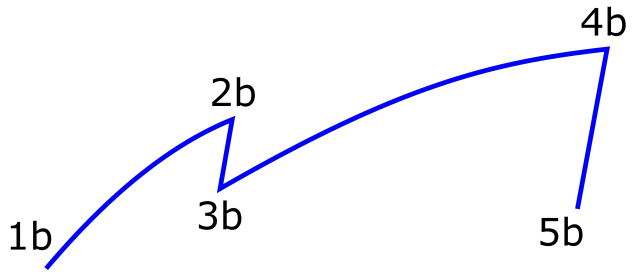

Figure 7.31: T-P chart of the second stage compression side with intercooler

in Fig. 7.30 which is computed as

$$P_i = \dot{m} c_{p_{He}} (T_2 - T_1) - \dot{m} c_{p_{He}} (T_3 - T_4) \tag{7.116}$$

In the hypothesis of constant helium specific heat $c_{p_{He}}$ and under the current assumptions, the input power minimization is equivalent to minimizing the temperature T_2. Indeed, the specific input power $P_i/(\dot{m} c_{p_{He}})$ is proportional to the input power P_i and has the unit of temperature.

While the expansion side in Fig. 7.30 has three constraints (p_4, T_4, T_3), on the compression side only the pressure p_1 and the temperature T_1 are defined by the model assumptions and requirements. Since the compressor needs several stages to increase the pressure from p_1 to p_2, an intercooler may be used between them with the aim of reducing temperature T_2. To prove that this configuration requires less input power than the original cryocooler, the compression side in Fig. 7.30 is modified as shown in Fig. 7.31. The key points are renamed with the terminology that will be used from now on in the model. The transformations represented in Fig. 7.31 are described by the relations:

$$T_{4b} = T_{2b} \left(\frac{p_{4b}}{p_{2b}} \right)^{\frac{\gamma-1}{\gamma} \frac{1}{\eta_c}} \tag{7.117}$$

$$p_{3b} = p_{2b}(1 - \Delta p) \tag{7.118}$$

$$T_{3b} = T_{2b} - \Delta T_i \tag{7.119}$$

$$T_{2b} = T_{1b} \left(\frac{p_{2b}}{p_{1b}} \right)^{\frac{\gamma-1}{\gamma} \frac{1}{\eta_c}} \tag{7.120}$$

where γ is the ratio between the specific heat at constant volume and the specific

heat at constant pressure of helium. Equations 7.117 and 7.120 express the relations between pressures and temperatures during the two polytropic compressions, whereas eqs. 7.118 and 7.119 describe the relations between pressures and temperatures across the heat exchanger (intercooler) respectively. The new unknowns introduced in the systems are pressures and temperatures at point 2 and 3 and the temperature T_{4b} at point 4.

To obtain an optimal design solution, the amount of heat that is exchanged in the intercooler and the position of the intercooler along the compression line must be determined. The heat transferred inside the heat exchanger is expressed by the difference ΔT_i between the inlet and outlet temperature of the intercooler. The heat exchanger position along the compression line in Fig. 7.31 is linked with the value of the pressure p_{2b} which in turns is correlated with the dimensions of the compressor stages. Since the dimensions of the compressor stages depend on the respective compression ratio the following variable is introduced

$$k_{pr} = \frac{p_{4b}/p_{3b}}{p_{2b}/p_{1b}} \tag{7.121}$$

where p_{2b}/p_{1b} is the first stage compression ratio and p_{4b}/p_{3b} is the second stage compression ratio. Using eqs. 7.117 to 7.120 all the unknowns of the system can be determined as a function of the independent variable k_{pr} and ΔT_i. The specific power required by the compression stages can be computed as

$$P_{sc} = T_{2b} - T_{1b} + T_{4b} - T_{3b} \tag{7.122}$$

Varying the pressure ratio k_{pr} and the temperature difference ΔT_i, the map of the specific compression power shown in Fig. 7.32 is obtained.

Fig. 7.32 also compares the analysis outcomes with the specific compression power of the system without regenerative cooling. The implementation of an intercooler is always convenient except when the second stage has a compression ratio lower than the first stage ($k_{pr} < 1$) or when the intercooler exchanges a small amount of heat. Thus, high performance can be achieved when the most of the heat is exchanged in the intercooler rather than in the heat exchanger before the turbine. Moreover, when most of the compression occurs in the second compressor (high k_{pr}) the system takes advantage of the lower slope of the polytropic

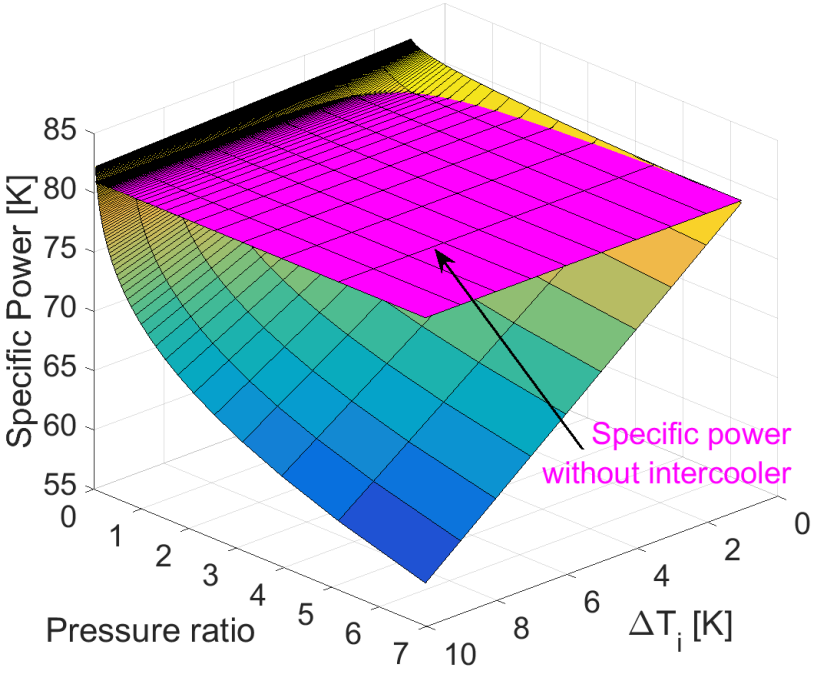

Figure 7.32: Specific input power variation with the pressure ratio between compression stages and with the intercooler temperature delta

transformation reducing the required input power.

However, not all the solutions are physically acceptable since the RBC's second stage under investigation interfaces with the first stage as shown in Fig. 7.33. In particular the temperature T_{3b} must be greater than the temperature T_{7a} to allow the heat to flow from the RBC's second stage to the first stage and not vice versa.

The temperature T_{7a} cannot be determined without investigating the heat transfer between the RBC's stages. The two helium cycles exchange heat according to the equations:

$$\begin{aligned} Q_1 &= \dot{m}_b c_{p_{He}}(T_{2b} - T_{3b}) = \dot{m}_a c_{p_{He}}(T_{1a} - T_{7a}) \\ Q_2 &= \dot{m}_b c_{p_{He}}(T_{4b} - T_{5b}) \\ \dot{m}_a &= \dot{m}_b \frac{Q_1 + Q_2}{c_{p_{He}}(T_{1a} - T_{6a}} \\ T_{1a} &= T_{2b} - \Delta T_{iHx} \\ T_{6a} &= T_{5b} - \Delta T_{iHx} \end{aligned} \tag{7.123}$$

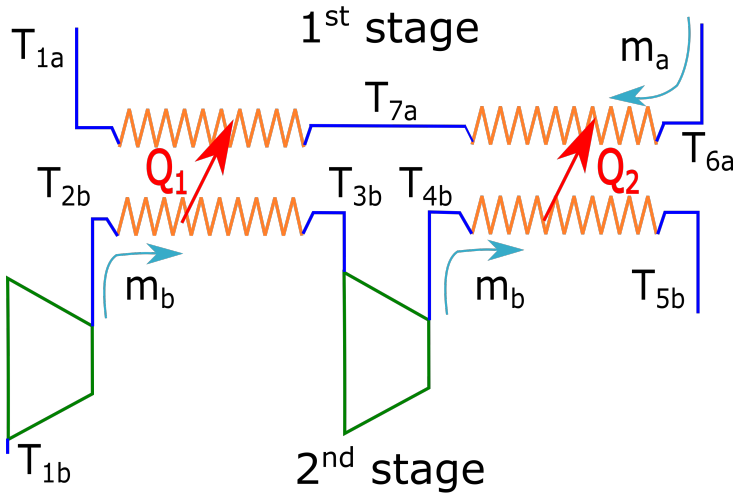

Figure 7.33: Schematic of the double-stage RBC interface

where $\dot{m}_a$ and $\dot{m}_b$ are the mass flow rates of the RBC's first stage and second stage, respectively.

The variation of the temperature T_{7a} can be expressed as a function of the second stage parameters combining eqs. 7.123 as

$$T_{7a} = T_{2b} - \Delta T_{iHx} - \frac{(T_{2b} - T_{5b})(T_{2b} - T_{3b})}{T_{2b} - T_{3b} + T_{4b} - T_{5b}} \tag{7.124}$$

The variations of the temperature T_{3b} and T_{7a} with respect to the design variables k_{pr} and ΔT_i are compared in Fig. 7.34. In particular, the areas where the temperature $T_{3b} > T_{7a}$ represent the set of conditions that can be implemented in the double-stage RBC to improve the performance of the cryocooler. The same analysis can be extended to the compression line of the RBC's first stage, splitting the heat sink in two heat exchangers, the first positioned between compressor stages and the second located before the turbine inlet.

The performances of the RBC with recuperative cooling and heat exchangers connected in series as shown in Fig. 7.33 strongly depend on the dimensions of the intercoolers and on their locations across the compression lines. Moreover, any change of operative condition entails a variation of the optimum proportion between compression ratios and would require a modification of the intercoolers dimensions that achieve the required temperature deltas. These dependencies are

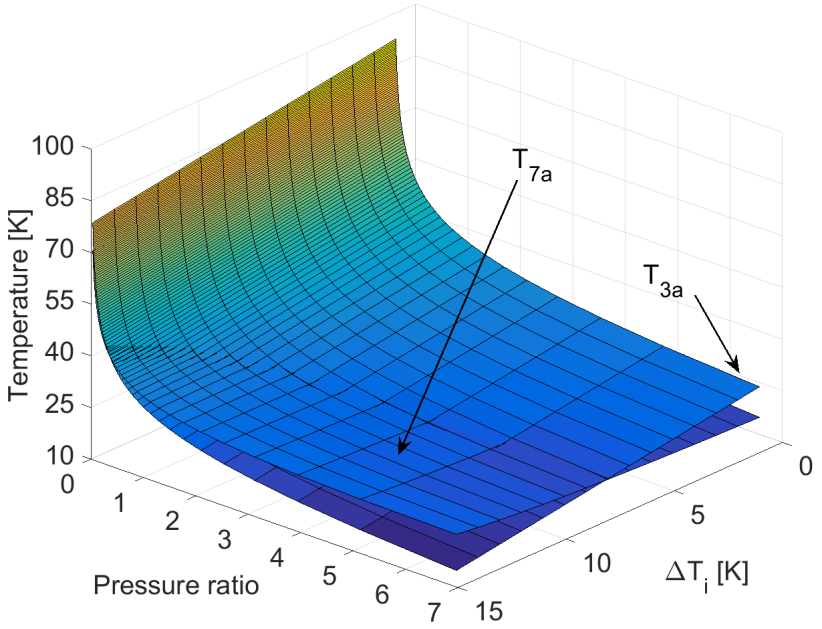

Figure 7.34: T_{7a} and T_{3b} temperatures variations with the pressure ration between compression stages and with the intercooler temperature delta

not beneficial for a system that is supposed to work under different situations and with different thermal loads. The system should be able to quickly respond to changes and automatically adapt to new situations. In particular, the dependency of the low pressure compressor outlet temperature T_{3b} on the outlet temperature of the first cold heat exchanger of the first stage T_{7a} limits the possible input power reduction that can be achieved with intercoolers.

When the heat exchangers are connected in series the inlet condition of the downstream heat exchanger depends on the amount of heat exchanged upstream. In order to have heat exchangers with the same inlet conditions the series connection scan be replaced with a parallel connection as shown in Fig. 7.35. With this configuration, the system can adapt to different operative conditions controlling the flow across the two heat exchangers with an upstream valve located were the flow separates. In this way, the two heat exchangers can be similarly sized since the valve is now responsible to redirect the flow across them to get the best performance in all the operative conditions. Fig. 7.35 shows the parallel connection between the RBC's second stage intercooler and the intermediate heat exchanger,

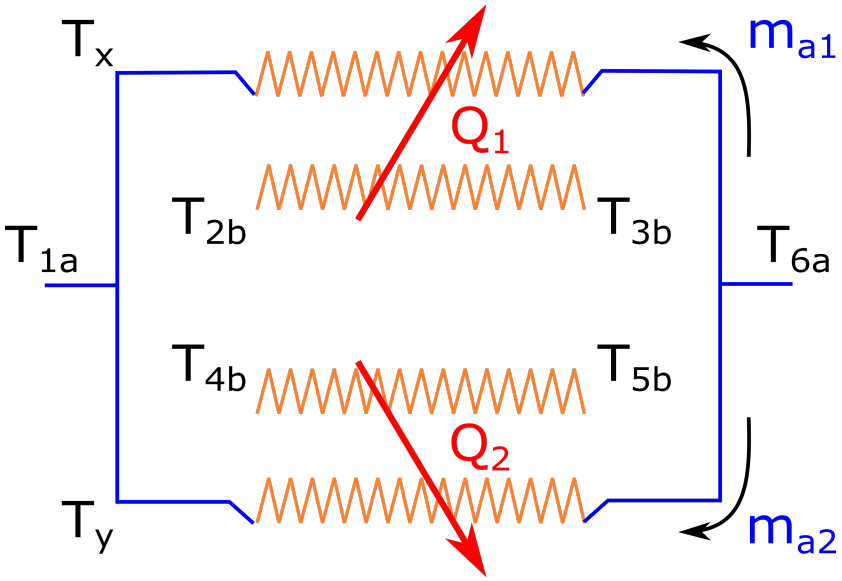

Figure 7.35: Schematic of the double-stage RBC interface with parallel-connected heat exchangers

but the same technique is applied to the RBC's first stage intercooler and heat sink.

Some additional assumptions are made on the heat exchangers inlet and outlet temperatures to make sure that the heat flows only from the colder stage to the hotter stage in respect of the second law of thermodynamics:

$$\begin{aligned} T_{3b} &= T_{6a} + \Delta T_{iHx2} \\ T_{2b} &= T_x + \Delta T_{iHx2} \\ T_{4b} &= T_y + \Delta T_{iHx} \end{aligned} \tag{7.125}$$

where T_x and T_y are the first stage heat exchangers outlet temperatures reported in Fig. 7.35 and T_{iHx2} is the second outlet-inlet temperature difference which is assumed approximately 1 K. With these additional assumptions it is not necessary to introduce a constant to define the pressure ratios of the compressor stages since the pressure p_{2b} is constrained by the temperature difference T_{iHx2}.

The performance of the RBC with parallel-connected heat exchangers depend on the amount of heat that is transferred among the independent flows in Fig. 7.35

which is expressed as

$$k_{Hxb} = \frac{Q_1}{Q_2} = \frac{T_{2b} - T_{3b}}{T_{4b} - T_{5b}} = \frac{\dot{m}_{a1}(T_x - T_{6a})}{\dot{m}_{a2}(T_y - T_{6a})} \tag{7.126}$$

The unknown pressures and temperatures (p_{2b}, p_{3b}, T_{2b} and T_{4b}) of the RBC's second stage can be expressed as a function of k_{Hxb} as

$$p_{2b} = \left[\frac{T_{3b} - k_{Hxb} T_{5b}}{2T_{1b}} + \sqrt{\left(\frac{T_{3b} - k_{Hxb} T_{5b}}{2T_{1b}} \right)^2 + k_{Hxb} \frac{T_{3b}}{T_{1b}} \left(\frac{p_{4b}}{p_{1b}(1-\Delta p} \right)^{\frac{\gamma-1}{\gamma\eta_c}} p_{1b}^{\frac{\gamma-1}{\gamma\eta_c}}} \right]^{\frac{\gamma\eta_c}{\gamma-1}}$$

$$\begin{aligned} p_{3b} &= p_{2b}(1 - \Delta p) \\ T_{2b} &= T_{1b} \left(\frac{p_{2b}}{p_{1b}} \right)^{\frac{\gamma-1}{\gamma\eta_c}} \\ T_{4b} &= T_{3b} \left(\frac{p_{4b}}{p_{3b}} \right)^{\frac{\gamma-1}{\gamma\eta_c}} \end{aligned} \tag{7.127}$$

The RBC's first stage pressure and temperatures are found solving the same system of equations in 7.127 for the respective variables, once the constant k_{Hxa} and the temperature at the compressor inlet T_{1a} are determined.

The constant k_{Hxa} represents the ratio between the heats transferred to the heat sink by the the first stage parallel-connected heat exchangers. k_{Hxa} can be defined as in eq. 7.126 replacing the respective variable of the RBC's first stage. The temperature T_{1a} is the temperature of the gaseous helium after the flows coming from the parallel-connected heat exchangers mingle. In the hypothesis, that the two flows perfectly mix the compressor inlet temperature can be computed as

$$T_{1a} = \frac{T_x \dot{m}_{a1} + T_y \dot{m}_{a2}}{\dot{m}_{a1} + \dot{m}_{a2}} \tag{7.128}$$

Considering the assumptions in eq. 7.125, the temperature T_{1a} can be rewritten as a function of known temperatures as

$$T_{1a} = \frac{\frac{T_{2b} - T_{3b}}{T_{2b} - \Delta T_{iHx2} - T_{6a}} (T_{2b} - \Delta T_{iHx2}) + \frac{T_{4b} - T_{5b}}{T_{4b} - \Delta T_{iHx} - T_{6a}} (T_{4b} - \Delta T_{iHx})}{\frac{T_{2b} - T_{3b}}{T_{2b} - \Delta T_{iHx2} - T_{6a}} + \frac{T_{4b} - T_{5b}}{T_{4b} - \Delta T_{iHx} - T_{6a}}} \tag{7.129}$$

In order to solve the model of the cryocooler with parallel-connected heat exchangers, the constants k_{Hxa} and k_{Hxb} must be selected. The optimum value of the constants minimizes the input power required by the cryocooler which coincides with the minimum of the specific power P_{sc}.

$$\begin{aligned} P_{sc}(k_{Hxa},k_{Hxb}) = T_{2a}(k_{Hxa},k_{Hxb}) + T_{1a}(k_{Hxb}) + T_{4a}(k_{Hxa}) - T_{3a} - T_{5a} \\ + T_{6a} + T_{2b}(k_{Hxb}) + T_{1b} + T_{4b}(k_{Hxb}) - T_{3b} - T_{5b} + T_{6b} \end{aligned} \tag{7.130}$$

Since the constants and the minimum input power depend on the mathematical model requirements and assumptions, the solution of the minimization problem is never univocal and changes with the variation of the operative conditions. However, whereas in RBCs with series-connected heat exchanger the design constant corresponded to the dimensions of the cryocooler components, the constants k_{Hxa} and k_{Hxb} represents the action of the distributing valves on the upstream flow and the ratio of the mass flow rates $\dot{m}_{a1}$ and $\dot{m}_{a2}$ across the heat exchangers as shown in eq. 7.126.

The investigation on the right valve setting to deal with any possible situation exceeds the intent of this research. It is accepted to consider a combination of constants that leads to a simple model whose results are close enough to the optimum condition. The selected value of the constants are $k_{Hxa} = 1$ and $k_{Hxb} = 1$ which means that the heat exchangers transfer the same amount of heat. This configuration leads to significant performance improvements, even though it should be kept in mind that recuperative cooling with parallel-connected heat exchangers has the potential to further improve the cryocooler performance.

7.6.2 Cryocooler Performance

The cold power Q_c is one of the requirements that main characterizes the performance of a cryocooler. The cryocooler for aerospace application designed by Palmer in [135] aims to remove 10 kW from a load at 20 K. The cryocooler uses liquid methane as heat sink since it is a good propellant that can be later used to fuel a gas turbine as shown in Fig. 7.29. Liquid methane has a low boiling temperature (110 K) and is particularly suitable as heat sink since the first helium expansion can already start from low temperature.

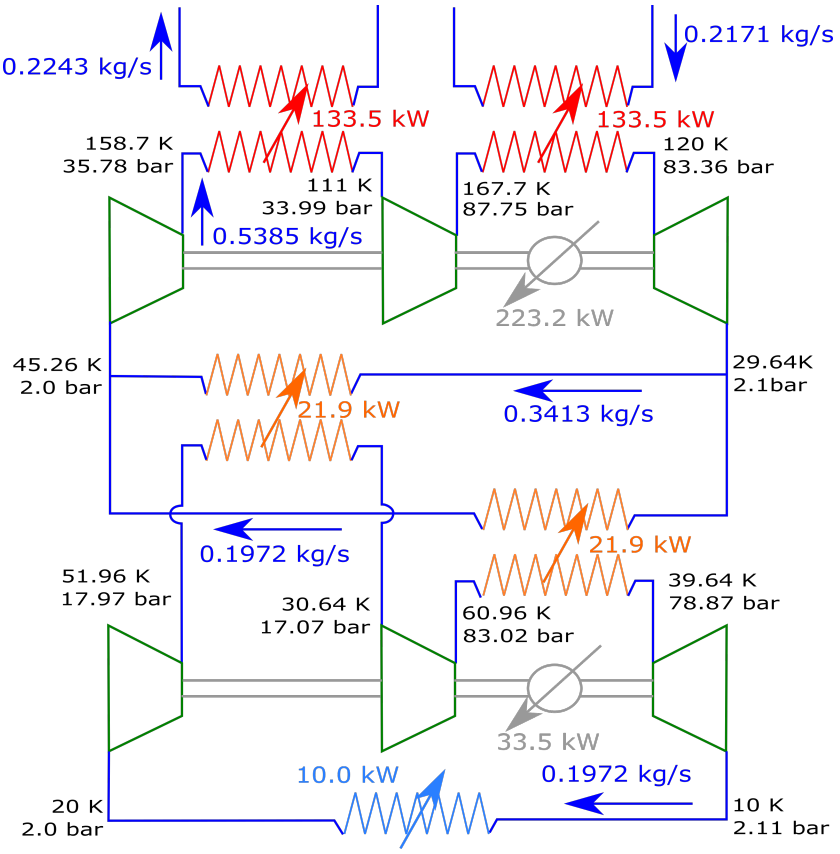

Figure 7.36: Schematic of the double-stage RBC with regenerative cooling and parallel connected heat exchangers

In order to compare the Palmer's RBC with the RBC developed in this chapter, the same power requirement and heat sink were implemented in the model of the cryocooler with regenerative cooling and parallel-connected heat exchangers leading to the results reported in Fig. 7.36. In particular, the heat transferred across the heat exchangers is the same according to the assumption on the design constants k_{Hxa} and k_{Hxb}.

In order to further highlight the power transfer across the double stage cryocooler, the T-P chart in Fig. 7.37 shows the helium transformations that occur in the cryocooler. The blue line in Fig. 7.37 represents the polytropic transformations of the coolant in the RBC's second stage whereas the helium cycle in the first stage is described by the red line. Starting from the cold power removed from the load (10 kW) in the RBC's second cycle, the two compressor stages need 63.9

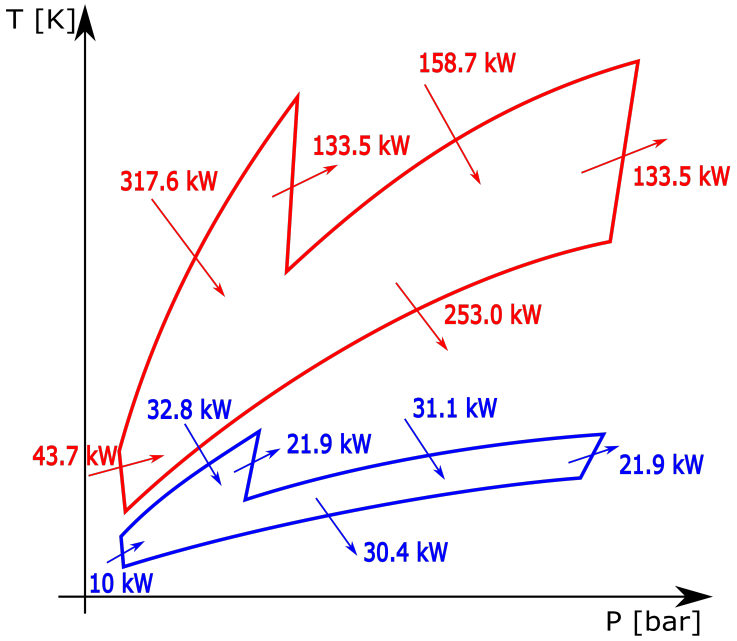

Figure 7.37: Temperature-pressure chart of the double-stage RBC with regenerative cooling and parallel connected heat exchangers

kW to increase the pressure, whereas the turbine recuperates 30.4 kW for a total net power of 33.5 kW. This power is supplied by the electric motor as shown in Fig. 7.36. Along the same cycle, helium transfers 21.9 kW per heat exchanger to the helium flowing in the RBC's first stage, for a total of 43.7 kW reported at the bottom of the red loop in Fig. 7.37. Moving along the first stage polytropic transformations, the compressor need 476.3 kW to rise the helium pressure while the turbine supplies 253.0 kW to the system for a net power of 223.0 kW. The superconducting electrical motor supplies the net power required by the first stage. The electric motor input powers shown in Fig. 7.36 are slightly bigger than the respective net powers because of the losses within the electrical motors themselves. 133.5 kW per heat exchanger are removed from the helium flow in the first RBC's cycle and transferred to the methane.

The input power P_i of the cryocooler is the sum of the power required by the electrical motors to move compressors and turbines of each cooling stage. The efficiency of the system represents of the ability of the cryocooler to remove heat

Table 7.6: Comparison between efficiencies achieved by different cryocooler configurations

	Double-stage RBC [135]	Series-connected heat exchanger	Parallel-connected heat exchanger	Carnot efficiency
Efficiency	2.83%	3.45%	3.90%	10.0%

for a given input power and can be computed as

$$\eta = \frac{Q_c}{P_i} \tag{7.131}$$

The efficiencies of the Palmer's model and of the RBC with parallel-connected heat exchangers are compared in Table 7.6. The same table reports the efficiency of an optimized RBC with series-connected heat exchangers and the ideal Carnot efficiency. The Carnot efficiency is the maximum efficiency that can be achieved by a fluid operating without any loss between the cycle maximum temperature T_H and minimum temperature T_C. It is computed as

$$\eta_C = \frac{T_C}{T_H} \tag{7.132}$$

In the model, losses are represented by the pressure drop Δp across the heat exchangers, by the difference between inlet and outlet temperature on the same side of the heat exchangers (ΔT_{wHx}, ΔT_{iHx}, ΔT_{iHx2}) and by the polytropic efficiencies η_c and η_t. These losses can be only reduced by an appropriate design, but they are never zero. Therefore the efficiency of the cryocooler is always lower than the Carnot efficiency, but the closer η gets to the Carnot efficiency the better is the refrigeration cycle.

7.7 SCLSM Design Results

The electromagnetic design, the AC losses model, the thermal model of insulation and the cryocooler model described in this chapter have been applied to different SCLSM configurations in order to select the final value of the airgap length. The airgap length is the result of an iterative procedure which considers different

counteracting thermal and electromagnetic effects. In this process the geometrical features listed in Table 7.2 remain constant and only the variables linked with the airgap length vary. The final machine layout aims to minimize the total input power required by the EML system.

The shorter the airgap length the greater is the magnetic flux that crosses the airgap and the lower the current intensity to achieve the same thrust level. On the other side, the intensity of secondary magnetic field harmonics in proximity of the superconductors is enhanced by the shorter distance between the mover and the stator. The larger the airgap the weaker is the electromagnetic interaction with the superconducting coils and the lower the AC losses in the superconductors (see Section 7.4). The additional heat load due to the AC losses is exacerbated by the increased heat flow across the thinner thermal insulation. The insulation has to keep the liquid hydrogen at its boiling temperature despite the heat flow coming from the external environment and the heat generated internally. The increased heat dissipation inside the cryostat demands additional cooling power to the cryocooler worsening the overall system performance.

In order to determine the airgap length of the motor, the electromagnetic features of the SCLSM must be estimated and compared. Since the stator coils are made of conventional conductors, their electric resistance is not zero and can be computed as

$$R = 4\frac{k_{skin}}{\sigma_c}\frac{l_s + l_{end}}{\pi d_w^2}N_1 \tag{7.133}$$

where

σ_c/k_{skin} is the equivalent conductivity that takes into account the skin affect. The skin effect coefficient is computed as done in Section 4.2 in Chapter 4;

l_{end} is the end-coil length, that for full-pitch distribute windings can be computed as (see also Fig. 4.12)

$$l_{end} = 1.05\sqrt{2\left(\frac{\tau}{\pi} - \frac{b_s}{2}\right)^2 + 2\left(\frac{\tau}{2} + \frac{b_s}{2}\right)^2 + \left(\frac{h_s}{2}\right)^2}; \tag{7.134}$$

N_1 is the number of turn per phase which is computed from the number of turns

per coil N_s as

$$N_1 = 2N_s(2p+1)q; \tag{7.135}$$

d_s is the diameter of each conductor which is computed as

$$d_w = \sqrt{\frac{2b_s h_s k_{fill}}{\pi N_s}}. \tag{7.136}$$

Since the armature MMF is notably smaller than that of the superconducting coils and the airgap of the motor is rather large, the leakage stator inductance per turn per phase L_{ph} may be calculated as for long electric power lines as [18]

$$L_{ph} = \frac{\mu_0}{\pi} 2p \left\{ l_s \ln \left[\frac{\tau}{d_w} + \sqrt{\left(\frac{\tau}{d_w}\right)^2 - 1} \right] + \frac{\tau}{2} \ln \left[\frac{l_s}{d_w} + \sqrt{\left(\frac{l_s}{d_w}\right)^2 - 1} \right] \right\} \tag{7.137}$$

The resultant inductance per phase considers the effect of all the conductors per coil and the influence of the other phases as

$$L_s = N_s L_{ph} \left(1 + \frac{1}{3} + \frac{1}{6}\right) \tag{7.138}$$

Once the stator phase resistance and inductance are determined, the active power P_a and the reactive power P_r can be computed as

$$P_a = F_{xc} v_s + 3RI^2 + AC_{loss} \tag{7.139}$$

$$P_r = 3\frac{\pi}{\tau} v_s L_s I^2 \tag{7.140}$$

where v_s is the synchronous speed at the end of the launch and F_{xc} is the corrected thrust (sum of the required thrust F_x and the force needed to accelerate the mover F_{mov}).

The efficiency of the whole EML system has to take into account not only the motor active power required by the launcher, but also the additional input power P_{RBC} required by the cryocooler as

$$\eta = \frac{F_{xc} v_s}{P_a + P_{RBC}} \tag{7.141}$$

Table 7.7: Efficiencies of double-stage cryocooler with different coolant as heat sink

	Efficiency	Carnot
Water	1.35%	3.66%
Liquid Nitrogen	5.52%	12.99%

The input power of the refrigeration system can be determined from the model illustrated in Section 7.6 using the cooling power needed by the liquid hydrogen as main requirements. However, is very likely that liquid methane will be replaced by water or liquid nitrogen as heat sink at the first helium loop in Fig. 7.36. Water is a common coolant with an excellent latent heat and specific heat capacity, but it is normally liquid above 273 K, temperature which is considered high for cryogenic application. Nitrogen is liquid a 77 K and is a coolant widely use for its high availability and affordability even though it does not have excellent thermal properties. Nitrogen could be bought and stored in a tank beside the launcher. The efficiencies of the cooling cycle with different heat sinks were estimated using the model in Section 7.6 and are reported in Table 7.7.

The total power required by the refrigeration system to remove the required amount of heat can be computed from the respective efficiency as

$$P_{RBC} = \frac{Q_c}{\eta_{RBC}} \tag{7.142}$$

where η_{RBC} can be one of the efficiencies reported in Table 7.7 and Q_c is the cooling power of the refrigeration system. The cryocooler is used after the mover is returned to its initial position. The cooling power of the refrigeration system Q_c must be enough to remove the heat absorbed by the coolant and restore the liquid hydrogen initial conditions in $t_c = 90$ s which is the minimum time between two consecutive launches. The cooling power can be computed as

$$Q_c = \frac{1}{t_c}\int_0^{t_{TOF}} AC_{loss}dt = \frac{AC_{loss\,(t=t_{TOF})}t_{TOF}}{2t_c} \tag{7.143}$$

where the second equality is valid considering the linear variation of the AC losses with time.

The required SCLSM input power can be computed from the active and reactive

Table 7.8: SCLSM performance with different airgap lengths

	g = 150 mm	g = 100 mm
Peak airgap magnetic flux density	1.009 T	1.334 T
Armature magnetic flux density	0.642 T	0.849 T
Mover Mass	7755 kg	7657 kg
Corrected thrust	548.55 kN	547.96 kN
Rated current per turn (RMS)	1482.3 A	1120.2 A
Peak Voltage	11425 V	15334 V
Current density	47.43 A/mm^2	35.85 A/mm^2
Resistance	0.166 Ω	0.166 Ω
Inductance	0.34 mH	0.34 mH
Peak AC loss	2.685 MW	3.953 MW
Active Power	50.79 MW	51.53 MW
Reactive power	1.201 MW	0.686 MW
Input power	50.80 MW	51.53 MW
Peak efficiency SCLSM	0.9259	0.9117
Power factor SCLSM	0.9997	0.9999
Cooling Power [kW]	217.27	319.33
Peak efficiency with LN_2-LH_2cryocooler	0.8593	0.8195
LN_2-LH_2 crycooler input power	3.936 MW	5.785 MW
Peak efficiency with H_2O-LH_2 cryocooler	0.7031	0.6245
H_2O-LH_2 crycooler input power	16.09 MW	23.69 MW
LH_2 boiling time	7 h 10 min	12.4 s
Additional LH_2	2.717 m ^{3}	4.049 m ^{3}

powers as

$$P_i = \sqrt{(P_a + P_{RBC})^2 + P_r^2} \tag{7.144}$$

whereas the voltage and the power factor are respectively

$$U = \frac{P_i}{3I} \tag{7.145}$$

$$\cos\phi = \frac{P_a}{\sqrt{P_a^2 + P_r^2}} \tag{7.146}$$

The active power in eq. 7.146 does not include the cryocooler input power P_{RBC} since the power factor is a property strictly related to the electrical machine.

The performance of the machine were estimated for two different values of the airgap length and the results of the analysis were reported in Table 7.8. In particular, the machine with 100 mm airgap has a lower rated current for the increased magnetic flux density in proximity of the armature coils. However, the active

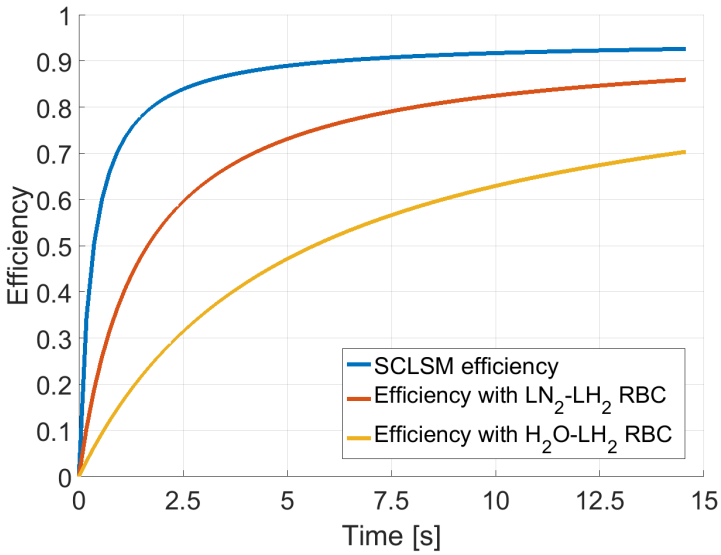

Figure 7.38: Comparison between SCLSM efficiency and the efficiencies of an EML system including RBC's input power

power and input power are almost equal to those of the machine with 150 mm airgap for the increased loss in the superconductors. Consequently, the applied voltage has to increase to allow the rated current to flow and produce the thrust. When the SCLSM has 100 mm airgap, the liquid hydrogen stored in the cryostat is not enough to cope with the exacerbated heat dissipation and full evaporation is reached only after 12.4 s as shown in Table 7.8. As indicated in eq. 7.20 the cryostat hosts a liquid hydrogen reservoir so that only 20% of the liquid hydrogen evaporates during launch. The volume of the spare liquid hydrogen reported in Table 7.8 is calculated as

$$v_{LH_2} = \frac{5}{L_{H_2}\rho_{H_2}} \int E_{H_2} dt \tag{7.147}$$

where E_{H_2} is the energy absorbed by the liquid hydrogen during the boiling time.

The efficiencies of the SCLSM and of the EML system including refrigeration are compared in Fig. 7.38 and the respective peak values are reported in Table 7.8. The efficiency of the EML system was computed considering both water and liquid nitrogen at the cryocooler heat sink. Since the liquid nitrogen is much colder than water, the cryocooler spends less energy to cool the hydrogen at the desire temperature and the efficiency of the EML system is much higher. In any

case when the refrigeration input power is considered the efficiency is drastically reduced with respect to the efficiency of the SCLSM alone.

From the comparison of the characteristics of the SCLSM in Table 7.8, the machine that presents better perfomance is the one with 150 mm airgap in particular for the lower AC losses. The analyses of the different aspects of the civil aircraft launcher presented in this chapter were developed assuming this value of the airgap length.

When water is employed at the cryocooler heat sink the required input power and the dimensions of the cryogenic system would require significant engineering challenges that can be significantly reduced adopting liquid nitrogen. Even in this case, the required input power would be hardly achieved by a single refrigeration system and multiple RBCs should be implemented.

7.8 Contribution to Knowledge

The implementation of a SCLSM for civil aircraft launch applications in a modern airport has been proposed and modelled in this chapter for the very first time. A new topology of SCLSM with MgB_2 superconducting cables hosted inside a moving cryostat has been thoroughly described and developed.

The presented modelling method is not only focused on the electromagnetic analysis of the machine as done in literature, but it is particularly concerned with the design of the thermal management system to prevent quenching of the superconducting material. In particular, the AC losses in superconductors that the thermal management system has to dissipated have been estimated with a simple analytical model. The temperature evolution of the superconductors during the launch has been investigated through static and transient thermal analysis of the cryostat insulation.

In order to quantify the input power of the EML system, the power required by the refrigeration system has to be estimated as well. This chapter proposed an RBC model that can be used to calculate the power required by a cryocooler for aerospace applications. The RBC model in this thesis improves and extends an existing model developed by a researcher in Rolls Royce.

Chapter 8

Conclusion

The growth in civilian air traffic in the last decades has led to several airports facing runway time availability issues that have been addressed by extending the runway length or by the construction of an additional runway. The growth of size at an airport often compels authorities to mandatory house purchase in the neighbouring area. People living beside busy airport also have to deal with noise and pollution caused by ground movements of aircraft, especially at take-off.

This thesis has quantified some of the possible benefits of the implementation of an electromagnetic launch system in a modern airport. The analysis of the take-off performance in Chapter 3 has shown that only 50% to 60% of the actual runway length is required with an electromagnetically assisted take-off system. Additionally, the reduced usage of the engines at take-off could allow a fuel saving of 48.5 kg, i.e. approximately 19.6% of the fuel normally burnt at take-off. The idle engine rating protracted to the initial part of the acceleration allows a noise emission reduction of 66% for an Airbus A320 sized aircraft. Considering the possibility of reducing the installed engine thrust, approximately 457 kg of fuel per flight can be saved leading to an exhaust emission reduction of 20.8% at ground level.

This thesis has proposed three practical linear electrical motor topologies to propel an A320-200 aircraft at take-off. The analytical and numerical design methods used to size a linear induction motor, a linear permanent magnet synchronous motor and a linear superconducting synchronous motor have been presented in Chapters 4, 5 and 7 respectively. The procedures used to design the induction mo-

tor were also experimentally validated through a working prototype of a reduced scale electromagnetic catapult presented in Chapter 6.

This final chapter compares the motor topologies developed in this research to achieve the challenging requirements of the launch of civil aircraft and presents ideas for future research work on this topic.

8.1 Launcher Topology Comparison

Since the electrical machines presented in this thesis are designed to achieve the same net output power (thrust multiplied by the mass of the A320-200 aircraft), the motor efficiency and power factor are the most important mean of comparison for the studied launcher topologies. The efficiency of an electrical motor represents the capability of the machine to produce mechanical energy for a given input energy. Since the lost energy is dissipated as heat, the efficiency is also closely connected to the thermal management of the electrical motor. High values of power factor have a significant bearing on the viability of electromagnetic launch system, as this directly affects the size and cost of the power conditioning and energy storage systems.

The electromagnetic performance and other key characteristics of the LIM, LPMSM and SCLSM are shown in Table 8.1. Looking at the efficiency and power factor of the linear electrical machines in Table 8.1, the SCLSM seems to be the ideal choice for EML applications since it requires less input power to operate. However, the input power of the cooling system has a great impact on the overall performance of the superconducting launcher. If the input power of the cryocooler is also considered then another 16 MW is required to cool down the hydrogen from room temperature to 20 K. This input power may be reduced by considering larger number of slot per pole per phase, but the final cryocooler power demand is expected to be similar.

Since the output power of the system is the product of the thrust and the catapult end-speed (which is always the same), the mass of the mover has to be as low as possible in order to transfer the major quantity of kinetic energy to the aircraft. Therefore, the difference between the output powers reported in Table 8.1 is related to the mass of the mover of the respective motor topologies. The SCLSM's

Table 8.1: Comparison between the electromagnetic performance of LIM, LPMSM and SCLSM with and without cryocooler

	LIM	LPMSM	SCLSM	SCLSM with cooler
Peak efficiency	0.8938	0.9875	0.9259	0.7031
Power Factor	0.8987	0.8277	0.9997	1.0000
Input Power [MW]	54.197	57.862	50.802	66.879
Output Power [MW]	43.534	47.295	47.023	47.023
Peak Thrust [kN]	508.01	551.67	548.55	548.55
Mover Mass [kg]	869	8286	7755	7755
Current RMS [A]	1086	1128	1482	1482
Peak Voltage [V]	16635	17093	11425	11425

mover is rather heavy for the high density materials that are hosted inside the cryostat shown in Fig. 8.1. The SCLSM's mover mass reported in Table 8.1 does not consider the weight of the pumps needed to force the hydrogen flow through the narrow duct of the cryostat. Moreover, the pressure increase due to hydrogen evaporation has not been considered in this work and the cryostat walls thickness and weight may need to increase to resist the internal pressure, even if implementing a pressure regulation valve. In conclusion, the complexity and weight of the mover structure and the difficulties introduced by the thermal management system discouraged the adoption of SCLSM to assist civil aircraft take-off until the technology matures.

The next best motor topology that achieves the highest product of efficiency and power factor is LPMSM as can be seen in Table 8.1. Nevertheless the input power required by the synchronous motor exceeds the input power needed by all the other motor topologies because of the mass of the mover. Compared to the SCLSM, the method used to estimate the mass of the mover is quite accurate and the value reported in Table 8.1 is considered to be very close to the value which would be found in the real application. The LPMSM also hosts materials with high densities which further increase the total mass. As a consequence of the high mass of the LPMSM's mover, the peak thrust needed to accelerate the A320-200 aircraft at the take-off speed exceeds that of all the other motor topologies shown in Table 8.1. Therefore the required output power and the respective input power are very large with respect to those for the other motors, despite the high efficiency and good power factor.

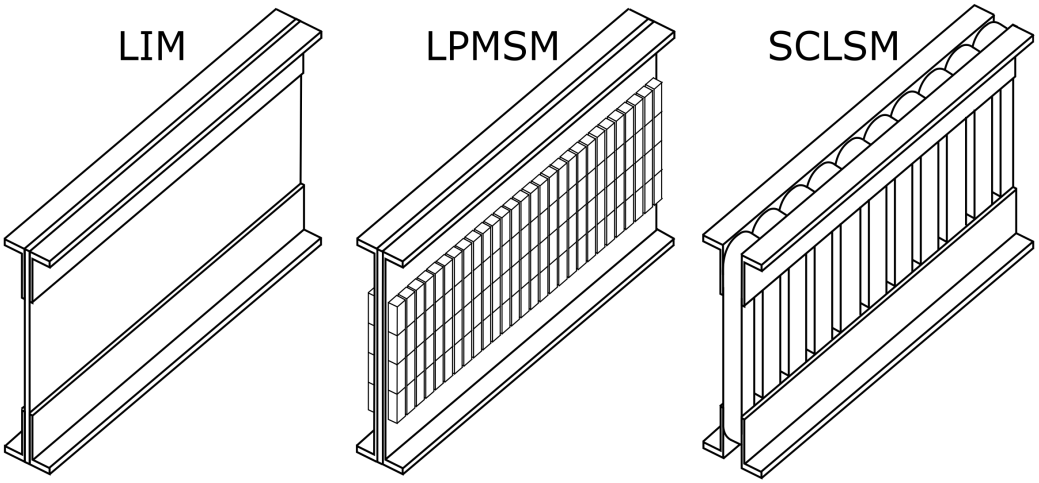

Figure 8.1: Schematic of the structure of LIM's, LPMSM's and SCLSM's movers

The LPMSM also requires close-loop control to keep the synchronism between the motion and the electromagnetic wave in the airgap. The position feedback from an encoder or resolver must be accurate and should also communicate the relative position between magnets and slots. If the encoder loses accuracy the control must be reinitialized. In addition to the difficulty of controlling the motor, the implementation of a LPMSM for EML applications is also affected by the cost of the NdFeB permanent magnets and by the complicated procedures needed to install them.

In comparison the mover of the LIM is very light, easy to install and presents a simple structure, as can be seen in Fig. 8.1. The design optimization method presented in Chapter 4 obtains peak efficiency and power factor which are comparable with those of the other motor topologies. Additionally, the induction motor can operate with open-loop control without the need of a position encoder and complex control techniques. Nevertheless a position feedback might be needed to determine the exact instant in which activate the several stages of the launcher. However, when the applied load is the same, LIMs perform in the exact same way across several launches, thus the encoder could be used only during the initial calibration rather than during the whole operational life.

The peak operating voltages of LIM and LPMSM shown in Table 8.1 cannot be easily handled by the current state of the art power converter switching devices and

power conditioning technology. In order to cope with the high operating voltage, three possible methods can be considered:

1. Since both LIM's and LPMSM's peak voltage were calculated considering a series connection between the sides of the stator, the operating voltage can be halved with this parallel connection;

2. The concentrated winding identical segments along a single side of the LPMSM's stator can be connected in parallel to further reduce the applied voltage;

3. If the peak voltage cannot exceed a predetermined threshold the machine may pass from "constant thrust" mode, where voltage and frequency increase with the speed, to "constant power" mode, where only the frequency increases with the speed.

Considering the first two option the peak operating voltage would reduce to 8.32 kV for LIM and 4.27 kV for LPMSM. The state of the art switching technology available today can handle up to 6.6 kV [110]. Series connected SiC super GTOs in the range of 10-20 kV and SiC p-IGBTs with 12 kV blocking voltage and switching time of a few μs are under development [111] and may be suitable for future EML applications.

In conclusion, when the technology will allow operating voltages in the range of 10-20 kV in the near future, LIM will represent the best solution for a civil aircraft launcher. With a maximum rated voltage of 6.6 kV available today, the LPMSM with all the identical winding segments connect in parallel could be used to assist civil aircraft take-off.

It is worth to mention that this conclusion is valid for the optimize induction and synchronous motor layouts, but the advantage of the induction motor could be still exploited designing the machine to achieve a peak voltage of 6.6 kV. Certainly, this motor configuration will required a much larger current, will have much lower performance and would need a much larger energy storage and power conditioning system, but it will be handled by the technology available today.

8.2 EML Systems Limitations

The research activities described in this thesis clearly define the methodology to follow to successfully design an electromagnetic catapult for civil aircraft. The author believes that this technology may bring significant improvements to modern civil aviation industry. In particular, the possibility of reducing the runway length required at take-off may represent a valuable alternative to the investments needed for the extension of existing airports.

Additionally, a reduced aircraft fuel consumption, exhaust emission and noise emission at ground level positively impact the local community living around airports reducing the environmental pollution. These aspects are also part of the objectives that civil aircraft designers aim to when proposing a new aircraft on the market.

Nevertheless, the installation of an electrical machine of such a size requires the interruption of the airport services for the time required by the construction of the EML system. The associated economic loss could be significant without considering the efforts required to re-route hundreds of flights to the nearest airports. For these reasons the author believes that EML systems would be easier to build at new airports or at airports where the space available is enough to avoid any runway obstruction during the catapult construction.

The research described in this work has also proved that EML system can operate in modern airports without compromising aircraft performance at take-off and passengers safety. However, new laws should be introduced to regulate aircraft operations with an assisted take-off system, since different procedures should be followed in the unfortunate case of engine failure or catapult damage. This work has conservatively adopted the regulation used for conventional take-off to estimate the performance of an aircraft connected to an EML system. The author believes that considering specific regulations that account for reliability, controllability and capability of electrical machines, take-off performance might be improved and in particular the runway length required at take-off might be even shorter than that presented in this thesis.

The electromagnetic catapult may allow future airports with shorter runways to occupy smaller areas. However, successful take-off would be completely depen-

dant on the EML system available at the airport. To prevent any ground movement interruption in the case of failure, all the catapult components should be redundant. Nevertheless, the electrical motor is a multi-stage machine which should attain the desired end-speed even when a section fails.

Since the landing distance is usually comparable or slightly shorter than the take-off distance, airports with a reduced runways length could be feasible in the future only when an external system is used to brake aircraft during landing. The author believes that this braking system may represent an interesting topic for future research to extend the work described in this thesis as it will be detailed in Section 8.3.

Although this thesis proposes a study of an EML system to accelerate the class of aircraft which has a major impact on the actual and future aviation market, the electromagnetic catapult should be able to launch heavier aircraft as well. Only in this case, smaller airports could host domestic and international hubs for all airlines and destinations.

The high voltage required by the electromagnetic catapult is the main factor that limits the weight of the aircraft that can be launched. The A320-200 aircraft with a maximum take-off weight of 73.5 tons represents a limit case for the voltage capability of actual technology. A catapult designed to launch an A380-800 aircraft with a maximum take-off weight of 560 tons would need a peak voltage 8-10 times greater than those shown in Table 8.1.

Significant technology breakthroughs are needed to make a launcher with such demanding requirements possible. On the other side, the catapult designed in this work is responsible of the initial acceleration without the need of using the aircraft engines. In the case part of the total thrust is provided by the engines, the electromagnetic catapult would allow larger aircraft to take-off in a shorter distance, but the benefit concerning noise, fuel consumption and exhaust emission reduction will be significantly reduced.

The engine size reduction allowed by the implementation of an EML system as described in Chapter 3 is a significant advantage in terms of fuel consumption and operational cost. However, the aircraft with a reduced installed thrust can take-off only from airports with an EML system. Consequently, departure and destination airports should have an assisted take-off system to allow the aircraft

with a reduced installed thrust to operate. The authors believes that this does not represent a big limitations as many aircraft today are used to fly along the same route, but an engine thrust reduction will be possible only when at least two EML systems are built at different destinations.

8.3 Future Research

This sections outlines where the design of the electrical machines presented in this thesis can be further improved. This research project can be also considered as the starting point for future researches on EML systems for civil aircraft applications. The research topics suggested in this section should also lead to the complete definition of an EML system to implement in modern airports.

8.3.1 Linear Synchronous Motor with Halbach PM Array

Section 8.1 has shown that linear permanent magnets synchronous motors are not an ideal choice for EML application because of the heavy mover. A Halbach permanent magnet array like the one shown in Fig. 5.1c could be implemented to increase the power density of this machine while reducing the quantity of magnetic material required to keep the magnetic field density in the airgap at the desired value. This new LPMSM topology could lead to the implementation of a small and light mover while achieving high efficiency and power factor.

The implementation of the Halbach array could be combined with an optimization procedure to select the concentrated winding sequence to reduce the leakage inductance associated with the stator harmonics. This thesis proposed a method for the selection of the winding sequence which was based on the observation on the MMF harmonic content and on the minimization of the magnetic material as shown in Section 5.2. However, an optimization procedure which is able to associate any winding sequence to the respective leakage inductance might be useful to reduce the reactive power of the machine. The reduction of the reactive power and the associated increase of the power factor would also allow the implementation of movers with a lower mass.

8.3.2 SCLSM Configuration with Lower Cooling Power

The main disadvantage of the superconducting motor designed in Chapter 7 is represented by the input power required by the cooling system. In order to remove the heat absorbed by the liquid hydrogen during the launch, the cooling system needs approximately 16 MW of power (see Table 7.8). The efficiency of the cryocooler and the cooling power required to extract heat at 20 K and release it at environmental temperature make the power requirement so demanding.

In order to model the current induced in the superconductors and accurately estimate the AC losses, the shielding effect caused by the aluminium structure of the cryostat should be considered. The only way to estimate the field intensity due to stator secondary harmonics in proximity of the superconducting magnets considering the shielding effects consists in the electromagnetic analysis of the SCLSM with finite element software. The simulation could be run without any superconducting magnets and while feeding the stator windings with the rated current. This method should allow a better estimation of AC losses in the superconductors and a precise calculation of the reduced cooling power.

The SCLSM might then become a valuable alternative to conventional synchronous and asynchronous machines for EML application presented in this thesis due to the reduced cooling power.

Approximately 98.5% of the heat absorbed by the liquid hydrogen during the launch is due to the coupling losses between MgB_2 wires. In order to partially eliminate the coupling losses and drastically reduce the power requirement of the cryocooler, another linear motor topology is proposed.

Future research might investigate the performance of a SCLSM where the MgB_2 coils are replaced by an array of superconducting magnets made out YBCO high temperature superconductor. The stator of this new motor topology will host winding at environmental temperature as for the double-sided SCLSM designed in Chapter 7. The cryostat could be built with a similar layered structure using liquid hydrogen as coolant. The theories presented in Chapter 7 can still be used to sized the machine, but they should be adapted to the new configuration. For instance, the technique employed to estimate the magnetic field across the machine should be updated to consider the new excitation field source, and different meth-

ods should be found to estimate AC losses inside YBCO magnets under oscillating magnetic field.

The SCLSM with YBCO superconducting magnets will have increased eddy current and hysteresis losses, but very low coupling losses. Since YBCO magnets are very brittle, the structural analysis of the cryostat of the new motor configuration is paramount. The structural analysis of the complex framework would also allow the sizing of all the cryostat components, especially the supports of the superconducting magnets under load. In particular the structural analysis should take into account the internal pressure increase due to hydrogen evaporation. The pressure increase will probably require an aluminium thickness redistribution to cope with the additional stress.

At the same time, the variation of the inner pressure changes the physical properties of the liquid and gaseous hydrogen improving the heat exchange. Indeed, high pressure increases the boiling temperature of the liquid hydrogen allowing the absorption of a larger quantity of heat from the superconductors before full evaporation. In order to fully characterize the behaviour of the coolant, the isochoric properties of hydrogen between 15 and 50 K at several pressures are needed. The online database of the thermo-physical properties of liquid hydrogen available at [136] could be useful to compile the lookup tables required for this purpose.

8.3.3 Definition of the Electromagnetic Catapult Subsystems

This thesis is concerned with the design of a launcher to assist civil aircraft take-off. An electromagnetic launch system is not only composed by an electrical motor, but it also includes a power conditioning system and an energy storage device.

Energy storage system An energy storage might be needed to supply the EML system with the required electrical power during the aircraft acceleration. Electricity can be stored electromagnetically, electrochemically, kinetically or as potential energy [137]. Energy storage systems can encompass a broad range of categories, but viable storage technologies for electromagnetic launch systems include batteries, superconducting magnetic energy storage systems (SMESs),

ultracapacitors and flywheels.

Batteries store energy electrochemically with high energy density and high energy capability. Even though they can hold the charge for years, they have short operational life especially with deep discharge cycles. Batteries can be low cost option for large storage systems, but they are not cost effective for high power applications [137].

SMES consists of a coil with many windings of superconducting wires cooled down to cryogenic temperature. The energy is stored in the magnetic field generated by the DC current flowing through the coils. The SMES is charged or discharged applying a positive or negative voltage across the superconducting coil. SMESs are attractive for their fast response and efficiency, but they require a refrigeration system with high input energy [137]. Thus SMES could be particularly indicated for SCLSMs for EML applications since cryocooler and cryogenic system would be already available.

Capacitors store electric energy accumulating positive and negative energy charges on parallel plates separated by a layer of dielectric material. The ratio between the charge and the voltage applied on the plates is call capacitance. The voltage is often limited by the dielectric breakdown, thus the amount of energy that a capacitor is able to store is proportional to its capacitance. For high voltage applications like EML systems, capacitors with high working voltage called supercapacitors or ultracapacitors are required. These capacitors connected in series might be a viable energy storage for induction and synchronous launchers.

Flywheels store kinetic energy into a large rotating inertia. In order to reduce friction and aerodynamic drag at high speed, high performance flywheels often operate in vacuum vessels using magnetic bearings. Flywheels could be a possible alternative to ultracapacitors to store the energy required by LIMs and LPMSMs. In particular, in place of few large flywheels it is possible to implement several flywheels along the track and separately feed the several stages of the launcher.

Power conditioning system The power conditioning system has the function to transfer the energy from the source to the motor with the right voltage and fre-

quency. It also permits EML systems to operate at their most efficient point at all speeds by allowing for a variable voltage, variable frequency supply. Since the track is sectioned, the power conditioning system is also responsible of energizing only the coils that can effect the launch.

When batteries, ultracapacitors and SMES discharge, the energy is released in the form of continuous current. The voltage and frequency required by the electrical motor can be provided by an inverter. When flywheels discharge, energy is often supplied as alternating current. In this case, rectifier could be used before the inverter to transform AC current into DC current. A cycloconverter, a voltage source converter or a matrix converter can transform a constant voltage and frequency waveform into another AC waveform without the need of a DC link. Even though the latter two opnions could be an ideal choice for civil EML applications, in literature a flywheel in combination with a cycloconverter was proposed to feed an EML system for military aircraft [8].

As discussed in several parts of this thesis, the switches that allow to feed the right section of the track and are used to regulate input voltage and frequency are the pivoting technology for EML systems. In order to reduce the required switches rating and to provide high level of control and redundancy, each separate phase winding in each section could be driven independently [30]. An adequate control method has to be developed in combination with the information provided by a position feedback sensor, to correctly feed the several sections of the linear motor.

The design of the test rig presented in Chapter 6 includes the description of the structural components of the stator housing. A similar procedure can be followed to size the framework of the launcher for EML applications. The structural analysis can be carried out on structural components similar to those studied in Chapter 6, considering the normal force shown in Fig. 8.2. LIM and LPMSM have similar peak normal forces which are approximately 3.8 MN. Considering a safety factor of 1.5, the frame of the stator housing should be designed to withstand a normal load of 5.7 MN.

The EML launcher needs some kind of braking system to decelerate the mover once the aircraft detaches. The mover also needs to be repositioned at the begin-

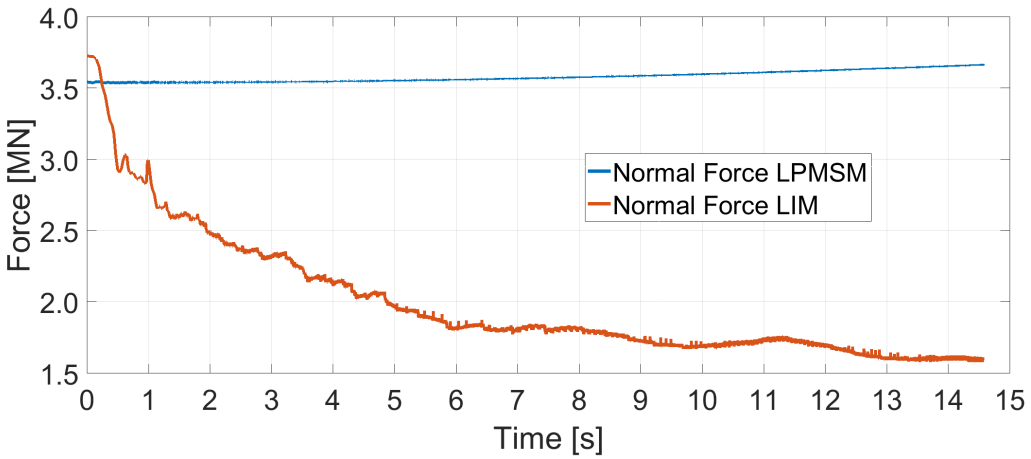

Figure 8.2: Variation of the normal force acting on the stator side of LIM and LPMSM during the launch

ning of the launch track before the next take-off. Future research could investigate several options that can be adopted for the braking and recovery systems.

The brake proposed in Chapter 6 for the catapult prototype is a fail-safe passive system that can be easily scaled up and implemented in a larger launcher. This system is preferable to a mechanical brake which suffers wear and need periodical maintenance and inspections.

Instead of using a passive system, the kinetic energy of the mover at the end of the launch could be partially recover by a special magnetic brake that would act as a generator. The energy recovery braking system is particularly convenient with LPMSM and SCLSM, for the large mass of the mover with respect to the aircraft. The energy recovery could be performed by a dedicated launcher section towards the end of the track.

Linear electrical motor can be used in reverse mode to reposition the mover at the beginning of the track. Future research could define the voltage and current ratings to efficiently perform this procedure.

8.3.4 Energy Recovery During Landing

The catapults on the deck of aircraft carriers and the launchers described in this thesis were designed to deliver intense thrust to propel the aircraft at take-off.

Nevertheless, if aircraft are required to operate in a confined space with a reduced runway length, strong decelerations are needed during landing. Civil aircraft can decelerate at 0.55 G or more with the aid of mechanical brake installed on the wheels of the aircraft undercarriage. The braking performance depends on the condition of the runway pavement and may decay in time because of the wear of brake pads. With a shorter runway length an auxiliary system may be needed to provide an additional braking force that does not depend on runway and environmental conditions.

Military aircraft commonly reduce their speed at landing with the aid of an elastic rope connected to turbines plunged into sea water. When an aircraft lands and catches the rope, the turbines are push into motion against the force exerted by the fluid. The aircraft kinetic energy is transferred to the turbines and dissipated into the water. Instead of wasting the aircraft energy at landing, it could be possible to partially recover it using generators in place of submerged turbines.

In order to slow down civil aircraft at landing, similar systems could be used to aid mechanical brakes to stop the vehicle within the runway length available. Since the kinetic energy of the aircraft at landing is rather large, future research might investigate and develop rotary generators push into motion by the aircraft through an elastic rope. The electricity produced by the generators could be used to charge the energy storage system that feeds the electromagnetic catapult at take-off.

Another research topic that might be of great interest is the aircraft kinetic energy recovery at landing through the same linear electrical machine used as catapult at take-off. Future research might investigate the best linear motor topology that can be used as a linear generator and that can provide the required breaking force to slow down the aircraft within the reduced runway length. The work presented in this thesis combined with a future research on energy generation at landing could define a self-sustaining system with little external energy inputs.

Bibliography

[1] ASTM, "Standard practice for design of amusement rides and devices," April 2006, designation: F 2291 - 06a.

[2] "Airports commission: Final report," Airports Commission, Tech. Rep., July 2015.

[3] "Current market outlook 2015-2034," Boing Commercial Airplanes, Tech. Rep., 2015.

[4] R. R. Bushway, "Electromagnetic aircraft launch system development consideration," *IEEE Transactions on Magnetics*, vol. 37, no. 1, pp. 52–54, January 2001.

[5] J. X. Jin, L. H. Zheng, Y. G. Guo, J. G. Zhu, C. Grantham, C. C. Sorrell, and W. Xu, "High-temperature supercondicting linear synchronous motors integrated with HTS magnetic levitation components," *IEEE Transactions on Applied Superconductivity*, vol. 22, no. 5, October 2012.

[6] M. Crawford, R. Subramanian, T. Watt, D. Surls, D. Motes, J. Mallick, D. Barnette, S. Satapathy, and J. Campos, "The design and testing of a large-caliber railgun," *IEEE Transactions on Magnetics*, vol. 45, no. 1, pp. 256–260, January 2009.

[7] G.A., "Railgun systems," 2016. [Online]. Available: http://www.ga.com/railgun-systems

[8] M. R. Doyle, T. Conway, R. R. Klimowski, and D. J. Samuel, "Electromagnetic aircraft launch system," *IEEE Transactions on Magnetics*, vol. 31, no. 1, pp. 528–533, January 1995.

[9] "An electric runway," *The Engineer*, pp. 379–380, Oct. 1946.

[10] A. M. Still, "Electromagnetic launchers for use in aircraft launch at sea," Master's thesis, The University of Texas, Austin, May 1998.

[11] H. P. S. Sodhi, "Electro magnetic aircraft launch system," *CAPS In Focus*, May 2015.

[12] B. Schweber, "Electronics poised to replace steam-powered aircraft launch system," *EDN Network*, April 2002.

[13] H. Robertson, M. Bolton, and M. Thomson, "An advanced linear motor system for electromagnetic launch: development and opportunities," in *The IEE Pulsed Power Symposium*, vol. 29. IET, 2005, pp. 1–6.

[14] G. Bellamy and E. Lewis, "The development of advanced linear induction motor systems," in *Power Electronics, Machines and Drives*, vol. 2. IET, 2004, pp. 876–878.

[15] A. Musolino, R. Rizzo, and E. Tripodi, "The double-sided tubular linear induction motor and its possible use in the electromagnetic aircraft launch system," *IEEE Transactions on Plasma Science*, vol. 41, no. 5, pp. 1193–1200, January 2013.

[16] G. Becherini, S. D. Fraia, and B. Tellini, "Design of multistage linear induction motor used as electromagnetic catapult," in *International Symposium on Power Electronics, Electric Drives, Automation and Motion*. IEEE, June 2010, pp. 1063–1068.

[17] G. Becherini, S. D. Fraia, and B. Tellini, "Analysis of the dynamic behaviour of a linear induction type catapult," *IEEE Transactions on Plasma Science*, vol. 39, no. 1, pp. 59–64, January 2011.

[18] I. Boldea, *Linear Electric Machines, Drives, and MAGLEVs Handbook*. CRC Press, Taylor & Francis Group, 2013.

[19] W. Xu, J. G. Zhu, Y. Zhang, Z. Li, Y. Li, Y. Wang, Y. Guo, and Y. Li, "Equivalent circuits for single-sided linear induction motor," *IEEE Transactions on Industry Applications*, vol. 46, no. 6, pp. 2410–2423, November 2010.

[20] H. Bolton, "Transverse edge effect in sheet-rotor induction motor," *Proc. IEE*, vol. 116, pp. 725–739, 1969.

[21] J. F. Gieras, G. E. Dawson, and A. R. Eastham, "A new longitudal end effect factor for linear induction motors," *IEEE Transactions on Energy Conversion*, vol. EC-2, no. 1, pp. 152 – 159, March 1987.

[22] J. Lu and W. Ma, "Research on two types of linear machines for covert airstrip electromagnetic catapult," *IEEE Transactions on Plasma Science*, vol. 39, no. 1, pp. 105–109, January 2011.

[23] G. Kang and K. Nam, "Field-oriented control scheme for linear induction motor with the end effect," in *IEE Proceedings of Electric Power Applications*, vol. 152, no. 6, November 2005, pp. 1565–1572.

[24] D. Hall, J. Kapinski, M. Krefta, and O. Christianson, "Transient electromechanical modeling for short secondary linear induction machines," *IEEE Transactions on Energy Conversion*, vol. 23, no. 3, pp. 789–795, September 2008.

[25] D. C. Meeker and M. J. Newman, "Indirect vector control of redundant linear induction motor for aircraft launch," *Proceedings of the IEEE*, vol. 97, no. 11, pp. 1768–1776, November 2009.

[26] E. R. Laithwaite and S. B. Kuznestov, "The asynchronous condeser: A brushless, adjustable power factor induction machine," *IEEE Transactions on Power Apparatus and Systems*, vol. 99, no. 6, pp. 2422–2432, December 1980.

[27] E. R. Laithwaite and S. B. Kuznestov, "Power factor improvement in linear induction motor," *IEE Proceedings in Electric Power Applications*, vol. 128, no. 4, pp. 190–194, July 1981.

[28] S. Kuznetsov and D. Marriott, "High velocity linear induction launcher with exit-edge compensation for testing of aerospace components," in *Proceedings of 14th Symposium of Electromagnetic Launch Technology*, 2008, pp. 1–8.

[29] J. F. Gieras, Z. J. Piech, and B. Z. Tomczuk, *Linear Synchronous Motor: Transportation and Automation System*, 2nd ed. CRC Press, Taylor & Francis Group, 2011.

[30] D. Patterson, A. Monti, C. W. Brice, R. A. Dougal, R. O. Pettus, S. Dhulipala, D. C. Kovuri, and T. Bertoncelli, "Design and simulation of a permanent-magnet electromagnetic aircraft launcher," *IEEE Transactions on Industry Applications*, vol. 41, no. 2, pp. 566–575, March 2005.

[31] K. B. Quan, H. X. Zhen, W. Hongxing, and L. Liyi, "Thrust and thermal characteristics of electromagnetic launcher based on permanent magnet linear synchronous motor," *IEEE Transactions on Magnetics*, vol. 45, no. 1, pp. 358–362, January 2009.

[32] J. R. Quesada and J. F. Charpentier, "Finite difference study of unconventional structures of permanent-magnet linear machines for electromagnetic aircraft launch system," *IEEE Transactions on Magnetics*, vol. 41, no. 1, pp. 478–483, January 2005.

[33] L. Liyi, J. Hong, Z. Lu, L. Ying, Y. Song, L. Rizhong, and L. Xiaopeng, "Fields and inductances of a sectioned permanent-magnet synchronous linear machines used in the EMALS," *IEEE Transactions on Plasma Science*, vol. 39, no. 1, pp. 87–93, January 2011.

[34] L. Liyi, H. Junjie, W. Hongxing, L. Peng, Z. Zhe, and L. Xiaopeng, "Section crossing drive with fuzzy-PI controller for the long stroke electromagnetic launcher," *IEEE Transactions on Magnetics*, vol. 45, no. 1, pp. 363–367, January 2009.

[35] S. Hao, Z. Tang, and M. Hao, "A decentralized linear motor for electromagnetic aircraft launch system," in *International Conference on Consumer*

Electronics, Communications and Networks (CECNet). IEEE, April 2011, pp. 3813–3818.

[36] M. Mirzaei and S. E. Abdollahi, "Design optimization of reluctance-synchronous linear machines for electromagnetic aircraft launch system," *IEEE Transactions on Magnetics*, vol. 45, no. 1, pp. 389–395, January 2009.

[37] M. Mirzaei, S. E. Abdollahi, and A. Vahedi, "Permanent magnet DC linear motor for aircraft electromagnetic launcher," in *Proceeding of the*. IEEE, 10-13 June 2008.

[38] G. Stumberger, D. Zarko, M. T. Aydemir, and T. A. Lipo, "Design and comparison of linear synchronous motor and linear induction motor for electromagnetic aircraft launch system," in *IEEE International Electric Machines and Drives Conference*, vol. 1. IEEE, 1-4 June 2003, pp. 494–500.

[39] W. V. Hassenzahl, "Superconductivity, an enabling technology for 21^{st} century power systems?" *IEEE Transactions on Applied Superconductivity*, vol. 11, no. 1, pp. 1447–1453, March 2001.

[40] S. S. Kalsi, *Applications of High Temperature Superconductors to Electric Power Equipment*. Wiley-IEEE Press, 2011, ch. HTS Superconductors, pp. 7–34.

[41] K. Sawada, "Outlook of the superconducting MAGLEV," *Proceeding of the IEEE*, vol. 97, no. 11, pp. 1881–1885, November 2009.

[42] M. Ono, S. Koga, and H. Ohtsuki, "Japan's superconducting MAGLEV train," *IEEE Instrumentation & Measurement Magazine*, vol. 5, no. 1, pp. 9–15, March 2002.

[43] S. Kusada, M. Igarashi, K. Nemoto, T. Okutomi, S. Hirano, K. Kuwano, T. Tominaga, M. Terai, T. Kuriyama, K. Tasaki, T. Tosaka, K. Marukawa, S. Hanai, T. Yamashita, Y. Yanase, H. Nakao, and M. Yamaji, "The project

overview of the HTS magnet for superconducting MAGLEV," *IEEE Transactions on Applied Superconductivity*, vol. 17, no. 1, pp. 2111–2116, June 2007.

[44] C. E. Oberly, G. Kozlowski, C. E. Gooden, R. X. Lenard, A. K. Sarkar, I. Martense, and J. C. Ho, "Principles of application of high temperature superconductors to electromagnetic launch technology," *IEEE Transactions on Magnetics*, vol. 27, no. 1, pp. 509–513, January 1991.

[45] G. Stumberger, D. Zarko, M. T. Aydemir, and T. A. Lipo, "Design of a linear bulk superconductor magnet synchronous motor fo electromagnetic aircraft launch systems," *IEEE Transactions on Applied Superconductivity*, vol. 14, no. 1, pp. 54–62, March 2004.

[46] J. M. Pina and J. Martins, "Control of an electromagnetic aircraft launch system based on a superconducting linear synchronous motor," in *8^{th} International Conference on Compatibility and Power Electronics (CPE)*. IEEE, June 2013, pp. 255–259.

[47] H. D. Fair, "Advances in electromagntic launch science and technology and its applications," *IEEE Transactions on Magnetics*, vol. 45, no. 1, pp. 225–230, 2009.

[48] S. Siceloff, "Emerging technologies may fuel revolutionary launcher," October 2010. [Online]. Available: http://www.nasa.gov/topics/technology/features/horizontallaunch.html

[49] J. Zhang, J. E. Thompson, Z. Lu, and N. Islam, "Analysis of the adavntages and disadvantages of multi-turn railgun," in *Proceedings of the 16^{th} international Symposium on Electromagnetic Launch Technology (EML)*. IEEE, October 2012.

[50] M. Bayati, A. Keshtkar, and S. V. A. Makki, "Analyzing the current distribuition, magnetic field and inductance gradient at the circular rail in comparison to the rectangular rail," in *Proceedings of the 16^{th} Symposium on Electromagnetic Launch Technology (EML)*. IEEE, May 2012.

[51] R. Murugan and K. Udayakumar, "Effect of rail dimensions on rail gun design parameters," in *Proceedings of annual IEEE INDICON*. IEEE, December 2005, pp. 623–626.

[52] R. A. Marshall, C. Persad, K. A. Jamison, and M. J. Matyac, "Observation of solid armature behavior," *IEEE Transactions on Magnetics*, vol. 31, no. 1, pp. 214–218, January 1995.

[53] B. Kim and K. Hsieh, "Effect of rail/armature geometry on current density distribution and inductance gradient," *IEEE Transactions on Magnetics*, vol. 35, no. 1, pp. 413–416, January 1999.

[54] M. S. Bayati, "Projectile geometry," in *Proceedings of the 16th International Symposium on Electromagnetic Launch Technology*. IEEE, May 2012.

[55] A. K. A. Keshtkar, S. Bayati, "Effect of rail's material on railgun inductance gradient and losses," in *Proceedings of the 14th Symposium on Electromagnetic Launch Technology*. IEEE, June 2008.

[56] I. McNab, "Pulsed power for electric guns," *IEEE Transactions on Magnetics*, vol. 33, no. 1, pp. 453–460, August 2002.

[57] T. Watt and M. Crawford, "Experimental results from a two-turn 40 mm railgun," *IEEE Transactions on Acoustics Speech and Signal Processing on Magnetics*, vol. 45, no. 1, pp. 490–494, January 2009.

[58] D. G. Bansal and J. L. Streator, "Behavior of copper-aluminium tribological pair under high current densities," *IEEE Transactions on Magnetics*, vol. 45, no. 1, pp. 244–249, January 2009.

[59] C. Persad, A. Yeoh, G. Prabhu, G. White, and Z. Eliezer, "On the nature of the armature-rail interface: Liquid metal effects," *IEEE Transactions on Magnetics*, vol. 33, no. 1, pp. 140–145, January 1997.

[60] I. Dutta, "Electric-current-induced liquid Al deposition, reaction and flow on Cu rails at rail-armature contacts in railguns," *IEEE Transactions on Magnetics*, vol. 45, no. 1, pp. 272–277, 2009.

[61] J. D. Cockcroft, "Skin effect in rectangular conductors at high frequencies," *Proceedings of Royal Society London*, vol. 122, pp. 533–542, February 1929.

[62] G. C. Long, "Railgun current density distributions," *IEEE Transactions on Magnetics*, vol. 22, no. 6, pp. 1597–1602, November 1986.

[63] F. J. Young and W. F. Hughes, "Rail and armature current distribution in electromagnetic launchers," *IEEE Transactions on Magnetics*, vol. 18, no. 1, pp. 33–41, January 1982.

[64] T. Chen, X. Long, I. Dutta, and C. Persad, "Effect of current crowding on microstructural evolution at rail-armature contacts in railguns," *IEEE Transactions on Magnetics*, vol. 43, no. 7, pp. 3278–3286, July 2007.

[65] G. C. Long, "Limits to the velocity of solid armatures in railguns," *IEEE Transactions on Magnetics*, vol. 25, no. 1, pp. 347–352, January 1989.

[66] J. P. Barber, A. Challita, B. Maas, and L. Thurmond, "Contact transition in metal armatures," *IEEE Transactions on Magnetics*, vol. 27, no. 1, pp. 228–232, January 1991.

[67] L. Brown, D. Xu, K. R. Chandar, and S. Satapathy, "Coefficient of friction measurement in the presence of high current density," *IEEE Transactions on Magnetics*, vol. 43, no. 1, pp. 334–337, January 2007.

[68] R. Watkins, K. R. Chandar, and S. Satapathy, "The mechanical behavior of conductors exposed to short-duration thermal loading," *IEEE Transactions on Magnetics*, vol. 41, no. 1, pp. 256–261, January 2005.

[69] S. Satapathy and C. Persad, "Thermal stress in EML rail-conductor overlays," *IEEE Transactions on Magnetics*, vol. 37, no. 1, pp. 269–274, January 2001.

[70] E. B. Rosa, "The self and mutual inductances of linear conductors," *Bulletin of the Bureau of Standards*, vol. 4, no. 2, pp. 301–344, January 1908. [Online]. Available: http://g3ynh.info/zdocs/refs/NBS/Rosa1908.pdf

[71] F. W. Grover, *Inductance Calculations: Working Formulas and Tables*. Dover Edition, 2004.

[72] FAR, "Part 25: Airworthiness standards: Transport category airplanes," 1970.

[73] PACE, "Pacelab aircraft preliminary design 3.5.1," March 2015.

[74] CFM, "CFM56-5A turbofan engine," April 2016. [Online]. Available: http://www.cfmaeroengines.com/engines/cfm56-5a

[75] ISO, "Standard atmosphere," May 1975.

[76] D. P. Raymer, *Aircraft Design: A Conceptual Approach*, J. S. Premienecki, Ed. AIAA: Education Series, 1992.

[77] IHS, "Estimation of drag arising from asymmetry in thrust or airframe configuration." Engineering Science Data Unit (ESDU), September 1989.

[78] E. Torenbeek, *Synthesis of subsonic airplane design*, D. U. Press, Ed., 1976.

[79] L. R. Jenkinson, P. Simpkin, and D. Rhodes, *Civil Jet Aircraft Design*. Arnold, 1999.

[80] FAR, "FAR 121: Operating requiremts: Domestic, flag, and supplemental operations," 1970.

[81] J. A. D. Atkin, E. K. Burke, J. S. Greenwood, and D. Reeson, "An examination of take-off scheduling constraints at London Heathrow airport," *Public Transport*, vol. 1, no. 3, pp. 168–187, 2009.

[82] EASA, "ICAO engine exhaust emissions data bank," February 2016.

[83] EPA, "Average annual emissions and fuel consumption for gasoline-fueled passenger cars and light trucks," October 2008.

[84] E. R. Laithwaite, *Induction machines for special purposes*. Chemical publishing Co. Inc. N.Y., 1966.

[85] J. C. West and D. E. Hesmondhalgh, "The analysis of thick-cylinder induction machines," *Proceedings of the IEE-Part C: Monographs*, vol. 109, no. 15, pp. 172–181, 1962.

[86] E. B. Moullin, *The Principles of Electromagnetism*. Clarendon Press, 1955.

[87] F. W. Carter, "The magnetic field threory of dynamo-electric machine," *IEE*, vol. Vol.64, pp. pp.1115–1138, 1926.

[88] E. Matagne, "Slot effect on the airgap reluctance carter-like calculation suitable for electric machines with large air-gap or surface mounted permanent magnet," *Electromotion*, vol. 15(4), pp. 171–176, 2008.

[89] J. Lu and W. Ma, "Research on end effect of linear induction machine for high-speed industrial transportation," *IEEE Transaction on Plasma Science*, vol. 39, no. 1, pp. 116–120, January 2011.

[90] D. Tipping, "The analysis of some special purpose electrical machines," Ph.D. dissertation, Victoria University of Manchester, 1964.

[91] S. Nonaka and M. Fuji, "The series connection of short stator LIMs for intercity transport," in *Record of International Conference on MAGLEV and Linear Devices*, 1987, pp. 23–29.

[92] C. P. Steinmetz, "On the law of hysteresis," *Transaction of the American Institute of Electrical Engineers*, vol. 9, no. 1, pp. 1–64, January 1892.

[93] R. H. Park, "Two-reaction theory of synchronous machines generalized method of analysis," *Transaction of the American Institute of Electrical Engineers*, vol. 48, no. 3, pp. 716–727, 1929.

[94] FAR, "Part 25.337: Limit maneuvering load factors," 1970.

[95] E. R. Stauffacher, "Short-time current carrying capacity of copper wire," *General Electric Review*, vol. 31, no. 6, June 1928.

[96] D. Brooks, "Fusing currents in traces," July 2015. [Online]. Available: http://www.ultracad.com/articles/fusingr.pdf

[97] "Heathrow our company: Facts and figures," January 2017. [Online]. Available: http://www.heathrow.com/company/company-news-and-information/company-information/facts-and-figures

[98] S. Spigarelli, "Creep of aluminium and aluminium alloys," European Aluminium Association, Tech. Rep., 1999.

[99] *ASHRAE Handbook - Fundamentals (I-P Edition)*, American Society of Heating, Refrigerating and Air-Conditioning Engineers, 2009.

[100] P. Salminen, "Fractional slot permanent magnet synchronous motors for low speed applications," Ph.D. dissertation, Lappeenranta University of Technology, 2004.

[101] K. Halbach, "Design of permanent multipole magnets with oriented rare earth cobalt material," *Nuclear Instruments and Methods*, vol. 169, pp. 1–10, 1980.

[102] N. Bianchi, M. D. Pre, L. Alberti, and E. Fornasiero, *Theory and Design of Fractional-Slot PM Machines*. IEEE-IAS, 2007.

[103] F. Magnussen and C. Sadarangani, "Winding factor and Joule losses of permanent magnet machines with concentrated windings," in *Electrical Machines and Drive Conference*, vol. 1, 2003, pp. 333–339.

[104] J. Pyrhonen, T. Jokinen, and V. Hrabovcova, *Design of Rotating Electrical Machines*. John Wiley & Sons Ltd, 2008.

[105] M. M. Liwschitz, "Distribution factors and pitch factors of the harmonics of a fractional-slot winding," *Transactions of the American Institute of Electrical Engineers*, vol. 62, no. 10, pp. 664–666, Oct. 1943.

[106] T. J. E. Miller, *Brushless Permanent-Magnet and Reluctance Motor Drives*. Oxford University Press, 1989.

[107] F. Libert and J. Soulard, "Investigation on pole-slot combinations for permanent-magnet machines with concentrated windings," in *International Conference on Electrical Machines (ICEM 04)*, 2004, pp. 530–535.

[108] J. Cros and P. Viarouge, "Synthesis of high performance PM motors with concentrated windings," *IEEE Transactions on Energy Conversion*, vol. 17, no. 2, pp. 248–253, 2002.

[109] H. VuXuan, D. Lahaye, H. Polinder, and J. A. Ferreira, "Improved model for design of permanent magnet machines with concentrated windings," in *2011 IEEE International Electric Machine & Drives Conference (IEMDC)*, vol. 1. Niagara Falls, ON: IEEE, May 2011, pp. 948–954.

[110] B. Backlund, M. Rahimo, S. Klaka, and J. Siefken, "Topologies, voltage ratings and state of the art high power semiconductor devices for medium voltage wind energy conversion," in *IEEE Power Electronics and Machines in Wind Applications (PEMWA)*. Lincoln, NE: IEEE, 2009, pp. 1–6.

[111] A. Agarwal, Q. Zhang, A. Burk, and R. Callanan, "Prospects of bipolar power devices in silicon carbide," in *34th Annual Conference of IEEE Industrial Electronics, 2008. IECON 2008.* IEEE, 2008, pp. 2879 – 2884.

[112] Z. Deng, I. Boldea, and S. A. Nasar, "Fields in permanent magnet linear synchronous machines," *IEEE Transactions on Magnetics*, vol. 2, pp. 107–112, 1986.

[113] Z. Q. Zhu and D. Howe, "Instantaneous magnetic field distribution in brushless permanent magnet dc motors, part III: Effect of stator slotting," *IEEE Transactions on Magnetics*, vol. 29, no. 1, pp. 143–151, January 1993.

[114] K. Yamazaki and Y. Fukushima, "Effect of eddy-current loss reduction by magnet segmentation in synchronous motors with concentrated windings," *IEEE Transactions on Industry Applications*, vol. 47, no. 2, pp. 779–788, April 2011.

[115] X. Wu, R. Wrobel, P. H. Mellor, and C. Zhang, "A computationally efficient PM power loss mapping for brushless AC PM machines with surface-mounted PM rotor construction," *IEEE Transactions on Industrial Electronics*, vol. 62, no. 12, pp. 7391–7401, December 2015.

[116] *Unmanned Aircraft System Operations in UK Airspace - Guidance CAP 722*, Safety and Airspace Regulation Group Std., Rev. Sixth Edition, March 2015.

[117] Bormatec, "Uav explorer," 2016. [Online]. Available: http://bormatec.com/shop/product_info.php?products_id=4

[118] E. N. Jacobs, K. E. Ward, and R. M. Pinkerton, "The characteristics of 78 related airfoil sections from tests in the variable-density wind tunnel," National Advisory Committee for Aeronautics, Tech. Rep. 460, 1935.

[119] D. M. Ma and J. K. Shiau, "The design of eddy-current magnet brakes," *Transactions of the Canadian Society for Mechanical Engineering*, vol. 35, no. 1, pp. 19–37, 2011.

[120] L. B. S. Silva, D. Rodrigues, G. D. Serrano, V. C. V. Metzner, M. T. Malachevsky, and A. Serquis, "MgB_2 superconductors with addition of other diborides and SiC," *IEEE Transactions on Applied Superconductivity*, vol. 21, no. 3, pp. 2639–2642, June 2011.

[121] X. Song, N. Mijatovic, B. B. Jensen, and J. Holboll, "Design study of fully superconducting wind turbine generators," *IEEE Transactions on Applied Superconductivity*, vol. 25, no. 3, 2015.

[122] C. Wen, M. Hu, H. Yu, T. Hong, H. Chen, R. Qu, and H. Fang, "Design of a MgB_2 superconsucting synchronous generator," *IEEE Transactions on Applied Superconductivity*, vol. 25, no. 3, 2015.

[123] O. N. Senkov, R. B. Bhat, and S. V. Senkova, *Metallic Materials with High Structural Efficiency*, O. N. Senkov, D. B. Miracle, and S. A. Firstov, Eds. NATO Science Series II: Mathematics, Physics and Chemistry, 2004, vol. 146.

[124] W. Goldacker and S. I. Schlachter, "HTS and MgB_2 cables for application in energy technology and magnets," Karlsruhe Institute of Technology, Tech. Rep., 2011.

[125] C. S. Yung and B. H. Moeckly, "Magnesium diboride flexible flat cables for cryogenic electronics," *IEEE Transactions on Applied Superconductivity*, vol. 21, no. 3, pp. 107–110, June 2011.

[126] M. Arata, M. Kawai, T. Yamashita, M. Fujita, and T. Hamajima, "Eddy current loss reduction of superconducting magnets for MAGLEV with a multilayer superconducting sheet," *IEEE Transactions on Applied Superconductivity*, vol. 7, no. 2, pp. 912–915, June 1997.

[127] M. Lyly, V. Lahtinen, A. Stenvall, L. Rostila, and R. Mikkonen, "A time-harmonic approach to numerically model losses in the metal matrix in twisted superconductors in external magnetic field," *IEEE Transactions on Applied Superconductivity*, vol. 24, no. 2, April 2014.

[128] R. S. Weaver, "The inductance of a helix of any pitch," Available online, March 2011. [Online]. Available: http://electronbunker.ca/DLpublic/HelicalInductance.pdf

[129] J. C. Maxwell, "On the geometrical mean distance of two figures on a plane," *Earth and Environmental Science Transactions of The Royal Society of Edinburgh*, vol. 26, no. 4, pp. 729–733, January 1872.

[130] W. J. Carr, *AC Loss and Macroscopic Theory of Superconductors*, second edition ed. Taylor & Francis, 2001.

[131] K. Cassel, M. Boghosian, E. Almasri, S. Ishimoto, and K. Yoshimura, "Natural-convection liquid-hydrogen absorber R&D," Illinois Institute of Technology, Tech. Rep., September 2001.

[132] L. A. Schwalbe and E. R. Grilly, "Thermal expansion of liquid normal hydrogen between 18.8 and 22.2 K," *Journal of Research of the National Bureau of Standards*, vol. 89, pp. 317–323, August 1984.

[133] Y. A. Cengel and A. J. Ghajar, *Heat and Mass Transfer: Fundamentals & Applications*, fourth edition ed. McGraw-Hill, 2011.

[134] W. S. Winters, G. H. Evans, S. F. Rice, and R. Greif, "An experimental and theoretical study of heat and mass transfer during the venting of gas from pressure vessels," *International Journal of Heat and Mass Transfer*, vol. 55, no. 1, pp. 8–18, January 2012.

[135] J. Palmer, "Distributed propulsion cryocooler models for aviation," 2014, restricted access.

[136] NIST, "Nist chemistry webbook," National Institute of Standard Technology, 2016. [Online]. Available: http://webbook.nist.gov/chemistry/

[137] P. F. Ribeiro, B. K. Johnson, M. L. Crow, A. Arsoy, and Y. Liu, "Energy storage system for advanced power applications," *Proceedings of the IEEE*, vol. 89, no. 12, pp. 1744–1756, 2001.